Author:
Zhong, Siying

Title:
Combining computational modelling, NMR spectroscopy and assembly-line synthesis for studying molecular conformations

University of Bristol – School of Chemistry

Combining Computational Modelling, NMR Spectroscopy, and Assembly–Line Synthesis for Studying Molecular Conformations

Siying Zhong

Supervisors: Professor Craig P. Butts and Professor Varinder K. Aggarwal, FRS

A dissertation submitted to the University of Bristol in accordance with the requirements for award of the degree of Doctor of Philosophy in the Faculty of Science.

School of Chemistry, January 2019

Word Count: 101,961

I. Abstract

This thesis reports the application of computational modelling, NMR spectroscopy and stereospecific iterative homologation of boronic esters to the three-dimensional structural elucidation of flexible organic small molecules, and the design and synthesis of flexible molecules with tailored conformations.

Firstly, the configuration of a recently isolated polyketide baulamycin A, which exhibits potent antibacterial activity, was reassigned using a combination of Density Functional theory (DFT) calculations, NMR spectroscopy and synthesis. In this work, DFT calculations were employed to predict the complex dynamic conformations of eight possible diastereomers of baulamycins and to compute the ensemble-averaged chemical shifts, ^{1}H-^{1}H scalar coupling constants and ^{1}H-^{1}H distances. Comparison between the computed NMR parameters of each diastereomer with the experimentally determined values eliminated 112 out of the possible 128 diastereomeric candidates. Finally, synthesis allowed the relative and absolute configuration of baulamycin A to be positively identified.

Secondly, inspired by the conformational control exerted by quaternary centres, a range of conformationally defined unnatural amino esters were designed with the aid of computational modelling. Two of the amino esters were synthesised and their solution state conformations were elucidated by a combination of DFT calculations and quantitative analysis of ^{1}H-^{1}H and ^{1}H-^{13}C scalar coupling constants. Their side chains are shown to take on defined orientations (*syn*-periplanar or turn a 120° corner) with controllable distances and could find application in areas such as drug design.

Finally, factors controlling the helical screw-sense of hydrocarbons with *all*-syn contiguous methyl substituents was investigated. The solution-state conformational behaviour of hydrocarbons with different numbers of methyl substituents (from six to 11) was studied using a combination of DFT calculations and quantitative analysis of ^{1}H-^{1}H scalar coupling constants and ^{1}H-^{1}H distances. It was discovered that only hydrocarbons with even numbers of methyl substituents adopt regular helical conformation, whereas hydrocarbons with odd number of methyl substituents do not have a strong preference for a particular conformation. The preference of screw sense (if any) in each case was rationalised by the minimisation of *gauche* interactions.

II. Contents

III. Author’s Declaration

I declare that the work in this dissertation was carried out in accordance with the requirements of the University's Regulations and Code of Practice for Research Degree Programmes and that it has not been submitted for any other academic award. Except where indicated by specific reference in the text, the work is the candidate's own work. Work done in collaboration with, or with the assistance of, others, is indicated as such. Any views expressed in the dissertation are those of the author.

SIGNED: ..... DATE:.....

IV. Acknowledgements

First, I would like to thank my supervisors Professors Craig Butts and Varinder Aggarwal for the opportunity to work across two research groups with very different research interests. When I was doing a lab rotation project as a CDT student in Varinder's group, I told him I would like to learn about computational modelling and NMR spectroscopy on top of organic synthesis. He clearly remembered our two minutes conversation and took advantage of this desire during the CDT project allocation week. Eventually, Craig happily obliged my request of sitting in front of a computer. Thank you both so much for the bravery to create such a multidisciplinary PhD studentship, for taking me on as your PhD student, and for all your guidance and nurturing during the ups and downs.

Next, I would like to thank Dr. Ikenna Ndukwe, Dr. Jessica Bame and Dr. Claire Dickson for introducing me to the beauty of NMR spectroscopy. Thank you, Dr Natalie Fay, for your guidance in computational chemistry. Thank you, Dr. Eddie Myers and Dr. Teerawut Bootwicha, for your patience and guidance which was critical for my development as a chemist. Thank you Johan for being my partner in crime during my PhD studies – you are a wonderful chemist, an awesome collaborator, and a dear friend to me. Thank you Craig, Adam, Alex, Steven, Joe, Johan and Rory for proof reading my thesis.

Finally, I would like to thank my parents who have been my solid support since the very first day I arrived in this island.

V. Acronyms and Abbreviations

ABNO	9-Azabicyclo[3.3.1]nonane *N*-oxyl
B3LYP	Becke exchange with Lee-Yang-Parr correlation
B3LYP-D2	B3LYP with Grimme's D2 dispersion correction
BRSM	based on recovered starting material
Cb	carbamate
CMAD	corrected mean average deviation
DFT	Density Functional Theory
DMP	Dess-Martin periodinane (p 117)
DQF-COSY	Double Quantum Filter COSY
ee	enantiomeric excess
e.g.	exempli gratia
et al.	*et alia*
er	enantiomeric ratio
es	enantiospecificity
ESI	electronspray ionisation
EXSIDE	Excitation-Sculptured Indirect-Detection Experiment
GC-MS	gas chromatography-mass spectrometry
GIAO	gauge-including atomic orbital
GP	general procedure
δ_H	^{1}H chemical shifts
δ_C	^{13}C chemical shifts
h	hour
HETLOC	heteronuclear long-range couplings

HIF-1α	hypoxia-inducible factor-1α
HPLC	high performance liquid chromatography
HRMS	high resolution mass spectrometry
HSQC	heteroneuclear single quantum coherence
HSQMBC	heteronuclear single-quantum multiple bond correlation
*i*Bu	*iso*-butyl
i.e.	in other words
IPAP	in-phase antiphase
J	coupling constants
$^{n}J_{HH}$	^{1}H-^{1}H scalar coupling constants
$^{n}J_{HC}$	^{1}H-^{13}C scalar coupling constants
LCMS	liquid chromatography-mass spectrometry
NMR	nuclear magnetic resonance
NOE	nuclear Overhauser effect
MAD	mean absolute deviation
MCMM	Monte Carlo Multi Minimum
MM	molecular mechanics
MP	melting point
MRSA	methicillin-resistant *Staphylococcus aureus*
MST	magnetic shielding tensor
PANIC	peak amplitude normalization for improved cross-relaxation
PSYCHE	pure shift yielded by chirp excitation
QM	quantum mechanics
RCSA	residual chemical shift anisotropy

RDC	residual dipolar coupling
ROE	rotating frame Overhauser effect
RSM	recovered starting material
SFC	supercritical fluid chromatography
StDev	standard deviation
*t*Bu	*tert*-butyl
TEMPO	2,2,6,6-tetramethylpiperidine 1-oxyl
TFAA	Trifluoroacetic anhydride
TIB	2,4,6-triisopropyl benzoate

Chapter 1 Introduction

1.1 Elements of conformational control in flexible molecules.

The three-dimensional arrangements, or conformations, of organic molecules dictate their molecular properties such as chemical reactivities and molecular functions. The organic chemistry community took little notice of conformational behaviour of molecules and did not appreciate the importance of conformational analysis until the 1950s, when Derek Barton rationalised the chemical reactivities of steroids based on their preferred conformations.[1-2] Since then, conformational analysis has become a fundamental area in chemistry and has been applied to the study of reaction mechanisms, in the prediction of reaction outcome in total syntheses, and in the structural elucidation of natural products.

Conformational analysis studies the energetic difference between conformational isomers arising from the free rotation around single bonds.[3] For example, rotation of the central C–C bond in ethane gives rise to conformations with different energies (Figure 1.1a and b), with the staggered conformer **1.1** being the minimum and the eclipsed conformer **1.2** being the maximum on a rotational energy diagram. The staggered conformer **1.1** is the lowest energy conformation due to the stabilising interactions between the C–H bonding orbital (σ_{C-H}) and the adjacent C–H antibonding orbital (σ^*_{C-H}) (Figure 1.1c). The eclipsed conformer **1.2** is the highest energy conformation because of the destabilising electronic repulsion of vicinal C–H bonds and inefficient orbital overlap between the σ_{C-H} orbital and the adjacent σ^*_{C-H} orbital (Figure 1.1c). Although steric repulsion between the eclipsing hydrogens could also contribute to the high conformer energy associated with eclipsed conformer **1.2**, steric factors are minor compared to hyperconjugation because hydrogen atoms are too small to impose severe steric clashes (Van der Waals radius of a hydrogen atom: 1.20 Å). This lack of steric repulsion is illustrated by the molecular model of the eclipsed and staggered forms of ethane (Figure 1.1d).[4]

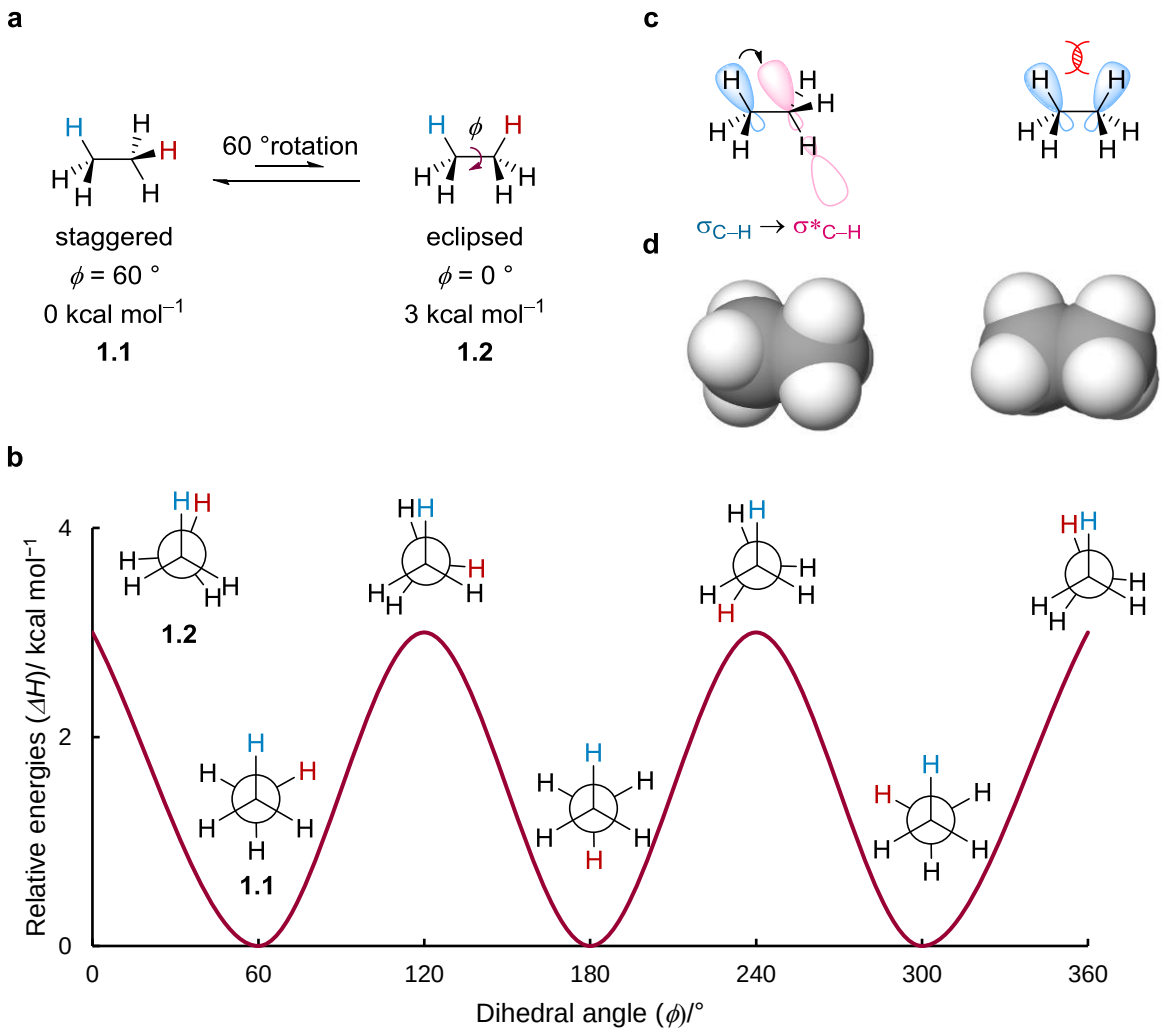

Figure 1.1: **a**, The eclipsed (**1.2**) and staggered (**1.1**) conformers of ethane with their relative conformer energies. **b**, Rotational energy diagram of ethane with the corresponding Newman projection for the maxima and minima. **c**, Orbital interactions in the eclipsed and staggered conformers of ethane. **d**, Space-filling model of the staggered (left) and eclipsed (right) conformers of ethane, showing lack of steric interaction.

When the hydrogens in ethane are replaced by other substituents, such as methyl groups or heteroatoms, a combination of steric and electronic factors controls the conformation of these flexible small molecules. In this section, several steric and electronic factors which influence molecular conformations will be discussed.

***Gauche*-butane interaction.**

In butane, the staggered conformations (**1.3** and **1.4**, Figure 1.2) which are free from eclipsing interactions are the minima in a rotational energy diagram as a result of minimising steric clashes between methyl groups and hydrogens. Conformer **1.4** with the two methyl groups furthest away from each other is the lowest in energy, whereas conformer **1.3** which

has the two methyl groups in *gauche* orientation was calculated to be 0.8 kcal mol^{-1} higher using *ab initio* methods (Møller–Plesset theory, MP4SDQ/6-31G(d)).[5] Steric hindrance, rather than hyperconjugation, is the major contributing factor which affects the relative energies of these two conformers. The steric hindrance between two methyl groups shown in **1.3** is often referred to as a *gauche*-butane interaction.

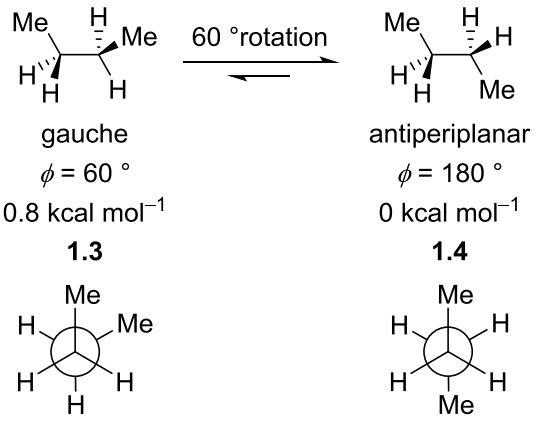

Figure 1.2: Staggered conformers of butane with the two methyl groups gauche (**1.3**) and antiperiplanar (**1.4**) to each other. The relative energies quoted were calculated using MP4SDQ 6-31G(d) level of theory.[5]

Syn-pentane interaction.

Steric hindrance also dictates the relative energies of pentane conformers (Figure 1.3). Staggered conformers arising from the rotation of the two central bonds (highlighted in blue, Figure 1.3) are considered and these four conformers of pentane are represented on a diamond lattice. Their relative energies were calculated using MP4SDQ/6-31G(d) level of theory.[5] Conformer **1.5**, with both the central bonds adopting antiperiplanar conformations (*ap ap*), is the lowest in energy, followed by the conformer which has one of the two bonds adopting a *gauche* conformation (g^+ *ap*, **1.6**). Conformer **1.6** experiences a gauche interaction between the two methyl groups which has an enthalpic penalty of 0.8 kcal mol^{-1} as discussed previously (*gauche*-butane interaction). The next higher energy conformer **1.7** is 1.4 kcal mol^{-1} above the global minimum **1.5**. The enthalpic cost of adopting conformer **1.7**, which has two consecutives *gauche*$^+$ dihedrals, is 0.2 kcal mol^{-1} smaller than twice the enthalpic penalty of the *gauche*-butane interaction (2 × 0.8 = 1.6 kcal mol^{-1}). The extra stabilisation associated with the g^+ g^+ conformer (**1.7**) was rationalised by the attractive van der Waals interactions between the terminal methyl groups. However, this attractive interaction becomes repulsive when the two methyl groups are synperiplanar to each other as in the case of conformer **1.8**, where the

backbone adopts a *gauche*$^{-}$ followed by a *gauche*$^{+}$ conformation ($g^{-}\,g^{+}$). The close proximity of the terminal methyl groups (2.5 Å) results in high strain in this conformer (3.4 kcal mol^{-1}) compared to the global minimum. Therefore **1.8** only has a 0.5% of conformer population at room temperature.[5]

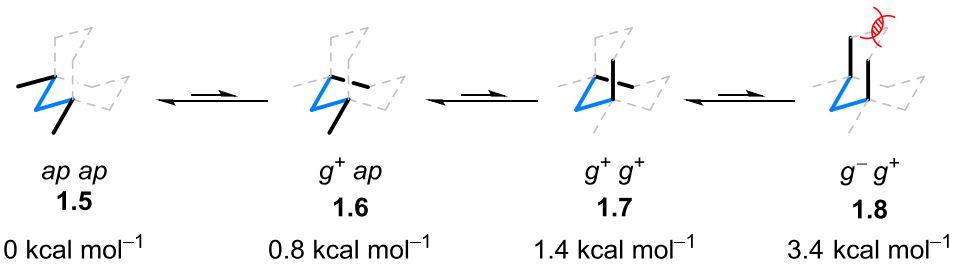

Figure 1.3: Conformational analysis of pentane. Relative energies of conformers were calculated using MP4SDQ 6-31G(d) level of theory.[5]

The destabilising interaction observed in **1.8** is known as a *syn*-pentane interaction and has been used in the design of molecules with tailored conformations. Still *et al.* designed conformationally defined tetracyclic podand ionophores (Figure 1.4e), based on the principle of destabilising undesired conformers using *syn*-pentane interactions.[6-7] According to MM2 calculations, ring annellation of a polyether chain (Figure 1.4a), and the introduction of methyl substituents at specific positions with defined stereochemistry, reduced the number of low energy conformers to within 3 kcal mol^{-1} above the global minimum from ~ 1000 to 25 (Figure 1.4c). Ring annellation provided covalent restriction, while the two methyl groups destabilised other accessible conformers by inducing the destabilising *syn*-pentane interactions between methyl groups and the endo C–O or C–C bonds (highlighted in red, Figure 1.4d). The bias toward a single conformation was further enhanced by destabilising other undesired conformers via the addition of another two methyl groups (Figure 1.4e and f). The tetracyclic ionophore Figure 1.4e) is a chiral version of 18-crown 6 (Figure 1.4b) and binds to 1-phenylethan-1-aminium cation with 40% ee.[6]

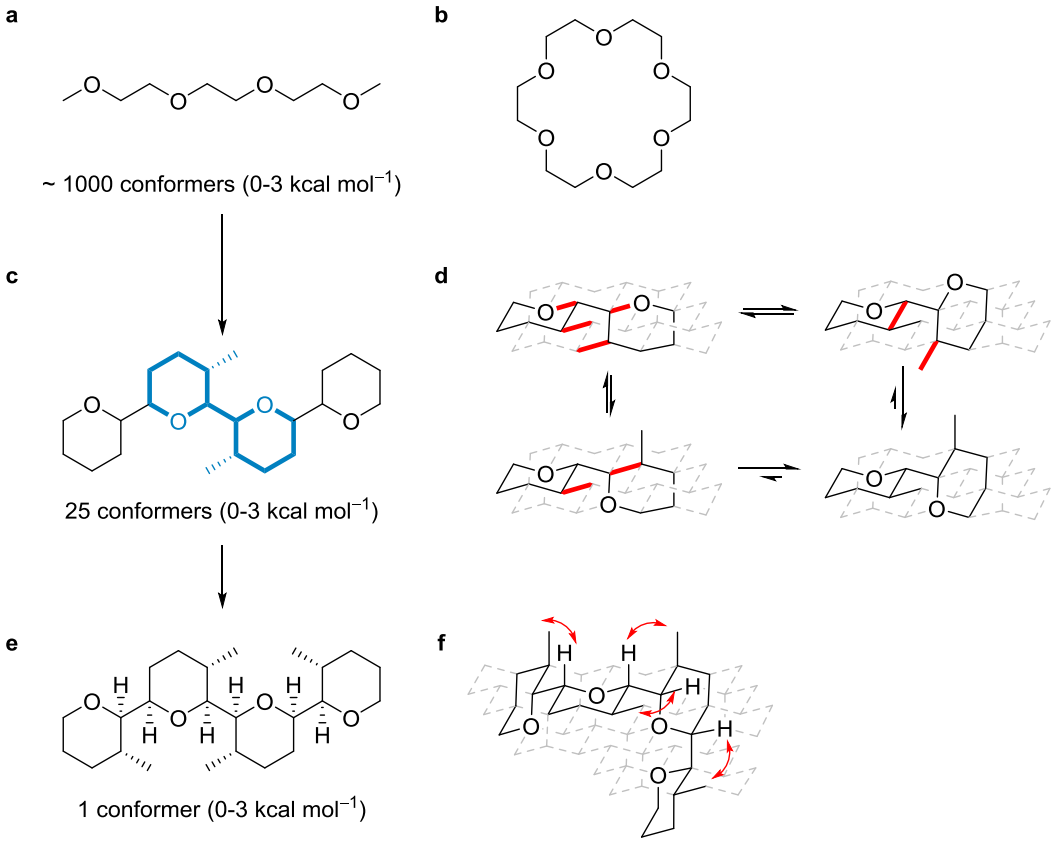

Figure 1.4 The design of Clark Still's podand ionophores.[6-7] **a**, A polyether chain with poorly defined conformations. **b**, Structure of achiral 18-crown 6. **c**, Ring annellation of the polyether chain together with the introduction of two methyl groups. The conformational analysis of the segment in blue is shown on a diamond lattice (**d**). **e**, Structure of the tetracyclic podand ionophores with the dominant conformation represented on a diamond lattice (**f**).

More recently, Aggarwal *et al.* reported the synthesis (section 1.4) and conformational analysis (section 1.3.4) of hydrocarbons with contiguous methyl substituents **1.9** and **1.10** (Figure 1.5a and b, respectively).[8] Due to the avoidance of *syn*-pentane interactions, The *syn-anti* isomer **1.9** was designed to preferentially adopt a linear conformation, whereas the all *syn* isomer **1.10** was designed to fold into a helical conformation. (Figure 1.5c and d, respectively). The solution-state conformations of both compounds were confirmed by using a combination of computational modelling and NMR spectroscopy, which will be discussed in section 1.3.4.

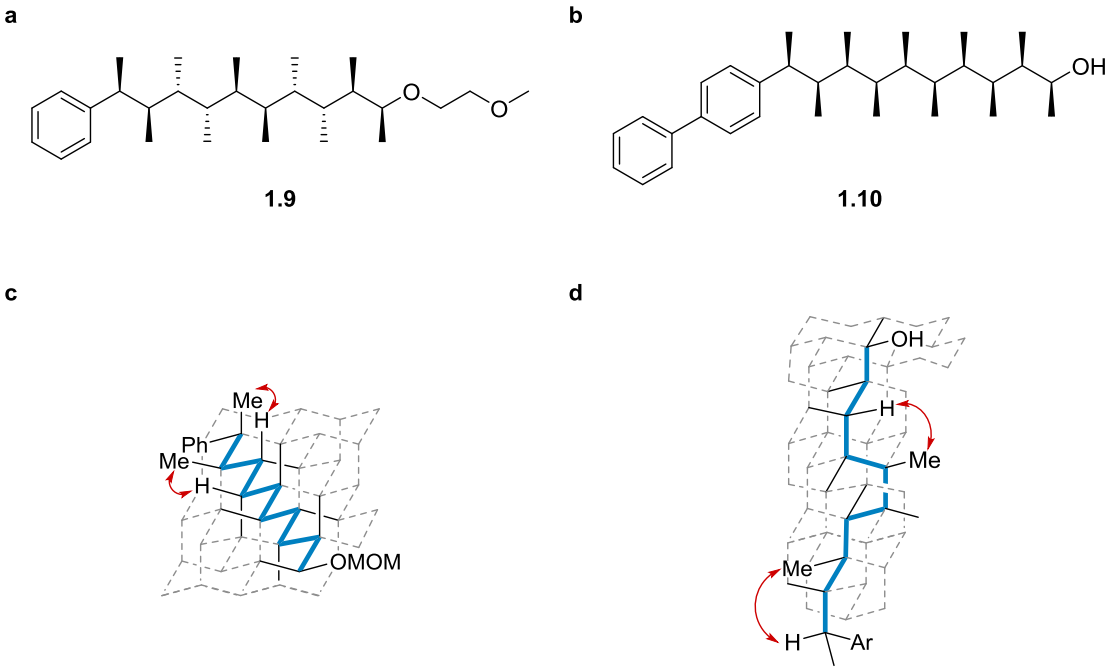

Figure 1.5 a, Chemical structure of the *syn-anti* isomer **1.9**. **b**, Chemical structure of the all *syn* isomer **1.10**. **c**, The dominant linear conformation of **1.9** represented on a diamond lattice. **d**, The dominant helical conformation of **1.10** represented on a diamond lattice**.**

Allylic strain ($A^{1,3}$ and $A^{1,2}$)

Compared to the highest energy conformer of pentane (**1.8**) where the two terminal methyl groups have a C–C distance of ~2.5 Å, the C–C distances of the methyl groups in (*Z*)-pent-2-ene (**1.11**) is even closer in space (~2.2 Å) because C–C double bonds are shorter than C–C single bonds. Therefore, the *syn*-pentane interaction between the methyl groups in **1.11** is even more costly and this strain is referred to as $A^{1,3}$ allylic strain.

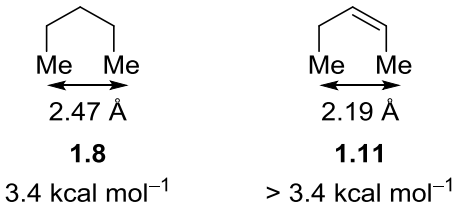

Figure 1.6: Chemical structure of the highest energy conformations of pentane and (*Z*)-pent-2-ene with the C–C distances between the terminal methyl groups labelled.

Figure 1.7a illustrates the effect of allylic 1,3-strain on the conformational behaviour of (*Z*)-4-methylpent-2-ene **1.12**. The relative energies of three conformers (**1.12**-1, **1.12**-2 and **1.12**-3) were calculated using MP2/6-31G(d) level of theory.[9] To avoid the $A^{1,3}$ strain which has an enthalpic penalty of 4.9 kcal mol^{-1} in the eclipsed conformer **1.12**-1, **1.12** would adopt

the eclipsed conformer **1.12**-2 which has the H–C–C=C dihedral angle within 0 ± 30°.[9-10] Unlike saturated hydrocarbons where staggered conformations are preferred, in unsaturated hydrocarbons (i.e. **1.12**) the eclipsed conformation **1.12**-2 is preferred due to the hyperconjugation of the $\sigma_{C\text{-}H}$ orbital to the $\pi^*_{C=C}$ orbital (Figure 1.7b). Therefore, although the $A^{1,3}$ strain could be avoided in the staggered conformer **1.12**-3, it is less energetically favourable due to the lack of stabilising hyperconjugation interactions. In the case of 2,3-dimethylbut-1-ene (**1.13**, Figure 1.7c), the avoidance of allylic 1,2 strain results in the preference for conformation **1.13**-2.[9]

Conformational preference in alkenes is a usually fine balance between the $A^{1,3}$ and $A^{1,2}$ strains, although $A^{1,3}$ strain outweighs $A^{1,2}$ strain due to a higher enthalpic penalty.

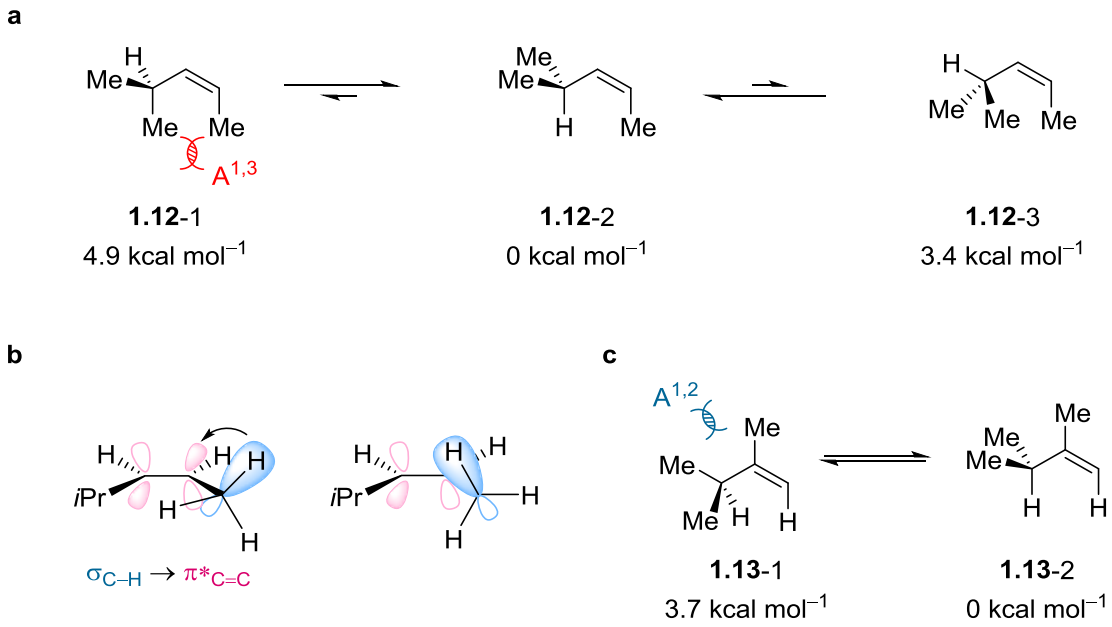

Figure 1.7: **a**, Three conformers of (*Z*)-4-methylpent-2-ene **1.12** with their relative energies. Allylic $A^{1,3}$ strain in conformer **1.12**-1 is highlighted in red. **b**, Orbital interactions of the eclipsed (**1.12**-2) and staggered (**1.12**-3) conformations of **1.12**. c, Two conformers of 2,3-dimethylbut-1-ene **1.13** with the allylic $A^{1,2}$ strain in conformer **1.13**-1 highlighted in blue. Relative energies of conformers were calculated using MP2/6-31G(d) level of theory. [9]

Hoffmann *et al.* demonstrated the design and synthesis of acyclic molecules with defined conformation utilising the conformational control exerted by *syn*–pentane interactions and $A^{1,3}$ strain (Figure 1.8). Analysis of $^nJ_{HH}$ values of both molecules showed that **1.14** preferentially adopts a Z-shaped conformation in which the two hydroxyl groups are on the

opposite face, while **1.15** adopts a U-shaped conformation in which the two hydroxyl groups are on the same face.[11]

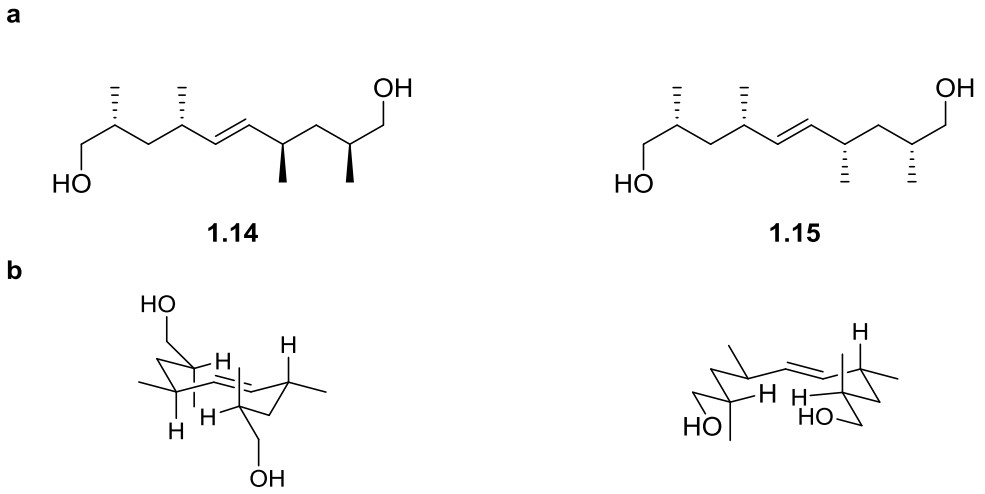

Figure 1.8: Chemical structure of (**a**) **1.14** and **1.15** with (**b**) the observed major conformations for each compound.

The effect of *syn*-pentane interactions and $A^{1,3}$ strain on molecular conformation was also observed in the X-ray structure of zincophorin, an antibiotic ionophore which binds to zinc cations.[12-13]

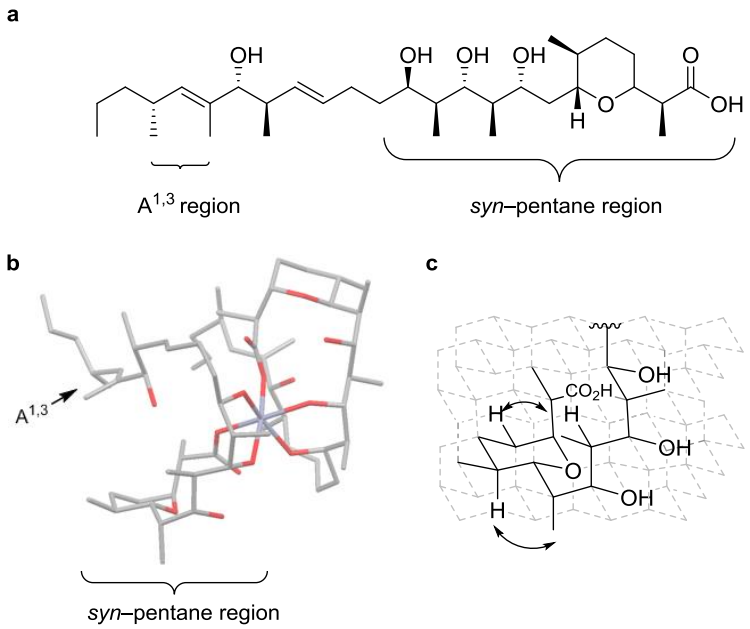

Figure 1.9: **a**, Chemical structure of zincophorin with regions controlled by $A^{1,3}$ strain and *syn*-pentane highlighted. **b**, Crystal structure of zincophorin dimer binding to a zinc cation.[14] **c**, Solid state conformation of the region controlled by *syn*-pentane interactions represented on a diamond lattice.

In the $A^{1,3}$ region, the proton is positioned in the eclipsed conformation to minimise $A^{1,3}$ strain. This can be clearly seen from the crystal structure of the zincophorin dimer with a zinc cation (Figure 1.9b). In addition, the avoidance of *syn*-pentane interactions (Figure 1.9c) preorganises the orientation of the 1,3-polyol segment for efficient binding to zinc cations.

***Gauche* effect**

As discussed, in acyclic saturated hydrocarbons the lowest energy conformers are the ones with the most sterically demanding substituents antiperiplanar to each other (X = Y = sp^3 carbon substituents, **1.16**, Figure 1.10a). However, a *gauche* conformation **1.17** is preferred over the antiperiplanar conformation if X and Y are electronegative substituents (Figure 1.10b). This conformational preference is known as the *gauche* effect.[15] For example, compounds containing F–C–C–F, F–C–C–O, and F–C–C–N fragments (**1.18** – **1.21**, Figure 1.10b) all experience the *gauche* effect. By adopting the gauche conformation **1.17**, the low-lying σ* antibonding orbital of the C–F bond is aligned to the adjacent σ bonding orbital of the C-H bond, thus allowing donation of electron density from the σ_{CH} orbital to the σ^*_{CF} orbital (Figure 1.10b). In the antiperiplanar conformation the σ^*_{CF} orbital is aligned with a less electron releasing σ_{CX} orbital, leading to poor hyperconjugation. [16-17]

When the atom Y is a chlorine atom (**1.22**, Figure 1.10), the antiperiplanar conformation is favoured instead in the gas-phase.[18] This is because the increased dipole repulsion between the C–F and C–Cl bonds outweighs the stabilisation provided by hyperconjugation. Nevertheless, MP2 calculations predicted that going from gas-phase to a polar environment (eg. acetone), the conformational preference of **1.22** will switch from antiperiplanar to the expected gauche conformation, due to the decreased energy penalty of the dipole repulsion in polar solvents.

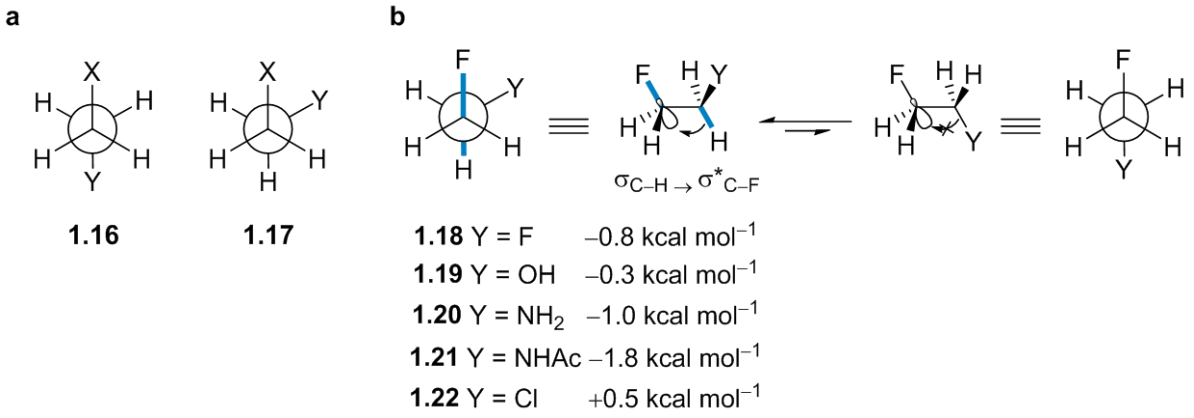

Figure 1.10: **a**, Newman projections of conformers with two nonhydrogen substituents antiperiplanar (**1.16**) and gauche (**1.17**) to each other. **b**, Newman projections of 1,2-disubstituted ethane in *gauche* and antiperiplanar conformations.

The *gauche* effect is general and applied to X–C–C–Y systems where X and Y are heteroatoms such as nitrogen and oxygen atoms. The conformational preference induced by the *gauche* effect is important in the regulation of the concentration of Hypoxia Inducible Factor 1 alpha (HIF-1α), which has been recognised as an important target for cancer therapy.[19]

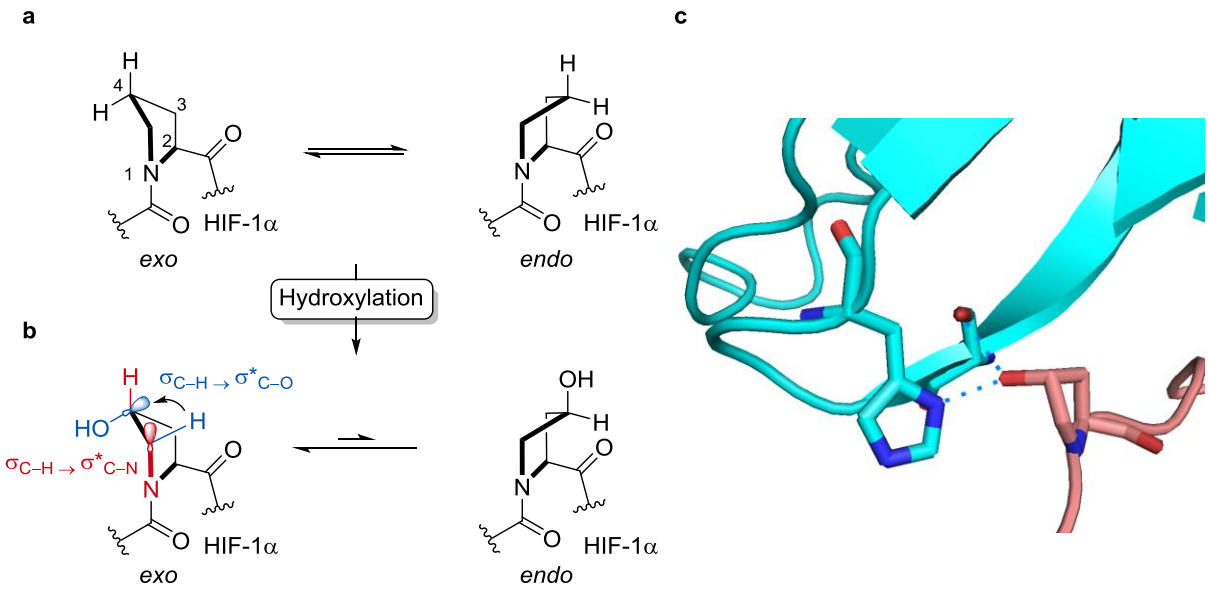

Figure 1.11: **a**, The *exo* and *endo* conformations of a proline residue in HIF-1α. **b**, The *exo* and *endo* conformations of a hydroxyproline residue in HIF-1α. The two key interactions shifting the conformational preference of the hydroxyproline is highlighted in red ($\sigma_{CH} \rightarrow \sigma^*_{CN}$) and blue ($\sigma_{CH} \rightarrow \sigma^*_{CO}$). **c**, Crystal structure of HIF-1α peptide bound to von-Hippel-Lindau protein, elongins C and B

(PDB: 1LQB)[20] showing the binding between the hydroxyproline residue of HIF-1α (in pink) and the histidine and serine residues of von-Hippel-Lindau protein (in blue).

Upon hydroxylation of the proline residues of HIF-1α under normal cellular oxygen levels, the *exo* conformation is favoured due to the stabilisation provided by hyperconjugation between the σ_{CH} and the σ^*_{CO} orbitals (highlighted in blue, Figure 1.11b), and between the σ_{CH} and the σ^*_{CN} orbitals (highlighted in red, Figure 1.11b). The shift in the conformational preference triggers the binding of HIF-1α to the von-Hippel-Lindau protein (blue, Figure 1.11c), which allows polyubiquitination and subsequent degradation of HIF-1α.[21]

Dipole–dipole interactions

Although in 1,2-difluoroalkanes two fluorine atoms are in proximity due to the *gauche* effect, in 1,3-difluoroalkanes the two fluorine atoms repel each other due to the destabilising dipole–dipole interactions between the two highly polarised C–F bonds. This can be illustrated using 1,3-difluoropropane as an example (Figure 1.12). The relative energies of the four staggered conformers were calculated using MP2/6-31G(d,p) level of theory[22] and it was found that the GG conformer is predicted to be the lowest in energy, presumably due to the stabilisation provided by two $\sigma_{CH} \rightarrow \sigma^*_{CF}$ interactions. The next low energy conformer GA only contains one such interaction and conformer AA contains none. When the two highly polarised C–F bonds are parallel to each other (ie. in GG' conformer), this results in a destabilising dipole–dipole interaction, which was predicted to have an energy penalty more than twice the energy of hyperconjugation stabilisation ($2 \times 1.16 = 2.32$ kcal mol^{-1}). Therefore, the dipole–dipole interaction is a more dominant factor in controlling the conformation of 1,3-difluorocompounds.

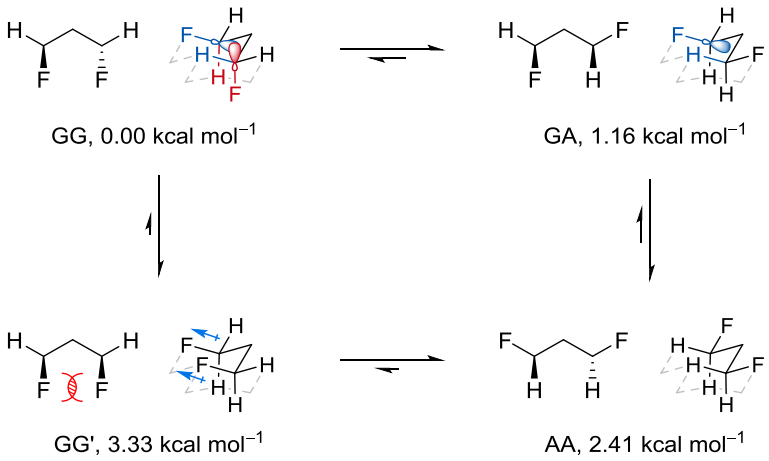

Figure 1.12: Four conformers (GG, GA, AA and GG') of 1,3-difluoropropane.

Utilising the conformational control exerted by the *gauche* effect and dipole–dipole interactions, multi-vicinal fluoroalkanes **1.23** and **1.24** with defined molecular conformations were designed and synthesised by O'Hagan *et al.*.[23] The X-ray structure of the all *syn* isomer **1.23** showed that it adopted a helical conformation while the *syn-anti* isomer **1.24** adopted a linear conformation. The conformational preference of both **1.23** and **1.24** was a result of maximising the *gauche* orientation between adjacent fluorine atoms while minimising 1,3 dipole–dipole repulsions arising from parallel C–F bonds. The solution-state conformational behaviour of **1.23** and **1.24** was also investigated using ^{1}H-^{1}H and ^{1}H-^{19}F scalar coupling constants. The preferred solution-state conformers in both compounds were found to be the same as that observed in the solid state.[23]

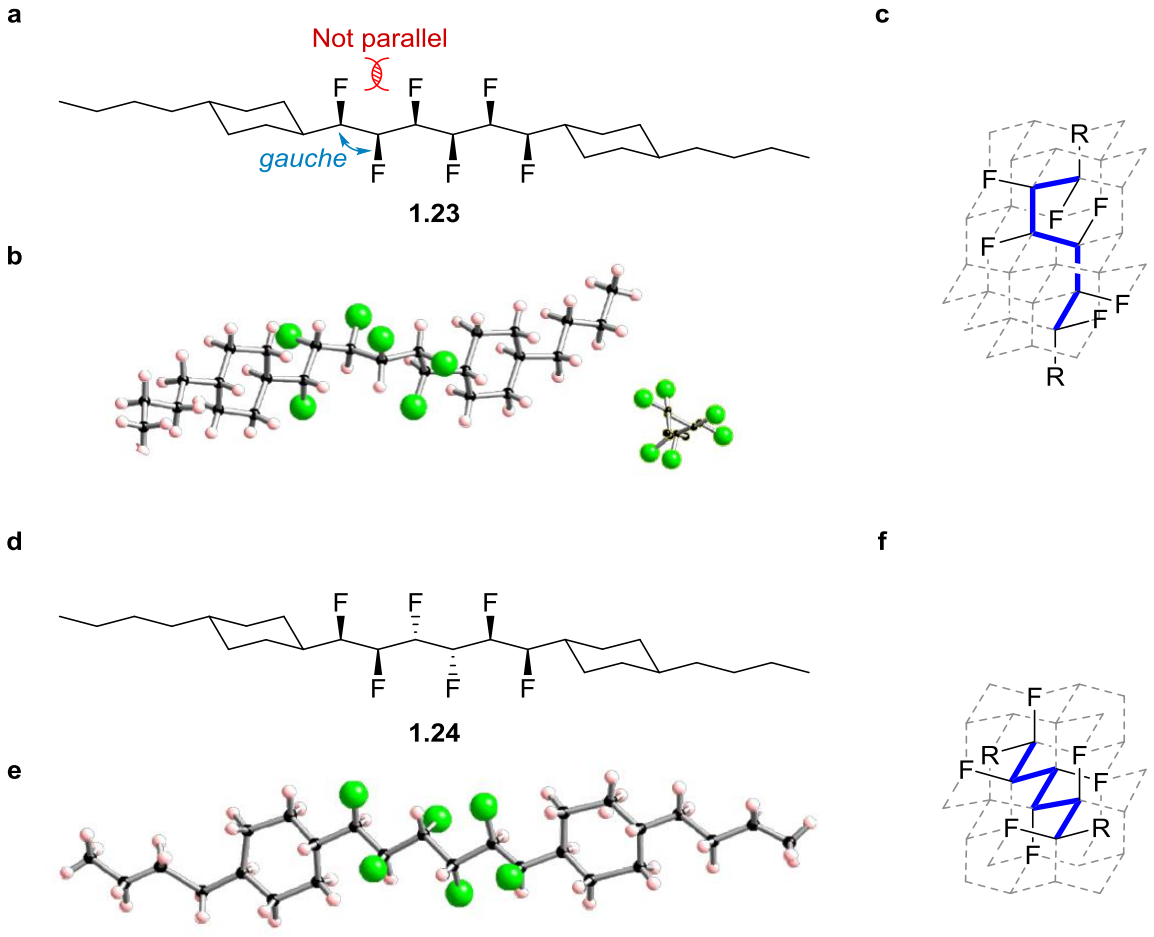

Figure 1.13: **a**, Chemical structure of **1.23**. **b**, X-ray crystal structure of **1.23** looking at the side, and down the helical wheel. **c**, Major conformation of **1.23** represented on a diamond lattice. **d**, Chemical structure of **1.24**. **e**, X-ray crystal structure of **1.24**. **f**, Major conformation of **1.24** represented on a diamond lattice.

Other interactions

Apart from the steric and electronic interactions discussed in this section, other non-covalent interactions also affect molecular conformations. Hydrogen bonds, one of the strongest non-covalent interaction, are electrostatic interactions between a δ^+ hydrogen atom and the lone pair of an electronegative element such as oxygen and nitrogen.[24] The strength of the interaction is highly dependent upon the nature of the donor and acceptor atoms, as well as the distance and angle between the donor and the acceptor atoms. A typical hydrogen bond (eg. ROH···O=C, ~ 1.9 Å) has an energy of 5–10 kcal mol^{-1}.[25] In contrast, the CH-π interaction between an aromatic π system (eg. benzene) and an aliphatic CH bond (eg. methane) is a lot weaker (1.03 – 1.13 kcal mol^{-1}, Figure 1.14).[26]

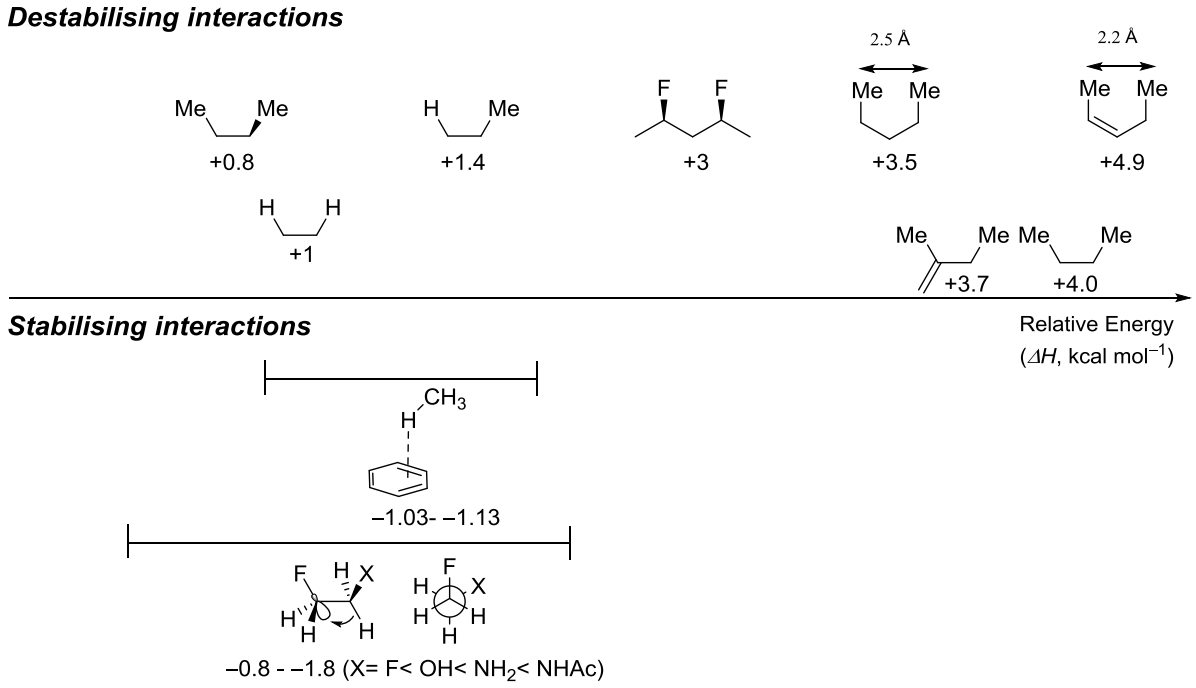

Figure 1.14: A selection of steric and electronic interactions.

In summary, conformational control in small molecules is a delicate balance between steric and electronic interactions. The energy of the eclipsing interaction increases (H/H: 1 kcal mol^{-1}, H/Me: 1.4 kcal mol^{-1}, Me/Me: 4 kcal mol^{-1}) with the increasing steric bulk of the substituents as illustrated in figure 1.14. Compared to *syn*-pentane interaction (3.5 kcal mol^{-1}), $A^{1,3}$ strain is slightly higher in energy (4.9 kcal/mol) due to the closer distance of the terminal methyl groups. Other non-covalent interactions including dipole-dipole, hyperconjugation (especially in the *gauche* effect) and CH-π interaction between benzene and aliphatic CH bonds are smaller in magnitude compared to allylic strain and *syn*-pentane interaction. However,

hydrogen bond interactions can possibly outweigh the destabilising interactions induced by $A^{1,3}$ strain.

1.2 Three-dimensional structural elucidation of small molecules using NMR spectroscopy.

Three-dimensional structural determination is also essential in conformational analysis. Although X-ray crystallography has been used for decades to determine the conformation of molecules at the atomic level, other factors, such as crystal packing, could influence the observed solid-state conformation. Therefore, NMR spectroscopy has been used routinely to study the dynamic behaviour and three-dimensional structures of small molecules in solution.

The elucidation of the 3D molecular structures consists of configurational and conformational analysis, which are interlinked. For a given molecular configuration, one could derive the preferred molecular conformations. At the same time, the knowledge of molecular conformations facilitates the configurational analysis by deducing the possible configurations of a given molecule.

In this section, the use of NMR parameters including chemical shifts (δ), scalar coupling constants (*J* values) and nuclear Overhauser effect (nOe) for the determination of configuration and conformation of flexible molecules will be discussed.

1.2.1 Chemical Shifts

While the value of the chemical shift of a nucleus provides information of the nature of the substituents directly attached to the nuclei, it also provides information about the nucleus' spacial environment. This forms the basis of the ^{13}C acetonide method (Figure 1.15), first described by Rychnovsky in 1990 for the assignment of the relative stereochemistry of 1,3-diols.[27]

In this approach, the *syn* or *anti* 1,3-diols (**1.25** and **1.26**, respectively Figure 1.15) were derivatised to the corresponding *syn* or *anti* acetonides. Depending on the stereochemistry of the 1,3-diol of interest, the derivatised acetonide would adopt different conformations, which give characteristic ^{13}C chemical shifts of the gem dimethyl groups, thus allowing the determination of the relative configuration of the 1,3-diol motif of interest.

The *syn* acetonide adopts a chair conformation so the gem dimethyl groups are chemically inequivalent and have different ^{13}C chemical shifts. The equatorial methyl group has a ^{13}C chemical shift around 30.0 ppm while the axial methyl group has a ^{13}C chemical shift around 19.6 ppm. On the other hand, the *anti* acetonide adopts a twist-boat conformation to avoid 1,3-diaxial interactions, thus both gem dimethyl groups are chemically equivalent and have ^{13}C chemical shifts around 24.6 ppm. The ^{13}C chemical shifts of the quaternary acetal

carbons could also be used to distinguish the *syn* and *anti* configurations. The acetal carbon of the *syn* acetonide has a ^{13}C chemical shift around 98.5 ppm, while the one of the *anti* acetonide has a ^{13}C chemical shift around 100.6 ppm. These characteristic chemical shifts of the gem dimethyl and the quaternary acetal carbons allows the assignment of the relative configuration (*syn* or *anti*) of 1,3-diol motifs.

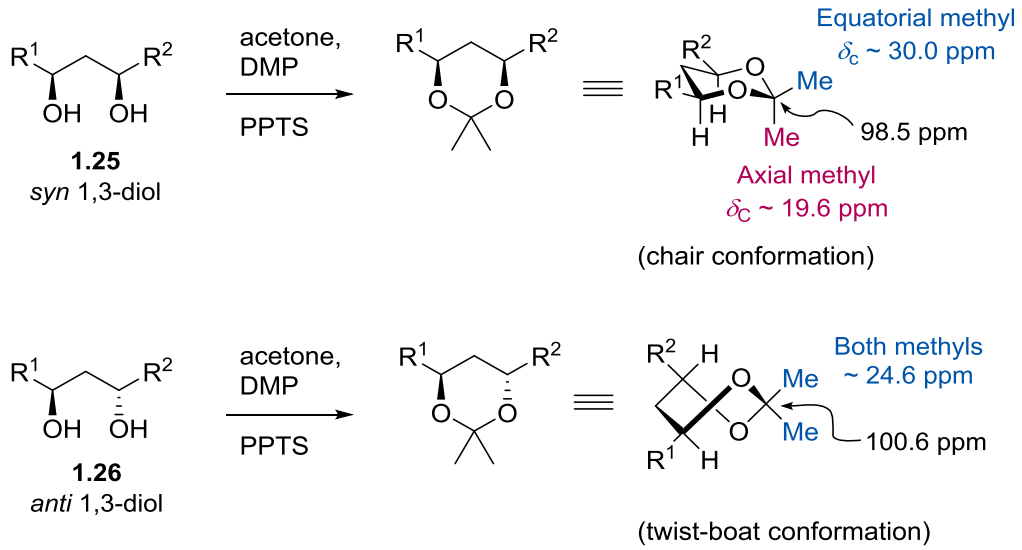

Figure 1.15: Derivatisation of the *syn* and *anti* 1,3-diol (**1.25** and **1.26**) using acetone, 2,2-dimethoxypropane (DMP) and pyridinium p-toluenesulfonate (PPST) to yield the corresponding *syn* and *anti* acetonides. The ^{13}C chemical shifts of the gem dimethyl groups and the acetal carbons are labelled.

Although the ^{13}C acetonide method originally described in 1990 allowed reliable assignment of the relative configuration of an isolated 1,3-diol motif, it is challenging to apply this approach to deconvolute the relative configuration of 1,3-polyol fragments in natural product, especially in the case of dermostatin A (**1.27**, Figure 1.16).[28] Application of the original ^{13}C acetonide method for the determination of the relative stereochemistry of the 1,3-polyol fragment of dermostatin A only revealed the number of *syn* and *anti* acetonides present in the molecule. Due to the lack of information of "which acetonides were *syn* and which are *anti*", the analysis of four derivatised acetonides **1.28** – **1.31** were required to reduce the number of possible stereoisomers of dermostatin A from 256 to six. Rychnovsky *et al*. showed that when the original ^{13}C acetonide method was used in combination of advanced 2D NMR methods such as DQF-COSY, HMQC, and NOESY/ROESY experiments, the positions of the *syn* and *anti* acetonides within the derivatised dermostatin A could be identified. The analysis

of only two of the four acetonides (**1.30** and **1.31**) allowed the unequivocal determination of the relative configuration of this polyol fragment.[28]

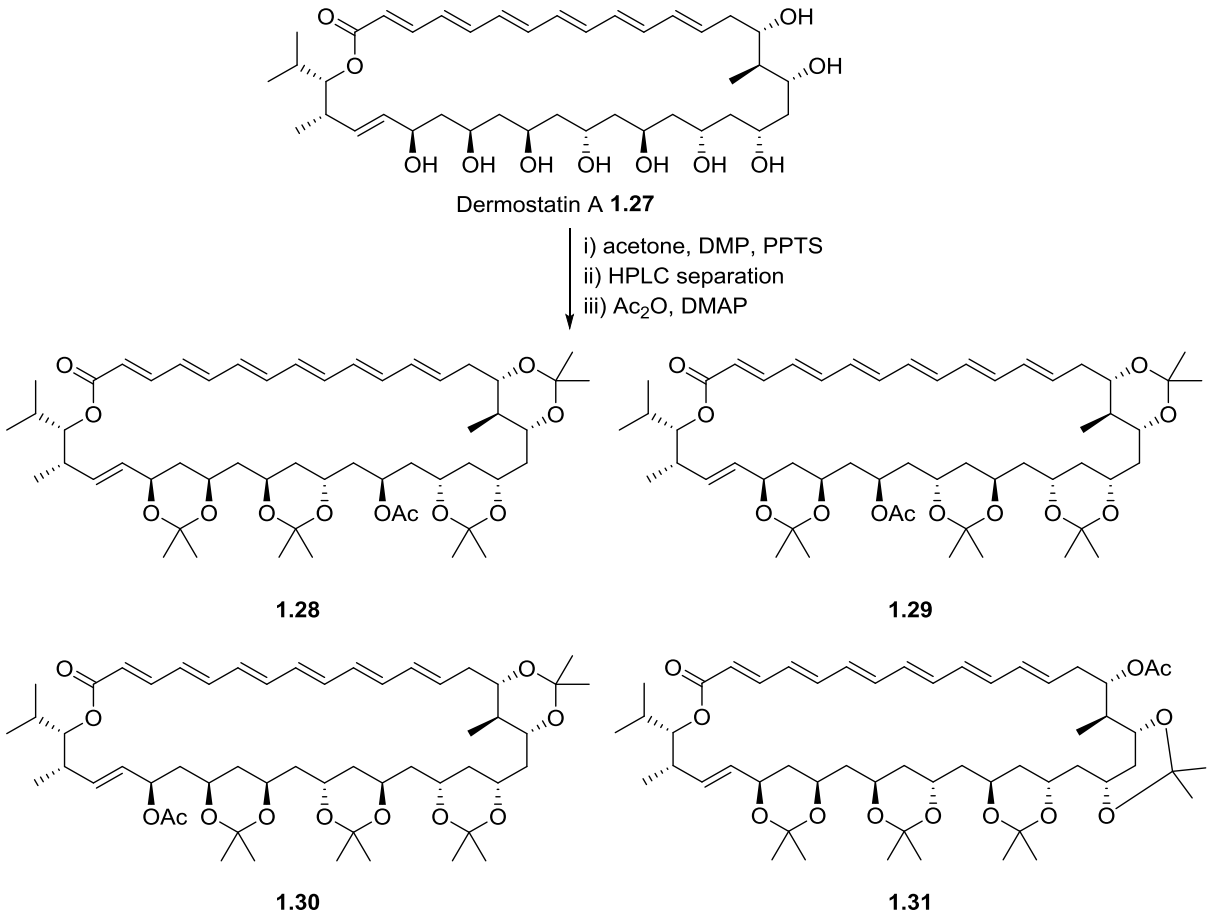

Figure 1.16: Chemical structure of dermostatin A (**1.27**) with the corresponding acetonide derivatives of dermostatin A **(1.28** – **1.31)**.

There are several limitations associated with the acetonide approach. It might be challenging to recording a high quality ^{13}C NMR spectrum with mass-limited samples due to the limited number of acetonides incorporated into the molecule. This could be circumvented by either the use of high field NMR instruments to record the ^{13}C NMR spectrum or the use of labelled 1,3-$^{13}C_2$-acetone in the derivatisation step. A cheaper alternative would be to use characteristic NOE correlations for the configurational assignment. Another drawback of the acetonide method is the requirement for derivatisation, which is undesirable for mass-limited samples.

Therefore, non-destructive techniques, or techniques which do not require derivationsation, such as the Universal NMR database (UDB) and *J*-based configurational analysis (which will be discussed in section 1.2.2) are highly desirable. Kishi *et al.* synthesised

a variety of polyols (Figure 1.17) with all possible stereochemistries to construct a database containing chemical shifts and ^{1}H-^{1}H coupling constants of each stereoisomer for the assignment of relative configuration of polyols.[29] The NMR data (often chemical shifts) of the polyol region of interest is compared to the NMR data of the structurally similar fragments in the database, and this allows the determination of the relative stereochemistry of the natural product fragment.

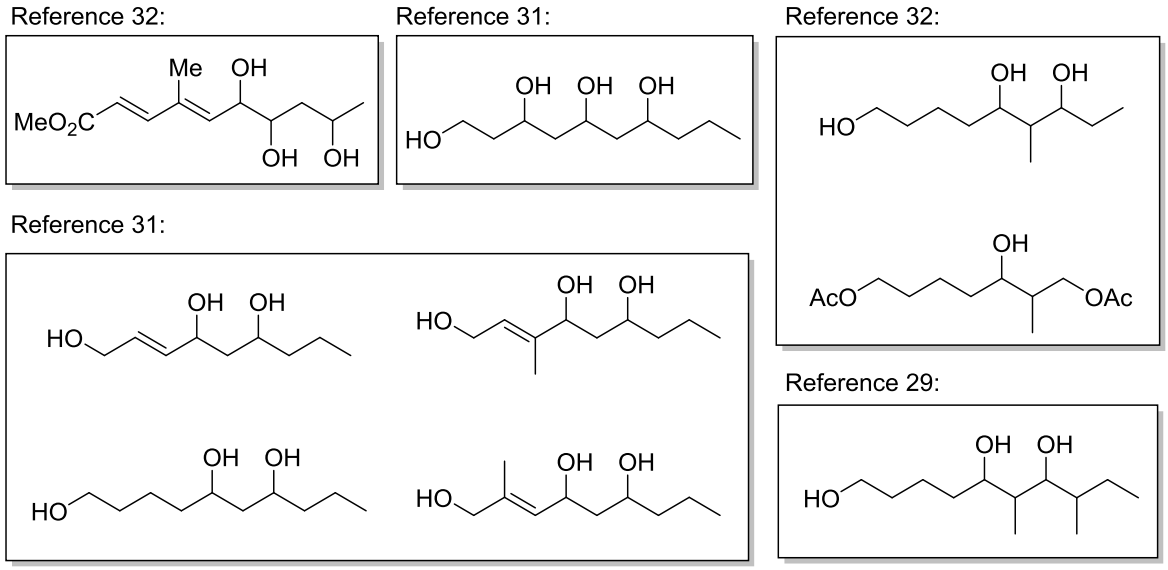

Figure 1.17: Representative examples of the polyol fragments in Kishi's universal NMR database.[29-32]

The use of the UDB for assigning relative stereochemistry of polyols was demonstrated using mycolactone B as an example (**1.32**, Figure 1.18). The truncated version of four diastereomers of the side chain of interest (C10' – C16' region of mycolactone B) were synthesised (**1.33** – **1.36**, Figure 1.18b) and the ^{13}C and ^{1}H chemical shifts of each diastereomer were compared to that of the natural product. The comparison was often presented as histograms in which the difference in chemical shifts between each diastereomer and the natural product ($\delta_{\mathbf{1.33\text{-}1.36}} - \delta_{\text{mycolacton B}}$) are plotted as the y-axis. The synthetic diastereomer with the smallest $\Delta\delta$ is assigned to have the same relative stereochemistry as the natural product. For example, the comparison of ^{13}C chemical shifts (δ_C) showed that both diastereomers **1.33** and **1.34** fitted well to the natural product data, while the other two diastereomers **1.35** and **1.36** fitted less well (Figure 1.18c). Comparison of the ^{1}H chemical shifts (δ_H) revealed that diastereomer **1.33** provides the best fit to the natural product data (Figure 1.18d), thus this diastereomer was assigned to possess the same relative stereochemistry as the corresponding mycolacton B fragment.[30]

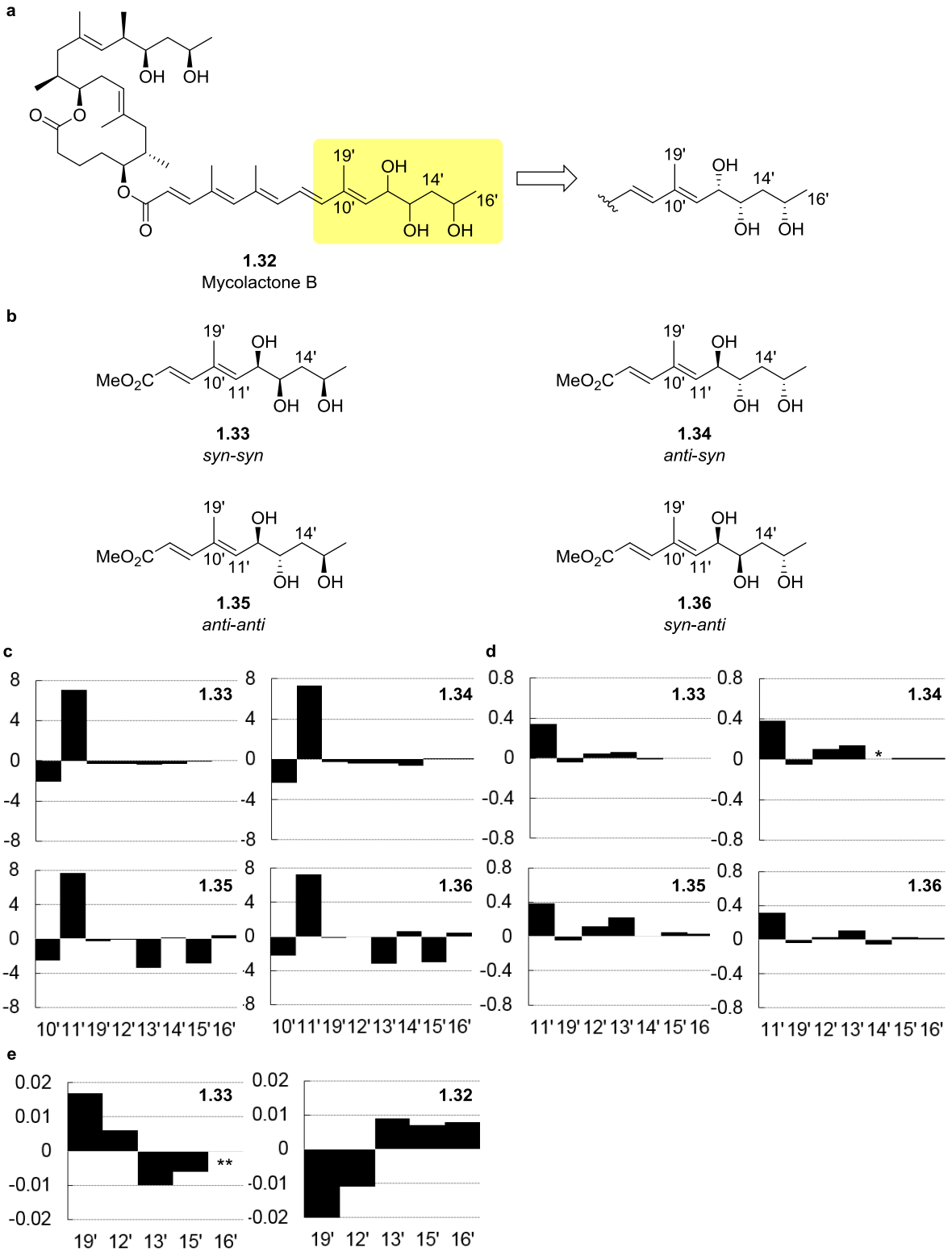

Figure 1.18: **a**, Chemical structure of mycolactone B (**1.32**) with the polyol region (C10' – C6') highlighted. **b**, Four structurally similar diastereomers (**1.33** – **1.36**) to the polyol fragment of mycolactone B **1.32** (C10' – C6' region). Comparison of the (**c**) ^{13}C chemical shifts and (**d**) ^{1}H chemical shifts of the four possible diastereomers (**1.33** – **1.36**) to the experimental values of the polyol region (C10' – C6') of mycolactone B **1.32**. **e**. Difference in ^{1}H chemical shifts of the *syn-syn* isomer **1.33** (left)

and mycolactone B **1.32** (right) between (*R*)- and (*S*)-DMBA-d_{13}. *: For **1.34**, H14' have two chemical shifts and this is not the case in mycolactone B. Therefore, the comparison of H14' was not made between **1.34** and that of mycolactone B. **Signal of $H_{16'}$ overlapped with solvent peaks.

Kishi *et al.* also demonstrated that the UDB approach could be extended to assign the absolute configuration of the C10' – C16' region of mycolactone B with the use of chiral deuterated solvents. Chemical shifts of **1.33** was measured in both deuterated *R*- and *S*- *N*,α-dimethylbenzylamine (DMBA) and the difference in chemical shifts ($\Delta\delta = \delta_R - \delta_S$) were compared to that of mycolactone B obtained in identical conditions. The comparison (Figure 1.18e) showed that **1.33** presented the opposite trend compared to the natural product, suggesting that **1.33** is the enantiomeric form of the C10' – C16' region of mycolactone B. This allowed for the assignment of the absolute configuration of this fragment of mycolactone B.[30]

The UDB approach is also used in the determination of the relative configuration of 1,3,5-triol moieties (Figure 1.19). It was found that the chemical shift of the central carbon atom (C_3, Figure 1.19a) is sensitive to the relative stereochemistry of the three hydroxyl groups. The *syn-syn* and *anti-anti* 1,3,5 triols could be differentiated solely on the basis of the chemical shifts of C_3 but the *syn-anti* and *anti-syn* configurations could not be differentiated. Nevertheless, this approach has been applied to determine the relative configuration of longer alternating polyol structures which could be conceptually treated as a series of overlapping 1,3,5-polyol segments. For example, the relative configuration of the alternating polyol segment of crypocaryol C (Figure 1.19b) was assigned using this approach[33] and was later verified by total synthesis.[34] This approach has also been applied to elucidate the relative configuration of the polyol segment of mycapolyol A (Figure 1.19c) containing 14 alternating hydroxyl groups.[35]

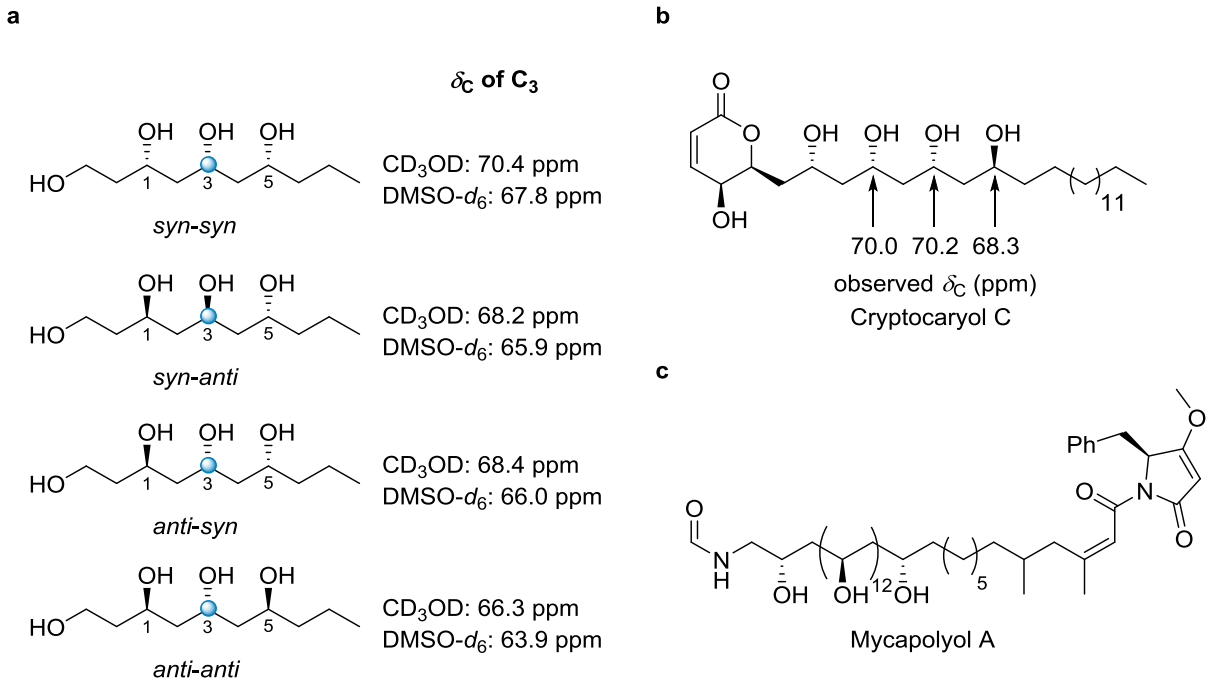

Figure 1.19: **a**, Chemical shifts of C_3 of 1,3,5-triols with different stereochemistries. **b**, Application of UDB in the determination of the stereochemistry of cryptocaryol C.[33] **c**, Proposed configuration of mycapolyol A.[35]

Successful application of the UDB approach in the assignment of relative configuration relies on comparing 'like with like' – not only the connectivity, but also the conformational behaviour of the motif of interest should closely match to the available fragments in the database. In the case of mycolactone B (Figure 1.18), all four synthetic isomers **1.33** – **1.36** provide poor match to the chemical shifts of position 11', presumably because position 11' in all the synthetic fragments does not possess the same chemical or conformational properties as that of mycolactone B. To provide the best chance for successful application of UDB approach, synthesis of all diastereomers of the matching fragments which closely mimic the target natural product is required. Scenarios like this, such as the case of baulamycins (which will be discussed in chapter 2), the synthesis of all possible isomers is not always trivial, thus leading to poor cost/benefit ratio.

Rather than generating a database by synthesising all possible stereoisomers of the stereo-undefined molecular fragments, the chemical shifts of all possible stereoisomers could be computed using quantum mechanical (QM) calculations. Chemical shift-based methods coupled with QM calculations will be discussed in section 1.3.4.

1.2.2 *J* values (^{1}H-^{1}H and ^{1}H-^{13}C scalar coupling constants)

In 1959, Karplus showed that the vicinal ^{1}H–^{1}H scalar coupling constants in ethane ($^{3}J_{\text{H-C-C-H}}$) has a dependency on the H–C–C–H dihedral angle based on valence bond calculations.[36] After the pioneering work published by Karplus, several generalised Karplus-type equations aiming to calculate vicinal coupling constants in organic molecules were proposed. One of the commonly used Karplus-type equations is described by Haasnoot, Leeuw and Altona (blue line, Figure 1.20a) which accounts for the effect of electronegativity and position of substituents on the vicinal coupling constants.[37] Vicinal ^{1}H–^{13}C coupling constants ($^{3}J_{\text{HC}}$), which have a dependency on the H–C–C–X dihedral angle (red line, Figure 1.20a), are less routinely used in structural determination but complement the use of $^{3}J_{\text{HH}}$ and provide additional information where $^{3}J_{\text{HH}}$ is not applicable, such as the cases of quaternary centres. Generally speaking, larger vicinal *J* values are expected for coupled nuclei in an antiperiplanar orientation ($^{3}J_{\text{HH}}$ = 9 – 12 Hz and $^{3}J_{\text{HC}}$ = 6-8 Hz respectively, φ = 180 °, Figure 1.20b) whereas smaller vicinal *J* values are expected for coupled nuclei in a *gauche* orientation ($^{3}J_{\text{HH}}$ = 2 – 4 Hz and $^{3}J_{\text{HC}}$ = 1 – 3 Hz respectively, φ = 60°,Figure 1.20b).

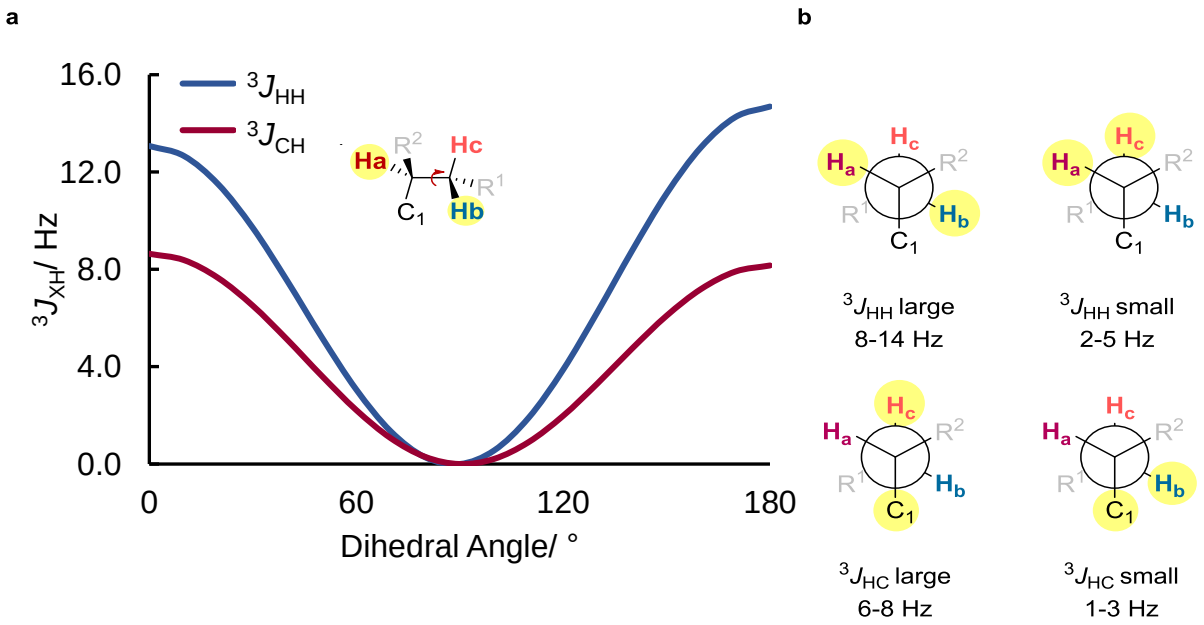

Figure 1.20: **a**. Correlation between $^{3}J_{\text{HH}}$ and the H–C–C–H dihedral angle in ethane (blue line)[37] and correlation between $^{3}J_{\text{HC}}$ and the H–C–C–C dihedral angle in propane (red line)[38]. **b**, Expected large and small $^{2}J_{\text{HC}}$ in ethanol.

Similar to vicinal H-C couplings ($^{3}J_{\text{HC}}$), two-bond H-C couplings also have a dependency on H-C-Cα-X dihedral angle and it is especially useful for the stereochemical

analysis when Cα is substituted by electronegative groups such as a hydroxyl moiety (ie. X = OH, Figure 1.21a).[39] When the proton (H_b) and hydroxyl group attached to the Cα are in a *gauche* orientation, a larger coupling constant (−5 – −7 Hz) is expected. On the other hand, when they are in an antiperiplanar orientation, a smaller coupling constant (0 – −2 Hz) is expected (Figure 1.21b).

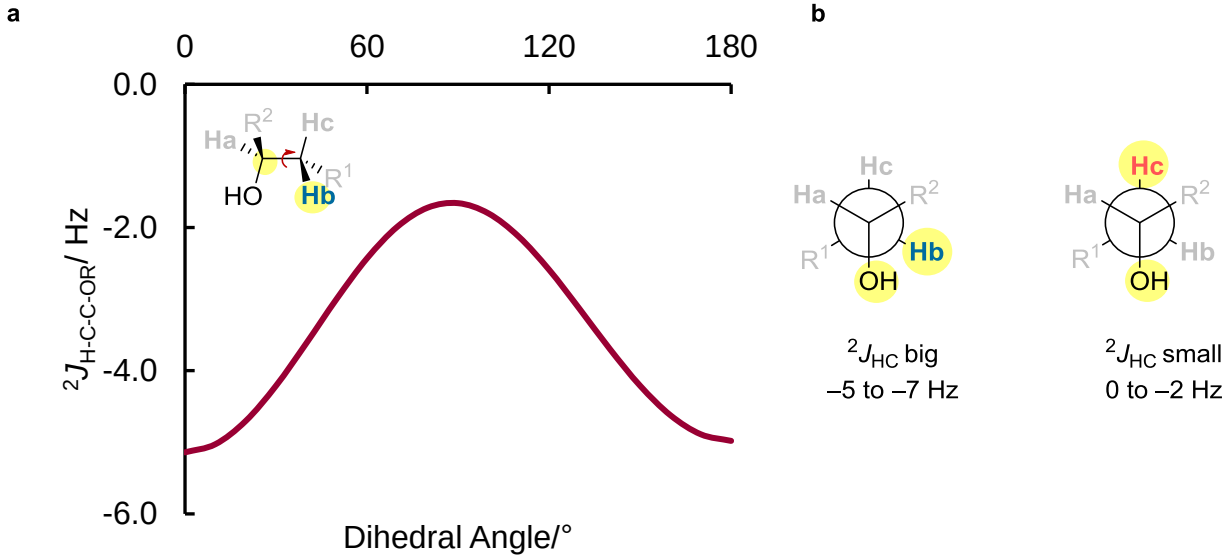

Figure 1.21: **a**, Correlation between $^2J_{HC}$ and the H-C-C-O dihedral angle in ethanol.[39] **b**, Expected large and small $^2J_{HC}$ in ethanol.

In terms of experimental measurements of *J* values, vicinal ^1H – ^1H scalar coupling constants ($^3J_{HH}$) can be measured from well-defined signals in a 1D ^1H NMR spectrum. For compounds with crowded ^1H NMR spectra, several two-dimensional techniques such as double-quantum filtered COSY (DQF-COSY)[40] and *J*-resolved experiments (PSYCHE-2D-J)[41] could be used to extract $^nJ_{HH}$.

Large $^nJ_{HC}$ such as one bond coupling ($^1J_{HC}$) can be measured directly from the 1D ^1H NMR spectrum because they usually appear as satellites. However, the intensity of these satellites are weak due to the low abundance of ^{13}C and can be further complicated by the satellites overlapping with other ^1H resonances in the spectrum. Alternatively, $^nJ_{HC}$ can also be measured from coupled ^{13}C spectra. However, it is a very insensitive technique and usually complex multiplets are observed for highly protonated carbon centres. It can also be difficult to assign $^nJ_{HC}$ for a given coupled partner. Therefore, two-dimensional techniques such as eCOSY, HSQMBC and EXSIDE were developed to measure $^nJ_{HC}$.[42] Among all these techniques, EXSIDE[43] provides the most accurate $^nJ_{HC}$ after some post-processing "tilting" of

the data when compared to the values obtained from coupled carbon spectrum (mean averaged deviation: 0.14 Hz).[44] However, EXSIDE experiments require selective irradiation of protons which are not coupled with each other, and this is not convenient when dealing with compounds with crowded ^{1}H NMR spectra. To overcome this limitation, broad-band techniques such as HSQMBC could be used instead, although the $^{n}J_{HC}$ values measured from HSQMBC spectra are slightly less accurate than those obtained from EXSIDE spectra (for example, mean averaged deviation = 0.35 Hz for in phase anti phase (IPAP) accordion HSQMBC[44]).

The use of a combination of $^{3}J_{HH}$, $^{3}J_{HC}$ and $^{2}J_{HC}$ to assign the relative configuration of acyclic compounds was reported by Murata *et al.*.[45] This method is known as "*J*-based configurational analysis" and can be used to determine the relative configuration of two adjacent or alternate stereogenic centres in acyclic systems. This approach relies on the characteristic patterns of spin-spin coupling constants yielded by each rotamer from the *threo* (*syn*) and the *erythro* (*anti*) configuration, as figure 1.22b illustrates. By comparing the magnitude of the expected scalar coupling constants of each rotamer to that of the experimentally observed values, the conformation, and subsequently the configuration, of the C–C bond can be assigned. Additional NOE/ROE correlations are used to distinguish the *anti* rotamers from the opposite configuration because these rotamers cannot be unambiguously assigned based solely on scalar coupling constants.

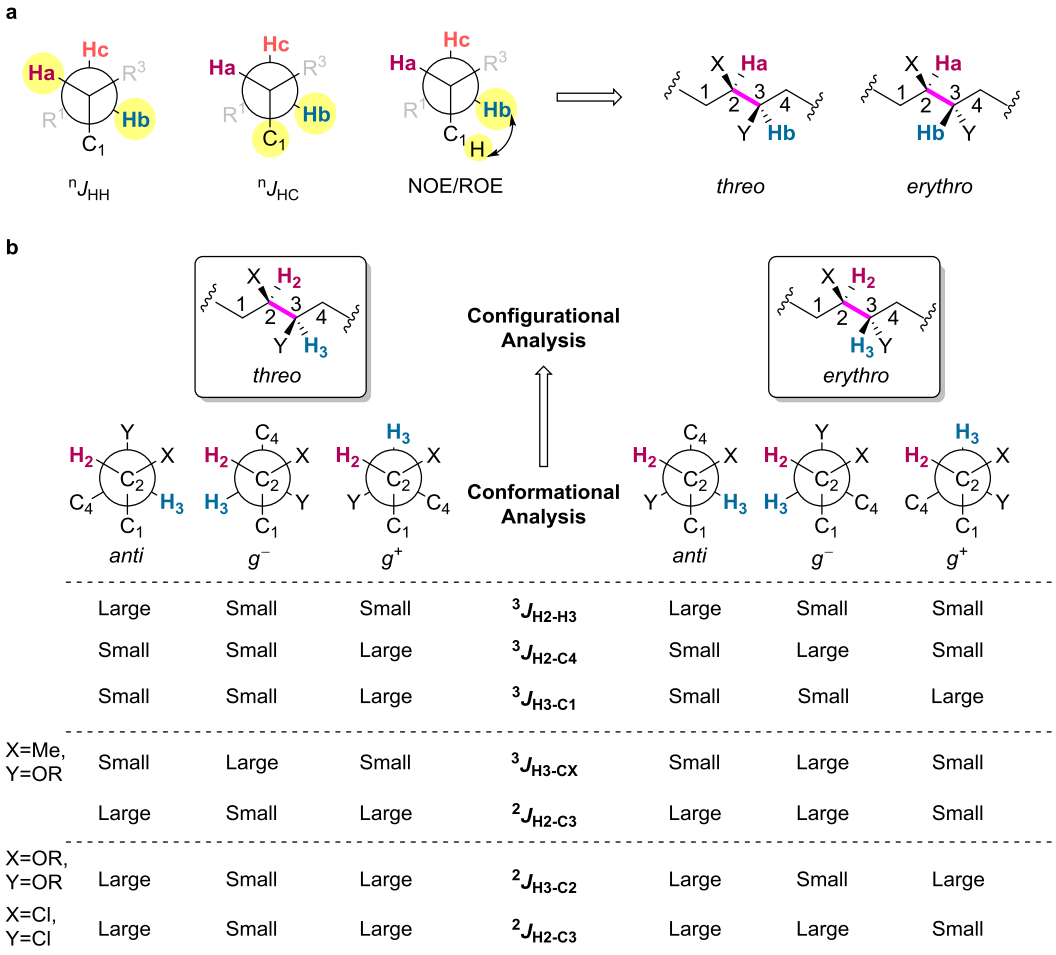

	Large	Small	Small	$^{3}J_{H2\text{-}H3}$	Large	Small	Small
	Small	Small	Large	$^{3}J_{H2\text{-}C4}$	Small	Large	Small
	Small	Small	Large	$^{3}J_{H3\text{-}C1}$	Small	Small	Large
X=Me, Y=OR	Small	Large	Small	$^{3}J_{H3\text{-}CX}$	Small	Large	Small
	Large	Small	Large	$^{2}J_{H2\text{-}C3}$	Large	Large	Small
X=OR, Y=OR	Large	Small	Large	$^{2}J_{H3\text{-}C2}$	Large	Small	Large
X=Cl, Y=Cl	Large	Small	Large	$^{2}J_{H2\text{-}C3}$	Large	Large	Small

Figure 1.22. a, NMR parameters used in *J*-based configurational analysis. **b**, Two possible configurations (*threo* and *erythro*) with the corresponding rotamers and the magnitude of the expected $^{n}J_{HX}$ of each rotamer in 1,2-methine systems.

J-based configurational analysis has been used widely in literature[46] as a routine method for the determination of the relative configuration of natural products. For example, it has been applied to elucidate the relative configuration of the C7 – C10 region of kalkitoxin **1.37** (Figure 1.23), and the assignment was confirmed by total synthesis.[47] It has also been applied to assign the relative configuration of the C5' – C16' region of a cytotoxic sulfolipid **1.38**.[48]

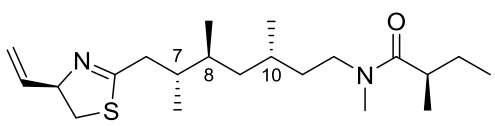

1.37

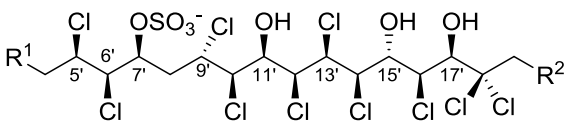

1.38

Figure 1.23: Chemical structure of (+)-kalkitoxin **1.37** and the C5'–C17' region of a cytotoxic sulfolipid **1.38**.

However, there are several limitations associated with *J*-based configurational analysis. Only staggered rotamers are considered and if the dihedral angle between the vicinal protons deviates by >15° from the ideal staggered angles (which is 60°), the magnitude of $^{3}J_{HH}$ will change substantially, from "small" to "medium". This will affect the accuracy of the conformational analysis of a given dihedral. In addition, the range of $^{2}J_{HC}$ is narrow and the magnitude of the *J* values strongly depends on the substitution along the coupling pathway (substituent $R^1$and R^2, Figure 1.21).[39] The final flaw of this approach is that all the dihedrals in a molecule are analysed in isolation, and inconclusive answers are obtained for cases where multiple conformers are in equilibrium, which will be detailed in chapter 2 of this thesis.

1.2.3 Quantitative analysis of interproton distances using Nuclear Overhauser Effect (NOE)

NOESY (Nuclear Overhauser Effect SpectroscopY) provides information of the spatial arrangement of protons and has been used for structure elucidation since the 1990s in either a qualitative[49] (NOE/no NOE) or a semi-quantitative[50](strong/medium/weak) fashion.

Butts *et al.* demonstrated that ^{1}H-^{1}H distances can be accurately determined from correlations measured from both 1D and 2D NOE spectra for both rigid[51] and flexible[52] small molecules. This methodology assumes that in the fast molecular tumbling regime with a short experimental NOE mixing time (τ_m), the observed NOE intensity between a pair of protons (η_{IS} between I and S) is only proportional to the IS cross relaxation rate (σ_{IS}) as equation 1.1 describes.

$$\boldsymbol{\eta_{IS} = \sigma_{IS}\tau_m} \qquad \textbf{Equation 1.1}$$

The cross relaxation rate (σ_{IS}) is inversely proportional to the distance between the pair of protons I and S to the sixth power (equation 1.2). If one assumes the values defining k (γ - gyromagnetic ratio, τ_c - rotational correlation time and ω - Larmour frequency) are constants, the observed NOE intensity (η_{IS}) is proportional to the distance between the pair of protons (r_{IS}). Therefore, the ratio of intensity of a pair of NOE signals (n_{IS} and n_{ref}) is also proportional to the ratio of their internuclear distances (r_{IS} and r_{ref}). By using a known rigid distance, which is insensitive to the change of conformer population, as a reference distance (r_{ref}, Equatoin 1.3), such as the distance between methylene protons (~ 1.78 Å), the distance between dipolar coupled nuclei for the rest of the molecule (r_{IS}, Equation 1.3) can be

determined by comparing the relative intensity of the peak of interest ($n_{IS,}$ Equarion 1.3) with the relative intensity of the peak corresponding to the rigid distance (n_{ref}, Equarion 1.3).[52]

$$\sigma_{IS} = kr_{IS}^{-6}, \text{ where } k = \left(\frac{\mu_0}{4\pi}\right)^2 \frac{\hbar^2\gamma^4}{10}\left(\frac{6\tau_c}{1+4\omega^2\tau_c^2} - \tau_c\right) \qquad \textbf{Equation 1.2}$$

$$r_{IS} = r_{ref}\left[\frac{n_{IS}}{n_{ref}}\right]^{-\frac{1}{6}} \qquad \textbf{Equation 1.3}$$

The NOE intensities could be obtained from either 1D or 2D NOE/ROE spectra. In order to compare all the NOESY intensities taken from the same molecule, the Peak Amplitude Normalisation for Improved Cross-relaxation (PANIC)[53] method was employed to correct for the differing rates of external relaxation for each proton. This was achieved by setting the integral of irradiated peaks to a fixed arbitrary value, usually 1000.

For strychnine (Figure 1.24a), a mean absolute deviation of 3.5% (corresponding to ~0.1 Å) and standard deviation of 2.7% were observed when comparing the experimentally determined NOE-distances (in C_6D_6) to those obtained from DFT calculations and X-ray crystallography. Although the overall fit was excellent, comparison of the interproton distance between H_{11b} and H_{23b} gave an error (14.9%) more than five times higher than the standard deviation. It was realised that the experimentally derived NOE-distance between H_{11b} and H_{23b} in C_6D_6 is 3.49 Å, which is shorter than the distances computed by DFT and measured from the X-ray crystal structure (4.10 and 4.12 Å, respectively). Since the observed NOE intensity is sensitive to short interproton distances (scaled with r^{-6}), Butts *et al.* showed that the shorter experimental H_{11b}-H_{23b} distance was indicative of the presence of a second conformer which has a shorter H_{11b}-H_{23b} distance (Figure 1.24c). A combination of molecular mechanics conformational search and DFT calculations were used to locate the second conformer of strychnine, which was computed to have ~ 2.5% of conformer population and a short H_{11b}-H_{23b} distance (2.11 Å). This example demonstrated the use of NOE-distance analysis for quantifying conformer populations in solution and this offers opportunities to study the detailed conformational behaviour of organic molecules. [54]

a

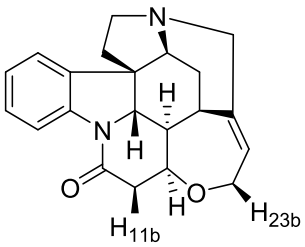

strychnine

b

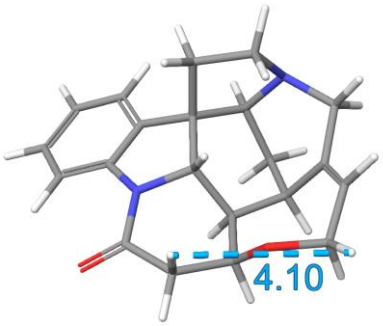

c

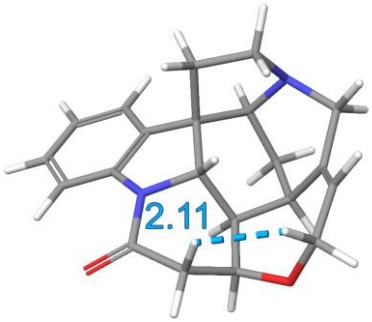

Figure 1.24:**a**, Chemical structure of strychnine. The major (**b**) and minor (**c**) conformers of strychnine in solution with the distance between H_{11b} and H_{23b} (in Å) labelled.

Apart from the isotropic NMR parameters discussed in this section (δ, J couplings and NOE-distances), other anisotropic NMR parameters, such as residual dipolar couplings (RDCs) and residual chemical shift anisotropies (RCSAs), could also be used for 3D structural elucidation. These anisotropic NMR parameters can be measured when the compound of interest is weakly aligned to the external magnetic field, with the aid of polymer gels swelled in deuterated NMR solvent as alignment media. The use of RCDs and RCSAs in structural elucidation of natural product complements the routinely used isotropic NMR parameters and it is a growing area of research. Unfortunately, a review of this field falls out of the scope of this thesis. Nevertheless, there are excellent articles in the literature that provide a general overview of these NMR parameters.[55-57]

1.3 A hybrid approach using quantum mechanical calculations and NMR (QM/NMR) for 3D structural elucidation.

Flexible small molecules often display time-averaged conformational behaviour in solution, due to the low interconversion barrier between conformers via C–C single bond rotation (3 kcal mol^{-1} in the case of ethane for example, Figure 1.1a). As a result, the rate of interconversion is fast compared to the NMR timescale and only the time-averaged signals are observed by NMR spectroscopy. Although the time-averaged signals could in principle be resolved at low temperature which allows the determination of conformer population, this is not often possible for flexible small molecules. Although the observed weighted-average NMR properties (such as *J* values) could be used for conformational analysis of flexible molecules, this requires knowledge of the NMR properties and conformer population of individual conformers, which are not trivial to estimate.

This challenge can be overcome by using quantum mechanical calculations to estimate conformer population and to compute the NMR properties (δ, *J* and internuclear distances) of individual conformers. The computed NMR properties of each conformer are Boltzmann-averaged to give the ensemble-averaged NMR properties of the molecule of interest. Quantitative comparison between the ensemble-averaged NMR properties with the experimentally measured data allows detailed conformational analysis of flexible small molecules. This integrated approach using quantum mechanical calculations and NMR spectroscopy for structural elucidation is referred to as the QM/NMR approach (Figure 1.25) in this thesis.

In this section, each stage of the QM/NMR approach (a – d ,Figure 1.25) will be discussed.

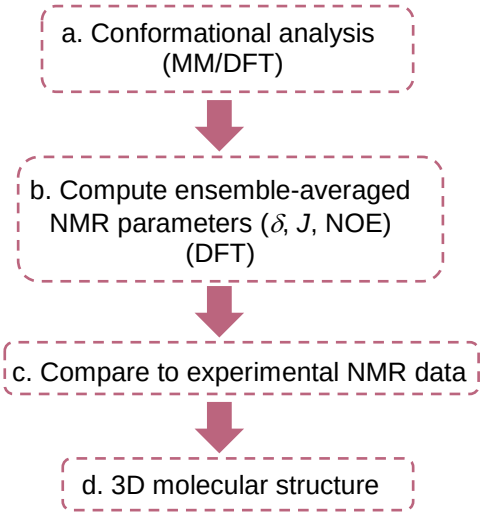

Figure 1.25: An outline of the QM/NMR workflow.

1.3.1 Conformational analysis (stage a): generating a library of low energy conformers by conformational search using Molecular Mechanics (MM) calculations.

One way to locate low energy conformers of a molecule is to employ molecular mechanics (MM) calculations. MM calculations treats molecules as a 'ball and spring' models. MM describes the strain energy of molecules as a sum of energies associate with bond stretching (E_{stretch}), bond angle bending (E_{bend}) , torsional angle rotations (E_{torsion}) , electrostatic interactions (E_{colombic}) and Van der Waals interactions (E_{VDW}) as equation 1.4 describes.[58]

$$E_{strain} = E_{stretch} + E_{bend} + E_{torsion} + E_{non-bonded}(r),$$

$$\text{where } E_{non-bonded}(r) = E_{coulombic}\,(r) + E_{VDW}(r) \qquad \textbf{Equation 1.4}$$

There are parameters associated with bond lengths, bond angles, torsional angles, as well as electrostatic properties and Van der Waals interactions between atoms. In the past few decades, several force fields were developed to describe these properties for different small organic molecules. MM2[59] and MM3[60] force fields were developed by Allinger *et al.* to calculate the strain energies of hydrocarbons. The Merck Molecular Force Field (MMFF), developed by Halgren, was parameterised based on results obtained from both *ab initio* calculations and X-ray crystallographic data of a range of organic molecules.[61]

However, the low energy conformer located using MM minimisation calculations depends on the geometry of the input structure. In the case of butane, if the input geometry is structurally similar to the *gauche* conformer **1.3**, minimisation of this input geometry would

only give the *gauche* conformer **1.3** as the low energy conformer of butane. On the other hand, if the input geometry is structurally similar to the antiperiplanar conformer **1.4**, minimisation of this input geometry would only give the antiperiplanar conformer **1.4** as the low energy conformer of butane. Therefore, to capture the lowest energy conformer (the global minimum) it is important to explore the entire potential energy surface of a molecule

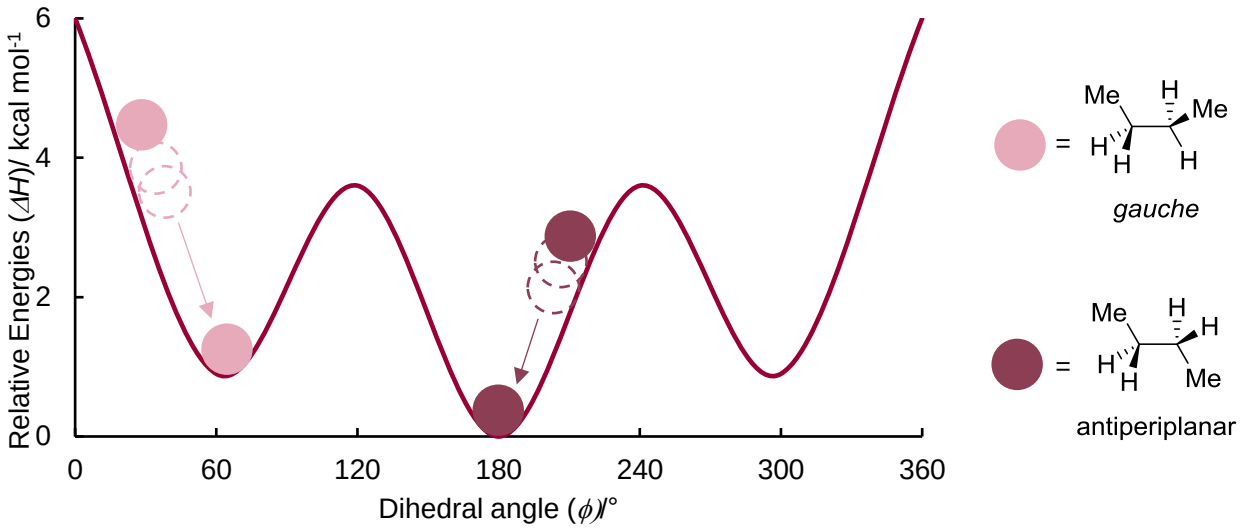

Figure 1.26: A schematic representation of MM minimisation calculations of butane.

In addition, a global minimum geometry determined by MM calculations based on strain energies may not remain to be the global minimum once entropy and solvation are considered. Further, often several low energy conformers contribute to the solution state behaviour of a molecule. Therefore, generation of a library of conformers is required to locate all low energy conformers of a molecule, that is, all local minima on a potential energy surface.

Two methods can be used to examine the conformational space of a molecule: MM conformational search and molecular dynamics simulation. In this thesis, only the former will be discussed in detail. Within MM conformational search, two approaches can be used: systematic and stochastic search. In the systematic search, either the Cartesian xyz coordinates of a molecule or the torsional angles of rotatable bonds are varied systematically. This leads to the examination of a very large number of conformers but most of these structures are high in energy due to destabilising steric interactions. Therefore it is time-consuming and not necessary to subject these conformers for minimisation to obtain low energy conformers.[62]

The stochastic search distorts the structure randomly and explores the conformational space in an iterative fashion. Figure 1.27 outlines one of the most frequently used methods (Monte Carlo Multi-Minimum (MCMM)). A starting structure is chosen and varied by either the distortion of Cartesian coordinates or torsional angles. The distorted structure is then minimised and the result is compared to the structure generated by the previous conformational search steps. The structure will either be stored as a new, unique structure or be discarded as a duplicate. This process is called Monte Carlo and the iteration of this process is called an MCMM search.[63] Unlike the systematic search, there is no defined end point for the stochastic search and usually a large number of iterations, or large number of steps, is set to ensure the examination of a large number of conformers arising from random distortions and hence maximising the chance of locating all the low energy conformers.

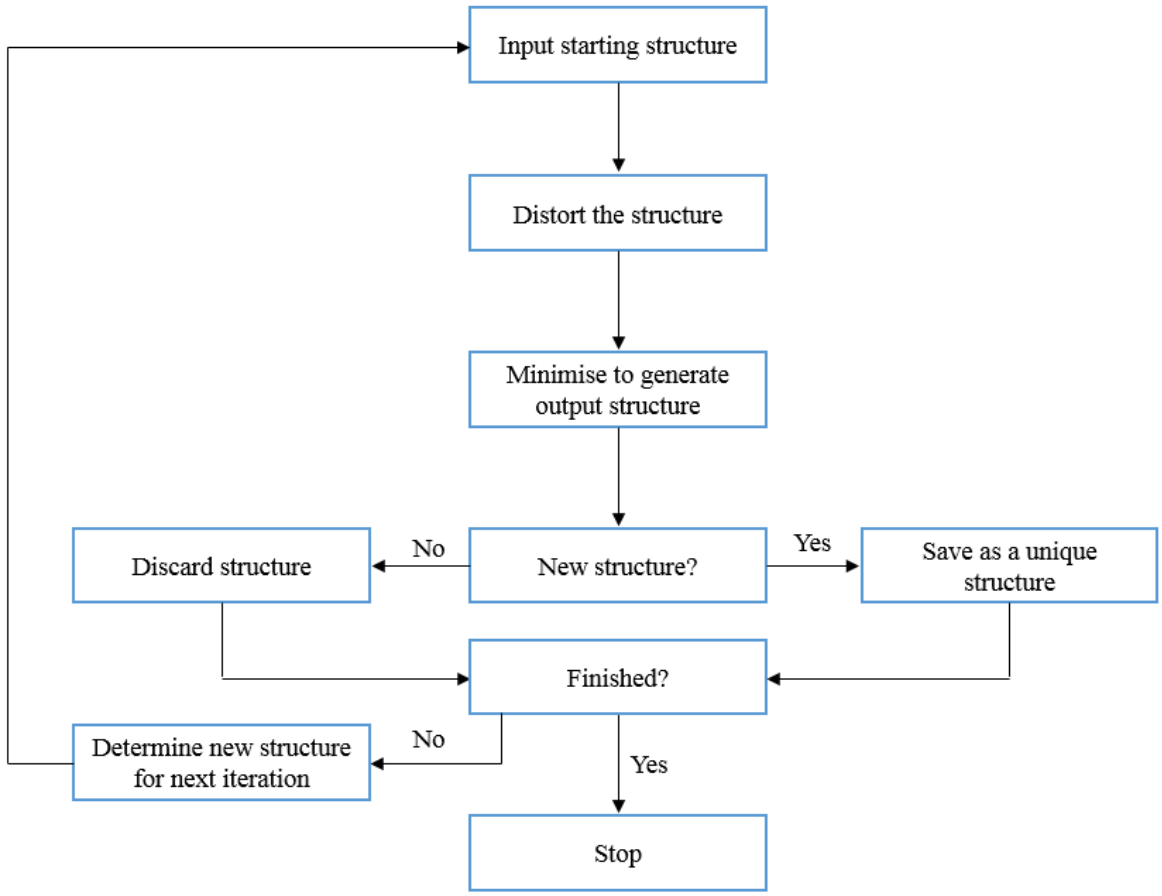

Figure 1.27: A flow describing the work flow of a Monte Carlo Multi-Minimum conformational search.[63]

1.3.2 Conformational analysis (stage a): evaluating conformer population using Density Functional Theory (DFT) geometry optimisation and frequency calculations.

After a conformational search, a library of conformers within a certain energy window above the global minimum is generated. DFT calculations are used to refine the geometries of conformers, and to compute the Gibbs free energies of conformers by taking into account zero-point energy correction, entropy and solvation.[64]

The physical properties such as the Gibbs free energy of a molecule, can be calculated by solving the time-independent Schrödinger equation (Equation 1.5), which encapsulates the physical behaviour of atoms and molecules, and describes the energy of a molecule as a function of the wave function.[65] However, practically it is impossible to solve the Schrödinger equation for polyatomic systems due to the time and computation power required.[66]

$$\hat{H}\psi = E\psi$$

Equation 1.5 The time-independent Schrodinger equation. $\hat{H}$ is the Hamiltonian operator, ψ is the wave function of the quantum system and E is the energy of the state ψ.

While the Schrödinger equation can be simplified by the Born-Oppenheimer approximation[67], which assumes that the electronic and nuclear motion in molecules can be separated due to the mass difference between electrons and nuclei, it is still challenging to solve the equation.

Fortunately, Density Functional Theory (DFT) provides a more practical solution to this problem. Hohenberg and Kohn[68] proposed that rather than trying to solve the Schrödinger equation itself to obtain the wave function, which describes the properties of a molecule, the Schrödinger equation can be reformulated to approximate the electron density of a molecule in order to determine the energy of a molecule. They also proposed that the initial approximation of the electron density, that is, the approximate solution to the Schrödinger equation, could be improved by an iterative process. Later, Kohn and Sham[69] took this theory to the application stage, and formulated a method to find the approximate answer. Although the exact exchange-correlation functional is unknown, approximate functionals such as B3LYP[70] and mPW1PW91[71] were developed and each functional has its strengths and weaknesses. For example, B3LYP is the most widely used functional due to its excellent accuracy/cost ratio and yet it does not account for dispersion interactions, which sometimes give misleading results in transition state calculation in organometallic chemistry.[72] The mPW1PW91 functional was proven to compute accurate chemical shifts and ^{1}H-^{13}C scalar coupling constants by Bifulco *et*

al..[46] In addition to functionals, different basis sets have also been developed as a mathematical description of atomic orbitals. The atomic orbitals, which can be used to build molecular orbitals, are approximated by either Slater-type orbitals or Gaussian-type orbitals. Polarisation functions and diffuse functions were also developed to better approximate the electron distribution and electron density of the atomic orbitals.

1.3.3 Computing ensemble-averaged NMR parameters (δ, J couplings and NOE-distances) using DFT calculations (stage b).

Prediction of NOE-distances is straight forward, and only the DFT-optimised geometries are required for computing internuclear distances. Prediction of chemical shifts is achieved by computing the magnetic shielding tensor (MST) values of each nucleus in the molecules of interest. The computed MST values can then be converted to chemical shift values by referencing to the MST values of tetramethylsilane (TMS) computed at the same level of theory. The gauge including atomic orbital (GIAO) method[73] has been widely used to compute accurate MST values. The calculation of *J* couplings is a lot more resource-intensive because it requires the evaluation of four terms: fermi contact, diamagnetic spin–orbit coupling component, paramagnetic spin–orbit coupling component and spin–dipolar operator. The contribution of these four terms varies depending on the nature of the coupling pathway (eg. geminal, vicinal) and therefore the calculations of all four terms are required to accurately predict the total *J* values between two coupled nuclei.

The computed NMR properties of all conformers are Boltzmann weighted based on the relative energies of the conformers to give the calculated ensemble-averaged NMR properties of a molecule. In the next section, examples of structural elucidation based on quantitative comparison between the ensemble-averaged NMR properties with the experimentally determined values will be discussed.

1.3.4 Application of the QM/NMR approach in 3D structural elucidation (stages c and d)

MAE-based comparison of computed vs experimental chemical shifts.

Tantillo *et al.* reported the structural reassignment of aquatolide (Figure 1.28)[74], a humulane-derived sesquiterpenoid lactone isolated from *Asteriscus aquaticus* in 1989. Aquatolide was originally assigned to have a rare [2]ladderane substructure on the basis of 1D and 2D NMR analysis[75] (**1.39**, Figure 1.28a). To verify the originally proposed structure, Tantillo *et al.* computed the ^{1}H and ^{13}C chemical shifts of the originally reported structure **1.39** and found a very large deviation between the computed values and reported natural product

data.[74] The comparison of ^{13}C chemical shifts showed a corrected mean averaged deviation (CMAD) of 7.23 ppm, with the largest deviation possessing a value of 24.33 ppm. The large discrepancy between the calculated and experimental data prompted Tantillo *et al.* to perform chemical shift based computational screening to elucidate the correct structure. This was achieved by computing the chemical shifts of 60 constitutional isomers arising from all possible [2+2] addition of the biosynthetic intermediate asteriscunolide C **1.40**. Finally, **1.41** (revised structure, Figure 1.28) was found to match the natural product chemical shifts well (CMAD of δ_C = 1.37 ppm with the largest deviation of 4.28 ppm) and was therefore assigned to be the structure of aquatolide. This assignment was further supported by the examination of $^{n}J_{HH}$, NOE correlations and X-ray crystal structure of the re-isolated natural product.[74] It later confirmed by total synthesis[76].

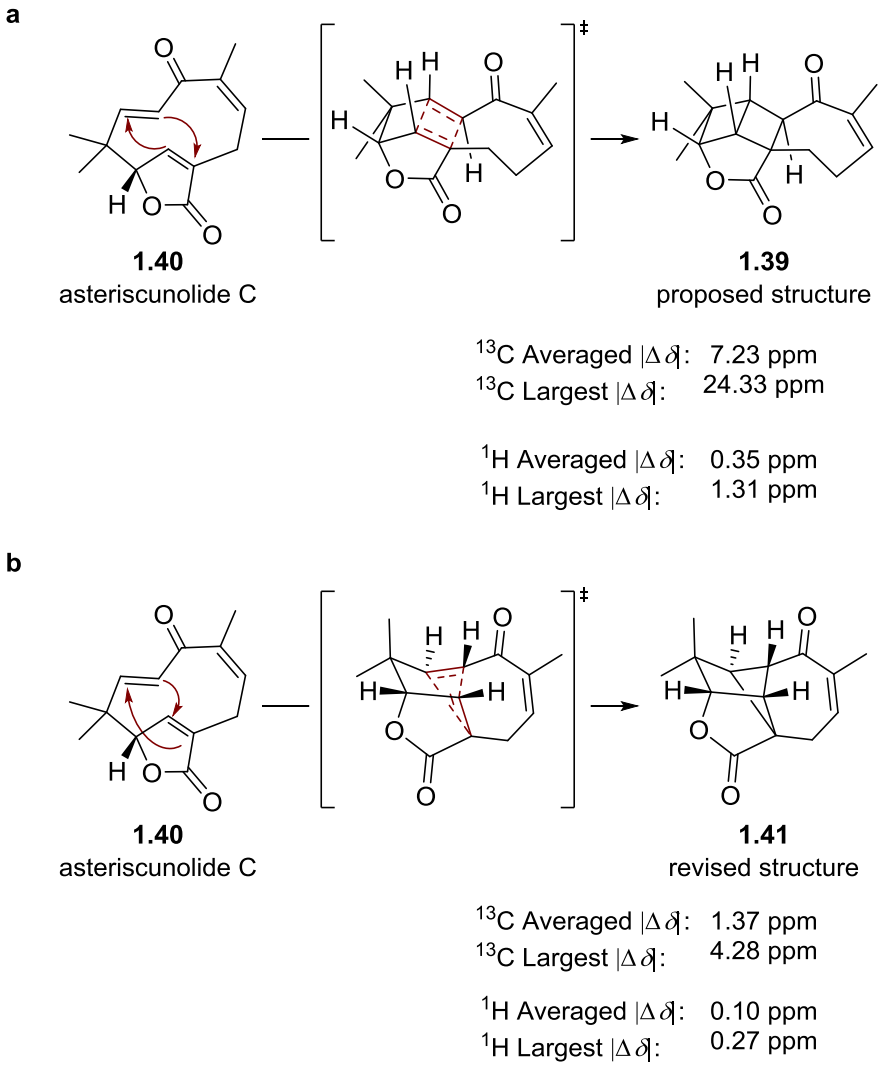

Figure 1.28: The (**a**) proposed (**1.39**) and (**b**) revised (**1.41**) structure of aquatolide. Both could be generated from asteriscunolide C **1.40** via [2+2] cycloaddition

When comparing the calculated chemical shifts to the observed values of the compounds of interest, the isomer showing the lowest error, that is, the lowest MAD value or the smallest error, would be assigned to be the matching isomer, such as in the case of aquatolide and examples discussed previously, for example, mycolactone B (Figure 1.18, section 1.2.1).

Probability-based comparison of computed vs experimental chemical shifts (DP4 and DP4+).

Although simple statistical analyses using R^2, mean averaged deviation (MAD) and standard deviation (StDev) values reflect the quality of the fit for the comparison, these numbers do not infer how likely it is that the matching isomer actually possess the stereochemistry of the stereo-undefined natural product. In addition, when dealing with cases where all possible isomers give similar MAD values (such as the case of baulamycins in chapter 2), the use of easy-to-perform statistical analysis for the comparison offers little advantage in discriminating possible stereoisomers. Smith and Goodman published the use of DP4 probability for the stereochemical assignment of organic small molecules in scenarios where only one set of experimental data is available.[77-78] Conformational search for possible stereoisomers were performed using the MMFFs forcefield in gas phase. The geometries obtained from MM calculations were then used to compute the magnetic shielding tensor (MST) values using the GIAO method, with B3LYP 6-31G(d,p) level of theory in gas phase. The computed MST values of each conformer were then Boltzmann averaged using the conformer energies calculated using DFT single point energy calculations with the same DFT method (B3LYP 6-31G(d,p)//MMFF). The ensemble-averaged MST values were converted to chemical shifts using the MST values of TMS computed using the same DFT method. The computed chemical shifts were then linearly scaled with respect to the experimentally observed values to remove systematic errors. Errors between the scaled chemical shifts of each nuclei and the experimental values ($\delta_{calc} - \delta_{exp}$, Figure 1.29) were converted to quantifiable probabilities of being the right answer using Bayes's theorem, with the expected standard deviations (σ) and degrees of freedom (ν).The σ and ν values used for calculating the DP4 probabilities ($\sigma_H = 0.185$ ppm, $\sigma_C = 2.306$ ppm, $\nu_H = 14.18$, $\nu_C = 11.38$) were obtained by fitting 1717 ^{13}C chemical shifts and 1794 ^{1}H chemical shifts of 177 known organic compounds computed using the same DFT method described previously (B3LYP 6-31G(d,p)//MMFF) to a *t* distribution. Finally, probabilities calculated for all nuclei of each stereoisomer were multiplied to give the DP4 probability of each isomer being the matching isomer (Figure 1.29).

To facilitate the use of DP4 probabilities in structural assignment of small organic molecules, an applet was made available at http://www.jmg.ch.cam.ac.uk/tools/nmr/DP4.[77]

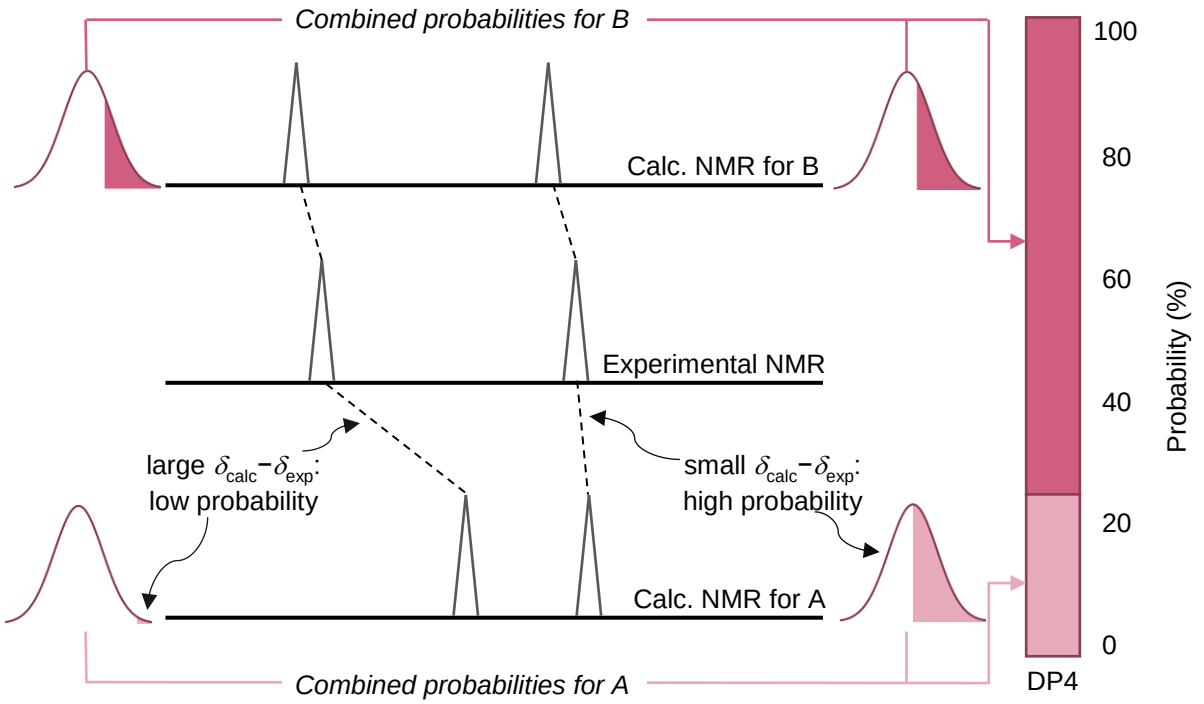

Figure 1.29: A schematic presentation (reproduced from literature[78]) of the DP4 probability.

Smith and Goodman demonstrated the application of DP4 probability to the assignment of tricholomalide A **1.42** (Figure 1.30)[77] Among 64 stereoisomers considered, the correct structure was assigned with very high confidence (99%). However, in the case of conformationally more flexible stereopentad **1.43** (Figure 1.30), DP4 probabilities often assigned the wrong stereoisomer with high confidence (>90%). The poor performance observed could be rationalised by the effect of improper description of solvent effects, which was not considered in the protocol, on conformer energies and the computed MST values.

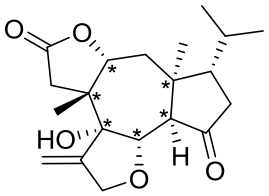

Tricholomalide A, **1.42**
64 stereoisomers compared
DP4: >99%

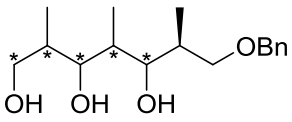

1.43
16 stereoisomers compared
Challenging for DP4

Figure 1.30: Application of DP4 probability in the stereochemistry assignment of **1.42** and **1.43**.

In addition, there are other drawbacks of the DP4 probability. The first one is associated with the accuracy of the expected σ values used in the calculation of probabilities, since the calculated chemical shifts used for the original fitting of the *t* distribution were computed using relatively low level of theory (B3LYP 6-31G(d,p)) in favour of low computational cost. Although the accuracy of the σ values might also be affected by the starting geometries, which were not re-optimised by DFT calculations.[79] In addition, the use of linear scaled chemical shifts for all atoms in the DP4 protocol ignored the fact that systematic errors for atoms with different hybridisations (sp^3 vs sp^2) are different and should not be treated using the same linear scaling process. Furthermore, scaling the chemical shifts of the wrong answer to the experimentally observed values might give false positive results, in cases where the calculated chemical shifts of the wrong isomer accidentally fit well to the experimentally observed values.

To address these issues, Sarotti *et al.* proposed an improved version of the DP4 probability (DP4+)[79]. To obtain more accurate σ values, 1219 ^{13}C and 1123 ^{1}H chemical shifts were computed on DFT optimised structures with 24 different levels of theory in gas phase and in implicit solvation (PCM). To address the issues with linear scaling for atoms with different hybridisations, another *t* distribution was fitted for sp^2 carbons. In addition, unscaled chemical shifts could also be used to calculate DP4+ probabilities and this was achieved by subtracting the errors ($\delta_{calc} - \delta_{exp}$) with the expected mean μ for the *t* distribution. To facilitate the use of DP4+ probabilities in structural assignment of small organic molecules, an Excel spreadsheet was made available as part of the supplementary information of the DP4+ publication.[79]

Although DP4-based methods offer new alternatives in structural assignment of natural product, both protocols start with gas conformational search which may not properly predict the conformational behaviour of flexible molecules, essentially when solvation has a big impact on the conformational behaviour. As Smith and Goodman pointed out, there are cases, such as the stereopentad **1.43**, where confident assignment of relative configuration is impossible solely based on chemical shifts.[77] Therefore, the analysis of other NMR parameters such as scalar coupling constants and NOE-distances, are required for the unequivocal determination of molecular structures.

Comparison using multiple NMR parameters (δ, *J* values and NOE-distances)

Butts and Bifulco *et al.* reported the use of both DFT-computed ^{13}C chemical shifts and quantitative NOE-distance analysis for the structural assignment of conicasterol F, which is a steroid isolated from marine sponge *Theonella swinhoei*.[80]

Two possible diastereomers **1.44** and **1.45** (Table 1.1) differing from the epoxy ring configuration were distinguished by quantitative NOE-distance analysis. Interproton distances of both diastereomers **1.44** and **1.45** were computed using DFT-optimised structures (mPW1PW91 6-31G(d)) and compared to the natural product NOE-distances derived from 1D-ROESY spectra. The goodness of fit was evaluated by mean absolute deviation (MAD), and it was found that diastereomer **1.45** fit better to the natural product data, with a MAD value of 3.0%, which correspond to approximately 0.1 Å. Therefore, diastereomer **1.45** was assigned to have the same relative configuration as the natural product. The NOE-distance derived configuration was further supported by the comparison of the calculated ^{13}C chemical shifts (mPW1PW91 6-31G(d,p)// mPW1PW91 6-31G(d)) of both diastereomer **1.44** and **1.45** with the natural product experimental data (MAD value of δ_C comparison for **1.45**: 0.8, Table 1.1).

Table 1.1: Comparison of NOE-distances and calculated chemical shifts of **1.44** and **1.45** to the natural product data.

	a	**b**
	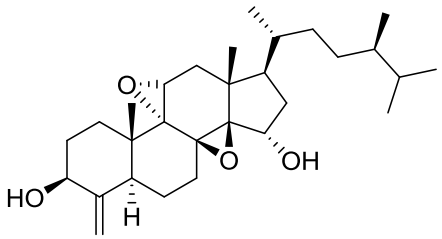 **1.44**	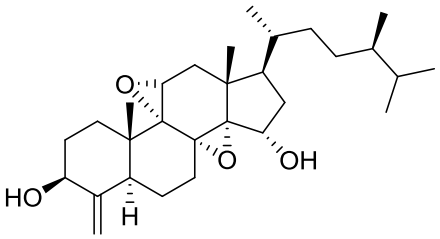 **1.45**
	MAD	MAD
NOE-distances	7.8%	3.0%
δ_C/ppm	3.7	0.8

The QM/NMR approach has also been applied to study molecular conformations of flexible molecules. Harvey and Butts *et al.* [8] demonstrated the application of QM/NMR approach for studying the conformational behaviour of molecules with 10 contiguous methyl substituents **1.9** and **1.10** (Figure 1.5).[8] As section 1.1 discussed, due to the avoidance of *syn*-pentane interactions the all *syn* isomer **1.9** was designed to adopt a linear conformation while the *syn-anti* isomer **1.10** was designed to adopt a helical conformation. The truncated version of both isomers **1.46** and **1.47** (Figure 1.31a) were studied computationally by conformational search using MM3 force field followed by DFT calculations (DF-LMP2-F12 VDZ-

F12//B3LYP-D2 6-311+G(d)). It was predicted that for isomer **1.46**, 95% of conformers adopt a linear conformation while for isomer **1.47**, 74% of conformers adopt a helical conformation. The DFT-predicted solution-state conformations for both compounds were confirmed by QM/NMR analysis using ^{1}H-^{1}H, ^{1}H-^{13}C scalar coupling constants and NOE-distances. For both compounds a good correlation was observed between the computed ensemble-averaged NMR parameters (mPW1PW91 6-311G(d,p)// B3LYP-D2 6-311+G(d)) and the experimental NMR data, with 1 Hz error in the comparison of *J* values and 5% error in the comparison of NOE-distances.[8]

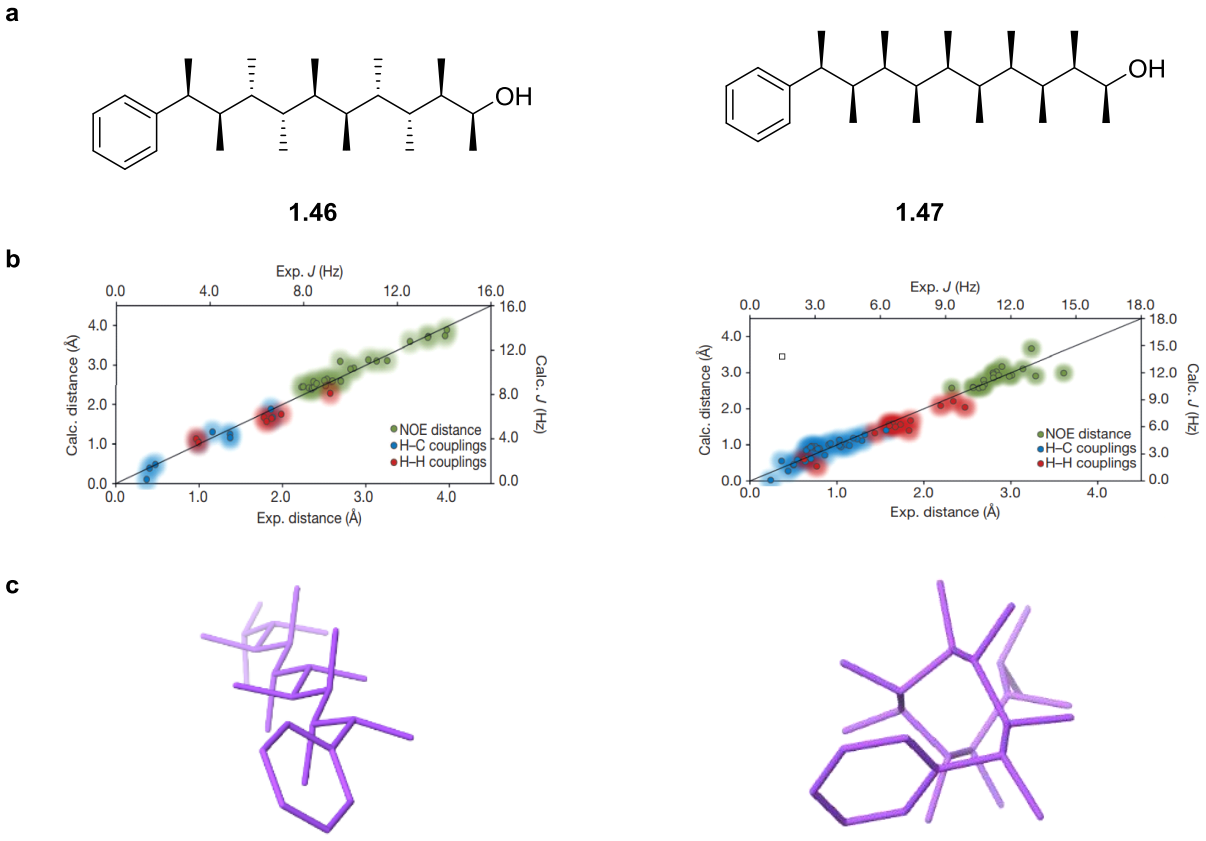

Figure 1.31: **a**, Chemical structure of the *syn-anti* isomer **1.46** and all-*syn* isomer **1.47**. **b**, correlation between the computed ensemble-averaged NMR data and the experimentally measured NMR data for both isomers. **c**, The lowest energy conformers of the *syn-anti* isomer **1.46** (left) and all-*syn* isomer **1.47** (right).

1.4 Synthesis of molecules with tailored conformations enabled by stereospecific iterative homologation of boronic esters.

With ever-increasing computing power and accuracy, the conformational behaviour of flexible small molecules can be routinely evaluated *in silico*, and their solution-state behaviour can be studied using a variety of NMR parameters discussed previously. However, one's ability to generate flexible small molecules with defined conformations is often limited, not only by one's understanding of conformational design, but also by the insufficient methods of stereoselective synthesis to create molecules with defined stereochemistry.

Organoboron chemistry is an attractive approach to stereoselective chemistry since there are numerous methods for their preparation in enantioenriched form, and they can be transformed to other functional groups with high stereospecificity.[81-82] Organoboron compounds, such as boranes (**1.48**, R^3 = alkyl groups) and boronic esters (**1.48**, R^3 = alkoxy groups) are electrophilic due to a vacant p-orbital on boron and can react with a nucleophile **1.49**, to form boronate complexes **1.50**, as a result of the donation of a pair of electrons from the nucleophile to the vacant p-orbital on boron (Scheme 1.1).[83] As a leaving group (LG, **1.49**) is present on the nucleophilic carbon, and if one of the substituents on boron can orientate itself antiperiplanar to the leaving group LG, a 1,2-metallate rearrangement can occur to give the homologated organoboron species **1.51**, with inversion of stereochemistry (Scheme 1.1).[83]

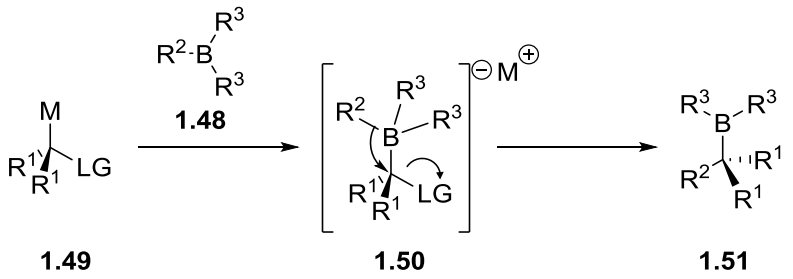

Scheme 1.1 Formation of a boronate complex followed by 1,2-metallate rearrangement.

Metal carbenoids are often used in the homologation of boronic esters and scheme 1.2 outlines some selected examples from the literature. Matteson developed a substrate-controlled strategy for the homologation of boronic esters.[84-89] In this method, boronic esters bearing a chiral diol ligand **1.52** were treated with dichloromethyl lithium in the presence of zinc chloride. The α-chloro boronic ester **1.53** could undergo further boronate complex formation with a Grignard reagent, then 1,2-rearrangement, to generate the homologated product **1.54**. Since the nature of the diol ligand on the boronic ester dictates the stereochemical outcome of the reaction,

the diol ligand needs to be exchanged to the opposite enantiomer to allow for generation of the opposite enantiomer of the homologated product. Rather than using (dichloromethyl)lithium as a homologating agent, Hoppe *et al.* demonstrated the use of chiral lithiated carbamates instead.[90] In this reagent-controlled approach, treatment of alkyl carbamate **1.55** with *sec*-butyllithium in the presence of a chiral diamine ligand such as (–)-sparteine, at –78 °C, gave an α-oxygen-stabilised organolithium **1.56**. This chiral, configurationally stable, organolithium carbenoid then reacted with B(O*i*Pr)$_3$, and the resulting boronic ester was transesterified, to give a chiral pinacol boronic ester **1.57**. This was then transformed to the homologated product **1.58** by the reaction with a Grignard reagent. Kocienski[91] and Aggarwal[83] developed the homologation of boronic esters in a single step, by the direct addition of a pinacol boronic ester to Hoppe's lithiated carbamates.

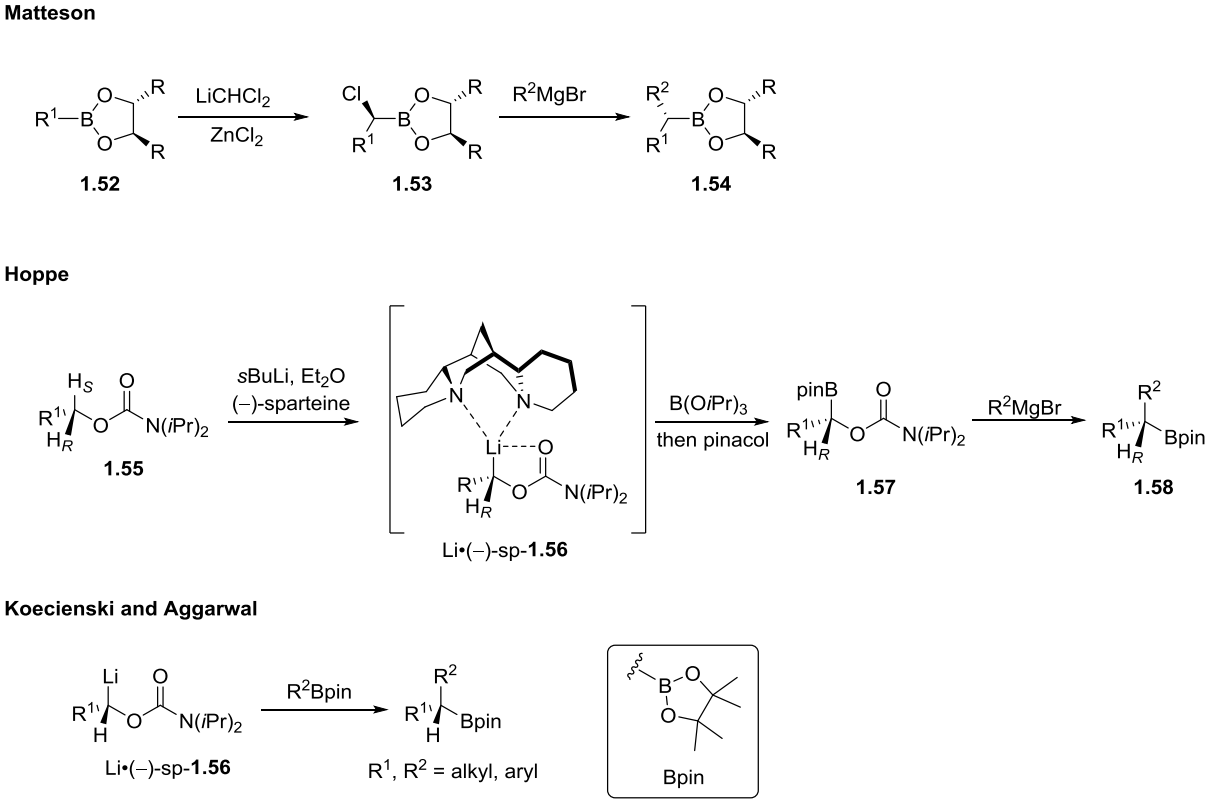

Scheme 1.2: Overview of homologations of boronic esters with lithium carbenoids.

The potential of performing iterative homologation using Hoppe's lithiated carbamates was investigated by the Aggarwal group (Scheme 1.3).[92] It was shown that triple homologation of boronic ester **1.59** with lithiated carbamate **1.56** gave boronic ester **1.62** in good yield over three steps (77%) and good *dr* (93.3:2.2). The homologation could be performed with either the isolation of each intermediate boronic ester (**1.60**, **1.61**, Scheme 1.3) or in an iterative fashion without column chromatographic purification between homologations.

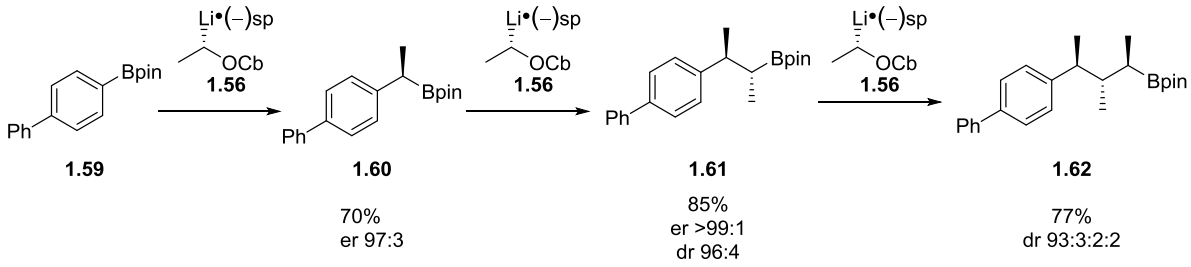

Scheme 1.3: Iterative homologation of boronic ester **1.59** with lithiated carbamate **1.56**.

However, further homologation of boronic ester **1.62** with lithiated carbamate **1.56** lead to the formation of a mixture of starting material **1.62**, desired product **1.63** and over homologated product **1.64** (Scheme 1.4a). A mechanism was proposed for this observation as scheme 1.4b illustrates. The lithiation–borylation of **1.62** with lithiated carbamate **1.56** gave boronate complex **1.65**, which generated the desired product **1.63** after 1,2-metallate rearrangement. However, if the 1,2-metallate rearrangement is slow, then the boronate complex **1.65** can reverse back to the lithiated carbamate **1.56**, which can react with product **1.63** again to generate the over homologated product **1.64**.

a

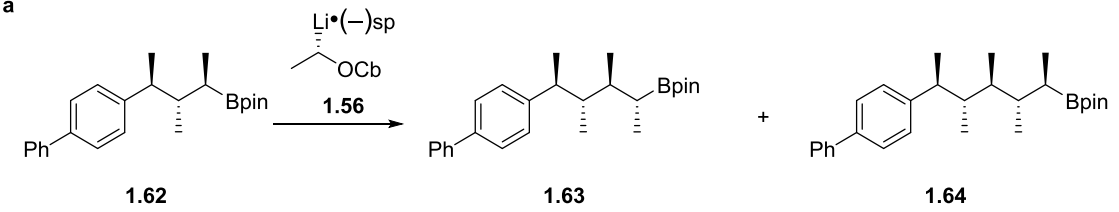

Product Distribution % (GC-MS)				
Entry	**1.62**	**1.63**	**1.64**	concentration
1	9	83.4	7.6	0.14M
2	7.4	84.1	7.5	0.05M

b

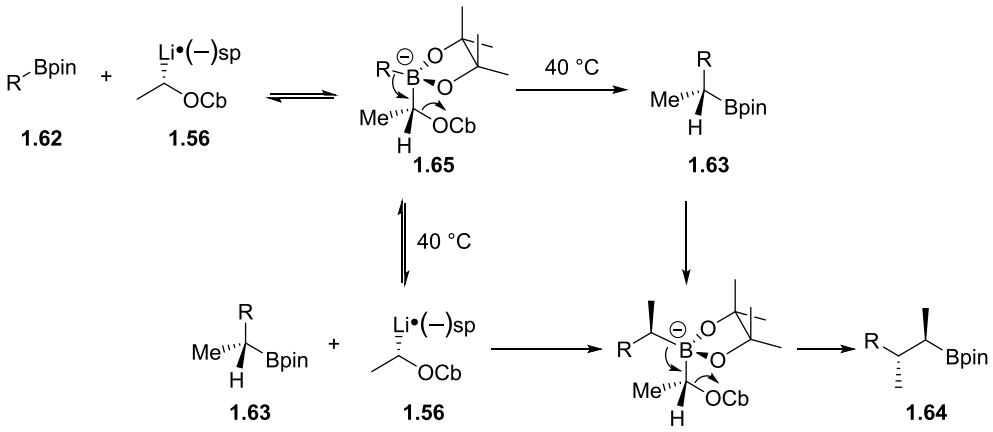

Scheme 1.4: **a**, Homologation of boronic ester **1.62** with lithiated carbamate **1.56**. **b**, Proposed mechanism for the formation of over homologated product **1.64**.

To overcome the problems associated with reversible 1,2-metallate rearrangement, the Aggarwal group demonstrated that another motif, the tri-isopropyl benzoate (TIB ester), developed by Beak *et al.*[93], could be used in place of carbamates. The TIB ester is a better leaving group so leads to a more facile 1,2-migration. In 2014, the Aggarwal group reported iterative homologations of boronic esters (assembly line synthesis) using α-lithioethyl tri-isopropyl benzoate to generate molecules with 10 contiguous methyl substituents with complete stereochemical control as scheme 1.5 illustrates.[8] To generate the lithiated species (*S*)-**1.67** in high er, ethyl tri-isopropylbenzoate **1.66** was lithiated in the presence of *sec*-BuLi and (−)- sparteine, which was trapped by trimethyltin chloride to give the α-stannyl benzoate (*S*)-**1.68** (91:9 er). The stannane (*S*)-**1.68** can be recrystalised to very high levels of enantiopurity (99.9:0.1 er). The subsequent tin–lithium exchange of this enantiomerically pure stannane (*S*)-**1.68** using *n*-BuLi is a convenient way to access the highly enantioenriched lithiated species (*S*)-**1.69**. The opposite enantiomer of the stannane could be prepared using the same procedure with (+)-sparteine instead. The enantiomerically enriched lithiated species (*S*)-

1.69 and (*R*)-**1.69** enabled the preparation of hydrocarbons with 10 contiguous methyl substituents (**1.70** and **1.71**) as single enantiomers and with only one column chromatography purification at the end of the homologation sequence. After further functionalisation of boronic ester **1.70** and **1.71**, **1.9** and **1.10** were obtained (Figure 1.4, section 1.1) and they were shown to adopt either linear or helical conformations as discussed previously (sections 1.1 and 1.3.3).[8]

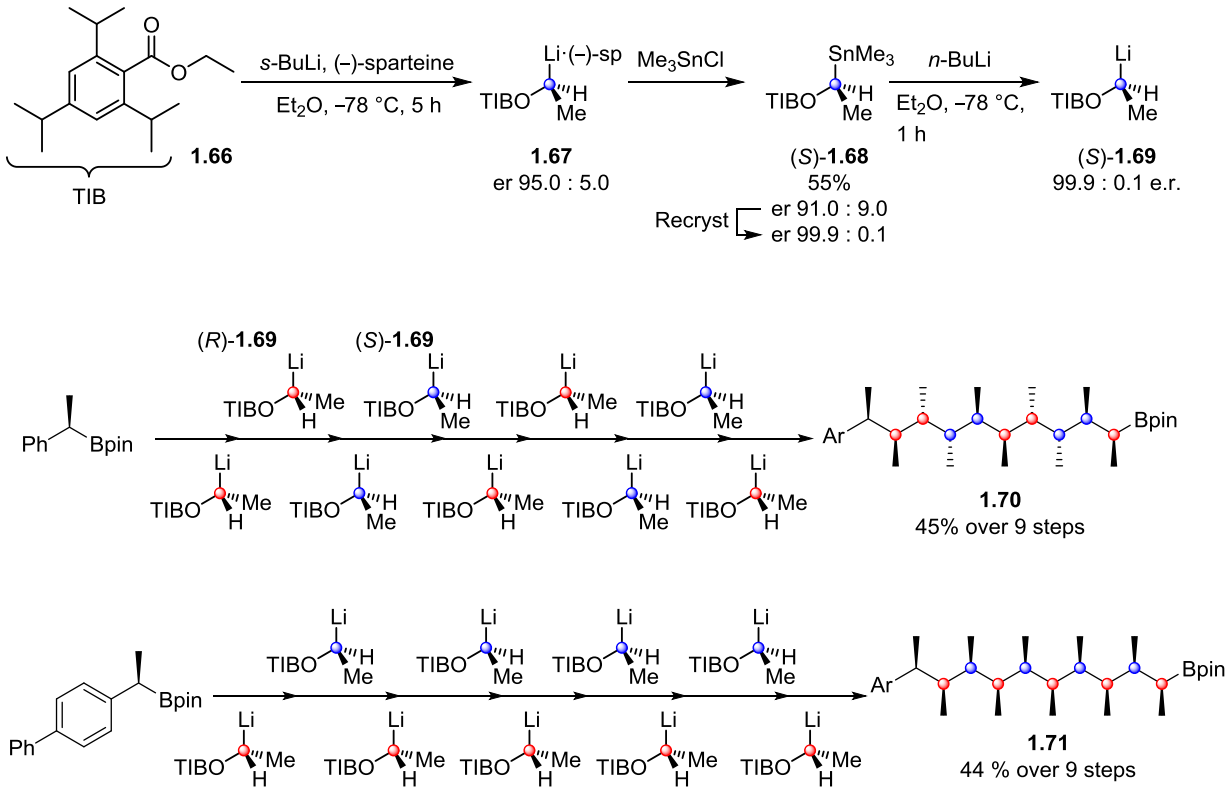

Scheme 1.5: Aggarwal's iterative homologation of boronic esters, referred to as the 'assembly-line synthesis'.

As matched and mismatched effects were not observed in this reagent-controlled strategy, the same methodology was applied to the total synthesis of two natural products (+)-kalkitoxin and (+)-hydroxyphthioceranic acid.[94] The fragments of both natural products were prepared with high stereocontrol and good yield. However, in the latter case, flash column chromatography was performed after every fourth homologation to ensure the efficiency of the assembly line process.

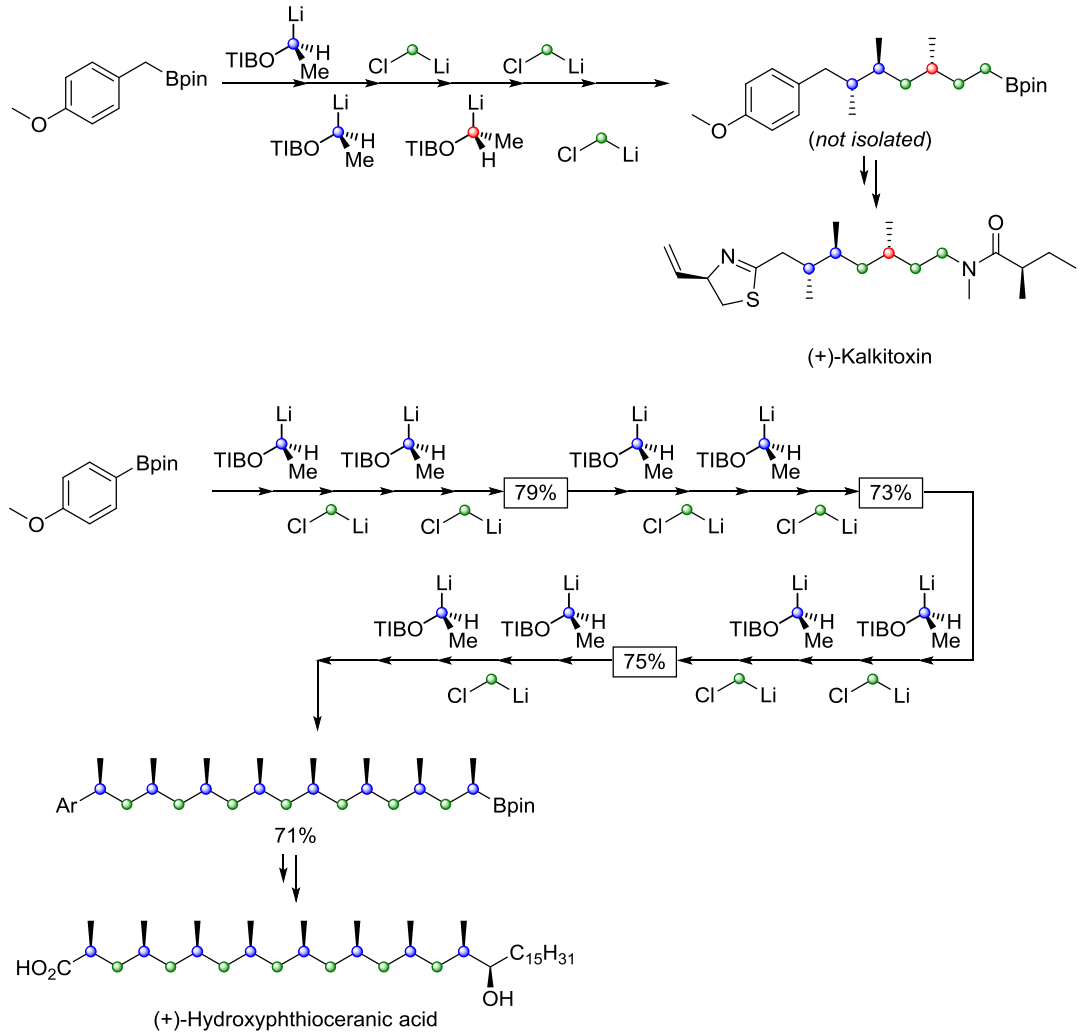

Scheme 1.6: Application of assembly line synthesis in total synthesis of natural products.

1.5 Conclusions

Conformational analysis of flexible small molecules is an interdisciplinary area of research. This requires chemists' understanding in stereoelectronic factors controlling molecular conformations, their ability to study the dynamic conformational behaviours of flexible molecules in solution using computational modelling and NMR spectroscopy, and their skills to synthesise molecules one have designed using advanced stereocontrolled synthetic methodology. The work described in this thesis aims at performing detailed conformational analysis of small flexible molecules using a combination of computational modelling, NMR spectroscopy and stereoselective iterative homologation of boronic esters. Conformational analysis was applied in the context of configurational assignment of highly flexible polyketide natural products (chapter 2), in the design and synthesis of molecules with defined conformations (chapter 3), and in the understanding of factors controlling helical screw-sense for the design of a new class of switchable helices (chapter 4).

Chapter 2 : The Synergy of Computational Modelling, NMR Spectroscopy and Synthesis to Elucidate the Correct Structure of Baulamycins

Parts of the work described in this chapter have been adapted from the following article:

Nature, **2017**, *547*, 436.

This project was conducted in collaboration with Dr. Jingjing Wu and Dr. Paula Lorenzo who have performed all the synthetic work. Parts of the synthetic work are included to provide a complete picture of the research.

2.1 Introduction

Baulamycin A and B were isolated in 2014 from *Streptomyces tempisquensis*, which was collected from sediments in Costa Rica.[95] They were shown to be active against both gram-positive and gram-negative bacteria and are active against superbug MRSA and *Bacillus anthracis* (IC_{50} values of baulamycin A: 130 μM and 110 μM). Two different modes of action of balamycin A in *Staphylococcus aureus* have been proposed: inhibition of siderophore synthesis[95] and membrane damage[96]. The unique biological activities of the baulamycins provide an opportunity for the development of a new class of broad-spectrum antibiotics to potentially help overcome the threat of antimicrobial resistance.

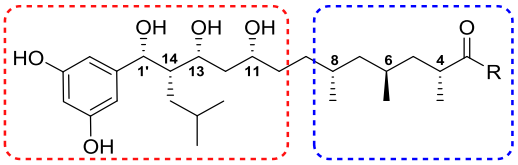

Baulamycin A: R = CH_2CH_3, **2.1**
Baulamycin B: R = CH_3

Figure 2.1: Sherman's proposed relative configuration of baulamycins with fragment A highlighted by a red box and fragment B highlighted by a blue box.

Due to their important biological activities, the Aggarwal group developed a 10-step enantioselective synthesis of the proposed structure of baulamycin A **2.1** (Figure 2.1). Unfortunately, both ^{1}H and ^{13}C spectra of the synthetic compound did not match those of the natural product (Figure 2.2). Further investigation of the literature reported spectra revealed that the connectivity of the molecules was correctly assigned. Thus at least one of the

stereogenic centres had been misassigned and re-evaluation of the relative configuration of the natural product was required.

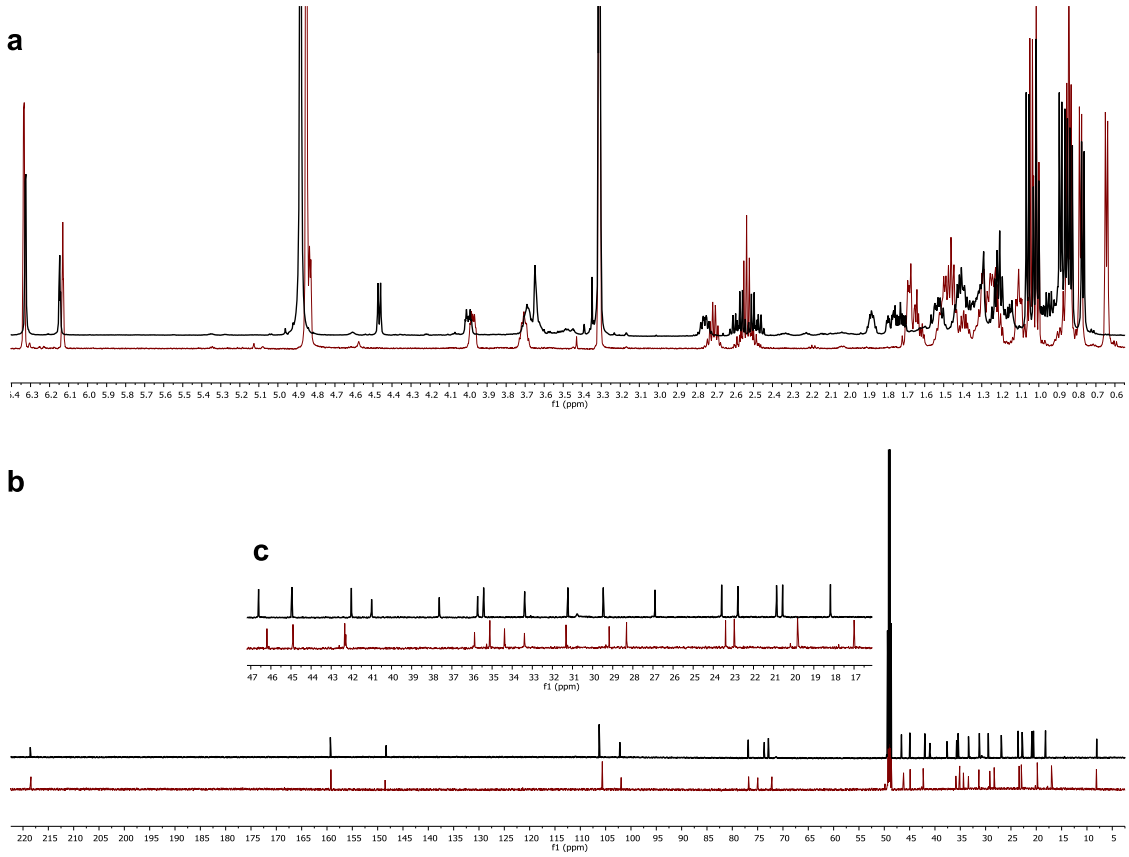

Figure 2.2: Comparison of **a**. ^{1}H NMR (CD_3OD, 500 MHz) and **b**. ^{13}C NMR (CD_3OD, 176 MHz) spectra of the synthetic proposed structure **2.1** (red) to that of the isolated baulamycin A (black). **c**. Zoom in of the ^{13}C NMR spectrum from 17 to 47 ppm.

In the original report, due to the limited availability of baulamycin A and B (3.6 mg and 2.1 mg, respectively), common structural elucidation techniques such as X-ray crystallography and chemical modification were precluded as means to gain stereochemical information of the natural product. Instead, the relative configuration of baulamycin A and B were elucidated entirely using *J*-based configurational analysis[45,95] (chapter 1, section 1.2.2).

Upon re-examination of Sherman *et al.*'s reported *J*-based configurational analysis[95], it was realised that the relative configuration of the natural product should be **2.2** (Figure 2.3b), with a *syn–syn–anti* configuration in fragment A and an *anti–syn* configuration in fragment B. During our investigation, Guchhait *et al.* reported a 17-step synthesis of **2.1** and also found that the data of **2.1** did not match that of the natural product. Their re-examination of the literature reported *J*-based configurational analysis also concluded that **2.2** was more appropriate. After

preparing **2.2**, they found that the experimental NMR data of **2.2** also did not match that of the natural product.[97]

A limitation of *J*-based configurational analysis is that it does not fully account for molecular flexibility and conformer stability, conformational analysis of each bond in isolation can lead to a molecular conformation which is highly energetically unfavourable. To illustrate this point, a 3D model of compound **2.2** was constructed using the Sherman proposed *J*-based configurational analysis.[95] In this model (Figure 2.3c), there are five *syn*-pentane interactions, each bearing an enthalpic penalty of 3.5 kcal mol^{-1} (Figure 2.3d). As a result, the literature proposed conformation has 17.5 kcal mol^{-1} (5 × 3.5 kcal mol^{-1}) of destabilising *syn*-pentane interactions, making this conformation inaccessible at room temperature. Therefore, it should not be observable using room temperature NMR experiments. Simply, **2.2** requires an impossible conformation in order to satisfy the experimentally observed natural product NMR data.

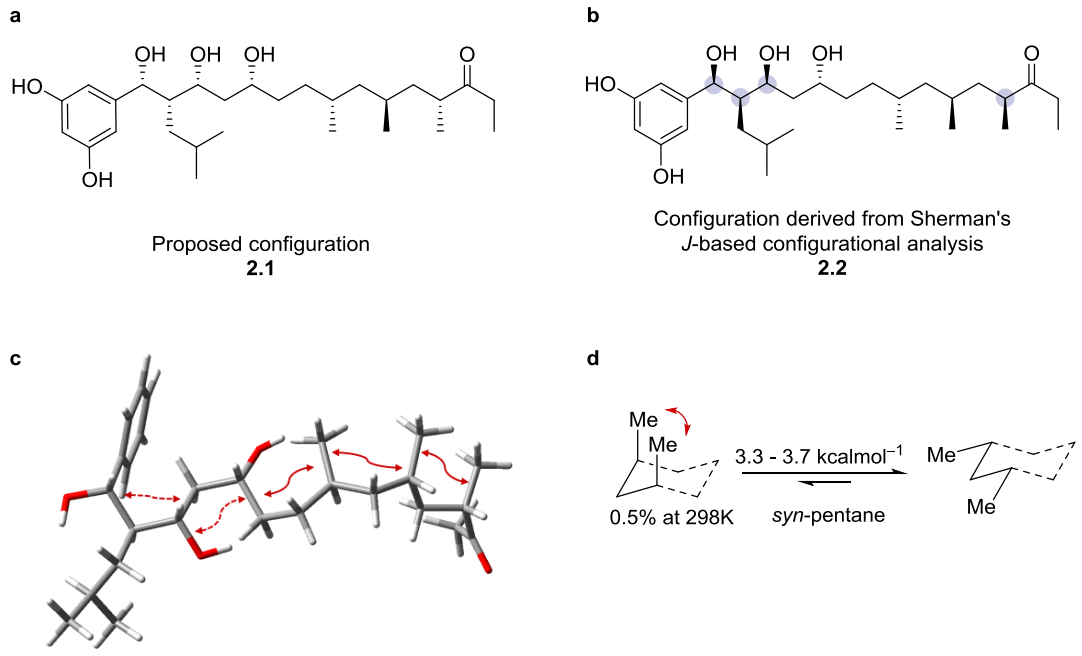

Figure 2.3: Literature proposed relative configurations of baulamycins and the limitation of *J*-based configurational analysis. **a**, Proposed structure (**2.1**) of baulamycin A. **b**, A diastereomer (**2.2**) of baulamycin A derived from the literature reported *J*-based configurational analysis with purple dots highlighting the revised stereocentres. **c**, A 3D conformation **2.2** proposed by Sherman[95] with red arrows highlighting unfavourable *syn*-pentane type steric interactions. Arrows with a dotted line highlight steric clash between an sp^2 and an sp^3 centre, and arrows with a solid line highlight steric clash between two sp^3 centres. **d**, Schematic representation of a *syn*-pentane interaction.

After the construction of the 3D model of **2.2** and thorough examination of both the PDF NMR spectrum and the original raw NMR data provided by David Sherman *et al.*, we realised that several published *J* values were incorrectly reported, meaning inaccurate values were used in the original *J*-based configurational analysis. For example, the vicinal coupling constant between H14 and H13 was reported to be a large value (7.7 Hz). The magnitude of the reported coupling constants, together with interproton correlations observed in the ROESY spectrum, led to the conclusion that the stereochemistry of the C14-C13 bond is *syn*.[95] However, the re-examination of the ^{1}H NMR spectrum of the natural product revealed that the vicinal coupling constant between H14 and H13 should be 3.3 Hz, which is substantially smaller than the originally reported value (7.7 Hz).

Taking the freshly extracted *J* values from Sherman's raw NMR data, a new qualitative analysis was undertaken for the C1'-C14 and C14-C13 configurational assignment. In the Sherman reported configurational analysis of the C1'-C14 bond, H1' and H14 were assigned to be anti-periplanar because a large vicinal coupling constant (6.8 Hz) was observed. Rotamer **2.3** (from the *syn* configuration, Figure 2.4b) fits with this H1-H14 coupling. Together with the NOE correlations observed between the aromatic protons (attached to C2') and H13, H13 and H1', and H1' and H15, the configuration of the C1'-C14 bond was assigned to be *syn* (Figure 2.4b).[95]

However, rotamer **2.4** (from the *anti* configuration, Figure 2.4g) also matches the magnitude of the natural product *J* values and lacks only a key NOE correlation between the aromatic protons (attached to C2') and H13. The lacking NOE correlation could be provided by rotamer **2.5**, which could be generated from bond-rotation of **2.4**. Providing that rotamer **2.5** is a minor conformation (<10% of global population), the magnitude of the Boltzmann averaged *J* values of rotamers **2.4** and **2.5** would be represented by rotamer **2.4**, while both rotamers would contribute to the observed NOE correlations since the experimentally observed NOE signals are very sensitive to minor conformers (<10% population) with close interproton contacts[54]. Therefore, the *anti* configuration could also provide matching NMR data to the experimentally observed natural product data. A qualitative analysis, therefore, could not unequivocally determine the configuration of the C1'-C14 bond. A quantitative analysis is thus required to determine whether the predicted NMR data of the *syn* or the *anti* configuration fits better to the natural product experimental data.

a

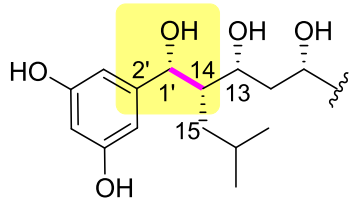

Literature proposed configuration

d

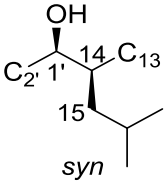

syn

f

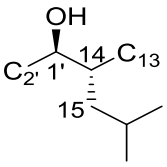

anti

b

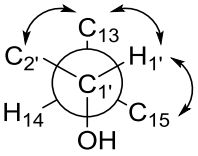

Sherman's proposed conformation

$H_{1'}$-H_{14} anti-periplanar

(from *syn*)

2.3

g

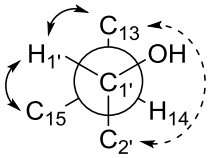

$H_{1'}$-H_{14} anti-periplanar

(from *anti*)

2.4

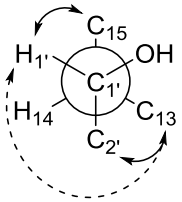

$H_{1'}$-H_{14} *gauche*

(from *anti*)

2.5

c

e Size of expected *J* values

$^{n}J_{HX}$	*J* values (size)	**2.3**	**2.4**		**2.5**
$^{3}J_{H1'\text{-}H14}$	6.8 Hz (large)	Large √	Large √		Small ×
$^{3}J_{H1'\text{-}C15}$	2.3 Hz (small)	Small √	Small √		Small ×
$^{3}J_{H1'\text{-}C13}$	4.3 Hz (small)	Small √	Small √		Large ×
$^{2}J_{H14\text{-}C1'}$	4.9 Hz (large)	Large √	Large √		Small ×

Figure 2.4: *J*-based configurational analysis of the C1'-C14 bond of baulamycins. **a**, Proposed configuration[95] of fragment A of baulamycins, highlighting the bond of interest (C1'-C14) in pink; **b**, Conformation proposed by Sherman[95], represented by a Newman projection with solid arrows indicating interproton NOE correlations observed in the natural product 2D ROESY spectrum; **c** *J* values (^{1}H-^{1}H and ^{1}H-^{13}C) of the natural product extracted from the ^{1}H spectrum provided by Sherman *et al.*[95] and an Accordion HSQMBC spectrum recorded using the synthetic baulamycin A; **d**, 2D structure of the *syn* configuration of the C1'-C14 bond, together with **e**, expected magnitude of *J* values of rotamer **2.3**; **f**, 2D structure of the *anti* configuration of the C1'-C14 bond; **g**, Newman projections of the *anti* configuration with H1'-H14 *trans* (**2.4**) and *gauche* (**2.5**) to each other, together with **e**, the expected magnitude of *J* values for each rotamer. A green tick represents a match in magnitude between the expected *J* values of the rotamer and the experimentally observed natural product data, while a red cross represents a mismatch in the magnitude of *J* values. Solid arrows in **b** and **g** represent matching interproton NOE correlations to the experimentally observed natural product data, while the dotted arrows indicate the 'missing' NOE correlations.

Secondly, when several conformations are in equilibrium it is challenging to estimate the magnitude of the expected *J* values for a given configuration, which hampers the accuracy of *J*-based configurational analysis. As figure 2.5 outlines, no single rotamer of the C14-C13 bond from either the *syn* or *anti* configuration provides the matching magnitude of *J* values to the natural product data, and the mismatched magnitude of *J* values suggests that neither rotamer is the major conformation. Therefore, the configuration of the C14-C13 bond could not be assigned using *J*-based configurational analysis. The same limitation was also observed by Paloma *et al.* for the configurational analysis of sapinofuranone A.[98]

a

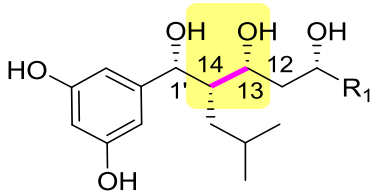

Literature proposed configuration

d

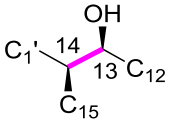

syn

f

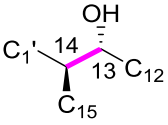

anti

b

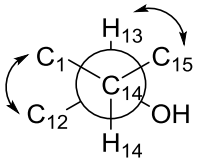

Literature proposed conformation based on inaccurate $^{3}J_{H14\text{-}H13}$

e

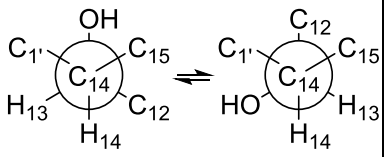

g

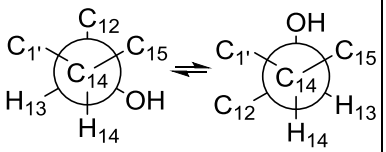

c

$^{n}J_{HX}$	*J* values (size)	Size of expected *J* values of each rotamer			
$^{3}J_{H13\text{-}H14}$	3.3 Hz (small)	Small √	Small √	Small √	Small √
$^{3}J_{H13\text{-}C1'}$	2.8 Hz (small)	Small √	Large ×	Small √	Large ×
$^{3}J_{H14\text{-}C12}$	3.8 Hz (small)	Small √	Large ×	Large×	Small √
$^{2}J_{H14\text{-}C13}$	5.0 Hz (large)	Small ×	Large √	Large √	Small ×

Figure 2.5: *J*-based configurational analysis of C14-C13 dihedral of baulamycins. **a**, Proposed configuration[95] of fragment A of baulamycins, highlighting the bond of interest (C14-C13) in pink; **b**, Conformation proposed by Sherman[95], represented by a Newman projection with solid arrows indicating interproton NOE correlations observed in the natural product 2D ROESY spectrum; **c**, *J* values (^{1}H-^{1}H and ^{1}H-^{13}C) of the natural product extracted from the ^{1}H spectrum provided by Sherman *et al.*[95] and an Accordion HSQMBC spectrum recorded using synthetic baulamycin A; **d**, 2D structure

of the *syn* configuration of the C14-C13 bond; **e**, Newman projections of the *syn* configuration with H14-H13 *gauche* to each other and the expected magnitude of *J* values for this rotamer; **f**, 2D structure of the *anti* configuration of the C14-C13 bond; and **g**, Newman projection of the *anti* configuration with H14-H13 *gauche* to each other, together with the expected magnitude of *J* values for each rotamer. A green tick represents a match in magnitude between the expected *J* values of the rotamer to the experimentally observed natural product data, while a red cross represents a mismatch in the magnitude of *J* values.

The key to achieving a reliable configurational analysis of flexible small molecules is to predict accurate NMR parameters of a given configuration of the molecule, and to quantitatively compare the calculated data with the experimentally measured data (QM/NMR approach, section 1.3). To obtain an accurate prediction of the Boltzmann averaged NMR data of a given configuration, quantum mechanics calculations could be employed to calculate the energies of all conformers, as well as to predict the Boltzmann averaged NMR parameters.[46,99] The comparison between the calculated Boltzmann averaged NMR data of different diastereomers and the natural product experimental data provides a quantitative assessment of the goodness of fit, which would then allow an unequivocal determination of the relative configuration of the natural product.

2.2 Results and Discussion

2.2.1 Validation study: Calculation of the proposed structure 2.1/2.6.

It will be challenging to model the conformational landscape of the baulamycins due to their flexible nature. Therefore, to establish whether the Boltzmann averaged calculated NMR properties would accurately describe the experimental coupling constants of a given diastereoisomer, NMR properties of the Sherman proposed structure with a phenyl and a methyl ketone end groups (**2.6**, Figure 2.6b) were calculated and compared to the experimental values of the corresponding synthetic product **2.1** prepared by Dr Jingjing Wu and Dr. Paula Lorenzo.

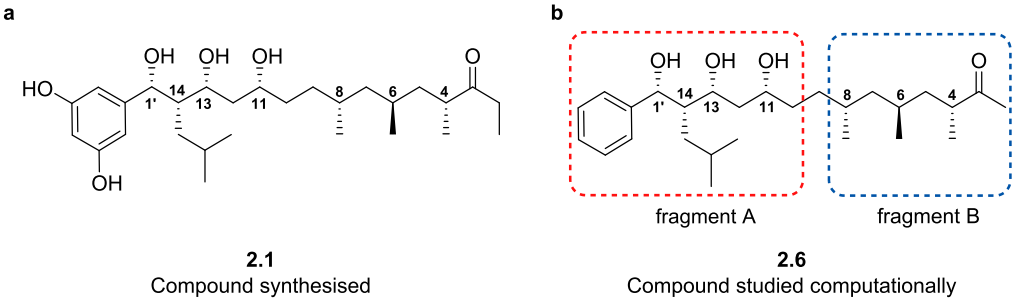

Figure 2.6. Structure of **2.1/2.6** with atom labels.

Conformational search of **2.6** using molecular mechanics (MM) with MMFFs forcefield[100] with 500,000 iterations in gas phase generated 2086 conformations. Conformers which have the same backbone conformation but differ in the rotation of phenyl, hydroxyl and isopropyl groups were treated as the same conformation (see experimental section for details). After redundant conformer elimination, 1674 conformers remained and 98 of these conformers had a potential energy within 10 kJ mol^{-1} of the global minimum. These 98 conformers, together with another 98 higher energy conformers randomly selected from the remaining pool (10-21 kJ mol^{-1}), were then reoptimised by Density Functional Theory (DFT) using mPW1PW91 functional and 6-31G (d) basis set in gas phase. To confirm that all 196 conformers were local minima after the DFT geometry optimisation calculations, frequency calculations were performed using the same DFT methods and the Gibbs free energies of all conformers were computed.

No significant conformational change was observed in this process. However, the relative energy of conformers changed dramatically upon going from MM to DFT calculations. For example, conformer **2.6**-5, which has a relative MM potential energy of 19.9 kJ mol^{-1} above the global minimum, became one of the low energy conformers (with $\Delta G^{BS1,\,gas}$ = 5.6 kJ

mol^{-1}, Table 2.1) after DFT geometry optimisation and frequency calculations, and ultimately was identified as the dominant conformer (30.1%) after single point calculation at a higher basis set (6-311G (d,p)) and solvation correction (the Integral Equation Formalism Polarizable Continuum Model (IEF-PCM) continuum dielectric solvation model using methanol) by single point calculations. After single point calculations, Boltzmann population analysis was performed using the approximate DFT–calculated relative Gibbs free energies ($\Delta G_{est}^{\mathrm{BS2,MeOH}}$, see equation 6.1 in experimental section) and it was found that the six lowest energy conformers have a combined population of 85.8%.

Table 2.1 DFT calculated energies (in kJ mol^{-1}) for the major conformers of **2.6** with a combined population of 85.8% with no population refinement.

Conformer	$\Delta E^{\mathrm{MMFFs,\ gas}}$	**Population(%)/** $E^{\mathrm{MMFFs,\ gas}}$	$\Delta G^{\mathrm{BS1,gas}}$	$\Delta G_{\mathrm{est.}}^{\mathrm{BS2,MeOH}}$	**Population(%)/** $\Delta G_{\mathrm{est.}}^{\mathrm{BS2,MeOH}}$
2.6-5	19.9	0.003%	5.6	0.0	30.1%
2.6-8	16.4	0.011%	3.4	0.7	22.3%
2.6-11	18.4	0.005%	6.5	1.3	17.8%
2.6-18	18.6	0.005%	9.9	3.6	7.1%
2.6-20	4.8	1.200%	0.0	4.4	5.1%
2.6-25	20.9	0.002%	12.8	5.4	3.4%

Conformers with intramolecular hydrogen bonding interactions between the three hydroxyl groups in fragment A dominate the DFT-determined conformations of this fragment (Figure 2.7), which is consistent with the molecular dynamics studies reported for the Sherman proposed structure **2.1**.[97] The six lowest energy conformers were then subjected to geometry reoptimisation using a larger basis set (6-311 G (d,p)) with methanol as implicit solvent and the NMR properties were calculated. Due to spectral overlap, it was challenging to extract accurate ^{1}H-^{1}H and ^{1}H-^{13}C coupling constants along the backbone for fragment B (C8-C4 region, Figure 2.6b), therefore in the validation study only the comparison of the NMR properties for fragment A (C1'-C10 region, Figure 2.6b) was investigated.

	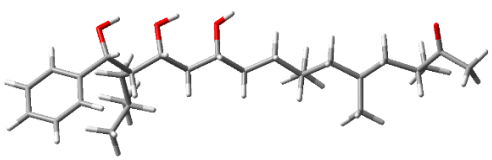	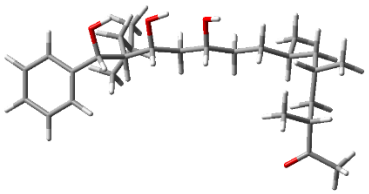
	2.6-5	**2.6**-8
$\Delta\Delta G_{est}^{BS2,MeOH}$	0.0	0.7
Population%	30.1%	22.3%
	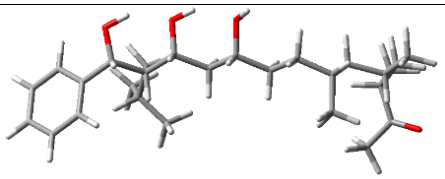	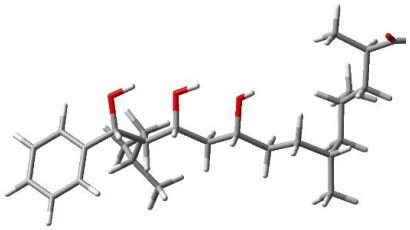
	2.6-11	**2.6**-18
$\Delta\Delta G_{est}^{BS2,MeOH}$	1.3	3.6
Population%	17.8%	7.1%
	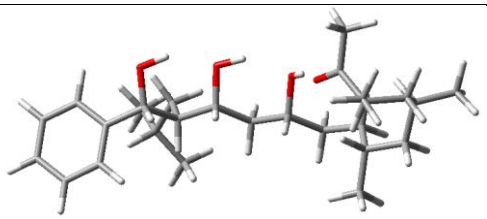	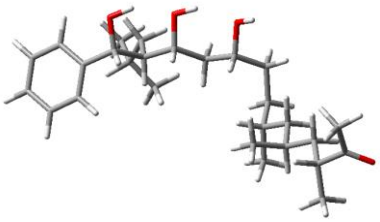
	2.6-20	**2.6**-25
$\Delta\Delta G_{est}^{BS2,MeOH}$	4.4	5.4
Population%	5.1%	3.4%

Figure 2.7. Selected conformers of **2.6** for NMR calculation.

All experimental natural product NMR data were re-extracted from the NMR spectrum provided by Sherman *et al.* to provide high accuracy (error of δ < 0.01 ppm and error of J < 0.5 Hz) experimental data for use in the quantitative comparison.

A good fit for the 'matched comparison' was observed between the calculated Boltzmann averaged ^{1}H-^{1}H coupling constants of **2.6** and the experimental data measured from the corresponding synthetic compound **2.1**, with both mean absolute deviation (MAD) and standard deviation (StDev) around 1.4 Hz (Table 2.2).

Table 2.2: Comparison of the calculated Boltzmann averaged $^{n}J_{HH}$ of **2.6** and the experimental ^{1}H-^{1}H scalar coupling constants of the C1'-C10 region for both synthetic **2.6** and baulamycin A with Mean Absolute Deviations (MAD, in Hz) and Standard Deviations (StDev, in Hz).

H	Hx	Calc. $^{n}J_{HH}$ of 2.6 /Hz	Exp. $^{n}J_{HH}$ of 2.6 /Hz	Deviation from 2.6	Exp. $^{n}J_{HH}$ of Baulamycin A /Hz	Deviation from Baulamycin A /Hz
$H_{1'}$	H_{14}	1.8	3.7	–1.9	6.8	–5.0
H_{14}	H_{13}	2.2	3.6	–1.4	3.5	–1.3
H_{13}	H_{12a}	1.1	3.6	–2.5	3.2	–2.1
	H_{12b}	9.1	9.1	0.0	10.0	–1.0
H_{12a}	H_{12b}	14.6	14.1	0.5	14.1	0.5
	H_{11}	2.2	4.3	–2.1	4.5	–2.3
H_{12b}	H_{11}	9.6	9.1	0.5	8	1.6
H_{11}	H_{10a}	2.1	4.3	–2.2	4.3	–2.2
	H_{10b}	9.1	8	1.1	8.0	1.2
			MAD	1.4	**MAD**	1.9
			StDev	1.4	**StDev**	2.0

Slightly larger values of MAD and StDev (1.9 and 2.0 respectively, Table 2.2) were observed when the calculated coupling constants of **2.6** were compared to the natural product experimental data, indicating a less good fit for the 'mismatched comparison'. Although the calculated value of H1'-H14 substantially deviates from that of the natural product (−5 Hz, Table 2.2), which suggests that **2.6** is unlikely to possess the stereochemistry of the natural product, the MAD value of the mismatched comparison only increased by 0.5 Hz. The impact of the large deviation was 'diluted' in the MAD-based comparison in which the absolute values of deviations were simply averaged. In order to give large deviations a higher weighting, the deviations were squared prior to averaging and the goodness of fit for all NMR parameters was evaluated by a statistical analysis using χ^2 (reduced) values, where an acceptable model must have a value approaching 1. The χ^2 (reduced) values can be calculated using equations 2.1 and 2.2

$$\chi^2 = \sum \frac{(a_{cal}^i - a_{exp}^i)^2}{\sigma^2} \qquad \textbf{Equation 2.1}$$

$$\chi^2(reduced) = \frac{\chi^2}{n-m} \qquad \textbf{Equation 2.2}$$

where a_{cal}^i is the Boltzmann averaged calculated NMR parameters (^{1}H or ^{13}C chemical shifts, *J* couplings, NOE-derived distances in flexible molecules), a_{exp}^i is the experimentally measured value, and σ^2 is the square of the expected standard deviation of the NMR parameter compared. As χ^2 values scale with the number of deviations used to calculate them, χ^2 (reduced) values were used to evaluate the overall quality of any model, where *n* is the number of

deviations used to calculate the χ^2 value, and *m* is the number of parameters fitted. A list of values of *n* and *m* used for this study can be found in table 6.1 in the experimental section.

Although there are no systematic studies reported for the expected standard deviation of NMR parameters (chemical shifts, *J* values and NOE-derived distances), one could define sensible values for the expected standard deviations (Table 2.3) based on related studies and Butts group in-house knowledge.

Table 2.3: A summary of estimated standard deviations for comparison between computed and experimental chemical shifts, scalar coupling constants and ^{1}H-^{1}H distances

NMR properties	Typical standard deviations
δ_H	0.15 ppm[77,79]
δ_C	1.5 ppm[79]
$^nJ_{HX}$ (X=H or C)	1 Hz [44]
r_{noe}	5%[101]

The χ^2 (reduced) values for both the matched and mismatched comparison for all calculated Boltzmann averaged NMR parameters (δ_H, δ_C, ^{1}H-^{1}H and ^{1}H-^{13}C scalar coupling constants) are shown in Figure 2.8. Unlike the MAD-based comparison (Table 2.2), χ^2 (reduced) values are more discriminating in the comparison of ^{1}H-^{1}H coupling constants (2.8 for the matched and 5.7 for the mismatched comparison, Figure 2.8), and therefore this statistical analysis was also applied to the comparison of other NMR parameters (δ_H, δ_C, and ^{1}H-^{13}C scalar coupling constants).

The calculated NMR parameters for fragment A (C1'-C10 region) of **2.6** are in moderate agreement with the experimental values of the synthetic compound **2.1** (χ^2(reduced) = 2.1, 1.0, 2.8 and 1.0 for comparison of δ_H, δ_C, ^{1}H-^{1}H and ^{1}H-^{13}C scalar coupling constants, respectively). However, χ^2(reduced) values for both δ_H and ^{1}H-^{1}H scalar coupling constants comparisons deviate substantially from the ideal value of 1. The poorer fit suggests that the conformer population derived from approximate DFT-calculated energies might not be accurate enough to describe the experimental chemical shifts and scalar coupling constants perfectly. In order to examine the accuracy of DFT energy derived conformer populations, quantitative NOE-distance analysis is required because the ensemble-averaged interproton distances are very sensitive to both conformer population and interproton distances (Chapter 1, section 1.2.3). Unfortunately, spectral overlap precluded the determination of ^{1}H-^{1}H distances

of compound **2.1** and thus it was not viable to probe the accuracy of the DFT-approximate conformer population on this validation system.

a) Matched comparison: **2.6** vs **2.1** b) Mismatched comparison: **2.6** to baulamycin A

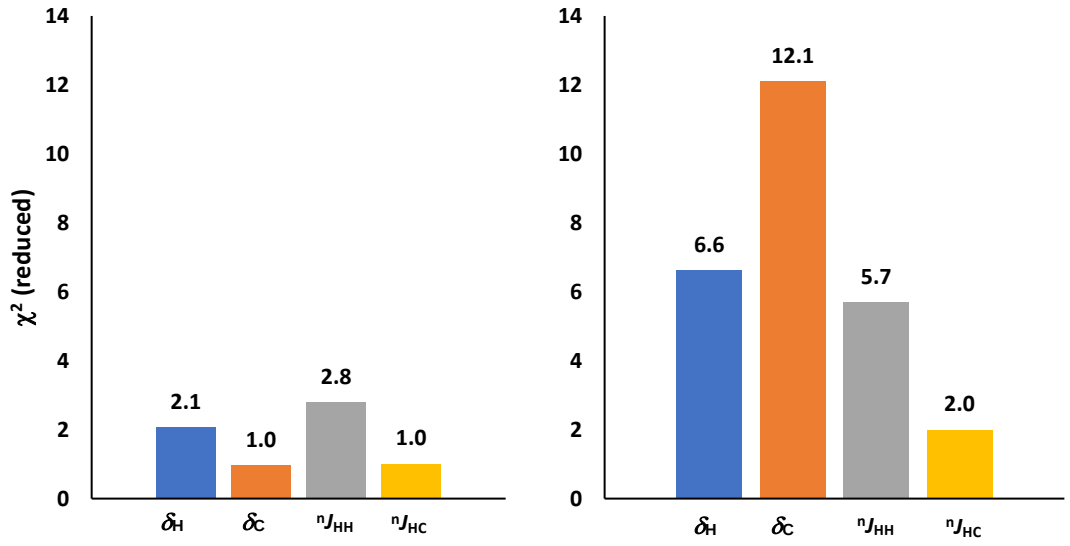

Figure 2.8. The fit for fragment A (C1'-C10) NMR parameters of diastereomer **2.6** to the **a** experimental data obtained from the corresponding synthetic compound **2.6** and to the **b** experimental data of the isolated natural product evaluated by χ^2 analysis without population refinement.

In contrast, the calculated NMR properties of Sherman's originally proposed **2.6** provides a very poor fit to the experimental data of baulamycins (χ^2(reduced) = 6.6, 12.1 and 5.7 for comparison of δ_H, δ_C, ^{1}H-^{1}H and ^{1}H-^{13}C scalar coupling constants, respectively). This suggests that one could indeed identify the relative stereochemistry of baulamycins by the comparison of the computed NMR properties of diastereomers of interest to the experimental data of the natural product.

Baulamycins contains seven stereogenic centres, which give rise to 128 possible stereoisomers. It is clearly not practical to synthesise all possible stereoisomers. Therefore, the QM/NMR hybrid approach (Chapter 1, section 1.3.4) will be applied to elucidate the relative configuration of baulamycins. First, conformational analysis will be performed using computational modeling on potential diastereomers of the natural product. The ensemble-averaged NMR properties including ^{1}H and ^{13}C chemical shifts, ^{1}H-^{1}H and ^{1}H-^{13}C scalar coupling constants, and ^{1}H-^{1}H distances of the potential isomer, will then be computed. Finally, comparison of the computed NMR properties of a given candidate and the experimental values

of the isolated natural product re-extracted from the spectrum provided by Sherman *et al.*[95] will allow the unequivocal determination of the relative configuration of baulamycins.

In order to reduce the number of isomers to be studied computationally, the molecule was considered in two halves (Figure 2.9a), fragment A (C1'-C10 region) and fragment B (C8-C4 region) which were assumed to behave independently. The configuration of fragment A was first considered. By comparing the observed coupling constants of the vicinal protons of C1'-C14 in the synthetic proposed structure **2.1** ($^3J_{H1'-H14}$ = 3.5 Hz) to that of the natural product ($^3J_{H1'-H14}$ = 6.8 Hz)[95], we hypothesised that the originally proposed *syn* relationship between C1' and C14 is more likely to be *anti* because of the large coupling constants observed, which is consistent with reports for related secondary benzylic alcohols ($^3J_{HH}$ = 6.4 to 9.2 Hz, Figure 2.9c).

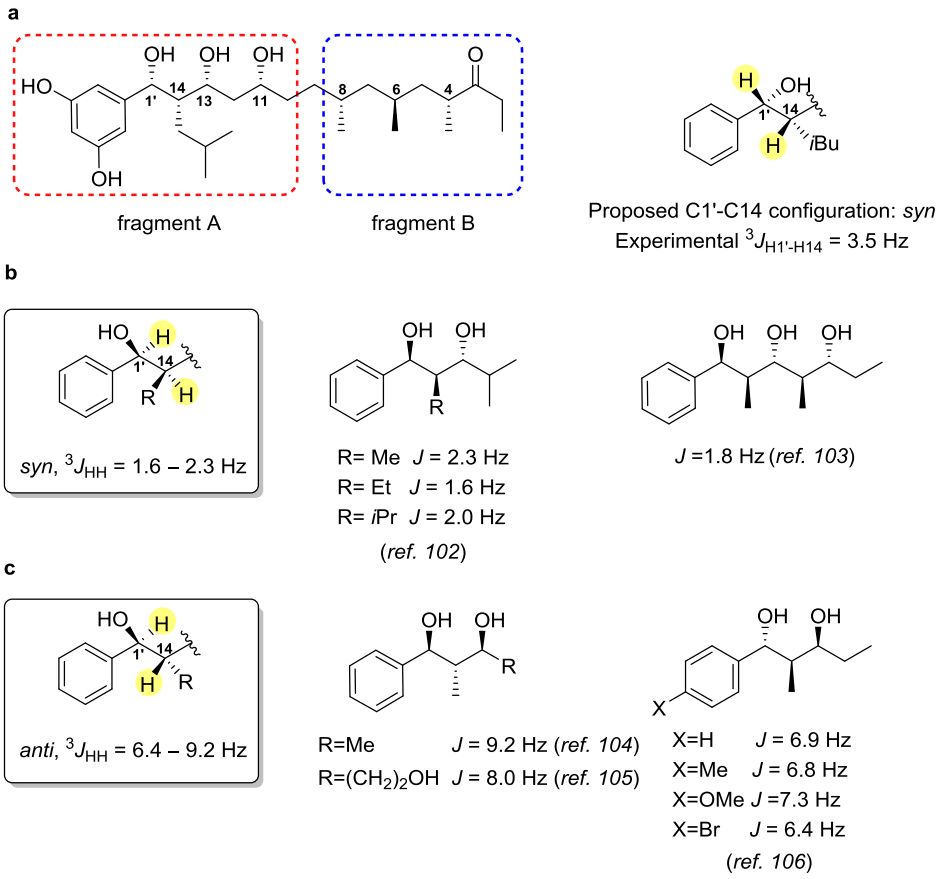

Figure 2.9: Coupling constants $^3J_{HH}$ reported for structurally related secondary benzyl alcohols with *syn* and *anti* configuration. **a**, Sherman's proposed configuration and the experimental $^3J_{H1'-H14.}$ **b**, 1,3-diols with *syn* configuration show small values for the corresponding coupling constants, $^3J_{HH}$ (~1.6 – 2.3 Hz).[102-103] **c**, 1,3-diols with *anti* configuration show large values for the corresponding coupling constants, $^3J_{HH}$ (~6.4 – 9.2 Hz). [104-106]

Therefore, the relative configuration of C1' and C14 was set as *anti*. The NMR properties of the four diastereomers (Figure 2.10b) which arise from the variation of the stereochemistry of the hydroxyl groups at C13 and C11 will be studied with Sherman's proposed fragment B configuration. The computationally derived fragment A will then be incorporated into all four variations of fragment B (Figure 2.10d) in a subsequent analysis of fragment B's configuration.

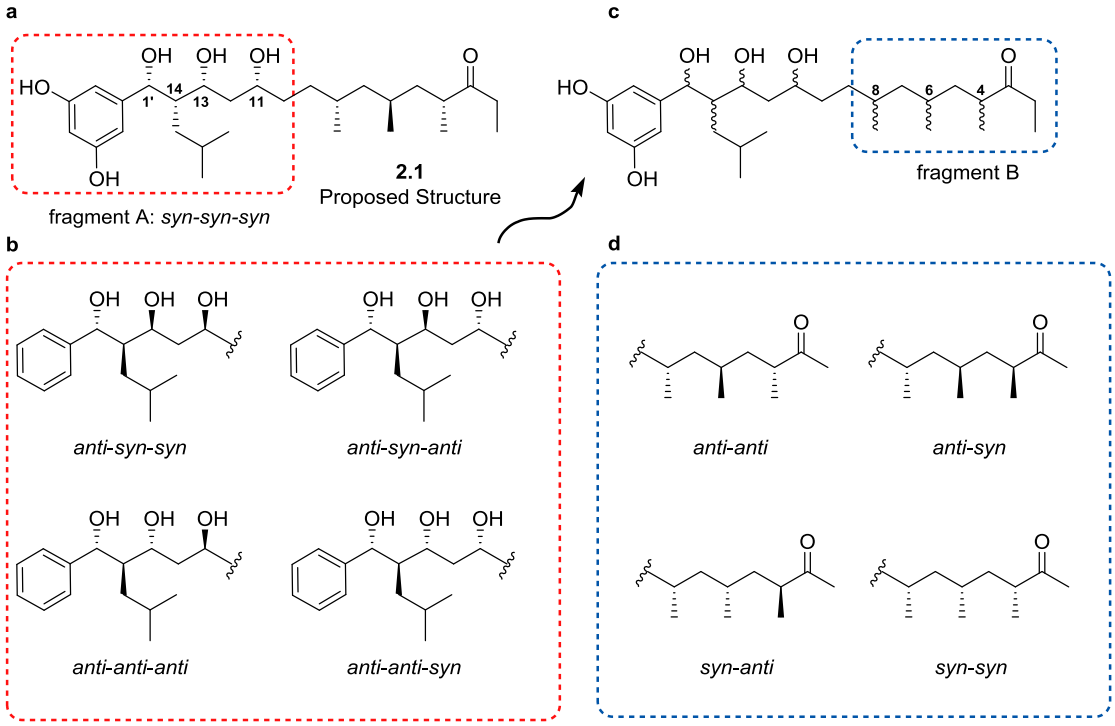

Figure 2.10. A list of diastereomers to be studied. **a**, Sherman's proposed configuration of baulamycin A.[95] **b**, The relative stereochemistry of isomers whose Boltzmann averaged NMR parameters will be computed using Sherman's proposed fragment B. **c**, Generic structure of baulamycin A, which will consist with a computationally derived fragment A and four variations of fragment B. **d**, The relative stereochemistry of isomers whose Boltzmann averaged NMR parameter will be computed with the computationally derived fragment A.

2.2.2 QM/NMR analysis of fragment A configuration starting from conformational search in gas phase (compounds 2.6, 2.7, 2.8, 2.9 and 2.10)

The freshly extracted set of accurate experimental NMR data including chemical shift, ^{1}H-^{1}H scalar coupling constants and ^{1}H-^{1}H distances were used for the QM/NMR analysis. Although the HETLOC spectrum, which provides ^{1}H-^{13}C scalar coupling constants, was also provided, the accuracy of the *J* values obtained from HETLOC spectrum is untested. Therefore, ^{1}H-^{13}C scalar coupling constants were not used in the initial study which instead focused on the analysis of ^{1}H-^{1}H coupling constants and ^{1}H-^{1}H distances for the analysis of the C10-C1' regions (fragment A, Figure 2.11a).

Conformational analysis of diastereomers **2.7** – **2.10** (Figure 2.11b) using molecular mechanics performed in gas phase found between 650 and 2455 conformations for each diastereomer. For each diastereomer, low-energy conformers (~84–196 conformers) were submitted to sequential DFT geometry optimisation and free-energy calculations as discussed in the validation study section (Figure 2.11c). The resulting low-energy conformers that were predicted to comprise 85 – 97% of the conformer populations of diastereomers **2.7** – **2.10** (6 ‑ 26 conformers per diastereomer) were subjected to DFT calculations for the prediction of NMR properties for the C10 ‑ C1' regions (fragment A).

Both the calculated ^{1}H-^{1}H scalar coupling constants and NOE-derived ^{1}H-^{1}H distances of diastereomer **2.6** – **2.10** were compared to the corresponding experimental data of the natural product (baulamycin A) using χ^2 analysis (Figure 2.11d). Based on the comparison of ^{1}H-^{1}H scalar coupling constants, there is a moderate fit for **2.7** and **2.10** isomers (χ^2 (reduced) = 2.2 and 2.1 respectively), and poor fits for **2.6**, **2.8** and **2.10** isomers ((χ^2 (reduced) = 5.7, 3.9 and 5.4 respectively). However, all isomers show a very poor fit (χ^2 (reduced) > 8) to the experimental ^{1}H-^{1}H distances derived from the 2D-ROESY spectrum provided by Sherman *et al.*[95] and no candidate fit both sets of experimental data simultaneously.

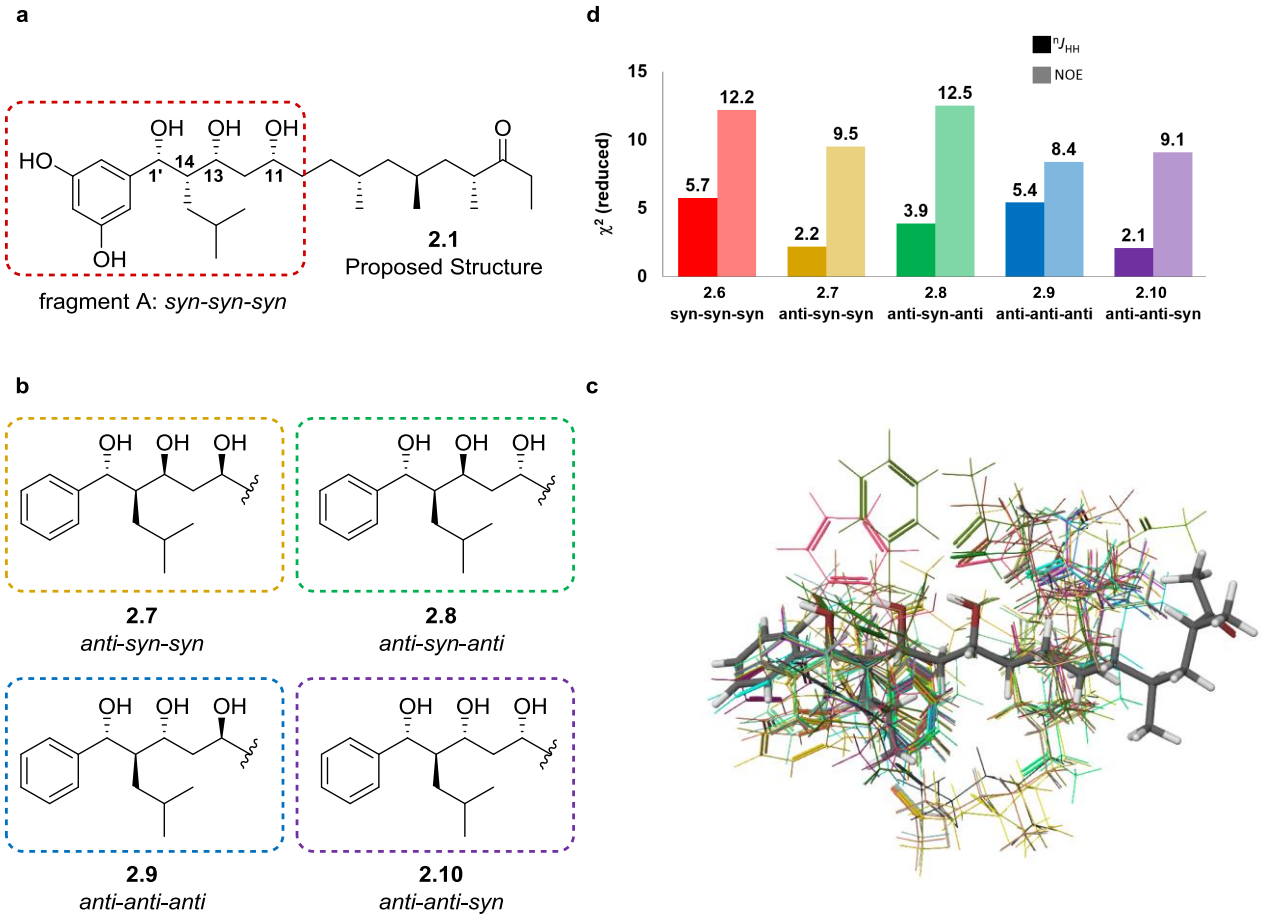

Figure 2.11. Analysis of the relative configuration of C1'-C10 region (fragment A) before population refinement. a, Sherman's proposed configuration of baulamycin A; b, The relative configurations of diastereomers computed for the study of fragment A; c, An overlay of conformations of isomer **2.10** analysed by DFT; d, Comparison of both Boltzmann averaged computed ^{1}H-^{1}H scalar coupling constants and ^{1}H-^{1}H distances* to the experimental data of baulamycin A using χ^2 analysis.

If the experimentally derived NOE-distances from the 2D ROESY spectrum provided by Sherman *et al.*[95] are an accurate reflection of the conformational landscape of the natural product, then the poor fit for ^{1}H-^{1}H distances for all isomers suggests the DFT energy-derived conformer population is not accurate enough to describe the conformational landscape of the matching isomer. This is because quantitative NOE-distance analysis is too sensitive to conformer populations and interproton distance (scales with r^{-6}).[54]

To correct the conformer populations (and thus the ensemble-averaged NMR parameters), the conformer populations for **2.6** – **2.10** were refined based on the experimental

* For each diastereomer, the reference distance used for NOE-derived distances were further optimised to give the best possible fit to the natural product data. Therefore, the χ^2 (reduced) values reported here differ slightly from the originally published values (difference < 1).

^{1}H-^{1}H distances of the natural product extracted from the 2D ROESY data provided by Sherman *et al.*[95] to obtain the best possible fit.

The conformers sampled by DFT for **2.6** – **2.10** (183, 97, 161, 153 and 84 conformers respectively) were clustered based on the four dihedral angles of the main chain in fragment A: ϕ_1- ϕ_4 (around the C1'-C14, C14-C13, C13-C12 and C12-C11 bonds respectively, Figure 2.12a). The populations of the resulting clusters (26, 13, 16, 29 and 17 respectively for **2.6** – **2.10**) were then refined by altering their relative ΔG values in a Generalised Reduced Gradient (GRG) non-linear least squares optimisation of the standard deviation between experimental and calculated NOE-distances (using the Solver element in Microsoft Excel 2016). In order to ensure physical and chemical sense in the refinement, a constraint ($\Sigma(\Delta\Delta G)^2$ = 400) was enforced to prevent unreasonably large changes in ΔG (not greater than 20 kJ mol^{-1}) away from the original DFT-calculated energies. The values of ϕ, initial populations of these clusters, the resulting $\Delta\Delta G$ and the refined populations for each diastereomer are listed in table 6.32 in the experimental section. A discussion of the changes in cluster populations can be found in section 2.2.3.

a)

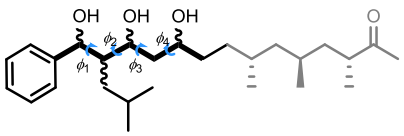

b)

Abbreviation used	Range of Dihedral Angles
sp (synperiplanar)	$-30° \leq \phi < 30°$
g^+ (gauche$^+$)	$30° \leq \phi < 90°$
+*ac* (+ anticlinal)	$90° \leq \phi < 150°$
ap (antiperiplanar)	$\pm 150° \leq \phi < 180°$
–*ac* (– anticlinal)	$-90° < \phi \leq -150°$
g^- (gauche$^-$)	$-30° < \phi \leq -90°$

Figure 2.12: a, Generic structure of diastereomers studied for fragment A analysis; **b,** Abbreviation of six clusters and the corresponding range of dihedral angles.

The refined ensemble-averaged ^{1}H-^{1}H distances were compared to the natural product data and there is an excellent fit for both **2.9** and **2.10** (χ^2 (reduced) = 1.4 and 1.6 respectively) while the remaining isomers **2.6**, **2.7** and **2.8** had poor fit (χ^2 (reduced) = 5.1, 4.8 and 5.4, respectively). Comparison of the refined ^{1}H-^{1}H scalar coupling constants revealed that both **2.6** and **2.10** provide a good fit (χ^2 (reduced) = 1.6 and 1.5 respectively), **2.7** and **2.8** provide a moderate fit (χ^2 (reduced) = 2.4 and 2.1, respectively), and **2.9** provides an unreasonable fit. (χ^2 (reduced) = 6.2). Therefore, **2.10** (*anti–anti–syn*) is the only isomer which simultaneously fits both sets of experimental NMR data for fragment A. Therefore, within the constraint

($\Sigma(\Delta\Delta G)^2$ = 400) applied, compounds **2.6**, **2.7** – **2.9** do not possess the correct fragment A stereochemistry and therefore the relative configuration of fragment A was assigned to be *anti–anti–syn*, rather than the all *syn* configuration originally proposed.

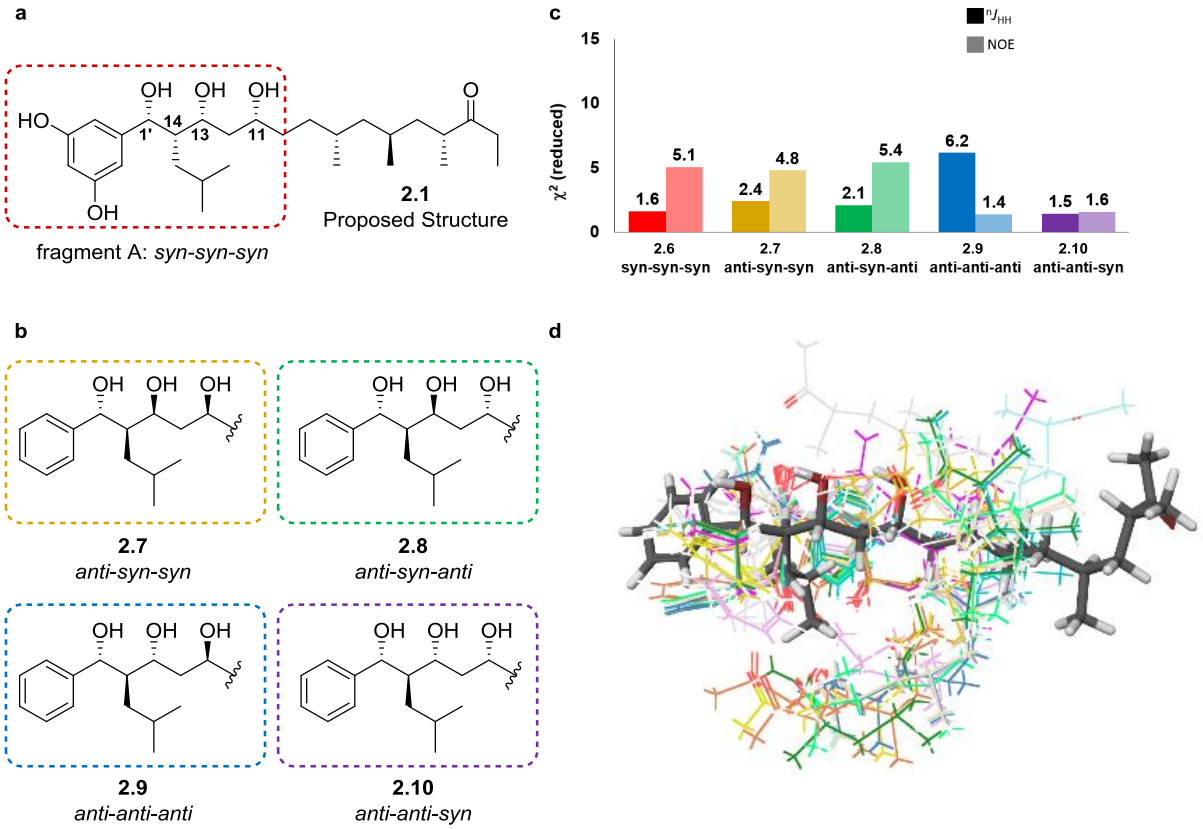

Figure 2.13 Analysis of the relative configuration of C1'-C10 region (fragment A) after population refinement. **a**, Sherman's proposed configuration of baulamycin A. **b**, The relative configurations of diastereomers computed for the study of fragment A. **c**, Comparison of both Boltzmann averaged computed ^{1}H-^{1}H scalar coupling constants and ^{1}H-^{1}H distances† to the experimental data of baulamycin A using χ^2 analysis; **d**, An overlay of conformations of isomer **2.10** (with a combined population of 92%) used for scalar coupling constant calculations.

Notably, comparison of calculated chemical shift (both ^{1}H and ^{13}C) with the experimental data of the natural product using methods described by Willoughby *et al.*[107] and Goodman *et al.* [77] was found to be non-discriminating. Figure 2.14 shows the results of the comparison between the calculated scaled chemical shifts (δ_H and δ_C) of compound **2.6** – **2.10**

† For each diastereomer, the reference distance used for NOE-derived distances were further optimised to give the best possible fit to the natural product data. Therefore, the χ^2 (reduced) values reported here differ slightly from the originally published values (difference < 0.5).

after NOE based population refinement and the experimental chemical shifts of baulamycin A using methods reported by both Willoughby *et al.*[107] and Goodman *et al.*[77].

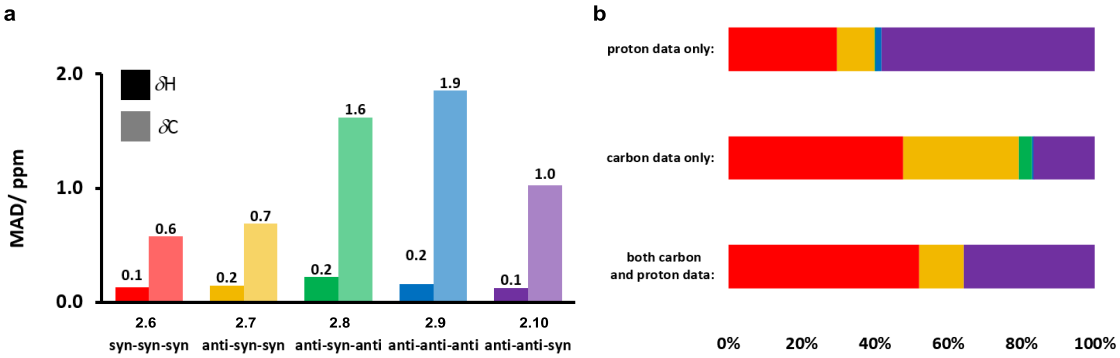

Figure 2.14: Comparison of calculated chemical shifts to the natural product experimental data. **a**, ^{1}H and ^{13}C chemical shifts of the C1'-C11 fragment. Mean absolute deviation (MAD) is plotted with the corresponding values above. **b**, Results of DP4 analysis using proton data only (top), using carbon data only (middle), and using both carbon and proton data (bottom). The size of the bar represents the probability (in percentage) of a given diastereoisomer being the 'correct answer' based on the five candidate structures compared. DP4 results using proton data only: **2.6**: 29.6%, **2.7**: 10.4%, **2.8**: 0.1%, **2.9**: 1.8%, **2.10**: 58.1%. DP4 results using carbon data only: **2.6**: 47.7%, **2.7**: 31.6%, **2.8**: 3.6%, **2.9**: 0.4%, **2.10**: 16.7%. DP4 results using both proton and carbon data: **2.6**: 52.0%, **2.7**: 12.2%, **2.8**: 0.0%, **2.9**: 0.0%, **2.10**: 35.8%.

For the Willoughby-style analysis, only the mean absolute deviations (MAD) were used for comparison. For comparison of ^{1}H chemical shifts, Willoughby *et al.* suggests that the correct answer should have an MAD less than 0.1 ppm and an incorrect answer can be identified by an MAD greater than 0.2 ppm. Figure 2.14c suggests that the a*nti–syn–anti* (**2.8**) isomer is unlikely to be the correct (MAD = 0.22 ppm), but the rest of the isomers have similar MAD values (MAD = 0.13 - 0.16 ppm) and therefore could not be discriminated. Although Willoughby *et al.* did not discuss the MAD values for the comparison of ^{13}C chemical shifts, it was found that *syn–syn–syn* (**2.6**), a*nti–syn–syn* (**2.7**) and *anti–anti–syn* (**2.10**) isomers all have comparable and reasonable MAD values (MAD = 0.6, 0.7 and 1.0 respectively) and so ^{13}C chemical shift is not considered to provide a clear discrimination between these structures.

The DP4 analysis of chemical shifts (Figure 2.14d) described by Goodman *et al.* determines the likelihood of an isomer being the matching isomer by the distribution of deviations of chemical shift comparisons. Although the DP4 analysis was found to show some

discrimination between diastereoisomers, no candidate shows a high probability (>95%) of matching on the basis of the DP4 analysis alone.

These results highlight the fact that care must be taken for NMR-based stereochemical analysis of dynamically complex flexible molecules.

To verify the computationally derived fragment A configuration experimentally, **2.11** (Figure 2.15) was synthesised by Dr. Paula Lorenzo and Dr. Jingjing Wu. Comparison of the NMR spectra between **2.11** with that of the natural product revealed that while the signals in the C1'-C10 region (fragment A) fitted very closely to the natural product data, a substantial difference in the C8-C2 region (fragment B) remained (Figure 2.15). Therefore, the relative configuration of fragment A could indeed be assumed to be *anti–anti–syn*, rather than the all *syn* configuration originally proposed. At this stage, the QM/NMR analysis has identified the relative configuration of four out of seven stereogenic centres, thus reducing 128 possible stereoisomers of baulamycin A down to 16.

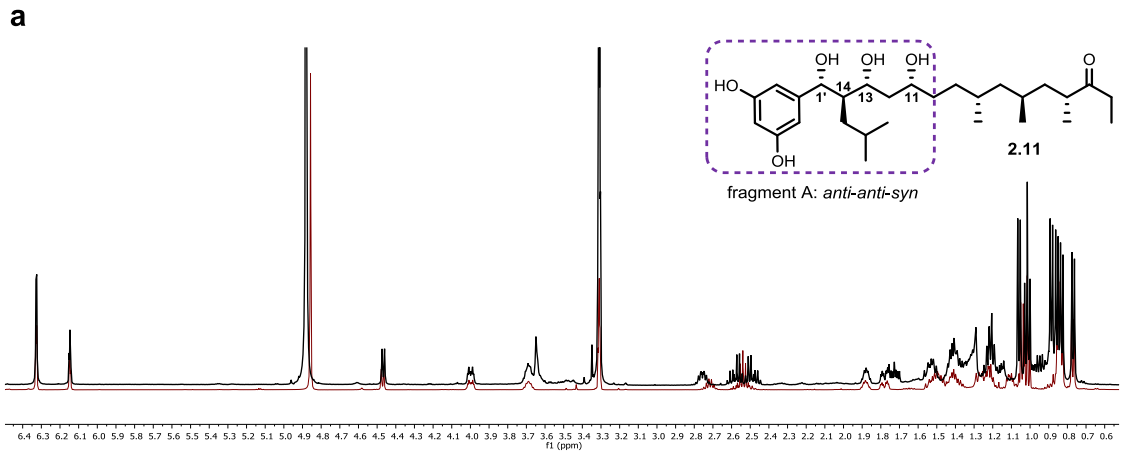

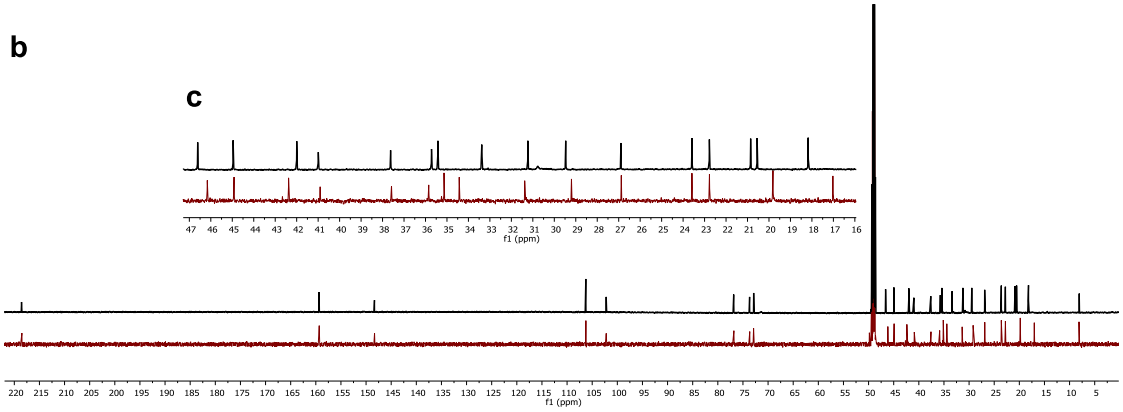

Figure 2.15. Chemical structure of **2.11** and the comparison of **a.** ^{1}H NMR (CD_3OD, 500 MHz) and **b.** ^{13}C NMR (CD_3OD, 176 MHz) spectra of **2.11** (red) and baulamycin A (black). **c**. Zoom in of the ^{13}C NMR spectrum from 17 to 47 ppm.

2.2.3 Population change of fragment A after NOE-refinement of 2.10.

Having established the relative configuration of fragment A of baulamycins, the change in conformational landscape of the fragment A matching isomer **2.10** after population refinement was investigated. The 84 conformers sampled by DFT calculations were divided into 17 clusters based on the dihedral angles of fragment A as described before and the relative Gibbs free energies (ΔG) were adjusted using $\Sigma\,(\Delta\Delta G)^2$ =400 as a constraint. After population refinement, conformer **2.10**-1 remains the lowest energy conformer but the number of conformers with a relative Gibbs free energy within 10 kJ mol^{-1} of the global minimum increased from 11 to 26, so the overall conformer population of **2.10** became more complex. The $\Delta\Delta G$ of four clusters changed substantially as figure 2.16a shows (7.2, −15.4, −5.7 and 6.3 kJ mol^{-1} for clusters 4, 6, 9, and 13 respectively). Within these four clusters, clusters 4 and 13 represent conformers with all three hydroxyl groups hydrogen bonded to each other (Figure 2.17c and d), while clusters 6 and 9 represent conformers with only two out of the three hydroxyl groups hydrogen bonded to each other (Figure 2.17e and f). Notably, the ΔG of groups 4 and 13 are increased ~ 6 kJ mol^{-1} by NOE fitting while the energies of both groups 6 and 9 decreases by > 5 kJ mol^{-1}. (Figure 2.16a).

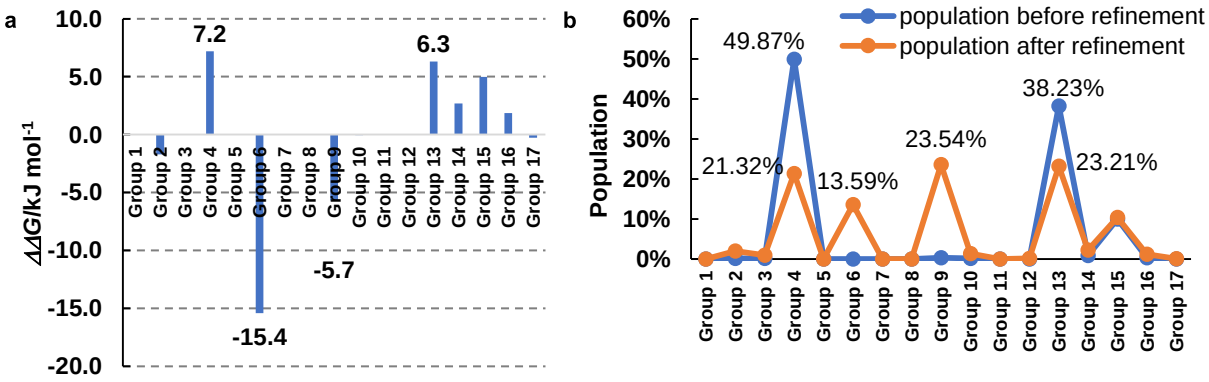

Figure 2.16: a, The change in relative Gibbs free energy ($\Delta\Delta G$) of each cluster after population refinement. **b** The comparison of the combined population of each cluster before and after population refinement.

Figure 2.17a shows the comparison between the calculated ^{1}H-^{1}H distances of **2.10** and the NOE derived experimental ^{1}H-^{1}H distances of the natural product before population refinement. A poor fit was observed (R^2 = 0.45, MAD = 9%, StDev = 15% and χ^2 (reduced) = 9.5) due to two outliers, which correspond to the distances between H1'-H12a and H14-H11 (orange and blue dots with 47% and 32 % deviation, respectively, Figure 2.17a).

a

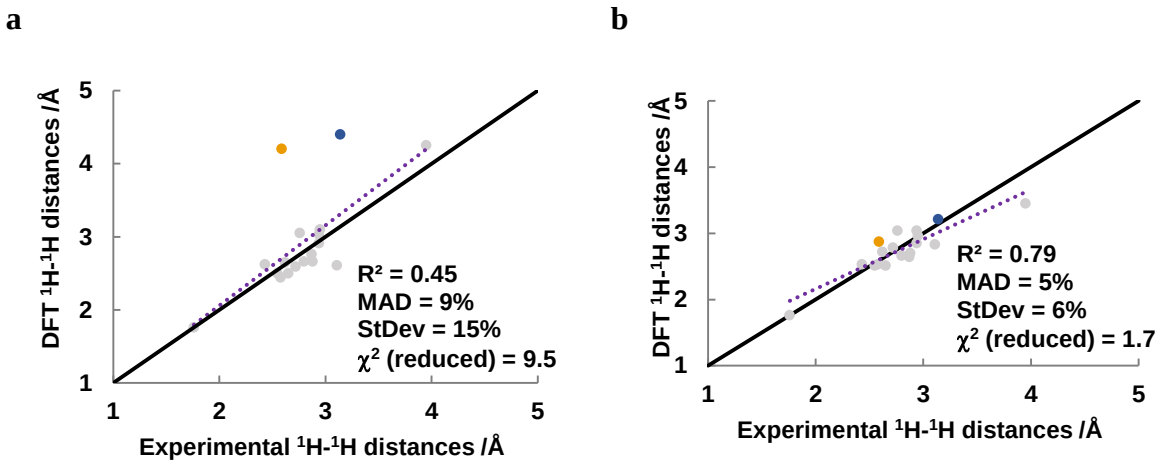

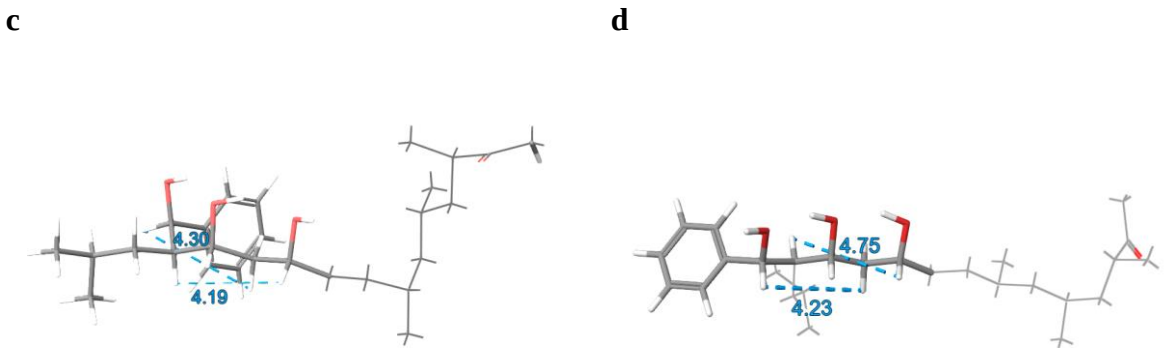

2.10-2 (from cluster 4)

2.10-1(from cluster 13)

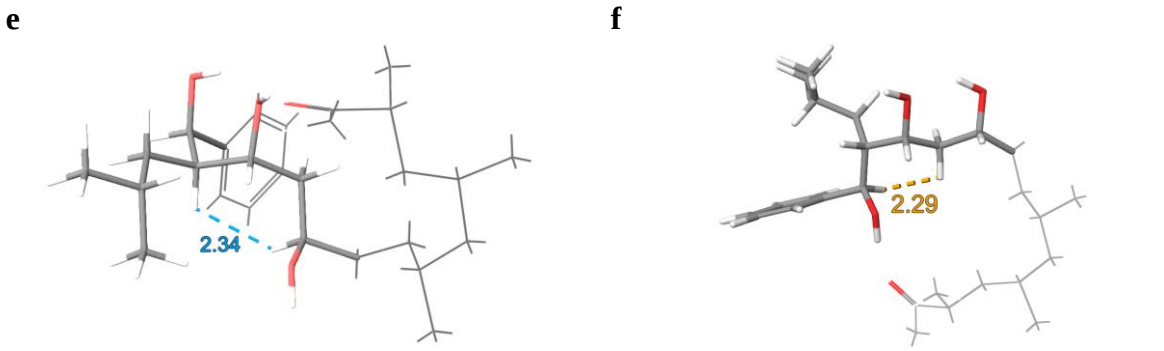

2.10-5(from cluster 6)

2.10-3 (from cluster 9)

Figure 2.17: Comparison of DFT calculated and experimental ^{1}H-^{1}H distances of compound **2.10** (**a**) before and (**b**) after population refinement. The ideal fit (calculated distances = experimental distances, y = x) is shown as solid black lines and the goodness of fit is evaluated by the mean absolute deviation (MAD), standard deviation (StDev) and χ^2 analysis using χ^2 (reduced) values. **c,** A representative conformer from cluster 4 with the distance between $H_{1'}$-H_{12a} and H_{14}-H_{11} labelled (4.30 and 4.19 Å, respectively). **d**, A representative conformer from cluster 13 with the distance between H1'-H12a and H_{14}-H_{11} labelled (4.23 and 4.75 Å, respectively). **e**, A representative conformer from cluster 6 with the distance between H_{14}-H_{11} labelled (2.34 Å). **f**, A representative conformer from cluster 9 with the distance between $H_{1'}$-H_{12a} labelled (2.29 Å).

In both cases, the experimental distances are shorter than the DFT estimated distances, which suggests that experimentally the population of conformers with short $H_{1'}$-H_{12a} and H_{14}-H_{11} distances are higher than what was predicted by DFT calculations. Indeed, cluster 6 and 9, which have conformers with short $H_{1'}$-H_{12} and H_{14}-H_{11} distances (< 2.5 Å, Figure 2.17e and f) were calculated to have only 0.31% of the global population, while the dominant conformations (cluster 4 and 13, 88% of the global population, Figure 2.16b), which have all three hydroxyl groups hydrogen bonded to each other, show long distances (>4 Å, Figure 2.17c and d). As a result, the ensemble-averaged distances derived from the DFT-approximate conformer population showed long $H_{1'}$-H_{12a} and H_{14}-H_{11} distances (>4 Å).

To minimise the deviation of the comparison of these two distances, the population of cluster 6 and 9, which have conformations with short $H_{1'}$-H_{12a} and H_{11}-H_{14} distances, were therefore increased from 0.00% and 0.31% to 14% and 24% respectively by NOE-based population refinement (Figure 2.16b). It is worth noting that while the fit for the comparison of these two distances has improved substantially, the good fit for the comparison of other distances remained, thus a substantial improvement was observed for the overall fit between the calculated and experimental distances of **2.10** (R^2 = 0.79, MAD = 5%, StDev = 6% and χ^2 (reduced) = 1.7, Figure 2.17b).

Clearly, the energies of conformers were poorly predicted either at the MM or the subsequent DFT calculations. If MM over-estimates the enthalpic benefit of forming intramolecular hydrogen bonds, this would result in under-representation of conformations which have less than two hydrogen bonding interactions between the three hydroxyl groups. Consequently, these conformations are not heavily represented in the subsequent DFT calculations. If the chosen DFT methods (discussed in validation study) are insufficient for calculating accurate conformer energies associated with intramolecular hydrogen bonding interactions, then better methods for calculations should be devised, since an adjustment of the calculated DFT conformer energies by 15 kJ mol^{-1} is outside the bounds of expected chemical accuracy (~ 4 kJ mol^{-1}).

To investigate this discrepancy, the calculated energies of conformers **2.10**-2 and **2.10**-1 (Figure 2.17c and d), which were ultimately found to have energies within 10 kJ mol^{-1} of the global minimum after population refinement (ΔG = 8.3 and 4.1 kJ mol^{-1}, respectively, Table 2.4), were compared at each stage of the calculations.

At the MM stage, both conformers 19 and 34 were calculated to have relative potential energies within 10 kJ mol^{-1} of the global minimum (ΔE_{MM} = 8.0 and 9.2 kJ mol^{-1}, respectively, Table 2.4) and were therefore captured in the subsequent DFT calculations. However, both conformers were calculated to have very high energies by DFT, with the relative Gibbs energy (ΔG_{DFT} > 13 kJ mol^{-1}, Table 2.4) above 10 kJ mol^{-1} of the global minimum, even with solvent correction by the mean of single point energy calculations (IEFPCM, methanol).

Although the 'fault' seems to lie in the DFT stage, it is unclear whether the 'fault' was caused by inappropriate choice of DFT calculation methods for dealing with intramolecular hydrogen bonding interactions, or the starting geometry for DFT calculations are genuinely energetically less favourable in protic solvent. Both conformers 19 and 34 show intramolecular H-bonding interaction between one of the three hydroxyl groups in fragment A and the ketone in fragment B (Figure 2.17e and f, respectively). This intramolecular H-bonding in protic solvent (methanol in this case) seems somewhat unlikely based on chemical intuition, and this could be the reason why both conformers were calculated to be high in energy by DFT even with implicit solvent correction (IEFPCM, methanol).

Table 2.4: Relative potential energies calculated by MM (ΔE_{MM}), relative Gibbs free energies calculated by DFT (ΔG_{DFT}), and the relative Gibbs free energies obtained after population refinement ($\Delta G_{refinement}$) of conformers 19 and 34.

Conformer	**ΔE_{MM}/ kJ mol^{-1}**	**ΔG_{DFT}/ kJ mol^{-1}**	**$\Delta G_{refinement}$/ kJ mol^{-1}**
19	8.0	25.1	4.1
34	9.2	13.9	8.3

2.2.4 Effect of implicit octanol on QM/NMR analysis of fragment A (compounds 2.6, 2.7, 2.8, 2.19 and 2.10)

The possibility of this discrepancy occurring in the MM conformational search stage was also examined, since the original MM conformational analysis was performed in gas phase. Out of the choices of implicit solvent available in the Maestro conformational search software (chloroform, octanol, water)[108], octanol would be the closest mimic to methanol, which is the solvent used for experimental NMR analysis.

Therefore, conformational analysis of **2.10** using MM was repeated in octanol and found 3670 non-redundant conformations. Amongst these conformations, 107 conformations are below 10 kJ mol^{-1} of the global minimum (c.t. 1353 conformers were found in gas phase, section 2.2.2). In the gas phase conformational search, conformers with no hydrogen bonds between the three hydroxyl groups (Figure 2.18c) were not present within 10 kJ mol^{-1} of the global minimum (Figure 2.18a), while 5 of these conformers were captured in the octanol conformational search (Figure 2.18b). The inclusion of implicit octanol in the conformational search has decreased the energies of conformations which do not have hydrogen bonds between hydroxyl groups (Figure 2.18a and b). This confirms that there is a bias towards the hydrogen bonded conformers when solvent polarity is ignored. It is likely that including explicit solvent in the conformational search would improve this further.

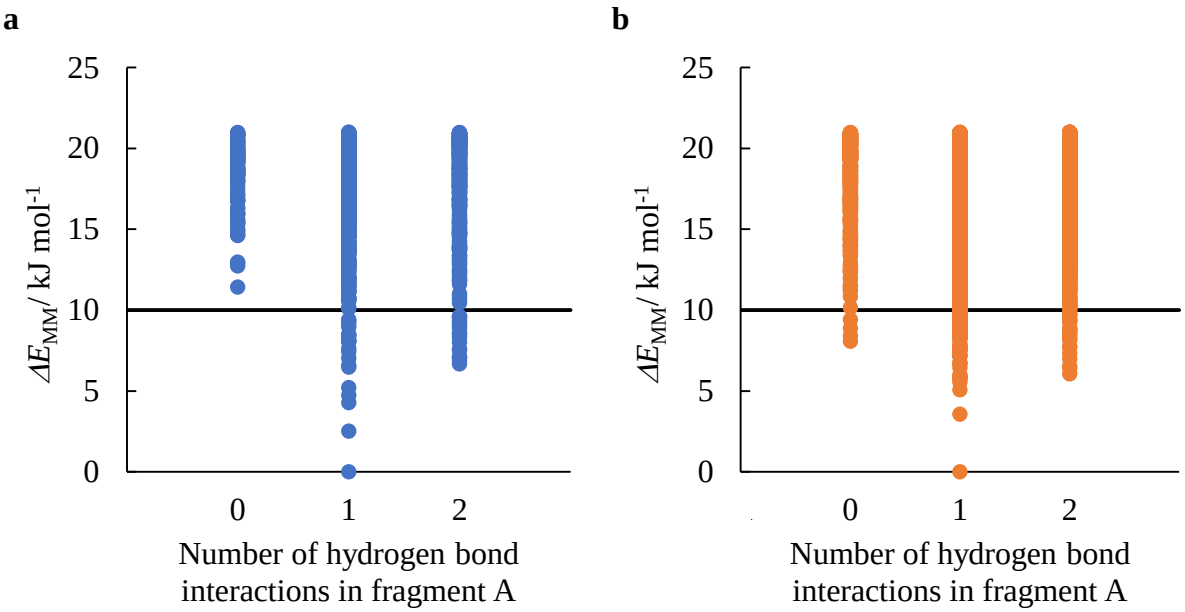

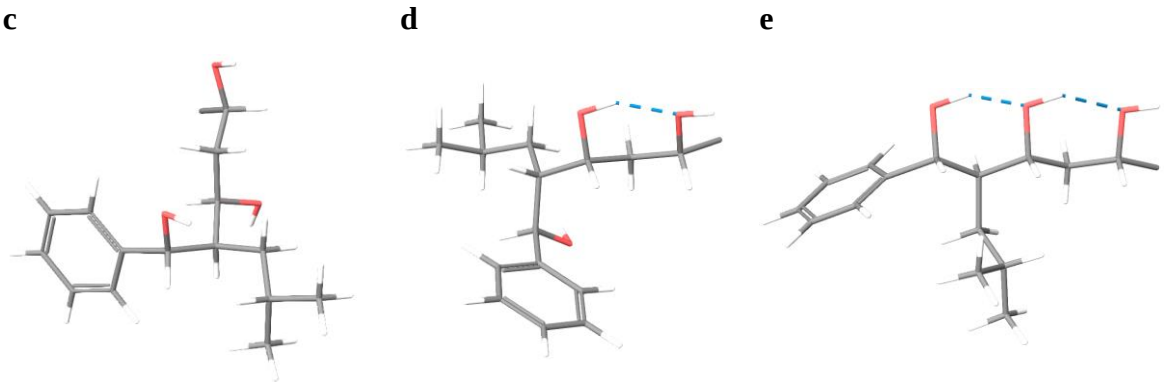

Figure 2.18: Analysis of fragment A conformations using conformers generated from **a** conformational search in gas phase and **b** conformational search with implicit octanol as solvent; **c**, **d**, and **e** are representative examples of conformers with none, one, or two hydrogen bond interactions (shown in blue dotted lines) between the hydroxyl groups in fragment A.

Although conformers above 10 kJ mol^{-1} of the global minimum are still partially captured by random sampling, conformers with high MM energies could easily be neglected due to the sheer number of conformations. Therefore, having a more diverse set of conformations within 10 kJ mol^{-1} of the global minimum would be desirable, since all conformations below this energy threshold would be subjected to the subsequent DFT calculations.

With a greater diversity of conformations in hand, the impact of including implicit octanol at the first stage of conformational analysis (ie. MM conformational search) on the resulting DFT predicted ensemble-averaged ^{1}H-^{1}H coupling and ^{1}H-^{1}H distances was investigated. For **2.10**, the 107 conformers below 10 kJ mol^{-1} of the global minimum, together with another 107 conformers randomly selected from the remaining pool (10-21 kJ mol^{-1} of the global minimum), were subjected to the subsequent geometry optimisation, frequency calculation and NMR prediction using DFT as previously described.

Both the calculated ensemble-averaged ^{1}H-^{1}H scalar coupling constants and ^{1}H-^{1}H distances were compared to the natural product experimental data using χ^2 analysis. While moderate fit was observed for the comparison of ^{1}H-^{1}H scalar coupling constants (χ^2 (reduced) = 3.0, Figure 2.19b), poor fit was again observed for ^{1}H-^{1}H distance comparison (χ^2 (reduced) = 5.3, Figure 2.19b). This result is similar to that obtained starting from the conformational search in gas phase (Section 2.2.2). Although the fit for ^{1}H-^{1}H distances has somewhat improved when the NMR parameters were calculated using conformers obtained from octanol

conformational search, with a χ^2 (reduced) value reducing from 9.1 to 5.3, the fit still deviates substantially from the ideal fit so population refinement is still required to correct for conformer population.

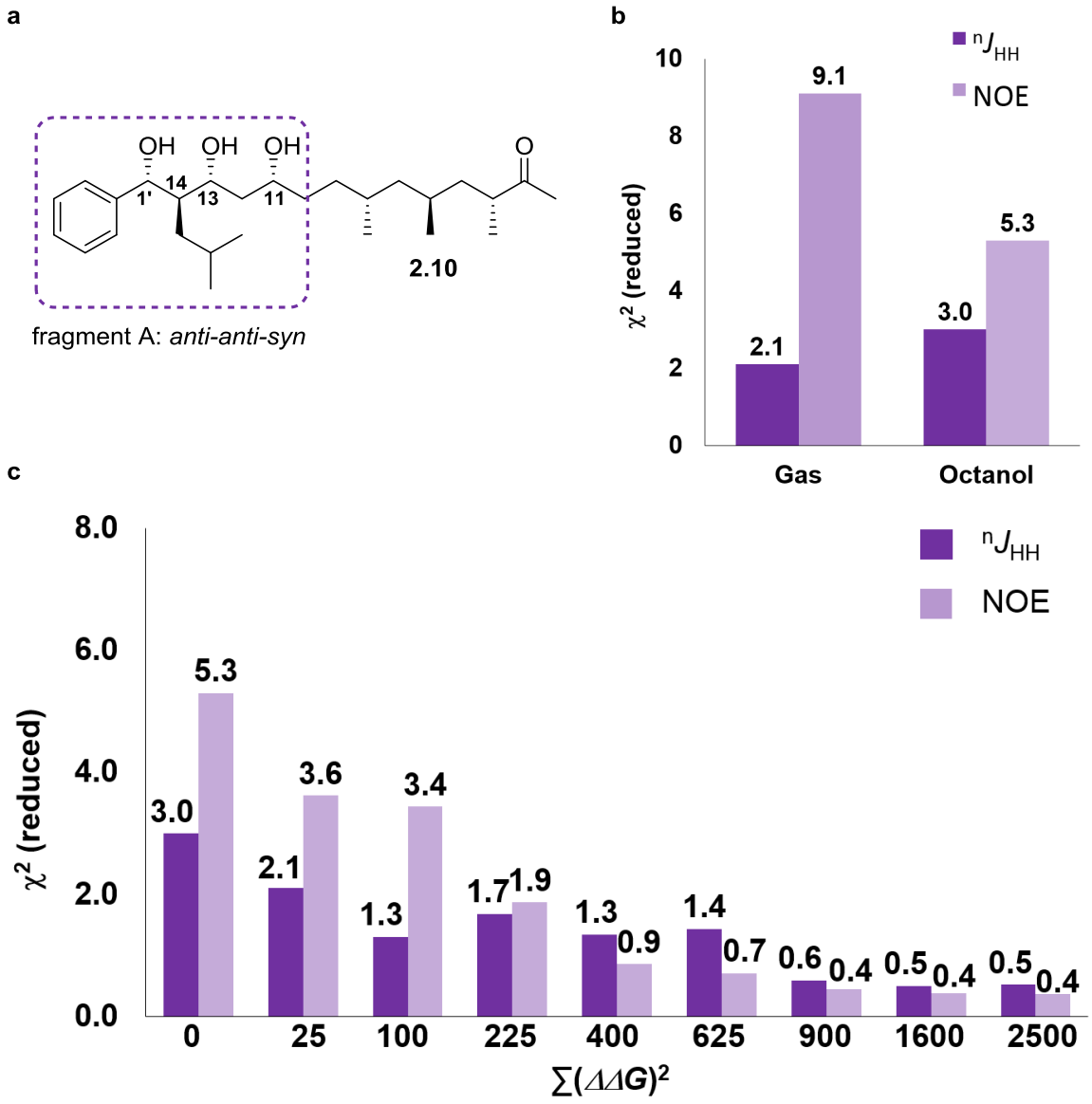

Figure 2.19: a, Chemical structure of **2.10**. **b**, Comparison of both Boltzmann averaged computed ^{1}H-^{1}H scalar coupling constants and ^{1}H-^{1}H distances to the experimental data of baulamycin A using χ^2 analysis; **c**, Comparison of both Boltzmann averaged computed ^{1}H-^{1}H scalar coupling constants and ^{1}H-^{1}H distances (based on refined conformer population obtained using different constraints) to the experimental data of baulamycin A using χ^2 analysis.

Next, the impact of varying the population refinement constraint was investigated to establish whether the constraint originally chosen ($\Sigma(\Delta\Delta G)^2$ =400) based on chemical intuition

was optimal, and what would happen if the constraint was loosened to a point where over-fitting could occur.

Conformations which were generated from octanol conformational search were chosen for this study because of the increased diversity of fragment A conformations (Figure 2.18b). The 214 conformations sampled by DFT were divided into 20 clusters based on the dihedral angle criteria described previously (Figure 2.12, also see table 6.43 in the experimental section for the corresponding dihedral sequence for each cluster). Population refinement were performed using eight different constraints ($\boldsymbol{\Sigma}(\Delta\Delta G)^2$ = 25, 100, 225, 400, 625, 900, 1600 and 2500, Figure 2.19c), which corresponds to the maximum change of ΔG for a particular cluster (out of the 20 clusters) from 5, 10, 15, 20, 25, 30, 40 and 50 kJ mol^{-1}. As the constraint increases from zero to 400, the fit for ^{1}H-^{1}H distances improves substantially, with the χ^2 (reduced) values reduceing from 5.3, which is a very poor fit, to 0.9, which is very close to the ideal fit (Figure 2.19c). In addition, the fit for ^{1}H-^{1}H coupling also improves from a moderate (χ^2 (reduced) = 3, Figure 2.19) to good (χ^2 (reduced) = 1.3, Figure 2.19c). Interestingly, when the constraint was increased beyond 400, no substantial improvement in the fit of ^{1}H-^{1}H was observed, indicating that overfitting might occur when a constraint of $\boldsymbol{\Sigma}(\Delta\Delta G)^2$ greater than 400 was used. However, in this case overfitting does not result in the erosion of the good fit in the comparison of ^{1}H-^{1}H scalar coupling constants, so the exact point when overfitting has occurred could not be determined. Therefore, the smallest constraint one could use to obtain the optimal fit lies somewhere around 225 and 400 and the constraint chosen originally ($\boldsymbol{\Sigma}(\Delta\Delta G)^2$ =400) seems to be reasonable.

Having established a sensible constraint for population refinement ($\boldsymbol{\Sigma}(\Delta\Delta G)^2$ = 400), conformational analysis of diastereomers **2.6** – **2.10** (Figure 2.11 a and b) using molecular mechanics was performed again using implicit octanol as solvent. For each diastereomer, between 2428 and 8794 conformations were found and the low-energy conformers (88-564 conformers) for each diastereomer were subjected to the subsequent geometry optimisation, frequency calculation and NMR prediction using DFT as described previously.

Both the calculated ensemble-averaged ^{1}H-^{1}H scalar coupling constants and NOE-derived ^{1}H-^{1}H distances of diastereomer **2.6** – **2.10** were compared to the corresponding experimental data of the natural product (baulamycin A) using χ^2 analysis (Figure 2.20c). The results are similar to that observed when starting from gas conformational search (section 2.2.2)

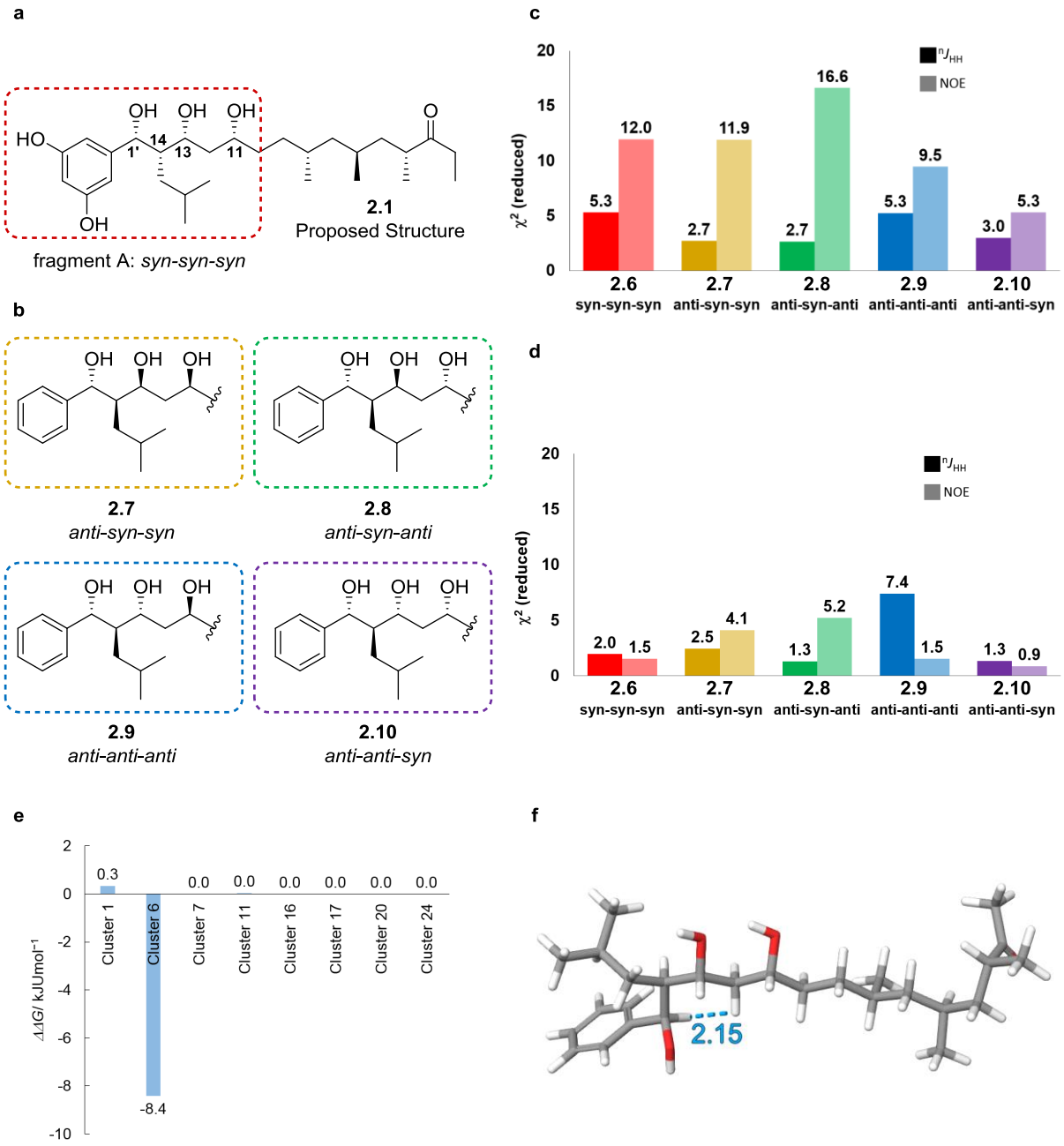

Figure 2.20: Analysis of the relative configuration of C1'-C10 region (fragment A) starting from octanol conformational search. **a**, Sherman's proposed configuration of baulamycin A. **b**, The relative configurations of diastereomers computed for the study of fragment A. Comparison of both Boltzmann averaged computed ^{1}H-^{1}H scalar coupling constants and ^{1}H-^{1}H distances to the experimental data of baulamycin A using χ^2 analysis **c** before population refinement and **d** after population refinement. **e**, The change in relative Gibbs free energy of the eight clusters after population refinement. **f**, Conformer 5515 from cluster 6, with the distance between $H_{1'}$-H_{12a} labelled (2.15 Å).

Based on the comparison of ^{1}H-^{1}H scalar coupling constants, there is a moderate fit for **2.7**, **2.8** and **2.10** isomers (χ^2 (reduced) = 2.7, 2.7 and 3.0, respectively), and no reasonable fit for **2.6**, **2.9** isomers ((χ^2 (reduced) = 5.3 for both isomers). Again, all isomers show a very poor fit (χ^2 (reduced) > 5) to the experimental ^{1}H-^{1}H distances derived from the 2D-ROESY spectrum provided by Sherman *et al.*[95] and no candidate fit both sets of experimental data simultaneously.

Next, population refinement was also applied to all diastereomers to correct for the DFT-approximate conformer population as described previously. The conformers sampled by DFT for **2.6** – **2.10** (564, 88, 204, 124 and 214 conformers, respectively) were clustered based on the four dihedral angles of the main chain in fragment A as discussed before (Figure 2.12) and a constraint of $\Sigma(\Delta\Delta G)^2$=400 was used for the refinement.

NMR properties were then recomputed based on the refined conformer population for each diastereomer. Figure 2.20d shows the comparison of ^{1}H-^{1}H scalar coupling constants and ^{1}H-^{1}H distances between the calculated data and the natural product experimental data. Comparison of ^{1}H-^{1}H distances showed that **2.6**, **2.9** and **2.10** fit well to the natural product data (χ^2 (reduced) = 1.5, 1.5 and 0.9, respectively) while **2.7** and **2.8** show poor fit (χ^2 (reduced) = 4.1 and 5.2, respectively). Comparison of the ^{1}H-^{1}H scalar coupling constants revealed that **2.8 and 2.10** provide a good fit (χ^2 (reduced) = 1.3 and 0.9, respectively), **2.6** and **2.7** provide a moderate fit (χ^2 (reduced) = 2.0 and 2.5, respectively, Figure 2.20), and a poor fit for **2.9** (χ^2 (reduced) = 7.4, Figure 2.20). As a result, both **2.6** and **2.10** could be considered as viable fits for both sets of experimental NMR data for fragment A.

Interestingly, the fit of ^{1}H-^{1}H distances of **2.6** (the originally proposed configuration by Sherman *et al.*), which previously could not be fitted using gas phase conformers (section 2.2.2), could now be fitted to the natural product data well (χ^2 (reduced) = 1.5, Figure 2.12d) when population refinement was performed using conformations obtained from octanol conformational search, due to the increased diversity of conformations obtained by including implicit octanol in the MM conformational search. For example, in the newly sampled eight clusters, cluster 6 was brought down in energy ($\Delta\Delta G$ = −8.4 kJ mol^{-1}, Figure 2.20e) by population refinement, with one of the conformers from this cluster (conformer 5515, Figure 2.11f) became the new global minimum and the population of this cluster increased from 0% to 17%. Examination of the fragment A conformation of this cluster reveals that conformations in this cluster have short interproton distance between $H_{1'}$-H_{12a} (eg. for conformer 5515: $H_{1'}$-

H_{12a} = 2.15 Å, Figure 2.20f), which is required to match the natural product experimental data ($H_{1'}$-H_{12a} = 2.55 Å).

2.2.5 QM/NMR Analysis of fragment B (compounds 2.10, 2.12, 2.13 and 2.14)

Computational analysis of the C8-C4 region (fragment B) was also performed, albeit without population refinement due to lack of usable NOE correlations. Therefore, the calculated ^{1}H and ^{13}C chemical shifts, together with ^{1}H-^{1}H scalar coupling constants without population refinement were used for the analysis of fragment B.

Conformational analysis of diastereomers **2.10** and **2.12**– **2.14** (Figure 2.21b) using molecular mechanics performed in gas phase found between 466 and 1641 conformations for each diastereomer. Low-energy conformers for each diastereomer (~84–152 conformers) were submitted to sequential DFT geometry optimisation and free-energy calculations. The resulting low-energy conformers that were predicted to make up 80% of the conformer populations of diastereomers **2.10** and **2.12**– **2.14** (9 ‑ 15 conformers per diastereomer) were subjected to DFT calculations for the prediction of NMR properties for the C8 ‑ C4 regions (fragment B, Figure 2.21a).

The Boltzmann averaged NMR properties were computed for the selected conformers of compound **2.10** and **2.12**– **2.14**. The ensemble-averaged calculated chemical shifts (δ_H, δ_C) and ^{1}H-^{1}H scalar coupling constants of the C4-C8 fragment for each candidate was compared to the experimental values of the natural product using χ^2 analysis (Figure 2.21c). Although isomer **2.10** shows the best fit (χ^2 (reduced) = 0.6, 0.5 and 0.9 for δ_H, δ_C and $^{n}J_{HH}$, respectively), the ^{1}H and ^{13}C spectrum of the synthetic isomer **2.10** does not fully match to that of the natural product, as discussed previously. The discrepancy observed suggests that isomer **2.10** is not the natural product and the configuration of fragment B is not *anti–anti*. It was found that intramolecular hydrogen bonded conformers (hydrogen bonded between the terminal ketone and C11-C14 hydroxyl groups, Figure 2.21) were over-represented in the initial MM conformational search of **2.10** and **2.12**– **2.14** while conformers which did not contain the H-bond were estimated by MM to have very high energies (and thus were not heavily represented in subsequent DFT procedures) despite the latter ultimately being found to have low, solvated free energies. Crucially the hydrogen-bonded forms had substantially different fragment B conformations to the non-hydrogen-bonded forms, suggesting a source for the poor fit between experiment and any of the calculated models.

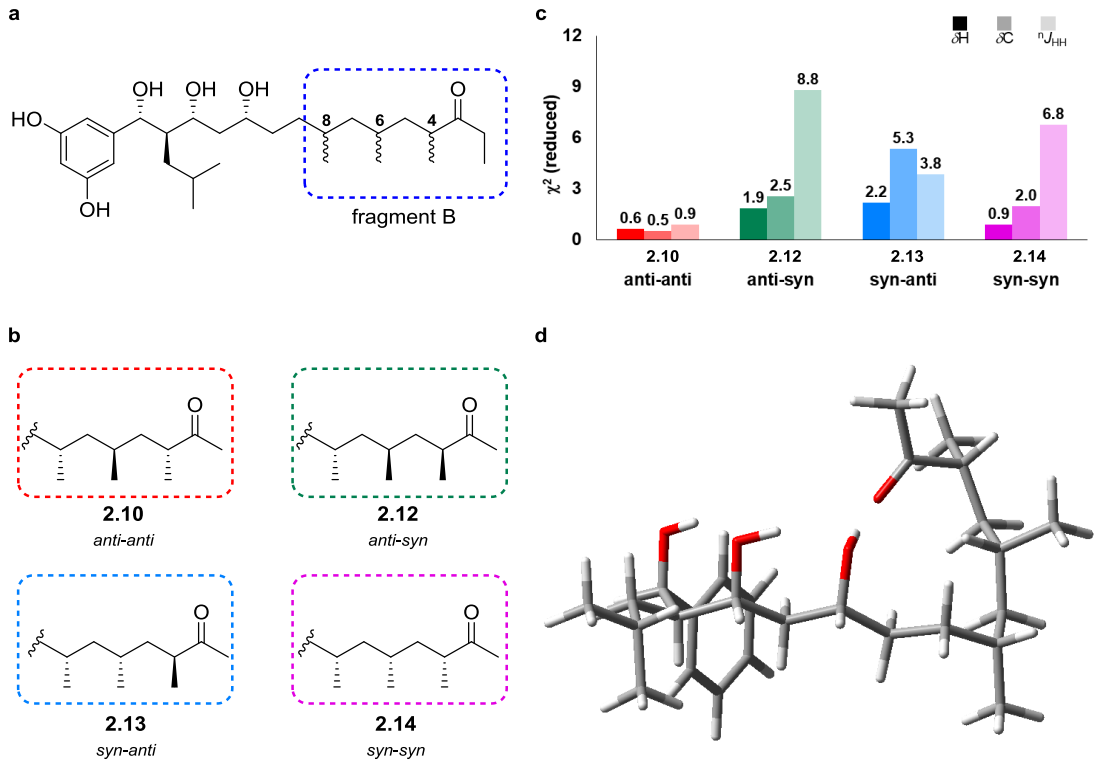

Figure 2.21. Analysis of the relative configuration of the C8-C4 region (fragment B). **a**, Isomer of baulamycin with computationally derived fragment A. **b**, Four possible stereoisomers of fragment B which were computed. **c**, χ^2 analysis comparing computed chemical shifts (^{1}H and ^{13}C) and ^{1}H-^{1}H scalar coupling constants with the experimental values of the natural product. **d**, Lowest energy conformation of **2.14**, dominated by the intramolecular hydrogen bond between the carbonyl carbon from fragment B and the hydroxyl group(s) in fragment A.

In order to provide a proper description of the conformational landscape of fragment B, conformational analysis of diastereomers **2.10** and **2.12**– **2.14** (Figure 2.22b) using molecular mechanics was performed in implicit octanol and found between 2086 and 8407 conformations for each diastereomer. Low-energy conformers for each diastereomer (~214–304 conformers) were submitted to sequential DFT geometry optimisation and free-energy calculations. The resulting low-energy conformers that were predicted to make up 80% of the conformer populations of diastereomers **2.10** and **2.12**– **2.14** (15 ‑ 33 conformers per diastereomer) were subjected to DFT calculations for the prediction of NMR properties for the C8 ‑ C4 regions (fragment B, Figure 2.21a).

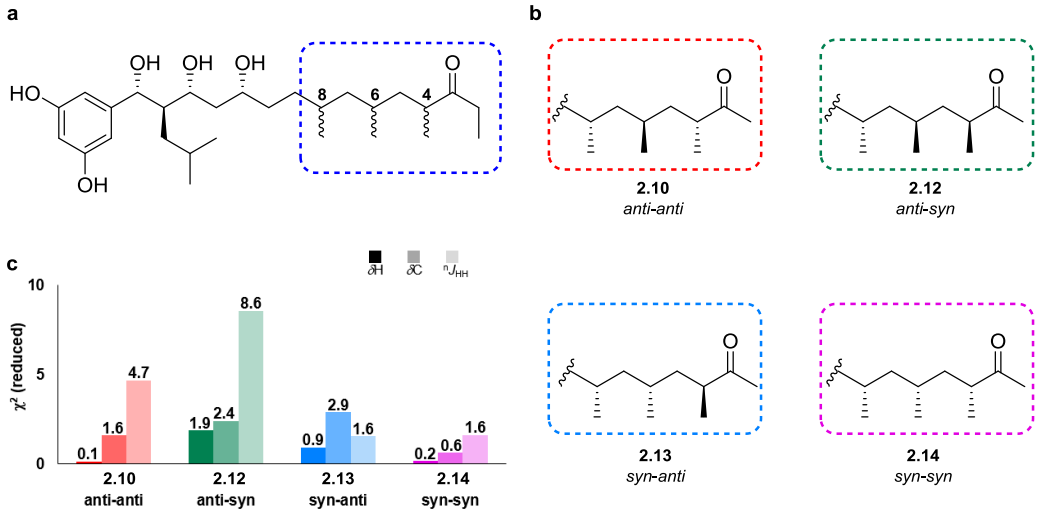

Figure 2.22. Analysis of the relative configuration of the C8-C4 region (fragment B). **a**, Isomer of baulamycin with computationally derived fragment A configuration. **b**, Four possible stereoisomers of fragment B which were computed. **c**, χ^2 analysis comparing computed chemical shifts (^{1}H and ^{13}C) and ^{1}H-^{1}H scalar coupling constants with the experimental values of the natural product. For the comparison of ^{1}H-^{13}C scalar coupling constant using data measured from the synthetic (+)-baulamycin A **2.17** see table 6.58 in the experimental section.

Based on ^{1}H-^{1}H scalar coupling constants, **2.10** and **2.12** fit poorly with the natural product experimental data (χ^2 (reduced) = 4.7 and 8.6, respectively), while both **2.13** and **2.14** provide a good fit (χ^2 (reduced) = 1.6 for both isomers). Based on the analysis of both ^{1}H and ^{13}C chemical shifts, it appears that **2.14** fits much better to the natural product experimental data (χ^2 (reduced) = 0.2 and 0.6 for δ_H and δ_C, respectively) while **2.13** fits less well (χ^2 (reduced) = 0.9 and 2.9, respectively).

Without conformer population refinement, one could not be confident that **2.14** would indeed simultaneously match all the NMR data of the natural product and possess the same fragment B configuration as the natural product. In parallel to the computational analysis, Dr. Jingjing Wu and Dr. Paula Lorenzo in the Aggarwal lab sought to determine the relative configuration of fragment B through synthesis. The idea was to exploit a reagent-controlled assembly-line synthesis[8] to generate an encoded mixture containing all four diastereomers of fragment B. The identity of each diastereomer in the mixture would be indicated by its relative population and thus the intensities of their peaks in a ^{13}C NMR spectrum. By comparison of the ^{13}C NMR spectrum of the mixture to that of the natural product, the identity of the natural product could be rapidly identified.

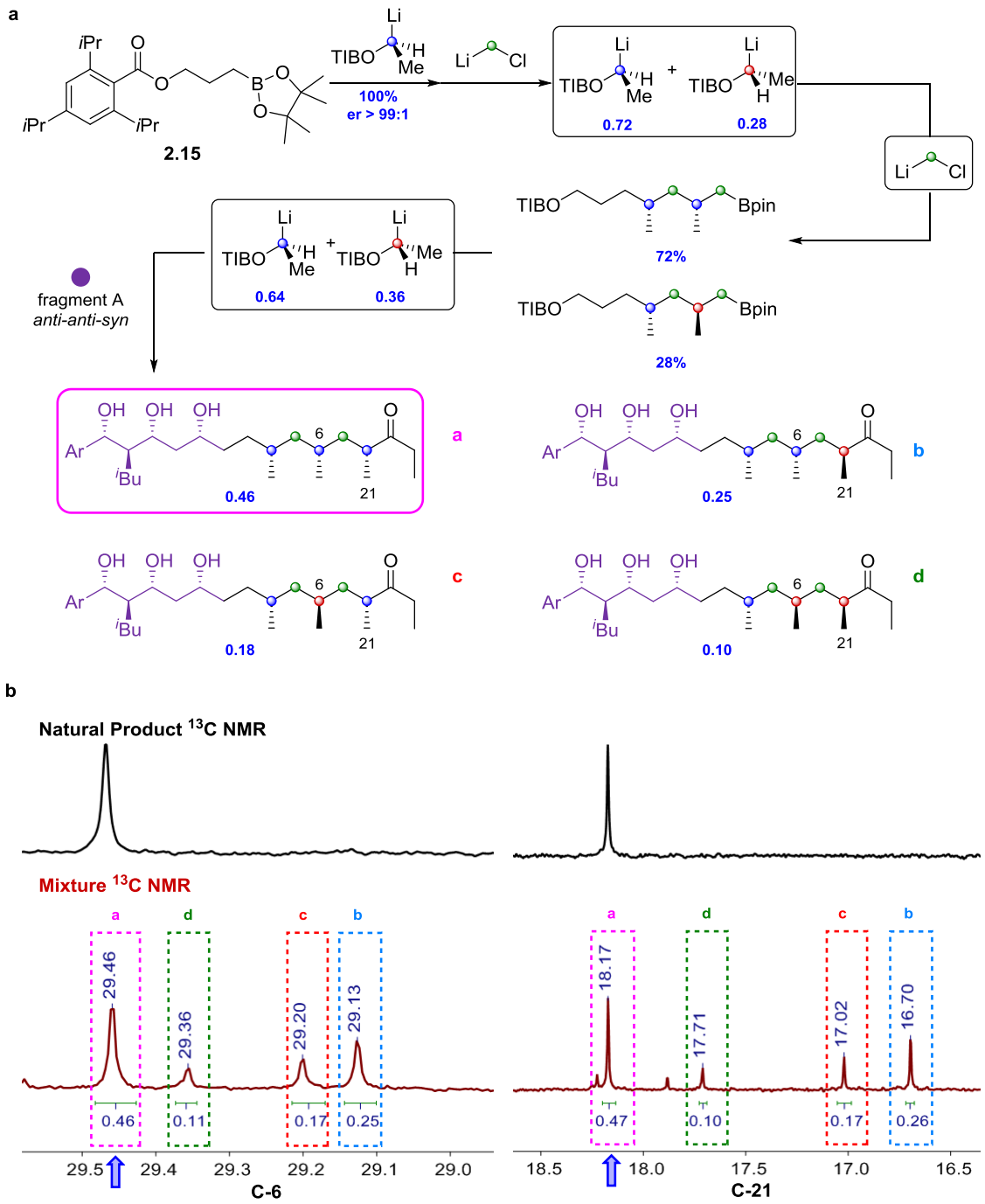

Figure 2.23. Determination of the relative stereochemistry of fragment B by assembly-line synthesis. **a**, synthesis of the encoded mixture of baulamycin A diastereomers (by virtue of known but inequivalent amounts of each isomer). **b**, Comparison of the mixture ^{13}C NMR spectrum (C6 and C21, red) with that of the natural product (black) indicating a match for signals corresponding to **2.14**.

In order to accurately quantify the mixture using NMR spectroscopy, the ratio between the four diastereomers was designed to be 46:25:18:10, where the difference in peak intensity is maximised. The desired ratio of diastereomers was achieved using different er values of >99.9:0.1, 72:28 and 64:36 for the α-stannyl ethyl benzoate in the assembly line synthesis

(discussed in Chapter1, Section 1.4) with primary boronic ester **2.15** to construct the C8, C6 and C4 stereocentres (Figure 2.23a). After the assembly-line synthesis, the mixture was coupled to the computationally derived fragment A to give a mixture of baulamycin A diastereomers with the desired ratio. The comparison of the ^{13}C NMR to that of the natural product at C6 and C21 revealed that chemical shifts of the diastereomer with the highest population (~46%, Figure 2.23b) matches very closely to that of the natural product. Therefore, in agreement with the DFT calculations, the relative configuration of fragment B is *syn–syn*, not *anti–anti* as originally proposed.

With the relative configuration within each fragment established, the configuration between C11 and C8 (*anti* or *syn*, Figure 2.24) was solved by synthesis. Compound **2.16** (C11/C8 *anti*) and **2.17** (C11/C8 *syn*) were synthesised. Although both compounds match the ^{13}C NMR spectrum of the natural product closely, there are significant differences in the ^{1}H NMR spectrum between **2.16** and that of the natural product for H-9 (**2.16**: 1.47 and 1.05 ppm; baulamycin A: 1.33 and 1.19 ppm) and H-10 (**2.16**: 1.48 and 1.33 pm; baulamycin A: 1.43-1.38 ppm), whereas the ^{1}H NMR spectrum of **2.17** match up perfectly with that of the natural product. However, the optical rotation of the synthetic matching diastereomer **2.17** is positive ($[\alpha]_D^{20}$= +6.25 (*c* 0.8, MeOH)) whereas the reported value of the isolate natural product is negative ($[\alpha]_D^{20}$= −10.3 (*c* 0.2, MeOH)). Therefore, the enantiomer of **2.17** was prepared and finally all analytical data fully matched that of the isolated natural product.

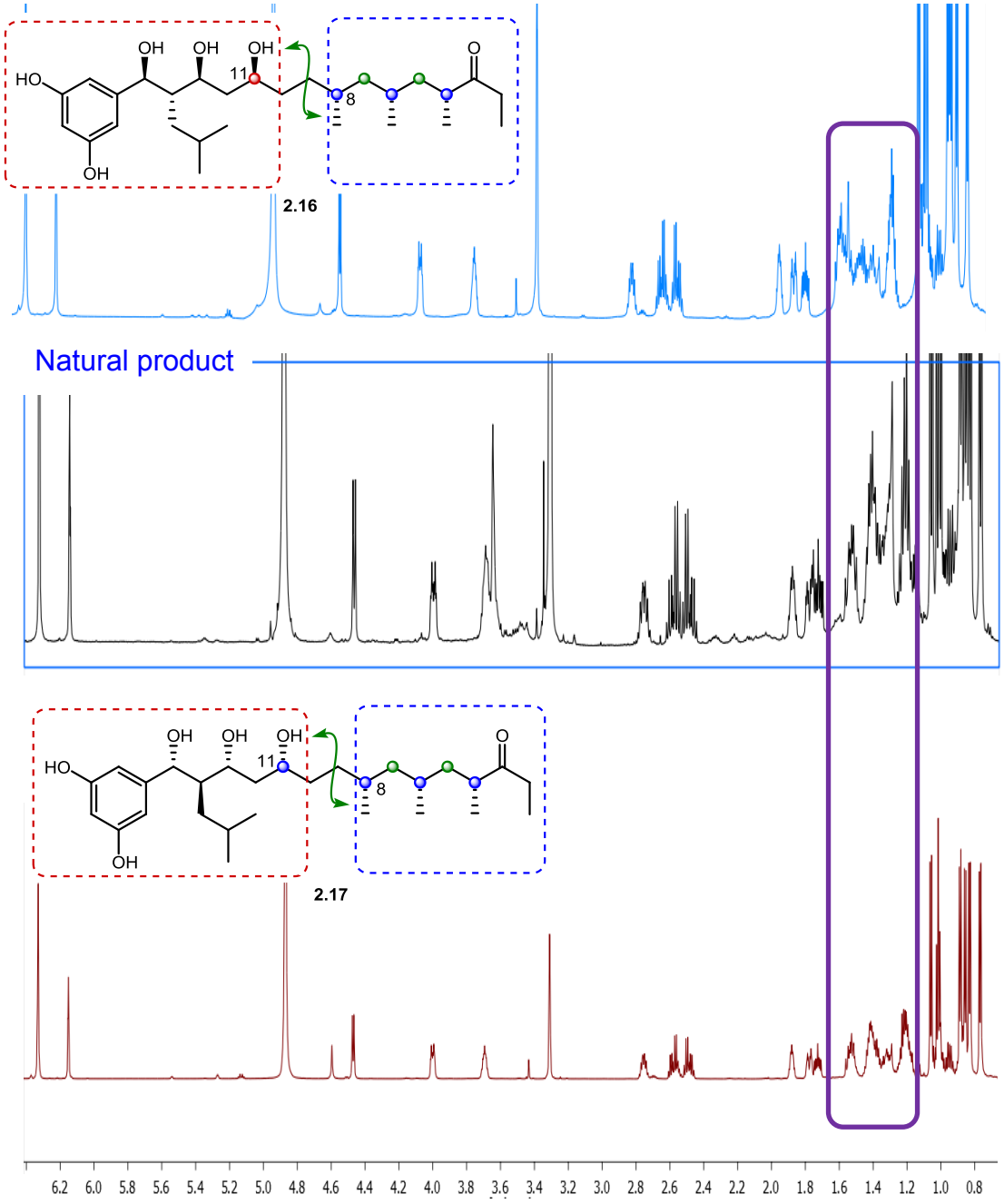

Figure 2.24. Determination of the relative configuration between C11 and C8. Top: ^{1}H NMR of synthetic **2.16** with C11-C8 *anti*. Middle: ^{1}H NMR of the isolate baulamycin A provided by Sherman *et al.* Bottom: ^{1}H NMR of the synthetic **2.17** with C11-C8 *syn*.

2.3 Conclusions and Future work

2.3.1 Conclusions

In conclusion, the relative and absolute configuration of baulamycins was revised using a combination of computation, NMR and synthesis. We have shown that by performing a detailed computational analysis of the NMR properties of 8 diastereomers, we were able to confidently exclude 112 out of 128 possible stereoisomers for baulamycin without heavily relying on chemical synthesis. While the lack of NMR data hindered the analysis of the relative configuration of fragment B, assembly-line synthesis allowed the rapid access to the correct relative configuration of fragment B. Finally, synthesis established the relative configuration between both fragments and the absolute configuration of the natural product.

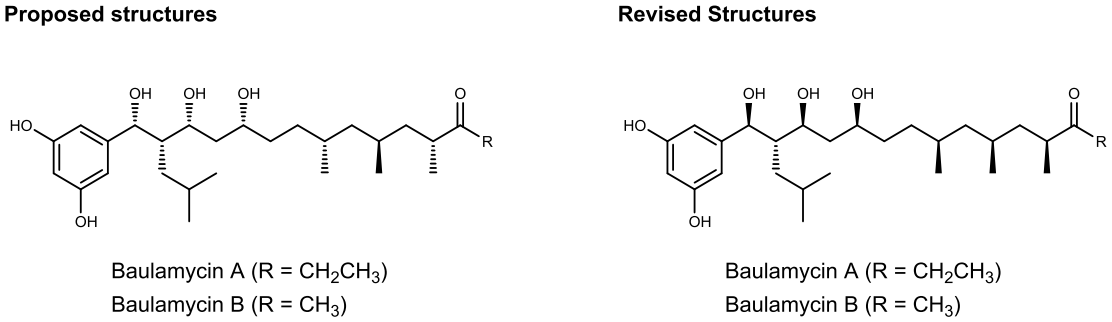

Figure 2.25. Structures of the originally proposed[95] and revised structures.

From this work, it is apparent that structural elucidation of flexible, acyclic natural products using either empirical *J*-based configurational analysis or solely the comparison of chemical shifts is inadequate due to the complex conformational landscape of these molecules. Further development in the accuracy of conformational analysis and the calculation of NMR parameters by computation, together with new NMR experiments for accessing hard-to-measure NMR properties, would allow one to determine the relative configuration of acyclic natural product (such as baulamycins) exclusively *in silico*.

2.3.2 Future work

It appears that the inclusion of implicit solvent in the initial molecular mechanics conformational search made a significant difference to the resulting DFT calculated ensemble-averaged NMR data (^{1}H-^{1}H scalar coupling constants and ^{1}H-^{1}H distances) Therefore, running the initial conformational search and the subsequent DFT calculations in explicit solvent should further improve the accuracy of the conformational analysis by properly accounting for energies of intramolecular hydrogen bonding interactions.

Although population refinement could be used (to an extent) to correct the DFT approximate conformer energies based on the natural product ^{1}H-^{1}H distances, care should be taken when applying this approach with an incomplete set of conformations. As section 2.2.4 discussed, comparison of ^{1}H-^{1}H distances of **2.6**, which was previously 'unoptimisable' (section 2.2.2), could be 'optimised' with a more diverse set of fragment A conformations. This result highlights the limitation of the randomly sample conformations by subsequent DFT calculations because it solely relies on chance to locate conformers which will eventually become low in energy at the stage of DFT calculations. Obviously, the ideal solution would be to perform DFT calculations on every single conformation found by molecular mechanics conformational search. However, this is a highly time-consuming and resource-intensive task when dealing with several diastereomers of a highly flexible small molecule, such as the case of baulamycins. Therefore, a sampling method should be devised to sample the maximum diversity of the conformational landscape of a given molecule. One way to achieve this would be doing a combination of molecular mechanics and molecular dynamics conformational search to maximise the chance to locate all local minima of a molecule, then cluster the output conformations based on structural similarity.

Now having access to some amount (~3 mg) of the natural product via chemical synthesis, it is possible to collect more NMR data of the natural product to determine the relative configuration of fragment B, as well as the relationship between fragment A and fragment B without the use of synthesis.

Due to the lack of resolution of the 2D-ROESY provided by Sherman *et al.*, quantitative NOE-distance analysis and the subsequent NOE-based population refinement of fragment B isomers were not viable. In theory, one could record a very high resolution 2D-ROESY using appropriate relaxation delay in a high field NMR instrument (> 700 MHz) and try to extract a reasonable number of ^{1}H-^{1}H distances from the spectrum. The experimental ^{1}H-^{1}H distances

will not only allow us to apply the NOE-based population refinement to a different motif, but also to access the accuracy of the DFT-derived conformer population of isomers computed for fragment B.

Lastly, it will be interesting to record NMR data of baulamycins in anisotropic conditions to obtain residual dipolar couplings, which provide global information of molecular conformation(s), and to explore the used of residual dipolar couplings in the determination of relative configuration of baulamycins, especially the determination of the relationship (*syn*/*anti*) between fragment A and fragment B, which was resolved by synthesis at this stage.[109]

Chapter 3 *tert*-Butyl group: effect on molecular conformation

3.1. Introduction and project outline.

In the 1990s, Alder and co-workers realised that the $C_{quaternary}$–***C–C***–C bond (C3–C4 of **3.1**, Scheme 3.1a) can only adopt an antiperiplanar conformation based on the MM2 calculation results of CEr_4 and CPr_4 together with examination of the crystal structure of several tetraammonium salts, including Et_4N^+, nPr_4N^+ and nBu_4N^+.[110] The conformational preference of the C2–C3–C4–C5 dihedral arises from the avoidance of *syn*-pentane interactions[5] between the C1–C2 bond and the terminal methyl group (C5). Since the quaternary centre (C2) is free to rotate around the C2–C3 bond and the resultant rotamers are energetically degenerate, there is always a C–C bond in place to induce destabilising *syn*-pentane interactions, thus the C2–C3 bond can only be antiperiplanar to the C4-C5 bond. This phenomenon is known as the *tert*-butyl effect.[13,110-112]

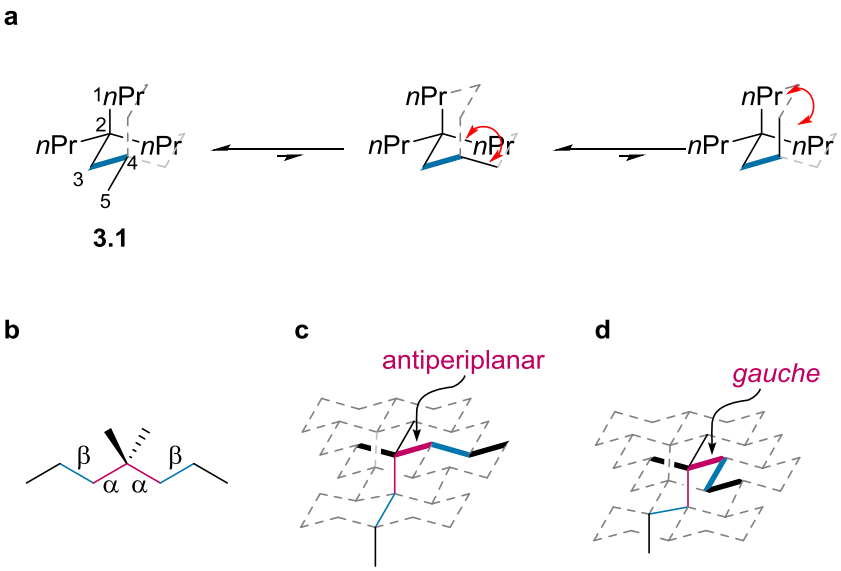

Scheme 3.1: a, Conformational control exerted by a quaternary centre in the case of CPr_4 **3.1**. **b**, Chemical structure of 4,4-dimethylheptane. **c** and **d**, Possible diamond lattice conformers of 4,4-dimethylheptane with the arrangement of the α bonds (*anti* or *gauche*) highlighted in red.

The same effect could also be observed in the case of 4,4-dimethylheptane (Scheme 3.1b), where the chains continue on both sides of a quaternary centre.[113] The two β dihedrals can only adopt an antiperiplanar conformation with respect to the quaternary centre but the α dihedrals can adopt either *anti* or *gauche* conformations (Scheme 3.1c and d). Therefore, the use of quaternary centres for the design of molecules with defined conformation is limited in

cases where the conformation of the α bond is controlled, or the quaternary centre is placed at the terminal position of the chain.

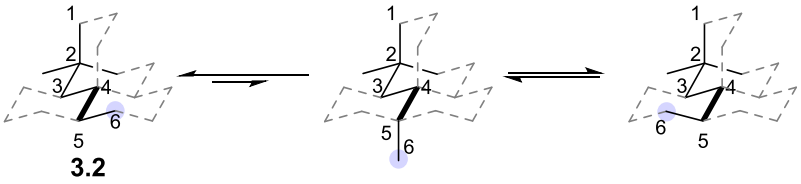

Scheme 3.2: Three possible diamond lattice conformers of 2,2-dimethyl hexane **3.2**.

Although the quaternary centre has exquisite control over the conformation of the $C_{quaternary}$–***C***–***C***–C bond (C3–C4, Scheme 3.1a), the control in conformation diminishes as one moves away from the quaternary centre. In the case of **3.2** (Scheme 3.2), the C4–C5 bond could adopt either an *anti* or *gauche* conformation because the terminal methyl group (C6) could be placed at either one of the three positions on a diamond lattice due to the lack of destabilising *syn*-pentane interactions. The diminishing control in conformation was observed in the examination of the crystal structures of nBu$_4$N$^+$ salts by Alder and co-workers[110], as well as the NMR studies of compound **3.3** (Figure 3.1) by Hoffmann and co-workers.[112-113]

Compound **3.3** (Figure 3.1a) bearing a terminal quaternary centre was designed to have a helical conformation. Its conformational behaviour in solution was investigated using ^{1}H-^{1}H scalar coupling constants. Due to spectral overlap, only the J values of one of the diastereotopic protons at the C4 and C6 positions were extracted. H_4 has vicinal coupling constants of 10.3 and 2.2 Hz and the magnitude of the values suggests a high preference of a single conformation in segment A. Slightly 'averaged' vicinal coupling constants were measured from H_6 (9.0 and 4.4 Hz), which implies a slight reduction in conformational preference in segment B.[112-113]. This experimental observation is further supported by calculation results of **3.4** – **3.6** (Figure 3.1b) using MM3 force field, which showed a dramatic decrease for the preference of the dominant helical conformation with longer chain length, attributed to the diminishing conformational control exerted by the terminal quaternary centre.[112]

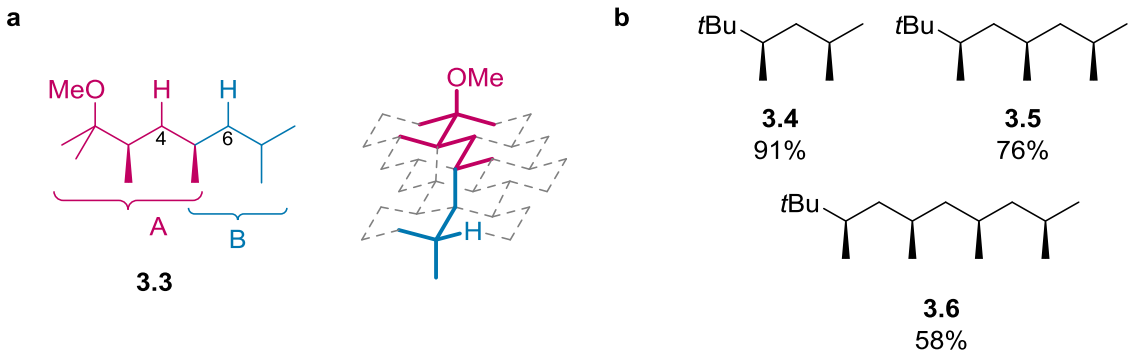

Figure 3.1: a, Chemical structure of **3.3** and its designed diamond–lattice type conformation.[112-113] **b**, Carbon chains bearing a terminal *t*Bu group and *syn*-1,3-dimethyl units with the calculated population of the conformational preference of a single dominant conformation.[112]

To achieve remote conformational control of extended hydrocarbon scaffolds, one could place quaternary centres at both ends of the chains to exert conformational control from both directions. The NMR analysis of $Me_3N^+(CH_2)_nN^+Me_3$ type ions (Figure 3.2a) in D_2O performed by Dufourcq and co-workers showed that when the two nitrogen quaternary centres are separated by three carbon units (i.e. n = 3, **3.7**, Figure 3.2a), only a single conformation is dominant in solution, with dihedrals a and b adopting *anti* conformations. Unfortunately, as discussed before, the conformational control exerted by nitrogen quaternary centres diminishes with increasing distance from the centres, thus when there are more than three carbon units between both quaternary centres, such as in the case of **3.8** and **3.9** (Figure 3.2a), more conformations are accessible due to free rotation of the central bond (bond d in **3.8** and bonds d and e in **3.9**, Figure 3.2a).[114]

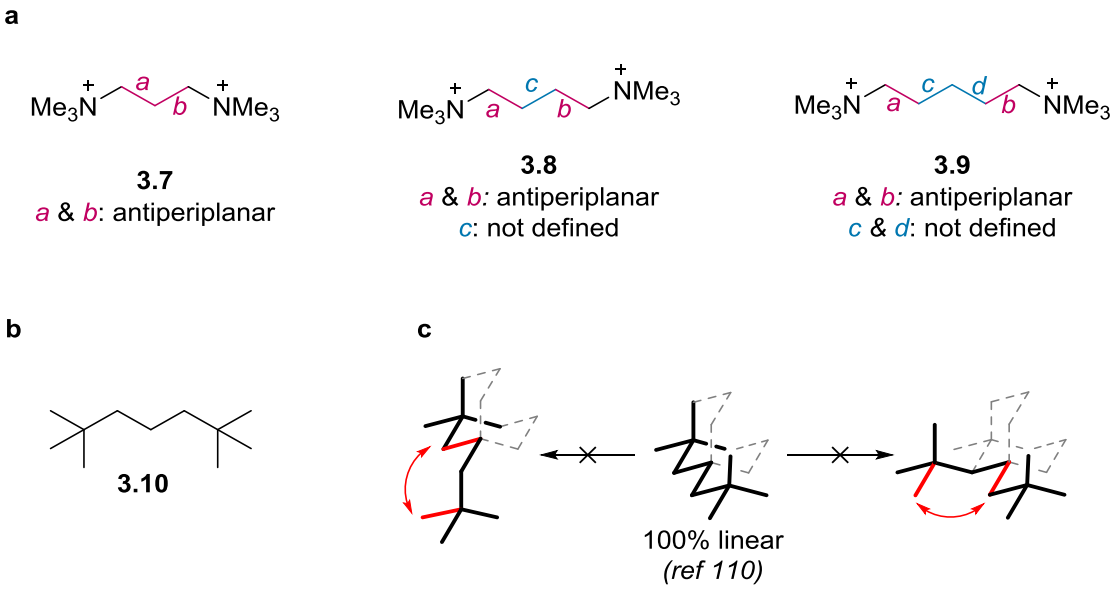

Figure 3.2: a, Preference of dihedral angles (ϕ_a – ϕ_e) derived from NMR studies of a series of $Me_3N^+(CH_2)_nN^+Me_3$ type ions in D_2O.[114] **b**, Chemical structure of 2,2,6,6-tetramethylheptane **3.10**. **c**, Dominant conformation represented on a diamond lattice with *syn*-pentane interactions (red arrows) highlighted in unfavourable conformations.

Alder and co-workers have proposed that by having two terminal carbon quaternary centres three carbons away from each other, one single conformation dominates. This is because the *t*Bu groups reinforce the conformation of the backbone from both directions and destabilise conformations with a non-linear backbone with *syn*-pentane interactions (Figure 3.2c). Although changing from nitrogen to carbon quaternary centres would change the enthalpic penalty of *syn*-pentane interactions due to different X_q–C bond lengths, the C–C bond length is somewhat similar to the N–C bond length (1.54 and 1.49 Å, respectively), therefore **3.10** should have a very similar conformational preference as **3.7** and should adopt a single conformation with a linear backbone (Figure 3.2b).[110-111]

Therefore, **3.10** could be used as a scaffold for the design of other molecules with tailored conformations. The *syn* isomer **3.11** would have both the ester and carbamate substituents s*yn* periplanar to each other ("U-shape"), while the *anti* isomer **3.12** would have both substituents turning a 120° corner ("L-shape"). The ester and carbamate groups were chosen initially to exploit their use as conformationally constrained unnatural amino acids.

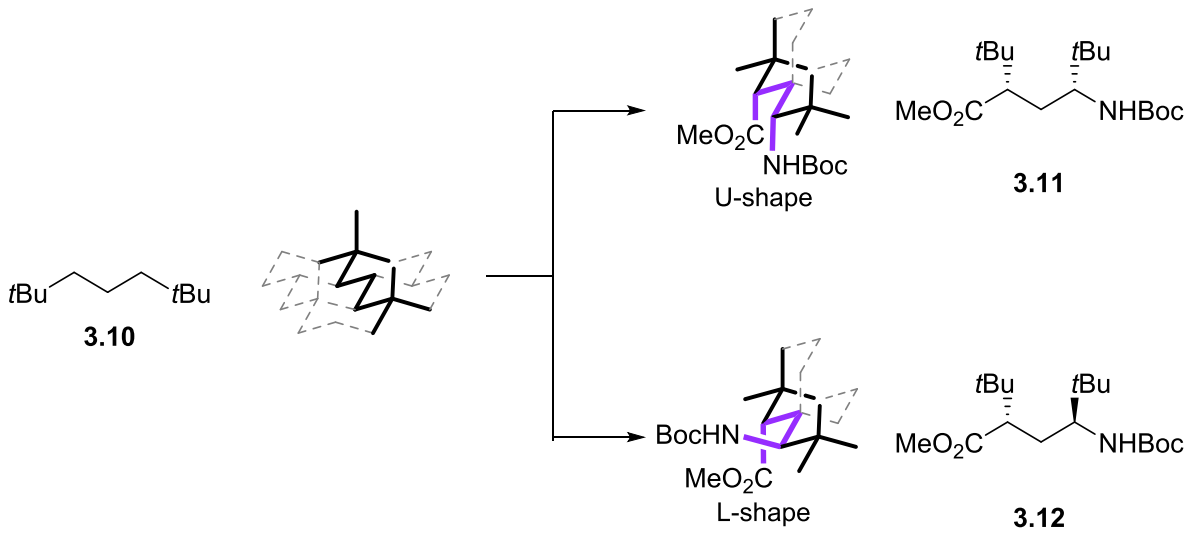

Scheme 3.3: Chemical structure and the expected diamond lattice conformation of **3.10**, **3.11** and **3.12**.

In this report, **3.11** (U-shaped molecule) and **3.12** (L-shaped molecule) will be synthesised using lithation–borylation methodology followed by functional group transformations. Their solution–state behaviours will be elucidated by quantitative analysis of ^{1}H-^{1}H, ^{1}H-^{13}C scalar coupling constants and NOE-derived ^{1}H-^{1}H distances using QM/NMR approach. It would be particularly interesting to establish the dominant conformation of **3.11** (U-shape), since the substituents also impose a destabilising *syn*-pentane interaction.

As discussed earlier, the conformational control exerted by both quaternary centres at the ends of the chain diminishes when there are more than three carbon units between the quaternary centres. It might be possible to regain the conformational control of the central bond(s) in **3.13** and **3.14** by adding destabilising *syn*-pentane interactions in undesired conformations. This in principle can be achieved by introducing substituents at specific positions with suitable stereochemistry. A combination of diamond lattice analysis and computational modelling will be used to guide the design of substituted analogues of **3.13** and **3.14**. Candidates showing strong preference (>80% of global population) towards a particular conformation by computational modelling will be synthesised and their solution–state behaviour will be studied using QM/NMR approach.

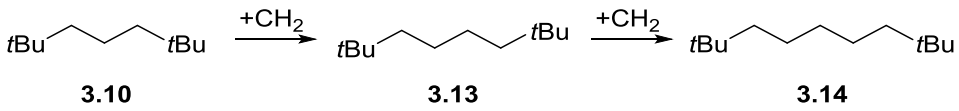

Scheme 3.4: Structure of **3.10**, **3.13** and **3.14** with different numbers of methylene units between two terminal quaternary centres.

3.2 Results and Discussion

Development of synthetic methodology and QM/NMR analysis of U-shaped and L-shaped molecules (Compounds 3.11 and 3.12).

3.2.1 Synthesis of 3.11 and 3.12.

To synthesise both target compounds **3.11** and *ent*-**3.12**, two retrosynthetic routes were proposed, utilising the reagent controlled lithiation–borylation methodology developed by the Aggarwal group[8], as scheme 3.5 outlines.

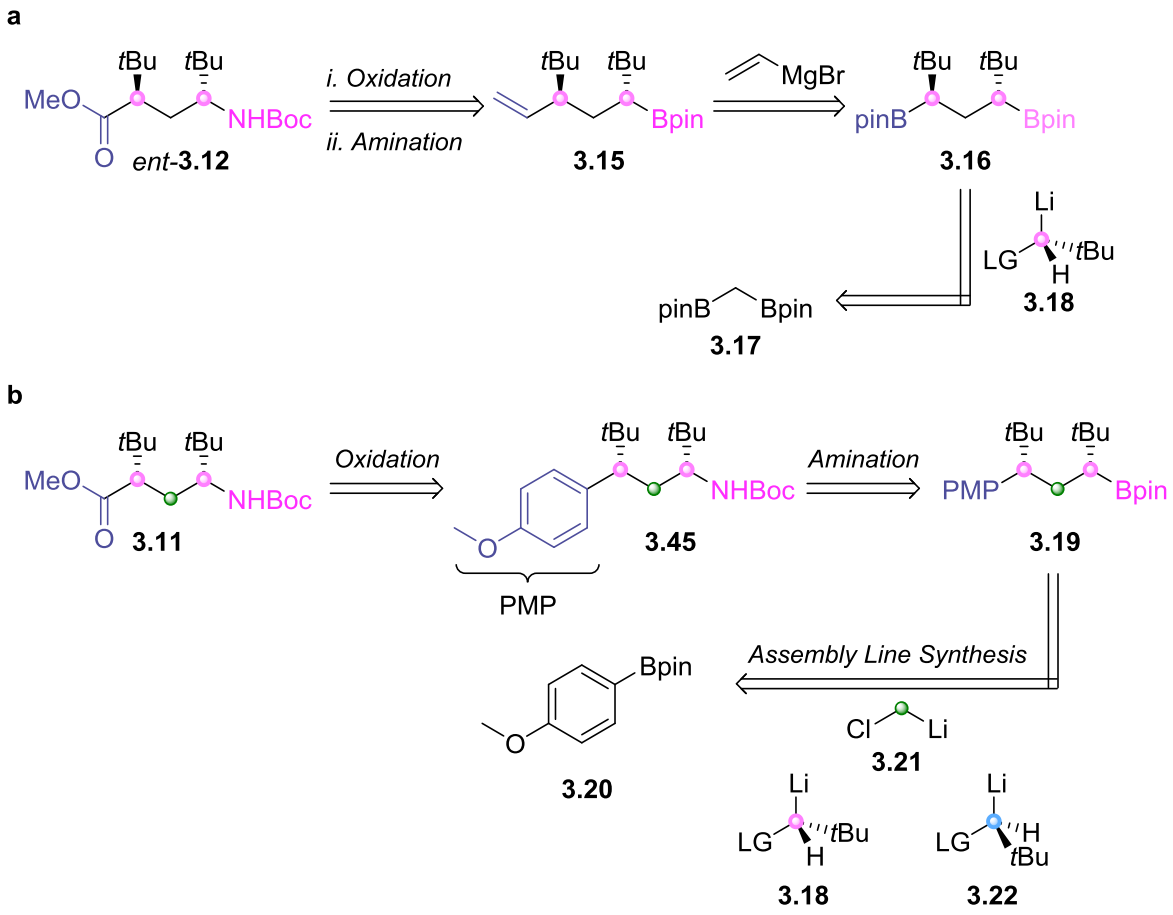

Scheme 3.5: Retrosynthetic analysis based on (**a**) bidirectional chain growth approach and (**b**) unidirectional chain growth approach.

In the bi-directional chain growth approach (Scheme 3.5a), the ester functionality would be unmasked via oxidation of terminal alkene **3.15** followed by methylation of the resultant carboxylic acid. The carbamate group would be installed via a stereospecific amination of the boronic ester in **3.15**.[115-116] The key intermediate **3.15** could be generated via desymmetrisation of a *C2* symmetric bis (boronic) ester **3.16** using Zweifel oliefination[117], and the bis boronic ester **3.16** could be synthesised by bi-directional homologation of

diborylmethane **3.17** with the requisite carbenoid **3.18**.[118] Although the bidirectional approach is only suitable for the enantioselective synthesis of *ent*-**3.12** (L-shaped), it is a short route to gain access to one of the two target molecules.

In the uni-directional approach (Scheme 3.5b), the ester functionally would be introduced via oxidation of a 4-methoxyphenyl group using $RuCl_3$ in the presence of $NaIO_4$.[94,119] Again, functional group interconversion of the carbamate would give the secondary boronic ester **3.19**, which can be constructed using assembly line synthesis with the requisite carbenoids starting from 4-methoxyphenyl pinacol boronic ester **3.20**.

For both routes the starting boronic ester could be synthesised following literature procedures[8,120] and the $ClCH_2Li$ carbenoid **3.21** could be generated *in situ* by the addition of *n*BuLi to bromochloromethane at −78 °C.[94] This only leaves with the synthesis of chiral building block **3.18** and **3.22**, with either Hoppe-type carbamate or Beak-type benzoate leaving groups.

Since asymmetric deprotonation of carbamates usually gives greater enantioselectivity (er ~ 98:2)[90,121-123] than that of the corresponding benzoate (er ~ 95:5)[93,124-125], the use of Hoppe-type carbamates as the leaving group was first considered. Unfortunately, Hoppe and co-workers demonstrated that neopentyl carbamate **3.23** could not undergo asymmetric deprotonation (within 4 hours) when (−)-sparteine **3.24** was used as the diamine ligand (Scheme 3.6).[126] Although the deprotonation is possible using a sterically less demanding diamine ligand **3.25**, the enantioselectivity of the lithiation was moderate (89.5:10.5, Scheme 3.6), which is undesirable for the development of the enantioselective synthesis of the target molecules **3.11** and **3.12**.

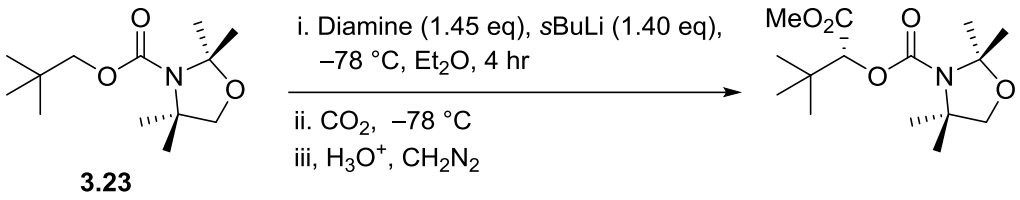

Diamine	Yield(%)	er
3.24	0	-
3.25	42	89.5:10.5

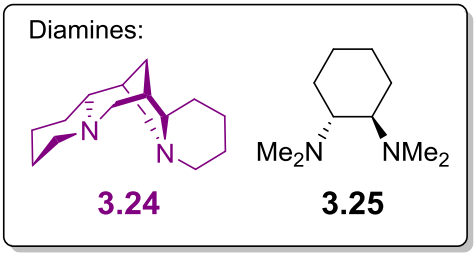

Scheme 3.6: Asymmetric deprotonation of neopentyl carbamate **3.23** using either **3.24** or **3.25** as the diamine ligand.

Fortunately, the neopentyl benzoate **3.26** undergoes steady asymmetric deprotonation with high enantioselectivity (er ≥99:1)[127] when (+)-sparteine is used as the diamine ligand, despite the fact that the α-proton of both **3.23** and **3.26** have similar p*K*a values.[128] The resultant lithiated species could then be trapped directly by a boronic ester with a very long borylation time ($t_{1/2}$ = 296 minutes, ~5 hours) to generate the homologated product **3.27**. Crucially, the use of excess organolithium base, which is required for efficient deprotonation of benzoate **3.26**, is undesirable for the homologation with precious boronic esters. Therefore, there is a need to develop a stable, convenient precursor of both enantiomeric forms of the neopentyl carbenoids.

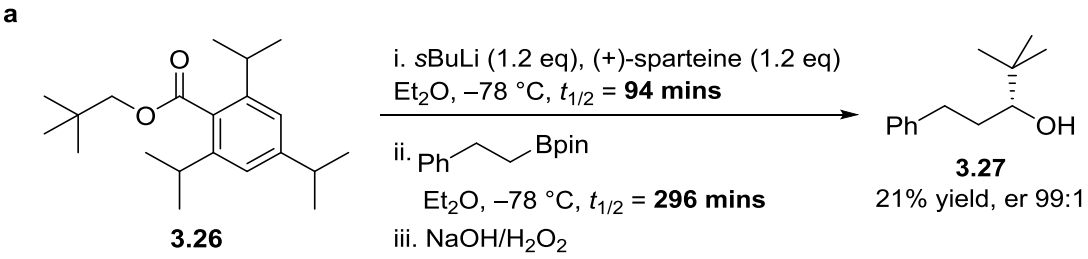

Scheme 3.7: Asymmetric deprotonation of neopentyl benzoate **3.26** using (+)-sparteine followed by trapping with phenyl ethyl pinacol boronic ester to give the homologated product **3.27** after oxidation.

The Aggarwal group has reported the use of both α-sulfinyl[129] and α-stannyl[8] benzoates (cf. **3.28** and (*S*)-**3.29**, respectively, Scheme 3.8) as bench-stable carbenoid precursors for the stereospecific homologation of boronic esters. For both classes of precursors, the carbenoid is unmasked by either sulfoxide– or tin–lithium exchange to give the configurationally stable neopentyl carbenoids (*S*)-**3.30**.

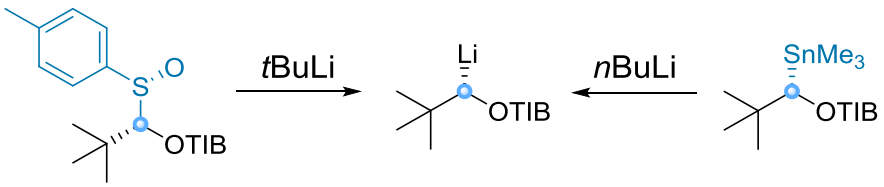

3.28 (*S*)-**3.30** (*S*)-**3.29**

Scheme 3.8: Two carbenoids precursors of neopentyl carbenoids (*S*)-**3.30**.

While the α-stannyl ethyl benzoates could be accessed in very high enantiopurity (> 99.9:0.1) via recrystallisation and used for the synthesis of molecules with 10 contiguous methyl stereogenic centres as single diastereomers (discussed in section 1.4), there are several drawbacks associated with the use of α-stannyl alkyl benzoates. First of all, in order to access these building blocks in very high enantiopurity, the α-stannyl alkyl benzoates must be crystalline solids. However, the physical state of the stannyl compounds are highly dependent on the nature of the pendant alkyl group. More importantly, in order to generate both enantiomers of the α-stannyl alkyl benzoate the use of both enantiomeric forms of sparteine is required. However, it is increasingly difficult to access the (–)-enantiomer of sparteine. Together with the toxicity associated with organotin compounds, the use of α-sulfinyl benzoates **3.28** as a precursor is very attractive because its synthesis does not require both chiral diamine ligands or highly toxic reagents. In addition, the *syn* isomer of α-sulfinyl benzoates is usually a crystalline solid, thus allowing access to enantiopure building blocks via recrystallisation.

The preparation of the α-sulfinyl benzoates began with the synthesis of the neopentyl benzoate **3.26** by a Mitsunobu reaction between 2,4,6-triisopropyl benzoic acid **3.31** and neopentyl alcohol (93% yield, Scheme 3.9a). The benzoate **3.26** was lithiated in the presence of tetramethylethylenediamine (TMEDA) followed by trasmetallation using $MgBr_2{\cdot}OEt_2$ to generate the corresponding magnesium carbenoids **3.32**, which was then trapped by Andersen's sulfonate to generate both *syn* and *anti* α-sulfinyl benzoates **3.28** and **3.33** in high enantiopurity with inversion of stereochemistry at the sulfur centre. The er of the *syn* isomer **3.28** could be further enhanced to > 99:1 by recrystallisation.[129]

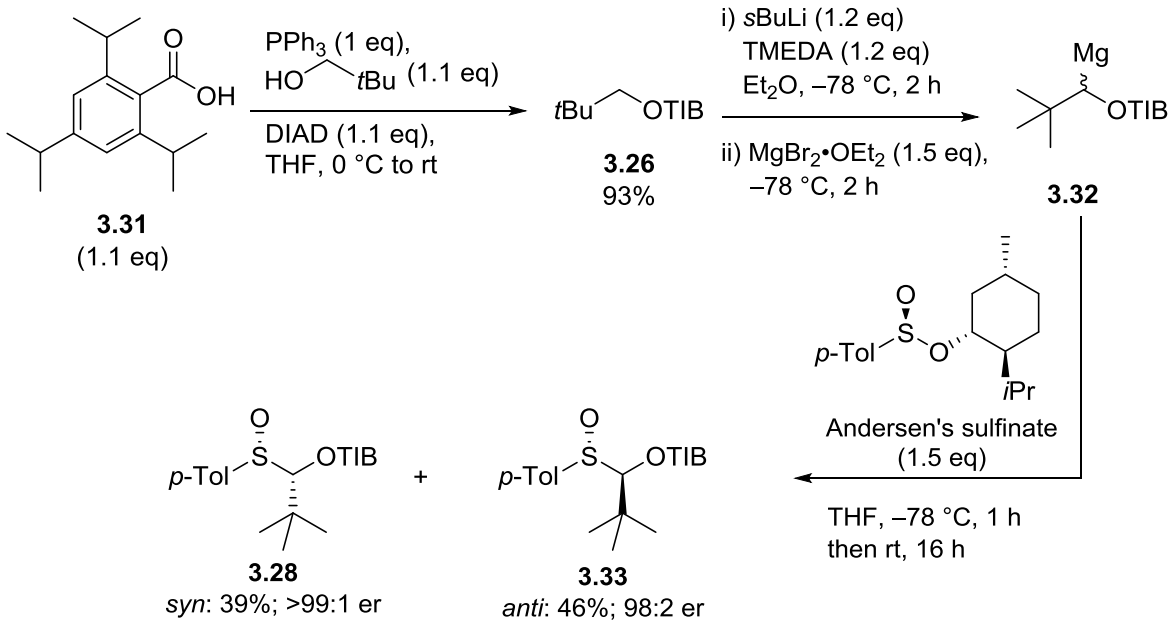

Scheme 3.9: Synthesis of neopentyl benzoate **3.26** and both diastereomers of α-sulfinyl benzoates **3.28** and **3.33**.

The use of α-sulfinyl benzoate **3.28** in lithiation–borylation was investigated by Dr. Murat Kucukdisli in the Aggarwal group (Scheme 3.10a). When *t*BuLi was added to a mixture of boronic ester **3.34**, α-sulfinyl benzoates **3.28** and *N*,*N*,*N*′,*N*″,*N*″-pentamethyldiethylenetriamine (PMDTA) in THF at −78 °C, the homologated product was not observed and only the neopentyl benzoate **3.26** (protodesulfinylation of the carbenoid precursor) was isolated. This suggests that the formation of the boronate complex **3.36** was slower than expected due to the hindered nature of the lithiated species (*S*)-**3.30**. Thus, the dominant pathway of the reaction was the protonation of the lithiated species (*S*)-**3.30**, presumably by the acidic α-proton of sulfinyl benzoate **3.28** or adventitious H_2O. To circumvent the quenching of the lithiated species (*S*)-**3.30** by the sulfinyl benzoate **3.28**, an inverse addition protocol was performed in which the α-sulfinyl benzoate **3.28** was added to a mixture of *t*BuLi and PMDTA in Et_2O followed by the addition of boronic ester **3.34**. The desired homologated product **3.35** was isolated in moderate yield (54%, Scheme 3.10a) but with reduced stereoselectivity (77% es).

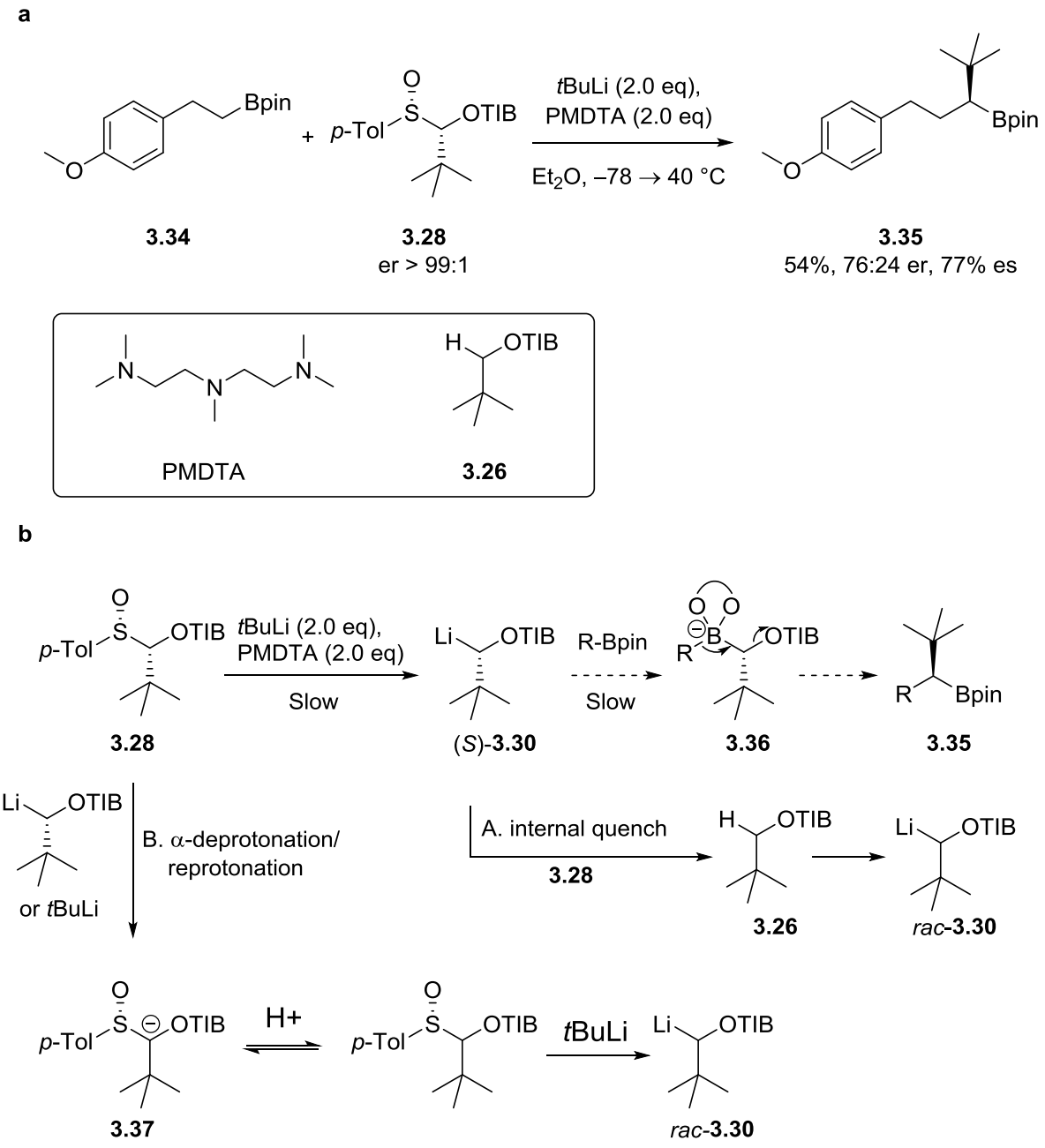

Scheme 3.10: Application of α-sulfinyl benzoate **3.28** in lithiation–borylation reactions. **a**: Reaction between the α-sulfinyl benzoate **3.28** and boronic ester **3.34**. **b**, Proposed competing reaction pathway which lead to reduced stereoselectivity observed in homologated product **3.35**.

The reduced stereoselectivity arises from a competing reaction pathway in which the racemic lithiated species *rac*-**3.30** is generated and engages in boronate complex formation with the boronic ester **3.34** (Scheme 3.10b). Due to steric hindrance of **3.28**, the rates of both sulfoxide–lithium exchange and the subsequent reaction of (*S*)-**3.30** with boronic ester **3.34** are slow. Therefore, newly generated chiral carbenoid (*S*)-**3.30** could deprotonate the acidic α-proton of any unreacted sulfinyl benzoate **3.28** to generate the protonated neopentyl benzoate

3.26, which could be deprotonated by *t*BuLi to generate racemic carbenoid *rac*-**3.30** (pathway A, Scheme 3.10b). The deprotonation of the unreacted chiral α-sulfinyl benzoate **3.28** generates an achiral anion **3.37**, which could be protonated by an internal proton source (for example **3.26**) and subsequently undergo sulfoxide–lithium exchange to generate the racemic carbenoid *rac*-**3.30** (pathway B, Scheme 3.10b). The racemic lithiated species *rac*-**3.30** ultimately leads to the formation of racemic homologated product and the observed erosion in er.

Next, the possibility of using α-stannyl neopentyl benzoate in the lithiation–borylation reaction sequence was considered. Since the α-deprotonation/reprotonation racemisation pathways observed for sulfoxide have not been observed with α-stannyl benzoate system, the use of the α-stannyl neopentyl benzoate should deliver the homologated product in perfect enantiospecificity.[8]

The α-stannyl neopentyl benzoate (*R*)-**3.29** was therefore synthesised by the lithiation of the neopentyl benzoate **3.26** in the presence of *s*BuLi (1.6 equivalents) and (+)-sparteine (1.6 equivalents) in anhydrous Et_2O at –78 °C for 24 hours followed by trapping with Me_3SnCl. The desired stannane (*R*)-**3.29** was obtained in good yield and with high enantioselectivity (92%, er 97.5:2.5, Scheme 3.11). The opposite enantiomer was synthesised by using (–)-sparteine in place of (+)-sparteine with identical yield and similar er (98:2). Unfortunately, both enantiomers of α-stannyl neopentyl benzoate are viscous oils and therefore cannot be re-crystallised to further improve their er.

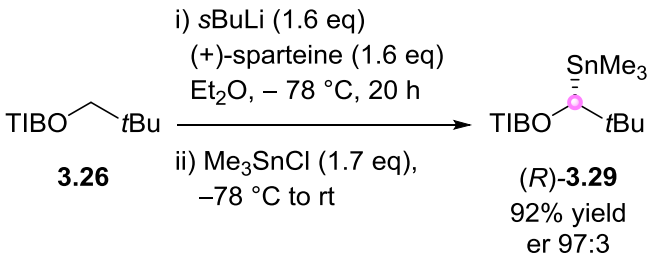

Scheme 3.11: Synthesis of α-stannyl neopentyl benzoate (*R*)-**3.29**.

With the α-stannyl neopentyl benzoates in hand, the bidirectional chain growth approach was first considered and the reaction between the lithiated species (*R*)-**3.30** and diborylmethane **3.17** was investigated (Scheme 3.12a). It was shown by the Aggarwal group that the reaction between diborylmethane **3.17** and a hindered carbenoid, for example the ones coordinated by a hindered diamine ligand (X = (+)-sparteine, Scheme 3.12b), would give

single-addition product **3.38**, whereas the reaction between **3.17** and an unhindered carbenoid, generated under diamine free conditions (X = Et_2O, Scheme 3.12b) would give double-addition product **3.39**.[118] Although the lithiated species (*R*)-**3.30** would be generated under diamine free conditions via tin–lithium exchange, it is sterically demanding and therefore it was not clear whether the reaction between (*R*)-**3.30** and **3.17** would give single- or double-addition product.

a

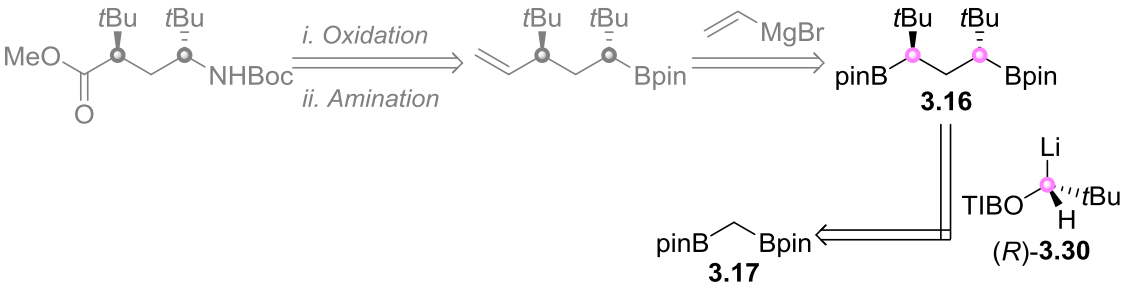

b

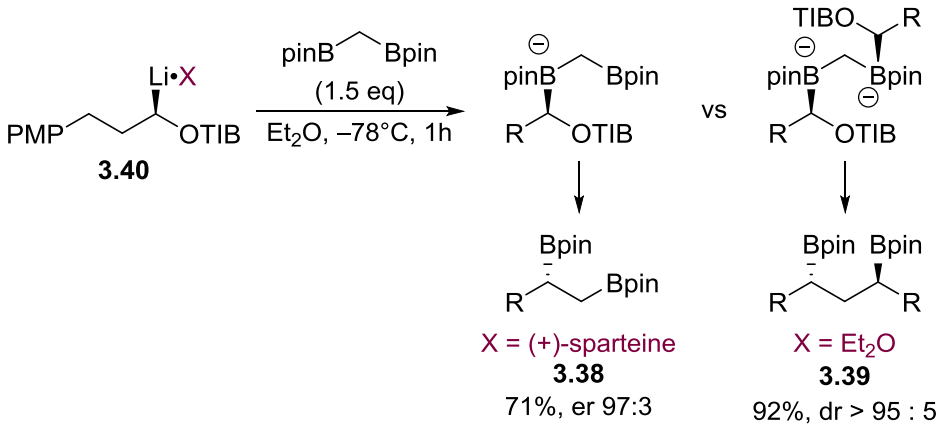

Scheme 3.12: a, Retrosynthetic analysis of bi-directional chain growth approach. **b**, Lithiation–borylation reaction between benzoate **3.40** with diborylmethane **3.17** in the presence of a diamine ligand (X = (+)-sparteine) or under diamine-free (X = Et_2O) conditions.

The lithiation–borylation reaction between diborylmethane **3.17** and α-stannyl benzoates (*R*)-**3.29** (Figure 3.3a) was monitored by the change of the carbonyl stretching frequencies ($\upsilon_{C=O}$) using *in situ* IR spectroscopy. The result was represented by plotting the concentration of each species observed in the reaction sequence (α-stannyl benzoates (*R*)-**3.29**, lithiated species (*R*)-**3.30**, boronate complex **3.41**) against time (Figure 3.3b).

The solution of α-stannyl benzoate (*R*)-**3.29** in Et_2O displayed a strong absorbance ($\upsilon_{C=O}$) at 1712 cm^{-1}. The addition of *n*BuLi to the solution initiated the tin–lithium exchange process and the above-mentioned signal (1712cm^{-1}) steadily disappeared with the appearance of a new signal at a lower wavenumber (1634 cm^{-1}) corresponding to the lithiated species (*R*)-**3.30**. The tin–lithium exchange was complete in ~1.5 hours and was found to be quicker towards (i.e. auto catalysis) the end of the exchange, reasons for which are currently unclear. Next, a solution of diborylmethane **3.17** in anhydrous diethyl ether was slowly added to the solution of lithiated species (*R*)-**3.30** at −78 °C and the formation of the boronate complex **3.41** (1658cm^{-1}) was found to be instantaneous (<15 s). Only ~50% of the lithiated species (*R*)-**3.30** was consumed, thus only one out of the two pinacol boronic esters engaged in boronate complex formation with the hindered lithiated species (*R*)-**3.30** to generate intermediate **3.41** (Figure 3.3c). Formation of the second boronate complex at the other unreacted boron centre was not observed at −78 °C with prolonged borylation time (3 hours) and at elevated reaction temperature (from −78 °C to −65 °C). Finally, the reaction was warmed to room temperature and stirred overnight for 1,2-migration to occur. The expected single-addition product **3.42** was isolated together with the secondary boronic ester **3.43**, which was generated via the fragmentation pathway, in moderate yields (33% each). Unfortunately, the addition of Lewis acid ($MgBr_2$ in anhydrous methanol) in the hope to promote the desired 1,2-migration pathway led to the formation of the secondary boronic ester **3.43** as the major product (52% isolated yield) and the desired single-addition product **3.42** as the minor product (< 5% isolated yield).

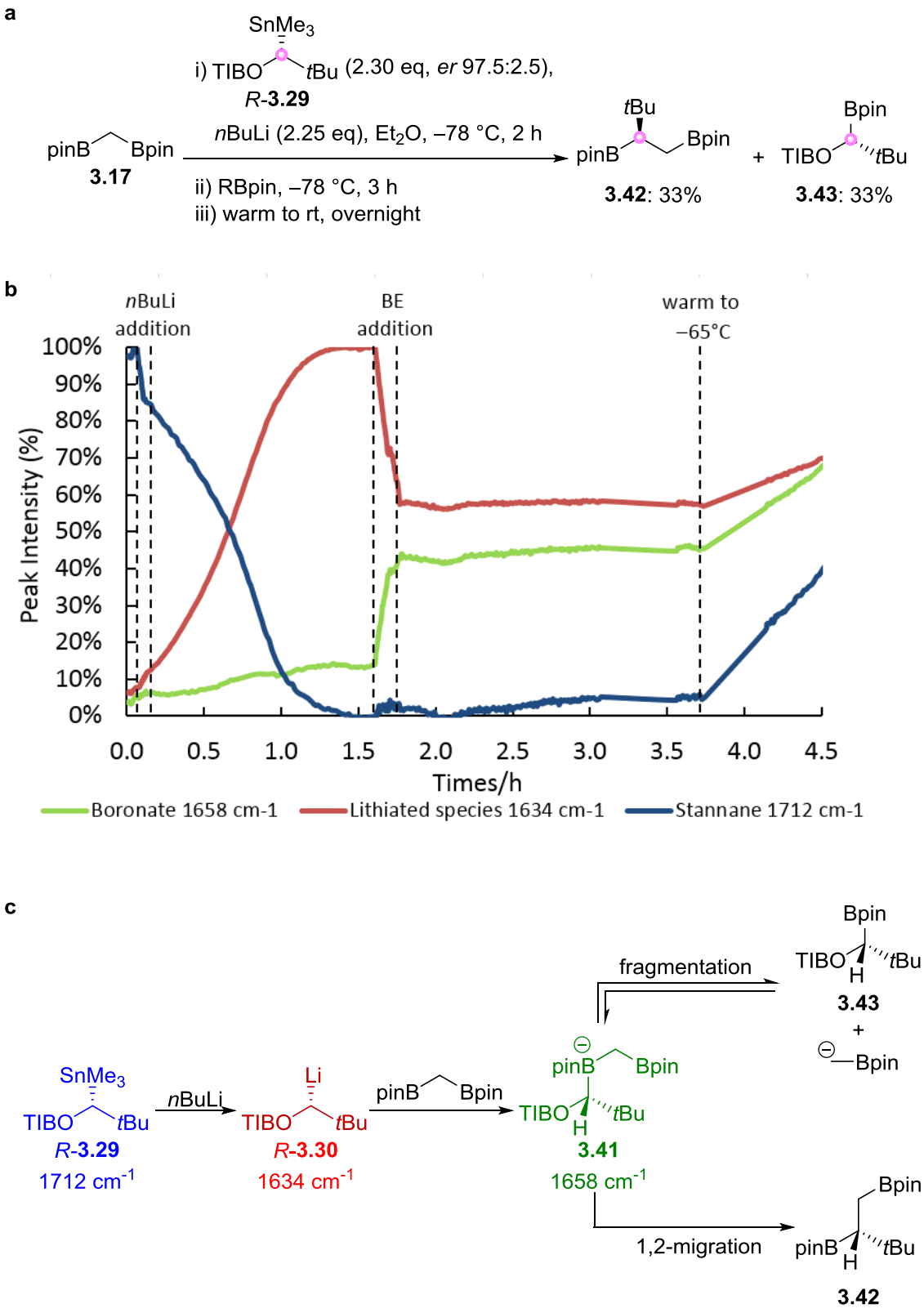

Figure 3.3: a, lithiation–borylation reaction investigated using react-IR spectroscopy. **b**, Traces of different species (blue: α-stannyl benzoates (*R*)-**3.29**; red: lithiated species (*R*)-**3.30;** green: boronate complex **3.41**) obtained from the react-IR study. **c**, Proposed reaction pathways which lead to the isolated products **3.42** and **3.43**.

Although the single-addition product **3.42** could be subjected to another lithiation–borylation reaction with lithiated species (*R*)-**3.30** and the less hindered primary boronic ester might preferentially undergo boronate complex formation, the fragmentation product **3.43** could not be eliminated and the single-addition product **3.42** was obtained in low yield (33%). Therefore, the bidirectional chain growth approach was abandoned and the unidirectional chain growth approach (Scheme 3.5b) was investigated instead.

As scheme 3.13 shows, the proposed synthesis of would start from boronic ester **3.20** and each carbon unit would be introduced using the requisite carbenoids for lithiation–borylation to deliver the key intermediates **3.19** and **3.44**. Boronic ester **3.19** will then be converted to carbamate **3.45**, using a stereospecific amination procedure developed by Morken and co-workers[115-116], and the electron-rich 4-methoxy phenyl group will be oxidised using $RuCl_3$ in the presence of $NaIO_4$ to yield the carboxylic acid **3.46**. [94,119] Methylation of the acid **3.46** using $TMSCHN_2$ would deliver the target compound **3.11** for QM/NMR analysis. The same synthetic sequence (amination & oxidation) could also be applied to the other diastereomer **3.44**.

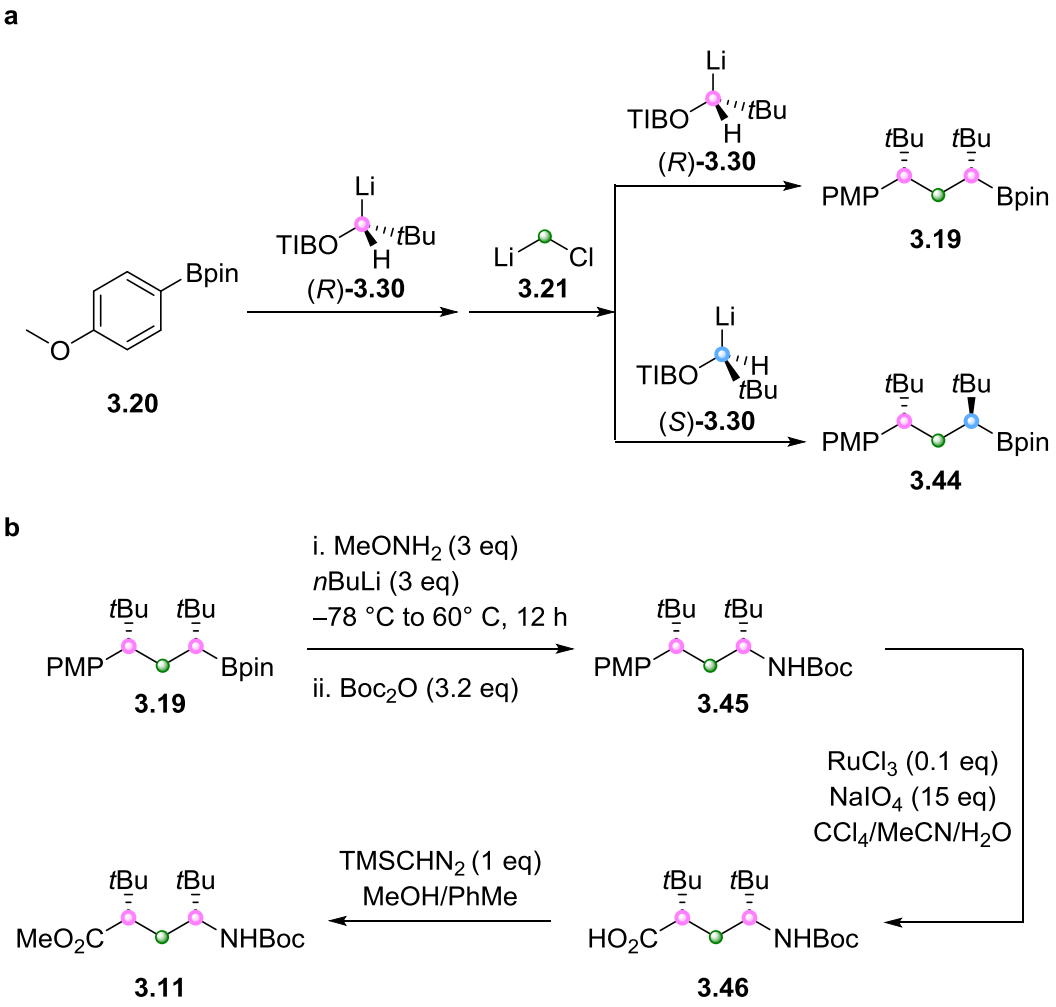

Scheme 3.13: Proposed synthesis of the unidirectional approach starting from 4-methoxyphenylboronic acid pinacol ester **3.20**.

A small scale lithiation–borylation reaction (0.2 mmol) between boronic ester **3.20** and α-stannyl benzoate (*R*)-**3.29** delivered the desired homologated product **3.47** in quantitative yield and high stereoselectivity (99.1% yield and 100% es, Scheme 3.14). Matteson homologation with **3.21**, which was generated *in situ* from bromochloromethane and *n*BuLi, led to the one carbon homologated boronic ester **3.48** with high conversion (>99%, monitored by GC–MS) and good yield (92%).

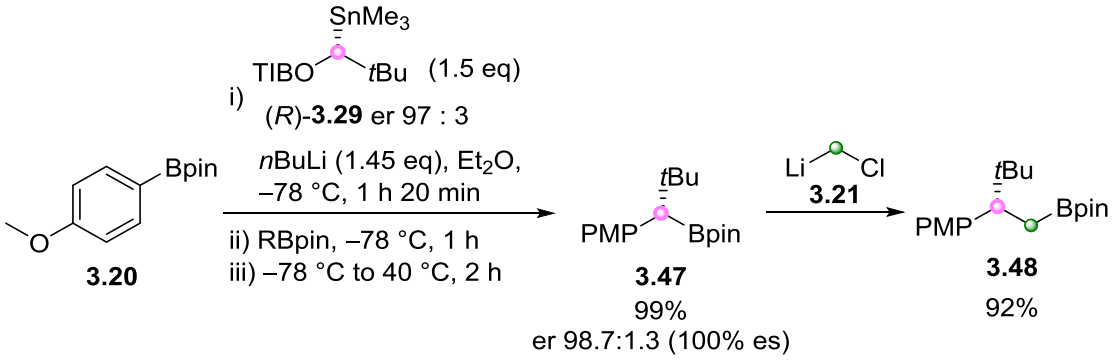

Scheme 3.14: Homologations of boronic ester **3.20**. Conditions for Matteson homologation: bromochloromethane (3 eq), *n*BuLi (2.5 eq), Et_2O (0.25 M of boronic ester), –78 °C for 20 minutes, then warm to room temperature for 1 hour.

However, when the Matteson homologation was performed to deliver boronic ester **3.48** on a larger scale (3.30 mmol, entry 2, Scheme 3.15), over homologated product **3.49** was also formed and the separation of these products was very challenging. Therefore, the possibility of eliminating the formation of over homologated product **3.49** was investigated.

Reduction of the reaction concentration may lead to slight increase in the formation of the desired product **3.48**, and a reduction of over homologated product **3.49** (entry 3, Scheme 3.15). It was thought that reducing the equivalents of the reactive lithiated species **3.21** would eliminate the possibility of the desired homologated product **3.48** undergoing further reaction to generate the undesired over homologated product **3.49**. Unfortunately, this led to the formation of a mixture containing unreacted starting boronic ester **3.47**, desired product **3.48** and over homologated product **3.49** (entry 4, Scheme 3.15). These two experiments suggest that reducing the reaction concentration lowered the amount of over homologated product **3.49** and a large excess of lithiated species **3.21** (2.5 eq) was required for full conversion of the starting boronic ester **3.47**.

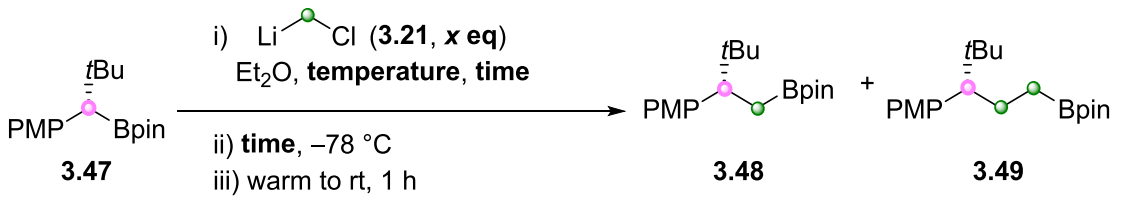

Entry	Scale	Concentration	Li Cl	Temp.	Total time at –78 °C	3.47:3.48:3.49 (GC-MS)
1	0.22 mmol	0.25 M	2.5	–78 °C	30 + 20 mins	0: 99.8 : 0.2
2	3.30 mmol	0.25 M	2.5	–78 °C	4.5 hr + 20 mins	0: 85 : 15
3	0.85 mmol	0.15 M	2.5	–78 °C	2 hr + 20 mins	0: 94 : 6
4	0.85 mmol	0.10 M	1.25	–78 °C	2 hr + 20 mins	2.8 : 92.3: 4.8
5	0.94 mmol	0.15 M	2.5	–95 °C	30 mins + 2hr	0 : 99.7: 0.3

Scheme 3.15: Optimisation of the Matteson homologation of **3.47** to form **3.48**.

Apart from the efficiency of heat transfer, one of the key differences between the small-scale and the large-scale Matteson homologations is the time the reaction mixture was left at –78 °C. Since the lithiated species **3.21** is very unstable even at –78 °C, *n*BuLi was added very slowly to the reaction mixture (1.2 mL/h) to avoid its decomposition. The formation of the over homologated product **3.49** suggests that during the formation of **3.21** at cryogenic temperature (< –70 °C), some of the boronate complex **3.50** underwent 1,2-migration to give the desired homologated product **3.48**, which then reacted with another lithiated species **3.21** to give the over homologated product **3.49** (Scheme 3.16).

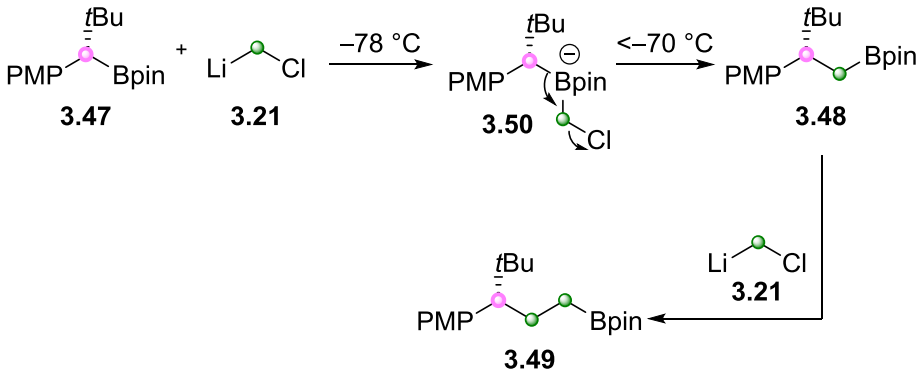

Scheme 3.16: Proposed mechanism for the formation of over homologated product **3.49**.

The solution to overcome this problem is to reduce the amount of 1,2-migration of the boronate complex **3.50** by shortening the reaction time at cryogenic temperature. This was achieved by a faster rate of *n*BuLi addition (2 mL/h) at reduced reaction temperature (from

–78 °C to –95 °C). This set of conditions led to product formation with good selectivity towards the desired product **3.48** (entry 5, Scheme 3.15).

Reaction between boronic ester **3.48** and the (*R*) enantiomer of the α-stannyl benzoate (*R*)-**3.29** gave the *syn* isomer **3.19** in moderate conversion (recovered 25% starting boronic ester **3.48**) and moderate isolated yield with good diastereoselectivity (66%, dr 95:5, entry 1, Scheme 3.17). The moderate conversion suggests that the boronate complex formation is reversible, presumably due to the hindered nature of the intermediate boronate complex. Therefore, the use of a Lewis acid additive ($MgBr_2$ in anhydrous methanol) to accelerate the rate of the desired 1,2-migration pathway[130] was explored. Pleasingly, the *syn* isomer **3.19** was obtained in good yield and good diastereoselectivity (73%, dr 95:5, entry 3, Scheme 3.17a). The same results (in terms of product yield and diastereoselectivity) could also be obtained when only 1.5 equivalents of α-stannyl benzoates (*R*)-**3.29** was used (entry 4, Scheme 3.17). The *anti* isomer **3.44** was synthesised using the (*S*) enantiomer of the α-stannyl benzoate (*S*)-**3.29** with no Lewis acid additive and the product was obtained in good yield and high diastereoselectivity (87% yield, dr 95:5, Scheme 3.17b).

a

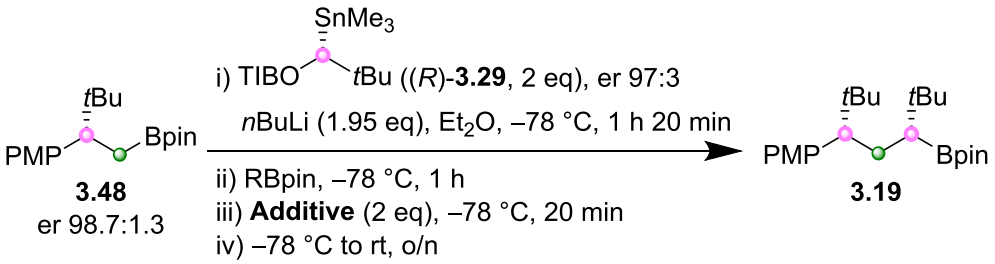

Entry	Eq of stannane	Additive	Yield (dr)
1	2	None	66% (95:5)
2	2	$MgBr_2$/MeOH	73% (95:5)
3*	1.5	$MgBr_2$/MeOH	76% (95:5)

b

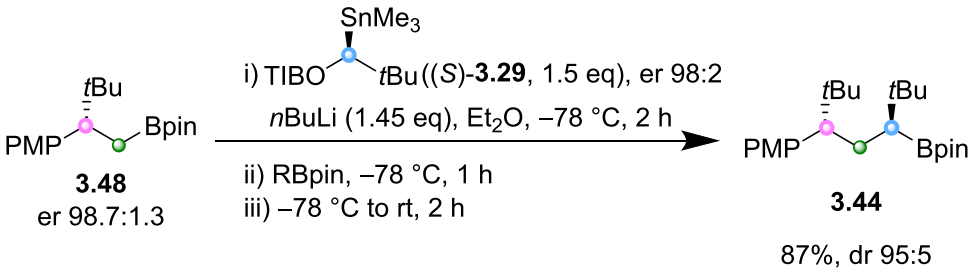

Scheme 3.17: a, Optimisation of lithiation–borylation reaction between boronic ester **3.48** and α-stannyl benzoate (*R*)-**3.29**. * Equivalents of *n*BuLi added: 1.45. **b**, Lithiation–borylation reaction between boronic ester **3.48** and stannane α-stannyl benzoate (*S*)-**3.29**.

With both key intermediates in hand, the amination of the *syn* isomer **3.19** was investigated using the first-generation conditions reported by Morken and co-workers, as scheme 3.18a illustrates[115]. First, methoxyamine **3.51** (Scheme 3.18b) was deprotonated by *n*BuLi to generate lithiated methoxyamine as the active aminating reagent, which then reacted with the boronic ester **3.19** to generate boronate complex **3.52**. The 1,2-migration of **3.52** at elevated temperature would generate intermediate **3.53** which could be converted to the desired carbamate **3.43** after Boc protection. However, the amination of **3.19** using the first-generation conditions only delivered the desired product **3.43** with moderate conversion (recovered 48% starting material) and low isolated yield (30%, Scheme 3.18a). This suggests that the association of the boronic ester **3.19** and the aminating reagent was inefficient owing to the steric hindrance of the boronic ester. Therefore, upon heating the aminating reagent might decompose to give the nitrene **3.54** prior to the association with the hindered boronic ester, leading to poor isolated yield of the desired product **3.43**.

To achieve efficient amination of **3.19**, transformation of boronic ester **3.19** to the corresponding borane **3.55** was investigated in the hope that this would alleviate the steric hindrance and increase the electrophilicity of the boron centre, thus allowing efficient amination with other aminating reagents such as chloramine (H_2NCl).[131] Unfortunately formation of borane **3.55** was not observed by ^{11}B NMR when methyl magnesium bromide was added to boronic ester **3.19**, presumably owing to the steric hindrance of the boronic ester.

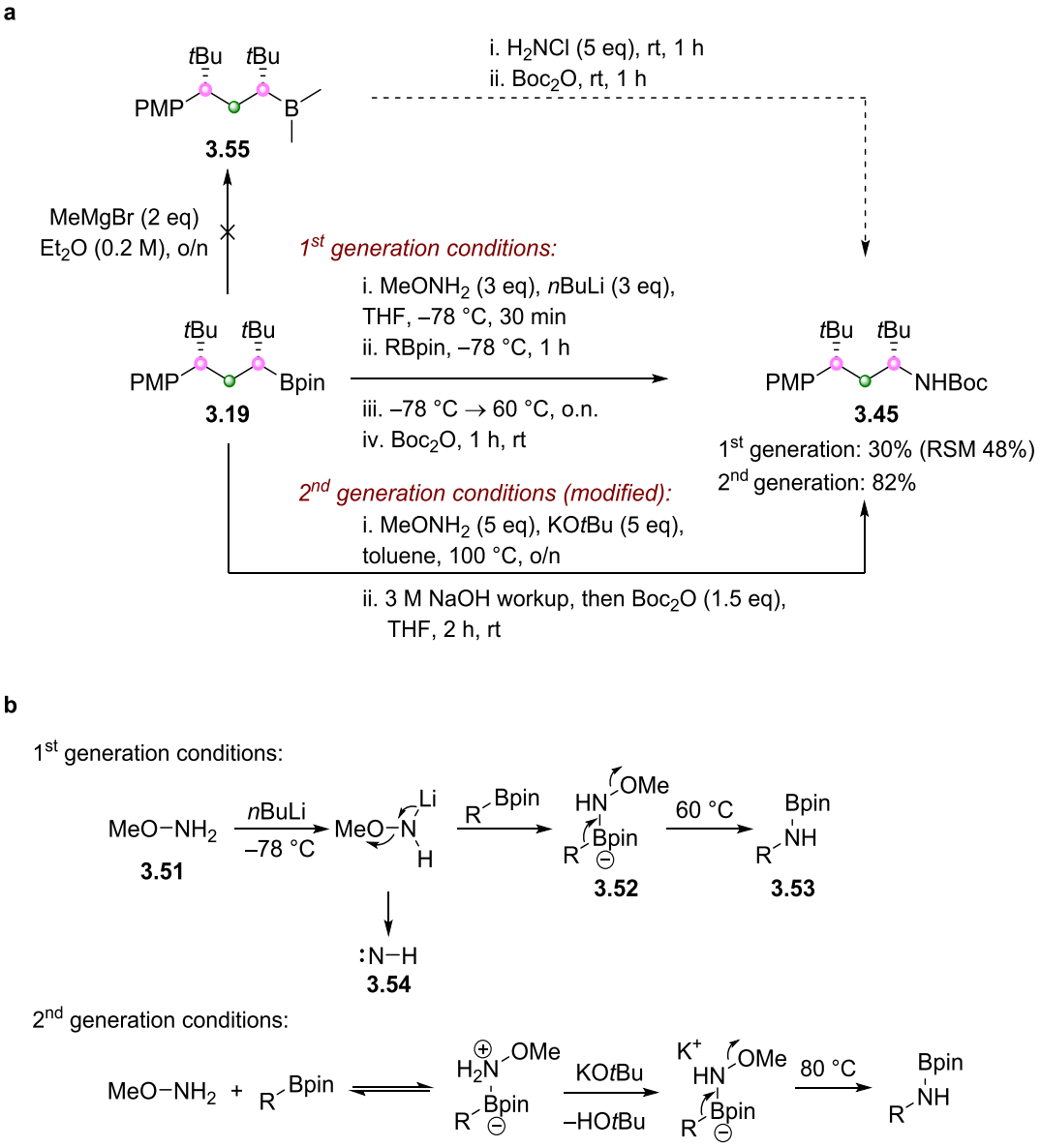

Scheme 3.18: a, Attempts of stereospecific amination of *syn* isomer **3.19**. **b**, Proposed reaction mechanisms of amination conditions developed by Morken and co-workers. [115-116]

Fortunately, Morken and co-workers published improved amination conditions (2nd generation conditions) for sterically demanding boronic esters (Scheme 3.18b).[116] Methoxyamine was used as a neutral aminating reagent together with an alkoxide base (KO*t*Bu)

so that the base could only deprotonate methoxyamine once the hydrogen is acidified by the coordination of methoxyamine to boron. The avoidance of the lithiated methoxyamine allowed the use of the higher temperatures required for more challenging aminations. Using a modified version of the reported second generation conditions, target compound **3.43** was obtained in good yield and the stereochemical integrity was preserved.

With the carbamate **3.43** in hand, the oxidation of the 4-methoxy phenyl group to a carboxylic acid moiety was investigated (Scheme 3.19). Unfortunately, formation of the desired carboxylic acid **3.46** was not observed in the crude reaction mixture (analysed by ^{13}C NMR) after treatment with $RuCl_3$ and $NaIO_4$. Instead, incomplete conversion together with non-specific decomposition of the starting material was observed. This transformation was not investigated further due to the lack of synthetic methods for the oxidation of 4-methoxyphenyl groups to carboxylic acids.

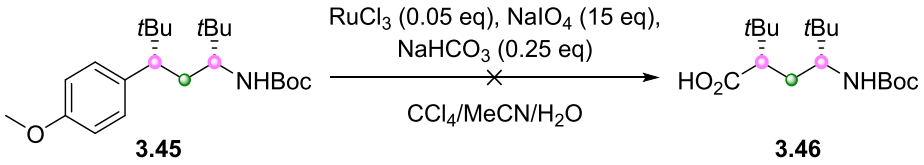

Scheme 3.19: Oxidation of the 4-methoxyphenyl group using a catalytic amount of $RuCl_3$ in the presence of $NaIO_4$.

A solution to the problem would be to use a different functional group as a precursor to the carboxylic acid, as scheme 3.20 outlines. The carboxylic acid functionality could be accessed via either ozonolysis of an alkene or oxidation of a primary alcohol. Again, the carbamate moiety could be installed by stereospecific amination of a boronic ester to give boronic esters **3.56** and **3.57**, which could be generated using lithiation–borylation reactions between the requisite carbenoids and boronic esters **3.58** and **3.59**, respectively.

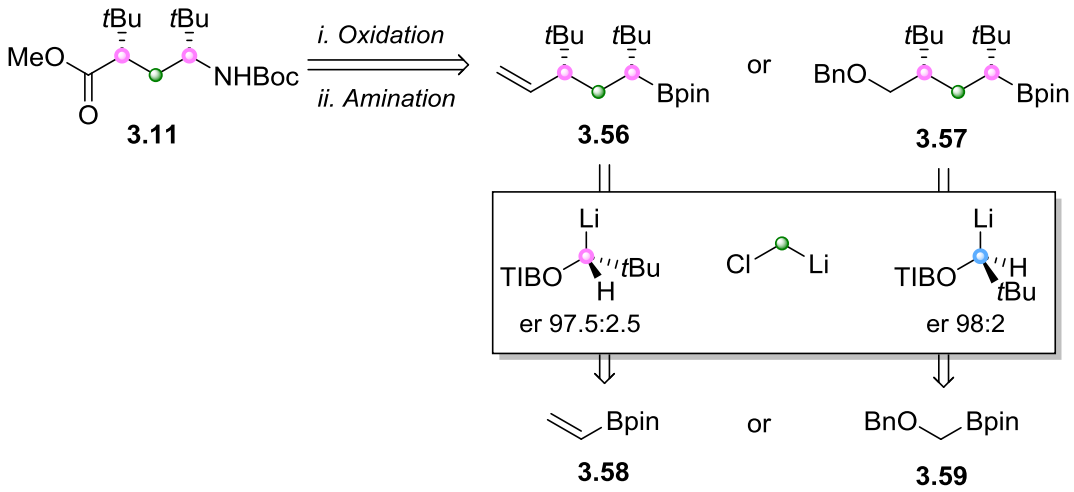

Scheme 3.20: Modified retrosynthetic analysis of unidirectional chain growth approach starting from boronic esters with masked oxygen functionality.

The use of commercially available vinyl pinacol boronic ester **3.58** was first considered and the lithiation–borylation reaction between **3.56** and the α-stannyl ethyl benzoates (*R*)-**1.68** was investigated by Dr Teerawut Bootwicha in the Aggarwal group (Scheme 3.21). Unfortunately, the 1,2-migration of the resultant boronate complex **3.60** was difficult, for reasons unknown, and only moderate conversion (50%) was observed, even with the use of a Lewis acid to enhance the efficiency of 1,2-migration. This suggests the use of boronic ester **3.58** as the starting point of the synthesis is not ideal for the future development of the iterative synthesis of the target compounds. Therefore, the use of boronic ester **3.59** bearing a protected oxygen moiety was investigated.

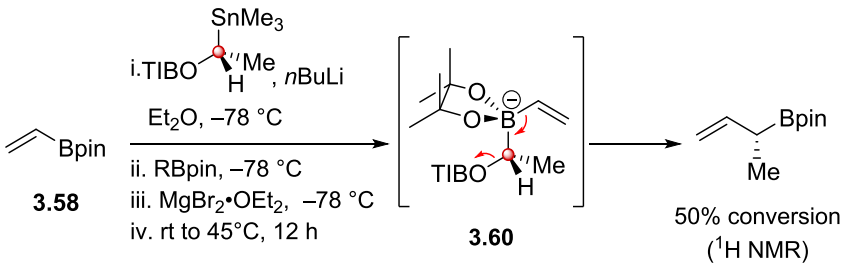

Scheme 3.21: Lithiation–borylation reaction between vinyl pinacol boronic ester **3.58** and α-stannyl ethyl benzoates (*R*)-**1.68** as investigated by Dr. Teerawut Bootwicha.

Boronic ester **3.59** was synthesised by reacting boronic ester **3.61** with sodium benzyl alkoxide, which was generated by deprotonating benzyl alcohol with sodium hydride in DMSO. The use of DMSO as solvent turned out to be crucial for high conversion (~80%)[132] because the use of THF as solvent (suggested by literature procedures[133-134]) always delivered product

in low conversion (<30%). Due to incomplete conversion, product **3.59** was obtained together with benzyl alcohol generated by the protonation of any unreacted sodium benzyl alkoxide. Due to the instability of **3.59** on silica, the product could not be purified by flash column chromatography. Although distillation could separate both compounds, it was found to be non-reproducible and sometimes benzyl alcohol could not be completely removed from the reaction mixture. Pleasingly, it was found that benzyl alcohol could be completely removed by repeatedly (four times) washing the crude mixture (dissolved in pentane) with water.

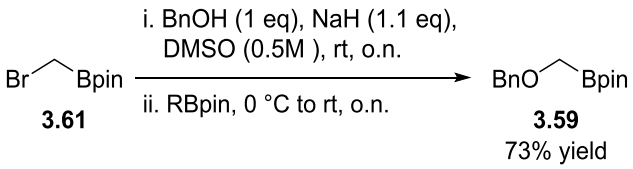

Scheme 3.22: Preparation of boronic ester **3.59**.

With pure boronic ester **3.59** in hand, the first homologation was investigated, and the desired homologated product **3.62** was isolated in good yield and stereoselectivity (Scheme 3.23a). It was found that the addition of methanol at the end of borylation prevented the formation of side product **3.63** by protonating any unreacted lithiated neopentyl benzoates (Scheme 3.23b). Although **3.63** was isolated in a small amount (<5%), eliminating the formation of **3.63** allowed easy purification of the desired product **3.62**. In addition, solvent switch (from Et_2O to $CHCl_3$) was required for efficient 1,2-migration at elevated temperature.[135]

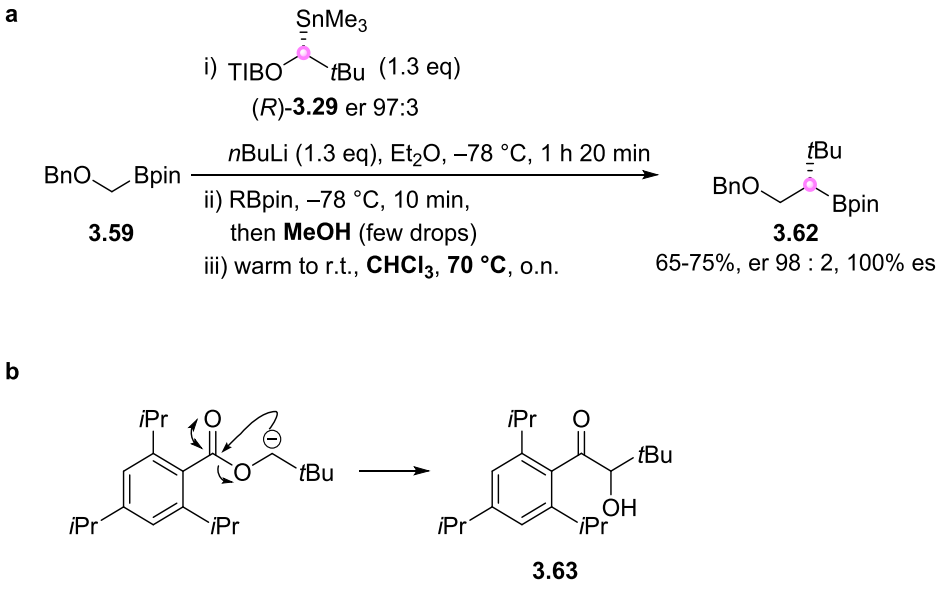

Scheme 3.23: a, Lithiation–borylation reaction between boronic ester **3.59** and α-stannyl neopentyl benzoates (*R*)-**3.29**. b, Proposed mechanism of the formation of side product **3.63**.

Next, Matteson homologation using boronic ester **3.62** was investigated. This reaction poses potential challenges because, apart from the desired 1,2-migration pathway, β-elimination could also occur due to the presence of an oxygen-based leaving group β to the boronic ester in the intermediate boronate complex **3.64** (Scheme 3.24a). The competing β-elimination pathway is undesirable and could lead to catastrophic decomposition of **3.64** (Scheme 3.23a).[136]

The Aggarwal laboratory has previously shown that it is possible to perform Matteson homologation with high efficiency in the presence of oxygen moieties at the β position when iodide was used as the leaving group (Scheme 3.24b).[137] With the encouraging literature precedent, Matteson homologation of boronic ester **3.62** was performed using the optimised conditions developed for the 4-methoxyphenyl analogue (3 eq bromochloromethane, 2.5 eq *n*BuLi, 0.25 M of boronic ester in anhydrous Et_2O at −78 °C for 0.2 mmol scale, Scheme 3.24c). The desired product **3.65** was isolated in good yield (86-89%) and no benzyl alcohol was observed in the crude reaction mixture, suggesting the competing β-elimination pathway did not occur under the reaction conditions.

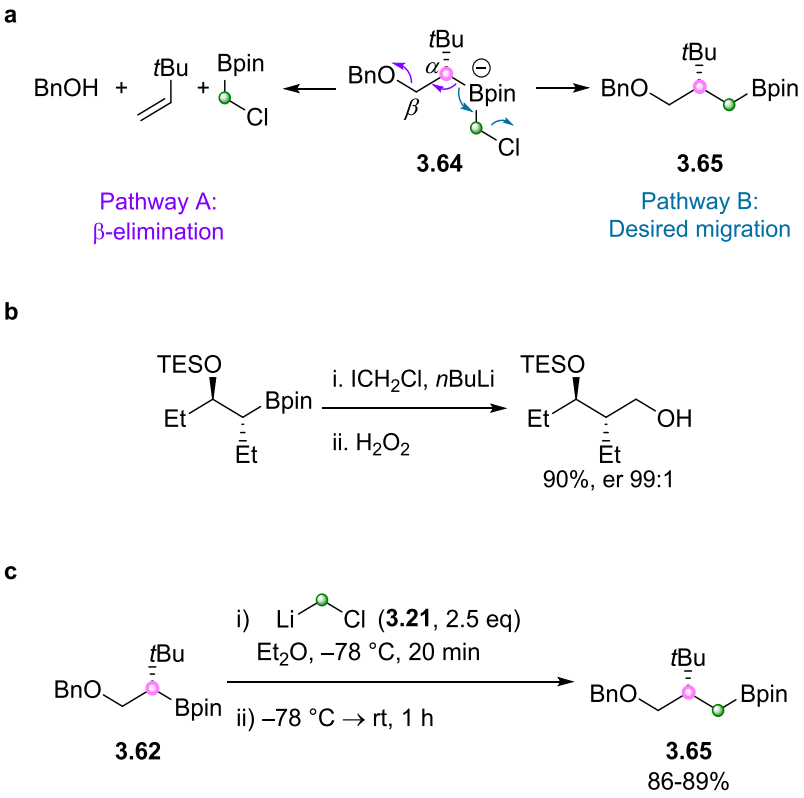

Scheme 3.24: **a**, Two possible reaction pathways for boronate complex **3.64**. **b**, Literature precedent[137] of Matteson homologation using boronic ester with potential leaving group at the position β to the pinacol boronic ester group. **c**, Matteson homologation of boronic ester **3.62**.

Finally, the *syn* isomer **3.57** was synthesised in good yield and diastereoselectivity (69%, dr 95:5, Scheme 3.25a) by lithiation–borylation reaction between boronic ester **3.65** and the (*R*) enantiomer of the *α*-stannyl benzoate (*R*)-**3.29**.

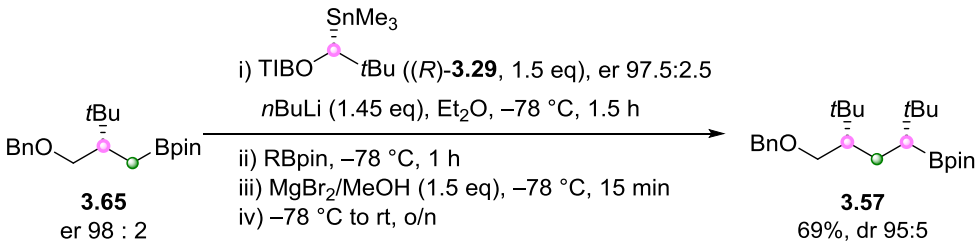

Scheme 3.25: Synthesis of **3.57**.

The *syn* isomer **3.57** was subjected to amination using the optimised conditions and the benzyl group was removed by hydrogenation using palladium on charcoal under an H_2 atmosphere, providing primary alcohol **3.66** as a single diastereomer in good yield after purification by flash column chromatography.

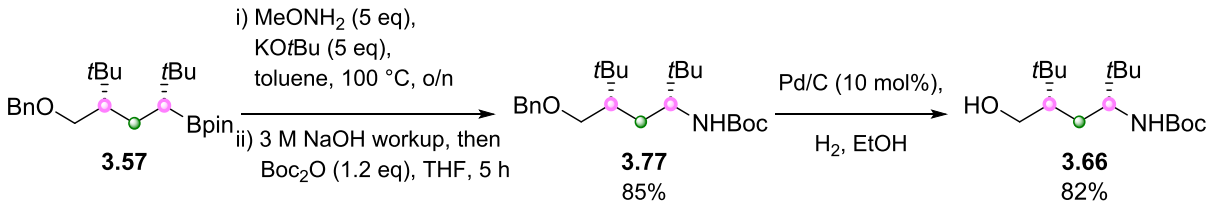

With the alcohol **3.66** in hand, the direct oxidation of the primary alcohol to the carboxylic acid **3.46** was investigated. Unfortunately, under TEMPO catalysed oxidation conditions the reaction either did not proceed or gave a complex mixture of products with a trace amount of desired product **3.11** isolated after methylation (<5% yield) in low purity. (Scheme 3.26)

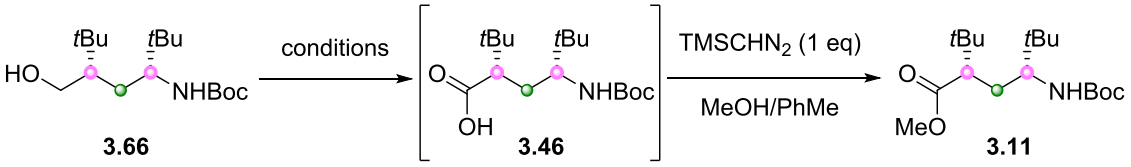

Entry	Conditions	Notes
1	$NaClO_2$ (2 eq), TEMPO (0.15 eq), NaOCl (0.02 eq), MeCN/phosphate buffer (0.67 M), 35°C, o/n	No conversion
2	TEMPO (0.01 eq), $NaHCO_3$ (4 eq), KBr (0.1 eq), Aliquat 336 (0.05 eq), NaClO (2.5 eq), DCM/H_2O, 0 °C	Complex mixture, trace amount of product

Scheme 3.26: Attempted direct oxidation of primary alcohol to **3.66** to carboxylic acid **3.46**, followed by methylation using $TMSCHN_2$ of the reaction crude mixture.

Next, stepwise oxidation (alcohol → aldehyde → carboxylic acid) was considered and the oxidation of primary alcohol **3.66** to aldehyde **3.67** was investigated. Under both Swern and DMP oxidation conditions, the desired aldehyde **3.67** was not obtained, instead, a cyclised product **3.68**, with loss of a stereogenic centre, was isolated.

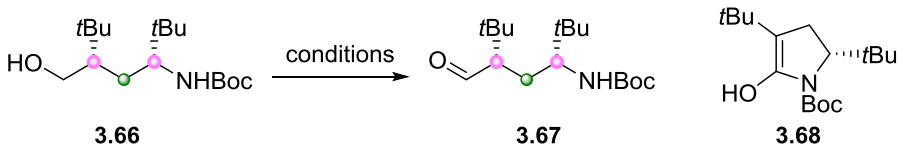

3.66 **3.67** **3.68**

Entry	Conditions	Notes
1	TFAA (3.5 eq), DMSO (5.0 eq), NEt_3 (5 eq), DCM, –78 °C	Isolated 54% **3.68**
2	DMP (2.0 eq), $NaHCO_3$ (10.0 eq), DCM, 0 °C	Isolated 65% **3.68**

Scheme 3.27: Oxidation of primary alcohol **3.66** to aldehyde **3.67** under Swern (entry 1) and DMP (entry 2) oxidation conditions.

The cyclised product **3.68** could be generated via a 5-*exo*-*trig* cyclisation of the carbamate nitrogen onto the aldehyde carbonyl followed by the loss of water (Scheme 3.28). The preferential formation of **3.68** via this pathway was surprising, since the carbamate nitrogen should be a poor nucleophile due to significant donation of the lone pair electron density to the adjacent carbonyl group. However, the *syn* isomer with two quaternary centres separated by three carbons, such as aldehyde **3.67**, was designed to have two substituents s*yn* periplanar to each other. Therefore, the energetic cost for the two reactive ends in aldehyde **3.67** to be close in proximity is low and the rate of intramolecular cyclisation was enhanced, leading to the preferential formation of the cyclised product **3.68**.

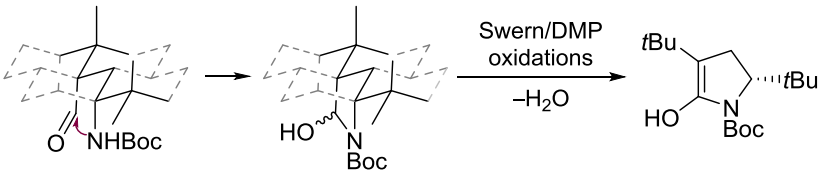

3.67 **3.70** **3.68**

Scheme 3.28: Proposed mechanism of the formation of **3.68**.

Acceleration of the rate of intramolecular cyclisation due to the effect of *tert*-butyl groups on molecular conformation has been reported for the **3.69** type of system, which undergoes an intramolecular Diels-Alder reaction upon heating in benzene at 80 °C (Figure 3.4a). When the 'anchoring' R group is a *tert*-butyl group (instead of a proton), both the furan and the alkyne moieties would orientate *anti* to the *tert*-butyl group (for the reasons discussed in section 3.1) and as a result they would be *syn* periplanar to each other and therefore close in proximity (Figure 3.4b). Compared to the rate of reaction of **3.69a**, which does not possess a

tert-butyl 'anchoring' R group, the conformational preference of **3.69b** (R=*t*Bu) leads to a 240-fold rate enhancement.[138]

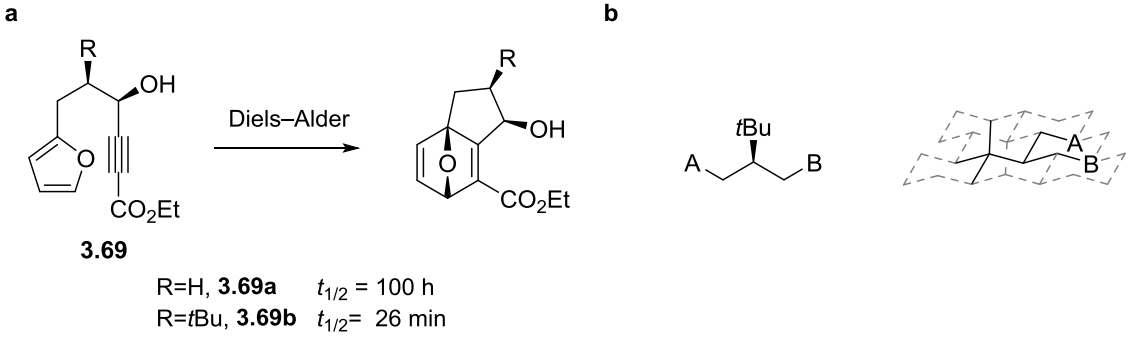

Figure 3.4: **a**, Intramolecular Diels-Alder reaction between furan and alkyne and the relative rates of cyclisation.[138] **b**, Carbon chain with a *t*Bu anchor in the middle of the chain.

Although the formation of hemiaminal **3.70** could be rationalised by the conformational preference of the aldehyde **3.67**, it was not entirely clear what the driving force for the loss of water to deliver the cyclised product **3.68** was. One could reason that under other oxidation conditions perhaps the loss of water would not occur so that the hemiaminal **3.70** could be further oxidised to the lactam **3.71**, which could be hydrolysed to deliver the desired carboxylic acid **3.46**.

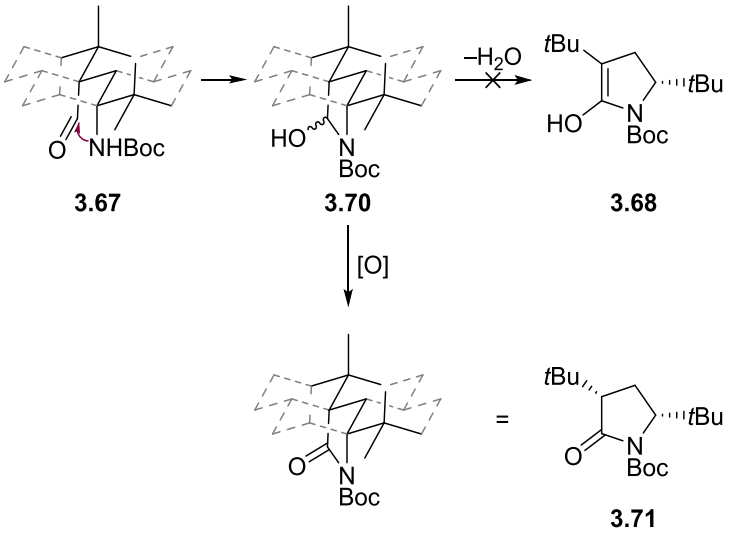

Scheme 3.29: Proposed alternative reaction pathway of oxidation of alcohol **3.66**.

It was found that oxidation of the primary alcohol under Stahl oxidation conditions, using catalytic amount of copper(I) and 9-azabicyclo[3.3.1]nonane *N*-oxyl (ABNO)[139], delivered the desired product as a mixture of aldehyde **3.67** and hemiaminal **3.70** (1:4 ratio in $CDCl_3$) in good yield (81%) without epimerisation of the stereogenic centre adjacent to the

aldehyde. The mixture of aldehyde and hemiaminal could be further oxidised to yield the lactam **3.71** by using an O_2 balloon and elevated temperature (70 °C). However full conversion was not observed presumably due to catalyst inhibition for unknown reasons. To ensure full conversion of the reaction (thus allowing easy purification by column chromatography), all catalytic components were reloaded every two hours until the reaction had gone to completion.

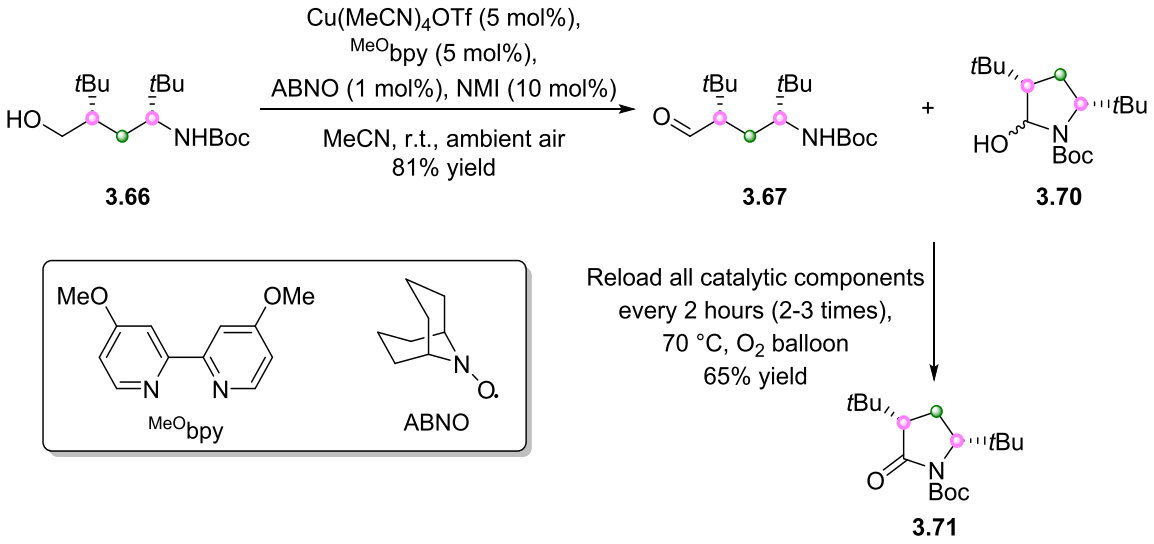

Scheme 3.30: Oxidation of primary alcohol **3.66** under Stahl oxidation conditions. NMI: *N*-methylimidazole.[139]

With sufficient material in hand, the hydrolysis of lactam **3.71** which would deliver the desired carboxylic acid **3.46** was investigated (Scheme 3.31). When the reaction was performed using LiOH in THF, no conversion was observed at 0 °C and room temperature (entry 1 and 2, Scheme 3.31). When a 1:1 mixture of THF and methanol was used as the reaction solvent, epimerisation of starting material was observed by ^{1}H NMR of the crude reaction mixture (entry 3, Scheme 3.31). This observation suggests that in a 1:1 mixture of THF and methanol, the basicity, rather than the nucleophilicity, of LiOH was enhanced, thus leading to deprotonation of the acidic α-proton of **3.71**, resulting epimerisation.

Next, the use of LiOOH for the hydrolysis of lactam **3.71** was investigated, because it is more nucleophilic due to the α-effect[140], and less basic (pK_a of [HOOH] = 11.6, compared to pK_a of [HOH] = 15.8.)[141]. Indeed, a trace amount of product was detected by LC-MS with the use of LiOOH at 0 °C (entry 4, Scheme 3.31). However, the efficiency of the hydrolysis could not be further improved by either performing the reaction at room temperature or with more equivalents of reagent (entry 5 and 6, Scheme 3.31). Unfortunately, heating the reaction

mixture at 60 °C overnight lead to epimerisation of starting material **3.71** (entry 7, Scheme 3.31).

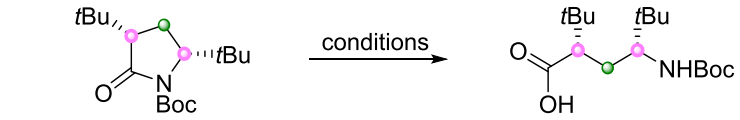

3.71
Single diastereomer (^{1}H NMR)

3.46

Entry	Conditions	Notes
1	LiOH (2 eq), THF, 0 °C, 10 h	No conversion
2	LiOH (2 eq), THF, **rt**, 10 h	No conversion
3	LiOH (2 eq), **THF/MeOH** (1:1), 0 °C, 12 h	epimerisation of starting material (*dr* 96:4, ^{1}H NMR)
4	**LiOOH**(2 eq), THF/H_2O (4:1), 0 °C, 12 h	Mass of **3.46** detected by LC-MS
5	LiOOH (2 eq), THF/H_2O (4:1), 0 °C, 1 h, **rt for 12 h**	Mass of **3.46** detected by LC-MS
6	LiOOH (**10 eq**), THF/H_2O (4:1), 0 °C, 1 h, rt for 3 h	Mass of **3.46** detected by LC-MS
7	LiOOH (10 eq), THF/H_2O (4:1) **60 °C o.n**	Mass of **3.46** detected by LC-MS & epimerisation of starting material **3.71** (*dr* 1 : 1, ^{1}H NMR)

Scheme 3.31: Attempts to hydrolyse lactam **3.71**.

The use of both hydroxide- or hydrogen peroxide-based nucleophiles were ineffective in the hydrolysis of lactam **3.71**, owing to the steric hindrance of the substrate. Therefore, the transformation of lactam **3.71** to the less sterically hindered thioester derivative was considered. Evans and co-workers reported the use of this approach for the removal of the chiral auxiliary in a sterically demanding substrate **3.72**, which did not undergo hydrolytic cleavage when LiOOH was used. The thioester derivative **3.73** was obtained in good yield (85%) and the subsequent hydrolysis using LiOOH delivered the desired carboxylic acid **3.74** in quantitative yield.[142]

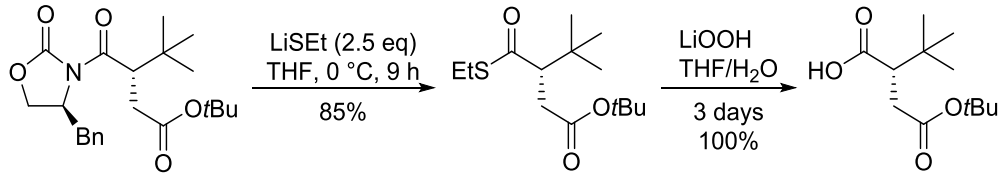

3.72 **3.73** **3.74**

Scheme 3.32: Cleavage of the chiral auxiliary of **3.72**.

Encouraged by the work done by David Evans and co-workers, the same conditions were applied to lactam **3.71** (5.0 mg scale) to synthesise the corresponding thioester derivative **3.75** for easier hydrolysis. Unfortunately, only the product arising from the cleavage of the Boc protecting group (**3.76**) was isolated in 51% yield.

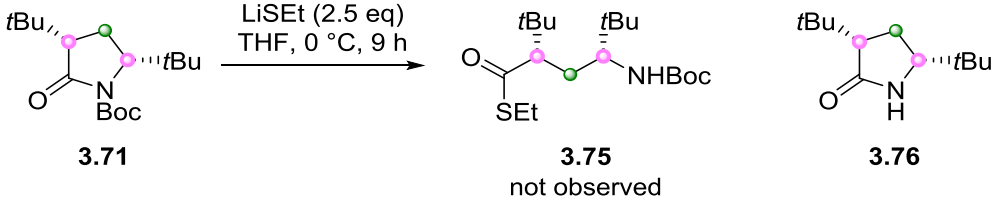

3.71 **3.75** not observed **3.76**

Scheme 3.33: Reaction between lactam **3.71** and LiSEt.

As discussed, all attempts to hydrolyse the lactam **3.71** failed due to steric hindrance. Therefore, an alternative approach was considered: if one could prevent the nucleophilic attack of the nitrogen of the carbamate at the aldehyde carbonyl, no cyclised product would form and the free aldehyde should be easily oxidised to the carboxylic acid. Therefore, carbamate **3.77** was subjected to another Boc-protection to yield **3.78** (Scheme 3.34). Again, due to the steric hindrance of **3.77** conventional methods (Boc_2O, DMAP in MeCN) for the second Boc-protection were unsuccessful. Finally, the desired product **3.78** was obtained in good yield (79%) using a modified literature procedure[143]. The use of DMAP was found to be essential for good conversion and the use of exactly one equivalent of *n*BuLi was crucial for eliminating a side product which was thought to arise from the deprotonation of the aromatic protons of the benzyl group.

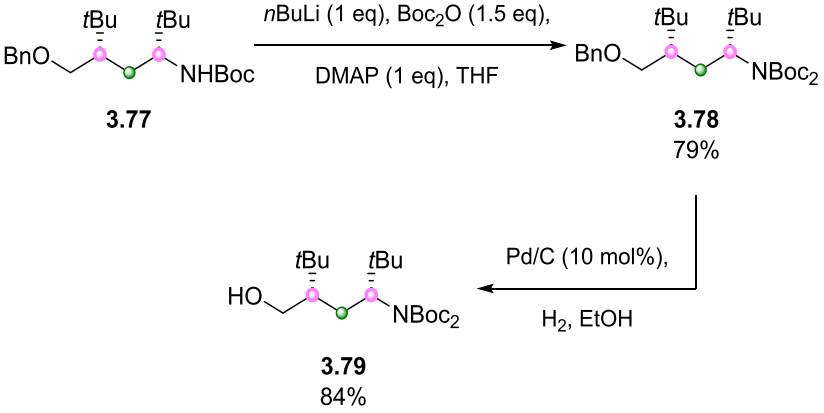

3.77 **3.78** 79% **3.79** 84%

Scheme 3.34: Second Boc protection of **3.77** followed by deprotection of the benzyl group.

Primary alcohol **3.79** was synthesised and the oxidation to the aldehyde was performed under Stahl oxidation conditions.[139] As hypothesised, the aldehyde **3.80** was isolated in good

yield (78%, Scheme 3.35a) and Pinnick oxidation of the aldehyde smoothly delivered the desire carboxylic acid **3.81**. The crude carboxylic acid **3.81** was subjected to methylation using $TMSCHN_2$ to deliver the methyl ester **3.82** in 77% yield over two steps. One of the Boc protecting groups was removed using TFA in DCM to deliver the U-shaped molecule **3.11** as a solid (Scheme 3.35b).

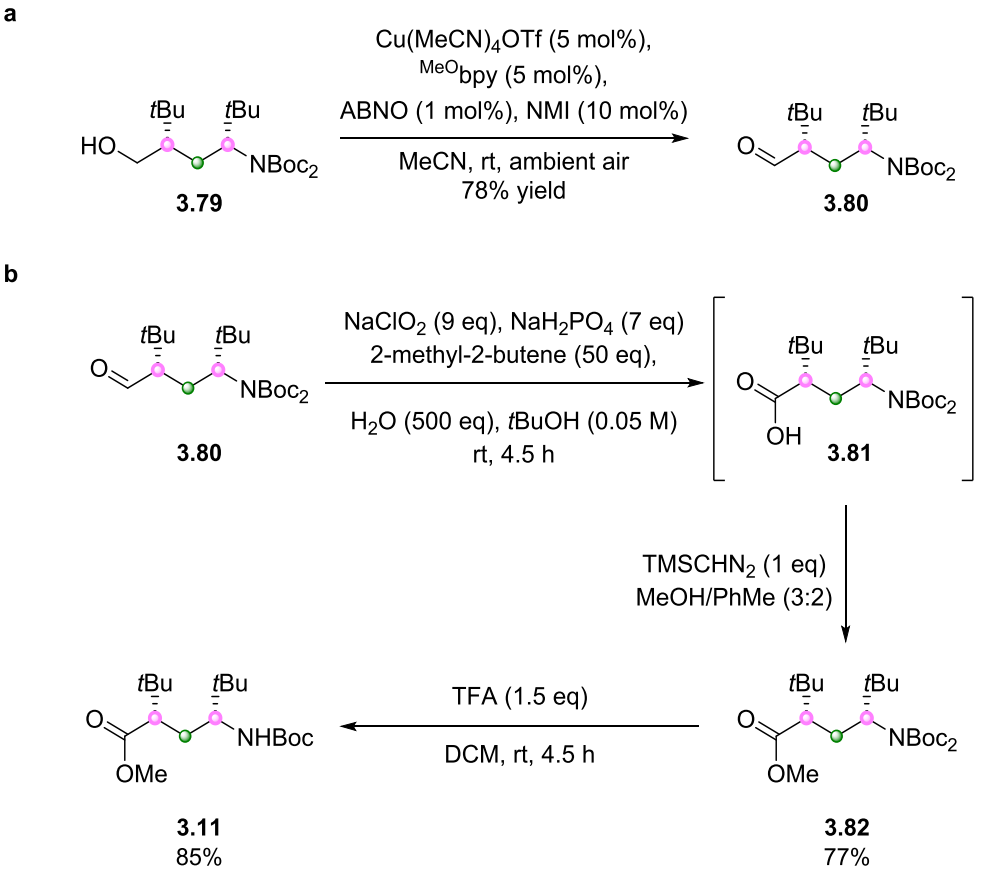

Scheme 3.35: **a**, Stahl oxidation of **3.79**. **b**, Pinnick oxidation of **3.80** followed by methylation of carboxylic acid **3.81** and the removal of one of the Boc protecting group to deliver U-shaped molecule **3.11**.

The solid-state structure of **3.11** was obtained via X-ray crystallography. Gratifyingly, the backbone conformation is linear with the two substituents synperiplanar to each other as designed (Figure 3.5).

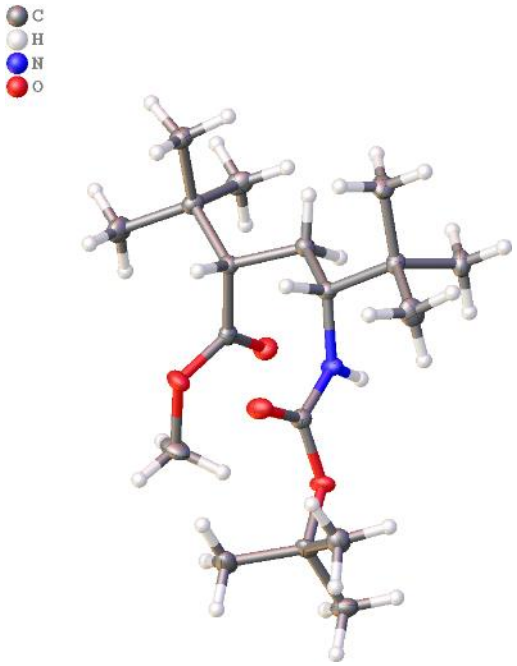

Figure 3.5: X-ray crystal structure of **3.11**. Thermal ellipsoids are shown at 50% probability.

Having established the synthetic route to prepare the *syn* isomer **3.11**, the optimised conditions were applied to the synthesis of the *anti* isomer **3.21**. Starting from boronic ester **3.62**, homologation with **3.21** followed by reaction with the (*S*) enantiomer of the α-stannyl benzoate (*S*)-**3.29** delivered the key intermediate **3.83** in good yield and diastereoselectivity (66%, dr 96:4, Scheme 3.36)

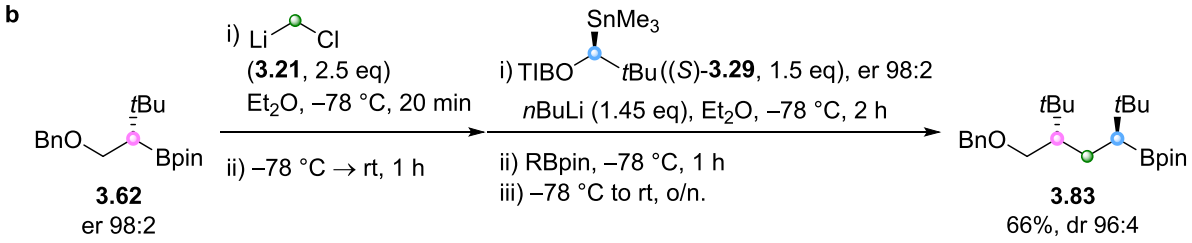

Scheme 3.36: Synthesis of boronic ester **3.83** by iterative homologation of **3.62**.

The key intermediate **3.83** was then subjected to the identical synthetic sequence described for the *syn* isomer (Scheme 3.37). Amination, second Boc protection and benzyl group deprotection gave primary alcohol **3.84**. Further functional group interconversions finally gave the L-shaped molecule **3.12** as an oil.

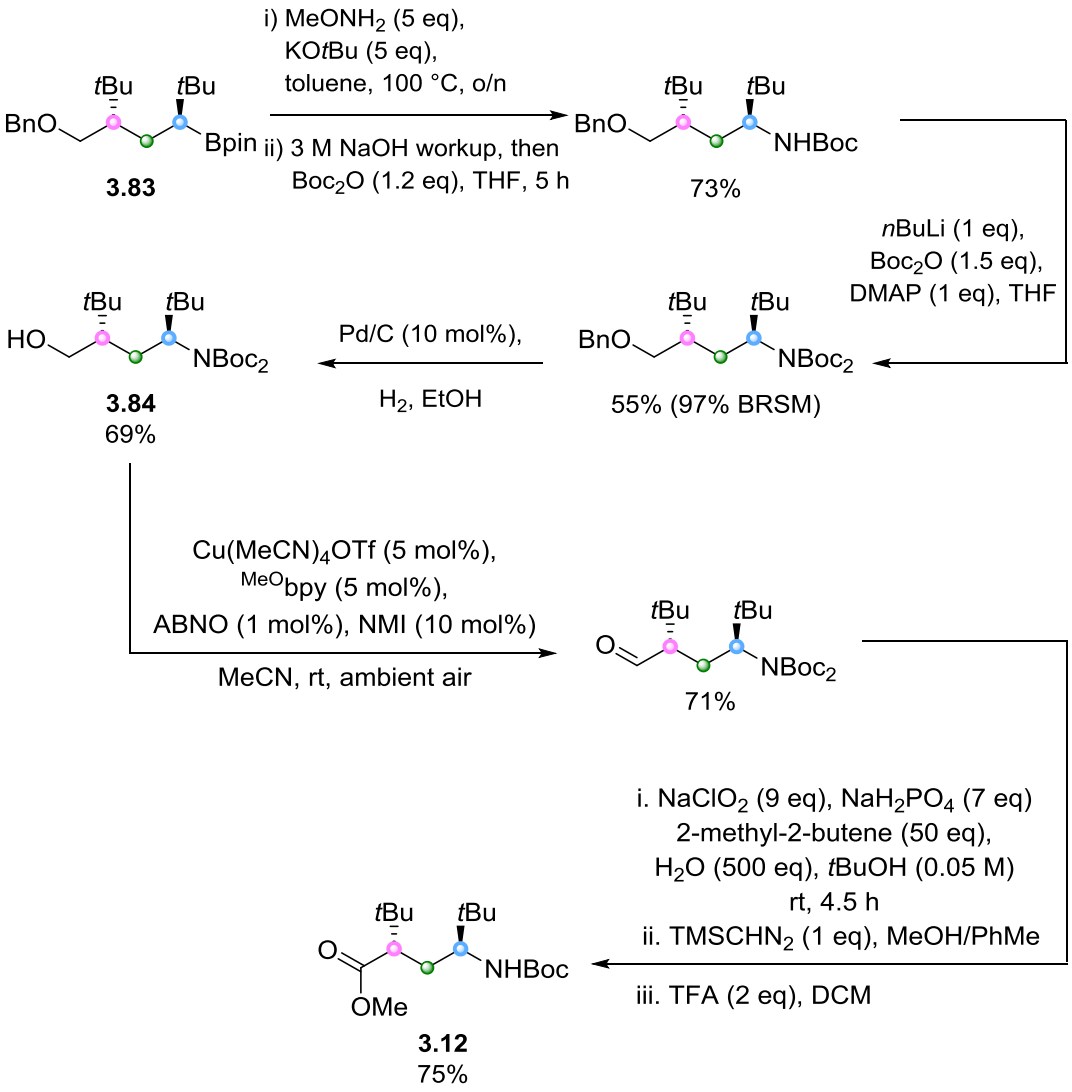

Scheme 3.37: Synthesis of L-shaped molecule **3.12** starting from boronic ester **3.83**.

3.2.2 QM/NMR analysis of U-shaped molecule 3.11.

The solution-state conformational behaviour of **3.11** was investigated using QM/NMR approach. A Monte Carlo conformational search using MM calculations with MMFFs force field and chloroform as implicit solvent was performed (see experimental section for details). For **3.11** (U-shaped), 6 conformers were found within 21 kJ mol^{-1} of the global minimum.

a

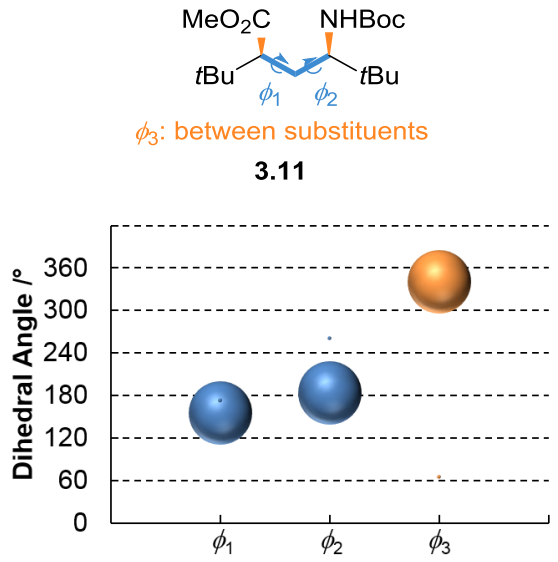

b

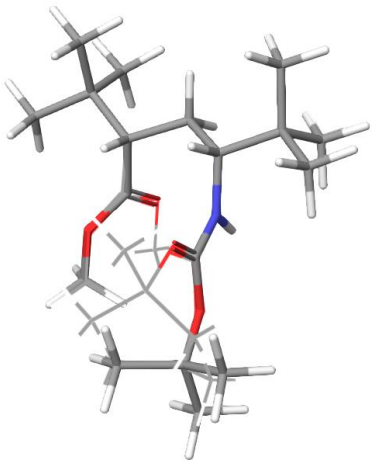

c

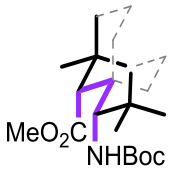

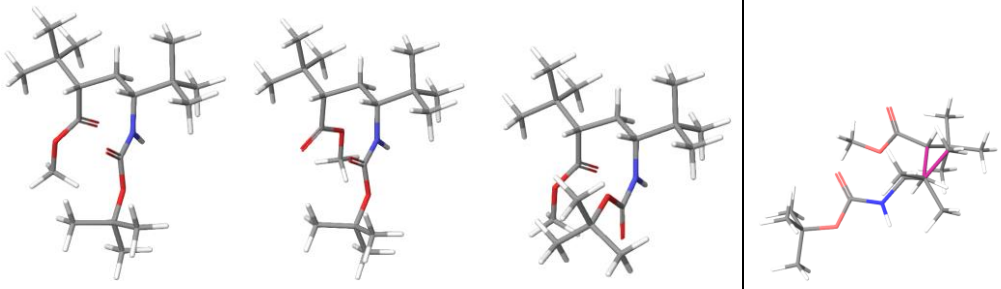

	3.11-1	**3.11**-2	**3.11**-3	**3.11**-4
Δ*G*/kJ mol^{-1}	0.0	7.1	9.3	14.1
Population (298 K)	92.2%	5.3%	2.2%	0.3%

Figure 3.6: a, Chemical structure of **3.11** and the DFT calculated conformational behaviour represented by a bubble plot. **b**, Overlaid structures of major conformers **3.11**-1, **3.11**-2 and **3.11**-3. **c**, Major conformation represented on a diamond lattice, DFT optimised structures, Δ*G* and population at 298 K.

All conformers were subjected to subsequent DFT geometry optimisation and frequency calculations using mPW1PW91 functional with 6-311G (d,p) basis set and chloroform as implicit solvent (IEFPCM). Values of relative Gibbs free energy (ΔG) of each conformer were used to calculate conformer populations.

The DFT predicted conformational behaviour of **3.11** is represented by a bubble plot (Figure 3.6a). The angles of dihedral in the backbone (ϕ_1 and ϕ_2, Figure 3.6a) and between the substituents (ϕ_3, Figure 3.6a) are shown and the size of the bubbles is proportional to the calculated Boltzmann population of that conformation.

The three dominant conformers **3.11**-1, **3.11**-2 and **3.11**-3 all adopt the designed U-shape conformation (Figure 3.6b) and have a combined population of 99.7% (Figure 3.6c). In all three conformers, ϕ_1 and ϕ_2 adopt *anti* conformations (Boltzmann averaged ϕ = 155 and 184°) with respect to the peripheral quaternary centres. The ester and the carbamate substituents are approximately *syn* periplanar to each other with a dihedral angle of −20°. The deviation of ϕ_1 (155°) and ϕ_3 (−20°) from the ideal angles of *anti* and *syn* periplanar conformations (180° and 0° respectively) alleviates the destabilising *syn*-pentane interaction between the ester and the carbamate groups.

The DFT predicted conformational behaviour of **3.11** also highlights the extent of conformational control provided by both peripheral quaternary centres. The first lowest energy conformer with a non-linear backbone (conformer **3.11**-4, Figure 3.6c) has a ΔG of 15 kJ mol^{-1} above the global minimum (0.3% of global population) with an distorted *syn*-pentane interaction between the methyl group of the one of the peripheral *t*Bu groups and the C–C bond of the backbone (Figure 3.6c).

To verify the major conformations of **3.11** in solution, QM/NMR analysis was performed using ^{1}H-^{1}H and ^{1}H-^{13}C scalar coupling constants. The NMR parameters of the three dominant conformers (**3.11**-1, **3.11**-2 and **3.11**-3, Figure 3.6) were computed by DFT using mPW1PW91 functional with 6-311G (d,p) basis set and chloroform as implicit solvent (IEFPCM). The experimental ^{1}H-^{1}H scalar coupling constants were extracted from the 1D ^{1}H NMR spectrum and the ^{1}H-^{13}C scalar coupling constants were measured from the traces extracted from the processed Accordion In-Phase and Anti Phase (IPAP) HSQMBC NMR spectra.[144]

A good agreement was observed for the comparison between the calculated ensemble-averaged ^{1}H-^{1}H and ^{1}H-^{13}C scalar coupling constants and the experimentally determined values (Figure 3.7) with root mean square deviation of 1.0 Hz for the comparison of ^{1}H-^{1}H scalar coupling constants and 0.41 Hz for the comparison of ^{1}H-^{13}C scalar coupling constants. The excellent correlation between the calculated ensemble-averaged scalar coupling constants and the experimental data confirms that indeed the solution-state major conformation of **3.11** is the designed U-shape conformation.

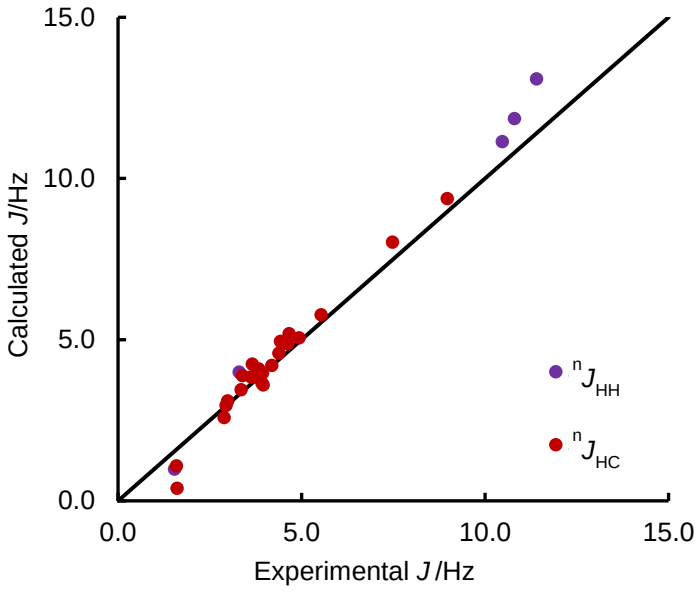

Figure 3.7: Correlation between the calculated and the experimentally determined ^{1}H-^{1}H and ^{1}H-^{13}C scalar coupling constants. Purple dots represent the comparison of ^{1}H-^{1}H scalar coupling constants while red dots represent the comparison of ^{1}H-^{13}C scalar coupling constants.

To investigate the detailed conformational behaviour of **3.11**, quantitative NOE analysis is required. However, due to the presence of rotameric signals of all proton resonances, the observed NOE intensities were complicated by chemical exchange between the irradiated proton and the corresponding rotameric signal. Therefore, quantitative NOE analysis was not performed.

3.2.3 QM/NMR analysis of L-shaped molecule 3.12.

A MM Monte Carlo conformational search of **3.12** (L-shaped) was performed using the identical protocol described for **3.11** and found 26 conformers within 21 kJ mol^{-1} of the global minimum. All conformers were subjected to DFT calculations using methods described for **3.11**.

a

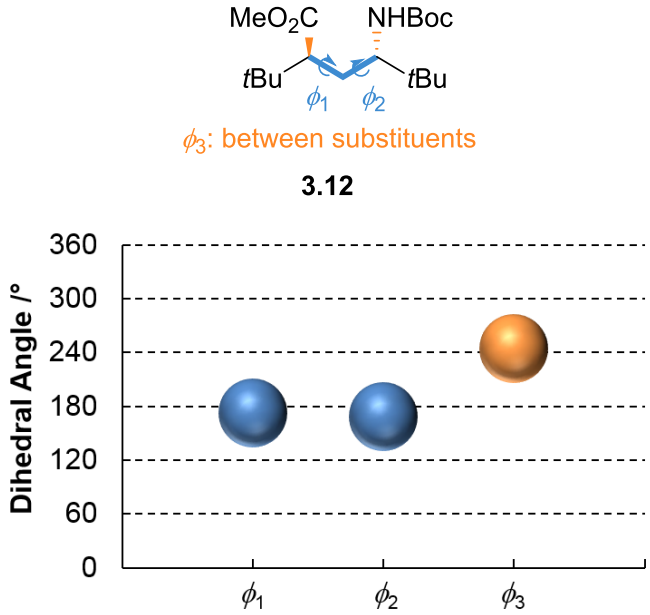

b

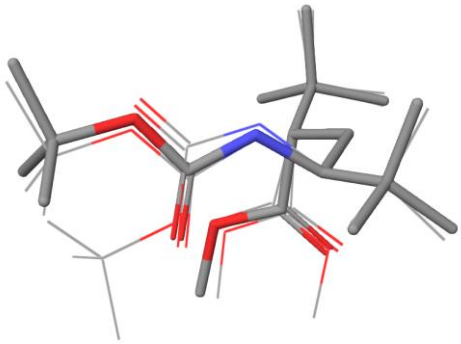

c

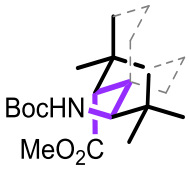

d

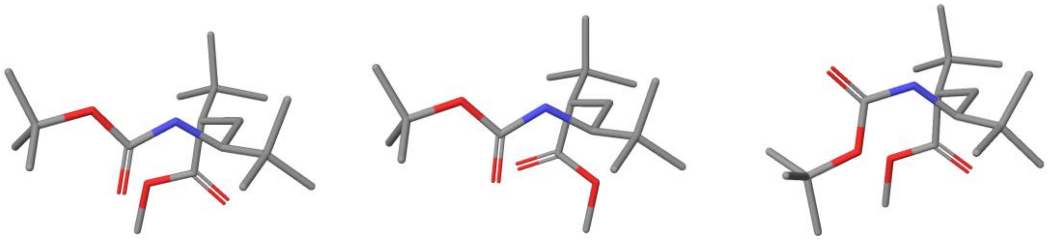

	3.12-1	**3.12**-2	**3.12**-3
ΔG/kJ mol^{-1}	0.0	9.5	12.9
Population (298 K)	97.0%	2.1%	0.5%

Figure 3.8: a, Chemical structure of **3.12** and the DFT calculated conformational behaviour represented by a bubble plot. **b**, Overlaid structures of conformer **3.12**-1, **3.12-2** and **3.12**-3. **c**, Major conformation represented on a diamond lattice, DFT optimised structures, ΔG and population at 298 K. Hydrogens are omitted for clarity.

The DFT predicted conformational behaviour of **3.12** was represented by a bubble plot (Figure 3.8a). The three dominant conformers **3.12**-1, **3.12**-2 and **3.12**-3 (Figure 3.8d) all adopt the designed L-shaped conformation (Figure 3.8b) and have a combined population of 99.6% (Figure 3.8c). In all three conformers, ϕ_1 and ϕ_2 adopt *anti* conformations (Boltzmann averaged ϕ = 172 and 169°) with respect to the peripheral quaternary centres. The ester and the carbamate substituents turn a corner with a dihedral angle of −116° (i.e. 224° in Figure 3.8a). Unlike the U-shaped molecule **3.11**, the values of the backbone dihedral angles (ϕ_1 and ϕ_2, Figure 3.8a) in **3.12** are closer to the ideal value for the *anti* conformation (180°), presumably due to the absence of *syn*-pentane interactions between the ester and the carbamate groups.

To verify the DFT-predicted major conformations of **3.12** in solution, QM/NMR analysis was performed using ^{1}H-^{1}H and ^{1}H-^{13}C scalar coupling constants. The NMR parameters of the three dominant conformers (**3.12**-1, **3.12**-2 and **3.12**-3, Figure 3.8d) were computed using the methods described for **3.11** and the corresponding experimental NMR data were extracted as described for **3.11**. Again, an excellent agreement was observed for the comparison between the calculated ensemble-averaged ^{1}H-^{1}H and ^{1}H-^{13}C scalar coupling constants and the experimentally determined values (Figure 3.9), therefore indicating that the solution-state major conformation of **3.12** is the designed L-shaped conformation.

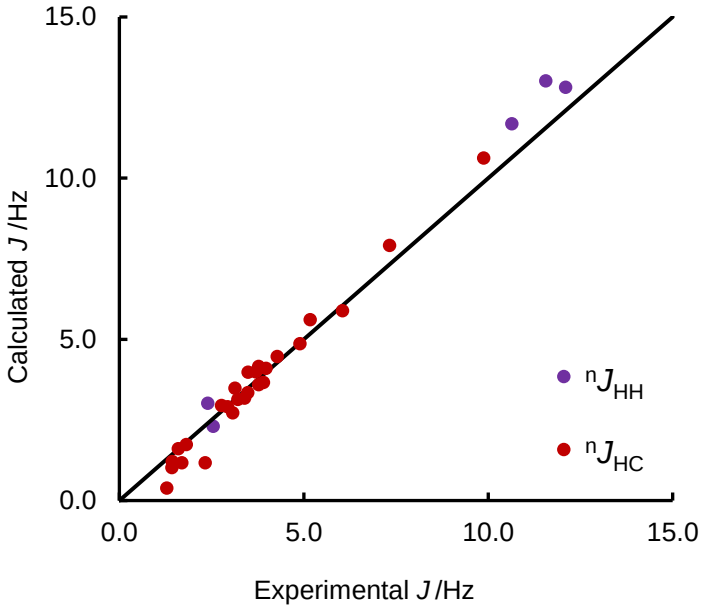

Figure 3.9: Correlation between the calculated and the experimentally determined ^{1}H-^{1}H and ^{1}H-^{13}C scalar coupling constants. Purple dots represent the comparison of ^{1}H-^{1}H scalar coupling constants while red dots represent the comparison of ^{1}H-^{13}C scalar coupling constants.

In summary, QM/NMR analysis showed that both **3.11** and **3.12** have a very high bias towards the desired U- and L-shaped conformations. With this encouraging result, remote conformational control of longer chains using terminal quaternary centres was considered next.

Designing conformationally biased molecules with terminal *tert*-butyl groups separated by four carbon units (Compounds 3.13, 3.86 – 3.99)

3.2.4 Conformational analysis of 3.13.

As discussed in section 3.1, the conformational control provided by both terminal quaternary centres declines when the two quaternary centres are separated by more than three carbon units. (Figure 3.2a). The extent of the loss in conformational control has not yet been quantified so the conformational behaviour of **3.13** (Scheme 3.38) was studied computationally.

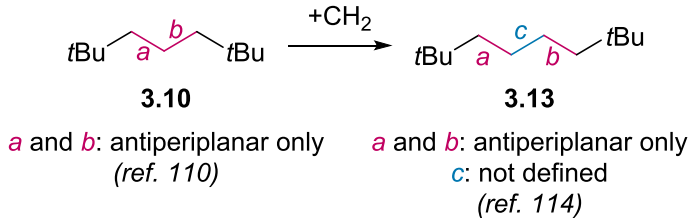

Scheme 3.38: Terminal *t*Bu groups separated by three (**3.10**) and four methylene units (**3.13**).

A MM Monte Carlo conformational search and DFT calculations were performed on **3.13** using procedures described previously (section 3.2.2) and found four conformers within 15.0 kJ mol^{-1} of the global minimum. Two of them have *syn*-pentane interactions and therefore have high relative Gibbs free energies above the global minimum (13.0 and 14.5 kJ mol^{-1}, respectively). The other two conformers, **3.13**-1 and **3.13**-2 (Figure 3.10b and c), have relative Gibbs energies within 10.0 kJ mol^{-1} of the global minimum thus dominating the conformer population of **3.13**.

Due to the symmetry of **3.13**, **3.13**-2 also has a degenerate mirror image conformer (**3.13**-3) which was eliminated by the initial MM conformational search. Therefore, **3.13**-3 was created manually to account for degeneracy in Boltzmann population calculation.

Compared to the conformational landscape of **3.10** in which conformers with a linear backbone heavily populated (100% of global population, Scheme 3.38), the conformer population of **3.13** is more complex (Figure 3.10a). Although conformer **3.13**-1 (Figure 3.10c) with a linear backbone is still the lowest energy conformer (blue dots, Figure 3.10a), it only has 63.1% of the global population due to the a small energy difference (ΔG = 3.1 kJ mol^{-1}) between this conformer and the next lowest energy conformers (**3.13**-2 and **3.13**-3, Figure 3.10c) which have backbone dihedral angles of *ap* g^- *ap* and *ap* g^+ *ap*. The diminishing conformational control predicted by DFT calculations is consistent with Alder's hypothesis,

which suggested that **3.13** should adopt multiple conformations based on the examination of nBu$_4$N$^+$ type crystal structures.[110]

a

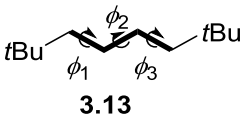

3.13

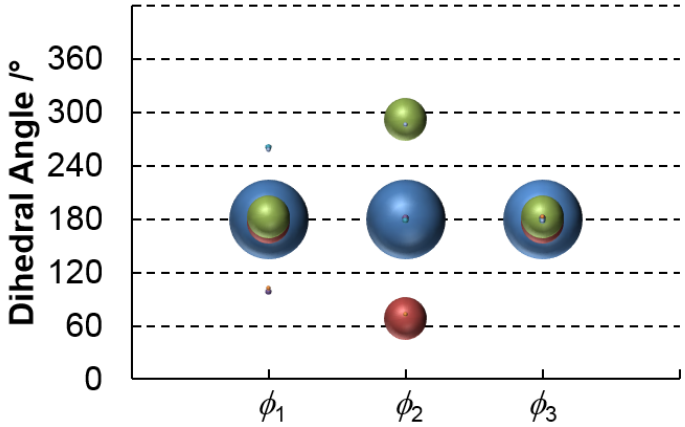

b

c

	3.13-1 (*ap ap ap*)	**3.13**-2 (*ap* g^- *ap*)	**3.13**-3 (*ap* g^+ *ap*)
ΔG/kJ mol^{-1}	0.0	3.1	3.1
Population (298 K)	63.1%	17.9%	17.9%

Figure 3.10: **a**, Chemical structure of **3.13** and the DFT predicted conformational landscape represented by a bubble plot. Blue dots represent conformer **3.13**-1, red dots represent conformer **3.13**-2 and green dots represent conformer **3.13**-3. **b**, 3D structure of **3.13**-1, **3.13**-2 and **3.13**-3. **c**, Major conformers of **3.13** represented on a diamond lattice together with the corresponding relative Gibbs free energies (ΔG) and population at 298 K.

3.2.5 Conformational analysis of 3.86 and 3.87.

Next, the possibility of enhancing the conformational bias towards a linear backbone conformation by introducing substituents at specific positions with appropriate stereochemistry was considered. Since the three lowest energy conformers **3.13**-1, **3.13**-2 and **3.13**-3 dominant the conformer population of **3.13** and have a combined population of 98.9%, only these three conformers were taken into consideration for the diamond lattice analysis.

Introduction of a methyl substituent adjacent to the quaternary centre would generate **3.85** (Figure 3.11a) and induce a destabilising *syn*-pentane interaction in the conformer with backbone dihedral angles of *ap* g^- *ap* (**3.85**-2, Figure 3.11b). Although **3.85** should show an enhanced bias towards the conformer with a linear backbone (**3.85**-1, Figure 3.11b), the other conformer with backbone dihedral angles of *ap* g^+ *ap* (**3.85**-3, Figure 3.11b) would still populate to an extent at room temperature due to the lack of destabilising *syn*-pentane interactions.

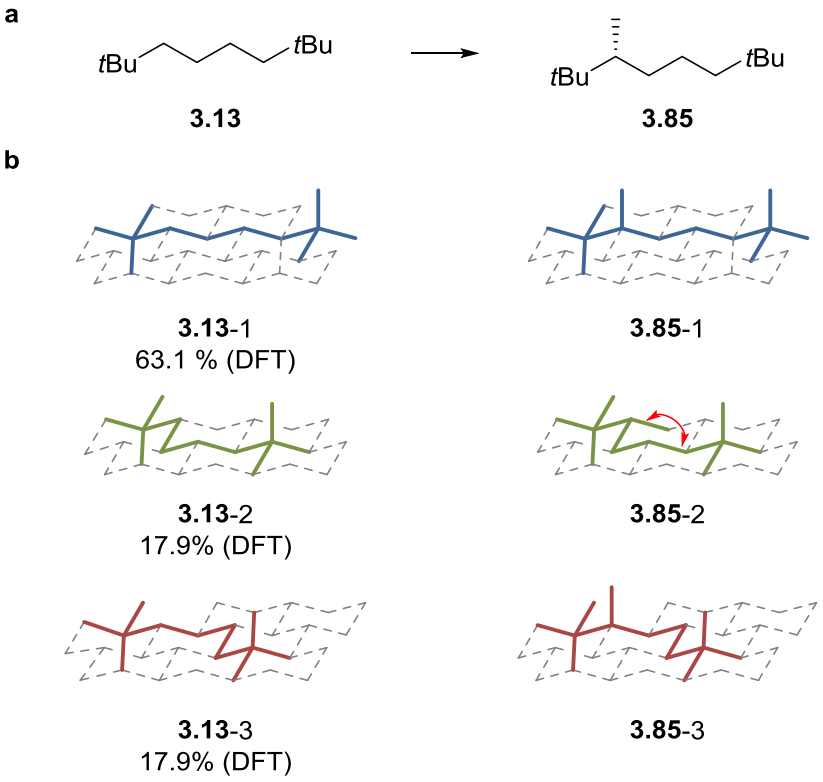

Figure 3.11: **a**, Introduction of a methyl substituent to **3.13**. **b**, Predicted conformers of **3.13** and **3.85** represented on a diamond lattice with *syn*-pentane interactions highlighted using red arrows.

To verify the conformational behaviour predicted by diamond lattice analysis of **3.85** (Figure 3.11b), a MM Monte Carlo conformational search and DFT calculations were

performed on **3.85** using procedures described previously (section 3.2.2). DFT calculations predicted that indeed the population of the conformation with a linear backbone (*ap ap ap ap*, Figure 3.12) has increased from 63.1% to 78.9% with the introduction of a methyl group. The other conformer which contributes 16.0% to the global population has backbone dihedral angles of *ap* g^+ *ap* (**3.85**-3, Figure 3.12b and c) as expected based on the diamond lattice analysis (Figure 3.11).

a

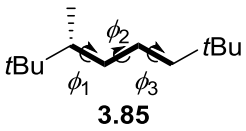

3.85

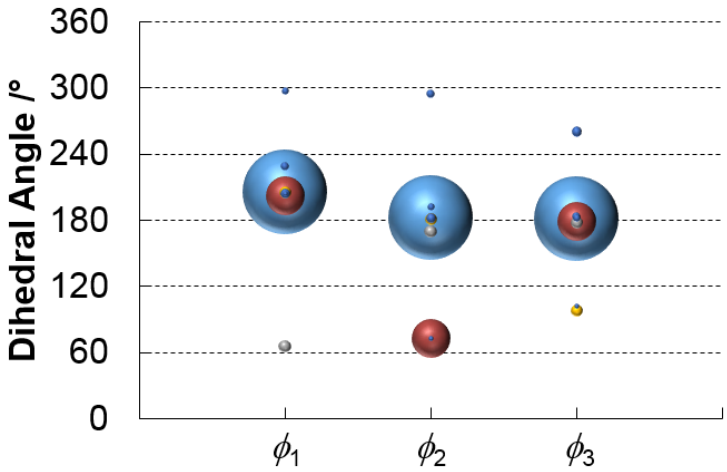

b

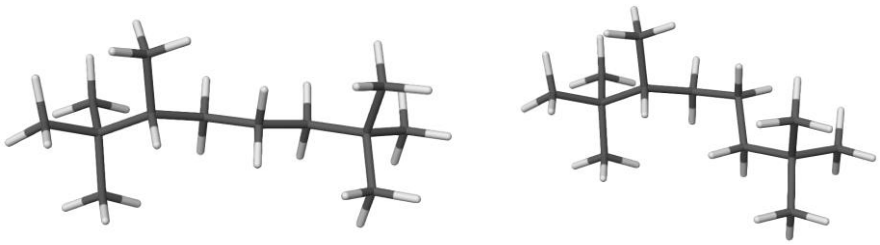

c

	3.85-1 (*ap ap ap*)	**3.85**-3, (*ap* g^+ *ap*)
ΔG/kJ mol^{-1}	0.0	4.0
Population (298 K)	78.9%	16.0%

Figure 3.12: **a**, Chemical structure of **3.85** and the DFT predicted conformational landscape represented by a bubble plot. Blue dots represent conformer **3.85**-1, red dots represent conformer **3.85**-3 and other colour dots represent minor conformers which have a combined population of 5.1%. **b**, 3D structure of **3.85**-1 and **3.85**-3. **c**, Major conformers of **3.85** represented on a diamond lattice together with the corresponding relative Gibbs free energies (ΔG) and population at 298 K.

If the conformer with backbone dihedral angles of *ap g+ ap* (for example, **3.85**-3, Figure 3.12b and c) could be destabilised by the introduction of another substituent, the preference to adopt a linear backbone conformation should be further enhanced. The diamond lattice analysis (Figure 3.13) suggested that if another substituent (R^2) was introduced *anti* to the existing one (R^1), this would create **3.86** (Figure 3.13b) and the conformer with backbone dihedral angles of *ap* g^+ *ap* (**3.86**-2, Figure 3.13b) should be destabilised by a *syn*-pentane interaction between the C-R^2 bond and the backbone C-C bond (highlighted in red, Figure 3.13b). Therefore, **3.86** should have a very strong preference to adopt the conformer with a linear backbone (**3.86**-1, Figure 3.13b).

In contrast, if the substituent R^2 is introduced *syn* to the existing R^1 substituent (Figure 3.13c), this configuration of R^2 would not induce any destabilising *syn*-pentane interactions and therefore **3.87** should have two accessible backbone conformations (**3.87**-1 and **3.87**-2, Figure 3.13c) and no strong bias towards either one would be achieved.

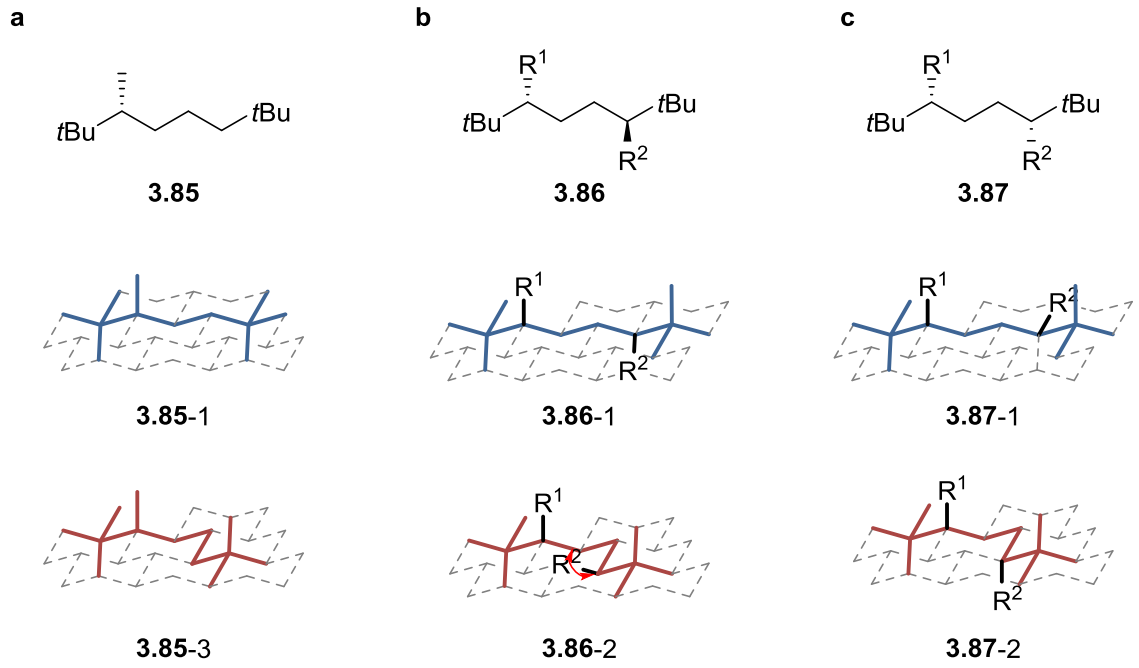

Figure 3.13: Introduction of another substituent (R^2) *anti* (**3.86**) or *syn* (**3.87**) to the existing substituent (R^1). The chemical structure and conformers of **3.85**, **3.86** and **3.87** are represented on a diamond lattice with the induced destabilising *syn*-pentane interaction highlighted in red.

3.2.6 QM analysis of 3.88 and 3.89.

The synthesis of **3.86** and **3.87** requires the use of the chiral α-stannyl neopentyl benzoates (*S*)-**3.29** generated using the hard-to-source (–)-sparteine. To maximise the use of

the chiral α-stannyl neopentyl benzoates (*R*)-**3.29** generated using the more abundant (+)-sparteine, conformational analysis and synthesis of the enantiomers of **3.86** and **3.87** (**3.88** and **3.89**, respectively) were considered instead.

a

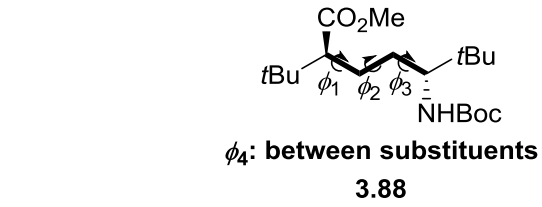

ϕ_4: between substituents

3.88

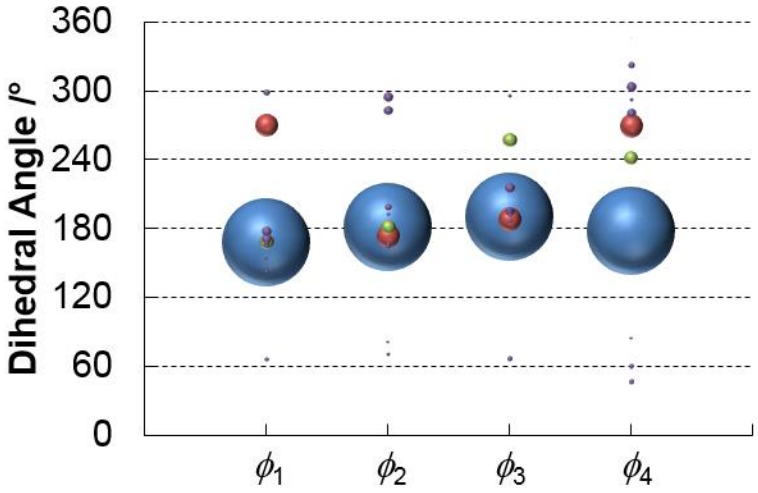

b

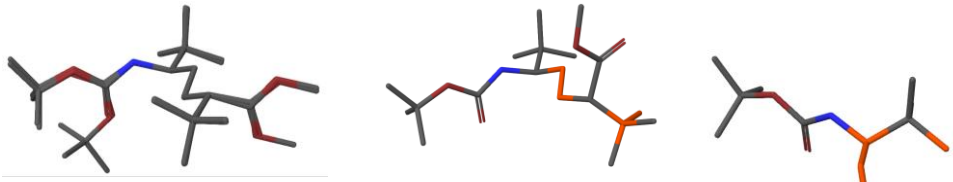

c

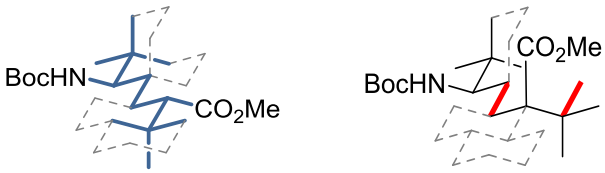

	3.88-1, **3.88**-2 and **3.88**-3	**3.88**-4	**3.88**-5
	(*ap ap ap*)	(g^- *ap ap*)	(*ap ap* −*ac*)
ΔG/kJ mol^{-1}	0, 2.5 and 3.7 respectively	5.5	8.4
Population (298 K)	88.1%*	5.9%	1.9%

Figure 3.14: Chemical structure of **3.88** and the DFT predicted conformational landscape represented by a bubble plot. Blue dots represent conformer **3.88**-1, **3.88**-2 and **3.88**-3 because they all have a linear backbone conformation. Red dots represent conformer **3.88**-4 and other colour dots represent minor conformers which have a combined population of 6.0%. **b**, 3D structure of **3.88**-1, **3.88**-2 and **3.88**-3 (overlaid) together with **3.88**-4 and **3.88**-5. **c**, Major conformers of **3.88** represented on a diamond lattice

together with the corresponding relative Gibbs free energies (ΔG) and population at 298 K. The distorted *syn*-pentane interactions in minor conformers (**3.88**-4 and **3.88**-5) are highlighted in red. *: Combined population of conformer **3.88**-1, **3.88**-2 and **3.88**-3. Hydrogens are omitted for clarity.

A MM Monte Carlo conformational search and DFT calculations were performed on **3.88** using procedures described previously (section 3.2.2). The DFT-predicted dominant conformers are **3.88**-1, **3.88**-2 and **3.88**-3 (Figure 3.14b and c) and they all possess a linear backbone conformation and only differ in the rotation of the pendant methyl ester and carbamate groups. In the dominant conformation, the substituents are antiperiplanar to each other, creating a 'Z-shaped' molecule.

Compared to **3.85**, which has one substituent on the backbone and has 78.9% of conformers with a linear backbone conformation, **3.88**, which has two substituents on the backbone *anti* to each other, shows a higher preference towards conformations with a linear backbone (88.1% population) and this is in line with what was predicted based on the diamond lattice analysis (Figure 3.13b). Compared to **3.13**, which has no substituent on the backbone, the introduction of two substituents adjacent to both quaternary centres in *anti* configuration enhanced the preference towards conformations with a linear backbone by 25%. Although the enhancement is substantial, minor conformers such as **3.88**-3 and **3.88**-4 still populate at room temperature (5.9% and 1.9% respectively, Figure 3.14c) because the distorted *syn*-pentane interactions observed in both conformers have a lower energy penalty than for a 'perfect' *syn*-pentane and are therefore less destabilising.

In contrast, **3.89** should not have a preference towards a particular conformation based on the diamond lattice analysis (Figure 3.13c). To validate this hypothesis, a MM Monte Carlo conformational search and DFT calculations were performed on **3.89** using procedures described previously (section 3.2.2). Surprisingly, DFT calculations predicted that **3.89** has a strong preference (89.6% population) to adopt the conformer with a linear backbone (*ap ap ap ap*, Figure 3.15a). in which the two substituents are *gauche* to each other (ϕ_4~ 60°C, Figure 3.15a). The DFT prediction contradicts the diamond lattice analysis, suggesting that the diamond lattice analysis (Figure 3.13) does not properly account for the effect of bulky, non-sp^3 substituents (e.g. NHBoc) on molecular conformations.

a

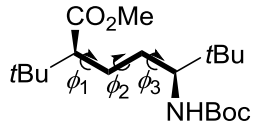

ϕ_4: between substituents

3.89

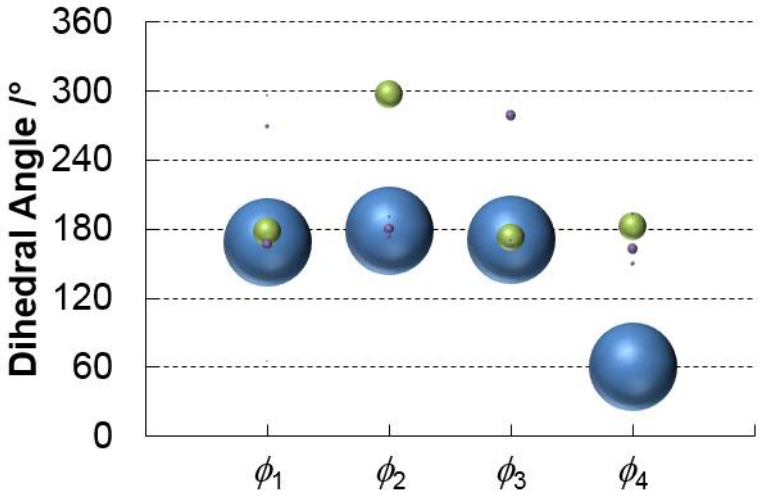

b

c

	3.89-1, **3.89**-2 and **3.89**-5	**3.89**-3 and **3.89**-4
	(*ap ap ap*)	(*ap* g^- *ap*)
ΔG/kJ mol^{-1}	0.0, 2.1 and 8.4 respectively	2.1 and 6.0 respectively
Population (298 K)	89.6%	8.4%

Figure 3.15: Chemical structure of **3.89** and the DFT predicted conformational landscape represented by a bubble plot. Blue dots represent conformer **3.89**-1, **3.89**-2 and **3.89**-5 and green dots represent conformer **3.89**-3 and **3.89**-4. Other colour dots represent minor conformers which have a combined population of 2.0%. **b**, 3D structure of **3.89**-1, **3.89**-2 and **3.89**-5 (overlaid) together with **3.89**-3 and **3.89**-4 (overlaid). **c**, Major conformers of **3.89** represented on a diamond lattice together with the corresponding relative Gibbs free energies (ΔG) and combined population of conformers with the same

backbone conformation at 298 K. Hydrogens of conformers **3.89**-1, **3.89**-2 and **3.89**-5 are omitted for clarity.

Summary of sections 3.2.4 – 3.2.6

As discussed, the conformational control exerted by quaternary centres diminishes with increasing chain length. DFT calculations predicted that going from **3.10** to **3.13**, the preference towards the linear backbone conformation decreased from 100% to 63.1% (Figure 3.10c), because the central dihedral (in blue, Scheme 3.9) could adopt either the *ap*, g^+ or g^-, conformations.

The conformational bias towards the linear backbone conformation could be restored by inducing destabilising *syn*-pentane interactions with substituents at specific positions with suitable stereochemistry. DFT calculations predicted that the introduction of a methyl group adjacent to a quaternary centre would increase the bias towards the linear backbone conformation from 63.1% to 78.9% (**3.85**-1, Figure 3.12). The introduction of a second substituent based on diamond lattice analysis suggested that while the *anti* isomer **3.86** should preferentially adopt the linear backbone conformation, the *syn* isomer **3.87** should adopt two conformations (Figure 3.13). However, when the methyl substituents were replaced by ester and carbamate moieties, DFT calculations predicted that both the *anti* isomer **3.88** and the *syn* isomer **3.89** preferentially adopt the linear backbone conformation with population greater than 88%.

3.2.7 Synthesis of 3.88.

The Z-shaped molecule **3.88** was synthesised to confirm the DFT-predicted molecular conformations. Matteson homologation of boronic ester **3.65** did not go to completion (93-97% conversion, Scheme 3.39) but due to time constraints, the Matteson homologation was not optimised and the crude material containing boronic esters **3.65** and **3.90** were subjected to another lithiation–borylation reaction with the *R* enantiomer of the α-stannyl benzoate (*R*)-**3.29**. The desired boronic ester **3.91** could be isolated from a crude mixture which also contained **3.11** (U-shaped molecule) by flash column chromatography.

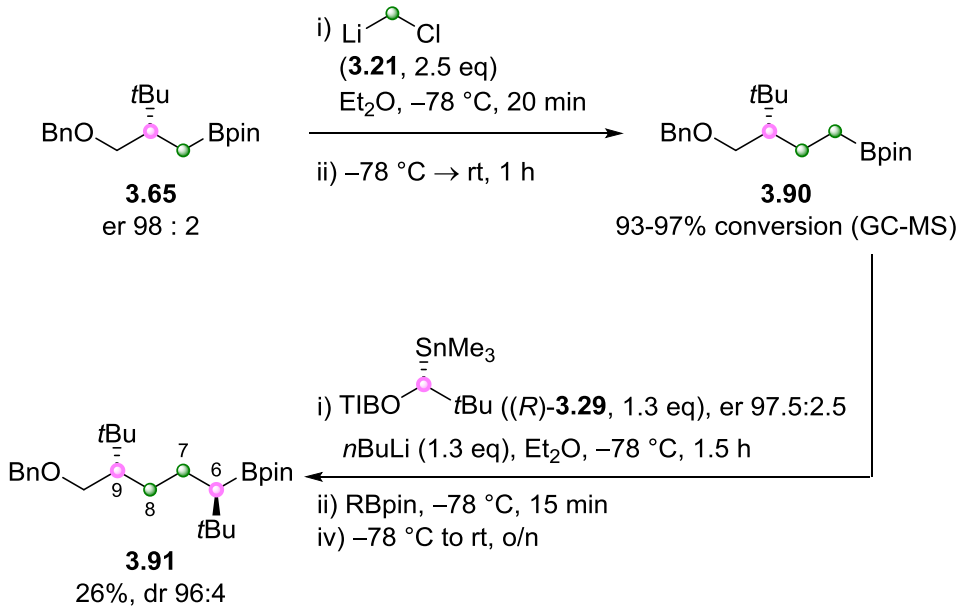

Scheme 3.39: Matteson homologation of boronic ester **3.65** followed by lithiation–borylation reaction with (*R*)-**3.29** to generate key intermediate **3.91**.

The ^{1}H NMR spectrum of **3.91** is relatively dispersed and ^{1}H-^{1}H scalar coupling constants of protons along the backbone (C6 – C9 region, Scheme 3.39) were extracted. The magnitude of the experimentally measured ^{1}H-^{1}H scalar coupling constants of **3.91** fits well with the magnitude of the designed major conformation (Z-shape) with the benzyl group and pinacol boronic ester antiperiplanar to each other (Table 3.1). Therefore, the two substituents are far away from each other and no cyclisation reaction should occur between the two ends after further functional group transformations.

Table 3.1: Predicted major conformation of **3.91** represented on a diamond lattice, together with the expected magnitude of ^{1}H-^{1}H scalar coupling constants in the C6 – C9 region and the experimentally measured values.

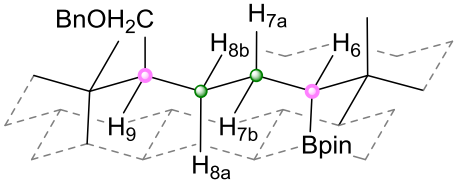

3.91

H_A	H_B	Magnitude of the expected J values	Experimental J values/ Hz
H_9	H_{8a}	Small	2.9
H_9	H_{8b}	Big	9.2
H_{8a}	H_{7b}	Small	4.6
H_{8a}	H_{7a}	Big	12.6
H_{8b}	H_{7b}	Big	12.0
H_{8b}	H_{7a}	Small	4.0
H_6	H_{7b}	Big	12.2
H_6	H_{7a}	Small	3.4

To verify this hypothesis, boronic ester **3.91** was transformed to the carbamate **3.92** using the optimised conditions described previously (Scheme 3.40). The benzyl group was deprotected in the absence of the second Boc protecting group to yield primary alcohol **3.92**. Stahl oxidation of primary alcohol **3.93** indeed exclusively yielded aldehyde **3.94**, which was oxidised and methylated to deliver the Z-shaped molecule **3.88** in good yield (90%). However, signal overlap of the methylene protons in **3.88** hindered the extraction of adequate amounts of $^{n}J_{HH}$ from the ^{1}H NMR spectrum to determine the major conformation of the backbone. Unfortunately, due to time constraints a full set of DFT NMR calculations of the Z-shaped molecule **3.88** was not undertaken and additional NMR experiments such as 1D-TOCSY and Accordion-HSQMBC were not performed to record additional $^{n}J_{HH}$ and $^{n}J_{HC}$. Therefore, QM/NMR analysis of the Z-shape molecule **3.88** could not be conducted to study its solution-state conformational behaviour. Nevertheless, the $^{n}J_{HH}$ of the intermediate boronic ester **3.91**, which has two bulky non-sp^3 substituents ($BnOCH_2$ and Bpin), suggested that it is very likely

to adopt the designated Z-shaped conformation. Therefore, the final product **3.88** should also adopt the designated Z-shaped conformation.

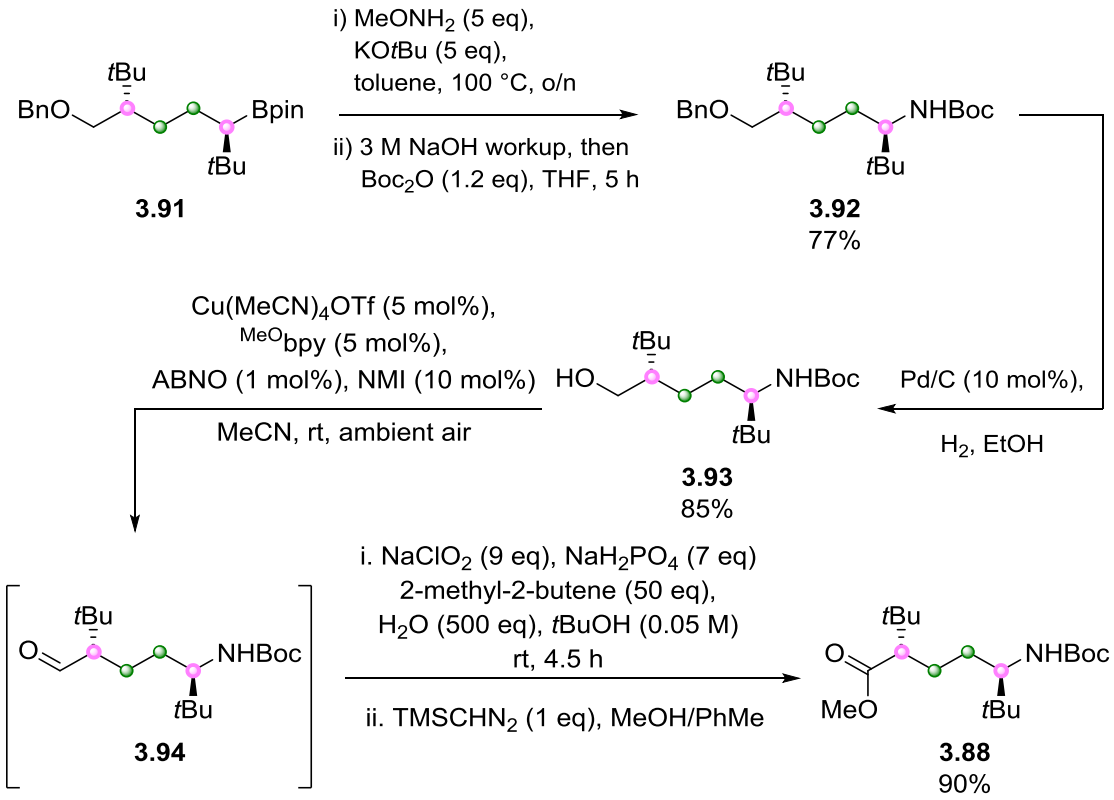

Scheme 3.40: Synthesis of Z-shaped molecule **3.88**.

Designing conformationally biased molecules with terminal *tert*-butyl groups separated by five carbon units. (Compounds 3.14, 3.95 – 3.105)

3.2.8 Conformational analysis of 3.14.

The introduction of another methylene group to **3.13** generates **3.14** (Figure 3.16) which should in theory have $3^2 = 9$ possible conformations due to the free rotation of the two central bonds (highlighted in blue, Figure 3.16). Only seven out of the nine conformers would be populated at room temperature because two of them would be destabilised by *syn*-pentane interactions, indicated by a g^+ dihedral angle followed by a g^- dihedral angle.

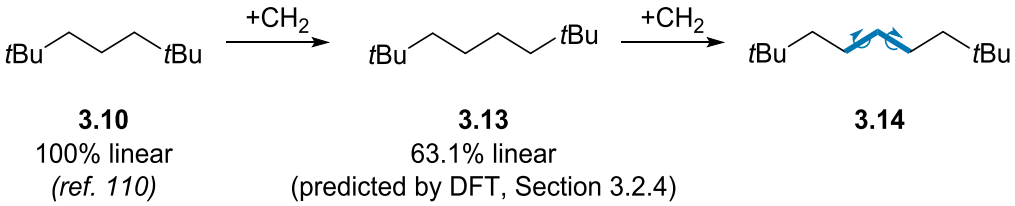

Figure 3.16: Terminal *t*Bu groups separated by three (**3.10**), four (**3.13**) and five methylene units (**3.14**).

A MM Monte Carlo conformational search and DFT calculations were performed on **3.14** using procedures described previously (section 3.2.2). It was found that three conformers (**3.14**-1, **3.14**-4 and **3.14**-6, Figure 3.17) have relative Gibbs free energies (ΔG) within 10 kJ mol^{-1} of the global minimum. Again, degenerate conformers (**3.14**-2, **3.14**-3, **3.14**-5 and **3.14**-7, Figure 3.17) were generated manually for the accurate description of conformer population.

When there are five methylene groups between the terminal *tert*-butyl groups, the preference for a particular conformation decreases to less than 40%. Although conformer **3.14**-1 with a linear backbone conformation is still the global minimum (Figure 3.17), it only has 37.6% population and the conformer population is even more complex. Therefore, it is more challenging to restore conformational control in **3.14**-type scaffold in which the two quaternary centres are separated by five carbon units.

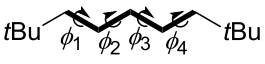

3.14

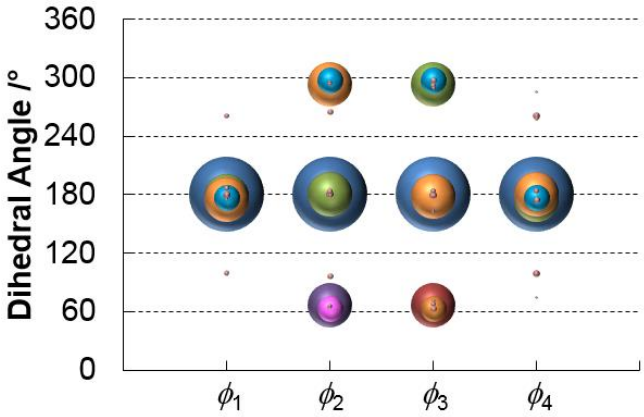

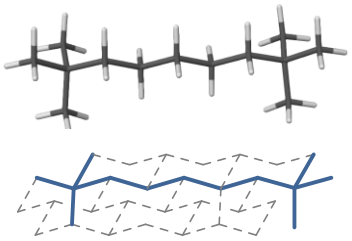

3.14-1, (*ap ap ap ap*)

ΔG = 0 kJ mol^{-1}

37.6% population

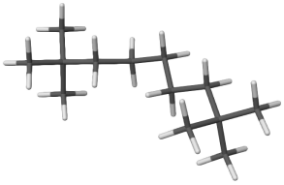

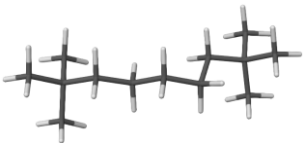

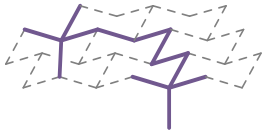

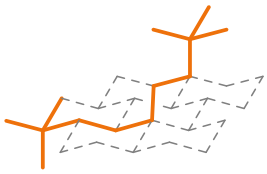

3.14-2
(*ap g*$^+$*ap ap*)
2.63
13.0%

3.14-3
(*ap g*$^-$ *ap ap*)
2.63
13.0%

3.14-4
(*ap ap g*$^+$ *ap*)
2.63
13.0%

ΔG/kJ mol^{-1}
Population
(298 K)

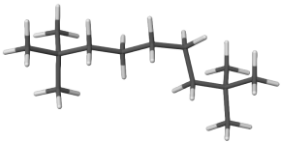

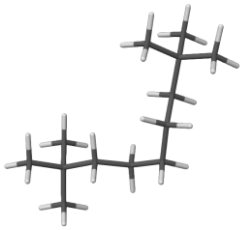

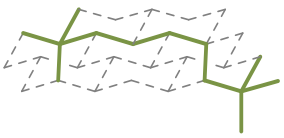

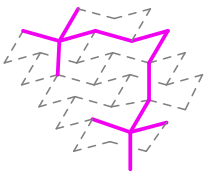

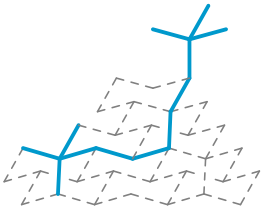

3.14-5
(*ap ap g*$^-$ *ap*)
2.63
13.0%

3.14-6
(*ap g*$^+$ *g*$^+$ *ap*)
5.38
4.3%

3.14-7
(*ap g*$^-$ *g*$^-$ *ap*)
5.38
4.3%

ΔG/kJ mol^{-1}
Population
(298 K)

Figure 3.17: Chemical structure of **3.14**, the DFT predicted conformational landscape represented by a bubble plot, 3D structures of major conformers of **3.14** and the corresponding relative Gibbs free energies (ΔG) and population at 298 K for each conformer. Different colour dots represent conformers with different backbone conformations.

3.3.9 Conformational analysis of compounds 3.95 – 3.105

Imposing conformational bias in an even longer, five-carbon chain was investigated. The seven low energy conformations (**3.14**-1 – **3.14**-7, Figure 3.17) were considered in the initial diamond lattice analysis of **3.14** (Figure 3.18). Although the introduction of a methyl group adjacent to the quaternary centre induces destabilising *syn*-pentane interactions in two conformers with backbone conformations of *ag*+*aa* and *ag*+*g*+*a* (**3.95**-2 and **3.95**-6 respectively, Figure 3.18b), the other seven conformers do not possess such destabilising interactions, thus will still populate substantially at room temperature. Therefore, based on diamond lattice analysis **3.95** does not have a strong preference (>80% population) towards a particular conformation.

a

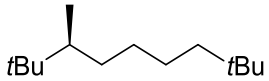

3.95

b

3.95-1
(*ap ap ap ap*)
√

3.95-2
(*ap* g^+ *ap ap*)
×

3.95-3
(*ap* g^- *ap ap*)
√

3.95-4
(*ap ap* g^+ *ap*)
√

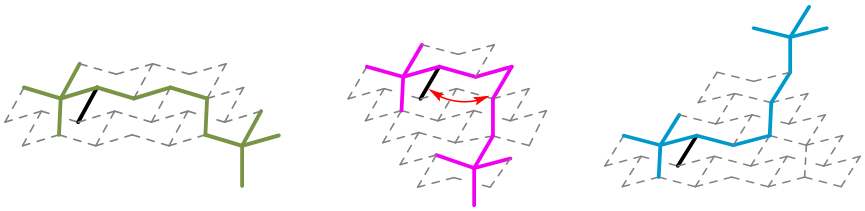

3.95-5
(*ap ap* g^- *ap*)
√

3.95-6
(*ap* g^+ g^+ *ap*)
×

3.95-7
(*ap* g^- g^- *ap*)
√

Figure 3.18: **a**, Chemical structure of **3.95**. **b**, Diamond lattice analysis of the seven potential conformers of **3.95**. Destabilising *syn*-pentane interactions induced by the introduction of a methyl group were highlighted using red arrows.

To destabilise more conformations, another methyl group was introduced adjacent to the other quaternary centres and this generated **3.96**. Diamond lattice analysis suggests that the

introduction of the second methyl group *syn* to the existing one induces destabilising *syn*-pentane interactions in four out of seven conformations (**3.96**-2, **3.96**-5, **3.96**-6 and **3.96**-7, Figure 3.19). Therefore, **3.96** should show a higher bias towards a particular conformation compared to **3.95**.

a

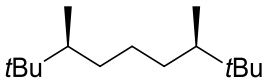

3.96

b

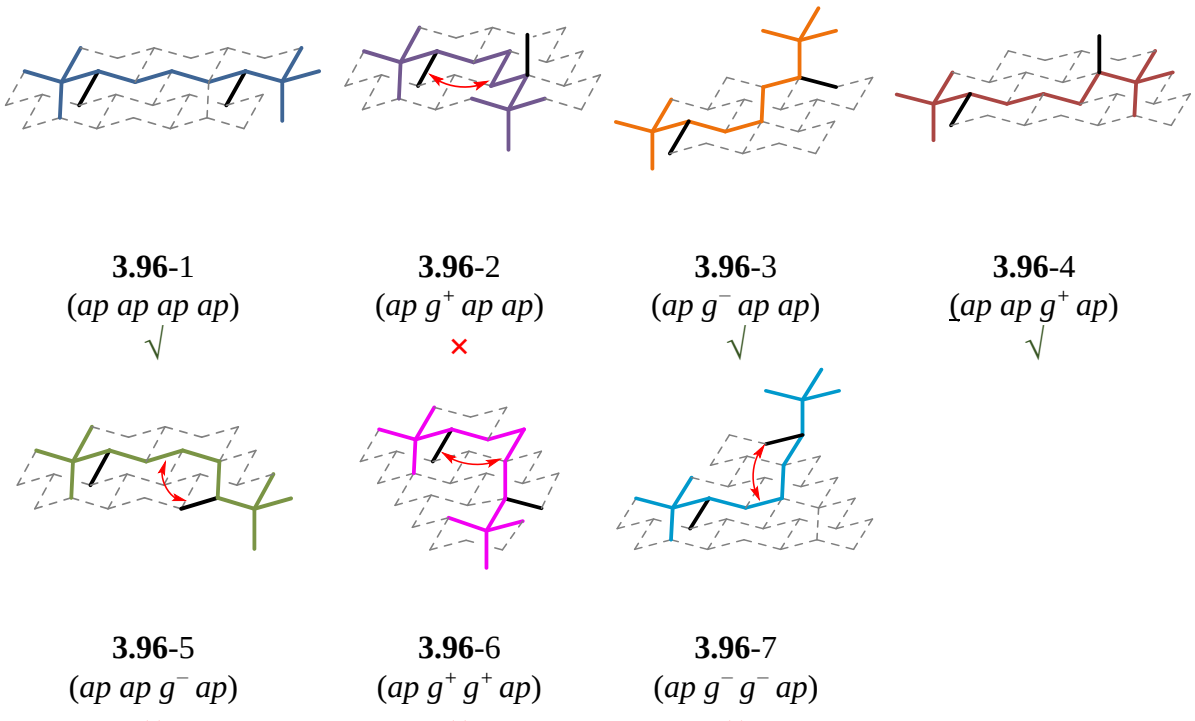

Figure 3.19: **a**, Chemical structure of **3.96**. **b**, Diamond lattice analysis of the seven potential conformers of **3.96**. Destabilising *syn*-pentane interactions induced by the introduction of methyl groups were highlighted using red arrows.

To further enhance the conformational bias of **3.96**, another methyl group was introduced in the centre of the chain (**3.97**, Figure 3.20). The introduction of the central methyl group *anti* to the existing ones should induce destabilising *syn*-pentane interactions in the conformers with backbone dihedral angles of *ap* g^- *ap ap* and *ap ap* g^+ *ap*. As a result, conformers **3.97**-3 and **3.97**-4 (Figure 3.20) should no longer populate at room temperature and therefore **3.97** would have a very strong preference (>80% of population) to adopt the conformation with a linear backbone (**3.97**-1, Figure 3.20).

a

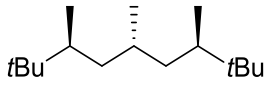

3.97

b

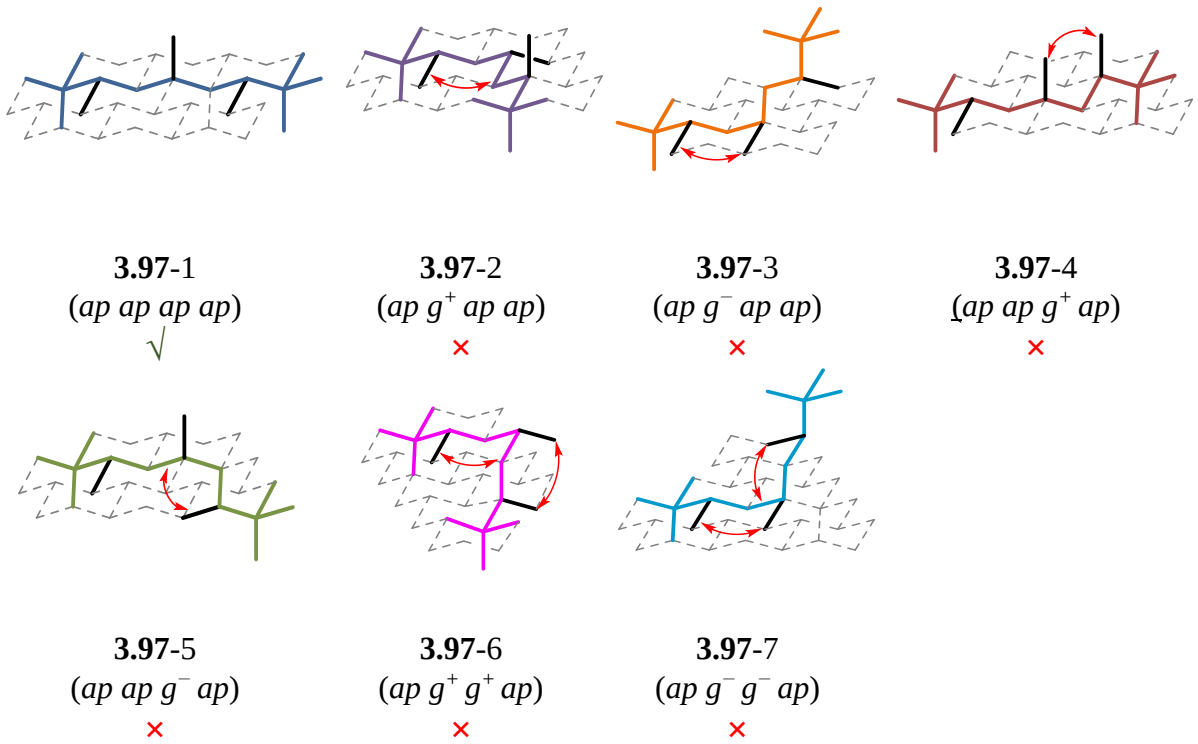

Figure 3.20: **a**, Chemical structure of **3.97**. **b**, Diamond lattice analysis of the seven potential conformers of **3.97**. Destabilising *syn*-pentane interactions induced by the introduction of methyl groups were highlighted using red arrows.

To verify the conformational behaviour of **3.97** predicted by diamond lattice analysis, conformational analysis of the analogue **3.98** (Figure 3.21) with the peripheral methyl groups replaced by ester and carbamate moieties were studied using the MM Monte Carlo conformational search and DFT methods as discussed previously (section 3.2.2). DFT calculations predicted that indeed conformers with a linear backbone (**3.98**-1 and **3.98**-3, Figure 3.21) dominate the conformer population of **3.98** with a combined population of 93.5%. The ester and carbamate groups are approximately *syn* periplanar to each other with a dihedral angle around −20°. Compared to **3.14** which has no substituents on the backbone and has 37.6% of conformers adopting the linear backbone conformation, the introduction of three substituents increases the preference to adopt the conformation with a linear backbone by 55.9% (**3.98**, Figure 3.21).

The first dihedral angle of the backbone (ϕ_1) in the minor conformer **3.98**-2 is +148° and this deviates from the ideal angle of 180° if the first bond would adopt an antiperiplanar conformation. As a result, the *syn*-pentane interaction observed between the C–C bond of the substituent and that of the backbone would have a smaller energetic penalty than expected thus conformer **3.98**-2 still populate (5%) at room temperature.

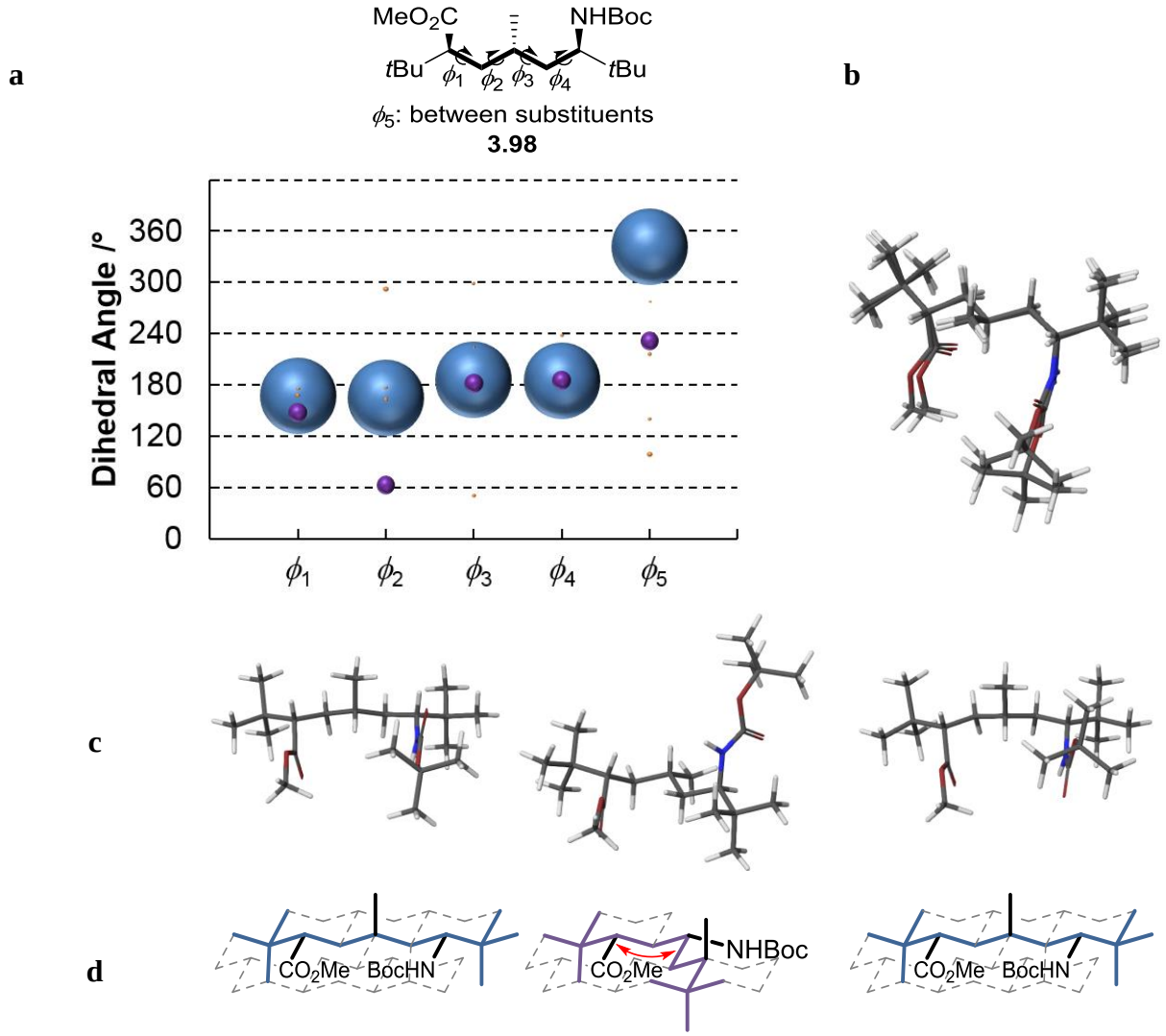

	3.98-1 (*ap ap ap ap*)	**3.98**-2* (*+ac g+ ap ap*)	**3.98**c-3 (*ap ap ap ap*)
ΔG/kJ mol^{-1}	0	7.2	9.6
Population (298 K)	91.6%	5.0%	1.9%

Figure 3.21: **a**, Chemical structure of **3.98** and the DFT predicted conformational landscape represented by a bubble plot. Blue dots represent conformer **3.98**-1 and c because they all have a linear backbone conformation (*ap ap ap ap*). Purple dots represent conformer **3.98**-2 and other colour dots represent minor conformers which have a combined population of 1.5%. **b**, Overlay of conformers **3.98**-1 and

3.98-3. **c**, 3D structure of **3.98**-1, **3.98**-2 and **3.98**-3. **d**, Major conformers of **3.98** represented on a diamond lattice together with the corresponding relative Gibbs free energies (ΔG) and population at 298 K. *: Conformer **3.98**-2 could not be truly represented on a diamond lattice because the first dihedral angle deviates from the ideal angle for an sp^3 carbon atom so the diamond lattice representation is for visualisation purpose only. The distorted *syn*-pentane interactions in conformer **3.98**-2 is highlighted using a red arrow.

The conformational landscape of the diastereomer **3.99** with two peripheral methyl groups in *anti* configuration was also considered (Figure 3.22). Based on the diamond lattice analysis, four out of seven conformers would still populate substantially at room temperature and therefore the conformer population is more complex compared to that of **3.96** (Figure 3.19)

a

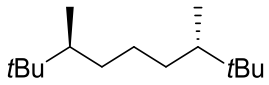

3.99

b

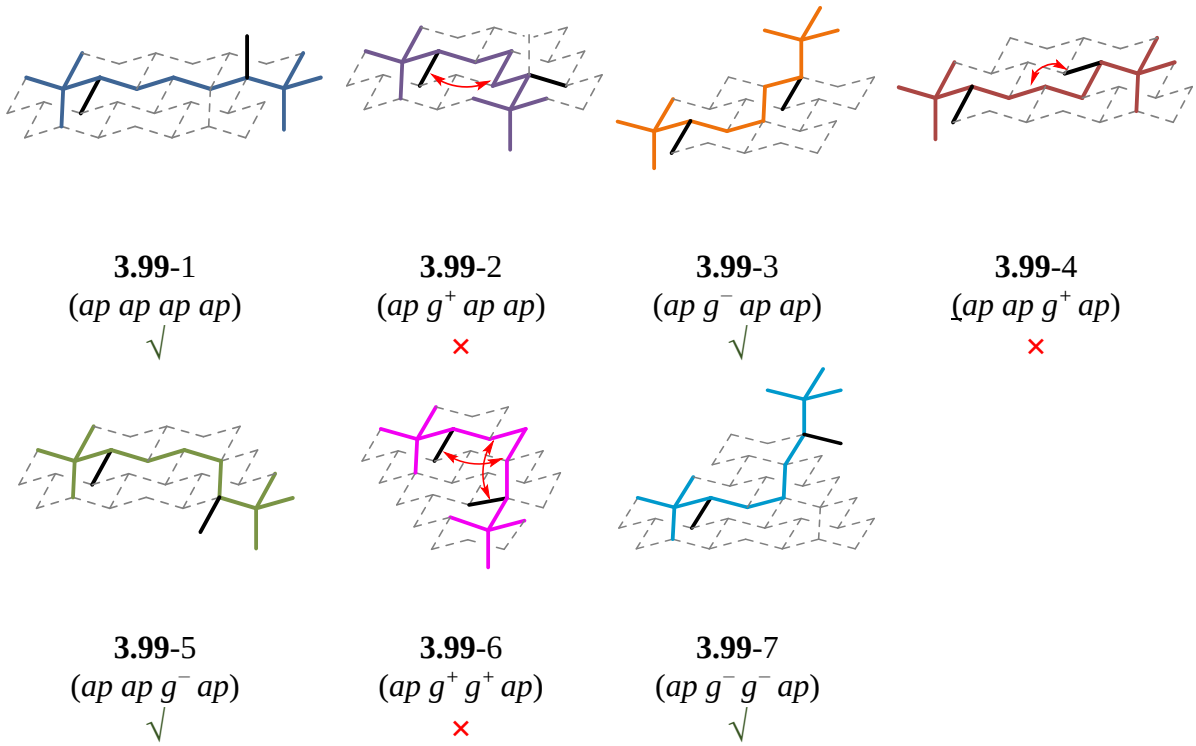

Figure 3.22: **a**, Chemical structure of **3.99**. **b**, Diamond lattice analysis of the seven potential conformers of **3.99**. Destabilising *syn*-pentane interactions induced by the introduction of methyl groups were highlighted using red arrows.

In addition to introducing substituents to the positions adjacent to the quaternary centres, the introduction of an isopropyl group to the centre of the chain was also investigated. Although

the methyl groups of the isopropyl group are free to rotate, in some conformers no matter what position the isopropyl group adopts, there will be an unavoidable *syn*-pentane interaction. Therefore, these conformations will be destabilised regardless of the exact position the isopropyl group since there will always be a methyl occupying a suitable position to induce the destabilising *syn*-pentane interactions. For example, the conformer with a linear backbone (**3.100**-1, Figure 3.23) will be destabilised by at least one *syn*-pentane interactions and the same logic also applies to conformer **3.100**-2 and **3.100**-4. The remaining four conformations (**3.100**-3, **3.100**-5, **3.100**-6 and **3.100**-7) could all in theory accommodate the isopropyl group without any destabilising *syn*-pentane interactions, however it is unclear whether they would populate heavily at room temperature because the rotation of the isopropyl group could still induce destabilising *syn*-pentane interactions.

a

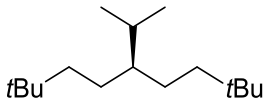

3.100

b

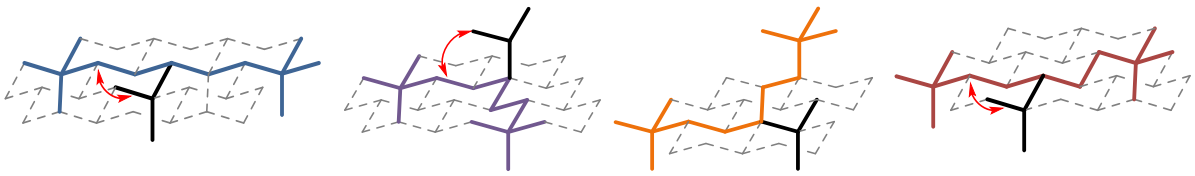

3.100-1
(*ap ap ap ap*)
×

3.100-2
(*ap* g^+ *ap ap*)
×

3.100-3
(*ap* g^- *ap ap*)
?

3.100-4
(*ap ap* g^+ *ap*)
×

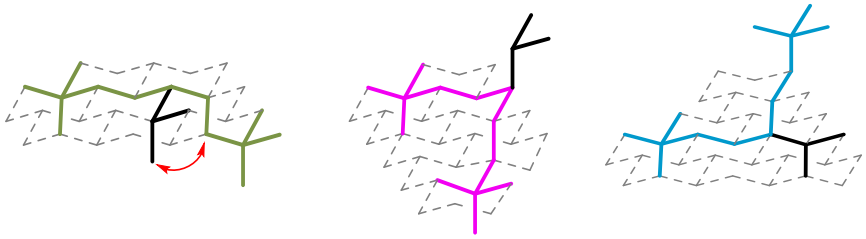

3.100-5
(*ap ap* g^- *ap*)
×

3.100-6
(*ap* g^+ g^+ *ap*)
?

3.100-7
(*ap* g^- g^- *ap*)
?

Figure 3.23: **a**, Chemical structure of **3.100**. **b**, Diamond lattice analysis of the seven potential conformers of **3.100**. Destabilising *syn*-pentane interactions induced by the introduction of the isopropyl group were highlighted using red arrows.

The conformational distribution of the enantiomer **3.101** was also analysed (Figure 3.24) and found to be same to that of **3.100**. Although both **3.100** and **3.101** are *meso* compounds and are therefore equivalent, their conformations were considered separately because subsequent combination of **3.99** and **3.100** (page 153-154) required the change in stereochemistry at the central carbon attached to the isopropyl group.

a

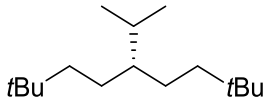

3.101

b

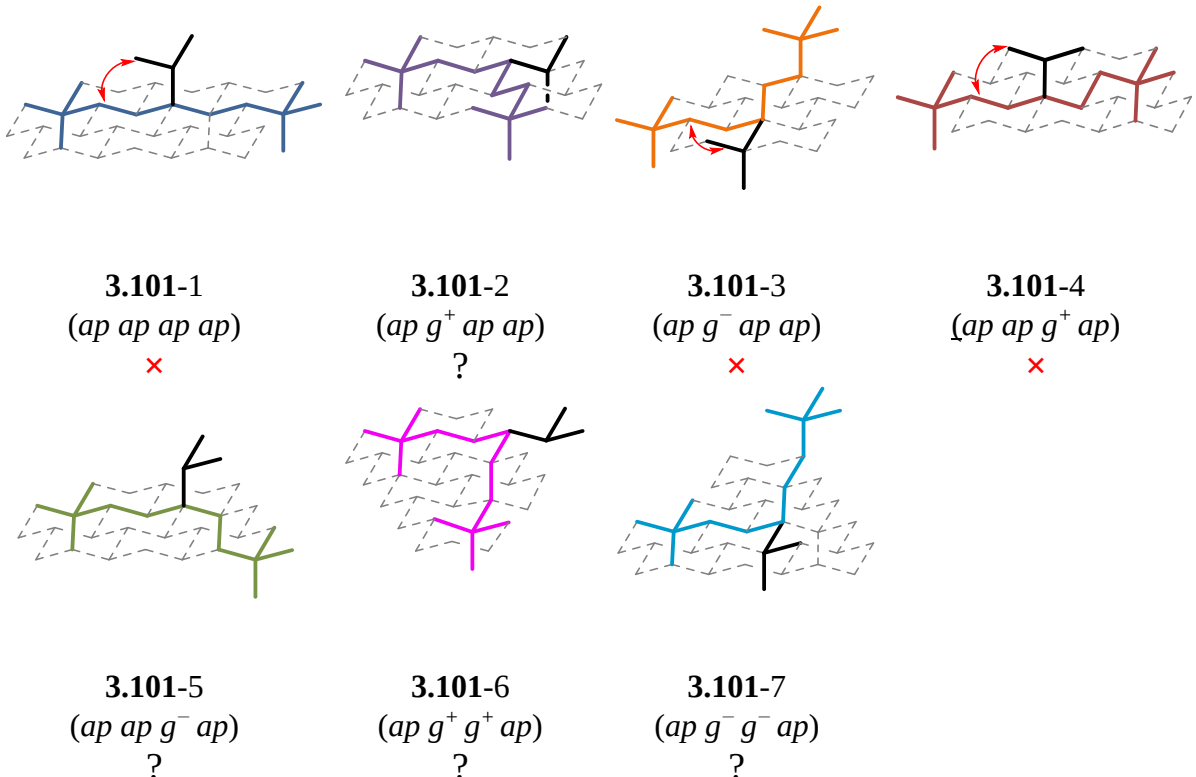

3.101-1
(*ap ap ap ap*)
×

3.101-2
(*ap* g^+ *ap ap*)
?

3.101-3
(*ap* g^- *ap ap*)
×

3.101-4
(*ap ap* g^+ *ap*)
×

3.101-5
(*ap ap* g^- *ap*)
?

3.101-6
(*ap* g^+ g^+ *ap*)
?

3.101-7
(*ap* g^- g^- *ap*)
?

Figure 3.24: **a**, Chemical structure of **3.101**. **b**, Diamond lattice analysis of the seven potential conformers of **3.101**. Destabilising *syn*-pentane interactions induced by the introduction of the isopropyl group were highlighted using red arrows.

Based on the diamond lattice analysis of **3.99**, **3.100** and **3.101**, one would expect that the combination of these scaffolds would lead to the generation of molecules with a single dominant conformation. For example, the combination of **3.99** and **3.100** would generate **3.102** (Figure 3.25a). Unfavourable backbone conformations of **3.99** predicted by diamond lattice analysis (**3.99**-2 and **3.99**-4, Figure 3.22) should be unfavourable in **3.102**. Therefore, for **3.102** conformers with backbone dihedral angles of *ap* g^+ *ap ap* and *ap ap* g^+ *ap* should be disfavoured.

Similarly, unfavourable conformations of **3.100** predicted by diamond lattice analysis (**3.100**-1, **3.100**-2 and **3.100**-4) again should also be unfavourable in **3.102**. Therefore, on top of conformers with backbone dihedral angles of *ap* g^+ *ap ap* and *ap ap* g^+ *ap*, conformers with backbone dihedral angles of *ap ap ap ap* would also be disfavoured in **3.102**.

Therefore, only three types of conformer with backbone dihedral angles of *ap* g^- *ap ap*, *ap ap* g^- *ap* and *ap* g^- g^- *ap* needs to be considered for the diamond lattice analysis (Figure 3.25). The combination of the terminal methyl groups with the central isopropyl group creates *syn*-pentane interactions between the substituents and this leads to the destabilisation of conformers **3.102**-5 and **3.102**-7. As a result, **3.102** should have a very high preference to adopt a conformation with backbone dihedral angles of *ap* g^- *ap ap*.

a

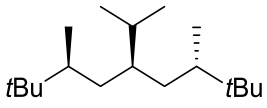

3.102

b

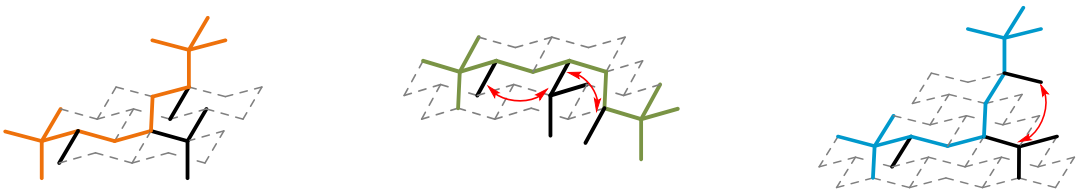

3.102-3 (*ap* g^- *ap ap*) √

3.102-5 (*ap ap* g^- *ap*) ×

3.102-7 (*ap* g^- g^- *ap*) ×

Figure 3.25: **a**, Chemical structure of **3.102**. **b**, Three potential conformers considered for the diamond lattice analysis of **3.102**.

To verify the conformational behaviour of **3.102** predicted by diamond lattice analysis, conformational analysis of the analogue **3.103** (Figure 3.26) with the methyl substituents replaced by ester and carbamate moieties was performed using the MM Monte Carlo conformational search and DFT calculations as described previously (section 3.2.2). DFT calculations predicted that indeed conformations with backbone dihedral angles of *ap* g^- *ap ap* (Figure 3.26b, c and d) dominate the conformer population of **3.103** with a combined population of 97.3%. The ester and carbamate groups are *syn* to each other with dihedral angles in the range from −20° to −45°. The enhancement of conformational preference observed in **3.103** is even more dramatic than was observed in **3.98**, which has three substituents in *anti*-

anti relationship. Compared to **3.14**, which has no substituents on the backbone and only has 13.0% of conformers adopting the conformation with backbone dihedral angles of *ap* g^- *ap ap*, the introduction of substituents increases the preference to adopt conformations with backbone dihedral angles of *ap* g^- *ap ap* by 84.5%.

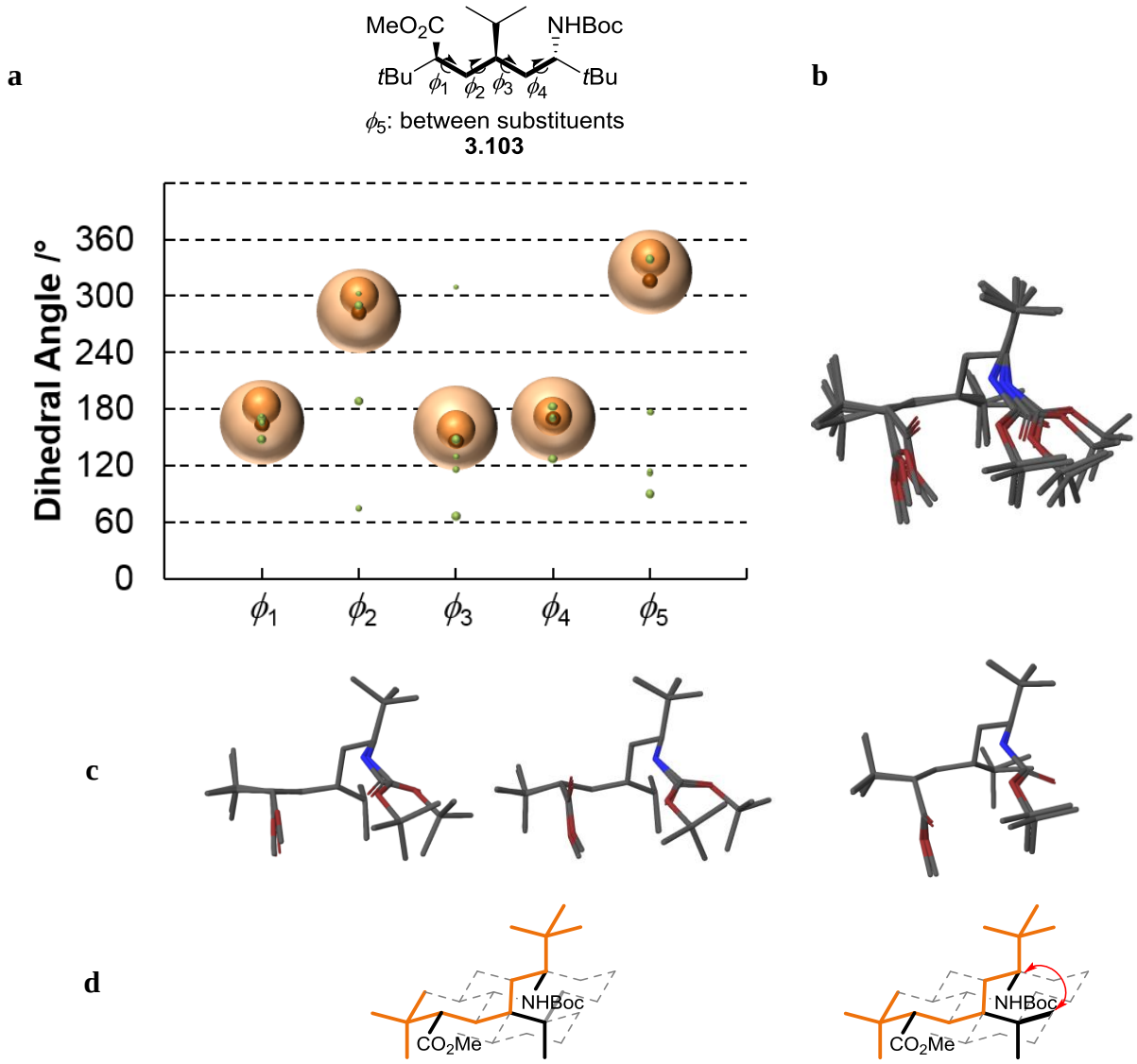

	3.103-1 and **3.103**-2	**3.103**-3 and **3.103**-6 (*ap* g^- *ap ap*)	**3.103**-4, **3.103**-8
ΔG/kJ mol^{-1}	0 and 2.1 respectively	3.1 and 10.7 respectively	8.3 and 11.7 respectively
Population (298 K)	78.7%	16.2%	2.4%

Figure 3.26: Chemical structure of **3.103** and the DFT predicted conformational landscape represented by a bubble plot. Conformers adopting similar backbone conformations (*ap* g^- *ap ap*) but differ in the rotation of substituents are represented in different shades of orange dots. Green dots represent minor conformers which have a combined population of 2.7%. **b**, Overlay of conformers **3.103**-1, **3.103**-2,

3.103-3, **3.103**-4, **3.103**-6 and **3.103**-8. **c**, 3D structure of **3.103**-1 and **3.103**-2 (overlaid), **3.103**-3 and **3.103**-6 (overlaid) together with **3.103**-4 and **3.103**-8 (overlaid). **d**, Major conformers of **3.103** represented on a diamond lattice together with the corresponding relative Gibbs free energies (ΔG) and population at 298 K. The *syn*-pentane interactions in conformer **3.103**-4 and **3.103**-8 are highlighted using a red arrow.

If **3.99** is combined with **3.101** instead, this would generate **3.104**. Again, the unfavourable conformations observed in both **3.99** and **3.101** would also be disfavoured in **3.104**. This led to the consideration of the remaining two accessible conformations with backbone dihedral angles of *ap ap* g^- *ap* and *ap* g^- g^- *ap* (**3.104**-5 and **3.104**-7, respectively, Figure 3.27).

a

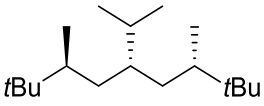

3.104

b

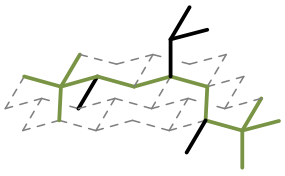

3.104-5
(*ap ap* g^- *ap*)
√

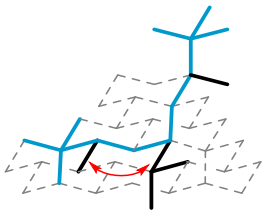

3.104-7
(*ap* g^- g^- *ap*)
×

Figure 3.27: **a**, Chemical structure of **3.104**. **b**, Two potential conformers considered for the diamond lattice analysis of **3.104**.

To verify the conformational behaviour of **3.104** predicted by the diamond lattice analysis (Figure 3.27), conformational analysis of the analogue **3.105** (Figure 3.26) with the methyl substituents replaced by ester and carbamate moieties were studied using the MM Monte Carlo conformational search and DFT calculations as described previously (section 3.2.2). DFT calculations predicted that indeed conformations with backbone dihedral angles of *ap ap* g^- *ap* dominate the conformer population of **3.105** with a combined population of 87.2%. The ester and carbamate groups are *syn* to each other with the dihedral angle (ϕ_5, Figure 3.28a) in the range of −70° to 7°.

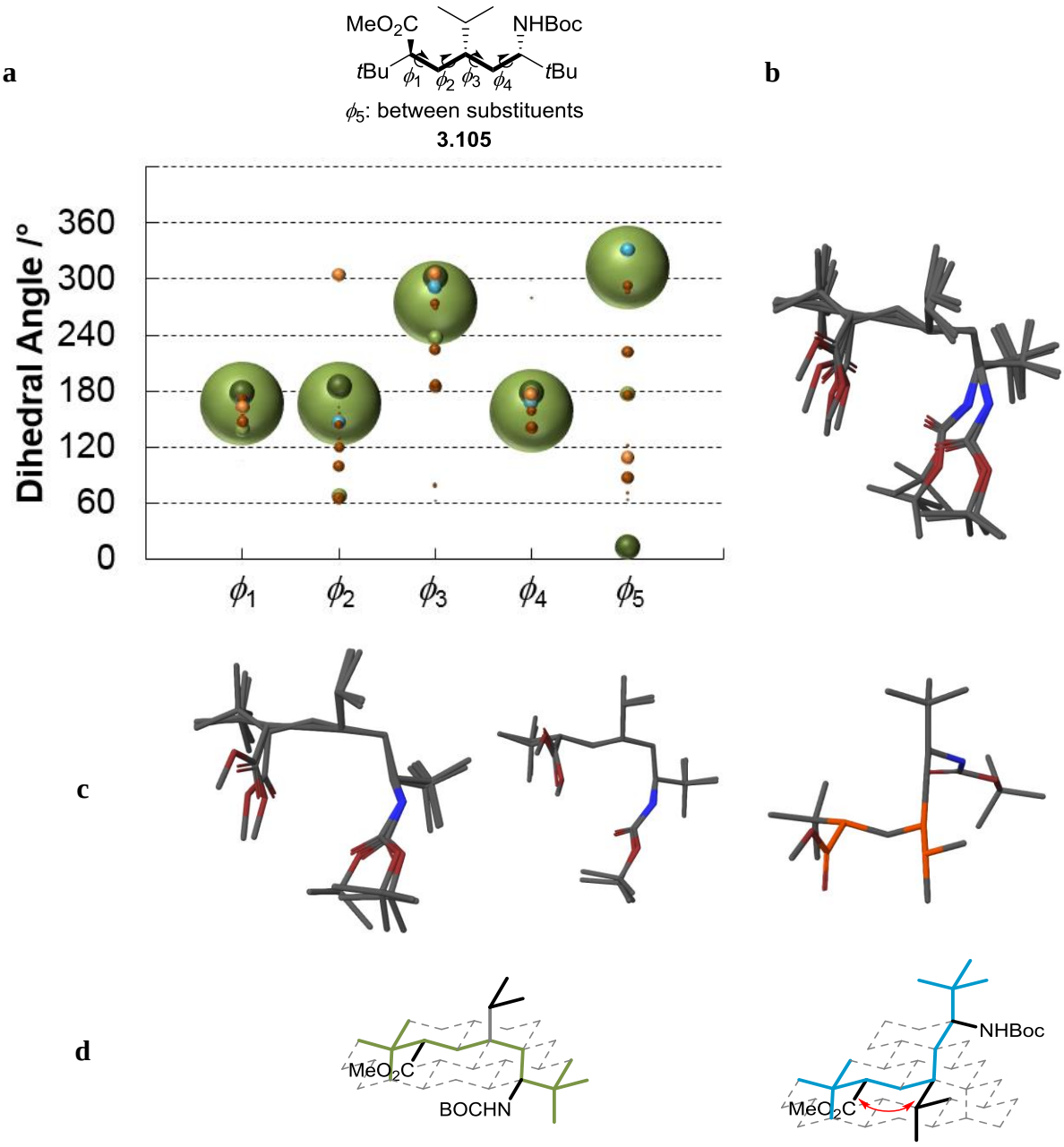

	3.105-1, **3.105**-2, **3.105**-3, and **3.105**-4 (*ap ap g*$^-$ *ap*)	**3.105**-5 and **3.105**-8	**3.105**-9 (*ap g*$^-$ *g*$^-$ *ap*)
ΔG/kJ mol^{-1}	0.0, 0.8, 1.9 and 1.9 repectively	4.4 and 7.3 respectively	7.4
Population (298 K)	80.4%	6.8%	1.5%

Figure 3.28: **a**, Chemical structure of **3.105** and the DFT predicted conformational landscape represented by a bubble plot. Conformers **3.105**-1, **3.105**-2, **3.105**-3, **3.105**-4, **3.105**-5 and **3.105**-8 have very similar backbone conformation and only differ in the rotation of the substituents and the dihedral angle between the substituents. Therefore, they are represented in different shades of green colours.

Blue dots represent minor conformers **3.105**-9 and the rest of the dots represent minor conformers which have a combined population of 11.3%. **b**, Overlay of conformers **3.105**-1, **3.105**-2, **3.105**-3, **3.105**-4, **3.105**-5 and **3.105**-8. **c**, 3D structure of **3.105**-1, **3.105**-2, **3.105** -3, **3.105**-4 (overlaid), **3.105**-5, **3.105** -8 (overlaid) and **3.105**-9. **d**, Conformers of **3.105** represented on a diamond lattice together with the corresponding relative Gibbs free energies (ΔG) and population at 298 K. The *syn*-pentane interactions in conformer **3.105**-9 is highlighted using a red arrow.

Unlike the exquisite conformational preference (97.3% population of a single backbone conformation) observed in **3.103**, **3.105** shows a slight reduced preference towards the designed conformation (87.2% population, Figure 3.28). This is because other conformations, which do not have ideal angles of a sp^3 carbons (109.5°), were not considered in the initial diamond lattice analyses and were ultimately found to populate to some extent by DFT calculations (e.g. 1% population each). In addition, although the qualitative diamond lattice analysis (Figure 3.27) suggested that conformers with backbone dihedral angles of ag^-g^-a should be destabilised by a *syn*-pentane interaction, DFT calculations predicted that such conformers (**3.105**-9, Figure 3.28c and d) would have a population of 1.5%, which is higher than what was expected. Therefore, the qualitative diamond lattice analysis failed to provide a quantitative representation of how destabilising the induced *syn*-pentane interaction would be when the methyl substituents were replaced by other groups.

Summary of section 3.2.8 and 3.2.9.

As discussed, when the two terminal quaternary centres are separated by five methylene groups (**3.14**, Figure 3.16), the conformational preference towards a particular conformation was less than 40% and the conformer population became more complex (Figure 3.17). Again, by inducing destabilising *syn*-pentane interactions, **3.98**, **3.103** and **3.105** were designed and they all have strong the conformational preference (>87% population) towards a single backbone conformation with the substituents pointing towards the same face (i.e. U-shaped molecules) were designed. All the U-shaped molecules designed so far shows different distances between the ester and carbamate substituents, ranging from 2.57 – 5.13 Å as figure 3.29 illustrates.

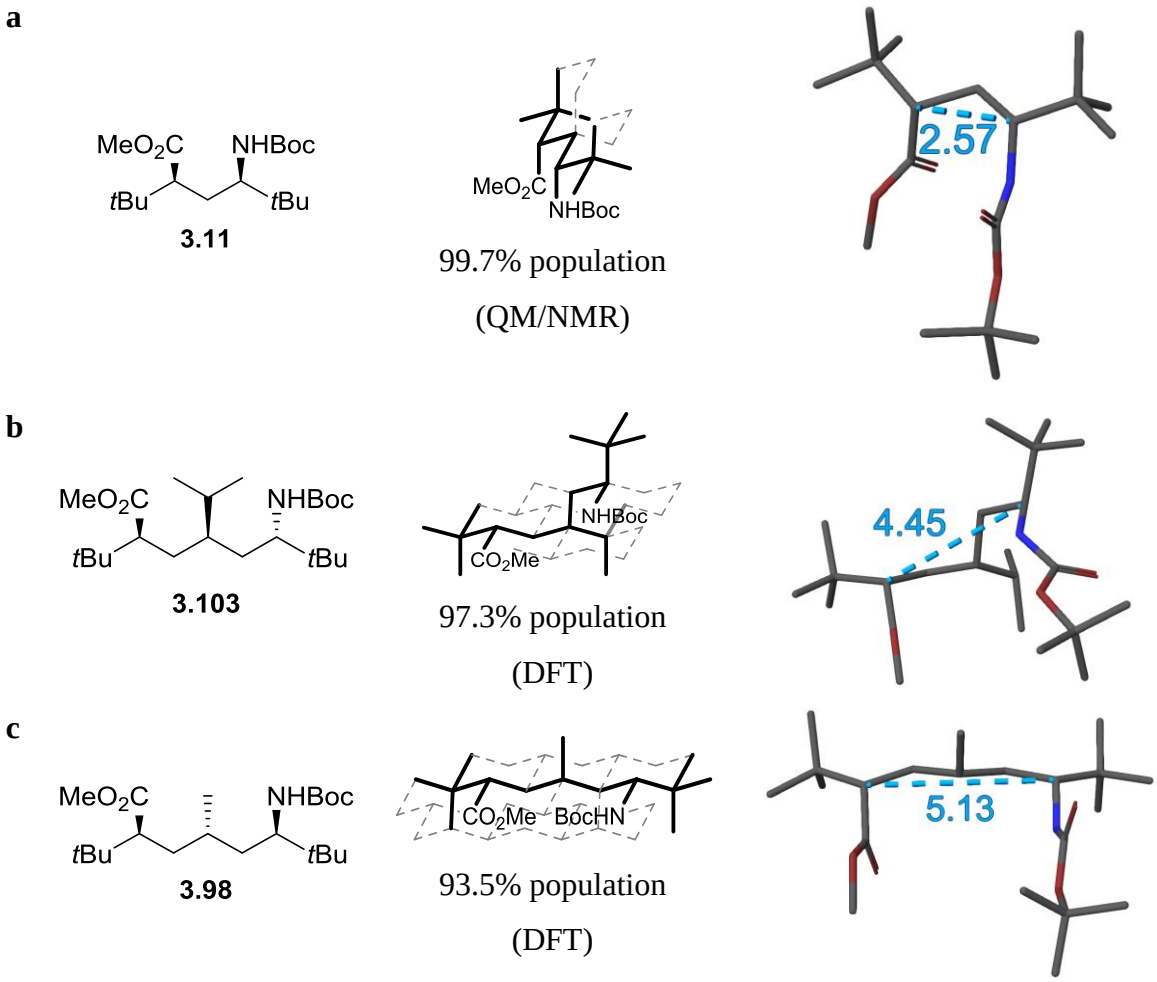

Figure 3.29: U-shaped molecules **3.11**, **3.103** and **3.98** with tuneable distances.

3.3. Conclusions and Future work

3.3.1 Conclusions

In summary, a unidirectional synthetic approach based on lithiation–borylation methodology was developed to prepare the U-shaped (**3.11**), L-shaped (**3.12**) and Z-shaped (**3.88**) molecules. The solution-state behaviour of both the U-shaped (**3.11**) and L-shaped (**3.12**) molecules were studied using a QM/NMR approach with ^{1}H-^{1}H and ^{1}H-^{13}C scalar coupling constants. It was found that both **3.11** and **3.12** have a very high preference to adopt the designed conformation with >99% of global population.

Remote conformational control using quaternary centres at both ends of a linear chain was explored. Although DFT calculations showed that the conformer population of **3.13** and **3.14** are complex, the conformational preference towards a single backbone conformation could be restored by introducing substituents at specific positions with appropriate stereochemistry. Based on the principle of inducing destabilising *syn*-pentane interactions, several molecules with tailored conformations (Table 3.2) were designed using a combination of diamond lattice analysis and MM/DFT calculations. Although the diamond lattice analysis was found to be sufficient to predict the preference of molecular conformations in a qualitative way in most cases, it does not take into account the impact of bulky substituents (such as a Boc protecting group) and this may lead to contradictive prediction of conformational behaviour of certain molecules, such in the case of **3.99** (section 3.2.6).

Table 3.2: A list of molecules designed with tailored conformations as discussed.

Compounds	Molecular Conformations
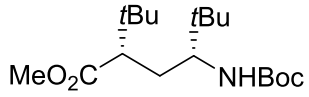 **3.11**	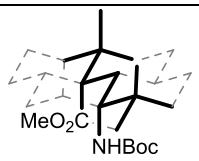 U-shape 99.7% (QM/NMR)
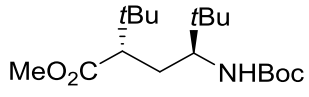 **3.12**	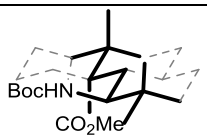 L-shape 99.6% (QM/NMR)
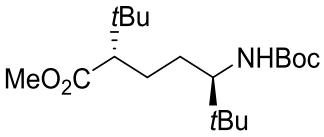 **3.88**	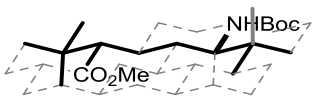 Z-shape 89.6% (DFT)
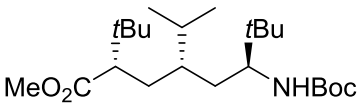 **3.105**	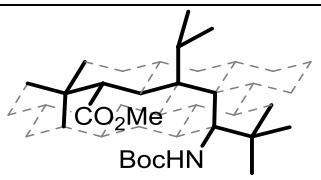 U-shape 87.2% (DFT)
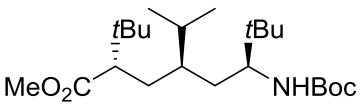 **3.103**	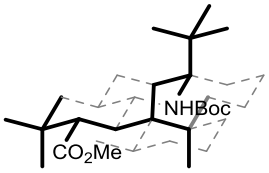 U-shape 97.3% (DFT)
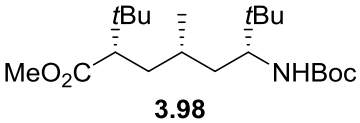 **3.98**	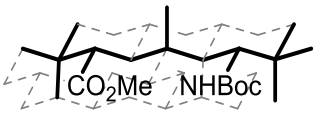 U-shape 93.5% (DFT)

3.3.2 Future work

Although the major conformations of the U-shaped (**3.11**) and L-shaped (**3.12**) molecules were confirmed by QM/NMR analysis using ^{1}H-^{1}H and ^{1}H-^{13}C scalar coupling constants, quantitative NOE analysis to gain detailed insight of the conformational landscapes of both molecules were not performed due to the complications arising from rotamers. If one could develop a method for the quantitative NOE analysis using conformationally defined molecules (i.e. **3.11** and **3.12**), this methodology could be applied to study the conformational behaviour of other small molecules which have carbamate rotamers.

While the Z-shaped molecule **3.88** was synthesised, the QM/NMR analysis was not performed due to time constraints. Therefore, QM/NMR analysis is required to verify the DFT predicted major conformations of **3.88**. In addition, the synthesis and QM/NMR analysis of both **3.99** and the corresponding free amine are required to determine whether the introduction of a bulky substituent (i.e. NHBoc) has indeed enhanced the conformational preference of the molecule as DFT calculations predicted. To confirm the DFT predicted U-shaped molecules with tuneable distances between the substituents, the synthesis and QM/NMR analysis of **3.98**, **3.103** and **3.105** are required.

After the synthesis and QM/NMR analysis of all molecules designed up to date, their use as linker units in bifunctional small-molecule protein degraders, known as PROteolysis TArgeting ChimeraS (PROTACs), will be explored. A functional PROTAC for selective protein degradation contains three components (Scheme 3.41a): a small-molecule ligand which binds to the target protein of interest (in blue, Scheme 3.41a), another small-molecule ligand which binds to an E3 ubiquitin ligase (in purple, Scheme 3.41a), and a linker unit (in pink, Scheme 3.41a) which connects the two ligands. Upon binding of a PROTAC with both the target protein and an E3 ligase, the formation of new protein–protein interactions between the target protein and the E3 ubiquitin ligase enables the ubiquitin tagging and subsequent proteasomal degradation of the target protein of interest.[145]

While several small-molecule ligands have been developed to engage both target proteins of interest and E3 ubiquitin ligase, no studies were performed to study the relationship between the conformations of the linker and the efficiency of PROTAC for selective protein degradation. Therefore, the incorporation of molecules with defined conformations, such as the ones discussed in this chapter, would offer valuable insight into the role of linker conformations in the function of PROTACs. For example, the polyethylene glycol linker in a known PROTAC

3.106 (Scheme 3.41a) could be replaced by an analogue of Z-shaped molecule (**3.88**, Figure 3.14) to generate another PROTAC analogue **3.107**. This analogue will not only allow one to study the conformational integrity of the linker unit when the substituents are large, but also to gain insight of the relationship between the linker conformation(s) and the physiochemical properties as well as potency of the PROTAC.

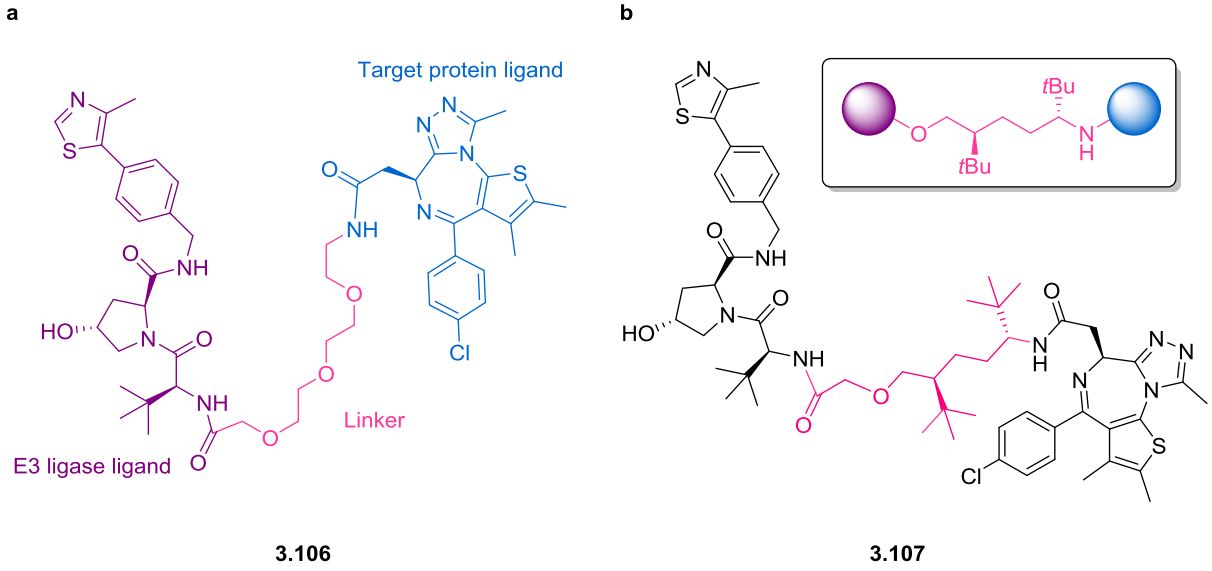

3.106 **3.107**

Scheme 3.41: **a**, Literature reported PROTAC **3.106.**[146] **b**, a PROTAC analogue **3.107** with conformationally defined linker unit.

Chapter 4 Investigation of factors controlling the helical screw-sense preference of all-*syn* methyl-substituted hydrocarbons

This project was conducted in collaboration with Johan A. Pradeilles who performed all the synthetic work and proposed the theoretical models (in section 4.2.1 and 4.2.4). The models and parts of the synthetic work are included to provide a complete picture of the research.

4.1. Introduction and project outline.

Helical structures, such as double-stranded DNA and α-helical peptides, are prevalent in Nature. For biopolymers, the formation of helical conformation does not only allow the efficient packing of genetic information,[147] as in DNA, but also displays functional groups at specific orientations, in the case of α-helical peptides, to maximise their interactions with other biological targets to regulate cellular functions.[148] Chemists have also designed, synthesised and studied non-peptidic helical molecules to take advantage of their chirality to induce asymmetry in organic synthesis[149] and to utilise their predictable molecular conformation for the development of chemical probes and inhibitors for interrogation and regulation of biological function of proteins[150].

Most of the non-peptidic helical scaffolds, such as achiral polyisocyanates, polysilanes and polyacetylenes, form equal populations of left-handed (*M* type) and right-handed (*P* type) helices. These helical polymers have low helix inversion barriers and therefore the *M* and *P* helices rapidly interconvert and exist as a dynamic mixture in solution.[151] Since the helical screw-sense (*M* or *P* helices) of helical scaffolds dictates molecular function, reversible interconversion between *M* and *P* helices in dynamic helical scaffolds, either via the change of solvent or other external stimuli such as light, allows modulation of molecular function.

For achiral helical scaffolds, the addition of chiral units induces a preference towards the *M* or *P* screw-sense. Suginome *et al.* have demonstrated the use of a chiral polyquinoxaline-based phosphine ligand (**4.1**), which folds into either the *M* or *P* helix depending on the choice of solvent, in the palladium catalysed asymmetric hydrosilylation of styrenes (Figure 4.1).[152]When the hydrosilylation reaction (Figure 4.1) was performed in chloroform, chiral ligand **4.1** adopted a *P* helical conformation and the reaction gave product in good yield with very high enantioselectivity (93% yield and 93% ee, Figure 4.1). When the screw-sense of **4.1** was inverted from *P* to *M* by heating at 60°C in a 2:1 mixture of 1,1,2-tetrachloroethane (TCE) and toluene for six hours, the hydrosilylation of styrene with the *M*-helical form of **4.1** in a

mixture of 1,1,2-TCE and toluene gave product in the opposite configuration with similar yield and enantioselectivity.

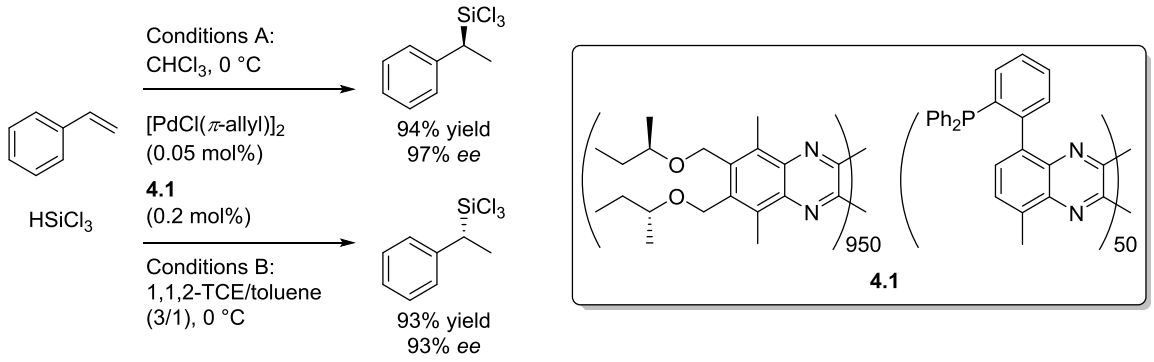

Figure 4.1: Solvent induced helical switch of a polyquinoxaline-based phosphine ligand (**4.1**), which can be used as a chiral ligand for a palladium catalysed hydrosilylation of styrene.

Clayden *et al.* have shown the use of a photoswitchable azobenzene moiety to control the helicity of a poly(aminoisobutyric acid) backbone, difluoroAiB (**4.2**, Figure 4.2), in lipid membranes.[153] The population distribution between the *M* and *P* helices was quantified by the difference in chemical shifts of the diastereotopic fluorine atoms at the C-termini in the fast exchange regime (ie. at a rate of greater than 6000 s^{-1} for this particular example[153]). When the azo unit adopted an *E* configuration, **4.2** preferentially folded into the *M* helix ((*E*,*M*)-**4.2**) with approximately 60-65% population. Upon irradiation using an LED with a wavelength of 365 nm, the azo unit isomerised from the *E* to *Z* configuration and this altered the geometry of the hydrogen bonding network along the polymer backbone, leading to a "more equal population" of *M* and *P* helices.[153] Subsequent irradiation using an LED with a wavelength of 455 nm isomerised the azo unit from the *Z* back to *E* configuration, restoring the conformational preference to the *M* helix.

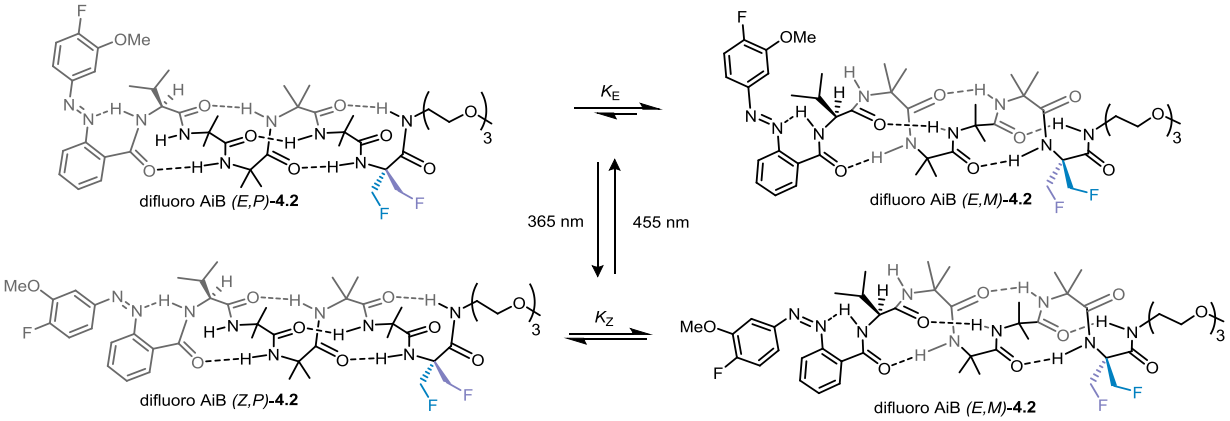

Figure 4.2: Light induced helical switch of difluoro AiB **4.2**.[153]

As discussed in the introduction (Sections 1.1, 1.3.3 and 1.5, Chapter 1), the Aggarwal group has developed the synthesis of hydrocarbons with 10 contiguous methyl substituents. The all-*syn* isomer **1.10** was shown to adopt a helical conformation. It was found that the preferred screw-sense of the all-*syn* isomer depends on the environment and the size of the end-group. In the solution state, alcohol **1.10** was found to be a right-handed (*P*) helix, whereas in the solid state the *para*-nitrobenzoate derivative of **1.10** was found to be a left-handed (*M*) helix.[8] The different helical screw-sense observed indicated the possibilities of developing a new class of helical scaffold which could reversibly switch between the *M* and *P* helical forms by chemical modification of the end groups. Although crystal packing was thought to control the helicity of the benzoate derivative of **1.10** in the solid state, the relationship between the nature of the end groups (ie. *para*-nitrobenoate and alcohol moieties) and the observed helical screw-sense was unclear in solution state.

A model which predicts the helical screw-sense based on the steric effect of the end groups was proposed by Huc *et al.*.[154] The helical screw-sense of a series of achiral quinoline-derived oligoamide foldamers with different end groups was studied using a combination of X-ray crystallography, NMR and circular dichroism spectroscopy. It was found that the introduction of a chiral end group, such as the (*R*) enantiomer of α-methylbenzylamine (Figure 4.3a) induced the oligoamide foldamer to preferentially adopt the *M* helical form with an *M* to *P* helical population ratio of 10 to 1. Examination of the X-ray crystal structures of **4.3** and other oligoamide foldamers with different end groups revealed that, for the chiral centre at the end group, the large group (aryl) pointed away from the helix, the medium group (methyl) aligned itself with the helical backbone, and the small group (H) points towards the helix. If

the chiral centre was assigned based on steric criteria (R^s, S^s) with the largest substituents having the highest priority (helix > aryl > methyl > H), rather than using the usual Cahn–Ingold–Prelog rules, it was found that oligoamide foldamers with R^s centres at the terminal group always adopted the *M* helical form, whereas the ones with S^s centres at the terminal group always adopted the *P* helical form.[154]

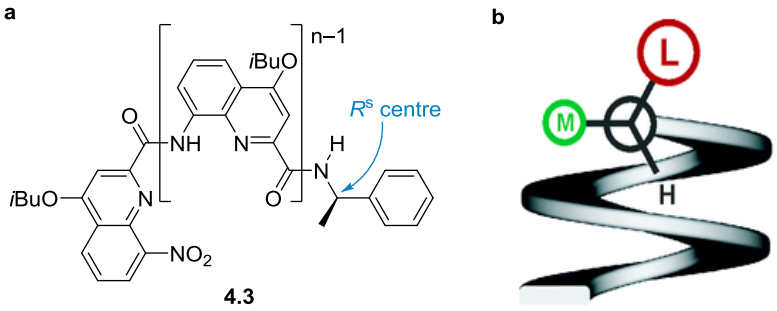

Figure 4.3: **a**, Chemical structure of quinoline derived oligoamide **4.3** with a chiral end group which has R^s configuration. **b**, Huc's model.[154]

Although the model proposed by Huc *et al.* offered insights into the relationship between the steric effect of the chiral end group and the preferred helical screw-sense of the achiral backbones of the quinoline-derived oligoamide foldamers, it could not be directly applied to the analysis of the all-*syn* isomer **1.10**, which has a chiral hydrocarbon backbone, which might dictate the inherent preference towards a particular helical screw-sense.

Therefore, a new model is required to establish the relationship between the configuration of *all*-syn methyl-substituted hydrocarbons and any inherent preference of the helical screw-sense. To validate the proposed model, such a hydrocarbon will be designed, synthesised and its preferred helical screw-sense in solution state will be studied using the QM/NMR approach. Having established the inherent preference, the relationship between the nature of the end group and the preferred helical screw-sense will be studied to enable the design and preparation of a hydrocarbon-based system with reversible switching between the *M* and *P* helical forms.

4.2 Results and Discussion

4.2.1 Theoretical model for predicting the preferred helical screw-sense.

Mr. Johan A. Pradeilles proposed that the minimisation of *gauche* interactions controlled the helicity of **4.4** (Figure 4.4a) in the solution state. In the case of both the *M* and *P* helices (Figure 4.4b), three *gauche* interactions occur between the non-hydrogen substituents for an *ap* backbone dihedral angle, whereas only two *gauche* interactions occur for both g^+ and g^- backbone dihedral angles. (Figure 4.4c) The total numbers of *gauche* interactions between non-hydrogen substituents can then be counted for both *M* and *P* helices. It was found that *M* helix **4.4**-1 has 23 *gauche* interactions whereas the *P* helix **4.4**-2 only has 22 *gauche* interactions. Therefore, the *P* helix **4.4**-2 is lower in energy, thus dominating the conformer population of **4.4** in solution.

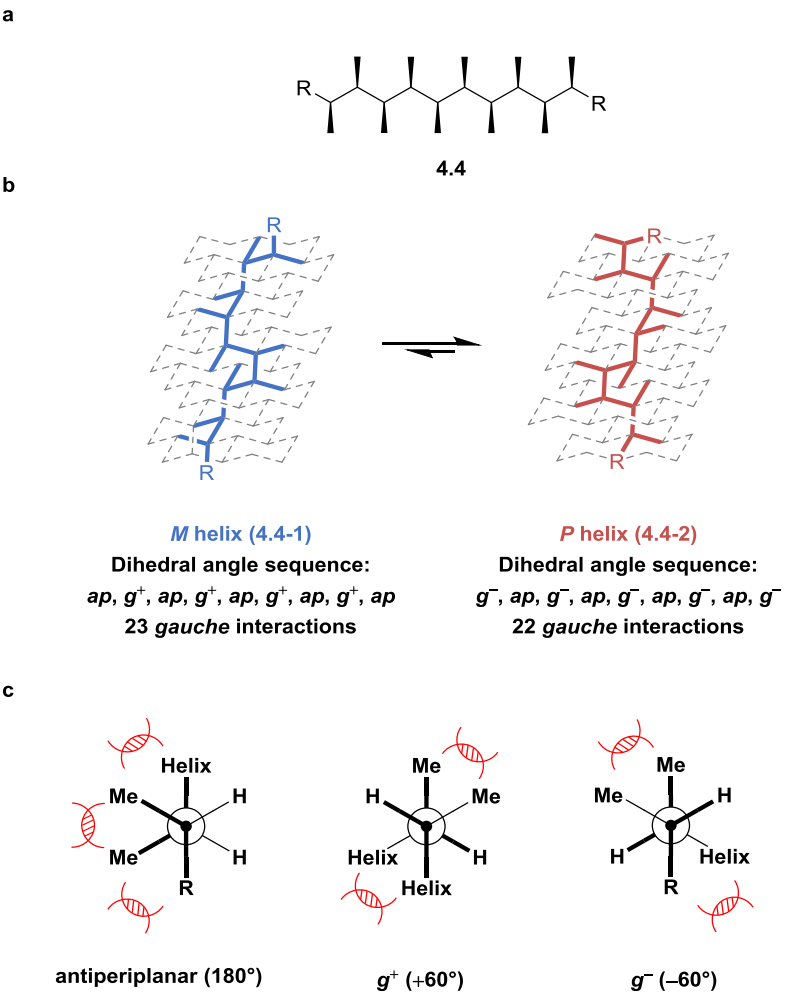

Figure 4.4: **a**, Chemical structure of **4.4**. **b**, *M* and *P* helices (**4.4**-1 and **4.4**-2, respectively) represented on a diamond lattice with the corresponding dihedral angle sequences of the backbones and the total number of *gauche* interactions between the non-hydrogen substituents. **c**, Newman projections representing the conformations of the first and second bonds (adopting *ap* and g^+ conformations

respectively) of the *M* helix together with the first bond (adopting g^- conformation) of the *P* helix. *Gauche* interactions between non-hydrogen substituents are highlighted in red.

4.2.2 QM/NMR analysis of compounds with even numbers of contiguous methyl substituents (4.5, 4.9 and 4.10)

To validate the model proposed by Mr. Johan A. Pradeilles, a *C2* symmetric compound **4.5** (Scheme 4.1) bearing alkyne moieties as small non-hydrogen end groups were designed as the model compound for the QM/NMR analysis. Synthesis of **4.5** started from a rhodium-catalysed asymmetric diboration[155] of *trans*-butene to deliver the 1,2-(bis boronic ester) **4.6** in perfect enantioselectivity. Bidirectional homologation of the 1,2-(bis boronic ester) **4.6** with the enantioenriched carbenoid (*R*)-**1.69** and then (*S*)-**1.69** generated from the corresponding stannyl compounds via tin–lithium exchange gave the homologated bis boronic ester **4.7**, which was converted to the target compound **4.5** using an alkynylation procedure developed by the Aggarwal group.[156]

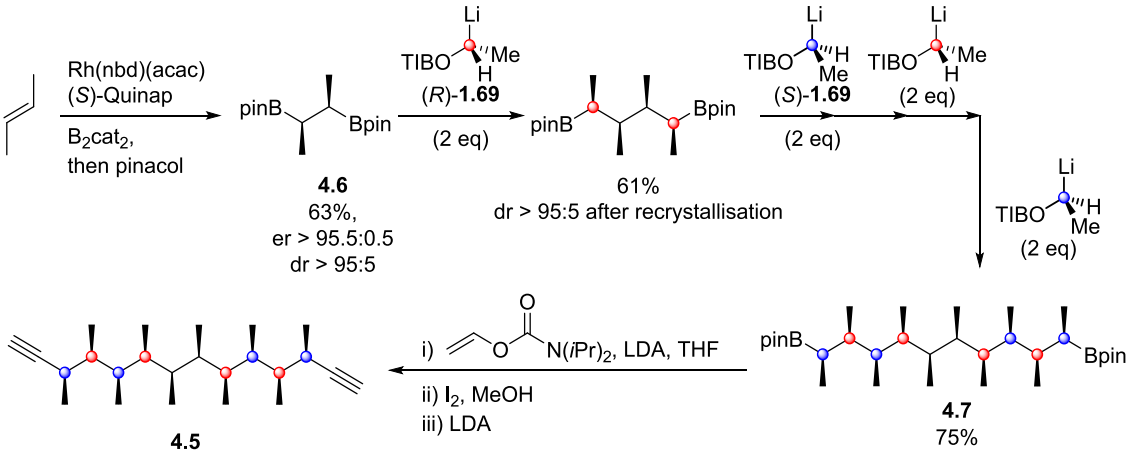

Scheme 4.1: Synthesis of target model compound **4.5**. nbd, nobornadiene; acac, acetylacetonate; cat, catacolato; pin, pinacolato; TIB, 2,4,6-triisopropylbenzoyl; LDA: lithium diisopropylamide.

4.2.2.1 Analysis of experimental ^{1}H-^{1}H scalar coupling constants.

With the compound in hand, the NMR analysis of **4.5** was investigated. The experimental measurements of $^nJ_{HH}$ values from the 1D ^{1}H NMR spectrum was straight forward for most of the protons, except the ones closest to the symmetry axis bisecting the molecule due magnetic inequivalence. For example, in **4.5** (Figure 4.5a) proton H_{11} and H_{13} are chemically equivalent and have the same chemical shifts. However, $^3J_{H11\text{-}H9}$ is different from $^4J_{H13\text{-}H9}$, thus H_{11} and H_{13} are magnetically inequivalent to each other. The H_{11}/H_{13} signal in the ^{1}H NMR spectrum appears as a complex multiplet, which is challenging to simulate

accurately using the spin simulation module implemented in MestreNova (Figure 4.5b). This is due to the high sensitivity of the line shape to the H_{11}-H_{13} coupling, as well as the $\Delta\delta$ of the magnetically inequivalent nuclei. Although *J* coupling values of symmetry related protons can be extracted from signals of rare isotope satellites (for example ^{13}C)[157], in the case of **4.5** the satellites of the H_{11}/H_{13} peak are overlapped with other signals in the spectrum, therefore the coupling constant between H_{11} and H_{13} was not extracted and the dihedral relationship between these two vicinal protons is unknown solely based on the analysis of *J* values.

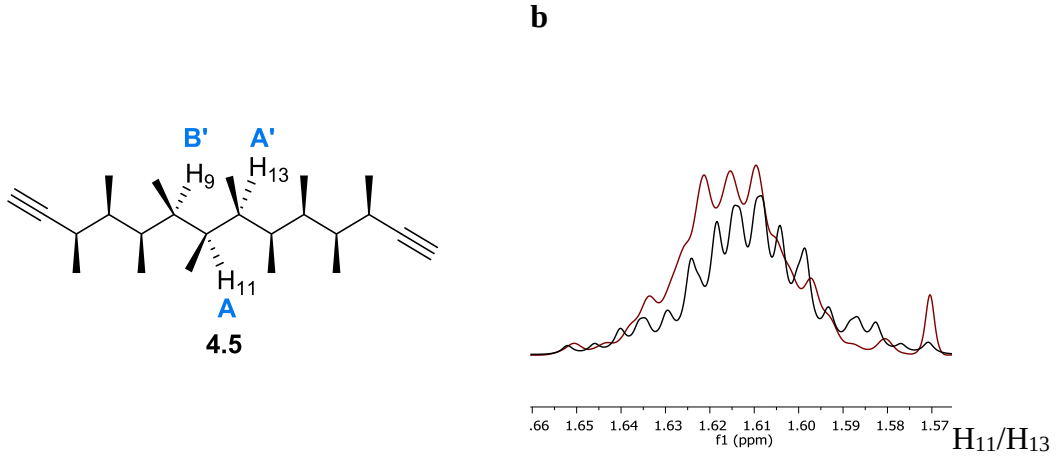

Figure 4.5: a, Structure of **4.5**, with H_{11}, H_9 and H_{13} highlighted as A, B' and A'. **b**, Experimental ^1H NMR spectrum showing the H_{11}/H_{13} multiplet in red, and the spin-simulated multiplet in black.

4.2.2.2 Analysis of the experimental ^1H-^1H NOE-distances.

Before the determination of NOE-distances using correlations obtained from 1D NOE spectra, the analysis of NOE-distances was first considered because special considerations must be taken of the symmetry-breaking NOEs in *C2* symmetric and *meso* compounds. For example, in the case of **4.5** (Figure 4.6a), the inter-subunit correlation between H_7 and H_{11} (H_A-H_B, Figure 4.6c) could not be distinguished from the intra-subunit correlation between H_7 and H_{13} (H_A-$H_{B'}$, Figure 4.6c), because both H_{11} (H_B) and H_{13} ($H_{B'}$) are chemically equivalent so both H_7-H_{11} and H_7-H_{13} correlations are observed at the same chemical shift (Figure 4.6b). Since H_7 and H_{17} are chemically equivalent, irradiation of H_7 also irradiates H_{17}. As a result, the observed NOE correlation upon irradiation of H_7 and H_{17} (H_A and $H_{A'}$) consists of the following four components: H_7-H_{11} (H_A-H_B), H_7-H_{13} (H_A-$H_{B'}$), H_{17}-H_{11} ($H_{A'}$-H_B) and H_{17}-H_{13} ($H_{A'}$-$H_{B'}$) (Figure 4.6c and d).

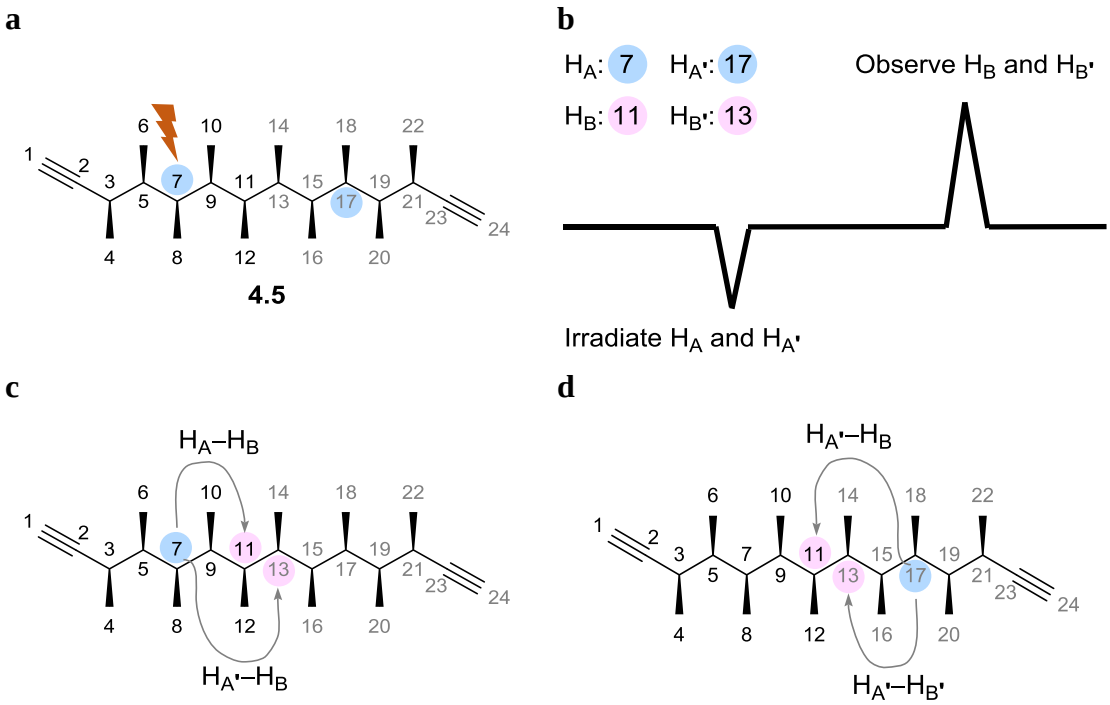

Figure 4.6: a, Chemical structure of **4.5**, with irradiated proton highlighted in blue. **b**, A schematic 1D NOE spectrum showing correlation between H_A and H_B. **c** and **d**, The four components which could contribute to the experimentally observed NOE correlation between H_A and H_B.

Appropriate treatment of the contributions arising from the four components towards an experimentally observed NOE signal is crucial for accurate conformational analysis, especially in determining the ratio between *M* and *P* helices. For example, in the case of **4.5**, the DFT computed interproton distances (discussed in more details in section 4.2.2.4.1) between H_7 and H_{11} (H_A-H_B) in both the *M* and *P* helices are around 3.3 Å (Figure 4.7). If only this distance was considered in conformational analysis, one would expect both helical conformers contribute equally to the experimentally observed NOE correlation intensity. However, the interproton distance between H_7 and H_{13} (H_A-$H_{B'}$), the latter being chemically equivalent to H_{11}, is 2.13 Å in *M* helix and 4.47 Å in *P* helix. Therefore, if *M* helix populates to some extent (>3% population), it would contribute more to the NOE correlation intensity due to the short contact (scaled by r^{-6}) between H_7 and H_{13}.

		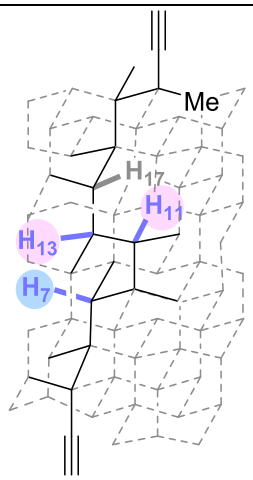 *M* helix	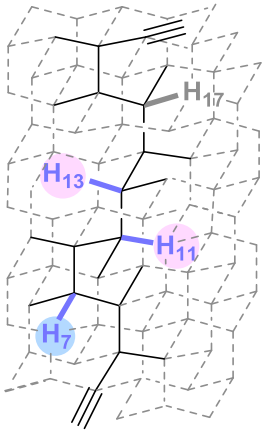 *P* helix
H	Hx	DFT computed ensemble-averaged distances/ Å	
H_7 (H_A)	H_{11} (H_B)	3.33	3.31
H_7 (H_A)	H_{13} ($H_{B'}$)	2.13	4.47

Figure 4.7: Diamond-lattice representation of both the *M* and *P* helices of **4.5**, together with the respective interproton distances between H_7-H_{11} and H_7-H_{13} computed using B3LYP-D2 6-311G(d) optimised geometries with corresponding conformer energies corrected by the mean of single point energy calculations using a larger basis set (6-311G(d,p)) and implicit toluene (IEFPCM).

Although the contribution of symmetry-breaking NOEs becomes more significant in the core of the molecule, the exact contributions of the individual components (H_A-H_B, $H_{A'}$-H_B, $H_{A'}$-$H_{B'}$, H_A-$H_{B'}$) towards a given observable correlation is unknown apriori, and thus requires some knowledge of the conformational landscape of the molecule. Therefore, the experimentally observed NOE correlations, which consist of some combinations of all four individual components outlined above, were converted into 'effective' distances[158] for quantitative comparison without averaging using equation 1.3 (Chapter 1, section 1.2.3). The reference distance (r_{ref}) was chosen to be the distance between H_3 and H_4, which is insensitive to change in molecular conformation.

The experimental NOE signal intensities (η_{NOE}) were derived from either 1D DPFGSE NOESY or CSSF-NOESY spectra. Values of PANIC corrections (discussed in Chapter 1, section 1.2.3) were chosen to account for the difference in the observed NOE intensities between a proton (for example, a CH group) and a methyl group when either the proton or the methyl group were irradiated. If a proton was irradiated and a correlation between this proton and a near-by methyl group was observed (CH→CH_3), the three equivalent protons of the methyl group would all contribute to the observed NOE signal intensity. On the other hand, if

the same methyl group was irradiated and the above-mentioned correlation between this methyl group and the proton was observed (CH_3→CH), the observed NOE signal intensity in this case would only arise from a single proton. Therefore, if the PANIC integration for both the proton (CH group) and the methyl group were set arbitrarily to the same value (e.g. 1000 for both), the resultant integrations for the same CH-methyl correlation would have different values, with the CH→CH_3 correlation being three times stronger than the CH_3→CH. The integration of the CH→CH_3 correlation could be divided by three to match that of the CH_3→CH correlation in order to weight average the three distances between the CH to each of the equivalent proton of the methyl group.[8,159]. To reduce confusion during the Boltzmann weighted averaging process in this study, rather than divide the resultant NOE correlation intensity by the number of equivalent spins which give rise to the signal, the PANIC integration was adjusted accordingly based on the total number of protons being irradiated in a NOE experiment.

When two protons were irradiated, such as the equivalent CHs in **4.5**, the PANIC integration of the irradiated peak was arbitrarily set to 2000. When six protons were irradiated, such as the equivalent methyl groups in **4.5**, the PANIC integration of the irradiated peak was arbitrarily set to 6000. (Table 4.1)

Table 4.1: A summary of PANIC integration values used in the study of *C2* symmetric compound **4.5**. Protons being irradiated are highlighted in blue.

Protons being irradiated	Number of protons being irradiated	PANIC integration values of irradiated peaks
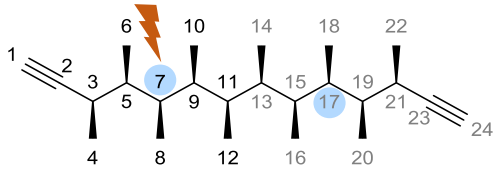 **4.5**	2	2000
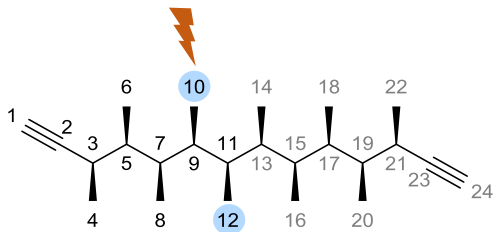 **4.5**	6	6000

4.2.2.3 Computational modelling of 4.5 - generation of mirror image conformations for *C2* symmetric molecules

A Monte Carlo MM conformational search of **4.5** was performed using the MMFFs forcefield with $CHCl_3$ as implicit solvent and found 45 conformers. All conformers found were subjected to DFT geometry optimization and free energy calculations using a combination of different exchange and correlation functionals and basis sets (discussed later in section 4.2.2.4.1).

Due to the symmetry of **4.5**, the computed distances for pairs of equivalent protons should be the same. For example, the distance between H_7 and H_{11} ($r_{HA\text{-}HB}$) should be the same as the distance between H_{17} and H_{13} ($r_{HA'\text{-}HB'}$). However, these two distances ($r_{H7\text{-}H11}$ = 2.99 Å and $r_{H17\text{-}H13}$ = 3.02 Å, Table 4.2) were initially found to be different after Boltzmann averaging regardless of which DFT calculation methods were used. Further examination of the distances of other equivalent pairs of protons revealed that indeed distances of equivalent pairs of protons were computed to be different ($r_{HA\text{-}HB} \neq r_{HA'\text{-}HB'}$).

Table 4.2: Structure of **4.5** and the computed ensemble-averaged distances of selected pairs of equivalent protons prior to the generation of degenerate conformations. The computed distances listed were obtained using B3LYP-D2/6-311G(d) geometries with conformer energies corrected by single point energy calculations using B3LYP-D2/6-311G(d,p) functional and implicit toluene (IEFPCM).

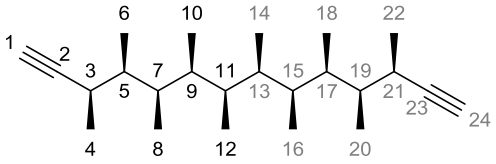

4.5

HA	HB	$r_{HA\text{-}HB}$ / Å	HA'	HB'	$r_{HA'\text{-}HB'}$ / Å
H3	H5	2.76	H21	H19	2.82
H3	H7	3.07	H21	H17	3.03
H3	H9	2.63	H21	H15	2.69
H5	H7	2.55	H19	H17	2.54
H5	H9	2.97	H19	H15	3.01
H5	H11	2.11	H19	H13	2.10
H7	H9	2.80	H17	H15	2.82
H7	H11	2.99	H17	H13	3.02

Although the differences between $r_{HA\text{-}HB}$ and $r_{HA'\text{-}HB'}$ are small (within 0.06 Å), this difference suggests that certain conformations might not have been captured in the initial MM conformational search. Although the option of retaining mirror image conformers had been

enabled in the initial conformational search, it was unclear whether the mirror image conformers would actually be kept separately for *C2* symmetric molecules, since both degenerate conformers would be superimposable and therefore could be treated as the same.

To probe whether all conformations were captured for *C2* symmetric molecules, conformational analysis of a truncated version of **4.5** (**4.8**, Table 4.3), which was desymmetrised *in silico* by the addition of a methyl group at one of the terminal alkynes, was performed using a MM conformational search under identical conditions (MMFFs force field, implicit $CHCl_3$ as solvent, TNCG, MCMM, 500,000 iterations). If both conformational searches give the same results in terms of numbers of conformations found, this would confirm that mirror image conformers were being retained during conformational search of **4.9**. On the other hand, if the conformational search of **4.8** gave more conformers than **4.9**, then the initial conformational search of **4.9** did not capture the entire conformational space of the molecule and might have eliminated degenerate mirror image conformations.

Table 4.3: Structure of **4.8** and **4.9**, with the number of conformers and clusters found by MM conformational search.

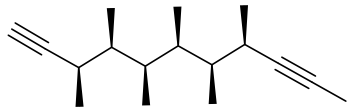

4.8

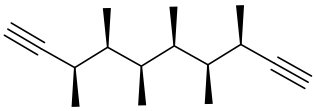

4.9

Compounds	Total number of conformers	Total number of clusters
4.8	47	46
4.9	29	28

In the event, the conformational search of **4.8** found more unique conformations, which was reflected by nearly double the numbers of dihedral clusters, which was grouped by dihedral angle of the backbone as discussed previously (Figure 2.12, Chapter 2). To investigate which conformations of **4.9** were 'missing', the dihedral angle sequence of all clusters found in the conformational search of **4.8** were compared to those found in the conformational search of **4.9**.

It then became apparent that the 'missing' conformations were, indeed, the mirror image conformers. For example, conformers with a backbone dihedral angle sequence of *ap*, g^+, *ap*, *+ac*, g^+ were found in both conformational searches (eg. conformer **4.8**-6, Figure 4.8a).

However, the mirror image conformer with the backbone dihedral angle sequence of g^+, *+ac*, *ap*, g^+, *ap* was only found in the conformational search of **4.8** (conformer **4.8**-9, Figure 4.8b). Although the backbone of conformers 6 and 9 could be superimposed in a 'head-to-tail' fashion (RMSD value of superimposition of backbone atoms < 0.02 Å, Figure 4.8c), they are not the same due to the presence of the terminal methyl group. Therefore, both conformers were treated as different conformers and stored separately in the conformational search output for **4.8**. In the case of **4.9**, when the terminal methyl group is absent the whole skeleton of both conformers would be superimposable and therefore even if both conformers were found, one would be eliminated as a redundant conformer and therefore not stored in the conformational search output result.

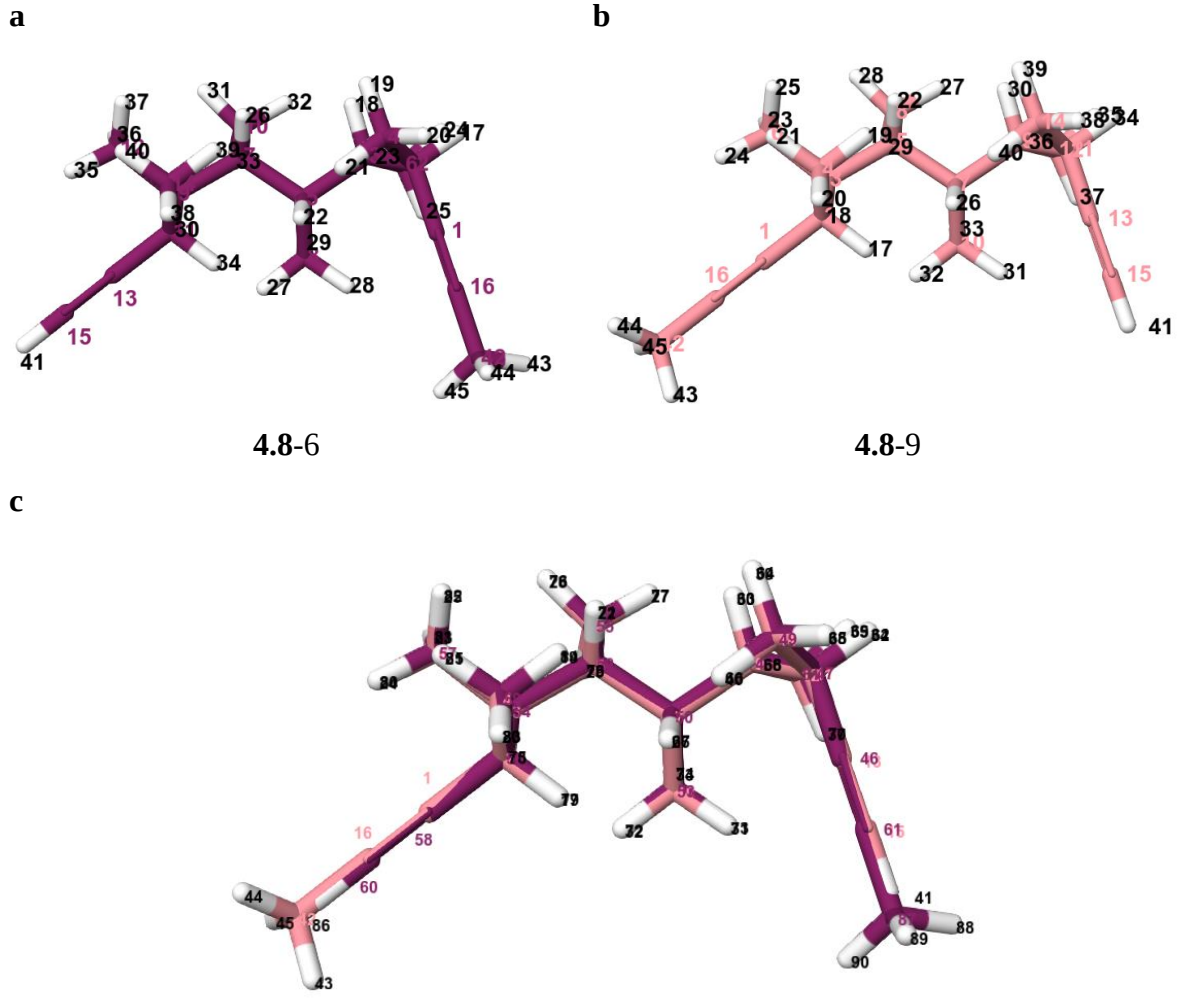

Figure 4.8: Representative output conformers of the conformational search of **4.8**. **a**, 3D structure of conformer **4.8**-6 with computational atom labels. **b**, 3D structure of conformer **4.8**-9 with computational atom labels. **c**, Overlap of conformers **4.8**-6 and **4.8**-9 in a 'head-to-tail' fashion.

The fact that two degenerate conformers could be overlaid in a 'head to tail' fashion suggests that the easiest way to generate the corresponding mirror image conformers would be to copy the geometry and swap the symmetry-equivalent atom labels. This was achieved by swapping the xyz coordinates of equivalent nuclei for all conformers using a python script written by Mr. William Gerrard.

The generation of the 'missing' 45 mirror image conformers for **4.5** was performed and the ensemble-averaged interproton distances were recomputed after the inclusion of degenerate conformations. As table 4.4 shows, the distances between selected equivalent pairs of protons are now the same. In addition, there was a slight improvement in the fit to the experimentally derived ^{1}H-^{1}H distances, reflecting the decreased values of MAD and StDev.

Table 4.4: Structure of **4.5** and the computed ensemble-averaged distances of selected pairs of equivalent protons after the generation of degenerate conformations. The computed distances listed were obtained using B3LYP-D2/6-311G(d) geometries with conformer energies corrected by single point energy calculations using B3LYP-D2/6-311G(d,p) functional and implicit toluene (IEFPCM).

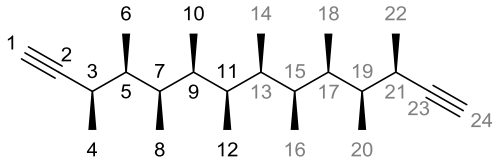

4.5

HA	HB	Computed Distances/ Å	HA'	HB'	Computed Distances/ Å
H3	H5	2.79	H21	H19	2.79
H3	H7	3.05	H21	H17	3.05
H3	H9	2.66	H21	H15	2.66
H5	H7	2.55	H19	H17	2.55
H5	H9	2.99	H19	H15	2.99
H5	H11	2.11	H19	H13	2.11
H7	H9	2.81	H17	H15	2.81
H7	H11	3.00	H17	H13	3.00

Comparison of the computed to the experimentally determined distances:			
	MAD	StDev	χ^2 (reduced)
Without degenerate conformations	4.10%	4.97%	2.04
With degenerate conformations	3.84%	4.92%	1.97

MAD: mean averaged deviation, StDev: standard deviation

4.2.2.4 QM/NMR analysis of 4.5.

4.2.2.4.1 Comparison of computed ensemble-averaged ^{1}H-^{1}H distances to the experimentally determined NOE-distances: effect of MM and DFT calculations on conformer geometries and energies.

MM calculations suggested that **4.5** preferentially adopts helical conformations (89.9% population) and both the *M* and *P* helices were found to be similar in energy (ΔE = 1.0 kJ mol^{-1}), thus have very similar conformer populations (Figure 4.9). The MM prediction contradicted with the expected helicity of **4.5** (ie. *P* helix) based on the minimisation of *gauche* interactions (section 4.2.1).

However, the conformer energies were found to change substantially going from MM to DFT. For example, DFT geometry optimisation and frequency calculations using B3LYP-D2 6-311G(d) level of theory predicted that **4.5** still preferentially adopts helical conformations (78.4% population) but with the *P* helix being the global minimum (68.3% population), and the energy difference between the *M* and *P* helices (with the same pitch) was calculated to be 4.3 kJ mol^{-1} (Figure 4.9). Unlike the MM prediction, the DFT prediction agreed with the expected helicity of **4.5** (*P* helix).

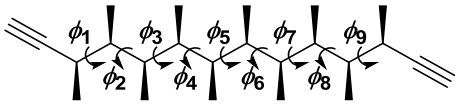

4.5

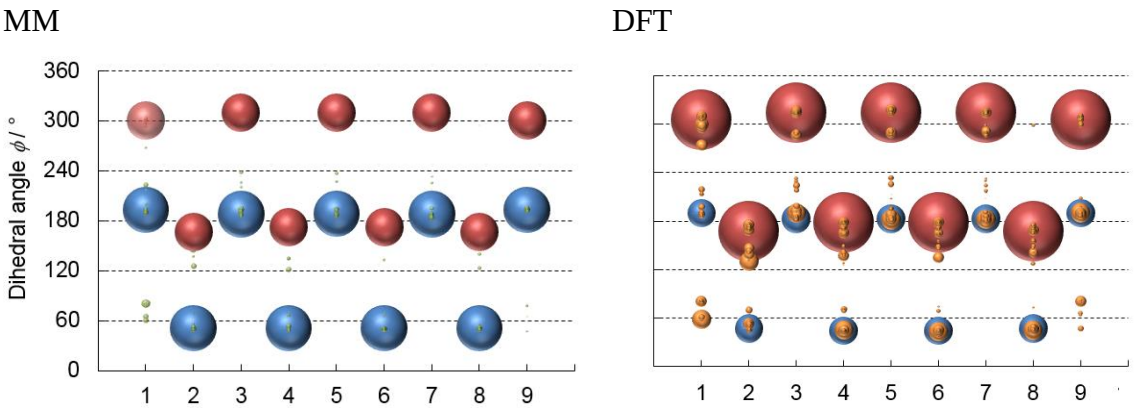

Figure 4.9: Chemical structure of **4.5** with the conformer population predicted by MM and DFT calculations represented by bubble plots. Red dots represent *P* helix while blue dots represent *M* helix.

To determine which predicted conformer population best describes the experimentally observed conformational behavior of **4.5**, the ensemble-averaged ^{1}H-^{1}H distances computed using MM geometries and energies were compared to the experimentally determined NOE-

distances. The goodness of fit was evaluated using χ^2 (reduced) values, where an acceptable model will have a value approaching 1. An expected standard deviation of 3.5% was chosen for the calculations of the χ^2 (reduced) values for **4.5**.[54] It was found that the MM predicted ensemble-averaged ^{1}H-^{1}H distances provided very poor fit to the experimental data with a χ^2 (reduced) value of 11.57. Therefore, care must be taken when using the MM calculated conformer energies to predict the conformational landscape of molecules.

The ensemble-averaged distances of **4.5** was also calculated using different DFT methods (Table 4.5). Compared to the MM calculated distances, all DFT-predicted distances provided better fit to the experimentally derived distances with χ^2 (reduced) values less than 6. In particularly, distances calculated using B3LYP-D2 6-311G(d) level of theory in gas phase provided a good fit to the experimentally derived distances with a χ^2 (reduced) value of 1.88. Therefore, on the basis of quantitative ^{1}H-^{1}H distance analysis, *P* helix is the major conformation of **4.5**.

The effect of different DFT calculation methods on conformer geometries and free energies was also investigated. Three different exchange and correlation functionals (mPW1PW91, B3LYP and M06-2X) and empirical dispersion correction (D2) in conjunction with the B3LYP functional were explored for geometry optimisation and frequency calculations. Selected combination of the four functionals with five different double- and triple-ζ basis sets (6-31G(d), 6-311G(d), 6-311+G(d), 6-311G(d,p), 6-311+G(d,p)) gave rise to 11 different sets of DFT methods. The ensemble-averaged ^{1}H-^{1}H distances predicted by these 11 sets of calculations were compared to the experimentally derived NOE-distances. The goodness of fit of the comparison was again evaluated using χ^2 (reduced) values, which were summarised in table 4.5.

The effect of basis set was first considered with the use of mPW1PW91 functional, which was the functional of use for NMR parameter calculations (entry 2 – 5, Table 4.5). The ensemble-averaged ^{1}H-^{1}H distances computed using the triple-ζ basis set (6-311G(d), χ^2(reduced) = 3.20, entry 3) gave better fit to that using the double-ζ basis set (6-31G(d), χ^2(reduced) = 5.08, entry 2), with an improvement of 1.88 in the χ^2 (reduced) value. The addition of polarisation function to the triple-ζ basis set was investigated and the ensemble-averaged ^{1}H-^{1}H distances gave worse fit (6-311G(d,p), χ^2(reduced) = 4.41, entry 4). Manual inspection of the optimised geometry with and without the use of polarisation function suggested that geometry optimisation with polarisation function seemed to change the

conformer geometries imperceptibly in most conformers (RMSD < 0.1 Å). Therefore, the erosion of fit ($\Delta\chi^2$(reduced) between entry 3 and 4 =−1.21) was presumably due to the change in conformer energies, which is within chemical accuracy (~ 4 kJ mol^{-1}) for all major conformer (ΔG < 10 mol^{-1}). Therefore, the inclusion of polarisation to the triple- ζ basis set, which required approximately 1.2 times more CPU time, is probably unnecessary for geometry optimisation and frequency calculations and the effect of polarisation function on conformer energies could be estimated using the less resource intensive single point energy calculations.

Table 4.5: Comparison between the computed ensemble-averaged ^{1}H-^{1}H distances of **4.5** and the experimentally derived NOE-distances.

Entry	**Force field**		**Solvation**	**χ^2 (reduced) NOE**
1	MMFFs		Chloroform	11.57
Entry	**DFT Functional**	**Basis set**	**Solvation**	**χ^2 (reduced) NOE**
2	mPW1PW91	6-31 G(d)	Gas	5.08
3		6-311 G(d)	Gas	3.20
4		6-311 G(d,p)	Gas	4.41
5		6-311+ G(d,p)	Gas	3.47
6	B3LYP	6-31 G(d)	Gas	NA
7		6-311 G(d)	Gas	5.12
8		6-311 G(d)	Toluene	5.22
9	M06-2X	6-31 G(d) finegrid	Gas	4.13
10		6-311 G(d) finegrid	Gas	3.81
11	B3LYP-D2	6-31 G(d)	Gas	2.08
12		6-311 G(d)	Gas	1.88

The inclusion of diffuse functions (6-311+G(d,p), χ^2(reduced) = 3.47, entry 5) substantially improves the fit of the computed distances to the experimentally determined NOE-distances ($\Delta\chi^2$(reduced) between entry 4 and 5 = 0.94). Although the use of the triple-ζ basis set with diffuse function and polarisation function (6-311+G(d,p), entry 5) provided a better fit, the inclusion of diffuse function requires approximately 3.5 times more CPU time. In addition, the goodness of fit is similar to that without the inclusion of polarisation and diffuse function (6-311+G(d), χ^2(reduced) = 3.20, entry 3) and it still deviated from the ideal fit.

Therefore, the addition of diffuse function to the triple-ζ basis set for geometry optimisation and frequency calculations seems to be uneconomical.

The effect of basis sets was also briefly explored using the other functionals (M06-2X and B3LYP-D2) and it was found that the ensemble-averaged ^{1}H-^{1}H distances computed using the triple-ζ basis set (6-311G(d), entry 10 and 12) gave a slightly better fit than that using the double-ζ basis set (6-31G(d), entry 9 and 11). Unfortunately, the same comparison could not be performed with the use of B3LYP functional because the geometry optimisation calculation for a major conformer did not converge to a stationary point when the double-ζ basis set was used. Manual inspection of the optimised conformer geometries with the use of double- and triple- ζ basis set suggested that the use of a bigger basis set sometimes gave slightly different conformer geometries (RMSD < 1.0 Å). Therefore, the improvement of fit when triple-ζ basis set was probably due to the better predicted conformer geometries and energies. Although the change is small and the use of triple-ζ basis set requires approximately 3 times more CPU time, the use of the larger triple- ζ basis set would be beneficial for geometry optimisation and frequency calculations.

The effect of inclusion of a dielectric continuum corresponding to toluene was also investigated with B3LYP functional and 6-311 G(d) basis set (entry 8). It was found that the inclusion of implicit toluene (with the deuterated version being the choice of solvent for NMR experiments) have minimal effect on the fit between the computed and experimental ^{1}H-^{1}H distances ($\Delta\chi^2$(reduced) between entry 7 and 8 = 0.1). Therefore, the inclusion of implicit toluene in geometry optimisation and frequency calculations are unnecessary and the effect of solvation on conformer energies, if there was any, could be included using the less resource intensive single point energy calculations

Finally, the effect of dispersion correction was considered (entry 9 – 12). Two different types of dispersion corrections were investigated: one which is parameterised to account for some dispersion (M06-2X) and the other one with empirical dispersion corrections (D2) to the existing B3LYP functional. The computed ensemble-averaged ^{1}H-^{1}H distances using conformer geometries and energies computed by M06-2X functional also provided unreasonable fit to the experimentally determined NOE-distances (χ^2(reduced) = 4.13 and 3.18 for double- and triple-ζ basis sets respectively, entry 9 and 10). In addition, the keyword "finegrid" was required for smoother convergence of conformer geometries to a stationary point (ie. imaginary frequency = 0). In contrast, the computed ensemble-averaged ^{1}H-^{1}H

distances using conformer geometries and energies computed using empirical dispersion correction (D2) in conjunction with B3LYP functional provided by far the best fit to the experimentally determined NOE-distances (χ^2(reduced) = 2.08 and 1.88 for double- and triple-ζ basis sets respectively, entry 9 and 10). The inclusion of D2 empirical dispersion correction had very little impact on the computational resource required and was found to affect both the optimised conformer geometries and the subsequently calculated free energies. Therefore, it is crucial to include dispersion correction in geometry and frequency calculations.

Balancing accuracy and computational economy for DFT calculations, the optimal method for geometry optimisation and frequency calculations was considered to be the B3LYP-D2 6-311(G) level of theory (entry 12). The computed ensemble-averaged ^{1}H-^{1}H distances using this method provided a good fit to the experimentally determined NOE-distances with reasonable time cost (~34 hours CPU time per calculations). The effect of a larger basis set (6-311G(d,p)) and implicit toluene (IEFPCM) on conformer energy was included by single point energy calculations and the fit of the computed ^{1}H-^{1}H distances to the experimental data was found to be very similar (χ^2(reduced) = 1.97).

4.2.2.4.2 Comparison between calculated and experimental $^nJ_{HH}$.

Having established the optimal DFT methods for calculating conformer geometries and energies, the scalar coupling constants of major conformers which were predicted to make up 90% of the conformer population were subjected to DFT calculations using mPW1PW91 6-311G(d,p) level of theory with implicit toluene (IEFPCM) to predict the ensemble-averaged scalar coupling constants. The DFT computed scalar coupling constants of equivalent pairs of protons were averaged with each other prior to Boltzmann averaging across all conformations. The long-range scalar coupling constants between H_1 and H_3 ($^4J_{H1\text{-}H3}$, see Figure 4.10a for atom labels) was not included in the analysis because this coupling constant does not provide insights into the conformational behaviour of **4.5**. In addition, the computed ensemble-averaged $^4J_{H1\text{-}H3}$ (4.18 Hz) was found to deviate substantially from the experimentally measured values (2.38 Hz), presumably due to the poor description of the alkyne sp orbital even when keyword "mixed" was used in the NMR parameter calculations to incorporate explicit mixing of core orbitals in the calculation of the fermi contact term.[160]

The computed NMR parameters are in good agreement with the experimentally measured values (^{1}H-^{1}H scalar coupling: MAD = 0.6 Hz, StDev = 0.7 Hz; χ^2(reduced) = 0.44. NOE distances: MAD = 3.8%, StDev = 4.9%, χ^2(reduced) = 1.97, Figure 4.10b) and the

goodness of fit is in line with those observed for conformational analysis of compounds with similar structural complexity.[8] Therefore, the dominant conformation of **4.5** in solution is the *P* helix (Figure 4.10c) as predicted (section 4.2.1). It was found that **4.5** also exists as a *P* helix in the solid state by X-ray crystallography (Figure 4.10d).

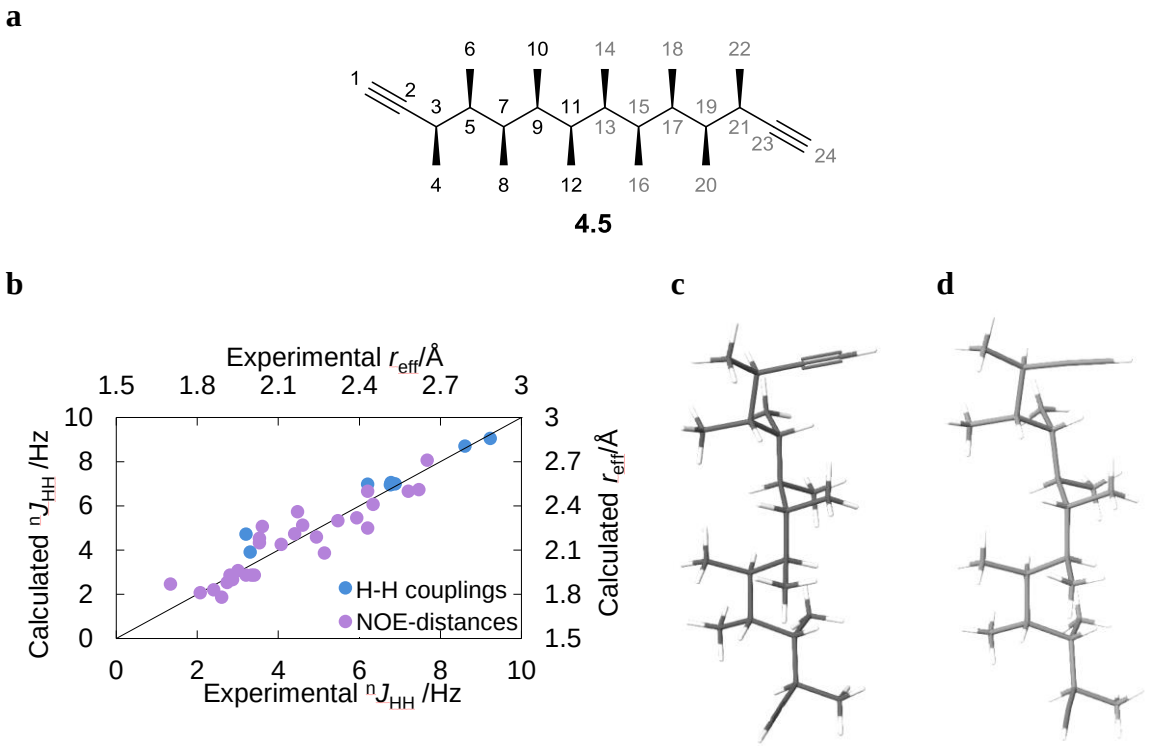

Figure 4.10: **a**, Chemical structure of **4.5** with assignment labels. **b**, Comparison of the DFT computed ensemble-averaged ^{1}H-^{1}H scalar coupling constants and ^{1}H-^{1}H distances to the experimentally determined values. **c**, DFT-predicted lowest energy conformer (a *P* helix) of **4.5**. **d**, X-ray crystal structure of **4.5**.

4.2.2.5 Achieving helical switch by bidirectional chain extension (QM/NMR analysis of 4.9and 4.10).

Next, the conformational behaviour of the synthetic intermediates in the bidirectional homologation of **4.6** was also considered. If the minimisation of *gauche* interactions dictates the helical screw-sense of an all-*syn* methyl substituted hydrocarbon, the intermediates **4.9** and **4.10** with different chain lengths (Figure 4.11) would preferentially fold into different helical conformers.

At the start of the sequence, **4.9** folds into a *P* helix with backbone dihedral angles of g^-, *ap*, g^-, *ap*, g^-, which has one less *gauche* interaction than the *M* helix (*ap*, g^+, *ap*, g^+, *ap*). If **4.10** were to adopt the same helicity as **4.9**, it would have backbone dihedral angles of *ap*, g^-, *ap*, g^-, *ap*, g^-, *ap* which give rise to 18 *gauche* interactions. To minimize the number of *gauche* interactions **4.10** would therefore undergo a conformational switch from the *P* helix to the *M* helix, which has backbone dihedral angles of g^+, *ap*, g^+, *ap*, g^+, *ap*, g^+ giving rise to 17 *gauche* interactions. Consequently, the homologated products were expected to switch from *P* (**4.9**) to *M* (**4.10**) then back to *P* (**4.5**). One could view this as switching in helical screw-sense via bidirectional chain growth of the bis boronic ester **4.6**.

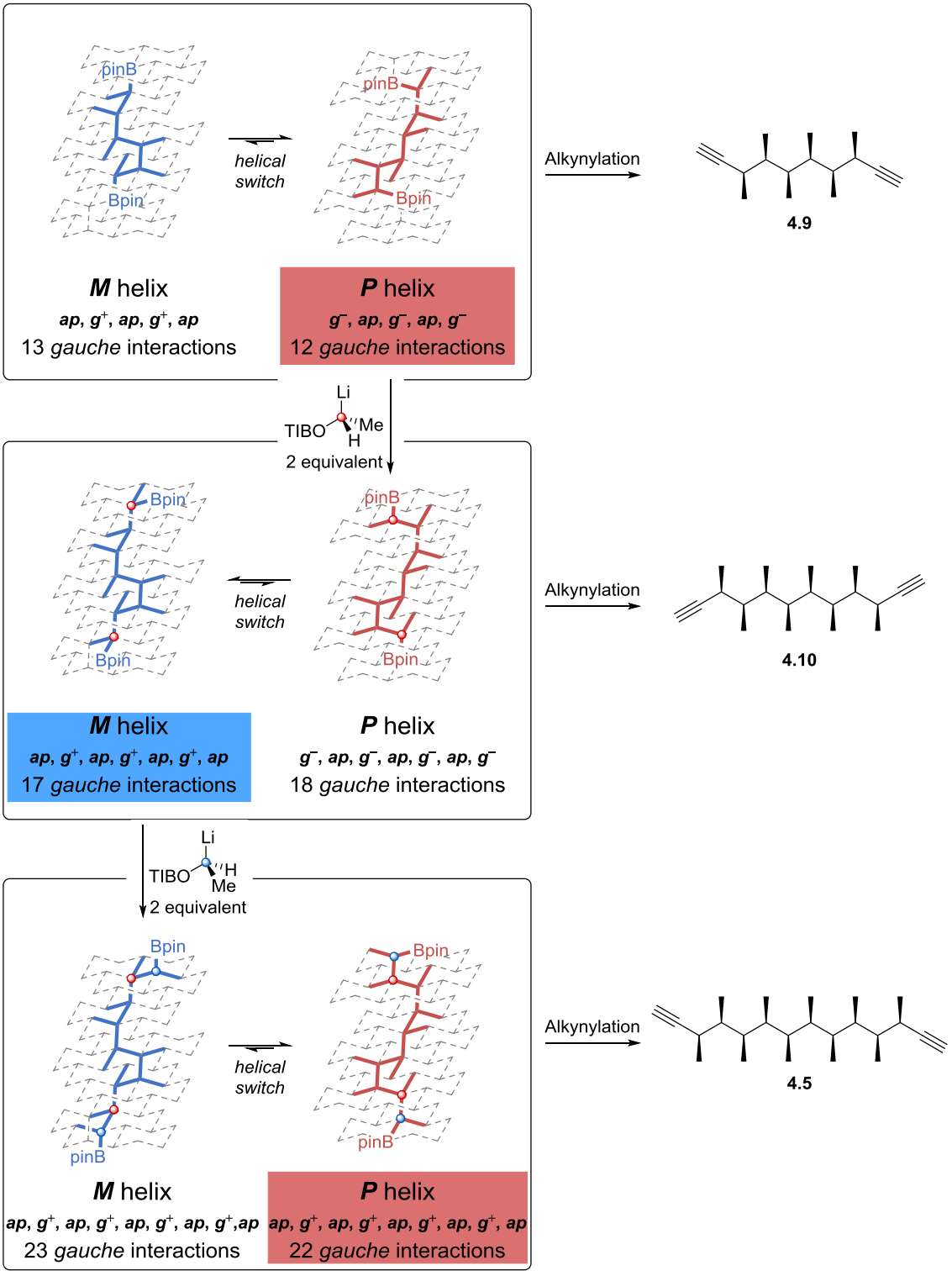

Figure 4.11: Key intermediates in the bidirectional iterative homologation of boronic ester **4.6**.

Therefore, **4.9** and **4.10** were synthesised and computation was performed using a Monte Carlo MM conformational search followed by the generation of mirror image conformers as described previously (section 4.2.2.3). Subsequent DFT calculations were performed using the same methods as described previously (B3LYP-D2 6-311G(d) with single

point energy calculations with a bigger basis set (6-311G(d,p)) and solvation (toluene, IEFPCM), section 4.2.2.4.1). It was found that both compounds have a strong conformational preference towards helical conformations (86% and 71% of the population adopting helical conformation for **4.9** and **4.10** respectively). The slight increase in helical population of **4.9** (86% vs ~70% observed for both **4.10** and **4.5**) could be the result of the decreasing entropic cost for adopting defined conformations associated with reducing the number of freely rotatable bonds. As predicted, the major conformers are the *P* helix for **4.9** and the *M* helix for **4.10**. The computed energy difference between *M* and *P* helices for both **4.9** and **4.10** respectively were about 1 kcal mol^{-1}, which is similar to that observed for **4.5**.

Comparing the computed Boltzmann averaged NMR parameters to the experimentally measured values gave good agreement for both **4.9** and **4.10** (Figure 4.12c and f, respectively. See figure title for MAD, StDev and χ^2(reduced) values), confirming the dominant conformations of each compound in solution, as well as the change in screw sense when **4.9** was extended bidirectionally by two carbon units.

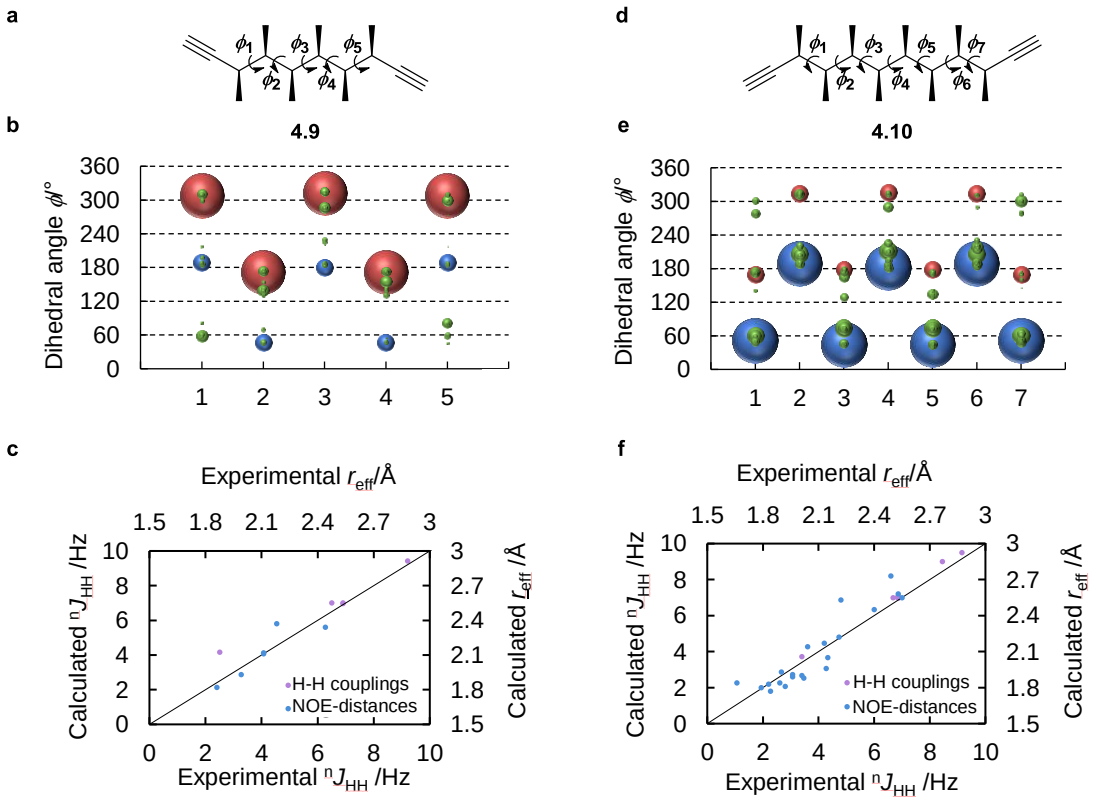

Figure 4.12: Chemical structures of (**a**) **4.9** and (**d**) **4.10**. DFT calculated conformer population of (**b**) **4.9** and (**e**) **4.10** represented by bubble plots. Red dots represent the *P* helix while blue dots represent the *M* helix. Comparison between DFT calculated ensemble-averaged ^{1}H-^{1}H scalar coupling constants and ^{1}H-^{1}H distances of (**c**) **4.9** and (**f**) **4.10**. Comparison for **4.9**: ^{1}H-^{1}H scalar coupling: MAD = 0.5 Hz,

StDev = 0.7 Hz; χ^2(reduced) = 0.8. NOE distances: MAD = 2.9%, StDev = 1.8%, χ^2(reduced) = 1.64. Comparison for **4.10**: ^{1}H-^{1}H scalar coupling: MAD = 0.1 Hz, StDev = 0.1 Hz; χ^2(reduced) = 0.02. NOE distances: MAD = 4.3%, StDev = 5.4%, χ^2(reduced) = 2.6.

In Summary, a theoretical model based on the minimisation of *gauche* interactions was proposed to rationalise the preferred helicity of **4.5** in solution-state. QM/NMR analysis of **4.5** showed that indeed the *P* helix, which has one less *gauche* interaction than the *M* helix, was observed as predicted by the theoretical model.

By exploiting the idea of minimising *gauche* interactions, switching between *P* and *M* helices was achieved going from **4.9** to **4.10** then to **4.5**. QM/NMR analysis of **4.9** and **4.10** showed that indeed the *P* helix was observed for **4.9** whereas the *M* helix was observed for **4.10**.

4.2.3 QM/NMR analysis of compounds with odd numbers of contiguous methyl substituents (compounds 4.11, 4.12 and 4.13).

4.2.3.1 QM/NMR analysis of 4.11.

In section 4.2.2, QM/NMR analysis showed that compounds with even numbers of contiguous methyl substituents (**4.9**, **4.10** and **4.5**) all adopt helical conformations with conformer population greater than 70%. Next, the conformational behaviour of compounds with odd numbers of contiguous methyl substituents, such as **4.11** (Figure 4.13a), was considered.

Since **4.11** is a *meso* compound, it was expected that both *M* and *P* helices would have the same numbers of *gauche* interactions (Figure 4.13b). Therefore, they are energetically degenerate and should be present in a 1:1 ratio.

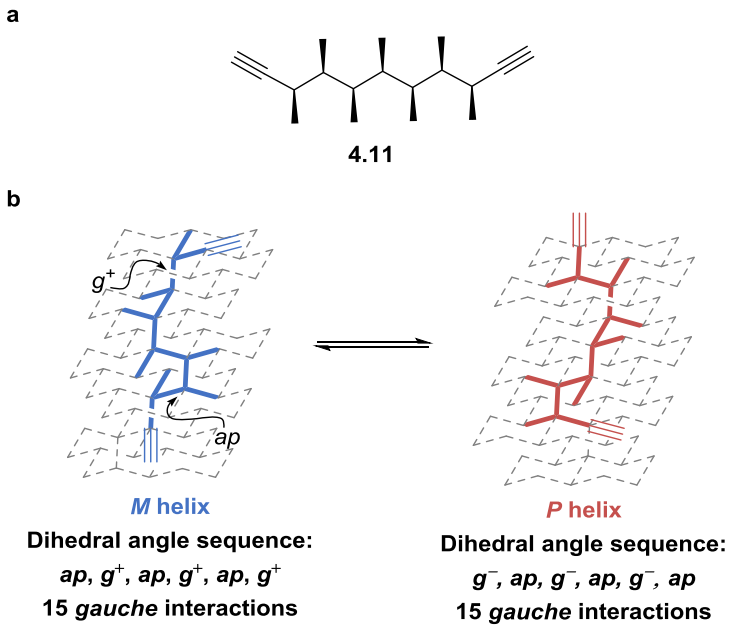

Figure 4.13: **a**, Chemical structure of **4.11**. **b**, *M* and *P* helical conformations of **4.11** represented on diamond lattices.

Unlike **4.9**, **4.10** and **4.5**, in which the preferred helical conformations have both alkyne end groups adopting *gauche* conformations with respect to the helix (Figure 4.11), both the *M* and *P* helices of **4.11** have one of the alkyne end groups adopting a *gauche* conformation with respect to the helix, while the other alkyne end group adopting an antiperiplanar conformation with respect to the helix. Since the antiperiplanar conformation has one extra *gauche* interaction compared to each of the *gauche* conformations (Figure 4.4b), to minimise *gauche* interactions both alkyne end groups of **4.11** would preferentially adopt the energetically more

favourable *gauche* conformations with the expense of breaking the helicity of the molecule. If the minimisation of *gauche* interactions indeed reduces the energy difference between the helical and non-helical conformers, one would expect to observe higher population of non-helical conformers for **4.11** compared to **4.5**, **4.9** and **4.10**. (14–30%)

To establish whether there is a break in helicity, conformational analysis of **4.11** using a Monte Carlo MM conformational search and DFT calculations was performed with procedures described previously (section 4.2.2.5). The ensemble-averaged scalar coupling constants of **4.11** were computed using DFT methods described previously (section 4.2.2.4.2). It was predicted that for **4.11**, 63% of the conformers adopt helical conformations and the ratio between M and P helices is 1:1. The DFT computed ensemble-averaged ^{1}H-^{1}H coupling constants gave good fit to the experimentally observed values (both MAD and StDev < 0.25 Hz, χ^2 (reduced) = 0.08).

However, the ensemble-averaged ^{1}H-^{1}H coupling constants based on a 1:1 mixture of *M* and *P* helices with no non-helical conformations also gave good fit to the experimental data (both MAD and StDev < 0.36 Hz, χ^2 (reduced) = 0.24, Table 4.6). Therefore, the analysis of ^{1}H-^{1}H coupling constants alone is insufficient to establish the presence, let alone the populations, of non-helical conformations in solution.

Table 4.6: Comparison of the ^{1}H-^{1}H coupling constants computed based on the DFT-derived conformer energies and a 1:1 mixture of M and P helices to the experimentally measured values.

			DFT derived ensemble-averaged *J* values		***M* and *P* helices only (50% : 50%)**	
H_A	**H_B**	**Exp. $^{n}J_{HH}$/Hz**	**Calc. $^{n}J_{HH}$/Hz**	**Dev./Hz**	**Calc. $^{n}J_{HH}$/Hz**	**Dev./Hz**
H3	**H4**	6.99	7.13	0.14	7.10	0.11
H3	**H5**	6.90	6.54	−0.36	7.00	0.10
H5	**H6**	6.80	7.00	0.20	6.96	0.16
H5	**H7**	5.40	5.79	0.39	6.51	1.11
H7	**H8**	6.80	6.99	0.19	6.95	0.15
H7	**H9**	6.70	6.94	0.24	7.08	0.38
H9	**H10**	6.80	7.04	0.24	6.97	0.17
			MAD	0.25	**MAD**	0.31
			StDev	0.24	**StDev**	0.36
			χ^2	0.08	χ^2	0.24

To investigate whether any NMR parameters (δ_H, δ_C, J values and NOE derived ^{1}H-^{1}H distances) could be used to detect the presence of non-helical conformations, two sets of ensemble-averaged NMR parameters were calculated and compared to the experimentally measured data. One set of calculated data was based on the DFT-derived conformer population, which consists of a mixture of equally populated *M* and *P* helices as well as non-helical conformations, while the other set was based on a 50%:50% mixture of *M* and *P* helices. The comparison of both sets of calculated data to the experimentally measured values showed very similar fit and both gave very similar χ^2 (reduced) values with the differences in χ^2 (reduced) values less than 0.3 for the comparison of δ_H, δ_C and ^{1}H-^{1}H coupling constants (Figure 4.14). Therefore, these NMR parameters are insensitive to the change in conformational space in the case of **4.11** and could not be used to establish the presence of non-helical conformations in solution.

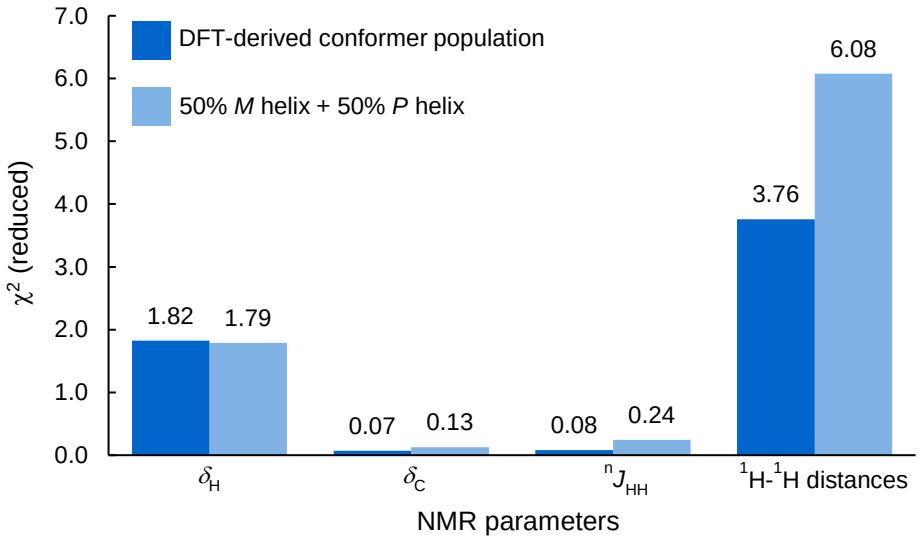

Figure 4.14 Comparison of two sets of ensemble-averaged δ_H, δ_C, ^{1}H-^{1}H couplings and ^{1}H-^{1}H distances to the experimentally measured values. The goodness of fit was evaluated by a statistical analysis using χ^2 analysis.

On the other hand, NOE derived ^{1}H-^{1}H distances are sensitive to the presence of non-helical conformations (χ^2 (reduced) = 6.08 for 50:50 *M*:*P* helices and 3.76 for DFT-derived population, Figure 4.14). Although the computed distances based on DFT-derived conformer population fits better to the experimentally measured distances (χ^2 (reduced) value = 3.76, Figure 4.14), it still deviates substantially from the ideal fit (χ^2 (reduced) value = 1.00) and

therefore population refinement based on the experimentally derived NOE-distances (discussed in section 2.2.2, Chapter 2) was applied to correct for the DFT-approximate conformer population. Unlike the case of baulamycins, in which the entire conformational space was not computed by DFT due to the sheer number of conformations found by the initial MM conformational search (Chapter 2), population refinement should be more robust for **4.11** since all conformations found by the initial MM conformational search were subjected to the subsequent DFT calculations.

Constraints of 0, 100, 225 and 625 (Figure 4.15) were examined for $\Sigma(\Delta\Delta G)^2$ and each represents a maximum change of 0, 10, 15 and 25 kJ mol^{-1} in the ΔG of a particular dihedral cluster (out of 21 clusters). The ratio between the *M* and *P* helical conformers was enforced to 1:1 during the refinement process. The ensemble-averaged ^{1}H-^{1}H coupling constants and ^{1}H-^{1}H distances were recomputed after each refinement and compared to the experimentally measured values. After population refinement, the fit for the ^{1}H-^{1}H distances dramatically improved as the constraint increased from 0 to 100, with the χ^2 (reduced) values decreased from 3.76 to 1.42 (Figure 4.15). In addition, the excellent fit for the ^{1}H-^{1}H coupling constants was retained with essentially no change in χ^2 (reduced) values (0.08 and 0.07 for constraint = 0 and 100 respectively, Figure 4.15). As the constraint of Sum$(\Delta\Delta G)^2$ was increase further from 100 to 225 then to 625, only a slight improvement in the fit for the ^{1}H-^{1}H distances was observed (χ^2 (reduced) values = 1.42, 1.04 and 0.77 for Sum$(\Delta\Delta G)^2$ = 100, 225 and 625 respectively, Figure 4.15). However, slight erosion in the fit for ^{1}H-^{1}H coupling constants was also observed with the χ^2 (reduced) values increased gradually from 0.07 to 0.36 (Figure 4.15). The erosion of the fit for the ^{1}H-^{1}H coupling constants might be an indication of over-fitting as the ΔG (and thus populations) of the dihedral clusters were allowed to deviate substantially from the DFT computed values.

In terms of population refinement, the optimal constraint for the refinement lies somewhere around 100 and 225 before overfitting takes place. A constraint of 100 was chosen as the optimal constraint for the refinement value because this value would give refined conformer energies closest to the DFT computed conformer energies.

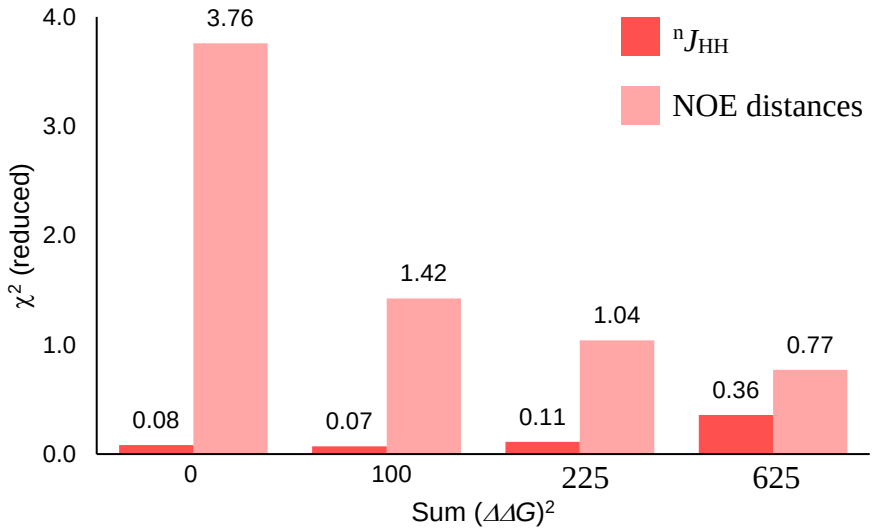

Figure 4.15: Comparison of ensemble-averaged ^{1}H-^{1}H couplings and ^{1}H-^{1}H distances based on conformer energies after population refinement using different constraints to the experimentally measured values. The goodness of fit was evaluated by χ^2 analysis.

The change in the conformational landscape of **4.11** after population refinement using a constraint of 100 was considered in more detail. The combined population of helical conformations (*M* + *P*) dropped from 63.0% to 44.5% after refinement, while the population of two clusters, which shows a break in helicity (indicated by +*ac*/−*ac* dihedral angles) along the backbone have increased from nearly zero to 24.9% and 18.5% respectively. Helical conformers (*M* and *P* helices) remained to be the global minimum and the energy of four clusters changed for ~ 6 kJ mol^{-1}, which is approaching chemical accuracies (~4 kJ mol^{-1}). In the absence of strong intramolecular interactions (e.g. intramolecular hydrogen bonds in the case of baulamycins, Chapter 2), a very small change in the *ΔG* of the three clusters resulted in a dramatic improvement of the fit in ^{1}H-^{1}H distances (Figure 4.15) because DFT calculations should provide a reasonably accurate description of conformer energies for these systems.

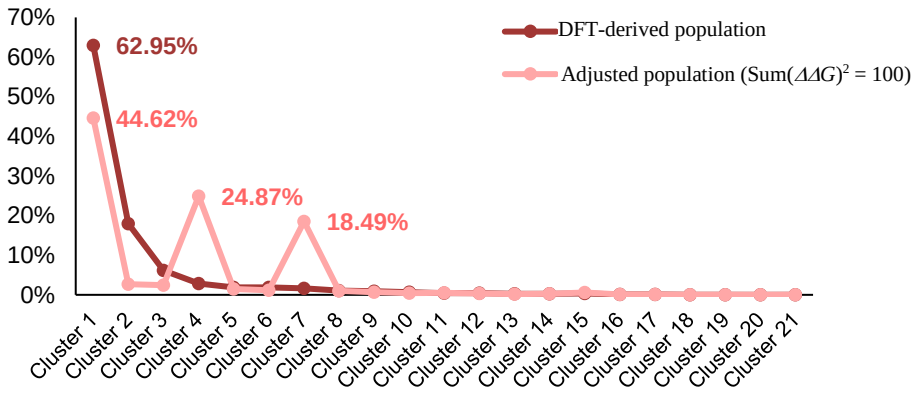

Figure 4.16: Population of each cluster of conformations before and after NOE-based population refinement using a constraint (sum($\Delta\Delta G$)^2) of 100.

Therefore, the presence and the conformer population of non-helical conformation was established by refining the DFT-computed ensemble-averaged ^{1}H-^{1}H distances based on the experimentally derived NOE distances. Although both helical conformations are still the lowest energy conformers after population refinement, the free energy difference between the helical and non-helical conformers is very small (1.4 kJmol^{-1}), thus the minimisation of *gauche* interactions indeed reduced the level of helical conformers of **4.11**.

4.2.3.2 Investigation of the effect of entropy on conformational preference (QM/NMR analysis of 4.12 and 4.13).

The *meso* compounds with odd numbers of contiguous methyl substituents provide the opportunity to directly explore the contribution of entropy on the conformational landscape of these systems. To examine this, compounds **4.12** and **4.13** (Scheme 4.2) with longer chain lengths were synthesised and their conformational behaviour was calculated using the MM conformational search and DFT calculation methods as described previously (section4.2.2.4.2).

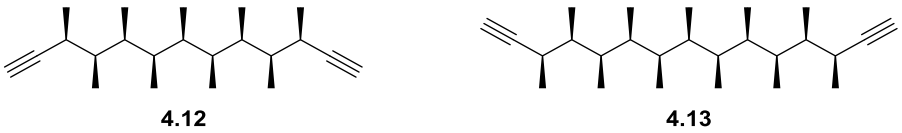

Scheme 4.2: Chemical structure of **4.12** and **4.13**.

The DFT-derived conformer energies were further refined based on the experimentally determined NOE-derived interproton distances using a constraint of 100 for $\Sigma(\Delta\Delta G)^2$. A mixture of equally populated *M* and *P* helices, as well as non-helical conformations were observed for both **4.12** and **4.13**. The combined population of helical conformers decreases with increasing chain length (from 44.6% to 29.6%, Figure 4.17), presumably because of the increasing entropic cost for adopting a regular helical conformation.

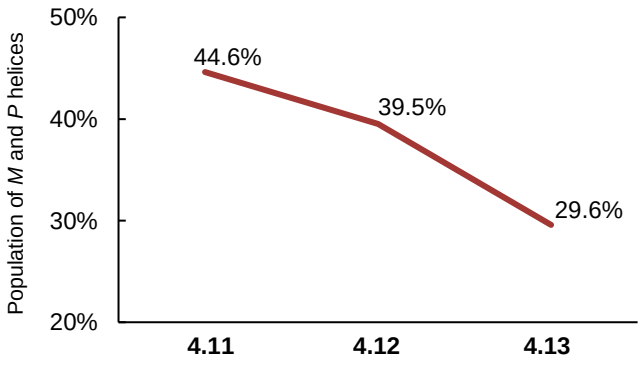

Figure 4.17: Combined helical conformer population of **4.11**, **4.12** and **4.13**.

In summary, the QM/NMR analysis of **4.11** found that neither chemical shifts nor scalar coupling constants were sensitive enough to establish the presence and the conformer population of non-helical conformers. Only NOE-distances, which are sensitive to conformer populations with short interproton distances (scaled with r^{-6}), could establish the presence of non-helical conformers and ultimately determine their conformer populations. The QM/NMR analysis also showed that molecules with odd numbers of contiguous methyl substituents (**4.11**,

4.12 and **4.13**) have poor conformational bias toward helical conformers because of the reduced free energy difference between the helical and non-helical conformers.

4.2.4 Helical switch by altering end groups (QM/NMR analysis of 4.14).

As discussed in section 4.2.2, the minimisation of *gauche* interactions dictates which helical conformation is preferred for compounds with even number of contiguous methyl substituents. To gain a deeper understanding of the actual energetic difference between the *M* and *P* helices, Mr. Johan A. Pradeilles re-visited the originally proposed model (Figure 4.4) and categorised the *gauche* interactions found in both helical screw-sense into five types (Table 4.7): between two methyl substituents (Me-Me); between the end group and the methyl substituent (R-Me); between the methyl substituent and the helical backbone (Me-Helix), between the end group and the helical backbone (R-Helix); and between the helical backbones (Helix-Helix). Cancellations of the same types of *gauche* interactions found in both helical screw-sense revealed the actual difference in the *gauche* interactions.

Table 4.7: A list of different types of *gauche* interactions observed in the *M* helix (**4.4**-1) and *P* helix (**4.4**-2) in compound **4.4**.

	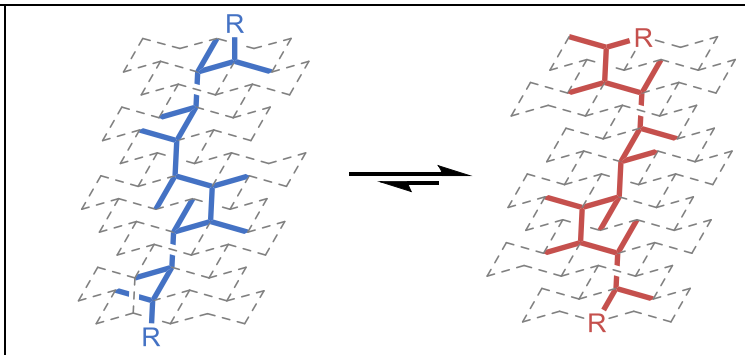	
	M helix (**4.4**-1)	*P* helix (**4.4**-2)
Types of *gauche* interactions	Numbers of *gauche* interactions	
Me-Me	9	9
R-Me	2	0
Me-Helix	8	8
R-Helix	0	2
Helix-Helix	4	3
Interactions left after cancellations	2×(R-Me) + (Helix-Helix)	2×(R-Helix)

If the energy arises from two *gauche* interactions between the end group and the methyl substituent plus a *gauche* interaction between the helical backbones (2×(R-Me) + (Helix-Helix)) is larger than that which arises from the two *gauche* interactions between the end group and the helical backbone (2×(R-Helix)), the *P* helix will be lower in energy and dominate the conformer population.

Although a *P* helix was observed for **4.5**, the enthalpic costs of each type of *gauche* interactions (alkyne-Me, Helix-Helix and alkyne-Helix) which dictates the preference of helicity are currently unknown, thus hindering the quantitative assessment of the mathematical description of the model (Table 4.7). Nevertheless, the preference towards the *M* helix could be enhanced by increasing the enthalpic cost of the *gauche* interaction between the end group and the helical backbone (R-Helix).

In addition to increasing the enthalpic penalty for adopting the *P* helical conformation, one could also reinforce the preference of the first backbone dihedral to adopt an antiperiplanar conformation to maximise the preference towards the *M* helical conformation. Therefore, using a *tert*-butyl group would not only substantially increase the enthalpic cost of the 'R-Helix' term, thus increasing the enthalpic penalty for adopting the *P* helical conformation, but would also reinforce the first backbone dihedral to adopt an antiperiplanar conformation due to the effect of a *tert*-butyl group on molecular conformation (Chapter 3).

Therefore, the *tert*-butyl analogue **4.14** was studied computationally using a Monte Carlo MM conformational search as described previously (section 4.2.2.3). Compared to the MM calculation results of **4.5** (Figure 4.18a), which predicted that both *M* and *P* helices have equal conformer populations, the MM calculation results of **4.14** showed an enhanced bias towards the *M* helical conformation (75.7% of conformer population, ignoring end-group rotamers, Figure 4.18b). However, synthesis of **4.14** was challenging due to the lack of synthetic methods to directly introduce the terminal *tert*-butyl group. In addition, it would also be challenging to analyse the NMR spectra of **4.14** due to signal overlap. Therefore, an analogue **4.15** was designed and MM calculations predicted that the *M* helical conformation still dominated the conformer population of **4.15** with a conformer population of 69.9%.

According to MM calculations, the introduction of a *tert*-butyl group indeed would enhance the preference to adopt the *M* helix as expected. However, MM predicted conformer energies were proven to be inaccurate in this type of system (section 4.2.2.4.1).

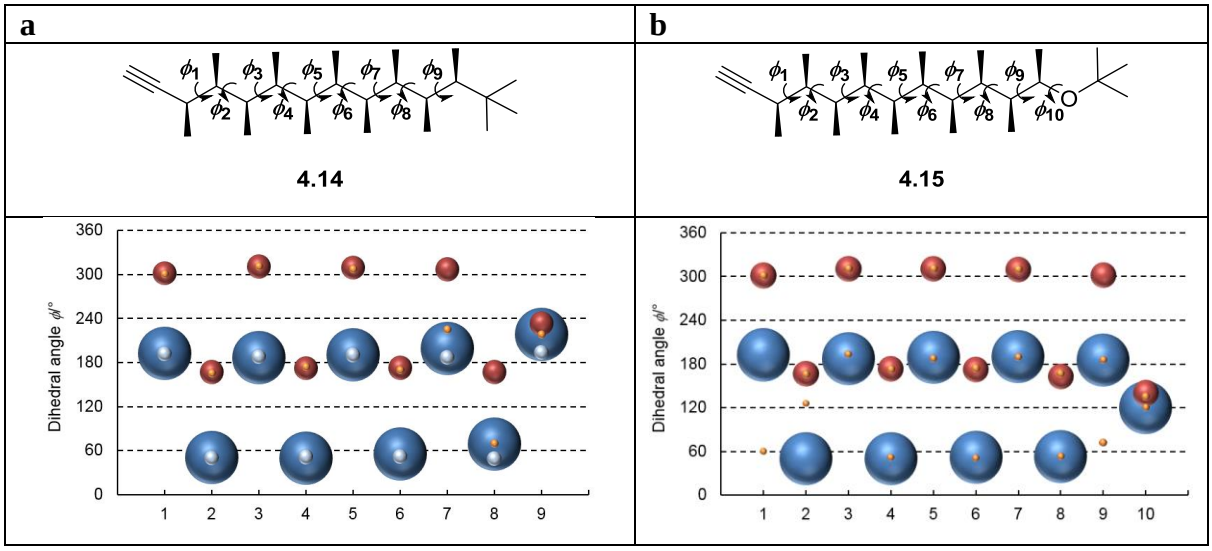

Figure 4.18: **a**, Chemical structure of **4.14** and the MM predicted conformer population represented by a bubble plot. **b**, Chemical structure of **4.15** and the MM predicted conformer population represented by a bubble plot. Red dots represent *P* helix while blue dots represent *M* helix.

Therefore, DFT calculations were also performed to obtain a better picture of the conformational behaviour of **4.15** using the procedures described previously (section 4.2.2.5). Again, the conformer energies were found to change substantially going from MM to DFT calculations. (section 4.2.2.4.1). Although the *M* helix was predicted to be the dominant conformation with a 69.9% of conformer population by MM calculations (Figure 4.18b), DFT calculations predicted that the *M* helix only has a 7.9% of conformer population with *P* helix representing 42.4% of the helical conformer population. In addition, the predicted combined population of helical conformers decreased from 86.2% (Figure 4.18b) to 50.3% (Figure 4.19c) going from MM to DFT calculations. The DFT-predicted conformer population was not in line with the expected conformational behaviour of **4.15** based on the mathematical description.

To confirm the DFT-predicted conformational behavior of **4.15** in solution, the computed ensemble-averaged ^{1}H-^{1}H scalar coupling constants and ^{1}H-^{1}H distances were computed using DFT calculation methods described previously (sections 4.2.2.4.1 and 4.2.2.4.2). The computed ensemble-averaged ^{1}H-^{1}H scalar coupling constants fit well to the experimentally determined values (MAD = 0.7 Hz, StDev = 0.9 Hz, χ^2 (reduced) = 0.9 Hz). However, the computed ensemble-averaged ^{1}H-^{1}H distances fits less well to the experimentally determined NOE-distances (MD = 5.7%, StDev = 7.5%) with a χ^2 (reduced) value of 4.6. The poor fit for NOE-distances arise from an outlier which corresponds to the distances between H_3 and H_9. (highlighted by a red circle, Figure 4.19b). The experimentally determined NOE distance between H_3 and H_9 is 2.27 Å, which is substantially shorter than the DFT-computed

ensemble-averaged distance (2.76 Å). This suggests that experimentally, one or more conformer populations with short H_3-H_9 distance are higher than what was predicted by DFT calculations. Since both the *M* helix and non-helical conformers of **4.15** show a short DFT-computed H_3-H_9 distance, it likely the large deviation observed reflects either an inaccurately predicted ratio between the *M* and *P* helices, or an inaccurately predicted ratio between the helical and non-helical conformers.

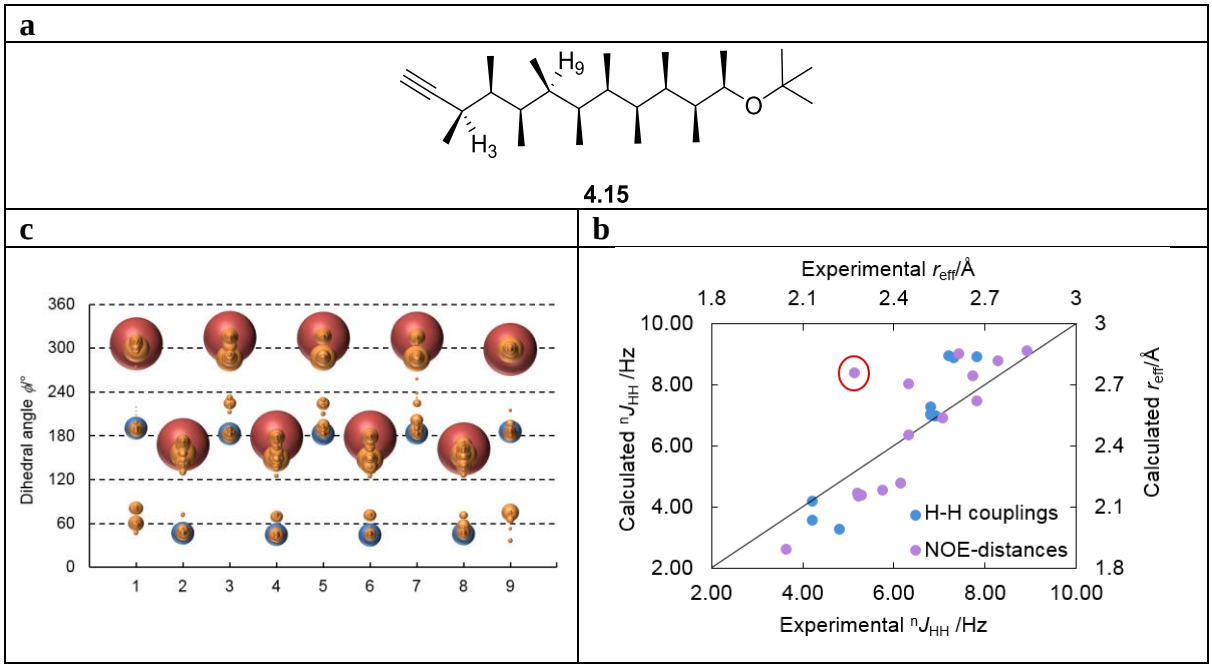

Figure 4.19: **a**, Chemical structure of **4.15** with H_3 and H_9 labelled. **b**, DFT-predicted conformer population of **4.15** represented by a bubble plot. Red dots represent *P* helix while blue dots represent *M* helix. **c**, Comparison of the DFT computed ensemble-averaged ^{1}H-^{1}H scalar coupling constants and ^{1}H-^{1}H distances to the experimentally determined values, with an outlier in the comparison of the ^{1}H-^{1}H distances highlighted using a red circle.

It seems that, experimentally, the major conformer of **4.15** is unlikely to be the *M* helical conformer as expected. Unfortunately, NOE-based population refinement was not performed on **4.15** to obtain a more accurate picture of the conformational landscape due to inadequate number of NOE-distances measured and time constraints. Only 17 NOE-distances could be measured from both 1D NOE and CSSF NOE spectra for **4.15** due to spectral overlap (c.t. 28 NOE-distances measured for **4.5**, which also has 10 contiguous methyl substituents), so the NOE-based population refinement would be less robust. Although other NOE techniques, such as pure shift NOESY[161], would overcome the spectral overlap problem by collapsing multiplets to 'pure shift' single peaks, thus enabling more NOE-distances to be measured, the accuracy of NOE-distances measured using this technique is currently untested. Therefore, validation

studies using rigid compounds such as strychnine is required to establish the accuracy of this method before application to structurally flexible compounds (such as **4.15**). It is with regret that due to time constraints, the validation study was not performed to establish the accuracy of using pure shift NOESY for NOE-distance determination because at the time all the attention was focused on completing the synthetic work discussed in chapter 3.

So, it was unclear at this stage whether the replacement of an alkyne end group by a *tert*-butyl group in **4.15** has enhanced the preference to adopt an *M* helical conformation, or has caused a break in helicity since it induces a different helicity to the alkyne end group at the other end of the chain. Therefore, **4.16** (Figure 4.20) was synthesised with *tert*-butyl groups at both ends of the chain to reinforce the same helicity (*M*) from both directions. Only the vicinal coupling constants between H_3 and H_5 were extracted for **4.16** due to spectral congestion. The value of J_{H3H5} is smaller than that of J_{H21H19} of **4.15** (Figure 4.20), therefore implying the change of both end groups to the *tert*-butoxy groups has decreased the conformer population of the *P* helix. However, the size of the observed J_{H3H5} was approaching that of averaged *J* values (~7 Hz), therefore it was unclear whether the rest of the conformer population of **4.16** was occupied by non-helical conformers or the *M* helix. Unfortunately, due to spectral overlap in ^{1}H NMR spectrum the measurement of experimental NOE distances was not possible, therefore population refinement based on NOE-distances could not be performed to study the detailed conformational behaviour of **4.16**.

a

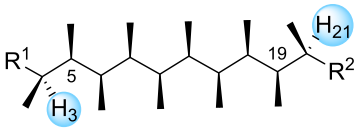

b

Compounds	R groups	Backbone *J* values/ Hz
4.5	$R^1 = R^2 =$ 	$J_{H3-H5} = J_{H21-H19} = 9.2$ Hz
4.15	$R^1 =$  $R^2 =$ 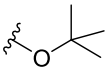	$J_{H3-H5} = 7.9$ Hz $J_{H21-H19} = 6.2$ Hz
4.16	$R^1 = R^2 =$ 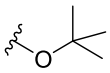	$J_{H3-H5} = J_{H21-H19} = 5.2$ Hz

Figure 4.20: a, Generic structure of a molecule with 10 contiguous methyl substituents, with protons at the peripheral positions (H_3 and H_{21}) highlighted. **b**, A summary of the observed ^{1}H-^{1}H scalar coupling constants of H_3 and H_{21} in compounds **4.5**, **4.15** and **4.16**.

4.3. Conclusions and Future work.

4.3.1 Conclusions

In conclusion, a theoretical model based on the minimisation of *gauche* interactions was proposed to account for the observed helicity of all-*syn* methyl-substituted hydrocarbons. Hydrocarbons with even numbers of methyl substituents were found to adopt regular helical conformations. Switching between the *M* and *P* helical forms was achieved by the bidirectional homologation of a *C2* symmetric bis(boronic ester) **4.6** followed by the transformation of the pinacol boronic esters to the alkyne moieties. The preferred helical screw-sense of **4.5**, and the change in screw-sense of hydrocarbons with six, eight and ten contiguous methyl substituents (**4.9**, **4.10** and **4.5**) were confirmed and followed by QM/NMR analysis using ^{1}H-^{1}H scalar coupling constants and ^{1}H-^{1}H distances. Hydrocarbons with odd numbers of methyl substituents were found to have a more diluted conformer population because of the break in helicity. Only the quantitative analysis of ^{1}H-^{1}H distances could be used to confirm the presence and the conformer population of non-helical conformers in the case of **4.11**. NOE-based population refinement of hydrocarbons with seven, nine and eleven methyl substituents (**4.11**, **4.12** and **4.13**) showed that the preference towards helical conformations decreased as chain length increased.

Spectroscopic and computational methods were developed to aid the accurate conformational analysis of the all-*syn* methyl-substituted hydrocarbons. Care must be taken with the NOE-distance analysis of *C2* symmetrical compounds (**4.9**, **4.10** and **4.5**) due to the symmetry-breaking NOE correlations. The effect of different functionals and basis sets on the computed ensemble-averaged ^{1}H-^{1}H distances were explored. It was found that the use of triple- ζ basis sets consistently gave computed ensemble-averaged ^{1}H-^{1}H distances that fits better to the experimentally determined NOE-distances. The use of diffuse function, polarisation and solvation were found to have little impact on computed conformer free energies and the optimised geometries, and the three different functionals investigated (B3LYP, mPW1PW91 and M06-2X) all showed similar performance in terms of the fit of the computed ensemble-averaged ^{1}H-^{1}H distances to the experimentally determined NOE-distances. However, the inclusion of empirical dispersion correction (D2) in conjunction with the B3LYP functional was found to have a substantial impact on both the computed conformer geometries and free energies and gave the computed ensemble-averaged distances which fitted the experimentally measured NOE-distances the best.

Finally, a revised version of the theoretical model was proposed (section 4.2.4) and it formed the basis of achieving helical switch by altering the size of the end groups of molecules with 10 contiguous methyl substituents. While the use of *tert*-butyl groups was thought to increase the energetic penalty for adopting a *P* helical conformation and the additional conformational effect of a *tert*-butyl group would further enhance the bias towards an *M* helical conformation, DFT calculations predicted that replacing an alkyne end group in **4.5** by a *tert*-butoxy moiety resulted in a break in helicity, rather than an enhanced preference towards the *M* helix. To remove the possibility of conflicts arising from different helicities being induced by different end groups, both alkyne end groups were replaced by *tert*-butoxy moieties to generate **4.16**. Unfortunately, due to spectral overlap and the conformational behaviour of **4.16**, it could not be studied in detail using QM/NMR approach. The magnitude of the only *J* value extracted (J_{H3H5} = 5.2 Hz) for **4.16** suggested that while the introduction of two sterically hindered *tert*-butoxy moieties decreases the preference toward the *P* helical conformation, the exact population of the *M* helical conformation could not be determined solely based on this value. The result obtained so far indicates the delicate balance between the preference towards either *M* or *P* helix is still poorly understood.

4.3.2 Future work

Having established the inherent preference of **4.5**-type systems, a deeper understanding between the nature of the end group and the preferred helical screw-sense is required for the design and synthesis of switchable hydrocarbon-based helices. While the use of *tert*-butyl groups as end groups has indicated that a sterically demanding group has reduced the conformer population of helical conformations, it was unclear whether the steric hindrance, or the introduction of destabilising *syn*-pentane interactions caused the break in helicity. The analysis of end groups bearing different size by QM analysis (Scheme 4.3a) would hopefully offer insight into the relationship between the steric hindrance of the end group and the preferred helical screw-sense. It was also unclear whether the hybridisation of the end groups would have an impact on helicity, since most of the systems studied so far have an alkyne end group with an sp carbon attached to the helix. Therefore, investigation of molecules bearing end groups with sp^2 carbons directly attached to the helix (Scheme 4.3b) was required. In addition, by introducing heteroatoms on the aryl rings or the use of triazole moieties would hopefully shed light on the effect of electronics on the preferred helical screw-sense.

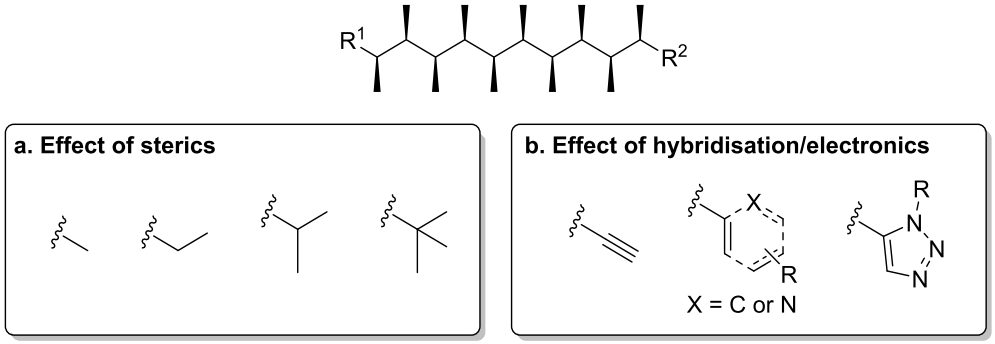

Scheme 4.3: Proposed target compounds to establish the relationship between the steric, hybridisation and electronic properties of the end group and the preferred helical screw-sense.

In addition, spectral overlap has hindered the measurements of adequate number of accurate NOE-distances for the NOE-based population refinement in the case of **4.15**. Therefore, one should investigate other NMR techniques (eg. pure shift NOESY[161]) which could circumvent the problems associated with spectral overlap.

Chapter 5 Conclusions

This thesis set out to use a quantitative QM/NMR approach together with synthesis as a tool to probe and predict flexible molecules' solution state conformational behaviours.

This tool was applied to investigate the complex dynamic conformational behaviour of baulamycin antibiotics which have long, flexible carbon chains. The comparison between the computed NMR parameters with the experimentally measured data enabled the elimination of 112 out of 128 possible stereoisomers. The synthesis of an encoded mixture of the natural product finally enabled the correct configuration of baulamycins to be unambiguously identified.

This tool was also applied to the design and conformational analysis of unnatural amino acids which project side chains in a predictable manner with tuneable distances based on the conformational control exerted by quaternary centres. Synthetic methodology utilising the stereoselective homologation of boronic ester was developed to install *tert*-butyl groups in a highly precise fashion. The predictable molecular conformation of these unnatural amino acid could, in principle, be utilised to generate novel chemical probes to interrogate other chemical or biological systems.

Detailed conformational analysis using the quantitative QM/NMR approach offered insight into factors controlling the helical screw-sense of all-*syn* methylated hydrocarbons, which would allow the design and synthesis of a new system where the helical screw-sense can be switched between *M* and *P* forms. Although the minimisation of *gauche* interactions was found to be the major factor controlling the preference of the helical screw-sense of these molecules, further QM/NMR analysis of other all-*syn* methylated hydrocarbons with different end groups is required to establish the relationship between the nature of the end groups and the preferred helical screw-sense.

The work outlined in this thesis demonstrated one's ability to predict and probe complex dynamic conformational behaviours of flexible molecules using a combination of computational modelling, NMR spectroscopy and synthesis. Further developments in accurate conformational analysis by computation and NMR methods to extract hard-to-measure NMR parameters are required to enable us to confidently and reliably determine the structures of flexible open chain-molecules exclusively *in silico*, and to create molecules with bespoke conformations for drug design and materials applications.

Chapter 6 Experimental

General Information

Molecular mechanics calculations were performed using the MacroModel software package[162] (version 9.9) accessed through the Maestro[108] (version 9.2) program. All geometry optimisations, frequency calculations and NMR calculations were performed using the Gaussian 09 Software package.[158] All molecular mechanics calculations were performed using the Unix computational resource of the School of Chemistry, University of Bristol. All DFT calculations were performed using either the Unix computational resource or the computational facilities of the advanced computing research centre at the University of Bristol (http://www.bris.ac.uk/acrc).

^{1}H- and ^{13}C- nuclear magnetic resonance (NMR) spectra were acquired at various field strengths as indicated using JEOL ECS 300MHz, JEOL ECS 400MHz, Varian 400 MR, Varian VNMRS 500MHz NMR spectrometers equipped with direct observe two-channel probes, a Bruker Avance III HD^{TM} 700MHz NMR Spectrometer with a 1.7 mm inverse triple resonance micro-Cryo Probe or a Bruker AVANCE III HD 500 MHz NMR Spectrometer with 5 mm DCH ^{13}C^{1}H/D Cryo Probe. ^{1}H chemical shifts (δ_H) are quoted in parts per million (ppm) and are referenced to the residual protio solvent resonance ($CHCl_3$ = 7.26 ppm, MeOH = 3.31 ppm, toluene = 2.09 ppm). Data are reported as follows: chemical shift, integration, multiplicity (s = singlet, br. s = broad singlet, d = doublet, t = triplet, q = quartet, pent = pentet, sext = sextet, hept = heptet, m = multiplet, dd = doublet of doublet, etc.), coupling constant(s), and assignment. ^{13}C chemical shifts (δ_C) are quoted in parts per million (ppm) and are referenced to the residual protio solvent resonance ($CHCl_3$ = 77.0 ppm, MeOH = 49.0 ppm, toluene = 20.4 ppm). ^{11}B NMR spectra were measured using Norell S-200-QTZ quartz NMR tubes at 96 or 128 MHz with complete proton decoupling.

Analytical TLC was performed on aluminium backed silica plates (Merck, Silica Gel 60 F_{254}, 0.25 mm). Compounds were visualised by fluorescence quenching or by staining the plates with either 5% solution of phosphomolybdic acid ($H_3PMo_{12}O_{40}$) in EtOH, KMnO4, ninhydrin, or anisaldehyde followed by heating. Flash column chromatography was performed on either silica gel (Merk, Silica Gel 60, 40–63 μm) or Biotage SNAP prepacked columns. All mixed solvent eluents are reported as *v*/*v* solutions.

GCMS was performed using an Agilent HP-5MS column (15 m × 0.250 mm), an Agilent 6890 GC, and Agilent 5973 MS system. Compounds were identified through extract ion

chromatogram and molecular ion analysis. Method **70-1X**: Inlet temperature 250 °C; Flow rate: 1.0 mL/min; hold at 70 °C for 0 min; ramp 20 °C/min to 200 °C; ramp 45.0 °C/min to 300 °C; hold at 300 °C for 2 min.

Mass spectra were recorded by the University of Bristol, School of Chemistry departmental mass spectrometry service using electrospray ionisation (ESI) techniques for low- and high-resolution mass spectra. HRMS ESI was performed on either a Bruker Daltonics Apex IV, 7-Tesla FT-ICR or microTOF II. Samples were submitted in Et_2O, pentane or $CHCl_3$.

All infrared spectra were recorded on the neat compounds using a PerkinElmer Spectrum One FT-IR spectrometer, irradiating between 4000 cm^{-1} and 600 cm^{-1}. Only strong and selected absorbances (ν_{max}) are reported.

Optical rotations were obtained using a Bellingham + Stanley Ltd. ADP220 polarimeter at 589 nm (Na D-line) in a cell with a path length of 1 dm. Specific rotation values are given in (deg mL)/(g dm). Melting points were measured with a Stuart SMP30 melting point apparatus and are uncorrected.

Chiral high performance liquid chromatography (HPLC) separations were performed on an Agilent 1100 Series HPLC unit equipped with UV-vis diode-array detector monitored at 210.8 nm, using Daicel Chiralpak IA, IB or IC columns (4.6 × 250 mm^2, 5 µm) fitted with respective guards (4 × 10 mm^2). Supercritical fluid chromatography (SFC) was performed on a Thar SFC investigator using a Daicel Chiralpak IA, IB, IC columns or a Whelk-O1 (4.6 × 250 mm^2, 5 µm).

Single crystal X-ray diffraction experiments were carried out at 100(2) K on a Bruker APEX II CCD diffractometer using Mo-K α radiation (λ = 0.71073 Å). Intensities were integrated[163] and absorption corrections were based on equivalent reflections using SADABS.[164] The structure was solved using Superflip[165-166] and refined against F 2 in SHELXL[167-168] using Olex2[169].All of the non-hydrogen atoms were refined anisotropically. While all of the hydrogen atoms were located geometrically and refined using a riding model. Crystal structure and refinement data are given in Table 6.69.

Chapter 2

General computational procedures

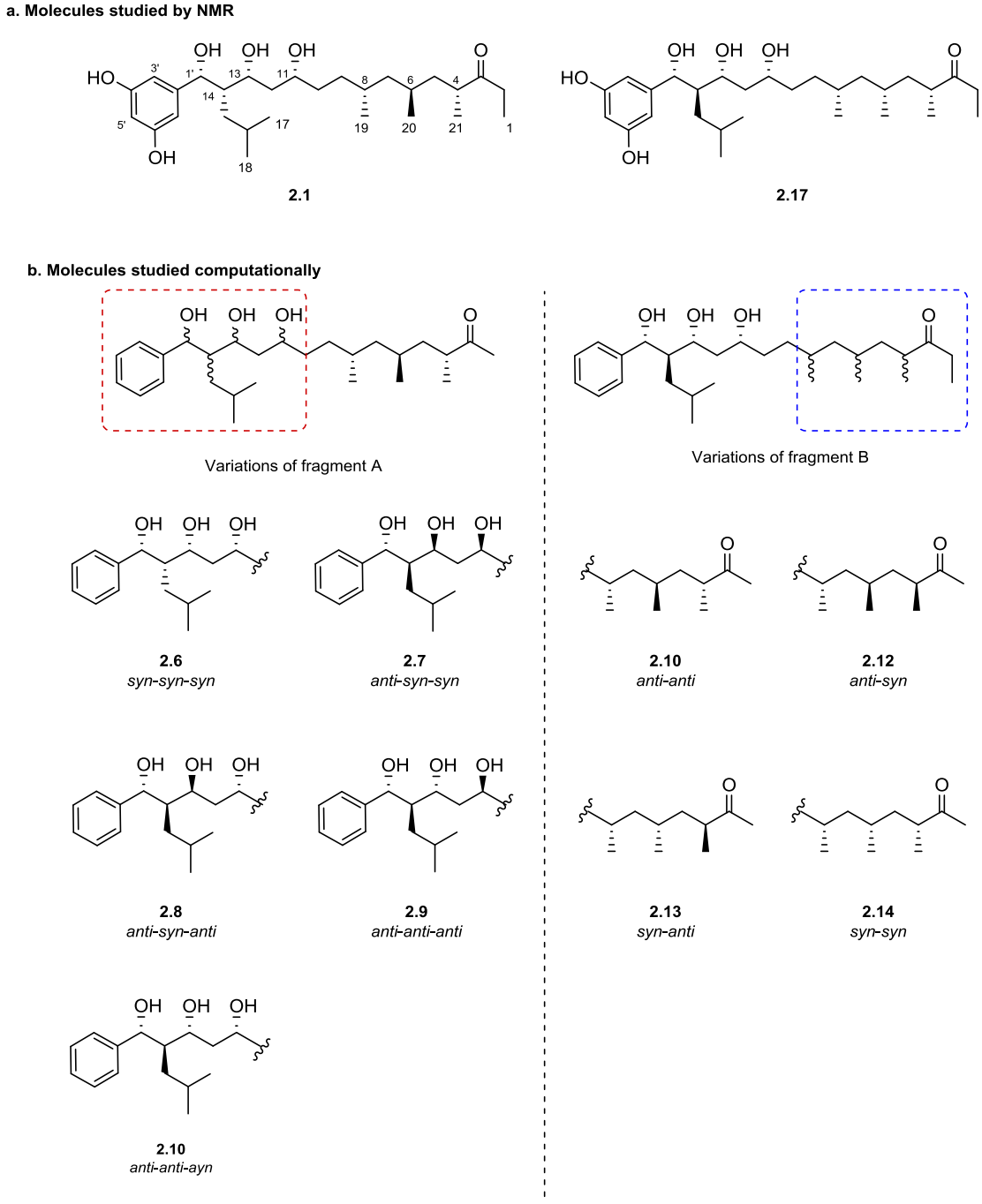

Figure 6.1: Compounds studied by NMR and computational modelling. All calculations were performed with terminal phenyl and methyl ketone end groups as shown in the figure.

A Monte Carlo multiple minimum (MCMM)[63] conformational search was used along with Merck Molecular Force Field (MMFFs)[61,170] and structures were minimised using the truncated Newton Conjugate Gradients (TNCG) method with 500 iterations with a gradient convergence criteria of 0.05. Conformers within 21.0 kJ mol^{-1} of the lowest energy conformer

found were stored. The searches were performed on all candidates outlined in Figure 6.1 with the conditions described above with a number of steps large enough that conformers below 10 kJ mol^{-1} were found more than 10 times on average. Conformers which have the same backbone conformation but differ in Ph, OH and *i*Pr rotations only were eliminated as redundant conformers based on maximum deviation for any pair of the corresponding atoms (NOT marked X in Figure 6.2) exceeding 0.5 Å, or energies differing by greater than 1 kJ mol^{-1}.

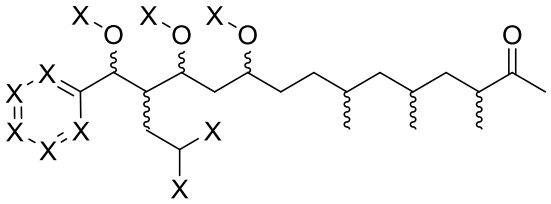

Figure 6.2: Atoms selected for redundant conformer elimination.

Conformers with a molecular mechanics potential energy below 10 kJ mol^{-1}, together with the same number of conformers between 10-21 kJ mol^{-1} in the remaining pool (see table 6.2, 6.8, 6.14 and 6.18 for details), were subjected to Density Functional Theory (DFT) geometry optimisation and frequency calculations with the mPW1PW91 functional using the 6-31 G (d) basis set (Basis set 1, BS1). Where the number of conformers below 10 kJ mol^{-1} was less than 50, the first 50 conformers, together with a further randomly sampled 50 conformers were subjected to the subsequent calculations.

In order to obtain a more accurate description of conformer energies, additional single point calculations were performed using the BS1 optimised structures. The effect of a larger basis set on conformer energy was evaluated by performing single point calculations using mPW1PW91 functional and 6-311G (d,p) basis set (BS2). Solvation effects were also evaluated by performing single point calculations using mPW1PW91/BS1 with the Integral Equation Formalism Polarizable Continuum Model (IEF-PCM) continuum dielectric solvation model using methanol as solvent (ε=32.63).[171-172]

At this stage, low energy conformers with a combined population of greater than 80%, based on their Gibbs free energies (see below), were subjected to further geometry optimisation by DFT using mPW1PW91 6-311 G (d, p) level of theory with methanol as solvent (IEF-PCM) and then NMR properties (magnetic shielding tensor and total nuclear spin-spin coupling constants) were computed with GIAO (gauge-independent atomic orbitals) method with mPW1PW91 functional using the 6-311G (d, p) basis set[173] with methanol as solvent (IEF-

PCM). Cartesian coordinates for conformers subjected to NMR calculations can be found at the CD attached to this thesis.

Calculation of estimated Gibbs free energies ($G_{est}^{\mathbf{BS2,MeOH}}$) and Boltzmann population

Due to the size of the molecules (77 atoms) and large number of geometry optimisation and frequency calculations required to perform in this study (~100 for each diastereoisomer), the nature of the stationary point and the Gibbs free energy of each conformer were calculated using a lower basis set (BS1) and the effect of a higher basis set (BS2) and solvation (methanol) on energies were incorporated by single point calculations. Gibbs free energies (in kJ mol^{-1}) of each conformer ($G_{est}^{\mathrm{BS2,MeOH}}$, in kJ mol^{-1}) were estimated according to

$$G_i^{\mathrm{BS2,MeOH}} = E_i^{\mathrm{BS2,gas}} + (G_i^{\mathrm{BS1,gas}} - E_i^{\mathrm{BS1,gas}}) + (E_i^{\mathrm{BS1,MeOH}} - E_i^{\mathrm{BS1,gas}}) \qquad \textbf{Equation 6.1}$$

where $G_i^{\mathrm{BS1,gas}}$ is the Gibbs free energy of conformer *i* with basis set 1 in gas phase, $E_i^{\mathrm{BS1,gas}}$ is the potential energy of conformer *i* with basis set 1 in gas phase, $E_i^{\mathrm{BS2,gas}}$ is single point energy of conformer *i* with basis set 2 in gas phase, $E_i^{\mathrm{BS1,MeOH}}$ is the single point energy of conformer *i* with basis set 1 in methanol. This approximation of Gibbs free energies is based on the assumption that the change in basis set and solvation has minimal impact on the change in both zero-point energy correction and entropy ($G_i^{\mathrm{BS1,gas}} - E_i^{\mathrm{BS1,gas}}$, Equation 6.1).

The estimated Gibbs free energies ($G^{\mathrm{BS2,MeOH}}$) of each conformer were then used in the Boltzmann analysis of population according to

$$p_i = \frac{g e^{-\frac{\Delta G_i^{\mathrm{BS2,MeOH}}}{RT}}}{\sum_{i=1}^{n} g e^{-\frac{\Delta G_i^{\mathrm{BS2,MeOH}}}{RT}}} \qquad \textbf{Equation 6.2}$$

where $\Delta G_i^{\mathrm{BS2,MeOH}}$ is the estimated Gibbs free energy (relative to the global minimum, in kJ mol^{-1}) of conformer *i*, *R* is the Boltzmann constant (8.314 × 10^{-3} kJ mol^{-1}), *T* is temperature of the system (298K) and *g* is the degeneracy of conformer *i* (which is 1 for every conformer in this study).

Calculation of Boltzmann averaged scaled chemical shifts.

The Boltzmann averaged magnetic shielding tensors were calculated according to

$$\sigma^x = \frac{\sum_i (\sigma_i^x \times p_i)}{\sum p}$$ **Equation 6.3**

where σ_i^x is the magnetic shielding tensor of nucleus *x* in conformer *i*, p_i is the Boltzmann population of conformer *i* and $\sum p$ is the combined population of conformers involved.

Chemical shifts were calculated according to

$$\delta_{calc}^x = \frac{\sigma^{TMS} - \sigma^x}{1 - \frac{\sigma^{TMS}}{10^6}}$$ **Equation 6.4**

where σ^x is the Boltzmann averaged magnetic shielding tensors for nucleus *x*, σ^{TMS} is the magnetic shielding tensor of either proton (31.92128) or carbon (189.5456) nuclei in tetramethylsilane (TMS) computed at the same level of theory (mPW1PW91, 6-311G(d,p), IEF-PCM (methanol)).

In order to remove systematic errors, the calculated chemical shifts (δ_{calc}^x) were then scaled according to

$$\delta_{scaled} = \frac{(\delta_{calc} - \text{intercept})}{slope}$$ **Equation 6.5**

where intercept and slope were obtained by plotting the calculated chemical shifts (δ_{calc}) for each diastereoisomer (as y-axis) against the re-extracted experimental chemical shifts of baulamycin A[95] (as x-axis) unless otherwise stated. Chemical shifts of nuclei at positions 1, 2', 3', 4', 5', 16, 17, 18 and 3 were not used for either scaling the data or further comparison.

These scaled chemical shifts were used for the Willoughby-type, DP4 and χ^2 analysis described below.[77,107]

Calculation of Boltzmann averaged scalar coupling constants

Total nuclear spin-spin coupling constants for each conformer were used to obtain the Boltzmann averaged ^{1}H-^{1}H and ^{1}H-^{13}C scalar coupling constants according to

$$^{n}J_{HX,calc} = \frac{\sum_i J_{HX,i} \times p_i}{\sum p} \qquad \textbf{Equation 6.6}$$

where $J_{HX,i}$ is the total calculated nuclear spin-spin coupling constant (in Hz) of interest in conformer i with a 6% linear scaling correction[44,160], p_i is the Boltzmann population of conformer i and $\sum p$ is the combined population of conformers involved.

Calculation of Boltzmann averaged ^{1}H-^{1}H distances

Interproton distances were extracted from the BS1 optimised geometries for compound **2.1**, **2.7 – 2.10** to obtain the Boltzmann averaged ^{1}H-^{1}H distances. Because quantitative NOE-distance analysis is very sensitive to conformer populations (interproton distances scale with r^{-6}), all conformations sampled by DFT were subjected to the quantitative NOE-distance analysis and the subsequent NOE-distance based population refinement. (For more details see the NMR procedure section). Boltzmann averaged distances from one proton (H) to another proton (H_x) were calculated according to:

$$r_{H-H_x,calc} = \left(\sum_i \left(r_{H-H_x,i}\right)^{-6} \times p_i\right)^{-\frac{1}{6}} \qquad \textbf{Equation 6.7}$$

where $r_{H-H_x,i}$ is the computed ^{1}H-^{1}H distances (in Å) of interest in conformer i and p_i is the Boltzmann population of conformer i.

To Boltzmann average distances from a single proton (H) to a pair of methylene protons (H_{ab}) which are overlapped *e.g.* H10 or H15, giving rise to a single NOE correlation, the following equation is used:

$$r_{H-H_{ab},calc} = \left(\frac{\sum_i \left(\left(r_{H-H_a,i}\right)^{-6} \times p_i + \left(r_{H-H_b,i}\right)^{-6} \times p_i\right)}{2}\right)^{-\frac{1}{6}} \qquad \textbf{Equation 6.8}$$

where $r_{H-H_a,i}$ is the computed ^{1}H-^{1}H distances (in Å) from proton H to one of the methylene protons H_a, $r_{H-H_b,i}$ is the computed ^{1}H-^{1}H distances (in Å) from the proton H to the other methylene proton H_b in conformer *i* and p_i is the Boltzmann population of conformer *i*.

χ^2 Analysis

Table 6.1: A summary of values of *n* and *m* used to calculate χ2(reduced) in fragment A and fragment B studies.

Fragment A	δ_H	δ_C	$^nJ_{HH}$	$^nJ_{HC}$	r_{noe}
n	8	7	9	16	18
m	1				
Fragment B	δ_H	δ_C	$^nJ_{HH}$	$^nJ_{HC}$	r_{noe}[a]
n	10	9	13	10	0
m	1				

[a]Quantitative noe-distance analysis was not performed on fragment B. For more details see the NMR section.

Calculated data for fragment A studies starting from gas conformational search (2.6 and 2.7 – 2.10)

Conformational search was performed in gas phase using 500,000 iterations. Table 6.2 gives the numbers of conformers found by molecular mechanics conformational search, numbers of non-redundant conformers derived from these, resulting numbers of conformers found below 10 kJ mol^{-1}, numbers of conformers selected for DFT geometry optimisation and frequency calculations, and (from these last) the number of conformers selected for NMR calculations for compound **2.6** and **2.7** – **2.10**. Total CPU time of ~ 18656 hours (~2.1 years) were spent on computing these compounds.

Table 6.2: Summary of numbers of conformers found by molecular mechanics conformational search and conformers sampled by DFT calculations for compound **2.6 and 2.7** – **2.10**.

Compound	Conformer Found	non-Redundant Conformer	Conformers < 10 kJ mol^{-1}	Conformers Sampled by DFT	Conformers used for NMR Calculations before Population refinement (DFT)	Conformers used for NMR Calculations after Population refinement (DFT)
2.6	2086	1674	98	196	6	32
2.7	650	444	18	100	8	8
2.8	2215	1620	85	170	25	18
2.9	2455	1730	82	164	9	10
2.10	1353	1015	42	84f	9	25

Calculated data for 2.6 (gas MM conformational search)

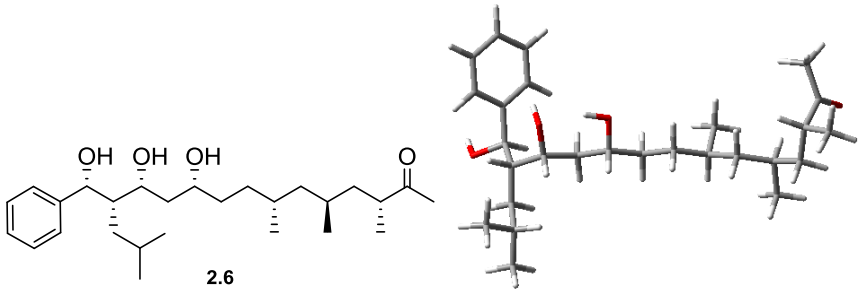

Figure 6.3: 2D structure of **2.6** and 3D structure of its lowest energy conformer **2.6**-1 obtained after population refinement using ^{1}H-^{1}H distances derived from the 2D-ROESY spectrum of the natural product.

Table 6.3: Calculated energies (in kJ mol^{-1}) and population for the major conformers of **2.6** before and after population refinement. All conformers listed were used to calculate the NMR properties of **2.6** after population refinement. For the NOE-refined $\Delta\Delta G$ (in kJ mol^{-1}) for each dihedral group, see Table 6.32.

Conformer	$\Delta E^{\mathrm{MMFFs,\ gas}}$	$\Delta E^{\mathrm{BS1,gas}}$	$\Delta G^{\mathrm{BS1,gas}}$	$\Delta E^{\mathrm{BS2,gas}}$	$\Delta E^{\mathrm{BS1,MeOH}}$	$\Delta G_{\mathrm{est.}}^{\mathrm{BS2,MeOH}}$	Population(%)/ $\Delta G_{\mathrm{est.}}^{\mathrm{BS2,MeOH}}$	Dihedral cluster	Population after refinement
2.6-1	18.7	29.8	17.5	28.6	23.9	15.1	0.07%	Cluster 26	12.17%
2.6-2	8.9	13.2	15.3	13.4	11.2	18.3	0.02%	Cluster 9	10.38%
2.6-3	20.3	32.3	18.2	30.7	26.7	15.9	0.05%	Cluster 26	8.97%
2.6-4	2.9	11.9	18.9	10.8	11.7	22.5	0.00%	Cluster 5	6.34%
2.6-5[a]	19.9	17.7	5.6	16.3	8.6	0.0	30.11%	Cluster 14	5.90%
2.6-6	20.9	30.7	19.6	29.4	24.7	17.3	0.03%	Cluster 26	5.09%
2.6-7	20.9	33.3	20.3	29.4	27.4	15.4	0.06%	Cluster 23	4.92%
2.6-8[a]	16.4	17.9	6.9	16.4	8.5	0.7	22.29%	Cluster 14	4.37%
2.6-9	20.8	34.9	28.4	33.5	23.6	20.5	0.01%	Cluster 9	4.27%
2.6-10	11.8	11.4	15.1	9.4	12.1	18.7	0.02%	Cluster 17	3.58%
2.6-11[a]	18.4	19.4	6.5	17.6	11.1	1.3	17.75%	Cluster 14	3.48%

2.6-12	9.1	10.6	17.7	8.5	13.4	23.3	0.00%	Cluster 3	3.40%
2.6-13	9.1	17.0	21.1	15.4	16.8	24.1	0.00%	Cluster 5	3.21%
2.6-14	10.4	15.9	14.8	13.3	16.1	17.2	0.03%	Cluster 23	2.30%
2.6-15	9.5	15.0	15.1	12.7	15.3	17.9	0.02%	Cluster 23	1.79%
2.6-16	0.0	11.0	13.2	9.2	7.0	12.2	0.22%	Cluster 20	1.52%
2.6-17	8.0	12.1	20.0	12.6	9.9	23.1	0.00%	Cluster 9	1.46%
2.6-18[a]	18.6	19.9	9.9	17.3	11.4	3.6	7.08%	Cluster 14	1.39%
2.6-19	7.8	10.4	20.3	9.0	12.6	26.0	0.00%	Cluster 3	1.14%
2.6-20[a]	4.8	1.7	0.0	1.1	1.9	4.4	5.07%	Cluster 14	0.99%
2.6-21	2.6	1.0	0.0	0.8	1.1	4.7	4.58%	Cluster 14	0.90%
2.6-22	7.4	24.9	21.5	21.1	21.9	19.8	0.01%	Cluster 15	0.87%
2.6-23	4.0	1.7	0.3	1.1	2.0	4.8	4.27%	Cluster 14	0.84%
2.6-24	2.7	12.0	16.9	11.2	11.1	20.1	0.01%	Cluster 7	0.76%
2.6-25[a]	20.9	24.6	12.8	22.6	14.2	5.4	3.43%	Cluster 14	0.67%
2.6-26	20.7	37.0	27.1	33.0	29.2	20.3	0.01%	Cluster 23	0.67%
2.6-27	7.0	19.5	22.8	17.2	15.2	21.0	0.01%	Cluster 15	0.52%
2.6-28	15.7	15.0	22.1	15.9	13.1	26.1	0.00%	Cluster 9	0.44%
2.6-29[b]	16.3	22.1	21.1	19.2	20.5	21.5	0.01%	Cluster 23	0.42%
2.6-30	19.9	32.3	27.4	29.2	24.8	21.6	0.00%	Cluster 23	0.39%
2.6-31	9.2	15.1	20.2	13.6	13.4	21.8	0.00%	Cluster 15	0.38%
2.6-32	16.5	23.4	19.5	20.7	23.6	21.8	0.00%	Cluster 7	0.38%

[a]These conformers were used to calculate the Boltzmann averaged NMR parameters before population refinement

[b]Geometry optimisation using basis set 2 with methanol for this conformer did not converged thus the subsequent NMR calculation was not performed to get chemical shifts and scalar coupling consants.

Calculated data for 2.7 (gas MM conformational search)

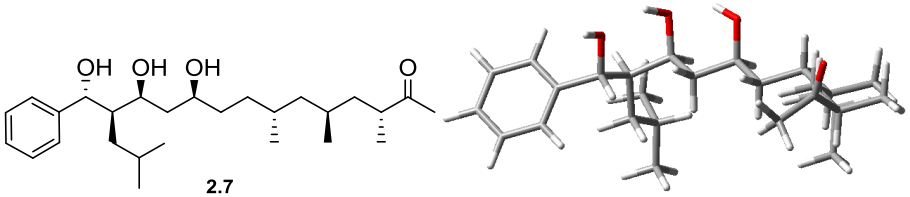

Figure 6.4: 2D structure of **2.7** and 3D structure of its lowest energy conformer **2.7**-1 obtained after population refinement using ^{1}H-^{1}H distances derived from the 2D-ROESY spectrum of the natural product.

Table 6.4: Calculated energies (in kJ mol^{-1}) and population for the major conformers of **2.7** before and after population refinement. The first 8 conformers with the combined population of 95.92% were used to calculate the NMR properties of **2.7** after population refinement. For the NOE-refined $\Delta\Delta G$ (in kJ mol^{-1}) for each dihedral group, see Table 6.32.

Conformer	$\Delta E^{\mathrm{MMFFs,\ gas}}$	$\Delta E^{\mathrm{BS1,gas}}$	$\Delta G^{\mathrm{BS1,gas}}$	$\Delta E^{\mathrm{BS2,gas}}$	$\Delta E^{\mathrm{BS1,MeOH}}$	$\Delta G_{\mathrm{est.}}^{\mathrm{BS2,MeOH}}$	Population(%)/ $\Delta G_{\mathrm{est.}}^{\mathrm{BS2,MeOH}}$	Dihedral cluster	Population after refinement
2.7-1[a]	18.8	20.0	4.5	17.4	11.3	0.4	22.44%	Cluster 4	35.61%
2.7-2[a]	20.7	23.8	7.2	20.3	14.7	1.9	12.07%	Cluster 4	19.15%
2.7-3	9.3	27.5	23.9	25.2	21.3	22.8	0.00%	Cluster 6	18.12%
2.7-4[a]	19.8	27.9	8.2	24.9	19.5	4.3	4.73%	Cluster 4	7.50%
2.7-**2.7**[a]	20.8	24.0	9.6	21.1	15.2	5.3	3.11%	Cluster 4	4.94%
2.7-6[a]	12.6	3.6	0.0	2.4	2.8	5.4	2.93%	Cluster 4	4.65%
2.7-7[a]	18.1	23.3	3.0	21.6	14.7	0.0	26.32%	Cluster 9	3.37%
2.7-8[a]	12.3	21.1	2.3	19.5	13.8	0.7	20.17%	Cluster 9	2.58%
2.7-9[a]	0.0	0.0	0.4	0.0	0.0	7.7	1.18%	Cluster 9	0.15%
2.7-10[a]	18.5	24.4	10.5	22.3	16.8	8.2	0.96%	Cluster 9	0.12%
2.7-11[a]	9.5	3.2	2.0	3.1	3.2	9.1	0.66%	Cluster 9	0.08%

[a]These conformers were used to calculate the Boltzmann averaged NMR parameters before population refinement.

Calculated data for 2.8 (gas MM conformational search)

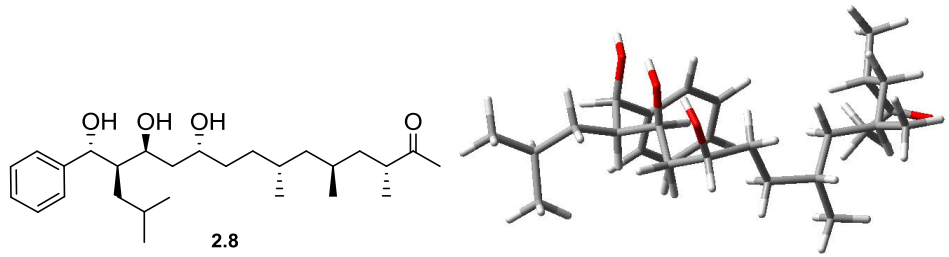

Figure 6.5: 2D structure of **2.8** and 3D structure of its lowest energy conformer **2.8**-1 obtained after population refinement using ^{1}H-^{1}H distances derived from the 2D-ROESY spectrum of the natural product.

Table 6.5: Calculated energies (in kJ mol^{-1}) and population for the major conformers of **2.8** before and after population refinement. The first 18 conformers with the combined population of 85.84% were used to calculate the NMR properties of **2.8** after population refinement. For the NOE-refined $\Delta\Delta G$ (in kJ mol^{-1}) for each dihedral group, see Table 6.32.

Conformer	$\Delta E^{\text{MMFFs, gas}}$	$\Delta E^{\text{BS1,gas}}$	$\Delta G^{\text{BS1,gas}}$	$\Delta E^{\text{BS2,gas}}$	$\Delta E^{\text{BS1,MeOH}}$	$\Delta G_{\text{est.}}^{\text{BS2,MeOH}}$	Population(%)/ $\Delta G_{\text{est.}}^{\text{BS2,MeOH}}$	Dihedral cluster	Population after refinement
2.8-1	8.3	27.9	9.8	26.8	16.8	8.3	20.98%	Cluster 3	17.63%
2.8-2	5.6	20.9	17.2	19.1	18.9	16.1	0.03%	Cluster 5	15.00%
2.8-3	9.8	24.5	20.0	21.9	21.8	17.4	0.02%	Cluster 5	8.86%
2.8-4[a]	12.1	22.7	11.0	20.9	13.1	2.2	8.53%	Cluster 3	7.17%
2.8-5[a]	8.5	0.0	0.0	0.0	0.0	2.6	7.24%	Cluster 3	6.08%
2.8-6	14.1	41.9	25.6	39.2	32.5	16.1	0.03%	Cluster 1	4.71%
2.8-7	7.0	38.8	25.8	35.6	30.1	16.7	0.02%	Cluster 1	3.73%
2.8-8[a]	3.9	8.9	2.6	7.5	8.9	4.0	4.23%	Cluster 3	3.56%
2.8-9[a]	9.1	23.9	10.6	22.2	16.5	4.1	3.99%	Cluster 3	3.35%
2.8-10[a]	18.0	28.3	14.5	25.9	18.3	4.7	3.10%	Cluster 3	2.61%
2.8-11[a]	8.7	20.6	11.6	19.9	12.2	5.1	2.66%	Cluster 3	2.23%

2.8-12[a]	19.9	25.8	11.7	26.0	16.5	5.1	2.66%	Cluster 3	2.23%
2.8-13	8.1	39.5	27.1	36.4	31.0	18.2	0.01%	Cluster 1	2.04%
2.8-14[a]	3.4	10.3	5.4	8.5	9.6	5.6	2.18%	Cluster 3	1.83%
2.8-15	6.4	20.2	12.6	18.6	13.0	6.4	1.60%	Cluster 3	1.34%
2.8-16	6.1	4.4	4.8	4.7	5.7	9.2	0.52%	Cluster 10	1.24%
2.8-17[a]	16.3	32.0	16.7	30.0	21.5	6.8	1.33%	Cluster 3	1.12%
2.8-18	20.4	25.1	23.9	23.5	22.7	22.5	0.00%	Cluster 5	1.10%
2.8-19[a]	7.3	4.8	2.4	6.8	1.4	3.6	4.92%	Cluster 8	0.26%
2.8-20[a]	9.6	28.6	10.9	28.3	19.8	4.3	3.75%	Cluster 8	0.20%
2.8-21[a]	9.8	25.3	11.4	24.7	16.8	4.9	2.91%	Cluster 8	0.15%
2.8-22[a]	9.4	28.4	15.2	28.9	15.1	5.1	2.64%	Cluster 8	0.14%
2.8-23[a]	5.7	24.8	12.2	25.2	15.0	5.3	2.44%	Cluster 8	0.13%
2.8-24[a]	18.2	28.2	13.1	27.4	18.7	5.5	2.26%	Cluster 8	0.12%
2.8-25[a]	9.4	15.4	14.1	12.5	7.4	5.8	2.00%	Cluster 7	0.48%
2.8-26[a]	2.3	14.5	12.8	11.6	8.2	6.2	1.69%	Cluster 7	0.40%
2.8-27[a]	10.4	20.2	14.0	17.0	13.3	6.5	1.50%	Cluster 7	0.36%
2.8-28[a]	17.6	32.1	17.0	30.4	21.2	7.0	1.23%	Cluster 3	1.03%
2.8-29[a]	20.4	30.8	14.0	28.7	23.4	7.1	1.22%	Cluster 7	0.29%
2.8-30[a]	19.9	28.1	14.5	26.9	19.5	7.4	1.06%	Cluster 3	0.89%
2.8-31[a]	17.7	28.0	14.4	28.2	18.1	7.4	1.05%	Cluster 8	0.06%
2.8-32[a]	2.5	13.3	7.7	13.7	10.2	7.7	0.95%	Cluster 8	0.05%
2.8-33[a]	14.0	19.3	13.1	16.1	14.6	7.8	0.89%	Cluster 7	0.21%

[a]These conformers were used to calculate the Boltzmann averaged NMR parameters before population refinement.

Calculated data for 2.9 (gas MM conformational search)

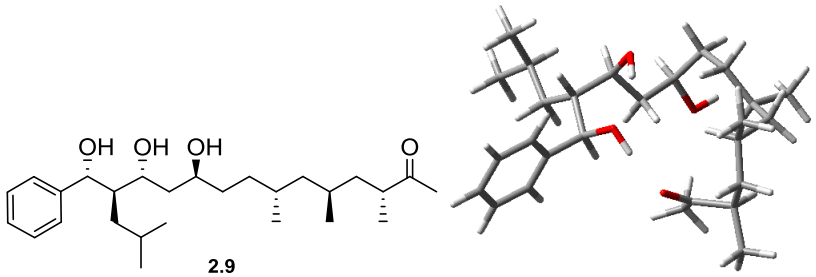

Figure 6.6: 2D structure of **2.9** and 3D structure of its lowest energy conformer **2.9**-1 obtained after population refinement using ^{1}H-^{1}H distances derived from the 2D-ROESY spectrum of the natural product.

Table 6.6: Calculated energies (in kJ mol^{-1}) and population for the major conformers of **2.9** before and after population refinement. The first 9 conformers with the combined population of 92.28% were used to calculate the NMR properties of **2.9** after population refinement. For the NOE-refined $\Delta\Delta G$ (in kJ mol^{-1}) for each dihedral group, see Table 6.32.

Conformer	$\Delta E^{\text{MMFFs, gas}}$	$\Delta E^{\text{BS1,gas}}$	$\Delta G^{\text{BS1,gas}}$	$\Delta E^{\text{BS2,gas}}$	$\Delta E^{\text{BS1,MeOH}}$	$\Delta G_{\text{est.}}^{\text{BS2,MeOH}}$	Population(%)/ $\Delta G_{\text{est.}}^{\text{BS2,MeOH}}$	Dihedral cluster	Population after refinement
2.9-1	8.9	23.4	20.4	17.7	18.1	19.3	0.03%	Cluster 7	22.18%
2.9-2[a]	19.5	32.7	13.8	27.2	22.0	7.5	3.51%	Cluster 15	15.89%
2.9-3	7.1	21.9	21.0	15.5	17.5	20.2	0.02%	Cluster 7	15.38%
2.9-4[a]	16.2	19.4	3.2	15.9	9.7	0.0	73.79%	Cluster 18	14.03%
2.9-5[a]	0.0	13.6	9.8	7.4	9.6	9.8	1.43%	Cluster 23	11.93%
2.9-6[a]	20.1	25.0	9.4	21.3	16.1	6.9	4.61%	Cluster 10	8.70%
2.9-7	9.6	15.7	11.9	12.3	10.4	13.1	0.37%	Cluster 15	1.67%
2.9-8	16.6	20.6	12.7	17.3	15.0	13.6	0.30%	Cluster 15	1.37%
2.9-9	3.1	12.0	12.4	8.7	7.0	14.1	0.25%	Cluster 15	1.13%

2.9-10[a]	18.6	25.3	10.4	22.5	14.0	6.3	5.67%	Cluster 18	1.48%
2.9-11[a]	4.6	0.0	0.0	0.0	0.2	10.2	1.20%	Cluster 20	0.23%
2.9-12[a]	16.2	19.2	8.2	13.7	16.8	10.3	1.16%	Cluster 17	0.15%
2.9-13[a]	9.2	19.0	10.1	15.5	13.3	11.0	0.86%	Cluster 1	0.31%

[a]These conformers were used to calculate the Boltzmann averaged NMR parameters before population refinement.

Calculated data for 2.10 (gas MM conformational search)

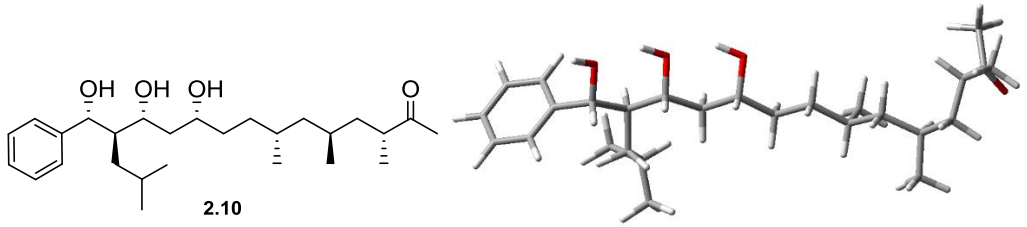

Figure 6.7: 2D structure of **2.10** and 3D structure of its lowest energy conformer **2.10**-1 obtained after population refinement using ^{1}H-^{1}H distances derived from the 2D-ROESY spectrum of the natural product.

Table 6.7: Calculated energies (in kJ mol^{-1}) and population for the major conformers of **2.10** before and after population refinement. All conformers with the combined population of 92.28% were used to calculate the NMR properties of **2.10** after population refinement. For the NOE-refined $\Delta\Delta G$ (in kJ mol^{-1}) for each dihedral group, see Table 6.32.

Conformer	$\Delta E^{\text{MMFFs, gas}}$	$\Delta E^{\text{BS1,gas}}$	$\Delta G^{\text{BS1,gas}}$	$\Delta E^{\text{BS2,gas}}$	$\Delta E^{\text{BS1,MeOH}}$	$\Delta G^{\text{BS2,MeOH}}_{\text{est.}}$	Population(%)/ $\Delta G^{\text{BS2,MeOH}}_{\text{est.}}$	Dihedral cluster	Population after refinement
2.10-1[a]	17.0	26.6	4.7	21.2	13.7	0.00	38.14%	Cluster 13	23.16%
2.10-2 [a]	20.6	27.6	7.4	20.8	14.1	0.6	29.66%	Cluster 4	12.68%
2.10-3	9.2	21.1	15.9	14.8	11.8	13.9	0.14%	Cluster 9	10.52%
2.10-4[a]	17.6	15.2	0.7	12.3	7.2	3.4	9.79%	Cluster 15	10.23%
2.10-5	8.0	27.6	25.1	21.1	21.2	25.8	0.00%	Cluster 6	4.42%
2.10-6	20.9	50.3	33.8	43.2	35.8	25.9	0.00%	Cluster 6	4.36%
2.10-7	8.5	23.3	18.1	18.0	13.2	16.2	0.05%	Cluster 9	4.16%
2.10-8	20.4	29.0	21.8	24.0	14.9	16.3	0.05%	Cluster 9	4.03%
2.10-9	18.1	30.2	20.5	23.6	20.1	17.2	0.84%	Cluster 9	2.77%
2.10-10	8.3	3.6	1.8	0.7	0.5	17.3	0.04%	Cluster 14	2.20%
2.10-11[a]	17.6	24.1	10.3	18.9	10.4	5.1	4.90%	Cluster 4	2.09%

2.10-12[a]	8.4	11.1	1.9	7.3	4.6	5.1	4.79%	Cluster 4	2.05%
2.10-13	15.5	41.7	28.7	33.9	35.0	27.8	0.00%	Cluster 6	2.02%
2.10-14	16.9	43.2	29.7	37.0	34.0	27.9	0.00%	Cluster 6	1.95%
2.10-15[a]	8.9	10.5	2.9	6.2	4.5	6.2	3.10%	Cluster 4	1.33%
2.10-16	11.3	36.0	24.1	27.4	26.2	19.30	0.02%	Cluster 9	1.21%
2.10-17	9.4	23.8	14.3	17.3	14.1	11.77	0.33%	Cluster 16	1.20%
2.10-18	8.1	26.7	18.0	20.7	16.6	15.38	0.08%	Cluster 2	1.18%
2.10-19	11.5	25.1	14.5	18.6	17.6	14.25	0.12%	Cluster 3	0.95%
2.10-20	17.4	29.1	26.8	22.8	25.0	29.95	0.00%	Cluster 6	0.84%
2.10-21[a]	8.0	9.5	3.9	5.6	3.3	7.35	1.96%	Cluster 4	0.84%
2.10-22[a]	14.5	25.6	9.9	21.2	14.4	7.97	1.53%	Cluster 4	0.65%
2.10-23[a]	7.6	10.0	4.4	6.4	3.7	8.10	1.45%	Cluster 4	0.62%
2.10-24	20.4	36.0	24.2	29.5	25.7	21.07	0.008%	Cluster 9	0.59%
2.10-25	7.6	21.0	13.6	15.6	15.1	15.77	0.07%	Cluster 10	0.52%

[a]These conformers were used to calculate the Boltzmann averaged NMR parameters before population refinement.

Calculated data for fragment A studies starting from octanol conformational search (2.6 and 2.7 – 2.10)

Conformational search was performed with octanol as implicit solvent using 500,000 iterations for **2.7**, **2.8**, and **2.9**, 300,000 iterations for **2.6** and **2.10**. Table 6.8 gives the numbers of conformers found by molecular mechanics conformational search, numbers of non-redundant conformers derived from these, resulting numbers of conformers found below 10 kJ mol^{-1}, numbers of conformers selected for DFT geometry optimisation and frequency calculations, and (from these last) the number of conformers selected for NMR calculations for compound **2.6** and **2.7** – **2.10**. Total CPU time of ~ 24283 hours (~2.7 years) were spent on computing these compounds.

Table 6.8: Summary of numbers of conformers found by molecular mechanics conformational search and conformers sampled by DFT calculations for compound **2.6** and **2.7** – **2.10**.

Compound	Conformer Found	non-Redundant Conformer	Conformers < 10 kJ mol^{-1}	Conformers Sampled by DFT	Conformers used for NMR Calculations before Population refinement (DFT)	Conformers used for NMR Calculations after Population refinement (DFT)
2.6	8698	5901	282	564	36	21
2.7	2428	1114	44	100	12	8
2.8	4272	1946	102	204	20	11
2.9	5742	3280	62	124	5	10
2.10	8794	3670	107	214	18	25*

* Using a constraint of 400

Calculated data for 2.6 (octanol MM conformational search)

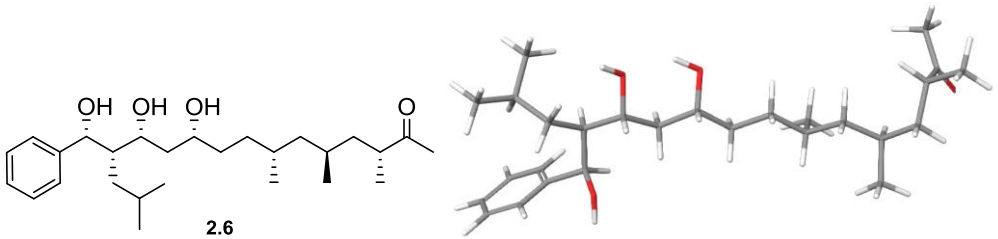

Figure 6.8: 2D structure of **2.6** and 3D structure of its lowest energy conformer **2.6**-1 obtained after population refinement using ^{1}H-^{1}H distances derived from the 2D-ROESY spectrum of the natural product.

Table 6.9: Calculated energies (in kJ mol^{-1}) and population for the major conformers of **2.6** before and after population refinement. All conformers listed were used to calculate the NMR properties of **2.6** after population refinement. For the NOE-refined $\Delta\Delta G$ (in kJ mol^{-1}) for each dihedral group, see Table 6.44.

Conformer	$\Delta E^{\mathrm{MMFFs,\,gas}}$	$\Delta E^{\mathrm{BS1,gas}}$	$\Delta G^{\mathrm{BS1,gas}}$	$\Delta E^{\mathrm{BS2,gas}}$	$\Delta E^{\mathrm{BS1,MeOH}}$	$\Delta G_{\mathrm{est.}}^{\mathrm{BS2,MeOH}}$	Population(%)/ $\Delta G_{\mathrm{est.}}^{\mathrm{BS2,MeOH}}$	Dihedral cluster	Population after refinement
2.6-1a	20.67	35.28	19.56	30.66	27.69	18.19	0.02%	Cluster 6	15.57%
2.6-2a	14.73	39.69	31.61	25.09	22.11	10.26	0.39%	Cluster 13	11.84%
2.6-3a	9.60	31.05	12.69	26.72	23.99	12.13	0.18%	Cluster 21	9.60%
2.6-4a	9.90	28.68	19.18	26.65	18.88	18.19	0.02%	Cluster 19	8.69%
2.6-5a	15.00	31.50	15.14	27.05	23.95	13.97	0.09%	Cluster 21	4.56%
2.6-6a	9.98	39.38	22.11	34.29	28.68	17.15	0.02%	Cluster 5	4.42%
2.6-7a	16.00	33.43	22.77	31.07	22.36	20.16	0.01%	Cluster 19	3.93%
2.6-8a	15.40	36.92	22.54	34.50	26.14	20.16	0.01%	Cluster 19	3.92%
2.6-9a	18.97	39.75	22.52	35.10	29.38	18.34	0.02%	Cluster 5	2.74%
2.6-10a[a]	3.25	17.62	0.00	15.32	9.09	0.00	24.71%	Cluster 3	2.50%
2.6-11a	14.57	33.46	24.76	31.24	22.16	22.07	0.00%	Cluster 19	1.82%

2.6-12a	16.68	32.91	17.00	28.52	25.78	16.31	0.03%	Cluster 21	1.77%
2.6-13a	8.89	33.30	17.33	29.07	26.07	16.71	0.03%	Cluster 21	1.51%
2.6-14a	11.69	17.37	18.60	15.78	13.79	24.27	0.00%	Cluster 6	1.33%
2.6-15a	17.64	38.25	21.07	33.66	28.65	17.72	0.02%	Cluster 4	1.16%
2.6-16a	8.45	31.03	24.00	28.70	21.87	23.33	0.00%	Cluster 19	1.09%
2.6-17a	8.84	43.22	26.81	38.07	31.96	21.22	0.00%	Cluster 5	0.85%
2.6-18a[a]	6.64	20.32	2.78	17.85	11.86	2.69	8.33%	Cluster 3	0.84%
2.6-19a	16.84	34.51	20.03	30.23	26.20	18.27	0.02%	Cluster 21	0.81%
2.6-20a	8.45	15.35	16.09	14.64	13.61	24.47	0.00%	Cluster 19	0.69%
2.6-21a	20.47	38.79	20.97	34.81	29.65	18.67	0.01%	Cluster 21	0.69%
2.6-22a[a]	6.83	19.43	4.57	17.13	9.91	3.58	5.82%	Cluster 3	0.59%
2.6-23a[a]	7.75	20.38	5.93	18.08	10.91	4.99	3.29%	Cluster 3	0.33%
2.6-24a[a]	9.41	20.28	5.55	17.78	11.67	5.28	2.93%	Cluster 3	0.30%
2.6-25a[a]	5.05	18.04	5.61	15.54	9.66	5.55	2.63%	Cluster 3	0.27%
2.6-26a[a]	8.83	20.10	6.74	17.46	10.83	5.65	2.53%	Cluster 3	0.26%
2.6-27a[a]	8.84	20.10	6.74	17.46	10.83	5.65	2.53%	Cluster 3	0.26%
2.6-28a[a]	7.58	22.96	7.51	20.51	12.85	5.78	2.40%	Cluster 3	0.24%
2.6-29a[a]	9.02	18.78	5.08	15.96	11.92	6.24	1.99%	Cluster 3	0.20%
2.6-30a[a]	8.54	20.77	6.78	18.54	11.91	6.52	1.77%	Cluster 3	0.18%
2.6-31a[a]	5.88	21.13	7.47	18.58	12.04	6.66	1.68%	Cluster 3	0.17%
2.6-32a[a]	9.46	20.86	7.91	18.28	11.51	6.80	1.58%	Cluster 3	0.16%
2.6-33a[a]	5.84	20.11	7.70	17.66	10.99	6.95	1.50%	Cluster 3	0.15%
2.6-34a[a]	16.65	43.97	35.02	27.69	21.63	7.23	1.33%	Cluster 3	0.13%
2.6-35a[a]	7.81	21.56	8.16	18.33	13.05	7.25	1.32%	Cluster 3	0.13%
2.6-36a[a]	7.16	21.54	7.31	18.86	13.59	7.51	1.19%	Cluster 3	0.12%
2.6-37a[a]	5.98	20.44	8.19	17.45	12.03	7.62	1.14%	Cluster 3	0.12%
2.6-38a[a]	5.70	22.30	9.50	20.10	12.00	7.84	1.04%	Cluster 3	0.11%
2.6-39a[a]	4.34	19.79	8.46	17.09	11.11	7.91	1.01%	Cluster 3	0.10%
2.6-40a[a]	9.93	22.90	10.18	19.83	12.97	8.00	0.98%	Cluster 3	0.10%

2.6-41a[a]	4.75	20.49	8.14	17.87	12.27	8.12	0.93%	Cluster 3	0.09%
2.6-42a[a]	7.83	20.59	9.02	17.83	11.64	8.15	0.92%	Cluster 3	0.09%
2.6-43a[a]	4.39	18.41	8.29	16.16	9.80	8.26	0.88%	Cluster 3	0.09%
2.6-44a[a]	2.41	19.85	8.64	17.77	10.89	8.44	0.82%	Cluster 3	0.08%
2.6-45a[a]	6.64	21.23	8.67	18.29	13.13	8.47	0.81%	Cluster 3	0.08%
2.6-46a[a]	8.91	25.60	9.76	22.64	16.54	8.58	0.77%	Cluster 3	0.08%
2.6-47a[a]	8.87	24.14	10.84	21.18	14.09	8.67	0.75%	Cluster 3	0.08%
2.6-48a[a]	4.12	20.28	9.22	17.93	11.52	8.94	0.67%	Cluster 3	0.07%
2.6-49a[a]	3.85	20.61	9.49	18.38	11.56	9.05	0.64%	Cluster 3	0.06%
2.6-50a[a]	8.42	22.82	10.53	20.04	13.34	9.10	0.63%	Cluster 3	0.06%
2.6-51a[a]	6.31	18.84	9.38	16.34	10.26	9.14	0.62%	Cluster 3	0.06%

[a]These conformers were used to calculate the Boltzmann averaged NMR parameters before population refinement

Calculated data for 2.7 (octanol MM conformational search)

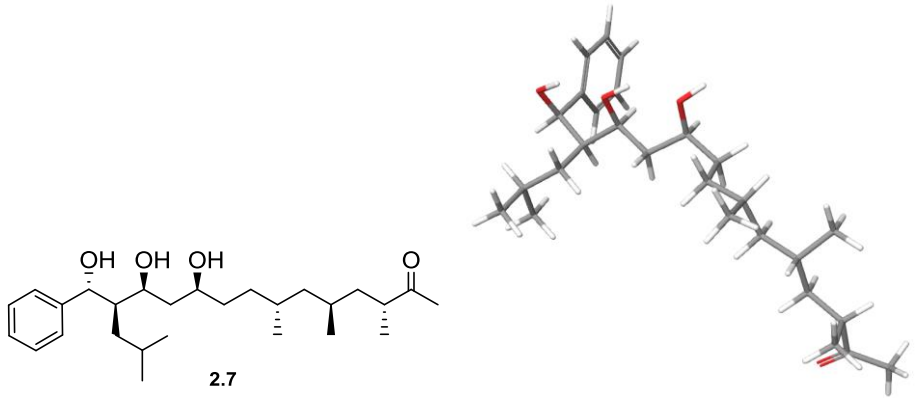

Figure 6.9: 2D structure of **2.7** and 3D structure of its lowest energy conformer **2.7** -1 obtained after population refinement using ^{1}H-^{1}H distances derived from the 2D-ROESY spectrum of the natural product.

Table 6.10: Calculated energies (in kJ mol^{-1}) and population for the major conformers of **2.7** before and after population refinement. All conformers listed were used to calculate the NMR properties of **2.7** after population refinement. For the NOE-refined *ΔΔG* (in kJ mol^{-1}) for each dihedral group, see Table 6.44.

Conformer	$\Delta E^{\mathrm{MMFFs,\,gas}}$	$\Delta E^{\mathrm{BS1,gas}}$	$\Delta G^{\mathrm{BS1,gas}}$	$\Delta E^{\mathrm{BS2,gas}}$	$\Delta E^{\mathrm{BS1,MeOH}}$	$\Delta G_{\mathrm{est.}}^{\mathrm{BS2,MeOH}}$	Population(%)/ $\Delta G_{\mathrm{est.}}^{\mathrm{BS2,MeOH}}$	Dihedral cluster	Population after refinement
2.7-1a[a]	16.72	25.89	9.12	22.51	16.22	2.98	8.19%	Cluster 4	40.01%
2.7-2a	9.42	30.31	25.42	27.97	22.38	22.08	0.00%	Cluster 3	8.89%
2.7-3a	15.80	29.79	13.52	26.89	19.09	6.85	1.71%	Cluster 4	8.37%
2.7-4a	15.51	31.22	26.51	29.25	22.38	22.64	0.00%	Cluster 3	7.08%
2.7-5a	18.73	30.53	12.90	27.49	21.38	7.63	1.25%	Cluster 4	6.12%
2.7-6a	17.48	33.47	16.05	29.74	22.93	8.69	0.81%	Cluster 4	3.98%

2.7-7a[a]	6.65	27.91	6.93	26.75	15.22	0.00	27.26%	Cluster 1	3.73%
2.7-8a	18.95	47.30	20.95	41.61	35.65	10.53	0.39%	Cluster 2	2.97%
2.7-9a[a]	8.46	20.12	3.38	18.54	12.67	1.29	16.21%	Cluster 1	2.22%
2.7-10a[a]	9.42	29.27	10.83	27.11	17.27	3.58	6.42%	Cluster 1	0.88%
2.7-11a[a]	9.90	30.04	11.11	28.93	17.42	4.31	4.79%	Cluster 1	0.66%
2.7-12a[a]	7.09	25.98	11.20	24.84	13.93	4.93	3.72%	Cluster 1	0.51%
2.7-13a[a]	8.31	30.19	13.06	29.02	16.40	5.03	3.57%	Cluster 1	0.49%
2.7-14a[a]	8.50	28.91	13.07	27.13	16.15	5.45	3.02%	Cluster 1	0.41%
2.7-15a[a]	4.97	31.60	13.20	30.56	18.54	6.02	2.40%	Cluster 1	0.33%
2.7-16a[a]	15.41	22.71	6.94	20.82	16.76	6.04	2.38%	Cluster 1	0.33%
2.7-17a[a]	19.94	30.80	14.37	28.69	18.17	6.56	1.93%	Cluster 1	0.26%
2.7-18a[a]	8.89	32.14	13.80	31.01	19.10	6.57	1.92%	Cluster 1	0.26%

[a]These conformers were used to calculate the Boltzmann averaged NMR parameters before population refinement

Calculated data for 2.8 (octanol MM conformational search)

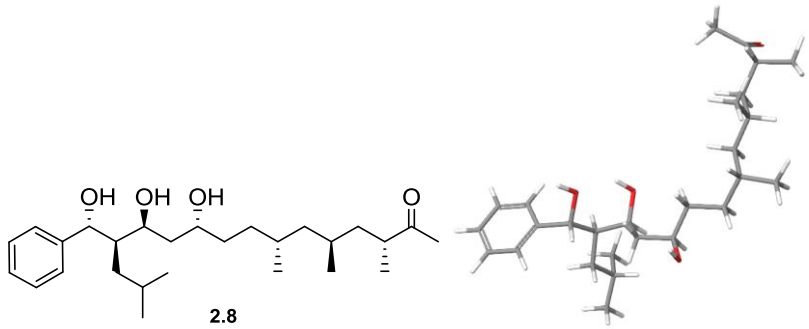

Figure 6.10: 2D structure of **2.8** and 3D structure of its lowest energy conformer **2.8** -1 obtained after population refinement using ^{1}H-^{1}H distances derived from the 2D-ROESY spectrum of the natural product.

Table 6.11: Calculated energies (in kJ mol^{-1}) and population for the major conformers of **2.8** before and after population refinement. All conformers listed were used to calculate the NMR properties of **2.8** after population refinement. For the NOE-refined *ΔΔG* (in kJ mol^{-1}) for each dihedral group, see Table 6.44.

Conformer	$\Delta E^{\mathrm{MMFFs,\,gas}}$	$\Delta E^{\mathrm{BS1,gas}}$	$\Delta G^{\mathrm{BS1,gas}}$	$\Delta E^{\mathrm{BS2,gas}}$	$\Delta E^{\mathrm{BS1,MeOH}}$	$\Delta G_{\mathrm{est.}}^{\mathrm{BS2,MeOH}}$	Population(%)/ $\Delta G_{\mathrm{est.}}^{\mathrm{BS2,MeOH}}$	Dihedral cluster	Population after refinement
2.8-1a	19.96	33.26	18.99	29.96	22.87	13.43	0.09%	Cluster 3	32.83%
2.8-2a[a]	11.13	14.62	4.72	13.70	6.90	4.20	3.83%	Cluster 6	7.51%
2.8-3a[a]	13.02	16.49	6.18	16.14	7.18	4.65	3.20%	Cluster 6	6.27%
2.8-4a[a]	15.13	16.76	5.83	15.59	8.65	4.67	3.17%	Cluster 6	6.22%
2.8-5a[a]	9.04	17.81	6.72	17.45	8.28	4.96	2.82%	Cluster 6	5.54%
2.8-6a[a]	8.67	19.10	7.39	19.37	8.56	5.25	2.51%	Cluster 6	4.93%
2.8-7a[a]	3.64	12.62	5.36	13.09	4.52	5.86	1.96%	Cluster 6	3.85%
2.8-8a[a]	8.88	12.62	5.36	13.09	4.52	5.86	1.96%	Cluster 6	3.85%

2.8-9a	19.05	38.11	25.91	36.07	23.83	17.72	0.02%	Cluster 8	3.84%
2.8-10a[a]	6.26	19.09	8.19	19.22	8.70	6.06	1.81%	Cluster 6	3.55%
2.8-11a	9.70	31.26	21.09	30.00	22.37	19.06	0.01%	Cluster 8	2.23%
2.8-12a[a]	5.63	20.75	2.70	21.63	9.04	0.00	20.92%	Cluster 4	0.61%
2.8-13a[a]	7.31	13.25	0.40	14.04	5.48	1.55	11.19%	Cluster 4	0.33%
2.8-14a[a]	8.40	21.56	6.92	22.42	8.99	3.34	5.43%	Cluster 4	0.16%
2.8-15a[a]	6.87	17.23	4.01	18.21	8.17	4.06	4.07%	Cluster 4	0.12%
2.8-16a[a]	7.22	23.16	7.34	23.57	11.49	4.20	3.84%	Cluster 4	0.11%
2.8-17a[a]	4.73	19.58	7.67	20.52	7.65	4.80	3.01%	Cluster 4	0.09%
2.8-18a[a]	20.65	13.43	3.69	14.27	5.58	4.81	3.00%	Cluster 4	0.09%
2.8-19a[a]	7.76	13.43	3.69	14.27	5.58	4.81	3.00%	Cluster 4	0.09%
2.8-20a[a]	3.07	21.08	9.11	22.64	8.21	5.92	1.92%	Cluster 4	0.06%
2.8-21a[a]	9.16	21.87	9.35	22.78	10.00	6.50	1.52%	Cluster 4	0.04%
2.8-22a[a]	9.28	22.43	10.70	23.16	9.72	6.84	1.32%	Cluster 4	0.04%

[a]These conformers were used to calculate the Boltzmann averaged NMR parameters before population refinement

Calculated data for 2.9 (octanol MM conformational search)

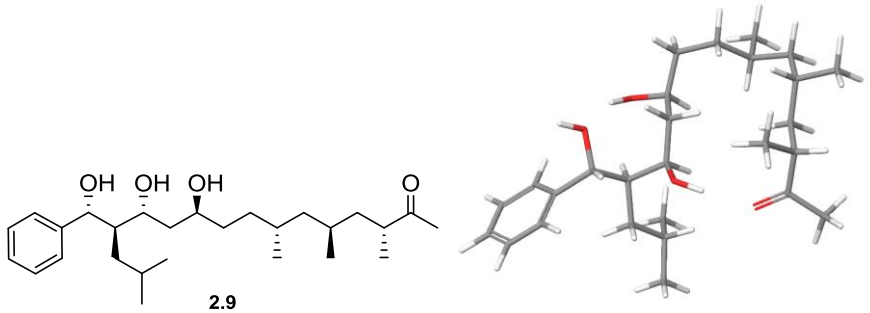

Figure 6.11: 2D structure of **2.9** and 3D structure of its lowest energy conformer **2.9**-1 obtained after population refinement using ^{1}H-^{1}H distances derived from the 2D-ROESY spectrum of the natural product.

Table 6.12: Calculated energies (in kJ mol^{-1}) and population for the major conformers of **2.9** before and after population refinement. All conformers listed were used to calculate the NMR properties of **2.9** after population refinement. For the NOE-refined *ΔΔG* (in kJ mol^{-1}) for each dihedral group, see Table 6.44.

Conformer	$\Delta E^{\text{MMFFs, gas}}$	$\Delta E^{\text{BS1,gas}}$	$\Delta G^{\text{BS1,gas}}$	$\Delta E^{\text{BS2,gas}}$	$\Delta E^{\text{BS1,MeOH}}$	$\Delta G_{\text{est.}}^{\text{BS2,MeOH}}$	Population(%)/ $\Delta G_{\text{est.}}^{\text{BS2,MeOH}}$	Dihedral cluster	Population after refinement
2.9-1a	4.92	1.54	5.55	0.00	2.60	9.21	0.97%	Cluster 11	25.03%
2.9-2a	7.07	7.03	10.47	10.53	0.07	11.15	0.45%	Cluster 5	15.97%
2.9-3a	20.28	26.91	13.46	24.50	17.44	5.73	3.98%	Cluster 17	8.96%
2.9-4a[a]	17.76	9.78	2.02	11.19	4.29	2.07	17.43%	Cluster 18	7.95%
2.9-5a	20.00	25.45	18.06	23.46	18.37	13.13	0.20%	Cluster 8	4.14%
2.9-6a	19.68	25.57	17.38	24.78	19.81	14.98	0.09%	Cluster 19	4.12%
2.9-7a	15.02	11.98	10.72	15.40	6.21	12.51	0.26%	Cluster 4	3.85%
2.9-8a	18.80	25.88	17.10	24.42	19.46	13.36	0.18%	Cluster 8	3.76%
2.9-9a	5.87	0.00	8.07	1.33	0.00	13.55	0.17%	Cluster 8	3.50%

2.9-10a[a]	17.25	8.48	0.00	9.36	3.46	0.00	40.15%	Cluster 6	3.00%
2.9-11a[a]	17.38	10.34	4.03	11.42	4.17	3.09	11.52%	Cluster 7	0.81%
2.9-12a[a]	17.76	14.11	5.97	17.41	4.68	3.97	8.09%	Cluster 7	0.57%
2.9-13a[a]	17.51	17.02	8.25	18.96	8.20	5.51	4.33%	Cluster 6	0.32%

[a]These conformers were used to calculate the Boltzmann averaged NMR parameters before population refinement

Calculated data for 2.10 (octanol MM conformational search)

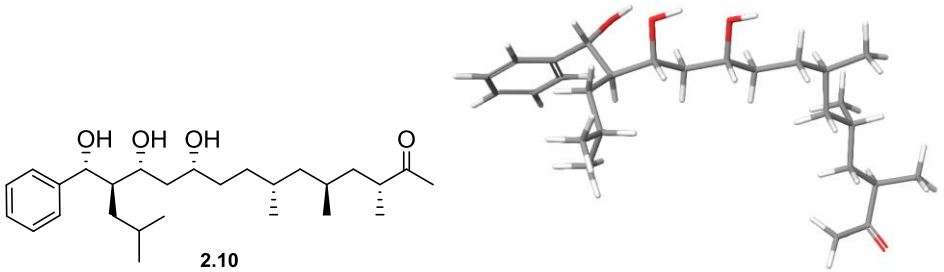

Figure 6.12: 2D structure of **2.10** and 3D structure of its lowest energy conformer **2.10**-1 obtained after population refinement (constraint $\Sigma(\Delta\Delta G)^2$ =400) using ^{1}H-^{1}H distances derived from the 2D-ROESY spectrum of the natural product.

Table 6.13: Calculated energies (in kJ mol^{-1}) and population for the major conformers of **2.10** before and after population refinement. All conformers listed were used to calculate the NMR properties of **2.10** after population refinement. For the NOE-refined $\Delta\Delta G$ (in kJ mol^{-1}) for each dihedral group, see Table 6.43.

Conformer	$\Delta E^{\text{MMFFs, gas}}$	$\Delta E^{\text{BS1,gas}}$	$\Delta G^{\text{BS1,gas}}$	$\Delta E^{\text{BS2,gas}}$	$\Delta E^{\text{BS1,MeOH}}$	$\Delta G_{\text{est.}}^{\text{BS2,MeOH}}$	Population(%)/ $\Delta G_{\text{est.}}^{\text{BS2,MeOH}}$	Dihedral cluster	Population after refinement $\Sigma(\Delta\Delta G)^2$ =25
2.10-1a^{a-g}	9.37	19.36	0.72	17.05	11.35	0.00	22.82%	Cluster 15	17.62%
2.10-2a^{a-g}	8.75	16.88	2.11	14.72	8.69	1.35	13.24%	Cluster 15	10.22%
2.10-3a^{a-f}	9.77	17.85	3.21	15.75	9.53	2.37	8.76%	Cluster 15	6.76%
2.10-4a^{a-e}	8.20	19.04	2.86	16.62	12.37	3.34	5.92%	Cluster 6	4.79%
2.10-5a^{a-e}	10.22	21.08	2.66	18.42	14.84	3.35	5.90%	Cluster 6	4.77%
2.10-6a^{a-i}	19.73	23.28	5.93	22.04	12.90	3.89	4.74%	Cluster 3	3.07%
2.10-7a^{a-e}	19.64	27.40	6.06	25.56	17.97	4.37	3.90%	Cluster 6	3.15%

2.10-8a[a – c]	7.72	22.65	6.53	19.94	14.39	5.16	2.84%	Cluster 15	2.19%
2.10-9a[a – c]	6.07	17.68	5.41	15.69	10.42	5.75	2.24%	Cluster 15	1.73%
2.10-10a[a – c]	8.67	17.48	6.14	15.40	9.84	6.00	2.02%	Cluster 15	1.56%
2.10-11a[a – c]	9.66	18.89	6.37	16.53	11.44	6.14	1.91%	Cluster 15	1.48%
2.10-12a[a – f]	19.70	25.33	9.54	23.34	14.38	6.18	1.88%	Cluster 10	0.84%
2.10-13a[a – f]	9.36	39.67	16.31	33.54	26.40	6.51	1.65%	Cluster 13	1.10%
2.10-14a[a – f]	7.72	36.51	15.54	30.12	24.94	7.15	1.27%	Cluster 13	0.85%
2.10-15a[a, d]	16.78	25.68	8.36	23.17	17.54	7.29	1.20%	Cluster 6	0.97%
2.10-16a[b – i]	7.15	32.34	11.66	27.36	23.45	7.37	1.16%	Cluster 8	6.14%
2.10-17a[b – i]	6.44	31.56	12.19	26.61	22.97	8.24	0.82%	Cluster 8	4.32%
2.10-18a[b – i]	9.72	34.25	13.22	29.48	25.17	8.95	0.62%	Cluster 8	3.25%
2.10-19a[b – i]	8.75	34.58	14.31	29.62	25.81	10.18	0.37%	Cluster 8	1.98%
2.10-20a[b – h]	9.58	36.84	15.43	31.93	26.99	10.25	0.36%	Cluster 8	1.92%
2.10-21a[b – g]	9.42	33.70	14.90	28.44	24.85	10.38	0.34%	Cluster 8	1.82%
2.10-22a[b – g]	9.90	38.91	15.98	33.50	29.19	10.42	0.34%	Cluster 8	1.79%
2.10-23a[b, e, f, g]	8.40	35.48	16.71	30.85	25.10	11.28	0.24%	Cluster 8	1.27%
2.10-24a[b, e, f, g]	8.70	33.68	14.99	28.38	25.70	11.30	0.24%	Cluster 8	1.26%
2.10-25a[c, f]	14.84	40.05	17.10	35.00	30.71	12.29	0.16%	Cluster 7	0.21%
2.10-26[da, e]	8.98	34.25	14.29	28.07	24.94	8.39	0.77%	Cluster 13	0.51%
2.10-27a[d, e]	9.05	39.93	17.03	33.52	28.16	8.45	0.75%	Cluster 13	0.50%
2.10-28a[d]	12.90	40.60	18.75	34.40	27.26	8.79	0.66%	Cluster 13	0.44%
2.10-29a[d]	7.23	35.87	17.11	29.67	24.29	8.91	0.62%	Cluster 13	0.42%
2.10-30a[d]	9.03	36.42	16.06	29.66	26.66	9.11	0.58%	Cluster 13	0.38%
2.10-31a[d]	20.82	26.56	10.63	24.64	15.58	7.32	1.19%	Cluster 10	0.53%
2.10-32a[d]	16.57	32.51	10.42	27.24	25.54	7.76	0.99%	Cluster 10	0.44%
2.10-33a[d]	9.72	36.39	16.51	30.09	26.42	9.84	0.43%	Cluster 13	0.29%
2.10-34a[d – f]	19.01	48.48	29.44	43.00	38.14	23.19	0.00%	Cluster 16	0.00%
2.10-35a[e, f]	9.67	34.10	25.76	30.20	26.73	24.07	0.00%	Cluster 16	0.00%
2.10-36a[e, f]	9.34	35.61	15.61	30.59	27.31	11.87	0.19%	Cluster 8	1.00%

2.10-37a[e, f]	20.83	36.15	16.43	31.54	26.79	12.05	0.18%	Cluster 8	0.93%
2.10-38a[f – i]	17.18	43.58	24.39	39.30	33.20	19.30	0.01%	Cluster 17	0.01%
2.10-39a[f – i]	9.99	40.57	23.43	36.84	31.08	19.79	0.01%	Cluster 17	0.01%
2.10-40a[f]	7.71	36.15	16.44	31.54	26.79	12.05	0.18%	Cluster 8	0.93%
2.10-41a[g – i]	16.98	53.69	32.30	46.48	40.31	21.29	0.00%	Cluster 14	0.00%
2.10-42a[g – i]	17.76	44.83	27.96	40.41	34.46	22.77	0.00%	Cluster 5	0.00%
2.10-43a[g]	18.84	57.76	37.98	49.34	45.91	27.29	0.00%	Cluster 14	0.00%
2.10-44a[h, i]	18.58	43.18	24.14	38.12	31.76	17.24	0.02%	Cluster 18	0.02%

Conformer populations after population refinement (continues)

conformer	$\Sigma(\Delta\Delta G)^2$ =100	$\Sigma(\Delta\Delta G)^2$ =225	$\Sigma(\Delta\Delta G)^2$ =400	$\Sigma(\Delta\Delta G)^2$ =625	$\Sigma(\Delta\Delta G)^2$ =900	$\Sigma(\Delta\Delta G)^2$ =1600	$\Sigma(\Delta\Delta G)^2$ =2500
2.10-1a	15.15%	6.60%	4.00%	3.99%	2.19%	0.29%	0.03%
2.10-2a	8.79%	3.83%	2.32%	2.32%	1.27%	0.17%	0.01%
2.10-3a	5.81%	2.53%	1.53%	1.53%	0.84%	0.11%	0.01%
2.10-4a	2.91%	5.27%	3.87%	0.77%	1.17%	0.06%	0.00%
2.10-5a	2.90%	5.25%	3.85%	0.77%	1.16%	0.06%	0.00%
2.10-6a	4.72%	6.29%	11.63%	14.44%	14.02%	17.55%	18.16%
2.10-7a	1.92%	3.47%	2.55%	0.51%	0.77%	0.04%	0.00%
2.10-8a	1.88%	0.82%	0.50%	0.50%	0.27%	0.04%	0.00%
2.10-9a	1.49%	0.65%	0.39%	0.39%	0.21%	0.03%	0.00%
2.10-10a	1.34%	0.58%	0.35%	0.35%	0.19%	0.03%	0.00%
2.10-11a	1.27%	0.55%	0.34%	0.33%	0.18%	0.02%	0.00%
2.10-12a	1.39%	2.71%	1.29%	1.36%	1.10%	0.10%	0.01%
2.10-13a	1.63%	5.36%	2.69%	1.80%	0.52%	0.04%	0.00%
2.10-14a	1.26%	4.13%	2.07%	1.38%	0.40%	0.03%	0.00%
2.10-15a	0.59%	1.07%	0.79%	0.16%	0.24%	0.01%	0.00%
2.10-16a	5.80%	4.85%	7.45%	7.40%	6.66%	6.91%	6.94%
2.10-17a	4.08%	3.41%	5.24%	5.21%	4.69%	4.86%	4.89%
2.10-18a	3.07%	2.57%	3.94%	3.92%	3.52%	3.66%	3.67%

2.10-19a	1.87%	1.56%	2.40%	2.38%	2.14%	2.23%	2.24%
2.10-20a	1.81%	1.52%	2.33%	2.31%	2.08%	2.16%	2.17%
2.10-21a	1.72%	1.44%	2.21%	2.19%	1.97%	2.05%	2.06%
2.10-22a	1.69%	1.41%	2.17%	2.16%	1.94%	2.01%	2.02%
2.10-23a	1.20%	1.00%	1.54%	1.53%	1.38%	1.43%	1.43%
2.10-24a	1.19%	0.99%	1.53%	1.52%	1.37%	1.42%	1.42%
2.10-25a	7.86%	0.62%	1.11%	2.00%	1.10%	0.10%	0.01%
2.10-26a	0.76%	2.51%	1.26%	0.84%	0.24%	0.02%	0.00%
2.10-27a	0.75%	2.45%	1.23%	0.82%	0.24%	0.02%	0.00%
2.10-28a	0.65%	2.13%	1.07%	0.71%	0.21%	0.01%	0.00%
2.10-29a	0.62%	2.03%	1.02%	0.68%	0.20%	0.01%	0.00%
2.10-30a	0.57%	1.87%	0.94%	0.63%	0.18%	0.01%	0.00%
2.10-31a	0.88%	1.71%	0.81%	0.86%	0.70%	0.06%	0.01%
2.10-32a	0.73%	1.43%	0.68%	0.72%	0.58%	0.05%	0.00%
2.10-33a	0.42%	1.39%	0.70%	0.47%	0.13%	0.01%	0.00%
2.10-34a	0.00%	1.22%	6.20%	6.60%	0.02%	0.01%	0.00%
2.10-35a	0.00%	0.85%	4.35%	4.63%	0.01%	0.00%	0.00%
2.10-36a	0.94%	0.79%	1.21%	1.20%	1.08%	1.12%	1.13%
2.10-37a	0.88%	0.73%	1.13%	1.12%	1.01%	1.04%	1.05%
2.10-38a	0.02%	0.03%	0.07%	4.59%	3.43%	4.32%	4.39%
2.10-39a	0.01%	0.03%	0.05%	3.78%	2.82%	3.56%	3.61%
2.10-40a	0.88%	0.73%	1.12%	1.12%	1.01%	1.04%	1.05%
2.10-41a	0.01%	0.01%	0.03%	0.10%	19.11%	20.94%	21.21%
2.10-42a	0.01%	0.01%	0.02%	0.03%	10.03%	10.13%	10.14%
2.10-43a	0.00%	0.00%	0.00%	0.01%	1.70%	1.86%	1.89%
2.10-44a	0.04%	0.07%	0.15%	0.30%	0.25%	4.74%	4.89%

[a]These conformers were used to calculate the Boltzmann averaged NMR parameters before population refinement

[b]These conformers were used to calculate the Boltzmann averaged NMR parameters after population refinement using a constraint $(\Sigma(\Delta\Delta G)^2) = 25$

[c]These conformers were used to calculate the Boltzmann averaged NMR parameters after population refinement using a constraint $(\Sigma(\Delta\Delta G)^2) = 100$

[d]These conformers were used to calculate the Boltzmann averaged NMR parameters after population refinement using a constraint ($\Sigma(\Delta\Delta G)^2$) = 225

[e]These conformers were used to calculate the Boltzmann averaged NMR parameters after population refinement using a constraint ($\Sigma(\Delta\Delta G)^2$) = 400

[f]These conformers were used to calculate the Boltzmann averaged NMR parameters after population refinement using a constraint ($\Sigma(\Delta\Delta G)^2$) = 625

[g]These conformers were used to calculate the Boltzmann averaged NMR parameters after population refinement using a constraint ($\Sigma(\Delta\Delta G)^2$) = 900

[h]These conformers were used to calculate the Boltzmann averaged NMR parameters after population refinement using a constraint ($\Sigma(\Delta\Delta G)^2$) = 1600

[i]These conformers were used to calculate the Boltzmann averaged NMR parameters after population refinement using a constraint ($\Sigma(\Delta\Delta G)^2$) = 2500

Calculated data for fragment B studies (2.10 and 2.12 – 2.14, gas conformational search)

The conformational searches for compounds **2.10** and **2.12** – **2.14** were conducted with octanol as solvent (500,000 iterations). Total CPU time of ~ 11220 hours (~1.3 years) were spent on computing these compounds.

Table 6.14: A summary of numbers of conformers found (starting from octanol conformational search) at each stage of calculations for compound **2.10** and **2.12 – 2.14**.

Compound	Conformer Found	Non-Redundant Conformer	Conformers < 10 kJ mol^{-1}	Conformers Sampled by DFT	Conformers used for NMR Calculations
2.10	1353	1015	42	100	9
2.12	466	347	23	100	15
2.13	926	633	47	100	10
2.14	1641	1186	84	168	13

Calculated data for 2.12 (gas MM conformational search)

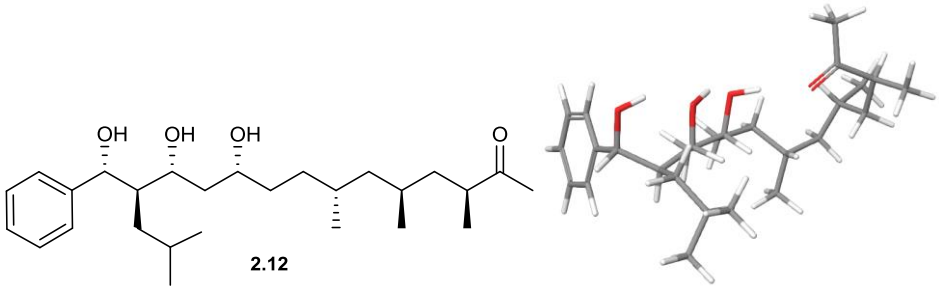

Figure 6.13: 2D structure of **2.12** and 3D structure of its lowest energy conformer **2.12-**1.

Table 6.15: Calculated energies (in kJ mol^{-1}) for the major conformers of **2.12** with a combined population of 95.1%.

Conformer	$\Delta E^{\text{MMFFs, gas}}$	$\Delta E^{\text{BS1,gas}}$	$\Delta G^{\text{BS1,gas}}$	$\Delta E^{\text{BS2,gas}}$	$\Delta E^{\text{BS1,MeOH}}$	$\Delta G_{\text{est.}}^{\text{BS2,MeOH}}$	Population (%)/ $\Delta G_{\text{est.}}^{\text{BS2,MeOH}}$
2.12-1	15.99	1.81	0.01	1.65	0.98	0.00	23.75%
2.12-2	5.33	0.00	0.00	0.00	0.00	0.98	16.00%
2.12-3	4.86	0.55	0.33	0.96	0.28	1.45	13.23%
2.12-4	9.50	3.85	2.08	3.97	2.39	1.72	11.85%
2.12-5	11.97	4.65	1.54	6.02	2.87	2.10	10.17%
2.12-6	11.50	8.07	4.35	8.95	5.03	3.18	6.58%
2.12-7	18.27	4.81	0.85	4.57	7.65	4.44	3.96%
2.12-8	6.93	3.74	4.04	3.01	6.06	6.60	1.65%
2.12-9	9.37	16.83	9.51	13.51	16.62	6.97	1.43%
2.12-10	17.55	6.13	3.77	5.42	9.08	6.99	1.41%
2.12-11	6.59	4.44	3.02	4.01	7.91	7.04	1.39%
2.12-12	12.57	13.73	8.81	10.97	14.40	7.70	1.06%
2.12-13	8.84	19.71	12.22	16.82	17.41	8.00	0.94%
2.12-14	11.69	20.00	13.84	16.96	16.34	8.13	0.89%
2.12-15	8.90	17.38	14.72	14.01	13.78	8.72	0.70%

Calculated data for 2.13 (gas MM conformational search)

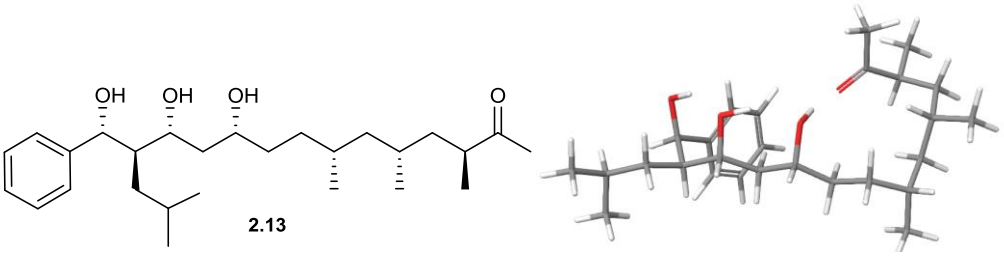

Figure 6.14: 2D structure of **2.13** and 3D structure of its lowest energy conformer **2.13**-1.

Table 6.16: Calculated energies (in kJ mol^{-1}) for the major conformers of **2.13** with a combined population of 96.8%.

Conformer	$\Delta E^{\text{MMFFs, gas}}$	$\Delta E^{\text{BS1,gas}}$	$\Delta G^{\text{BS1,gas}}$	$\Delta E^{\text{BS2,gas}}$	$\Delta E^{\text{BS1,MeOH}}$	$\Delta G_{\text{est.}}^{\text{BS2,MeOH}}$	Population (%)/ $\Delta G_{\text{est.}}^{\text{BS2,MeOH}}$
2.13-1	0.00	0.00	0.00	0.79	0.26	0.00	60.64%
2.13-2	7.11	0.82	5.09	1.10	0.44	3.93	12.39%
2.13-3	7.77	3.36	4.42	5.46	2.58	4.68	9.17%
2.13-4	0.37	0.16	5.89	1.24	0.48	6.23	4.90%
2.13-5	7.61	0.13	7.63	0.00	0.00	6.32	4.73%
2.13-6	6.68	3.26	9.34	4.26	2.37	8.40	2.04%
2.13-7	20.27	20.03	17.92	18.93	14.53	10.26	0.96%
2.13-8	5.43	7.28	13.21	6.61	6.65	10.86	0.75%
2.13-9	14.20	2.71	10.73	2.68	3.96	10.91	0.74%
2.13-10	6.72	17.04	18.67	14.72	13.76	12.02	0.47%

Calculated data for 2.14 (gas MM conformational search)

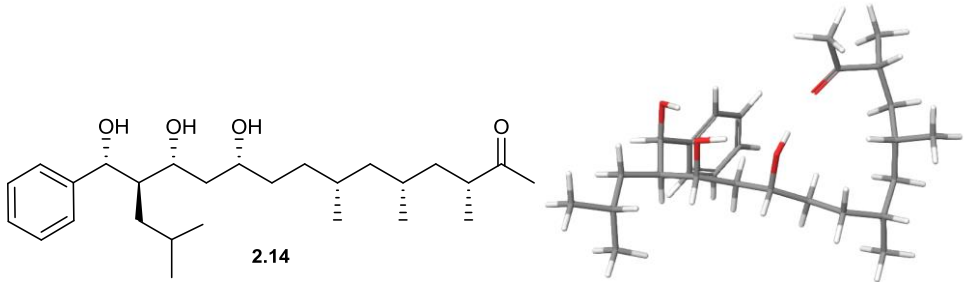

Figure 6.15: 2D structure of **2.14** and 3D structure of its lowest energy conformer **2.14**-1.

Table 6.17: Calculated energies (in kJ mol^{-1}) for the major conformers of **2.14** with a combined population of 88.8%.

Conformer	$\Delta E^{\text{MMFFs, gas}}$	$\Delta E^{\text{BS1,gas}}$	$\Delta G^{\text{BS1,gas}}$	$\Delta E^{\text{BS2,gas}}$	$\Delta E^{\text{BS1,MeOH}}$	$\Delta G_{\text{est.}}^{\text{BS2,MeOH}}$	Population (%)/ $\Delta G_{\text{est.}}^{\text{BS2,MeOH}}$
2.14-1	8.6	0.00	0.00	0.09	0.00	0.00	40.30%
2.14-2	7.8	3.05	1.48	4.22	2.32	1.83	19.23%
2.14-3	19.3	9.94	8.18	8.58	8.21	5.00	5.35%
2.14-4	5.6	16.42	12.09	13.05	13.31	5.53	4.33%
2.14-5	8.8	5.88	8.24	4.32	4.89	5.59	4.21%
2.14-6	7.4	3.30	4.52	4.96	2.93	5.72	4.00%
2.14-7	20.5	20.85	15.73	18.17	14.47	6.58	2.82%
2.14-8	18.8	19.88	15.93	17.55	12.98	6.61	2.79%
2.14-9	7.8	6.91	8.07	8.12	5.04	7.31	2.10%
2.14-10	9.9	0.21	7.06	0.00	1.42	7.97	1.62%
2.14-11	9.0	8.38	10.26	7.13	7.50	8.04	1.57%
2.14-12	9.0	21.05	16.32	18.51	16.70	9.35	0.92%
2.14-13	9.6	16.09	15.19	13.38	13.07	9.37	0.92%

Calculated data for fragment B studies (2.10 and 2.12 – 2.14, octanol conformational search)

The conformational searches for compounds **2.10** and **2.12** – **2.14** were conducted with octanol as solvent (100,000 iterations, except compound **2.10** which requires 300,000 iterations in order to find conformers below 10 kJ mol^{-1} more than 10 times on average). Total CPU time of ~ 21456 hours (~2.5 years) were spent on computing these compounds.

Table 6.18: A summary of numbers of conformers found (starting from octanol conformational search) at each stage of calculations for compound **2.10** and **2.12 – 2.14**.

Compound	Conformer Found	Non-Redundant Conformer	Conformers < 10 kJ mol^{-1}	Conformers Sampled by DFT	Conformers used for NMR Calculations
2.10	8794	5350	107	214	18
2.12	3060	1844	108	216	15
2.13	3129	1871	117	234	18
2.14	2086	1238	152	304	33

Calculated data of 2.12 (octanol MM conformational search)

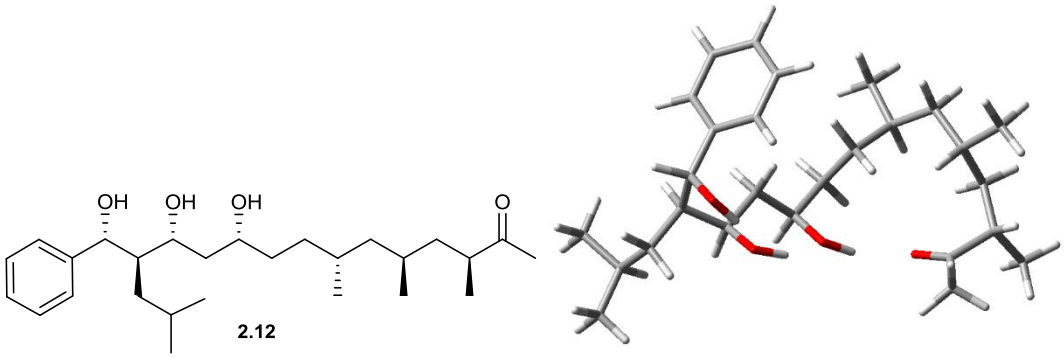

Figure 6.16: 2D structure of **2.12** and 3D structure of its lowest energy conformer **2.12**-1.

Table 6.19: Calculated energies (in kJ mol^{-1}) for the major conformers of **2.12** with a combined population of 90.2%.

Conformer	$\Delta E^{\text{MMFFs, gas}}$	$\Delta E^{\text{BS1,gas}}$	$\Delta G^{\text{BS1,gas}}$	$\Delta E^{\text{BS2,gas}}$	$\Delta E^{\text{BS1,MeOH}}$	$\Delta G_{\text{est.}}^{\text{BS2,MeOH}}$	Population (%)/ $\Delta G_{\text{est.}}^{\text{BS2,MeOH}}$
2.12-1a	1.9	0.0	0.0	0.0	0.0	0.0	18.4%
2.12-2a	1.2	0.6	0.3	1.0	0.3	0.5	15.2%
2.12-3a	2.5	3.8	2.1	4.0	2.4	0.7	13.6%
2.12-4a	5.7	4.7	1.5	6.0	2.9	1.1	11.7%
2.12-5a	6.2	4.7	1.5	6.0	2.9	1.1	11.7%
2.12-6a	3.9	8.1	4.4	9.0	5.0	2.2	7.5%
2.12-7a	3.9	20.9	14.6	17.2	15.4	5.5	2.0%
2.12-8a	5.2	3.7	4.0	3.0	6.1	5.6	1.9%
2.12-9a	4.3	16.8	9.5	13.5	16.6	6.0	1.6%
2.12-10a	5.9	4.4	3.0	4.0	7.9	6.1	1.6%
2.12-11a	15.8	5.3	6.1	4.5	6.9	6.9	1.1%
2.12-12a	1.8	19.7	12.2	16.8	17.4	7.0	1.1%
2.12-13a	4.5	20.0	13.8	17.0	16.3	7.1	1.0%
2.12-14a	18.9	28.4	16.4	28.3	19.3	7.2	1.0%
2.12-15a	2.0	17.4	14.7	14.0	13.8	7.7	0.8%

Calculated data of 2.13 (octanol MM conformational search)

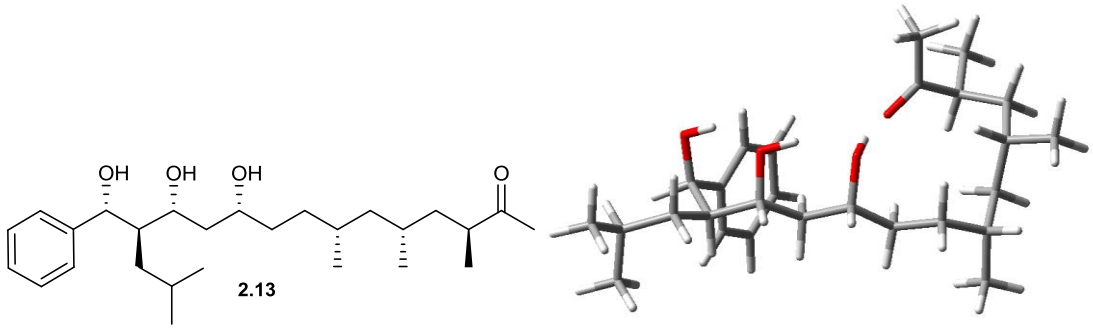

Figure 6.17: 2D structure of **2.13** and 3D structure of its lowest energy conformer **2.13**-1.

Table 6.20: Calculated energies (in kJ mol^{-1}) for the major conformers of **2.13** with a combined population of 80.8%.

Conformer	$\Delta E^{\text{MMFFs, gas}}$	$\Delta E^{\text{BS1,gas}}$	$\Delta G^{\text{BS1,gas}}$	$\Delta E^{\text{BS2,gas}}$	$\Delta E^{\text{BS1,MeOH}}$	$\Delta G_{\text{est.}}^{\text{BS2,MeOH}}$	Population (%)/ $\Delta G_{\text{est.}}^{\text{BS2,MeOH}}$
2.13-1a	0	1.6	0.0	1.8	1.9	0.0	19.9%
2.13-2a	5.4	0.7	2.2	1.1	0.4	1.8	9.8%
2.13-3a	6.5	3.2	1.5	5.5	2.6	2.5	7.2%
2.13-4a	6.8	3.9	5.1	4.0	2.2	2.8	6.3%
2.13-5a	11.8	22.8	13.3	20.9	15.7	3.7	4.5%
2.13-6a	0.8	0.0	3.0	1.2	0.5	4.1	3.9%
2.13-7a	5.7	0.0	4.7	0.0	0.0	4.1	3.7%
2.13-8a	15.3	25.9	16.1	23.2	17.2	4.3	3.5%
2.13-9a	7.2	21.2	13.6	19.2	14.9	4.6	3.1%
2.13-10a	12.3	21.2	13.6	19.2	14.9	4.9	2.8%
2.13-11a	16.2	27.4	13.7	26.0	20.6	5.1	2.5%
2.13-12a	17.3	26.5	16.1	24.5	18.0	5.3	2.4%
2.13-13a	4.3	26.7	15.1	25.9	18.3	5.4	2.3%
2.13-14a	5.7	6.9	5.6	9.2	4.9	5.6	2.1%
2.13-15a	15.5	26.7	17.7	24.0	18.0	5.7	2.0%
2.13-16a	7.9	8.3	8.6	9.2	5.2	5.8	1.9%
2.13-17a	2.3	3.1	6.4	4.3	2.4	6.2	1.6%
2.13-18a	14.8	46.2	25.7	40.3	33.3	6.4	1.5%

Calculated data of 2.14 (octanol MM conformational search)

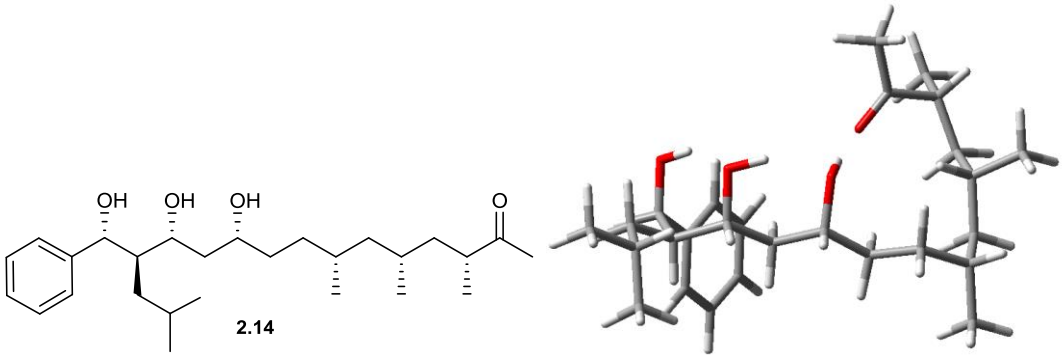

Figure 6.18: 2D structure of **2.14** and 3D structure of its lowest energy conformer **2.14**-1.

Table 6.21: Calculated energies (in kJ mol^{-1}) for the major conformers of **2.14** with a combined population of 83.7%.

Conformer	$\Delta E^{MMFFs,gas}$	$\Delta E^{BS1,gas}$	$\Delta G^{BS1,gas}$	$\Delta E^{BS2,gas}$	$\Delta E^{BS1,MeOH}$	$\Delta G_{est.}^{BS2,MeOH}$	Population (%)/ $\Delta G_{est.}^{BS2,MeOH}$
2.14-1a	8.3	0.4	0.0	0.9	0.3	0.0	13.5%
2.14-2a	14.7	18.1	10.5	16.1	11.4	1.2	8.3%
2.14-3a	13.4	3.4	1.5	5.1	2.7	1.8	6.5%
2.14-4a	17.6	27.2	14.1	26.2	17.0	2.4	5.2%
2.14-5a	13.5	20.2	12.1	18.2	13.3	2.7	4.6%
2.14-6a	13.8	22.3	13.4	20.5	14.1	2.8	4.4%
2.14-7a	18.6	24.5	15.7	22.2	14.8	3.2	3.7%
2.14-8a	15.5	18.5	12.3	16.6	12.0	3.3	3.5%
2.14-9a	13.1	16.5	11.9	12.4	12.8	3.5	3.3%
2.14-10a	14.1	17.0	13.4	14.8	10.3	3.9	2.8%
2.14-11a	13.8	38.8	20.1	34.3	27.7	3.9	2.8%
2.14-12a	9.8	3.8	5.1	4.4	3.0	4.3	2.4%
2.14-13a	14.8	26.8	15.3	25.3	18.0	4.4	2.3%
2.14-14a	17.8	26.6	15.5	24.5	18.6	4.8	2.0%
2.14-15a	12.2	6.2	8.2	5.2	5.2	5.6	1.4%
2.14-16a	13.5	3.6	4.5	5.8	3.3	5.7	1.3%
2.14-17a	18.6	26.0	17.4	23.7	17.3	5.7	1.3%
2.14-18a	15.6	34.3	22.1	29.2	25.1	7.2	1.3%
2.14-19a	17.5	41.8	24.2	35.9	30.5	6.3	1.1%
2.14-20a	18.8	23.8	15.8	21.4	17.5	6.5	1.0%
2.14-21a	20.1	29.9	17.4	28.6	20.8	6.5	1.0%
2.14-22a	19.7	27.4	14.2	23.4	24.3	6.6	1.0%
2.14-23a	12.8	18.0	15.8	15.7	11.5	6.6	1.0%
2.14-24a	19.3	24.5	17.0	23.2	16.1	6.7	0.9%
2.14-25a	13.3	10.3	10.7	9.6	7.4	6.7	0.9%
2.14-26a	18.6	37.2	21.6	31.6	28.4	6.7	0.9%
2.14-27a	13.8	24.4	16.3	22.2	17.8	6.8	0.9%
2.14-28a	20.2	30.5	19.4	28.6	20.6	7.0	0.8%

2.14-29a	15.4	34.3	22.1	29.2	25.1	7.2	0.8%
2.14-30a	19.7	25.2	18.2	23.2	16.9	7.2	0.7%
2.14-31a	13.2	39.8	25.9	34.1	27.5	7.3	0.7%
2.14-32a	13.7	25.2	18.3	24.2	15.9	7.4	0.7%
2.14-33a	13.5	40.1	26.0	34.3	27.8	7.4	0.7%

General NMR procedures

Determination of scalar coupling constants.

^{1}H-^{1}H scalar coupling constants were measured manually from multiplets in ^{1}H spectra and selective 1-dimensional TOCSY spectra. For the natural product these were also checked against the homonuclear 2D*J* NMR spectrum provided by Sherman *et al.*[95] To maximise the accuracy of the coupling constants (experimental error < 0.5 Hz), spin simulations were performed using the MestreNova (Version 11.0.2-18153) Spin Simulation module. Methylene protons (H_{12a}/H_{12b}, H_{10a}/H_{10b}, H_{7a}/H_{7b} and H_{5a}/H_{5b}) for each diastereomer computed were assigned based on the best fit to the experimental scalar coupling constants of the natural product.

^{1}H-^{13}C scalar coupling constants of synthetic compounds **2.1** and **2.17** were measured from the Accordion In-Phase and Anti Phase (IPAP) HSQMBC NMR spectra[174] (~19 mg in 0.7 mL CD_3OD, 12 scans, 1600 f1 increments and 8192 t2 data points, f1 spectra width 224.5 ppm (28249Hz), f2 spectra width 7 ppm (3501Hz), matching J_{LR} from 3Hz to 8 Hz) Both IP and AP spectra were recorded interleaved. The sum and difference spectra were created by adding/subtracting the AP and IP spectra. The offset between the sum (red, Figure 6.19) and the difference (blue, Figure 6.19) spectra allows the extraction of the ^{1}H-^{13}C scalar coupling constants.

$^{3}J_{H13\text{-}C1'}$ = 4.2 Hz

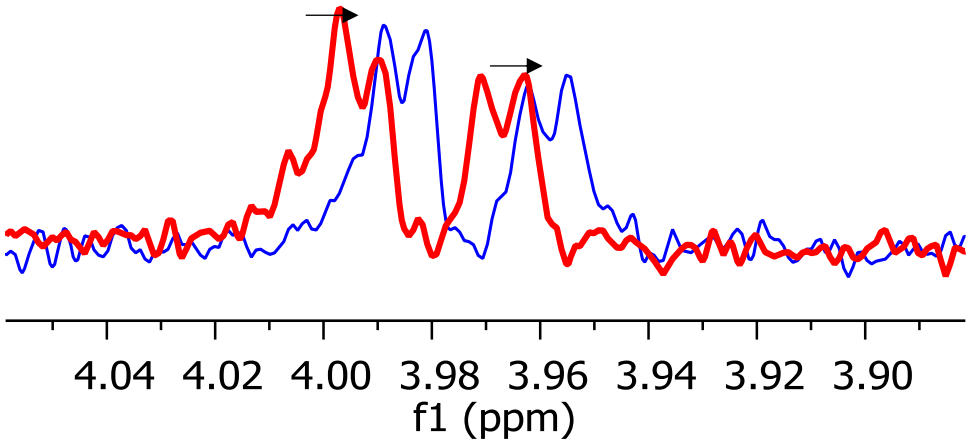

Figure 6.19: Overlay of the sum (red) and difference (blue) HSQMBC traces for C-1' (76.8 ppm) to H-13 (3.98 ppm) of compound **2.17**. The traces were taken at 76.8 ppm and the offset between the traces suggest $^{3}J_{H13\text{-}C1'}$ = 4.2 Hz.

Determination of ^{1}H-^{1}H distances.

The interproton distances of baulamycin A were determined using Equation 6.9[52] and the 2D ROESY spectrum provided by *Sherman et al.*[95] (reprocessed using the following parameters: f1 phasing: PH0 = 178.97°, PH1 = 4.14°; f2 phasing: PH0 = -165.92° and PH1 = 1.72°; Apodisation along t1: sine bell 90.00° and sine squre 90.00°; Apodisation along t2: sine bell 90.00°; t2 zero fill to 2K and t1 zero fill to 2K and forward linear predict from 128 to 384 data points; Polynomial fit baseline correction was applied to both f1 and f2.)

$$r_{NOE} = r_{ref}\left[\frac{\eta_{NOE}}{\eta_{ref}}\right]^{-\frac{1}{6}} \qquad \textbf{Equation 6.9}$$

Where r is interproton distance and η is NOE signal intensity derived from the 2D-ROESY spectrum In order to compare ROE intensities across all traces taken from the 2D ROESY spectrum and correct for different rates of external relaxation for each proton in the molecule, peak amplitude normalisation for improved cross-relaxation (PANIC) [53,175-176] was employed by setting the irradiated peak in each slice of the 2D ROESY spectrum to a single value (arbitrarily 1000 intensity units in this analysis) as Figure 6.20 shows.

Butts *et al.* have reported that by using a known distance between two protons as the reference distance in the same molecule, r_{ref}, the distance between other dipolar coupled protons for the rest of the molecule, r_{NOE}, can be determined by comparing the relative intensity of the peak of interest (η_{NOE}) and the relative intensity of the reference distance (η_{ref}).[51-52] For each diastereoisomer studied computationally (compound **2.6**, **2.7** – **2.10**, the reference distance (r_{ref}) was chosen to be the distance between methylene protons $H1_{2a}$ and H_{12b}. The reference distances for each diastereoisomer were optimised to give the best fit to the natural product data.

Slices were taken for all resolved resonances in the processed 2D ROESY spectrum for baulamycin A. Figure 6.20 shows the slice of H_{12a} of baulamycin A, showing a correlation to other protons within ~4 Å such as $H_{1'}$ at 4.47 ppm. Taking H_{12a}-H_{12b} as the reference distance (r_{ref}, 1.76 Å), the corresponding H_{12a}-H_{12b} intensity (η_{ref}, 207.99), and the H_{12a}-$H_{1'}$ intensity (η_{NOE}, 23.31), one could calculate the H_{12a}-$H_{1'}$ distance using **Equation 6.9**:

$$r_{H12a-H1'} = 1.76\ \text{Å} \times \left[\frac{23.31}{207.99}\right]^{-\frac{1}{6}} = 2.53\ \text{Å}$$

This H_{12a}-$H_{1'}$ distance was subsequently averaged with the $H_{1'}$-H_{12a} distance (2.66 Å) determined from the slice of $H_{1'}$ from the 2D-ROESY spectrum to give the final experimental value of 2.59 Å.

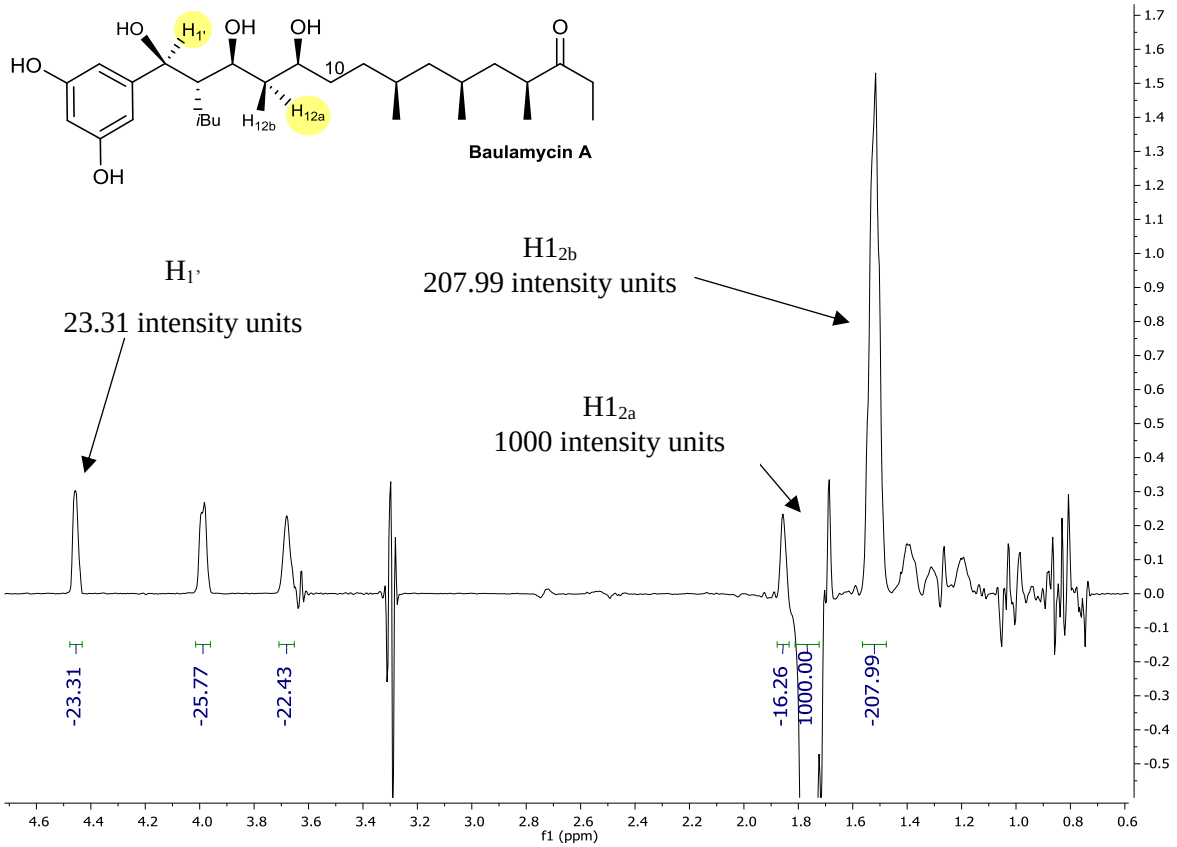

Figure 6.20: 2D-ROESY f2 slice at f1 chemical shifts (700MHz, CD_3OD) of $H_{1'}$ of baulamycin A with blue integrals as the intensity units of each proton.

To determine the distance from a given proton to pairs of methylene protons H_{15} and H_{10}, the intensities of peaks corresponding to H_{15} (or H_x-H_{10}) were divided by 2 to correct for the two protons contributing to the signals. Distances from any proton to H_{16}, H_{17} and H_{18} were not used for comparison because conformations arising from the rotation of the *i*Pr group were excluded were eliminated in redundant conformer elimination (see 'general information' in the computation section).

In this study, only interproton distances in fragment A (C1'-C10 section) of baulamycin A were determined. Unfortunately, spectral overlap precluded the determination of interproton distances in fragment B (C8-C4 section).

Comparison of NMR of synthetic baulamycin diastereomers and that of the isolated natural product.

Table 6.22: Comparison of the ^{1}H and ^{13}C NMR spectra of **2.1** and the isolated natural product.

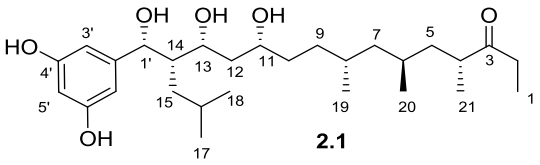

2.1

	δ_H			δ_C	
	Natural[a] (500 MHz)	**Synthetic (700 MHz)**		**Natural[a] (176 MHz)**	**Synthetic (176 MHz)**
1	1.02, t (7.3)	1.01, t (7.3)		8.1	8.1
2	2.57, dq (18.0, 7.4), 2.49, dq (17.8, 7.3)	2.56, dp (18.2, 7.3) 2.51, dp (18.0, 7.2)		35.4	35.1
3	-	-		218.6	218.4
4	2.76, dqd (9.1, 6.9, 5.3)	2.71, hept (6.9)		45.0	44.9
5	1.73, ddd (13.8, 9.1, 5.0) 1.00, ddd (13.8, 8.8, 5.3)	1.48, ddd (13.2, 8.1, 6.4) 1.21, ddd (13.2, 7.6, 5.4)		42.0	42.3
6	1.43, ddqdd (8.8, 7.2, 7.0, 6.8, 5.0)	1.55-1.49, m		29.5	29.2
7	1.22, ddd (13.8, 6.8, 6.8) 0.95, dt (13.8, 7.2)	1.14-1.08, m		46.6	46.2
8	1.53, m	1.53-1.48, m		31.2	31.3
9	1.32, m 1.19, m	1.32-1.27, m		33.4	34.4
10	1.43-1.38, m	1.49-1.44 m		35.7	35.9
11	3.69, dddd (8.2, 8.0, 4.5, 4.3)	3.71, dddd (8.5, 7.1, 4.7, 4.1)		72.9	72.2
12	1.78, ddd (14.1, 4.5 3.2) 1.54, ddd (14.1, 10.0, 8.2)	1.68, dt (14.1, 9.1) 1.63, dt (14.1, 4.4)		41.0	42.3
13	4.00, dt (10.0, 3.3)	3.98, dt (9.1, 3.6)		73.7	74.9
14	1.88, dddd (7.2, 6.8, 5.0, 3.5)	1.71-1.67, m		48.8	49.3
15	1.21, m	1.43-1.37, m		37.6	33.4
16	1.38, m	1.27-1.23, m		26.9	28.3
17	0.77 d (6.5)	0.78, d (6.2)		23.6	23.4
18	0.83, d (6.6)	0.64, d (6.3)		22.8	22.9
19	0.86, d (6.6)	0.85, d (6.9) or		20.6	19.81/19.79
20	0.88, d (6.6)	0.85, d (6.9) or		20.9	19.81/19.79
21	1.06, d (6.9)	1.04, d(3.9)		18.2	17.0
1’	4.47, d (6.8)	4.83, d (3.5)		76.9	76.8
2’	-	-		148.3	148.5
3’	6.33, d (2.1)	6.32, d (2.1)		106.3	105.7
4’	-	-		159.3	159.2
5’	6.15, t (2.2)	6.13, t (2.2)		102.2	101.9

a. ^{1}H and ^{13}C chemical shifts were re-extracted from the spectra provided by Sherman *et al.*[95] referenced to CD_3OD (3.31 and 49.000 ppm respectively).

As Figure 6.21, there are significant differences between the ^{13}C chemical shift values of synthetic **2.1** and those of the isolated natural product. There were large differences (~1 ppm or more) for C-9, C-12, C-13, C-15, C-16, C-19, C-20, C-21, suggesting that both the relative configuration of the hydroxyl-rich region and methyl-rich region had been mis-assigned.

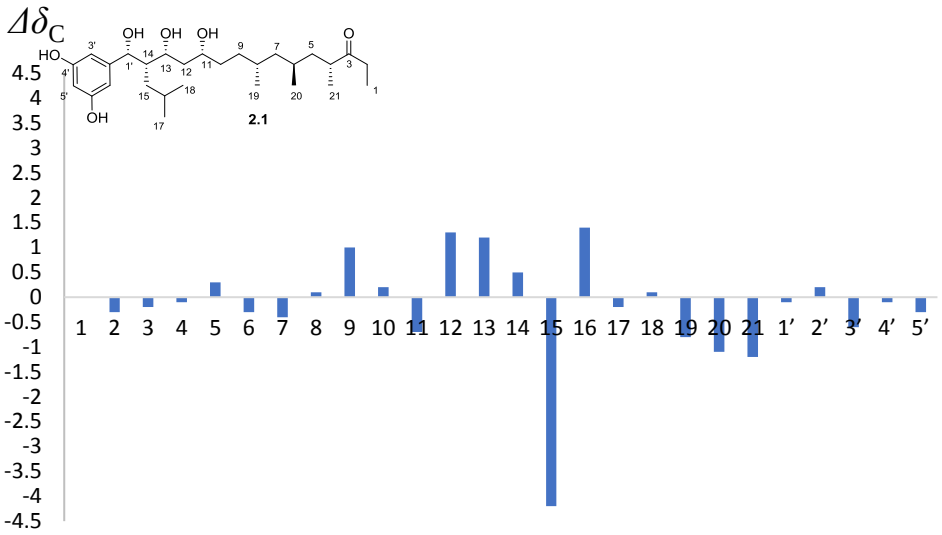

Figure 6.21: Differences between ^{13}C NMR spectra of **2.1** (CD_3OD, 175MHz) and the natural product (CD_3OD, 175 MHz). Natural product chemical shifts were re-extracted from the spectra provided by Sherman *et al.*, referenced to CD_3OD (49.00 ppm).[95]

Table 6.23: Comparison of the ^{1}H and ^{13}C NMR spectra of **2.11** and the natural product.

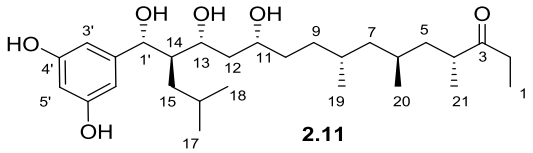

2.11

	δ_H			δ_C	
	Natural[a] (500 MHz)	**Synthetic (700 MHz)**		**Natural[a] (176 MHz)**	**Synthetic (176 MHz)**
1	1.02, t (7.3)	1.02, t (7.2)		8.1	8.1
2	2.57, dq (18.0, 7.4), 2.49, dq (17.8, 7.3)	2.56, dq (18.0, 7.1) 2.52, dq (18.0, 7.1)		35.4	35.1
3	-	-		218.6	218.5
4	2.76, dqd (9.1, 6.9, 5.3)	2.72, hept (6.8)		45.0	44.9
5	1.73, ddd (13.8, 9.1, 5.0) 1.00, ddd (13.8, 8.8, 5.3)	1.51-1.46, m 1.25-1.20, m		42.0	42.4
6	1.43, ddqdd (8.8, 7.2, 7.0, 6.8, 5.0)	1.54-1.49, m		29.5	29.2
7	1.22, ddd (13.8, 6.8, 6.8) 0.95, dt (13.8, 7.2)	1.15-1.07, m		46.6	46.2
8	1.53, m	1.52-1.47, m		31.2	31.4
9	1.32, m 1.19, m	1.30-1.24, m		33.4	34.4
10	1.43-1.38, m	1.45-1.39, m		35.7	35.9
11	3.69, dddd (8.2, 8.0, 4.5, 4.3)	3.71-3.67, m		72.9	72.9
12	1.78, ddd (14.1, 4.5 3.2) 1.54, ddd (14.1, 10.0, 8.2)	1.78, dt (14.1, 4.2, 3.4) 1.56-1.50, m		41.0	40.9
13	4.00, dt (10.0, 3.3)	4.00, dt (10.0, 3.4)		73.7	73.7
14	1.88, dddd (7.2, 6.8, 5.0, 3.5)	1.88, dddd		48.8	48.8
15	1.21, m	1.26-1.18, m		37.6	37.6
16	1.38, m	1.41-1.36, m		26.9	26.8
17	0.77 d (6.5)	0.77, d (6.7)		23.6	23.6
18	0.83, d (6.6)	0.83, d (6.5)		22.8	22.8
19	0.86, d (6.6)	0.85, d (6.4) or 0.84 d (6.3)		20.6	19.83/19.81
20	0.88, d (6.6)	0.85, d (6.4) or 0.84 d (6.3)		20.9	19.83/19.81
21	1.06, d (6.9)	1.04, d (6.8)		18.2	17.0
1’	4.47, d (6.8)	4.47, d (6.8)		76.9	76.8
2’	-	-		148.3	148.3
3’	6.33, d (2.1)	6.33, d (2)		106.3	106.3
4’	-	-		159.3	159.3
5’	6.15, t (2.2)	6.15, t (2.1)		102.2	102.2

a. ^{1}H and ^{13}C chemical shifts were re-extracted from the spectra provided by Sherman *et al.*[95] referenced to CD_3OD (3.31 and 49.000 ppm respectively).

Table 6.24: Comparison of the ^{1}H and ^{13}C NMR spectra of **2.16** and the natural product.

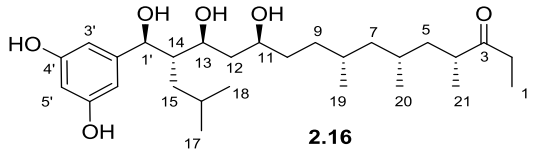

2.16

	δ_H			δ_C	
	Natural[a] (500MHz)	**Synthetic (700MHz)**		**Natural[a] (175MHz)**	**Synthetic (175MHz)**
1	1.02, t (7.3)	1.01, t (7.3)		8.1	8.1
2	2.57, dq (18.0, 7.4), 2.49, dq (17.8, 7.3)	2.58, dq (18.2, 7.4) 2.48, dq (18.1, 7.3)		35.4	35.4
3	-	-		218.6	218.5
4	2.76, dqd (9.1, 6.9, 5.3)	2.75, dqd (9.1, 6.9, 5.3)		45.0	44.9
5	1.73, ddd (13.8, 9.1, 5.0) 1.00, ddd (13.8, 8.8, 5.3)	1.72, ddd (13.8, 9.1, 4.9) 1.00, ddd (13.8, 8.6, 5.3)		42.0	41.9
6	1.43, ddqdd (8.8, 7.2, 7.0, 6.8, 5.0)	1.44-1.40, m		29.5	29.5
7	1.22, ddd (13.8, 6.8, 6.8) 0.95, dt (13.8, 7.2)	1.26-1.18, m 0.94, dt (14.0, 7.2)		46.6	46.4
8	1.53, m	1.53-1.49, m		31.2	31.3
9	1.32, m 1.19, m	1.48-1.43, m 1.08-1.03, m		33.4	33.4
10	1.43-1.38, m	1.51-1.47, m		35.7	35.7
11	3.69, dddd (8.2, 8.0, 4.5, 4.3)	3.71-3.65, m		72.9	73.1
12	1.78, ddd (14.1, 4.5 3.2) 1.54, ddd (14.1, 10.0, 8.2)	1.78, ddd (14.1, 4.5, 3.0) 1.56-1.51, m		41.0	40.9
13	4.00, dt (10.0, 3.3)	4.00, dt (10.0, 3.5)		73.7	73.8
14	1.88, dddd (7.2, 6.8, 5.0, 3.5)	1.88, dddd (7.0, 6.9, 5.3, 3.8)		48.8	48.8
15	1.21, m	1.26-1.18, m		37.6	37.6
16	1.38, m	1.41-1.36, m		26.9	26.9
17	0.77 d (6.5)	0.77, d (6.5)		23.6	23.5
18	0.83, d (6.6)	0.83, d (6.6)		22.8	22.8
19	0.86, d (6.6)	0.87, d (6.6)		20.6	20.6
20	0.88, d (6.6)	0.88, d (6.6)		20.9	20.9
21	1.06, d (6.9)	1.06, d (6.9)		18.2	18.2
1’	4.47, d (6.8)	4.47, d (6.9)		76.9	76.8
2’	-	-		148.3	148.3
3’	6.33, d (2.1)	6.33, d (2.2)		106.3	106.3
4’	-	-		159.3	159.3
5’	6.15, t (2.2)	6.12 t (2.2)		102.2	102.2

a. ^{1}H and ^{13}C chemical shifts were re-extracted from the spectra provided by Sherman *et al.*[95] referenced to CD_3OD (3.31 and 49.000 ppm respectively).

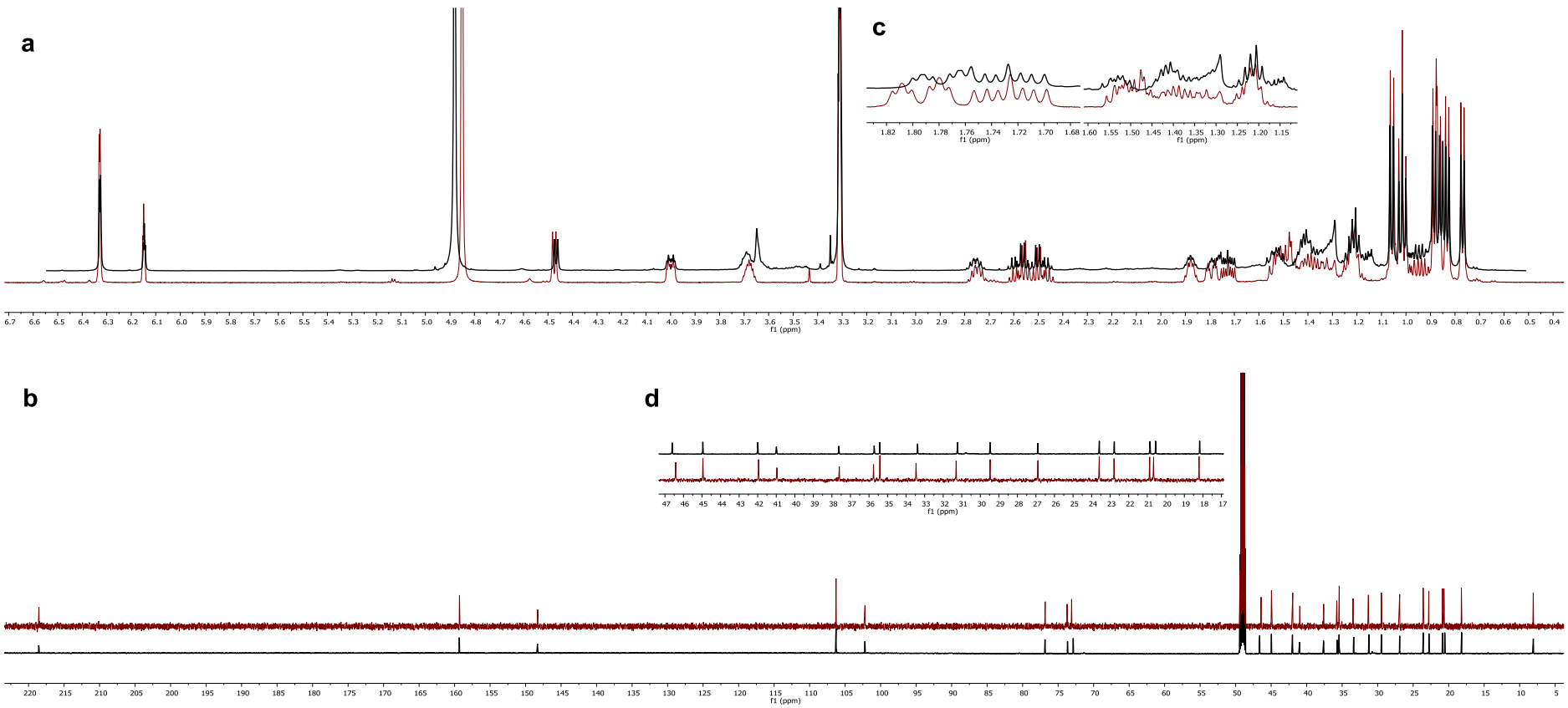

Figure 6.22: Comparison of (**a**) ^{1}H NMR (CD_3OD, 500 MHz) and (**b**) ^{13}C NMR (CD_3OD, 176 MHz) spectrum of **2.16** (red) and baulamycin A (black). **c**. Zoom in of ^{1}H NMR spectra from 1.6 – 1.8 ppm. **d**. Zoom in of ^{1}H NMR spectra from 1.1-1.6 ppm. **e**. Zoom in of ^{13}C NMR spectra from 17 to 47 ppm.

Table 6.25: Comparison of the ^{1}H and ^{13}C NMR spectra of **2.17** and the natural product (CD_3OD).

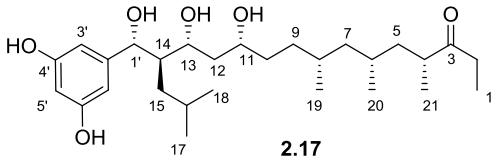

2.17

	δ_H			δ_C	
	Natural[a] (500 MHz)	**Synthetic (700 MHz)**		**Natural[a] (175 MHz)**	**Synthetic (175 MHz)**
1	1.02, t (7.3)	1.02, t (7.3)		8.1	8.1
2	2.57, dq (18.0, 7.4), 2.49, dq (17.8, 7.3)	2.58, dq (17.9, 7.2), 2.48, dq (18.0, 7.2)		35.4	35.4
3	-	-		218.6	218.6
4	2.76, dqd (9.1, 6.9, 5.3)	2.76, dqd (9.1, 6.9, 5.3)		45.0	44.9
5	1.73, ddd (13.8, 9.1, 5.0) 1.00, ddd (13.8, 8.8, 5.3)	5a (*pro-R*):1.73, ddd (13.5, 9.1, 5.0) 5b (*pro-S*):1.00, ddd (13.8, 8.8, 5.3)		42.0	42.0
6	1.43, ddqdd (8.8, 7.2, 7.0, 6.8, 5.0)	1.42, ddqdd (8.8, 7.2, 7.0, 6.8, 5.0)		29.5	29.5
7	1.22, ddd (13.8, 6.8, 6.8) 0.95, dt (13.8, 7.2)	7a (*pro-R*):1.22, ddd (13.8, 6.6, 6.8) 7b: (*pro-S*):0.95, dt (13.8, 7.2)		46.6	46.6
8	1.53, m	1.52, dddqd (8.5, 7.2, 6.8, 6.6, 4.8)		31.2	31.2
9	1.32, m	1.35-1.30, m, 1H		33.4	33.4
10	1.43-1.38, m	1.42-1.39, m		35.7	35.7
11	3.69, dddd (8.2, 8.0, 4.5,	3.68, dddd (8.2, 8.0, 4.5, 4.3)		72.9	72.9
12	1.78, ddd (14.1, 4.5 3.2) 1.54, ddd (14.1, 10.0, 8.2)	12a (*pro-R*):1.78, ddd (14.1, 4.5 3.2) 12b: (*pro-S*):1.54, ddd (14.1, 10.0,		41.0	41.0
13	4.00, dt (10.0, 3.3)	4.00, dt (9.9, 3.3)		73.7	73.7
14	1.88, dddd (7.2, 6.8, 5.0,	1.88, dddd (7.2, 6.8, 5.0, 3.5)		48.8	48.8
15	1.21, m	1.23-1.2, m		37.6	37.6
16	1.38, m	1.40.1.35, m		26.9	26.9
17	0.77 d (6.5)	0.77, d (6.5)		23.6	23.6
18	0.83, d (6.6)	0.83, d (6.6)		22.8	22.8
19	0.86, d (6.6)	0.86, d (6.6)		20.6	20.6
20	0.88, d (6.6)	0.89, d (6.6)		20.9	20.9
21	1.06, d (6.9)	1.06, d (6.9)		18.2	18.2
1’	4.47, d (6.8)	4.47, d (6.8)		76.9	76.8
2’	-	-		148.3	148.3
3’	6.33, d (2.1)	6.32, d (2.1)		106.3	106.3
4’	-	-		159.3	159.3
5’	6.15, t (2.2)	6.15, t (2.2)		102.2	102.2

a. ^{1}H and ^{13}C chemical shifts were re-extracted from the spectra provided by Sherman *et al.*[95] referenced to CD_3OD (3.31 and 49.000 ppm respectively).

NMR data computed vs experimental values of baulamycin A

NMR data used for validation study

Table 6.26: Calculated Boltzman averaged ^{1}H chemical shifts (δ_H) for **2.6** and experimental ^{1}H chemical shifts of C1'-C10 region for both synthetic **2.1** and baulamycin A with Mean Absolute Deviations (MAD, in ppm), Standard Deviations (StDev, in ppm) and χ^2 (reduced) values (χ^2 (red.)).

	Cal. 2.6[a]	Exp. δ_H of 2.1	Deviation	Exp. δH of Baulamycin A	Deviation
$H_{1'}$	4.78	4.83	–0.05	4.47	0.31
H_{14}	1.48	1.69	–0.21	1.88	–0.4
H_{13}	4.14	3.98	0.16	4.00	0.14
H_{12a}	1.42	1.63	–0.21	1.78	–0.36
H_{12b}	1.69	1.68	0.01	1.54	0.15
H_{11}	3.73	3.71	0.02	3.69	0.04
H_{10a}	1.32	1.46	–0.14	1.41	–0.09
H_{10b}	1.55	1.46	0.09	1.39	0.16
		MAD	0.11	**MAD**	0.21
		StDev	0.14	**StDev**	0.26
		χ^2(red.)	2.06	**χ^2(red.)**	6.62

[a] Experimental chemical shifts of compound **3** were used to scale the calculated chemical shift of **3a** using **Equation 6.5**.

Table 6.27: Calculated Boltzman averaged ^{13}C chemical shifts (δ_C) for **2.6** and experimental ^{1}H chemical shifts of C1'-C10 region for both synthetic **2.1** and baulamycin A with Mean Absolute Deviations (MAD, in ppm), Standard Deviations (StDev, in ppm) and χ^2 (reduced) values (χ^2 (red.)).

	Cal. 2.6[a]	Exp. δC of 2.1	Deviation	Exp. δC of Baulamycin A	Deviation
$C_{1'}$	82.89	76.78	–0.47	76.85	6.04
C_{14}	52.18	49.26	–0.37	48.82	3.36
C_{15}	31.50	33.39	–2.98	37.63	–6.13
C_{10}	37.97	35.87	0.32	35.72	2.25
C_{11}	79.03	72.18	0.69	72.87	6.16
C_{12}	43.76	42.27	–0.90	40.99	2.77
C_{13}	83.77	74.97	2.14	76.38	7.39
		MAD	1.12	**MAD**	4.87
		StDev	1.57	**StDev**	4.52
		χ^2(red.)	0.97	**χ^2(red.)**	12.10

[a] Experimental chemical shifts of compound **2.1** were used to scale the calculated chemical shift of **2.6** using **Equation 6.5** .

Table 6.28: Calculated Boltzman averaged $^{n}J_{HC}$ for **2.6** and experimental ^{1}H-^{13}C scalar coupling constants of C1'-C10 region for both **2.1** and baulamycin A with Mean Absolute Deviations (MAD, in Hz), Standard Deviations (StDev, in Hz) and χ^2 (reduced) values (χ^2 (red.)). For details on determination of scalar coupling constants see general information in NMR procedure section.

H	C	Calc. $^{n}J_{HC}$ of 2.6/Hz	Exp. $^{n}J_{HC}$ of 2.1 /Hz	Deviation from 2.1	Exp. $^{n}J_{HC}$ of Baulamycin A[b]/Hz	Deviation from Baulamycin A /Hz
$H_{1'}$	C_{15}	4.4	4.5	–0.1	2.3	2.1
	C_{13}	4.0	2.9	1.2	4.3	–0.3
H_{13}	C_{14}	2.2	2.5	–0.2	3.5	–1.3
	$C_{1'}$	3.8	4.2	–0.5	2.8	1.0
H_{14}[a]	C_{12}	2.0	-	-	3.8	–1.8
	C_{13}	2.2	-	-	5.0	–2.7
	$C_{1'}$	2.9	-	-	4.9	–2.0
H_{12a}	C_{14}	2.3	2.6	–0.3	1.8	0.4
	C_{13}	1.8	2.9	–1.1	2.3	–0.5
	C_{10}	1.2	3.2	–1.9	2.5	–1.3
	C_{11}	1.5	3.0	–1.5	3.3	–1.7
H_{12b}	C_{14}	0.9	2.6	–1.7	2.5	–1.6
	C_{13}	6.0	6.6	–0.6	6.2	–0.2
	C_{10}	2.7	2.4	0.3	3.3	–0.6
	C_{11}	6.3	6.0	0.4	6.0	0.3
H_{11}	C_{13}	2.7	2.7	0.1	3.1	–0.4
			MAD	0.7	**MAD**	1.1
			StDev	0.9	**StDev**	1.2
			χ^2(red.)	1	**χ^2(red.)**	2.0

[a] Due to spectral overlap in the f2 dimention, it is not viable to extract $^{n}J_{HC}$ of H14 in compound **1**.

[b] Experimental $^{n}J_{CH}$ values reported here were extracted from NMR spectra measured on the synthetic baulamycin A **2.17**.

Assignments of all diastereomers computed.

Table 6.29 – 32 show the assignments of all diastereomers computed in this study. Methylene protons (H_{12a}/H_{12b}, H_{10a}/H_{10b}, H_{7a}/H_{7b} and H5a/H5b) were assigned based on the best fit to the natural product NMR data.

Table 6.29: Assignments of fragment A of compounds **2.6** and **2.7 – 2.10** (gas conformational searches)

a) Before population refinement						
	Bmc A d_H, Mult. (J /Hz)	**2.6 d_H, Mult. (J /Hz)***	**2.7 d_H, Mult. (J /Hz)**	**2.8 d_H, Mult. (J /Hz)**	**2.9 d_H, Mult. (J /Hz)**	**2.10 d_H, Mult. (J /Hz)**
$H_{1'}$	4.47, d (6.8)	4.71, d (1.8)	4.72, d (6.8)	4.68, d (4.7)	4.33, d (8.9)	4.65 d (6.1)
H_{14}	1.88, dddd (7.2, 6.8, 5.0, 3.5)	1.49, dddd (1.8, 2.2, 4.6, 3.3)	1.87, dddd (6.8, 2.6, 6.9, 8.4)	1.65, dddd (4.7, 2.2, 8.4, 5.6)	1.78, dddd (8.9, 6.6, 7.6, 1.4)	1.81, dddd (6.1, 3.5, 6.7, 5.7)
H_{13}	4.00, dt (10.0, 3.3)	4.08, ddd (2.2, 1.1, 9.0)	3.81, ddd (2.6, 9.7, 1.5)	3.97, ddd (2.2, 10.4, 2.0)	4.17, ddd (6.6, 2.9, 10.1)	4.03, ddd (3.5, 1.6, 9.9)
H_{12a}	1.78, ddd (14.1, 4.5 3.2)	1.44, ddd(14.6, 1.1, 2.2)	1.19, ddd (14.5, 1.5, 1.7)	1.18, ddd (15.0, 2.0, 3.3)	1.65, ddd (14.4, 2.9, 4.6)	1.16, ddd (14.7, 1.6, 1.7)
H_{12b}	1.54, ddd (14.1, 10.0, 8.2)	1.69, ddd (14.6, 9.0, 9.6)	1.74, ddd (14.5, 9.7, 9.0)	1.98, ddd (15.0, 10.4, 4.3)	1.90, ddd (14.4, 10.1, 3.1)	1.20, ddd (14.7, 9.9, 9.1)
H_{11}	3.69, dddd (8.2, 8.0, 4.5, 4.3)	3.68, dddd (2.2, 9.6, 2.1, 9.1)	3.71, dddd (9.0, 1.7, 8.8, 2.2)	3.65, dddd (4.3, 3.3, 7.0, 6.5)	3.54, dddd (4.6, 3.1, 8.9, 2.8)	3.70, dddd (1.7, 9.1, 2.4, 9.1)
H_{10a}	1.41, m	1.33, m	1.38, m	1.43, m	1.32, m	1.15, m
H_{10b}	1.39, m	1.55, m	1.39, m	1.45, m	1.89, m	1.25, m
b) After population refinement						
	Bmc A d_H, Mult. (J /Hz)	**2.6 d_H, Mult. (J /Hz)***	**2.7 d_H, Mult. (J /Hz)**	**2.8 d_H, Mult. (J /Hz)**	**2.9 d_H, Mult. (J /Hz)**	**2.10 d_H, Mult. (J /Hz)**
$H_{1'}$	4.47, d (6.8)	4.69, d (5.3)	4.66, d (4.8)	4.83, d(4.7)	4.57, d (5.4)	4.51, d (6.7)
H_{14}	1.88, dddd (7.2, 6.8, 5.0, 3.5)	1.89, dddd (5.3, 3.2, 8.4, 4.2)	1.94, dddd (4.8, 2.4, 9.5, 6.0)	1.64, dddd (4.7, 2.1, 8.6, 5.7)	1.97, dddd (5.4, 4.5, 7.4, 5.7)	1.88, dddd (6.7, 3.7, 6.6, 4.8)

H_{13}	4.00, dt (10.0, 3.3)	4.01, ddd (9.3, 3.2, 2.4)	3.86, ddd (2.4, 8.1,2.9)	3.83, ddd (2.1, 9.2, 2.9)	4.00, ddd (4.5, 3.0, 8.8)	4.19, ddd (3.7, 3.6, 8.9)
H_{12a}	1.78, ddd (14.1, 4.5 3.2)	1.25, ddd (14.8, 2.4, 1.8)	1.40, ddd (14.7, 2.9, 2.3)	1.28, ddd (14.8, 2.9, 3.1)	1.16, ddd (14.8, 3.0, 7.1)	1.44, ddd (14.6, 3.6, 1.7)
H_{12b}	1.54, ddd (14.1, 10.0, 8.2)	1.41, ddd (14.8, 9.3, 9.0)	1.74, ddd (14.7, 8.1, 9.8)	1.87, ddd (14.8, 9.2, 6.8)	1.77, ddd (14.8, 8.8, 2.2)	1.33, ddd (14.6, 8.9, 9.0)
H_{11}	3.69, dddd (8.2, 8.0, 4.5, 4.3)	3.71, dddd (1.8, 9.0, 3.4, 8.4)	3.81, dddd (9.8, 2.3, 6.5, 4.2)	3.67, dddd (6.8, 3.1, 5.3, 5.9)	3.73, dddd (7.1, 2.2, 5.3, 8.0)	3.65, dddd (1.7, 9.0, 4.5, 6.8)
H_{10a}	1.41, m	1.25, m	1.49, m	1.34, m	1.54, m	1.19, m
H_{10b}	1.39, m	1.40, m	1.33, m	1.48, m	1.34, m	1.40, m

.

Table 6.30: Assignments of fragment A of compounds **2.6** and **2.7 – 2.10** (octanol conformational search)

a) Before population refinement						
	Bmc A d_H, Mult. (J /Hz)	**2.6 d_H, Mult. (J /Hz)***	**2.7 d_H, Mult. (J /Hz)**	**2.8 d_H, Mult. (J /Hz)**	**2.9 d_H, Mult. (J /Hz)**	**2.10 d_H, Mult. (J /Hz)**
$H_{1'}$	4.47, d (6.8)	4.68, d (1.78)	4.43, d (8.38)	4.46, d (7.34)	4.49, d (7.31)	4.61, d (4.15)
H_{14}	1.88, dddd (7.2, 6.8, 5.0, 3.5)	1.49, dddd (1.78, 2.15, 4.94, 2.82)	1.86, dddd (8.38, 2.91, 4.71, 10.60)	1.78, dddd (7.34, 2.81, 5.78, 9.41)	1.81, dddd (7.31, 6.52, 7.45, 2.18)	1.96, dddd (4.15, 3.10, 4.12, 9.64)
H_{13}	4.00, dt (10.0, 3.3)	4.05, ddd (2.15, 1.15, 9.14)	3.98, ddd (2.91, 1.21, 9.47)	4.08, ddd (2.81, 1.53, 10.39)	4.19, ddd (6.52, 2.94, 8.53)	4.08, ddd (3.10, 1.44, 9.66)
H_{12a}	1.78, ddd (14.1, 4.5 3.2)	1.45, ddd (14.62, 2.07, 1.08)	1.59, ddd (14.79, 1.94, 1.14)	1.43, ddd (15.16, 2.63, 1.44)	1.42, ddd (14.91, 4.96, 2.78)	1.15, ddd (14.98, 1.70, 1.36)
H_{12b}	1.54, ddd (14.1, 10.0, 8.2)	1.69, ddd (14.62, 9.49, 9.14)	1.70, ddd (14.79, 9.53, 9.47)	2.12, ddd (15.16, 4.69, 10.39)	1.85, ddd (14.91, 3.28, 8.53)	1.34, ddd (14.98, 9.23, 9.66)
H_{11}	3.69, dddd (8.2, 8.0, 4.5, 4.3)	3.65, dddd (14.62, 2.07, 2.74, 8.46)	3.80, dddd (14.79, 1.94, 5.19, 5.74)	3.72, dddd (15.16, 2.63, 3.60, 8.44)	3.64, dddd (14.91, 4.96, 2.32, 9.22)	3.61, dddd (14.98, 1.70, 5.41, 6.35)
H10a	1.41, m	1.37, m	1.45, m	1.43, m	1.51, m	1.20, m
H10b	1.39, m	1.60, m	1.58, m	1.61, m	1.46, m	1.45, m
b) After population refinement (using a constraint of 400)						
	Bmc A d_H, Mult. (J /Hz)	**2.6 d_H, Mult. (J /Hz)***	**2.7 d_H, Mult. (J /Hz)**	**2.8 d_H, Mult. (J /Hz)**	**2.9 d_H, Mult. (J /Hz)**	**2.10 d_H, Mult. (J /Hz)**
$H_{1'}$	4.47, d (6.8)	4.71, d (4.72)	4.85, d (4.72)	4.84, d (5.51)	4.57, d (6.53)	4.37, d (6.93)
H_{14}	1.88, dddd (7.2, 6.8, 5.0, 3.5)	1.88, dddd (4.72, 4.20, 5.11, 5.46)	1.73, dddd (4.72, 2.25, 9.28, 4.87)	1.77, dddd (5.51, 2.30, 8.14, 6.17)	1.91, dddd (6.53, 4.13, 8.40, 4.16)	1.90, dddd (6.93, 2.63, 4.24, 9.36)
H_{13}	4.00, dt (10.0, 3.3)	3.97, ddd (4.20, 2.37, 9.41)	3.82, ddd (2.25, 3.09, 8.20)	3.84, ddd (2.30, 2.10, 9.40)	4.03, ddd (4.13, 5.01, 8.24)	4.27, ddd (2.63, 2.83, 9.17)

H_{12a}	1.78, ddd (14.1, 4.5 3.2)	1.36, ddd (14.71, 1.70, 1.08)	1.27, ddd (14.57, 2.36, 1.14)	1.51, ddd (14.59, 2.57, 1.44)	1.54, ddd (14.88, 7.19, 2.78)	1.47, ddd (14.75, 1.75, 1.36)
H_{12b}	1.54, ddd (14.1, 10.0, 8.2)	1.41, ddd (14.71, 8.96, 9.41)	1.67, ddd (14.57, 9.59, 8.20)	1.83, ddd (14.59, 6.94, 9.40)	1.75, ddd (14.88, 2.73, 8.24)	1.51, ddd (14.75, 9.04, 9.17)
H_{11}	3.69, dddd (8.2, 8.0, 4.5, 4.3)	3.61, dddd (14.71, 1.70, 3.34, 8.19)	3.80, dddd (14.57, 2.36, 3.52, 6.22)	3.52, dddd (14.59, 2.57, 4.66, 7.77)	3.70, dddd (14.88, 7.19, 7.11, 5.40)	3.62, dddd (14.75, 1.75, 4.13, 7.35)
H_{10a}	1.41, m	1.26, m	1.57, m	1.98, m	1.38, m	1.35, m
H_{10b}	1.39, m	1.47, m	1.30, m	1.04, m	1.65, m	1.39, m

Table 6.31: Assignments of fragment B of compounds **2.10** and **2.12 – 2.14**.

a) NMR parameters calculated using gas phase conformational search candidates					
	Bmc A d_H, multi (J /Hz)	**2.10 δ_H, multi (J /Hz)**	**2.12 δ_H, multi (J /Hz)**	**2.13 δ_H, multi (J /Hz)**	**2.14 δ_H, multi (J /Hz)**
H_8	1.53, m	1.74	1.84, ddddq (2.7, 10.1, 9.9, 2.0, 6.2)	1.73, ddddq (4.3, 4.3, 9.1, 3.6, 6.5)	1.67, ddddq (3.4, 5.1, 10.4, 3.8, 6.5)
H_{7a}	1.22, ddd (13.8, 7.5)	1.24, ddd (14.5, 6.3, 6.5)	1.11, ddd (14.5, 2.0, 10.3)	1.40, ddd (14.7, 3.6, 8.7)	1.08, ddd (14.6, 10.4, 1.7)
H_{7b}	0.95, dt (13.8, 7.2)	1.03, ddd (14.5, 7.7, 5.7)	0.99, ddd (14.5, 9.9, 1.9)	0.54, ddd (14.7, 9.1, 3.5)	0.97, ddd (14.6, 3.8, 9.5)
H_6	1.43, ddqdd (8.8, 7.5, 7.2, 6.6, 5.0)	1.43, ddddq (5.7, 6.5, 5.4, 7.4, 6.2)	1.12, ddddq (1.9, 10.3, 9.0, 0.8, 6.2)	1.19, ddddq (3.5, 8.7, 9.8, 2.9, 6.1)	1.11, ddddq (1.7, 9.5, 1.9, 9.8, 6.2)
H_{5a}	1.73, ddd (13.8, 9.1, 5.0)	1.53, ddd (14.2, 5.4, 7.8)	2.03, ddd (14.3, 0.8, 10.8)	1.75, ddd (14.8, 2.9, 10.8)	1.63, ddd (14.3, 1.9, 10.8)
H_{5b}	1.00, ddd (13.8, 8.8, 5.3)	1.18, ddd (14.2, 7.4, 5.7)	0.77, ddd (14.3, 9.0, 2.1)	1.31, ddd (14.8, 9.8, 4.2)	1.01, ddd (14.3, 9.8, 2.5)
H_4	2.76, dqd (9.1, 6.9, 5.3)	2.76, ddq (7.8, 5.7, 6.4)	2.82, ddq (2.1, 10.8, 6.8)	2.64, ddq (4.2, 10.8, 6.5)	2.88, ddq (10.8, 2.5, 6.8)
H_{19}	0.86, d (6.6)	0.85, d (6.2)	0.89, d (6.2)	0.78, d (6.5)	0.82, d (6.5)
H_{20}	0.88, d (6.6)	0.94, d (6.2)	0.95, d (6.2)	0.87, d (6.1)	0.78, d (6.2)
H_{21}	1.06, d (6.9)	1.10, d (6.4)	1.19, d (6.8)	1.21, d (6.5)	1.14, d (6.8)
b) NMR parameters calculated using octanol conformational search candidates					
	Bmc A d_H, multi (J /Hz)	**2.10 δ_H, multi (J /Hz)**	**2.12 δ_H, multi (J /Hz)**	**2.13 δ_H, multi (J /Hz)**	**2.14 δ_H, multi (J /Hz)**
H_8	1.53, m	1.43, ddddq (4.9, 7.4, 3.4, 10.1, 6.1)	1.87, ddddq (2.8, 10.1, 9.8, 2.1, 6.2)	1.67, ddddq (3.7, 6.8, 7.9, 4.8, 6.3)	1.52, ddddq (3.6, 7.2, 8.3, 5.8, 6.2)
H_{7a}	1.22, ddd (13.8, 7.5)	1.20, ddd (13.9, 10.1, 3.3)	1.11, ddd (14.5, 2.1, 10.2)	1.26, ddd (14.6, 7.9, 4.8)	1.19, ddd (14.3, 8.3, 5.0)
H_{7b}	0.95, dt (13.8, 7.2)	0.93, ddd(13.9, 3.4, 10.2)	1.00, ddd (14.5, 9.8, 1.9)	0.70, ddd (14.6, 4.8, 7.8)	0.98, ddd (14.3, 5.8, 7.6)
H_6	1.43, ddqdd (8.8, 7.5, 7.2, 6.6, 5.0)	1.39, ddddq (10.2, 3.3, 9.2, 3.3, 6.2)	1.13, ddddq (1.9, 10.2, 9.1, 0.9, 6.2)	1.35, ddddq (4.8, 7.8, 8.1, 3.8, 6.2)	1.41, ddddq (5.0, 7.8, 3.0, 9.4, 6.1)
H_{5a}	1.73, ddd (13.8, 9.1, 5.0)	1.79, ddd (14.2, 3.3, 9.8)	2.02, ddd (14.3, 0.9, 10.8)	1.88, ddd (14.7, 3.8, 9.7)	1.81, ddd (14.1, 3.0, 10.0)
H_{5b}	1.00, ddd (13.8, 8.8, 5.3)	0.97, ddd (14.2, 9.2, 3.3)	0.77, ddd (14.3, 9.1,2.1)	1.24, ddd (14.7, 8.1, 4.1)	0.90, ddd (14.1, 9.4, 3.2)
H_4	2.76, dqd (9.1, 6.9, 5.3)	2.83, ddq (3.3, 9.8, 6.6)	2.82, ddq (2.1, 10.8, 6.8)	2.69, ddq (4.1, 9.7, 6.5)	2.82, ddq (10.0, 3.2, 6.7)
H_{19}	0.86, d (6.6)	0.81, d (6.1)	0.91, d (6.2)	0.82, d (6.3)	0.92, d (6.2)
H_{20}	0.88, d (6.6)	0.89, d (6.2)	0.94, d (6.2)	0.90, d (6.2)	0.92, d (6.1)

H_{21}	1.06, d (6.9)	1.11, d (6.6)	1.18, d (6.8)	1.18, d (6.5)	1.13, d (6.7)

NMR data of fragment A (compounds 2.6 and 2.7 – 2.10, gas conformational search)

Table 6.32: Conformation clusters of compounds **2.6** and **2.7 – 2.10** with initial DFT energy derived population, NOE-refined $\Delta\Delta G$ (in kJ mol^{-1}) and NOE-refined population for each cluster.

	Cluster	Φ_1	Φ_2	Φ_3	Φ_4	Initial Population	NOE−refined $\Delta\Delta G$/kJ mol^{-1}	NOE−Refined Population
2.6	1	g^+	g^+	g^+	*ap*	0.00%	0.09	0.01%
	2	g^+	g^+	*ap*	*ap*	0.00%	–0.23	0.01%
	3	g^+	*ap*	g^-	*ap*	0.00%	–6.72	4.54%
	4	g^+	+*ac*	*ap*	g^+	0.00%	0.00	0.00%
	5	g^+	+*ac*	*ap*	*ap*	0.01%	–7.45	9.54%
	6	g^+	*ap*	*ap*	g^+	0.00%	–0.03	0.00%
	7	g^+	*ap*	*ap*	*ap*	0.01%	0.19	1.14%
	8	g^+	*ap*	g^-	*ap*	0.00%	–0.06	0.02%
	9	g^+	g^-	*ap*	*ap*	0.03%	–4.48	17.63%
	10	+*ac*	g^-	*ap*	*ap*	0.00%	0.00	0.00%
	11	*ap*	g^+	g^+	–*ac*	0.00%	0.01	0.00%
	12	*ap*	g^+	g^+	*ap*	0.00%	0.17	0.00%
	13	*ap*	*ap*	*ap*	g^+	0.00%	–0.03	0.00%
	14	*ap*	*ap*	*ap*	*ap*	99.11%	15.18	19.44%
	15	*ap*	*ap*	g^-	*ap*	0.04%	0.15	3.00%
	16	*ap*	*ap*	g^-	g^-	0.00%	–0.34	0.07%
	17	–*ac*	g^-	g^+	*ap*	0.02%	–2.28	3.58%
	18	*ap*	g^-	+*ac*	*ap*	0.00%	0.00	0.00%
	19	*ap*	g^-	*ap*	g^+	0.00%	0.00	0.00%
	20	*ap*	g^-	*ap*	*ap*	0.50%	6.34	3.45%
	21	g^-	g^+	*ap*	*ap*	0.00%	0.00	0.00%
	22	g^-	*ap*	*ap*	g^+	0.00%	–0.13	0.01%
	23	g^-	*ap*	*ap*	*ap*	0.14%	0.28	11.32%
	24	g^-	*ap*	g^-	*ap*	0.00%	–0.02	0.00%
	25	g^-	*ap*	g^-	g^-	0.00%	–0.02	0.00%
	26	g^-	g^-	*ap*	*ap*	0.15%	–1.72	26.23%
2.7	1	g^+	g^+	*ap*	*ap*	0.00%	0.00	0.00%
	2	g^+	*ap*	*g*+	*ap*	0.00%	–0.13	0.01%
	3	g^+	*ap*	*g*+	g^+	0.00%	0.00	0.00%
	4	g^+	*ap*	*ap*	*ap*	47.28%	4.87	75.05%
	5	g^+	*ap*	*ap*	g^-	0.00%	0.00	0.00%
	6	*ap*	g^+	g^+	*ap*	0.00%	–15.90	18.12%

	7	*ap*	g^+	*ap*	g^+	0.00%	0.03	0.03%
	8	*ap*	g^+	*ap*	*+ac*	0.00%	0.01	0.00%
	9	*ap*	g^+	*ap*	*ap*	52.71%	11.11	6.75%
	10	*ap*	g^+	*ap*	g^-	0.00%	0.04	0.02%
	11	*ap*	g^-	*ap*	*ap*	0.00%	0.00	0.00%
	12	g^-	*–ac*	*ap*	*ap*	0.00%	–0.02	0.00%
	13	g^-	g^-	*ap*	*ap*	0.00%	0.00	0.00%
2.8								
	1	g^+	*ap*	g^+	g^+	0.08%	–9.26	11.54%
	2	g^+	*ap*	*ap*	*ap*	0.01%	–0.10	0.05%
	3	g^+	*ap*	*ap*	g^-	65.48%	3.59	55.02%
	4	*+ac*	*ap*	*ap*	g^-	0.00%	0.00	0.00%
	5	*ap*	g^+	*ap*	g^+	0.06%	–12.08	28.49%
	6	*ap*	g^+	*ap*	*+ac*	0.00%	–0.07	0.01%
	7	*ap*	g^+	*ap*	*ap*	9.54%	6.72	2.27%
	8	*ap*	g^+	*ap*	g^-	24.28%	10.44	1.28%
	9	*ap*	g^+	*–ac*	*ap*	0.01%	0.14	0.04%
	10	*ap*	g^+	g^-	*ap*	0.52%	1.00	1.25%
	11	*ap*	*ap*	*ap*	g^-	0.01%	–0.54	0.05%
	12	*ap*	*–ac*	*ap*	g^-	0.00%	0.00	0.00%
	13	*ap*	g^-	g^-	*ap*	0.00%	0.00	0.00%
	14	g^-	g^+	*ap*	g^-	0.00%	0.00	0.00%
	15	g^-	*–ac*	*ap*	g^-	0.00%	–0.01	0.00%
	16	g^-	g^-	*ap*	g^-	0.00%	–0.03	0.00%
2.9								
	1	g^+	g^+	g^+	*ap*	1.09%	2.66	0.39%
	2	g^+	g^+	*ap*	g^+	0.38%	0.60	0.31%
	3	g^+	g^+	*ap*	*ap*	0.04%	0.00	0.05%
	4	g^+	*+ac*	*ap*	g^+	0.00%	0.00	0.00%
	5	g^+	*ap*	*ap*	g^+	0.00%	0.01	0.00%
	6	g^+	g^-	*ap*	g^+	1.66%	2.54	0.62%
	7	g^+	g^-	*ap*	*ap*	0.05%	–16.22	37.55%
	8	g^+	g^-	g^-	*ap*	1.17%	–0.37	1.41%
	9	g^+	g^-	g^-	g^-	0.03%	–0.60	0.04%
	10	*+ac*	*ap*	g^+	*ap*	4.61%	–1.48	8.70%
	11	*+ac*	*ap*	*ap*	g^+	0.09%	0.82	0.07%
	12	*+ac*	g^-	*ap*	*ap*	0.01%	0.01	0.01%

	13	+*ac*	g^-	*ap*	g^+	0.08%	0.59	0.06%
	14	*ap*	g^+	g^+	*ap*	0.62%	4.92	0.09%
	15	*ap*	g^+	*ap*	g^+	4.95%	–3.65	22.40%
	16	*ap*	*ap*	g^+	*ap*	0.04%	0.01	0.04%
	17	*ap*	g^-	*ap*	g^+	2.04%	4.54	0.34%
	18	*ap*	*ap*	*ap*	g^+	80.14%	4.20	15.24%
	19	*ap*	*ap*	*ap*	*ap*	0.03%	–0.18	0.03%
	20	*ap*	–*ac*	*ap*	*ap*	1.24%	3.58	0.30%
	21	*ap*	g^-	*ap*	*ap*	0.20%	1.92	0.10%
	22	*ap*	*ap*	*ap*	g^-	0.00%	0.00	0.00%
	23	*ap*	g^-	g^-	*ap*	1.46%	–5.17	12.21%
	24	*ap*	g^-	g^-	g^-	0.00%	–0.05	0.00%
	25	g^-	*ap*	g^+	*ap*	0.01%	–0.10	0.02%
	26	g^-	*ap*	*ap*	g^+	0.02%	0.11	0.02%
	27	g^-	*ap*	*ap*	*ap*	0.01%	0.11	0.01%
	28	g^-	g^-	*ap*	*ap*	0.00%	0.07	0.00%
	29	g^-	g^-	*ap*	g^+	0.01%	0.56	0.00%
2.10	1	g^+	g^+	*ap*	g^+	0.00%	0.00	0.00%
	2	g^+	g^+	*ap*	*ap*	0.13%	–1.70	1.99%
	3	g^+	+*ac*	g^-	*ap*	0.12%	–0.03	0.95%
	4	g^+	g^-	*ap*	*ap*	49.87%	7.19	21.32%
	5	+*ac*	g^-	*ap*	*ap*	0.00%	0.00	0.00%
	6	g^+	g^-	g^-	*ap*	0.00%	–15.42	13.59%
	7	g^+	g^-	g^-	g^-	0.00%	–0.02	0.01%
	8	*ap*	g^+	*ap*	g^+	0.00%	–0.02	0.00%
	9	*ap*	g^+	*ap*	*ap*	0.31%	–5.67	23.54%
	10	*ap*	g^+	g^-	*ap*	0.17%	–0.03	1.34%
	11	g^-	g^-	*ap*	*ap*	0.00%	0.00	0.00%
	12	g^-	*ap*	*ap*	*ap*	0.01%	0.04	0.11%
	13	*ap*	*ap*	*ap*	*ap*	38.23%	6.32	23.21%
	14	*ap*	–*ac*	*ap*	*ap*	0.86%	2.69	2.26%
	15	*ap*	–*ac*	*ap*	*ap*	9.96%	4.98	10.41%
	16	*ap*	g^-	*ap*	*ap*	0.33%	1.87	1.20%
	17	*ap*	g^-	g^-	g^-	0.01%	–0.27	0.06%

Table 6.33: Comparison of experimental ^{1}H chemical shifts re-extracted from the ^{1}H spectrum provided by Sherman *et al.*[95] with the calculated scaled ^{1}H chemical shifts before population refinement for compound **2.6**, **2.7** – **2.10** with Deviations (Dev., in ppm), Mean Absolute Deviations (MAD, in ppm), Standard Deviations (StDev, in ppm) and χ^2 (reduced) values (χ^2 (red.)).

	Lit. δ_H	**2.6**	**Dev.**	**2.7**	**Dev.**	**2.8**	**Dev.**	**2.9**	**Dev.**	**2.10**	**Dev.**
$H_{1'}$	4.47	4.70	0.23	4.72	0.25	4.68	0.21	4.33	–0.14	4.65	0.18
H_{14}	1.88	1.49	–0.39	1.87	–0.01	1.65	–0.23	1.78	–0.10	1.81	–0.07
H_{13}	4.00	4.08	0.08	3.81	–0.19	3.97	–0.03	4.17	0.17	4.03	0.03
H_{12a}	1.78	1.43	–0.35	1.19	–0.59	1.18	–0.60	1.64	–0.14	1.16	–0.62
H_{12b}	1.54	1.69	0.15	1.74	0.20	1.98	0.44	1.90	0.36	1.20	–0.34
H_{11}	3.69	3.68	–0.01	3.71	0.02	3.65	–0.04	3.54	–0.15	3.70	0.01
H_{10a}	1.41	1.33	–0.08	1.38	–0.03	1.43	0.02	1.32	–0.09	1.15	–0.26
H_{10b}	1.39	1.55	0.16	1.39	0.00	1.45	0.06	1.89	0.50	1.24	–0.15
		MAD	0.18	**MAD**	0.16	**MAD**	0.20	**MAD**	0.20	**MAD**	0.21
		StDev	0.24	**StDev**	0.26	**StDev**	0.31	**StDev**	0.26	**StDev**	0.25
		χ^2(red.)	2.51	**χ^2(red.)**	3.10	**χ^2(red.)**	4.17	**χ^2(red.)**	3.07	**χ^2(red.)**	3.95

Table 6.34: Comparison of experimental ^{13}C chemical shifts re-extracted from the ^{13}C spectrum provided by Sherman *et al.*[95] with the calculated scaled ^{13}C chemical shifts before population refinement for compound **2.6** and **2.7** – **2.10** with Deviations (Dev., in ppm), Mean Absolute Deviations (MAD, in ppm), Standard Deviations (StDev, in ppm) and χ^2 (reduced) values (χ^2 (red.)).

	Lit. δC	**2.6**	**Dev.**	**2.7**	**Dev.**	**2.8**	**Dev.**	**2.9**	**Dev.**	**2.10**	**Dev.**
$C_{1'}$	76.85	76.14	–0.7	76.60	–0.2	79.32	2.5	81.23	4.4	75.43	–1.4
C_{14}	48.82	48.95	0.1	48.43	–0.4	49.51	0.7	48.29	–0.5	47.14	–1.7
C_{15}	37.63	30.63	–7.0	36.01	–1.6	36.41	–1.2	36.90	–0.7	39.47	1.8
C_{10}	35.72	36.37	0.6	37.19	1.5	34.71	–1.0	34.71	–1.0	35.25	–0.5
C_{11}	72.87	72.73	–0.1	74.74	1.9	74.21	1.3	70.86	–2.0	71.85	–1.0
C_{12}	40.99	41.49	0.5	38.87	–2.1	37.22	–3.8	39.98	–1.0	42.60	1.6
C_{13}	73.68	76.92	3.2	74.43	0.8	71.13	–2.6	74.25	0.6	77.71	4.0
		MAD	1.77	**MAD**	1.21	**MAD**	1.86	**MAD**	1.46	**MAD**	1.72
		StDev	3.01	**StDev**	1.50	**StDev**	2.22	**StDev**	2.10	**StDev**	2.02
		χ^2(red.)	4.50	**χ^2(red.)**	1.00	**χ^2(red.)**	2.34	**χ^2(red.)**	1.96	**χ^2(red.)**	2.10

Table 6.35: Experimental $^{n}J_{HH}$ values (in Hz) of Balamycin A and Boltzmann averaged calculated $^{n}J_{HH}$ of C1'-C10 region (fragment A, in Hz) before population refinement for **2.6** and **2.7** – **2.10** with Deviations (Dev, in Hz), Mean Absolute Deviations (MAD, in Hz), Standard Deviations (StDev, in Hz) and χ^2 (reduced) values (χ^2 (red.)).

H	Coupled H	Exp. $^{n}J_{HH}$	Calc. 2.6	Dev.	Calc. 2.7	Dev.	Calc. 2.8	Dev.	Calc. 2.9	Dev.	Calc. 2.10	Dev.
$H_{1'}$	H_{14}	6.8	1.8	–5.0	6.8	0.0	4.7	–2.1	8.9	2.1	6.1	–0.7
H_{14}	H_{13}	3.5	2.2	–1.3	2.6	–0.9	2.2	–1.3	6.6	3.1	3.5	0.0
H_{13}	H_{12a}	3.2	1.1	–2.1	1.5	–1.7	2.0	–1.2	2.9	–0.3	1.6	–1.6
	H_{12b}	10.0	9.0	–1.0	9.7	–0.3	10.4	0.4	10.1	0.1	9.9	–0.1
H_{12a}	H_{12b}	14.1	14.6	0.5	14.5	0.4	15.0	0.9	14.4	0.3	14.7	0.6
	H_{11}	4.5	2.2	–2.3	1.7	–2.8	3.3	–1.2	4.6	0.1	1.7	–2.8
H_{12b}	H_{11}	8.2	9.6	1.4	9.0	0.8	4.3	–3.9	3.1	–5.1	9.1	0.9
H_{11}	H_{10a}	4.3	2.1	–2.2	2.2	–2.1	6.5	2.2	2.8	–1.5	2.4	–1.9
	H_{10b}	8.0	9.2	1.2	8.8	0.8	7.0	–1.0	8.9	0.9	9.1	1.1
			MAD	1.9	**MAD**	1.1	**MAD**	1.6	**MAD**	1.5	**MAD**	1.1
			StDev	2.0	**StDev**	1.3	**StDev**	1.8	**StDev**	2.3	**StDev**	1.3
			χ^2(red.)	5.7	**χ^2(red.)**	2.2	**χ^2(red.)**	3.9	**χ^2(red.)**	5.4	**χ^2(red.)**	2.1

Table 6.36: Experimental $^{n}J_{HC}$ values of synthetic baulamycin A (compound **2.17**, in Hz) and Boltzmann averaged calculated $^{n}J_{HC}$ of C1'-C10 region (fragment A, in Hz) before population refinement for **2.6** and **2.7** – **2.10** with Mean Absolute Deviations (MAD, in Hz), Standard Deviations (StDev, in Hz) and χ^2 (reduced) values (χ^2 (red.)).

H	C	Exp. $^{n}J_{HC}$[a]	Calc. 2.6	Dev.	Calc. 2.7	Dev.	Calc. 2.8	Dev.	Calc. 2.9	Dev.	Calc. 2.10	Dev.
$H_{1'}$	C_{15}	2.3	4.4	2.1	1.9	–0.4	2.1	–0.2	2.5	0.2	2.5	0.2
	C_{13}	4.3	4.0	–0.3	3.6	–0.7	4.9	0.6	2.3	–2.0	4.6	0.3
H_{13}	C_{14}	3.5	2.2	–1.3	2.9	–0.6	2.5	–1.0	1.5	–2.0	2.2	–1.3
	$C_{1'}$	2.8	3.8	1.0	5.0	2.2	4.2	1.4	4.3	1.5	5.0	2.3
H_{14}	C_{12}	3.8	2.0	–1.8	3.2	–0.6	2.8	–1.0	1.7	–2.0	2.4	–1.4
	C_{13}	5.0	2.2	–2.7	4.6	–0.3	3.8	–1.1	5.5	0.5	3.6	–1.3
	$C_{1'}$	4.9	2.9	–2.0	4.8	–0.1	3.4	–1.5	6.0	1.1	4.0	–0.9
H_{12a}	C_{14}	1.8	2.3	0.4	1.6	–0.2	1.6	–0.2	0.9	–0.9	1.6	–0.2
	C_{13}	2.3	1.8	–0.5	1.7	–0.7	1.3	–1.0	1.7	–0.7	1.8	–0.5
	C_{10}	2.5	1.2	–1.3	1.8	–0.7	0.9	–1.6	0.6	–1.9	1.8	–0.7
	C_{11}	3.3	1.5	–1.7	2.1	–1.2	2.1	–1.2	2.5	–0.7	1.9	–1.4
H_{12b}	C_{14}	2.5	0.9	–1.6	1.1	–1.4	1.7	–0.8	2.6	0.1	1.3	–1.2
	C_{13}	6.2	6.0	–0.2	6.0	–0.2	6.3	0.1	5.9	–0.3	6.0	–0.2
	C_{10}	3.3	2.7	–0.6	2.3	–1.0	5.5	2.2	5.4	2.1	2.3	–0.9
	C_{11}	6.0	6.3	0.3	6.1	0.1	5.2	–0.8	5.3	–0.7	6.1	0.1
H_{11}	C_{13}	3.1	2.7	–0.4	3.3	0.2	6.4	3.3	6.8	3.7	3.4	0.3
			MAD	1.1	**MAD**	0.7	**MAD**	1.1	**MAD**	1.3	**MAD**	0.8
			StDev	1.2	**StDev**	0.8	**StDev**	1.4	**StDev**	1.6	**StDev**	1.0
			χ^2(red.)	2.0	**χ^2(red.)**	0.8	**χ^2(red.)**	2.0	**χ^2(red.)**	2.7	**χ^2(red.)**	1.1

[a] Experimental $^{n}J_{CH}$ values reported here were extracted from NMR spectra measured on the synthetic baulamycin A **2.17**

Table 6.37: Experimental ^{1}H-^{1}H distances derived from 2D-ROESY spectrum provided by Sherman *et al.*[95] and the Boltzmann averaged computed ^{1}H-^{1}H distances of C1'-C10 region (fragment A, in Å) before population refinement for **2.6** and **2.7** – **2.10** with Mean Absolute Deviations (MAD), Standard Deviations (StDev) and χ^2 (reduced) values (χ^2 (red.)).

H	**H_x**	Exp *r* /Å	Calc.**2.6** / Å	% error[a]	Exp *r* /Å	Calc.**2.7** / Å	% error[a]	Exp *r* /Å	Calc.**2.8** / Å	% error[a]
$H_{1'}$	**H_{13}**	3.09	2.27	−30%	2.99	3.72	22%	3.04	3.70	20%
	H_{14}	2.75	2.46	−11%	2.66	2.64	−1%	2.71	2.56	−6%
	H_{12a}	2.72	4.22	43%	2.64	3.05	15%	2.68	3.24	19%
	H_{12b}	4.15	4.54	9%	4.02	2.58	−43%	4.08	2.77	−38%
	H_{15}	3.02	3.77	22%	2.92	2.87	−2%	2.97	2.96	−1%
H_{13}	**H_{11}**	2.71	2.45	−10%	2.62	2.43	−8%	2.66	3.54	28%
	H_{14}	2.55	2.41	−6%	2.47	2.45	−1%	2.51	2.44	−3%
	H_{12a}	2.68	2.53	−6%	2.60	2.53	−3%	2.64	2.51	−5%
	H_{12b}	3.09	3.05	−1%	2.99	3.05	2%	3.04	3.04	0%
	H_{15}	3.26	3.82	16%	3.16	3.40	7%	3.21	3.47	8%
H_{11}	**H_{14}**	3.31	4.16	23%	3.20	4.39	31%	3.25	4.82	39%
	H_{12a}	2.79	2.47	−12%	2.70	2.49	−8%	2.74	2.47	−10%
	H_{12b}	2.90	3.05	5%	2.81	3.05	8%	2.86	2.42	−17%
	H_{10}	2.95	2.66	−10%	2.85	2.61	−9%	2.90	2.65	−9%
	H_{9a}	3.03	2.58	−16%	2.93	2.59	−12%	2.98	2.65	−12%
	H_{9b}	3.10	3.26	5%	3.00	3.10	3%	3.05	2.92	−4%
H_{12a}	**H_{14}**	2.86	2.48	−14%	2.76	2.76	0%	2.81	2.65	−6%
	H_{12b}	1.85	1.77	−5%	1.79	1.77	−1%	1.82	1.76	−3%
			MAD/%	13.57%		**MAD/%**	9.78%		**MAD/%**	12.60%
			StDev/%	17.48%		**StDev/%**	15.44%		**StDev/%**	17.68%
			χ^2(red.)	12.23		**χ^2(red.)**	9.54		**χ^2(red.)**	12.50

[a]% error = $(r_{cal} - r_{NOE})/((r_{cal} + r_{NOE})/2)$

(Table 6.37 continued)

H	**H_x**	Exp *r* /Å	Calc.**2.9** / Å	% error[a]	Exp *r* /Å	Calc.**2.10** / Å	% error[a]			
$H_{1'}$	**H_{13}**	3.02	2.57	−16%	3.04	2.91	−4%			
	H_{14}	2.69	2.98	10%	2.71	2.65	−2%			
	H_{12a}	2.66	3.51	27%	2.68	4.20	44%			
	H_{12b}	4.06	4.10	1%	4.08	4.22	3%			
	H_{15}	2.96	2.63	−12%	2.97	2.76	−7%			
H_{13}	**H_{11}**	2.65	3.59	30%	2.66	2.44	−9%			
	H_{14}	2.50	2.87	14%	2.51	2.62	4%			
	H_{12a}	2.62	2.47	−6%	2.64	2.50	−5%			
	H_{12b}	3.02	2.93	−3%	3.04	3.03	0%			
	H_{15}	3.19	2.83	−12%	3.21	2.61	−21%			
H_{11}	**H_{14}**	3.23	3.64	12%	3.25	4.35	29%			
	H_{12a}	2.73	2.42	−12%	2.74	2.50	−9%			
	H_{12b}	2.84	2.46	−14%	2.86	3.05	7%			
	H_{10}	2.88	2.69	−7%	2.90	2.66	−9%			
	H_{9a}	2.96	2.54	−16%	2.98	2.66	−11%			
	H_{9b}	3.03	2.94	−3%	3.05	3.10	2%			
H_{12a}	**H_{14}**	2.79	3.23	14%	2.81	2.59	−8%			
	H_{12b}	1.81	1.77	−2%	1.82	1.76	−3%			
			MAD/%	11.81%		**MAD/%**	9.91%			
			StDev/%	14.47%		**StDev/%**	15.05%			
			χ^2(red.)	8.38		**χ^2(red.)**	9.06			

[a]% error = $(r_{cal} - r_{NOE})/((r_{cal} + r_{NOE})/2)$

Table 6.38: Comparison of experimental ^{1}H chemical shifts re-extracted from the ^{1}H spectrum provided by Sherman *et al.*[95] with the calculated scaled ^{1}H chemical shifts after population refinement for compound **2.6** and **2.7** – **2.10** with Deviations (Dev, in ppm) Mean Absolute Deviations (MAD, in ppm), Standard Deviations (StDev, in ppm) and χ^2 (reduced) values (χ^2 (red.)).

	Lit. δ_H	**2.6**	**Dev.**	**2.7**	**Dev.**	**2.8**	**Dev.**	**2.9**	**Dev.**	**2.10**	**Dev.**
$H_{1'}$	4.47	4.69	0.22	4.66	0.19	4.83	0.36	4.57	0.10	4.51	0.04
H_{14}	1.88	1.89	0.01	1.94	0.06	1.64	–0.24	1.97	0.09	1.88	0.00
H_{13}	4.00	4.01	0.01	3.86	–0.14	3.83	–0.17	4.00	0.00	4.19	0.19
H_{12a}	1.78	1.25	–0.53	1.40	–0.38	1.28	–0.50	1.16	–0.62	1.44	–0.34
H_{12b}	1.54	1.41	–0.13	1.74	0.20	1.87	0.33	1.77	0.23	1.33	–0.21
H_{11}	3.69	3.71	0.02	3.81	0.12	3.67	–0.02	3.73	0.04	3.65	–0.04
H_{10a}	1.41	1.25	–0.16	1.49	0.08	1.34	–0.07	1.54	0.13	1.19	–0.22
H_{10b}	1.39	1.40	0.01	1.33	–0.06	1.48	0.09	1.34	–0.05	1.40	0.01
		MAD	0.14	**MAD**	0.15	**MAD**	0.22	**MAD**	0.16	**MAD**	0.13
		StDev	0.22	**StDev**	0.19	**StDev**	0.29	**StDev**	0.26	**StDev**	0.17
		χ^2(red.)	2.33	**χ^2(red.)**	1.67	**χ^2(red.)**	3.75	**χ^2(red.)**	3.05	**χ^2(red.)**	1.58

Table 6.39: Comparison of experimental ^{13}C chemical shifts re-extracted from the ^{13}C spectrum provided by Sherman *et al.*[95] with the calculated scaled ^{13}C chemical shifts after population refinement for compound **2.6** and **2.7** – **2.10** with Deviations (Dev., in ppm) Mean Absolute Deviations (MAD, in ppm), Standard Deviations (StDev, in ppm) and χ^2 (reduced) values (χ^2 (red.)).

	Lit. δC	**2.6**	**Dev.**	**2.7**	**Dev.**	**2.8**	**Dev.**	**2.9**	**Dev.**	**2.10**	**Dev.**
$C_{1'}$	76.85	76.94	0.1	77.17	0.3	78.64	1.8	79.99	3.1	76.96	0.1
C_{14}	48.82	49.33	0.5	49.34	0.5	49.20	0.4	48.92	0.1	47.75	-1.1
C_{15}	37.63	36.57	-1.1	37.00	-0.6	36.25	-1.4	41.29	3.7	39.01	1.4
C_{10}	35.72	36.03	0.3	37.29	1.6	35.11	-0.6	36.75	1.0	36.48	0.8
C_{11}	72.87	72.76	-0.1	72.97	0.1	74.45	1.6	69.75	-3.1	71.38	-1.5
C_{12}	40.99	39.84	-1.2	39.37	-1.6	38.27	-2.7	40.17	-0.8	41.56	0.6
C_{13}	73.68	74.53	0.8	73.62	-0.1	70.80	-2.9	72.57	-1.1	75.47	1.8
		MAD	0.58	**MAD**	0.69	**MAD**	1.62	**MAD**	1.85	**MAD**	1.02
		StDev	0.76	**StDev**	0.99	**StDev**	1.90	**StDev**	2.41	**StDev**	1.21
		χ^2(red.)	0.26	**χ^2(red.)**	0.44	**χ^2(red.)**	1.77	**χ^2(red.)**	2.66	**χ^2(red.)**	0.70

Table 6.40: Experimental $^{n}J_{HH}$ values (in Hz) of balamycin A and population refined Boltzmann averaged calculated $^{n}J_{HH}$ of C1'-C10 region (fragment A, in Hz) for **2.6** and **2.7** – **2.10** with Deviations (Dev, in Hz), Mean Absolute Deviations (MAD, in Hz), Standard Deviations (StDev, in Hz) and χ^2 (reduced) values (χ^2 (red.)).

H	Coupled H	Exp. $^{n}J_{HH}$	Calc. 2.6	Dev	Calc. 2.7	Dev.	Calc. 2.8	Dev.	Calc. 2.9	Dev.	Calc. 2.10	Dev.
$H_{1'}$	H_{14}	6.8	5.3	–1.5	4.8	–2.0	4.7	–2.1	5.4	–1.4	6.7	–0.1
H_{14}	H_{13}	3.5	3.2	–0.3	2.4	–1.1	2.1	–1.4	4.5	1.0	3.7	0.2
H_{13}	H_{12a}	3.2	2.4	–0.8	2.9	–0.3	2.9	–0.3	3.0	–0.2	3.6	0.4
	H_{12b}	10.0	9.3	–0.7	8.1	–1.9	9.2	–0.8	8.8	–1.2	8.9	–1.1
H_{12a}	H_{12b}	14.1	14.8	0.7	14.7	0.6	14.8	0.7	14.8	0.7	14.6	0.5
	H_{11}	4.5	1.8	–2.7	2.3	–2.2	3.1	–1.4	7.1	2.6	1.7	–2.8
H_{12b}	H_{11}	8.2	9.0	0.8	9.8	1.6	6.8	–1.4	2.2	–6.0	9.0	0.8
H_{11}	H_{10a}	4.3	3.4	–0.9	4.2	–0.1	5.3	1.0	5.3	1.0	4.5	0.2
	H_{10b}	8.0	8.3	0.3	6.5	–1.5	5.9	–2.1	7.9	–0.1	6.8	–1.2
			MAD	1.0	**MAD**	1.3	**MAD**	1.2	**MAD**	1.6	**MAD**	0.8
			StDev	1.1	**StDev**	1.3	**StDev**	1.1	**StDev**	2.4	**StDev**	1.1
			χ^2(red.)	1.6	**χ^2(red.)**	2.4	**χ^2(red.)**	2.1	**χ^2(red.)**	6.2	**χ^2(red.)**	1.5

Table 6.41: Experimental $^{n}J_{HC}$ values of synthetic baulamycin A (compound **2.17**, in Hz) and the population refined Boltzmann averaged calculated $^{n}J_{HC}$ of C1'-C10 region (fragment A, in Hz) for **2.6** and **2.7** – **2.10** with Mean Absolute Deviations (MAD, in Hz), Standard Deviations (StDev, in Hz) and χ^2 (reduced) values (χ^2 (red.)).

H	C	Exp. $^{n}J_{HC}$[a]	Calc. 2.6	Dev	Calc. 2.7	Dev.	Calc. 2.8	Dev.	Calc. 2.9	Dev.	Calc. 2.10	Dev.
$H_{1'}$	C_{15}	2.3	3.1	0.8	1.8	–0.5	2.0	–0.3	3.2	0.9	2.7	0.4
	C_{13}	4.3	3.6	–0.7	5.4	1.1	4.7	0.4	3.1	–1.2	3.7	–0.6
H_{13}	C_{14}	3.5	2.7	–0.8	2.5	–1.0	2.2	–1.3	2.6	–0.9	2.1	–1.4
	$C_{1'}$	2.8	5.7	3.0	3.6	0.8	4.0	1.2	5.1	2.3	3.9	1.1
H_{14}	C_{12}	3.8	4.1	0.3	2.3	–1.5	2.4	–1.3	1.8	–2.0	3.2	–0.6
	C_{13}	5.0	4.5	–0.5	3.6	–1.4	3.6	–1.4	4.1	–0.9	3.9	–1.1
	$C_{1'}$	4.9	5.9	1.0	3.4	–1.5	3.2	–1.7	4.5	–0.4	4.9	0.0
H_{12a}	C_{14}	1.8	1.9	0.1	2.4	0.5	1.9	0.1	1.7	–0.1	1.6	–0.2
	C_{13}	2.3	2.1	–0.2	2.8	0.5	2.3	0.0	1.8	–0.5	2.5	0.2
	C_{10}	2.5	1.7	–0.8	1.2	–1.3	3.1	0.6	1.3	–1.2	1.8	–0.7
	C_{11}	3.3	1.9	–1.3	1.5	–1.8	3.6	0.3	4.8	1.5	1.9	–1.3
H_{12b}	C_{14}	2.5	1.5	–1.1	1.7	–0.8	2.0	–0.6	1.9	–0.6	2.4	–0.1
	C_{13}	6.2	5.6	–0.6	6.1	–0.1	5.9	–0.3	6.1	–0.1	5.8	–0.4
	C_{10}	3.3	2.4	–0.9	2.8	–0.5	4.6	1.3	3.3	0.0	2.4	–0.9
	C_{11}	6.0	6.1	0.1	6.3	0.3	5.4	–0.6	2.7	–3.3	6.3	0.3
H_{11}	C_{13}	3.1	3.2	0.1	2.6	–0.5	4.5	1.4	4.8	1.7	3.2	0.1
			MAD	0.8	**MAD**	0.9	**MAD**	0.8	**MAD**	1.1	**MAD**	0.6
			StDev	1.1	**StDev**	1.3	**StDev**	1.0	**StDev**	1.4	**StDev**	0.7
			χ^2(red.)	1.1	**χ^2(red.)**	1.1	**χ^2(red.)**	1.0	**χ^2(red.)**	2.1	**χ^2(red.)**	0.6

[a] Experimental $^{n}J_{CH}$ values reported here were extracted from NMR spectra measured on the synthetic baulamycin A **2.17**

Table 6.42: Experimental ^{1}H-^{1}H distances derived from 2D-ROESY spectrum provided by Sherman *et al.*[95] and the population refined Boltzmann averaged computed ^{1}H-^{1}H distances of C1'-C10 region (fragment A, in Å) for **2.6** and **2.7** – **2.10** with Mean Absolute Deviations (MAD), Standard Deviations (StDev) and χ^2 (reduced) values (χ^2 (red.)).

H	**H_x**	Exp *r* /Å	Calc.**2.6** / Å	% error[a]	Exp *r*/Å	Calc.**2.7** / Å	% error[a]	Exp *r* /Å	Calc.**2.8** / Å	% error[a]
$H_{1'}$	**H_{13}**	2.95	2.82	−5%	3.04	3.69	19%	2.95	3.70	23%
	H_{14}	2.62	2.67	2%	2.71	2.52	−7%	2.63	2.56	−3%
	H_{12a}	2.60	3.40	27%	2.68	3.03	12%	2.60	3.05	16%
	H_{12b}	3.96	2.92	−30%	4.08	3.51	−15%	3.96	2.86	−32%
	H_{15}	2.88	2.81	−2%	2.97	3.10	4%	2.88	2.98	3%
H_{13}	**H_{11}**	2.58	2.47	−4%	2.66	2.49	−7%	2.58	2.86	10%
	H_{14}	2.43	2.42	0%	2.51	2.43	−3%	2.43	2.45	1%
	H_{12a}	2.56	2.53	−1%	2.64	2.60	−2%	2.56	2.55	0%
	H_{12b}	2.94	2.91	−1%	3.04	2.85	−6%	2.95	2.89	−2%
	H_{15}	3.11	3.52	12%	3.21	3.58	11%	3.11	3.54	13%
H_{11}	**H_{14}**	3.15	3.16	0%	3.25	4.17	25%	3.15	3.13	−1%
	H_{12a}	2.66	2.48	−7%	2.74	2.48	−10%	2.66	2.46	−8%
	H_{12b}	2.77	3.04	9%	2.86	3.05	6%	2.77	2.56	−8%
	H_{10}	2.81	2.65	−6%	2.90	2.60	−11%	2.81	2.56	−9%
	H_{9a}	2.89	2.71	−7%	2.98	2.75	−8%	2.89	2.81	−3%
	H_{9b}	2.96	3.36	13%	3.05	3.11	2%	2.96	2.99	1%
H_{12a}	**H_{14}**	2.72	2.72	0%	2.81	2.58	−8%	2.72	2.71	−1%
	H_{12b}	1.763	1.76	0%	1.82	1.77	−3%	1.76	1.76	0%
			MAD/%	7.02%		**MAD/%**	8.90%		**MAD/%**	7.39%
			StDev/%	11.37%		**StDev/%**	11.00%		**StDev/%**	11.66%
			χ^2(red.)	5.14		**χ^2(red.)**	4.8		**χ^2(red.)**	5.44

[a]% error = $(r_{cal} - r_{NOE})/((r_{cal} + r_{NOE})/2)$

(Table 6.42 continued)

H	**H_x**	Exp *r* /Å	Calc.**2.9** / Å	% error[a]	Exp *r*/Å	Calc.**2.10** / Å	% error[a]			
$H_{1'}$	**H_{13}**	2.95	3.10	5%	2.91	3.04	5%			
	H_{14}	2.63	2.79	6%	2.59	2.72	5%			
	H_{12a}	2.60	2.83	9%	2.56	2.87	11%			
	H_{12b}	3.96	3.76	−5%	3.91	3.45	−12%			
	H_{15}	2.88	2.62	−10%	2.84	2.64	−7%			
H_{13}	**H_{11}**	2.59	2.82	9%	2.55	2.53	−1%			
	H_{14}	2.44	2.48	2%	2.40	2.53	5%			
	H_{12a}	2.56	2.55	0%	2.52	2.51	−1%			
	H_{12b}	2.95	2.79	−5%	2.91	2.85	−2%			
	H_{15}	3.12	2.93	−6%	3.07	2.83	−8%			
H_{11}	**H_{14}**	3.16	3.25	3%	3.11	3.21	3%			
	H_{12a}	2.66	2.66	0%	2.62	2.51	−5%			
	H_{12b}	2.77	2.51	−10%	2.73	3.04	11%			
	H_{10}	2.81	2.67	−5%	2.77	2.66	−4%			
	H_{9a}	2.89	3.00	4%	2.85	2.70	−6%			
	H_{9b}	2.96	2.92	−1%	2.92	2.96	1%			
H_{12a}	**H_{14}**	2.73	2.90	6%	2.69	2.78	3%			
	H_{12b}	1.77	1.76	0%	1.741	1.76	1%			
			MAD/%	4.83%		**MAD/%**	5.10%			
			StDev/%	5.91%		**StDev/%**	6.37%			
			χ^2(red.)	1.40		**χ^2(red.)**	1.62			

[a]% error = $(r_{cal} - r_{NOE})/((r_{cal} + r_{NOE})/2)$

The fit of all calculated NMR parameters for Fragment A of **2.6** and **2.7 – 2.10**, to those of the experimental parameters derived from the natural product is shown in Figure 6.23.

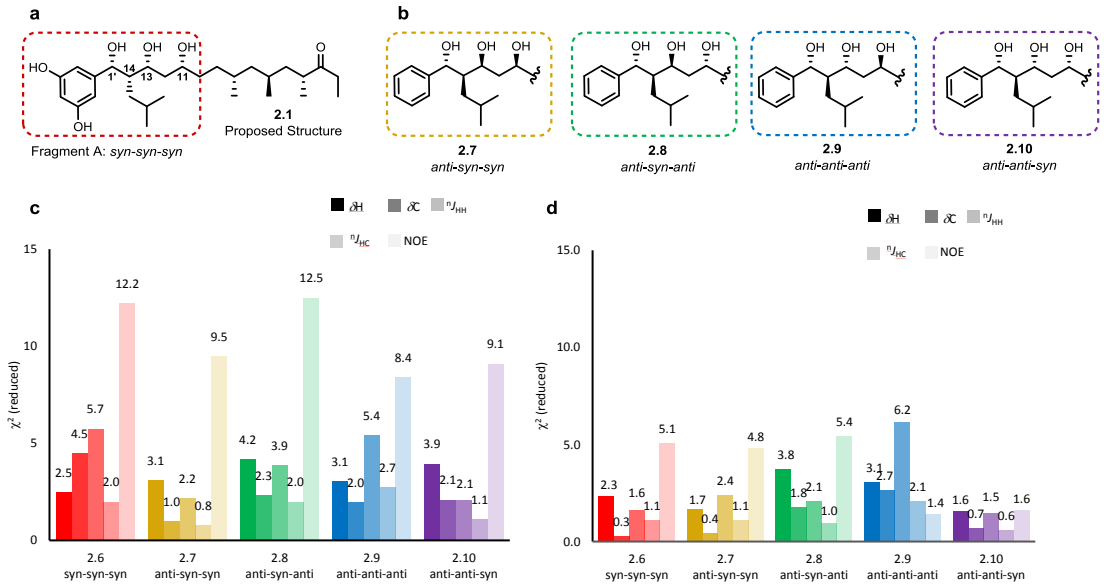

Figure 6.23: **a**. Generic structure of isomers studied for fragment A analysis using conformers obtained from gas MM conformational search. **b**. Relative stereochemistry of isomers studied for fragment A analysis. Results of comparison of NMR properties (^{1}H and ^{13}C chemical shifts, ^{1}H-^{1}H and ^{1}H-^{13}C scalar coupling constants, NOE distances) (**c**) before and (**d**) after population refinement.

NMR data of fragment A (compounds 2.6, 2.7 – 2.10, octanol conformational search)

Table 6.43: Conformation clusters of compounds **2.10** with initial DFT energy derived population, NOE-refined ΔΔ*G* (in kJ mol^{-1}) using different constraints and NOE-refined population for each cluster.

						$\Sigma(\Delta\Delta G)^2$ =25		$\Sigma(\Delta\Delta G)^2$ =100		$\Sigma(\Delta\Delta G)^2$ =225	
Cluster	Φ_1	Φ_2	Φ_3	Φ_4	Initial Population	NOE−refined ΔΔ*G*/kJ mol^{-1}	NOE−Refined Population	NOE−refined ΔΔ*G*/kJ mol^{-1}	NOE−Refined Population	NOE−refined ΔΔ*G*/kJ mol^{-1}	NOE−Refined Population
1	+*ac*	*ap*	*ap*	*ap*	0.01%	−0.01	0.01%	0.01	0.01%	0.02	0.02%
2	−*ac*	g^-	*ap*	*ap*	0.00%	0.00	0.00%	0.04	0.01%	0.01	0.01%
3	*ap*	−*ac*	*ap*	*ap*	4.77%	1.15	3.09%	1.59	4.75%	1.93	7.52%
4	*ap*	−*ac*	*ap*	g^+	0.00%	0.00	0.00%	0.00	0.00%	0.00	0.00%
5	*ap*	−*ac*	g^-	*ap*	0.00%	−0.44	0.00%	−0.46	0.01%	−0.05	0.01%
6	*ap*	*ap*	*ap*	*ap*	17.68%	0.60	14.32%	3.34	8.70%	3.15	17.01%
7	*ap*	*ap*	*ap*	g^+	0.16%	−0.66	0.22%	−8.08	7.92%	0.00	0.55%
8	*ap*	g^+	*ap*	*ap*	5.51%	−4.05	29.13%	−2.40	27.54%	−0.85	26.68%
9	*ap*	g^+	g^-	*ap*	0.01%	−0.02	0.01%	−0.01	0.01%	0.01	0.02%
10	*ap*	g^-	*ap*	*ap*	4.56%	2.08	2.03%	2.33	3.36%	2.01	6.97%
11	*ap*	g^-	g^-	*ap*	0.00%	−0.01	0.00%	−0.01	0.00%	−0.03	0.00%
12	*ap*	g^-	g^-	g^-	0.00%	0.00	0.00%	−0.01	0.00%	−0.03	0.01%
13	g^+	g^+	*ap*	*ap*	8.61%	1.07	5.76%	1.60	8.55%	1.82	14.18%
14	g^+	g^+	*ap*	g^+	0.00%	0.00	0.00%	−0.01	0.01%	−0.03	0.02%
15	g^+	g^-	*ap*	*ap*	58.61%	0.71	45.35%	2.59	38.99%	5.26	24.03%
16	g^+	g^-	g^-	*ap*	0.00%	−0.56	0.00%	−0.61	0.01%	−13.25	2.74%

17	g^-	$+ac$	ap	ap	0.02%	0.01	0.02%	−0.01	0.04%	−0.02	0.06%
18	g^-	ap	ap	ap	0.03%	0.02	0.03%	0.01	0.05%	0.02	0.09%
19	g^-	g^+	ap	ap	0.01%	0.01	0.01%	−0.01	0.02%	0.01	0.04%
20	g^-	g^-	ap	ap	0.01%	0.01	0.01%	0.10	0.02%	0.05	0.03%

	$\Sigma(\Delta\Delta G)^2$ =625		$\Sigma(\Delta\Delta G)^2$ =900		$\Sigma(\Delta\Delta G)^2$ =1600		$\Sigma(\Delta\Delta G)^2$ =1600	
Cluster	NOE−refined $\Delta\Delta G$/kJ mol^{-1}	NOE−Refined Population	NOE−refined $\Delta\Delta G$/kJ mol^{-1}	NOE−Refined Population	NOE−refined $\Delta\Delta G$/kJ mol^{-1}	NOE−Refined Population	NOE−refined $\Delta\Delta G$/kJ mol^{-1}	NOE−Refined Population
1	0.41	0.07%	0.21	0.05%	1.16	0.01%	2.68	0.00%
2	1.15	0.03%	0.78	0.02%	2.40	0.00%	3.95	0.00%
3	3.51	14.54%	2.54	14.11%	−0.67	17.68%	−4.76	18.29%
4	0.00	0.01%	−0.06	0.01%	−0.03	0.00%	−0.03	0.00%
5	−0.19	0.03%	−15.51	10.06%	−18.19	10.16%	−22.20	10.17%
6	11.32	2.31%	9.24	3.49%	13.74	0.19%	16.22	0.01%
7	0.00	2.02%	0.44	1.11%	3.73	0.10%	5.65	0.01%
8	1.68	35.15%	0.90	31.62%	−1.85	32.82%	−5.86	32.97%
9	0.03	0.08%	0.21	0.05%	0.04	0.02%	0.05	0.00%
10	7.08	3.29%	6.54	2.67%	9.82	0.24%	12.05	0.02%
11	−0.03	0.00%	−0.10	0.00%	−0.05	0.00%	−0.05	0.00%
12	−0.54	0.02%	−0.03	0.01%	−0.15	0.00%	−0.16	0.00%
13	6.05	9.41%	8.09	2.71%	12.09	0.18%	14.47	0.01%
14	−1.61	0.11%	−15.64	21.11%	−18.51	23.15%	−22.55	23.44%
15	10.58	10.28%	11.03	5.63%	13.40	0.74%	15.44	0.06%
16	−13.86	12.84%	−0.17	0.03%	0.05	0.01%	0.05	0.00%
17	−9.07	9.20%	−9.39	6.86%	−12.62	8.65%	−16.66	8.79%
18	−0.29	0.39%	−0.82	0.31%	−10.79	6.00%	−14.87	6.19%

19	−0.11	0.16%	0.02	0.10%	0.72	0.03%	1.25	0.00%
20	2.10	0.05%	1.62	0.04%	3.78	0.01%	5.55	0.00%

Table 6.44: Conformation clusters of compounds **2.6** and **2.7 – 2.10** with initial DFT energy derived population, NOE-refined $\Delta\Delta G$ (in kJ mol^{-1}) using a constraint of 400 and NOE-refined population for each cluster.

	Cluster	Φ_1	Φ_2	Φ_3	Φ_4	Initial Population	NOE−refined $\Delta\Delta G$/kJ mol^{-1}	NOE−Refined Population
2.6	1	$-ac$	g^-	ap	ap	0.00%	0.34	0.08%
	2	$-ac$	g^-	g^+	ap	0.00%	−0.04	0.04%
	3	ap	ap	ap	ap	97.94%	14.30	9.89%
	4	ap	ap	ap	g^+	0.02%	−1.53	1.39%
	5	ap	ap	g^-	ap	0.06%	−4.27	11.80%
	6	ap	g^+	ap	ap	0.02%	−8.42	16.90%
	7	ap	g^+	ap	g^+	0.00%	0.00	0.00%
	8	ap	g^+	g^+	$-ac$	0.00%	0.00	0.00%
	9	ap	g^-	ap	ap	1.04%	7.33	1.76%
	10	ap	g^-	ap	g^+	0.00%	0.00	0.00%
	11	ap	sp	ap	ap	0.00%	0.03	0.07%
	12	g^+	$+ac$	ap	ap	0.00%	0.00	0.01%
	13	g^+	ap	ap	ap	0.43%	0.18	13.14%
	14	g^+	ap	ap	g^+	0.00%	0.00	0.00%
	15	g^+	g^+	ap	ap	0.00%	−0.01	0.01%
	16	g^+	g^+	ap	g^+	0.00%	0.00	0.00%
	17	g^+	g^+	g^+	$+ac$	0.00%	0.00	0.00%
	18	g^+	g^+	g^+	ap	0.00%	−0.01	0.01%
	19	g^+	g^-	ap	ap	0.04%	−6.98	22.78%
	20	g^-	$+ac$	ap	ap	0.00%	0.00	0.01%
	21	g^-	ap	ap	ap	0.42%	−1.17	22.03%
	22	g^-	ap	g^-	ap	0.00%	0.00	0.00%
	23	g^-	g^-	ap	ap	0.00%	0.37	0.05%
	24	sp	ap	ap	ap	0.00%	0.00	0.03%
2.7	1	ap	g^+	ap	ap	86.44%	13.00	12.03%
	2	ap	g^+	ap	g^-	0.50%	3.04	3.82%
	3	ap	g^+	g^+	ap	0.01%	−11.22	15.93%
	4	g^+	ap	ap	ap	13.04%	4.15	63.58%
	5	g^+	ap	ap	g^-	0.02%	−0.15	0.45%
	6	g^+	ap	g^+	ap	0.00%	−8.86	4.19%
	7	g^+	g^+	ap	ap	0.00%	0.00	0.00%

	8	g^-	$-ac$	ap	ap	0.00%	−0.03	0.01%
	9	g^-	g^-	ap	ap	0.00%	0.00	0.00%
2.8	1	$+ac$	ap	ap	g^-	0.00%	0.00	0.00%
	2	ap	g^+	ap	ap	2.16%	5.55	1.35%
	3	ap	g^+	ap	g^+	0.09%	−10.16	32.84%
	4	ap	g^+	ap	g^-	71.82%	13.13	2.10%
	5	g^+	ap	ap	ap	0.06%	−1.54	0.65%
	6	g^+	ap	ap	g^-	25.80%	2.72	50.58%
	7	g^+	ap	g^+	ap	0.02%	−0.58	0.16%
	8	g^+	ap	g^+	g^+	0.05%	−9.13	12.32%
2.9	1	$+ac$	ap	$g+$	ap	0.11%	1.30	0.12%
	2	$-ac$	g^-	ap	g^+	0.00%	0.24	0.00%
	3	ap	$-ac$	ap	ap	0.04%	−0.14	0.08%
	4	ap	$-ac$	ap	g^+	0.33%	−5.07	4.96%
	5	ap	ap	ap	ap	0.45%	−7.23	16.03%
	6	ap	ap	ap	g^+	47.58%	8.06	3.56%
	7	ap	ap	g^+	ap	20.59%	8.20	1.45%
	8	ap	g^+	ap	g^+	0.81%	−5.86	16.82%
	9	ap	g^+	$g+$	ap	0.23%	4.31	0.08%
	10	ap	g^-	ap	g^+	0.37%	3.12	0.20%
	11	ap	g^-	$g-$	ap	0.97%	−6.40	25.03%
	12	ap	g^-	$g-$	g^-	0.01%	0.00	0.01%
	13	g^+	g^+	ap	$-ac$	0.00%	0.00	0.00%
	14	g^+	g^+	ap	ap	0.02%	0.16	0.03%
	15	g^+	g^+	ap	g^+	4.44%	−0.07	8.85%
	16	g^+	g^+	g^+	ap	0.05%	0.25	0.09%
	17	g^+	g^-	ap	ap	3.98%	−0.37	8.96%
	18	g^+	g^-	ap	g^+	17.73%	3.58	8.09%
	19	g^+	g^-	g^-	g^-	0.11%	−7.70	4.59%
	20	g^-	ap	ap	ap	0.00%	0.01	0.00%
	21	g^-	ap	g^+	ap	2.19%	3.47	1.04%
2.10	1	$+ac$	ap	ap	ap	0.01%	0.02	0.05%
	2	$-ac$	g^-	ap	ap	0.00%	0.01	0.03%
	3	ap	$-ac$	ap	ap	4.77%	2.58	11.71%
	4	ap	$-ac$	ap	g^+	0.00%	0.00	0.00%

	5	*ap*	*−ac*	g^-	*ap*	0.00%	−0.05	0.02%
	6	*ap*	*ap*	*ap*	*ap*	17.68%	5.86	11.58%
	7	*ap*	*ap*	*ap*	g^+	0.16%	0.00	1.12%
	8	*ap*	g^+	*ap*	*ap*	5.51%	0.20	35.38%
	9	*ap*	g^+	g^-	*ap*	0.01%	0.01	0.04%
	10	*ap*	g^-	*ap*	*ap*	4.56%	5.75	3.12%
	11	*ap*	g^-	g^-	*ap*	0.00%	−0.03	0.00%
	12	*ap*	g^-	g^-	g^-	0.00%	−0.03	0.01%
	13	g^+	g^+	*ap*	*ap*	8.61%	3.59	14.08%
	14	g^+	g^+	*ap*	g^+	0.00%	−0.03	0.03%
	15	g^+	g^-	*ap*	*ap*	58.61%	9.12	10.30%
	16	g^+	g^-	g^-	*ap*	0.00%	−15.16	12.07%
	17	g^-	*+ac*	*ap*	*ap*	0.02%	−0.02	0.13%
	18	g^-	*ap*	*ap*	*ap*	0.03%	0.02	0.19%
	19	g^-	g^+	*ap*	*ap*	0.01%	0.01	0.08%
	20	g^-	g^-	*ap*	*ap*	0.01%	0.05	0.06%

Table 6.45: Experimental $^{n}J_{HH}$ values (in Hz) of Balamycin A and Boltzmann averaged calculated $^{n}J_{HH}$ of C1'-C10 region (fragment A, in Hz) before population refinement for **2.6** and **2.7** – **2.10** with Deviations (Dev, in Hz), Mean Absolute Deviations (MAD, in Hz), Standard Deviations (StDev, in Hz) and χ^2 (reduced) values (χ^2 (red.)).

H	Coupled H	Exp. $^{n}J_{HH}$	Calc. 2.6	Dev.	Calc. 2.7	Dev.	Calc. 2.8	Dev.	Calc. 2.9	Dev.	Calc. 2.10	Dev.
$H_{1'}$	H_{14}	6.8	1.78	−5.02	8.38	1.58	7.34	0.54	7.31	0.51	4.15	−2.65
H_{14}	H_{13}	3.5	2.15	−1.35	2.91	−0.59	2.81	−0.69	6.52	3.02	3.10	−0.40
H_{13}	H_{12a}	3.2	1.15	−2.05	1.21	−1.99	1.53	−1.67	2.94	−0.26	1.44	−1.76
	H_{12b}	10.0	9.14	−0.86	9.47	−0.53	10.39	0.39	8.53	−1.47	9.66	−0.34
H_{12a}	H_{12b}	14.1	14.62	0.52	14.79	0.69	15.16	1.06	14.91	0.81	14.98	0.88
	H_{11}	4.5	2.07	−2.43	1.94	−2.56	2.63	−1.87	4.96	0.46	1.70	−2.80
H_{12b}	H_{11}	8.2	9.49	1.29	9.53	1.33	4.69	−3.51	3.28	−4.92	9.23	1.03
H_{11}	H_{10a}	4.3	2.74	−1.56	5.19	0.89	3.60	−0.70	2.32	−1.98	5.41	1.11
	H_{10b}	8.0	8.46	0.46	5.74	−2.26	8.44	0.44	9.22	1.22	6.35	−1.65
			MAD	1.73	**MAD**	1.38	**MAD**	1.21	**MAD**	1.63	**MAD**	1.40
			StDev	1.90	**StDev**	1.60	**StDev**	1.47	**StDev**	2.27	**StDev**	1.55
			χ^2(red.)	5.31	**χ^2(red.)**	1.56	**χ^2(red.)**	2.66	**χ^2(red.)**	5.26	**χ^2(red.)**	3.00

Table 6.46: Experimental ^{1}H-^{1}H distances derived from 2D-ROESY spectrum provided by Sherman *et al.*[95] and the Boltzmann averaged computed ^{1}H-^{1}H distances of C1'-C10 region (fragment A, in Å) before population refinement for **2.6** and **2.7** – **2.10** with Mean Absolute Deviations (MAD), Standard Deviations (StDev) and χ^2 (reduced) values (χ^2 (red.)).

H	**H_x**	Exp *r* /Å	Calc.**2.6** / Å	% error[a]	Exp *r* /Å	Calc.**2.7** / Å	% error[a]	Exp *r* /Å	Calc.**2.8** / Å	% error[a]
$H_{1'}$	**H_{13}**	3.09	2.28	−30%	3.00	3.77	23%	3.03	3.75	21%
	H_{14}	2.75	2.46	−11%	2.67	2.89	8%	2.70	2.78	3%
	H_{12a}	2.72	4.21	43%	2.64	2.73	3%	2.67	2.83	6%
	H_{12b}	4.15	4.50	8%	4.03	2.43	−50%	4.07	2.46	−49%
	H_{15}	3.02	3.75	22%	2.93	2.70	−8%	2.96	2.75	−7%
H_{13}	**H_{11}**	2.71	2.44	−10%	2.63	2.44	−7%	2.66	3.70	33%
	H_{14}	2.55	2.41	−6%	2.48	2.49	0%	2.50	2.47	−2%
	H_{12a}	2.68	2.52	−6%	2.60	2.54	−3%	2.63	2.54	−4%
	H_{12b}	3.09	3.00	−3%	3.00	3.05	2%	3.03	3.05	1%
	H_{15}	3.26	3.82	16%	3.17	3.26	3%	3.20	3.35	5%
H_{11}	**H_{14}**	3.31	4.17	23%	3.21	4.65	37%	3.24	5.16	46%
	H_{12a}	2.79	2.47	−12%	2.71	2.48	−9%	2.74	2.45	−11%
	H_{12b}	2.90	3.05	5%	2.82	3.04	8%	2.85	2.40	−17%
	H_{10}	2.95	2.64	−11%	2.86	2.59	−10%	2.89	2.65	−9%
	H_{9a}	3.03	2.62	−14%	2.94	2.76	−6%	2.97	2.64	−12%
	H_{9b}	3.10	3.01	−3%	3.01	2.95	−2%	3.04	2.82	−8%
H_{12a}	**H_{14}**	2.86	2.48	−14%	2.77	3.23	15%	2.80	3.01	7%
	H_{12b}	1.85	1.77	−5%	1.80	1.77	−2%	1.82	1.76	−3%
			MAD/%	13.43%		**MAD/%**	10.81%		**MAD/%**	13.42%
			StDev/%	17.30%		**StDev/%**	17.25%		**StDev/%**	20.20%
			χ^2(red.)	11.98		**χ^2(red.)**	11.90		**χ^2(red.)**	16.32

[a]% error = $(r_{cal} - r_{NOE})/((r_{cal} + r_{NOE})/2)$

(Table 6.46 continued)

H	**H_x**	Exp *r* /Å	Calc.**2.9** / Å	% error[a]	Exp *r* /Å	Calc.**2.10** / Å	% error[a]			
$H_{1'}$	**H_{13}**	2.99	2.66	−12%	3.01	3.19	6%			
	H_{14}	2.66	2.79	5%	2.68	2.58	−4%			
	H_{12a}	2.64	4.07	43%	2.65	3.48	27%			
	H_{12b}	4.02	4.26	6%	4.04	4.01	−1%			
	H_{15}	2.92	2.64	−10%	2.94	2.55	−14%			
H_{13}	**H_{11}**	2.62	3.59	31%	2.63	2.42	−8%			
	H_{14}	2.47	2.73	10%	2.48	2.50	1%			
	H_{12a}	2.60	2.46	−5%	2.61	2.51	−4%			
	H_{12b}	2.99	2.81	−6%	3.00	3.05	1%			
	H_{15}	3.16	2.78	−13%	3.18	3.05	−4%			
H_{11}	**H_{14}**	3.20	2.89	−10%	3.22	4.31	29%			
	H_{12a}	2.70	2.50	−8%	2.71	2.50	−8%			
	H_{12b}	2.81	2.46	−13%	2.83	3.05	8%			
	H_{10}	2.85	2.66	−7%	2.87	2.64	−8%			
	H_{9a}	2.93	2.62	−11%	2.95	2.78	−6%			
	H_{9b}	3.00	2.89	−4%	3.02	2.81	−7%			
H_{12a}	**H_{14}**	2.76	2.99	8%	2.78	2.59	−7%			
	H_{12b}	1.79	1.76	−2%	1.80	1.76	−2%			
			MAD/%	11.30%		**MAD/%**	8.07%			
			StDev/%	15.38%		**StDev/%**	11.54%			
			χ^2(red.)	9.47		**χ^2(red.)**	5.32			

[a]% error = $(r_{cal} - r_{NOE})/((r_{cal} + r_{NOE})/2)$

Table 6.47: Experimental $^{n}J_{HH}$ values (in Hz) of balamycin A and population refined (using different constraints) Boltzmann averaged calculated $^{n}J_{HH}$ of C1'-C10 region (fragment A, in Hz) for **2.10** with Deviations (Dev, in Hz), Mean Absolute Deviations (MAD, in Hz), Standard Deviations (StDev, in Hz) and χ^2 (reduced) values (χ^2 (red.))

			$\Sigma(\Delta\Delta G)^2$ =25		$\Sigma(\Delta\Delta G)^2$ =100		$\Sigma(\Delta\Delta G)^2$ =225		$\Sigma(\Delta\Delta G)^2$ =625		$\Sigma(\Delta\Delta G)^2$ =900	
H	**Coupled H**	**Exp. $^{n}J_{HH}$**	**Calc.**	**Dev.**	**Calc.**	**Dev.**	**Calc.**	**Dev.**	**Calc.**	**Dev.**	**Calc.**	**Dev.**
$H_{1'}$	**H_{14}**	6.8	5.44	−1.36	5.71	−1.09	6.17	−0.63	6.73	−0.07	6.75	−0.05
H_{14}	**H_{13}**	3.5	2.94	−0.56	3.06	−0.44	3.24	−0.26	1.85	−1.65	1.87	−1.63
H_{13}	**H_{12a}**	3.2	1.50	−1.70	1.57	−1.63	1.80	−1.40	2.79	−0.41	2.79	−0.41
	H_{12b}	10.0	9.74	−0.26	9.80	−0.20	9.74	−0.26	9.03	−0.97	9.21	−0.79
H_{12a}	**H_{12b}**	14.1	14.92	0.82	14.78	0.68	14.87	0.77	14.83	0.73	14.71	0.61
	H_{11}	4.5	1.60	−2.90	2.37	−2.13	1.54	−2.96	2.12	−2.38	4.03	−0.47
H_{12b}	**H_{11}**	8.2	9.07	0.87	8.62	0.42	8.96	0.76	9.12	0.92	7.58	−0.62
H_{11}	**H_{10a}**	4.3	4.95	0.65	4.58	0.28	4.34	0.04	4.24	−0.06	3.87	−0.43
	H_{10b}	8.0	6.78	−1.22	6.97	−1.03	6.99	−1.01	7.21	−0.79	7.63	−0.37
			MAD	1.15	**MAD**	0.88	**MAD**	0.90	**MAD**	0.89	**MAD**	0.60
			StDev	1.29	**StDev**	0.97	**StDev**	1.16	**StDev**	1.06	**StDev**	0.59
			χ^2(red.)	2.11	**χ^2(red.)**	1.30	**χ^2(red.)**	1.68	**χ^2(red.)**	1.43	**χ^2(red.)**	0.59

(Table 6.47 continued)

			$\Sigma(\Delta\Delta G)^2$ =1600		$\Sigma(\Delta\Delta G)^2$ =2500	
H	**Coupled H**	**Exp. $^{n}J_{HH}$**	**Calc.**	**Dev.**	**Calc.**	**Dev.**
$H_{1'}$	**H_{14}**	6.8	6.69	−0.11	6.62	−0.18
H_{14}	**H_{13}**	3.5	2.16	−1.34	2.16	−1.34
H_{13}	**H_{12a}**	3.2	2.71	−0.49	2.73	−0.47
	H_{12b}	10.0	9.07	−0.93	9.08	−0.92
H_{12a}	**H_{12b}**	14.1	14.73	0.63	14.74	0.64
	H_{11}	4.5	4.12	−0.38	4.18	−0.32
H_{12b}	**H_{11}**	8.2	7.66	−0.54	7.62	−0.58
H_{11}	**H_{10a}**	4.3	3.81	−0.49	3.65	−0.65
	H_{10b}	8.0	7.79	−0.21	7.92	−0.08
			MAD	0.57	**MAD**	0.57
			StDev	0.54	**StDev**	0.56
			χ^2(red.)	0.50	**χ^2(red.)**	0.52

Table 6.48: Experimental $^{n}J_{HH}$ values (in Hz) of balamycin A and population refined ($\Sigma(\Delta\Delta G)^2$ =400) Boltzmann averaged calculated $^{n}J_{HH}$ of C1'-C10 region (fragment A, in Hz) for **2.6** and **2.7** – **2.10** with Deviations (Dev, in Hz), Mean Absolute Deviations (MAD, in Hz), Standard Deviations (StDev, in Hz) and χ^2 (reduced) values (χ^2 (red.))

H	Coupled H	Exp. $^{n}J_{HH}$	Calc. 2.6	Dev	Calc. 2.7	Dev.	Calc. 2.8	Dev.	Calc. 2.9	Dev.	Calc. 2.10	Dev.
$H_{1'}$	H_{14}	6.8	4.72	−2.08	4.72	−2.08	5.51	−1.29	6.53	−0.27	6.93	0.13
H_{14}	H_{13}	3.5	4.20	0.70	2.25	−1.25	2.30	−1.20	4.13	0.63	2.63	−0.87
H_{13}	H_{12a}	3.2	2.37	−0.83	3.09	−0.11	2.10	−1.10	5.01	1.81	2.83	−0.37
	H_{12b}	10.0	9.41	−0.59	8.20	−1.80	9.40	−0.60	8.24	−1.76	9.17	−0.83
H_{12a}	H_{12b}	14.1	14.71	0.61	14.57	0.47	14.59	0.49	14.88	0.78	14.75	0.65
	H_{11}	4.5	1.70	−2.80	2.36	−2.14	2.57	−1.93	7.19	2.69	1.75	−2.75
H_{12b}	H_{11}	8.2	8.96	0.76	9.59	1.39	6.94	−1.26	2.73	−5.47	9.04	0.84
H_{11}	H_{10a}	4.3	3.34	−0.96	3.52	−0.78	4.66	0.36	7.11	2.81	4.13	−0.17
	H_{10b}	8.0	8.19	0.19	6.22	−1.78	7.77	−0.23	5.40	−2.60	7.35	−0.65
			MAD	1.06	**MAD**	1.31	**MAD**	0.94	**MAD**	2.09	**MAD**	0.81
			StDev	1.27	**StDev**	1.25	**StDev**	0.82	**StDev**	2.72	**StDev**	1.06
			χ^2(red.)	1.96	**χ^2(red.)**	2.46	**χ^2(red.)**	1.30	**χ^2(red.)**	7.40	**χ^2(red.)**	1.34

Table 6.49: Experimental ^{1}H-^{1}H distances derived from 2D-ROESY spectrum provided by Sherman *et al.*[95] and the population refined (using different constraints) Boltzmann averaged computed ^{1}H-^{1}H distances of C1'-C10 region (fragment A, in Å) for **2.10** with Mean Absolute Deviations (MAD), Standard Deviations (StDev) and χ^2 (reduced) values (χ^2 (red.)).

		$\Sigma(\Delta\Delta G)^2$ =25			$\Sigma(\Delta\Delta G)^2$ =100			$\Sigma(\Delta\Delta G)^2$ =225		
H	**H_x**	Exp *r* /Å	Calc./ Å	% error[a]	Exp *r*/Å	Calc./ Å	% error[a]	Exp *r* /Å	Calc./ Å	% error[a]
$H_{1'}$	**H_{13}**	2.98	3.10	4%	2.98	3.06	3%	2.96	3.05	3%
	H_{14}	2.65	2.65	0%	2.65	2.66	0%	2.64	2.68	2%
	H_{12a}	2.62	2.77	6%	2.62	2.80	6%	2.61	2.81	7%
	H_{12b}	4.00	3.84	−4%	4.00	3.84	−4%	3.98	3.83	−4%
	H_{15}	2.91	2.58	−12%	2.91	2.59	−12%	2.90	2.64	−9%
H_{13}	**H_{11}**	2.61	2.42	−7%	2.61	2.45	−6%	2.60	2.44	−6%
	H_{14}	2.46	2.50	2%	2.46	2.51	2%	2.44	2.53	4%
	H_{12a}	2.58	2.51	−3%	2.58	2.51	−3%	2.57	2.51	−2%
	H_{12b}	2.97	3.05	2%	2.97	3.05	2%	2.96	3.01	2%
	H_{15}	3.14	3.16	1%	3.14	3.14	0%	3.13	3.10	−1%
H_{11}	**H_{14}**	3.18	4.39	32%	3.18	4.39	32%	3.17	3.82	19%
	H_{12a}	2.69	2.50	−7%	2.69	2.52	−6%	2.67	2.50	−7%
	H_{12b}	2.80	3.05	8%	2.80	2.96	6%	2.78	3.04	9%
	H_{10}	2.84	2.64	−7%	2.84	2.64	−7%	2.82	2.63	−7%
	H_{9a}	2.92	2.76	−5%	2.92	2.73	−7%	2.90	2.76	−5%
	H_{9b}	2.99	2.83	−5%	2.99	2.85	−5%	2.97	2.86	−4%
H_{12a}	**H_{14}**	2.75	2.71	−1%	2.75	2.73	−1%	2.74	2.76	1%
	H_{12b}	1.78	1.76	−1%	1.78	1.76	−1%	1.77	1.76	−1%
			MAD/%	6.05%		**MAD/%**	5.76%		**MAD/%**	5.07%
			StDev/%	9.51%		**StDev/%**	9.27%		**StDev/%**	6.84%
			χ^2(red.)	3.65		**χ^2(red.)**	3.44		**χ^2(red.)**	1.87

[a]% error = $(r_{cal} - r_{NOE})/((r_{cal} + r_{NOE})/2)$

(Table 6.49 continued)

		$\Sigma(\Delta\Delta G)^2$ =625			$\Sigma(\Delta\Delta G)^2$ =900			$\Sigma(\Delta\Delta G)^2$ =1600		
H	**H_x**	Exp *r* /Å	Calc./ Å	% error[a]	Exp *r*/Å	Calc./ Å	% error[a]	Exp *r* /Å	Calc./ Å	% error[a]
$H_{1'}$	**H_{13}**	2.92	2.94	1%	2.94	2.99	2%	2.94	2.99	2%
	H_{14}	2.60	2.65	2%	2.62	2.65	1%	2.62	2.63	0%
	H_{12a}	2.57	2.69	5%	2.59	2.73	5%	2.59	2.72	5%
	H_{12b}	3.92	3.81	−3%	3.95	3.86	−2%	3.95	3.88	−2%
	H_{15}	2.85	2.70	−6%	2.87	2.75	−4%	2.88	2.80	−3%
H_{13}	**H_{11}**	2.55	2.48	−3%	2.57	2.54	−1%	2.58	2.55	−1%
	H_{14}	2.41	2.52	5%	2.43	2.52	4%	2.43	2.53	4%
	H_{12a}	2.53	2.55	1%	2.55	2.54	0%	2.55	2.55	0%
	H_{12b}	2.91	2.89	−1%	2.94	2.96	1%	2.94	2.96	1%
	H_{15}	3.08	3.08	0%	3.10	3.19	3%	3.11	3.15	2%
H_{11}	**H_{14}**	3.12	3.15	1%	3.14	3.14	0%	3.15	3.14	0%
	H_{12a}	2.63	2.49	−5%	2.65	2.57	−3%	2.65	2.57	−3%
	H_{12b}	2.74	3.02	10%	2.76	2.85	3%	2.76	2.84	3%
	H_{10}	2.78	2.63	−5%	2.80	2.64	−6%	2.81	2.65	−6%
	H_{9a}	2.86	2.72	−5%	2.88	2.72	−6%	2.88	2.73	−6%
	H_{9b}	2.92	2.87	−2%	2.95	2.95	0%	2.95	2.98	1%
H_{12a}	**H_{14}**	2.69	2.82	5%	2.72	2.84	4%	2.72	2.84	4%
	H_{12b}	1.74	1.76	1%	1.76	1.76	0%	1.76	1.76	0%
			MAD/%	3.30%		**MAD/%**	2.59%		**MAD/%**	2.33%
			StDev/%	4.21%		**StDev/%**	3.32%		**StDev/%**	3.06%
			χ^2(red.)	0.71		**χ^2(red.)**	0.44		**χ^2(red.)**	0.38

[a]% error = $(r_{cal} - r_{NOE})/((r_{cal} + r_{NOE})/2)$

(Table 6.49 continued)

		$\Sigma(\Delta\Delta G)^2$ =2500		
H	**H_x**	Exp *r* /Å	Calc./ Å	% error[a]
$H_{1'}$	**H_{13}**	2.94	2.99	1%
	H_{14}	2.62	2.63	0%
	H_{12a}	2.59	2.72	5%
	H_{12b}	3.95	3.88	−2%
	H_{15}	2.88	2.81	−3%
H_{13}	**H_{11}**	2.58	2.55	−1%
	H_{14}	2.43	2.53	4%
	H_{12a}	2.55	2.55	0%
	H_{12b}	2.94	2.96	1%
	H_{15}	3.11	3.15	1%
H_{11}	**H_{14}**	3.15	3.14	0%
	H_{12a}	2.65	2.57	−3%
	H_{12b}	2.76	2.84	3%
	H_{10}	2.81	2.65	−6%
	H_{9a}	2.88	2.73	−6%
	H_{9b}	2.95	2.98	1%
H_{12a}	**H_{14}**	2.72	2.84	4%
	H_{12b}	1.76	1.76	0%
			MAD/%	2.32%
			StDev/%	3.05%
			χ^2(red.)	0.37

[a]% error = $(r_{cal} - r_{NOE})/((r_{cal} + r_{NOE})/2)$

Table 6.50: Experimental ^{1}H-^{1}H distances derived from 2D-ROESY spectrum provided by Sherman *et al.*[95] and the population refined ($\Sigma(\Delta\Delta G)^2$ =400) Boltzmann averaged computed ^{1}H-^{1}H distances of C1'-C10 region (fragment A, in Å) for **2.6** and **2.7** – **2.10** with Mean Absolute Deviations (MAD), Standard Deviations (StDev) and χ^2 (reduced) values (χ^2 (red.)).

H	**H$_x$**	Exp *r* /Å	Calc.**2.6** / Å	% error[a]	Exp *r*/Å	Calc.**2.7** / Å	% error[a]	Exp *r* /Å	Calc.**2.8** / Å	% error[a]
H$_{1'}$	**H$_{13}$**	2.89	2.76	−5%	3.00	3.70	21%	2.94	3.70	23%
	H$_{14}$	2.57	2.49	−3%	2.67	2.55	−5%	2.62	2.57	−2%
	H$_{12a}$	2.55	2.85	11%	2.64	2.99	12%	2.59	3.02	15%
	H$_{12b}$	3.88	3.35	−15%	4.03	3.17	−24%	3.95	2.87	−32%
	H$_{15}$	2.83	2.86	1%	2.93	3.01	3%	2.87	2.96	3%
H$_{13}$	**H$_{11}$**	2.53	2.48	−2%	2.63	2.50	−5%	2.58	2.81	9%
	H$_{14}$	2.39	2.47	3%	2.48	2.44	−1%	2.43	2.45	1%
	H$_{12a}$	2.51	2.52	0%	2.60	2.59	0%	2.55	2.57	1%
	H$_{12b}$	2.89	2.93	1%	3.00	2.82	−6%	2.94	2.89	−1%
	H$_{15}$	3.05	3.22	5%	3.17	3.34	5%	3.11	3.52	12%
H$_{11}$	**H$_{14}$**	3.09	3.17	2%	3.21	3.61	12%	3.14	3.14	0%
	H$_{12a}$	2.61	2.50	−4%	2.71	2.49	−8%	2.65	2.47	−7%
	H$_{12b}$	2.72	3.03	11%	2.82	3.00	6%	2.76	2.58	−7%
	H$_{10}$	2.76	2.65	−4%	2.86	2.54	−12%	2.80	2.66	−5%
	H$_{9a}$	2.83	2.62	−8%	2.94	3.07	4%	2.88	2.72	−6%
	H$_{9b}$	2.90	2.92	1%	3.01	3.17	5%	2.95	2.75	−7%
H$_{12a}$	**H$_{14}$**	2.67	2.69	1%	2.77	2.63	−5%	2.72	2.73	0%
	H$_{12b}$	1.73	1.77	2%	1.80	1.77	−2%	1.76	1.76	0%
			MAD/%	4.46%		**MAD/%**	7.63%		**MAD/%**	7.33%
			StDev/%	6.17%		**StDev/%**	10.14%		**StDev/%**	11.43%
			χ^2(red.)	1.52		**χ^2(red.)**	4.11		**χ^2(red.)**	5.23

[a]% error = $(r_{cal} - r_{NOE})/((r_{cal} + r_{NOE})/2)$

(Table 6.50 continued)

H	**H_x**	Exp *r* /Å	Calc.**2.9** / Å	% error[a]	Exp *r*/Å	Calc.**2.10** / Å	% error[a]			
$H_{1'}$	**H_{13}**	2.96	3.07	4%	2.94	3.07	4%			
	H_{14}	2.63	2.76	5%	2.62	2.69	3%			
	H_{12a}	2.61	2.89	10%	2.59	2.69	4%			
	H_{12b}	3.97	3.69	−7%	3.95	3.82	−3%			
	H_{15}	2.89	2.69	−7%	2.88	2.67	−7%			
H_{13}	**H_{11}**	2.59	2.85	10%	2.58	2.47	−4%			
	H_{14}	2.44	2.51	3%	2.43	2.53	4%			
	H_{12a}	2.57	2.59	1%	2.55	2.54	−1%			
	H_{12b}	2.95	2.73	−8%	2.94	2.90	−2%			
	H_{15}	3.12	3.03	−3%	3.11	3.06	−2%			
H_{11}	**H_{14}**	3.16	3.19	1%	3.15	3.18	1%			
	H_{12a}	2.67	2.64	−1%	2.65	2.50	−6%			
	H_{12b}	2.78	2.50	−11%	2.76	3.03	9%			
	H_{10}	2.82	2.64	−7%	2.81	2.63	−6%			
	H_{9a}	2.90	3.01	4%	2.88	2.74	−5%			
	H_{9b}	2.97	3.00	1%	2.95	2.87	−3%			
H_{12a}	**H_{14}**	2.73	2.93	7%	2.72	2.86	5%			
	H_{12b}	1.77	1.76	−1%	1.76	1.77	0%			
			MAD/%	4.97%		**MAD/%**	3.87%			
			StDev/%	6.18%		**StDev/%**	4.64%			
			χ^2(red.)	1.53		**χ^2(red.)**	0.87			

[a]% error = $(r_{cal} - r_{NOE})/((r_{cal} + r_{NOE})/2)$

The fit of all calculated NMR parameters for fragment A of **2.6** and **2.7 – 2.10**, to those of the experimental parameters derived from the natural product is shown in Figure 6.24.

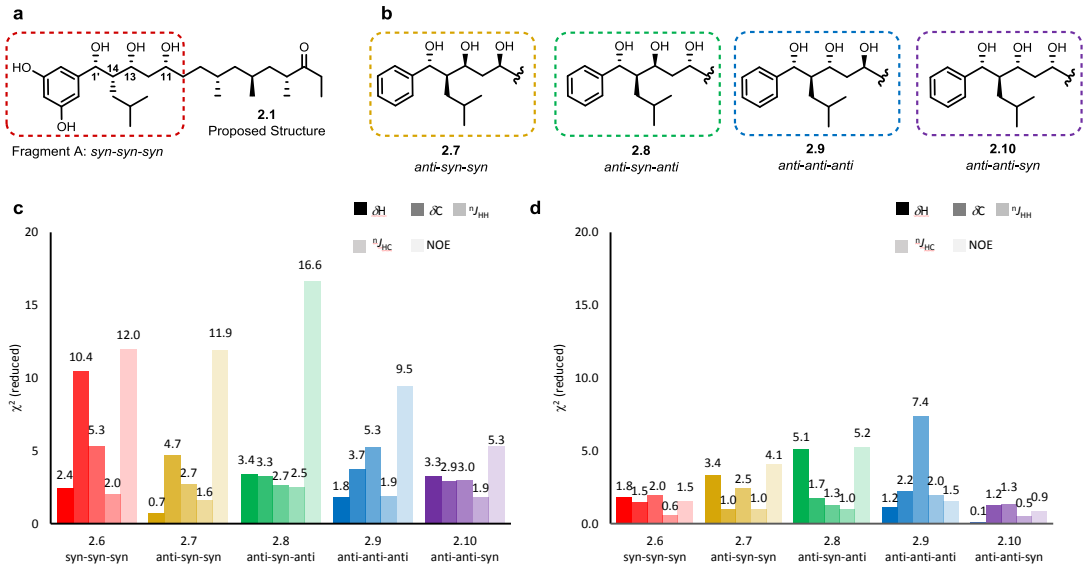

Figure 6.24: **a**. Generic structure of isomers studied for fragment A analysis using conformers obtained from octanol MM conformational search. **b**. Relative stereochemistry of isomers studied for fragment A analysis. Results of comparison of NMR properties (^{1}H and ^{13}C chemical shifts, ^{1}H-^{1}H and ^{1}H-^{13}C scalar coupling constants, NOE distances) (**c**) before and (**d**) after population refinement.

NMR data of fragment B (compounds 2.10 and 2.12 – 2.14, gas MM conformational search)

Table 6.51: Comparison of experimental ^{1}H chemical shifts re-extracted from the ^{1}H spectrum provided by Sherman *et al.*[95] with the calculated scaled ^{1}H chemical shifts for compound **2.10** and **2.12** – **2.14** obtained from conformers generated by gas conformational search with Deviations (Dev., in ppm), Mean Absolute Deviations (MAD, in ppm), Standard Deviations (StDev, in ppm) and χ^2 (reduced) values (χ^2 (red.)).

H	δ_H/ppm	2.10	Dev.	2.12	Dev.	2.13	2.14	Q	Dev.
H_8	1.53	1.74	0.21	1.84	0.31	1.73	0.20	1.67	0.14
H_{7a}	1.22	1.24	0.02	1.11	–0.11	1.40	0.18	1.08	–0.14
H_{7b}	0.95	1.03	0.08	0.99	0.04	0.54	–0.41	0.97	0.02
H_6	1.43	1.43	0.00	1.12	–0.31	1.19	–0.24	1.10	–0.33
H_{5a}	1.73	1.53	–0.20	2.03	0.30	1.75	0.02	1.63	–0.10
H_{5b}	1.00	1.18	0.18	0.77	–0.23	1.31	0.31	1.01	0.01
H_4	2.76	2.76	0.00	2.82	0.06	2.64	–0.12	2.88	0.12
H_{19}	0.86	0.85	–0.01	0.89	0.03	0.78	–0.08	0.82	–0.04
H_{20}	0.88	0.94	0.06	0.95	0.07	0.87	–0.01	0.78	–0.10
H_{21}	1.06	1.10	0.04	1.19	0.13	1.21	0.15	1.14	0.08
		MAD	0.08	**MAD**	0.16	**MAD**	0.17	**MAD**	0.11
		StDev	0.11	**StDev**	0.20	**StDev**	0.22	**StDev**	0.14
		χ^2(red.)	0.62	**χ^2(red.)**	1.85	**χ^2(red.)**	2.17	**χ^2(red.)**	0.90

Table 6.52: Comparison of experimental ^{13}C chemical shifts re-extracted from the ^{13}C spectrum provided by Sherman *et al.*[95] with the calculated scaled ^{13}C chemical shifts for compound **2.10** and **2.12** – **2.14** obtained from conformers generated by gas conformational search with Deviations (Dev., in ppm), Mean Absolute Deviations (MAD, in ppm), Standard Deviations (StDev, in ppm) and and χ^2 (reduced) values (χ^2 (red.)).

C	δC/ppm	2.10	Dev.	2.12	Dev.	2.13	2.14	Q	Dev.
C_9	33.38	32.47	–0.91	29.78	–3.60	29.24	–4.14	29.82	–3.56
C_8	31.23	30.95	–0.28	27.90	–3.33	29.84	–1.39	30.71	–0.52
C_7	46.61	44.24	–2.37	46.94	0.33	38.83	–7.78	43.87	–2.74
C_6	29.47	29.08	–0.39	30.57	1.10	30.84	1.37	29.85	0.38
C_5	42.00	41.38	–0.62	38.35	–3.65	43.08	1.08	42.42	0.42
C_4	44.96	44.74	–0.22	46.48	1.52	47.99	3.03	46.21	1.25
C_{19}	20.55	19.87	–0.68	20.78	0.23	21.03	0.48	22.08	1.53
C_{20}	20.85	22.17	1.32	21.98	1.13	21.78	0.93	18.99	–1.86
C_{21}	18.17	18.42	0.25	20.06	1.89	19.90	1.73	20.91	2.74
		MAD	0.78	**MAD**	1.86	**MAD**	2.44	**MAD**	1.67
		StDev	0.98	**StDev**	2.34	**StDev**	3.42	**StDev**	2.09
		χ^2(red.)	0.52	**χ^2(red.)**	2.55	**χ^2(red.)**	5.33	**χ^2(red.)**	1.98

Table 6.53: Experimental $^{n}J_{HH}$ values (in Hz) of balamycin A and Boltzmann averaged calculated $^{n}J_{HH}$ of C4-C8 region (fragment B, in Hz) for **2.10** and **2.12** – **2.14** obtained from conformers generated by gas conformational search with Mean Absolute Deviations (MAD, in Hz), Standard Deviations (StDev, in Hz) and χ^2 (reduced) values (χ^2 (red.)).

H	Coupled H	Exp. $^{n}J_{HH}$	Calc. 2.10	Deviation	Calc. 2.12	Deviation	Calc. 2.13	Deviation	Calc. 2.14	Deviation
H_8	**H_{7a}**	7.5	6.3	–1.2	2.0	–5.5	3.6	–3.9	10.4	2.9
	H_{7b}	7.2	7.7	0.5	9.9	2.7	9.1	1.9	3.8	–3.4
	H_{19}	6.6	6.2	–0.4	6.2	–0.4	6.5	–0.1	6.5	–0.1
H_{7a}	**H_{7b}**	13.8	14.5	0.7	14.5	0.7	14.7	0.9	14.6	0.8
	H_6	7.5	6.5	–1.0	10.3	2.8	8.7	1.2	1.7	–5.8
H_{7b}	**H_6**	7.2	5.7	–1.5	1.9	–5.3	3.5	–3.7	9.5	2.3
H_6	**H_{5a}**	5	5.4	0.4	0.8	–4.2	2.9	–2.1	1.9	–3.1
	H_{5b}	8.8	7.4	–1.4	9.0	0.2	9.8	1.0	9.8	1.0
	H_{20}	7	6.2	–0.8	6.2	–0.8	6.1	–0.9	6.2	–0.8
H_{5a}	**H_{5b}**	14	14.2	0.2	14.3	0.3	14.8	0.8	14.3	0.3
	H_4	9.1	7.8	–1.3	10.8	1.7	10.8	1.7	10.8	1.7
H_{5b}	**H_4**	5.3	5.7	0.4	2.1	–3.2	4.2	–1.1	2.5	–2.8
H_4	**H_{21}**	6.9	6.4	–0.5	6.8	–0.1	6.5	–0.4	6.8	–0.1
			MAD/Hz	0.8	**MAD/Hz**	2.1	**MAD/Hz**	1.5	**MAD/Hz**	1.9
			StDev/Hz	0.8	**StDev/Hz**	2.8	**StDev/Hz**	1.9	**StDev/Hz**	2.5
			χ^2(red.)	0.9	**χ^2(red.)**	8.8	**χ^2(red.)**	3.8	**χ^2(red.)**	6.8

Table 6.54: Experimental $^{n}J_{HC}$ values of synthetic baulamycin A(**2.17**, in Hz) and Boltzmann averaged calculated $^{n}J_{HC}$ of C4-C8 region (fragment B) for **2.10** and **2.12** – **2.14** obtained from conformers generated by gas conformational search with Mean Absolute Deviations (MAD, in Hz), Standard Deviations (StDev, in Hz) and χ^2 (reduced) values (χ^2 (red.)).

Proton	Coupled	Exp. $^{n}J_{HC}$[a]	Calc. 2.10	Deviation	Calc. 2.12	Deviation	Calc. 2.13	Deviation	Calc. 2.14	Deviation
H_{7a}	**C_9**	5.1	5.4	0.3	3.9	–1.2	5.8	0.7	2.3	–2.8
H_{7b}	**C_9**	4.8	2.7	–2.1	7.2	2.4	3.3	–1.5	6.2	1.4
H_6	**C_4**	4.3	2.2	–2.1	4.3	0.0	3.2	–1.1	3.6	–0.7
H_{5a}	**C_7**	3.3	5.4	2.1	4.3	1.0	6.1	2.8	4.6	1.3
	C_{20}	6.2	3.5	–2.7	1.8	–4.4	3.2	–3.0	6.8	0.6
	C_{21}	3.7	4.1	0.4	7.1	3.4	4.3	0.6	2.3	–1.4
H_{5b}	**C_7**	3.3	2.8	–0.5	0.4	–2.9	3.6	0.3	0.9	–2.4
	C_{21}	3.7	3.6	–0.1	5.8	2.1	1.9	–1.8	3.1	–0.6
	C_{20}	5.0	3.9	–1.1	3.4	–1.6	2.8	–2.2	4.4	0.7
H_4	**C_6**	2.6	2.1	–0.5	2.2	–0.4	1.3	–1.3	1.7	–0.9
			MAD/Hz	1.2	**MAD/Hz**	1.9	**MAD/Hz**	1.5	**MAD/Hz**	1.3
			StDev/Hz	1.4	**StDev/Hz**	2.5	**StDev/Hz**	1.7	**StDev/Hz**	1.5
			χ^2(red.)	2.5	**χ^2(red.)**	6.1	**χ^2(red.)**	3.4	**χ^2(red.)**	2.5

[a] Experimental $^{n}J_{CH}$ values reported here were extracted from NMR spectra measured on the synthetic Baulamycin A **2.17**

NMR data of fragment B (compounds 2.10 and 2.12 – 2.14, octanol MM conformational search)

Table 6.55: Comparison of experimental ^{1}H chemical shifts re-extracted from the ^{1}H spectrum provided by Sherman *et al.*[95] with the calculated scaled ^{1}H chemical shifts for compound **2.10** and **2.12** – **2.14** obtained from conformers generated by octanol conformational search with Deviations (Dev., in ppm), Mean Absolute Deviations (MAD, in ppm), Standard Deviations (StDev, in ppm) and χ^2 (reduced) values (χ^2 (red.)).

H	δ_H/ppm	2.10	Dev.	2.12	Dev.	2.13	2.14	Q	Dev.
H_8	1.53	1.43	–0.10	1.87	0.34	1.67	0.14	1.52	–0.01
H_{7a}	1.22	1.20	–0.02	1.11	–0.11	1.26	0.04	1.19	–0.03
H_{7b}	0.95	0.93	–0.02	1.00	0.05	0.70	–0.25	0.98	0.03
H_6	1.43	1.39	–0.04	1.13	–0.30	1.35	–0.08	1.41	–0.02
H_{5a}	1.73	1.79	0.06	2.02	0.29	1.88	0.15	1.81	0.08
H_{5b}	1.00	0.97	–0.03	0.77	–0.23	1.24	0.24	0.90	–0.10
H_4	2.76	2.83	0.07	2.82	0.06	2.69	–0.07	2.82	0.06
H_{19}	0.86	0.81	–0.05	0.91	0.05	0.82	–0.04	0.92	0.06
H_{20}	0.88	0.89	0.01	0.94	0.06	0.90	0.02	0.92	0.04
H_{21}	1.06	1.11	0.05	1.18	0.12	1.18	0.12	1.13	0.07
		MAD	0.05	**MAD**	0.16	**MAD**	0.11	**MAD**	0.05
		StDev	0.05	**StDev**	0.20	**StDev**	0.14	**StDev**	0.06
		χ^2(red.)	0.14	**χ^2(red.)**	1.88	**χ^2(red.)**	0.94	**χ^2(red.)**	0.16

Table 6.56: Comparison of experimental ^{13}C chemical shifts re-extracted from the ^{13}C spectrum provided by Sherman *et al.*[95] with the calculated scaled ^{13}C chemical shifts for compound **2.10** and **2.12** – **2.14** obtained from conformers generated by octanol conformational search with Deviations (Dev., in ppm), Mean Absolute Deviations (MAD, in ppm), Standard Deviations (StDev, in ppm) and χ^2 analysis.

C	δC/ppm	2.10	Dev.	2.12	Dev.	2.13	2.14	Q	Dev.
C_9	33.38	35.21	1.83	30.12	–3.26	30.23	–3.15	32.34	–1.04
C_8	31.23	31.76	0.53	27.75	–3.48	29.83	–1.40	32.14	0.91
C_7	46.61	42.98	–3.63	47.08	0.47	40.87	–5.74	44.76	–1.85
C_6	29.47	29.22	–0.25	30.55	1.08	30.53	1.06	29.44	–0.03
C_5	42.00	41.58	–0.42	38.54	–3.46	41.90	–0.10	40.23	–1.77
C_4	44.96	43.38	–1.58	46.50	1.54	46.13	1.17	44.52	–0.44
C_{19}	20.55	18.41	–2.14	20.71	0.16	20.59	0.04	20.29	–0.26
C_{20}	20.85	20.44	–0.41	21.92	1.07	21.47	0.62	20.46	–0.39
C_{21}	18.17	20.26	2.09	20.11	1.94	20.26	2.09	19.73	1.56
		MAD	1.43	**MAD**	1.83	**MAD**	1.71	**MAD**	0.92
		StDev	1.83	**StDev**	2.28	**StDev**	2.47	**StDev**	1.12
		χ^2(red.)	1.59	**χ^2(red.)**	2.42	**χ^2(red.)**	2.89	**χ^2(red.)**	0.63

Table 6.57: Experimental $^{n}J_{HH}$ values (in Hz) of balamycin A and Boltzmann averaged calculated $^{n}J_{HH}$ of C4-C8 region (fragment B, in Hz) for **2.10** and **2.12** – **2.14** obtained from conformers generated by octanol conformational search with Mean Absolute Deviations (MAD, in Hz), Standard Deviations (StDev, in Hz) and χ^2 analysis.

H	Coupled H	Exp. $^{n}J_{HH}$	Calc. 2.10	Deviation	Calc. 2.12	Deviation	Calc. 2.13	Deviation	Calc. 2.14	Deviation
H_8	**H_{7a}**	7.5	10.1	2.6	2.1	–5.4	7.9	0.4	8.3	0.8
	H_{7b}	7.2	3.4	–3.8	9.8	2.6	4.8	–2.4	5.8	–1.4
	H_{19}	6.6	6.1	–0.5	6.2	–0.4	6.3	–0.3	6.2	–0.4
H_{7a}	**H_{7b}**	13.8	13.9	0.1	14.5	0.7	14.7	0.9	14.3	0.5
	H_6	7.5	3.3	–4.2	10.2	2.7	4.9	–2.6	5.0	–2.5
H_{7b}	**H_6**	7.2	10.2	3.0	1.9	–5.3	7.8	0.6	7.6	0.4
H_6	**H_{5a}**	5	3.3	–1.7	0.9	–4.1	3.8	–1.2	3.0	–2.0
	H_{5b}	8.8	9.2	0.4	9.0	0.2	8.2	–0.6	9.4	0.6
	H_{20}	7	6.2	–0.8	6.2	–0.8	6.2	–0.8	6.1	–0.9
H_{5a}	**H_{5b}**	14	14.2	0.2	14.3	0.3	14.7	0.7	14.2	0.2
	H_4	9.1	9.8	0.7	10.8	1.7	9.7	0.6	10.0	0.9
H_{5b}	**H_4**	5.3	3.3	–2.0	2.1	–3.2	4.1	–1.2	3.2	–2.1
H_4	**H_{21}**	6.9	6.6	–0.3	6.8	–0.1	6.5	–0.4	6.7	–0.2
			MAD	1.6	**MAD**	2.1	**MAD**	1.0	**MAD**	1.0
			StDev	2.1	**StDev**	2.8	**StDev**	1.1	**StDev**	1.2
			χ^2(red.)	4.7	**χ^2(red.)**	8.6	**χ^2(red.)**	1.6	**χ^2(red.)**	1.6

Table 6.58: Experimental $^{n}J_{HC}$ values of synthetic baulamycin A(compound **2.17**, in Hz) and Boltzmann averaged calculated $^{n}J_{HC}$ of C4-C8 region (fragment B) for **2.10** and **2.12** – **2.14** obtained from conformers generated by octanol conformational search with Mean Absolute Deviations (MAD, in Hz), Standard Deviations (StDev, in Hz) and χ^2 analysis.

Proton	Coupled Carbon	Exp. $^{n}J_{HC}$[a]	Calc. 2.10	Deviation	Calc. 2.12	Deviation	Calc. 2.13	Deviation	Calc. 2.14	Deviation
H_{7a}	**C_9**	5.1	2.5	–2.6	7.2	2.1	5.8	0.7	2.3	–2.8
H_{7b}	**C_9**	4.8	2.8	–2.0	3.8	–1.0	3.3	–1.5	5.7	0.9
H_6	**C_4**	4.3	2.4	–1.9	4.2	–0.1	3.5	–0.8	2.7	–1.6
H_{5a}	**C_7**	3.3	6.6	3.3	4.2	0.9	5.1	1.8	3.4	0.1
	C_{20}	6.2	2.8	–3.4	1.8	–4.4	3.1	–3.1	7.0	0.8
	C_{21}	3.7	3.7	0.0	7.1	3.4	4.7	1.0	2.7	–1.0
H_{5b}	**C_7**	3.3	3.4	0.1	0.5	–2.8	4.0	0.7	2.0	–1.3
	C_{21}	3.7	2.4	–1.3	5.7	2.0	2.7	–1.0	3.3	–0.4
	C_{20}	5.0	3.4	–1.5	3.4	–1.6	3.5	–1.5	3.7	–1.2
H_4	**C_6**	2.6	1.8	–0.8	2.2	–0.4	1.8	–0.8	1.8	–0.8
			MAD	1.7	**MAD**	1.9	**MAD**	1.3	**MAD**	1.1
			StDev	1.8	**StDev**	2.4	**StDev**	1.5	**StDev**	1.1
			χ^2(red.)	4.6	**χ^2(red.)**	5.8	**χ^2(red.)**	2.4	**χ^2(red.)**	1.9

[a] Experimental $^{n}J_{CH}$ values reported here were extracted from NMR spectra measured on the synthetic baulamycin A **2.17**

The fit of all calculated NMR parameters for fragment B of **2.10** – **2.14** to those of the experimental parameters derived from the natural product is shown in Figure 6.25.

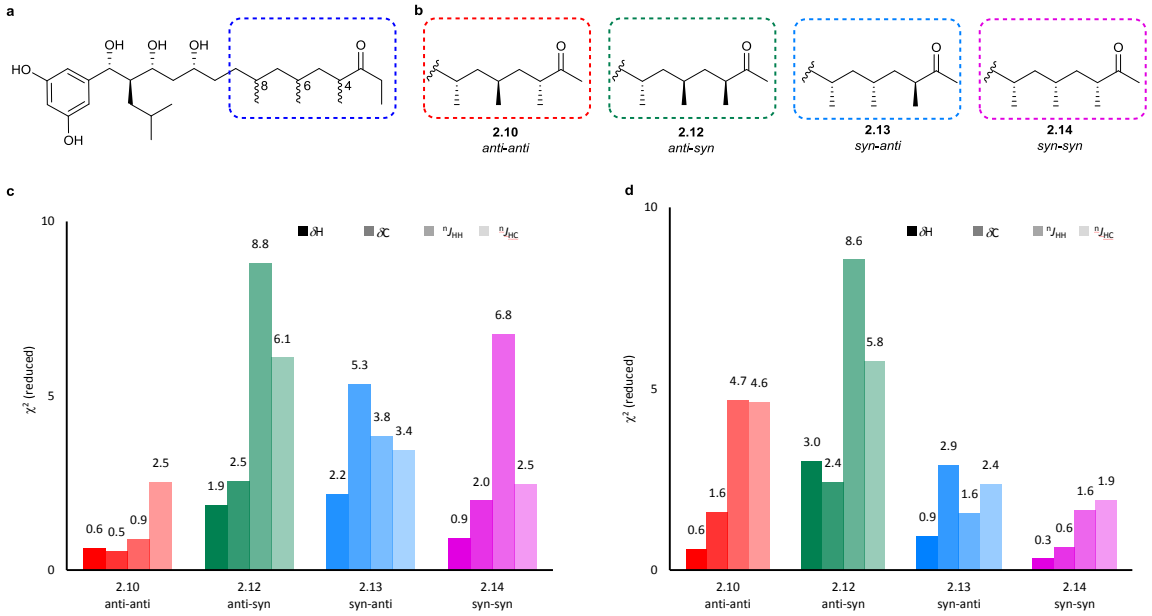

Figure 6.25: **a**. Generic structure of isomers studied for fragment B analysis. **b**. Relative stereochemistry of the isomers studied for fragment B analysis. **c**. Comparison of the calculated Boltzmann averaged chemical shifts (^{1}H and ^{13}C) and scalar coupling constants (^{1}H-^{1}H and ^{1}H-^{13}C) obtained from c gas conformational search candidates and (**d**) octanol conformational search versus the experimental data of the natural product for isomers **2.10** and **2.12** – **2.14.**

Chapter 3

Materials and Reagents

Reaction mixtures were stirred magnetically. Air- and moisture-sensitive reactions were carried out in flame-dried glassware under a N_2 atmosphere using standard Schlenk manifold technique. All required fine chemicals were purchased from Acros Organics, Alfa Aesar, Inochem-Frontier Scientific or Sigma-Aldrich and used as received unless otherwise mentioned. *n*-Butyllithium (*n*BuLi) was received from Acros Organics as a 1.6 M solution in *n*-hexane and the molarity was verified by titration with *N*-benzylbenzamide.[177] Solutions of *n*BuLi where precipitate had formed were discarded as these were found to not be effective in Sn-Li exchange reactions. (+)-Sparteine was obtained as the free base (Ark Pharm), distilled over CaH_2 and stored in a Young's tube under N_2. (−)-Sparteine was obtained as the free base (Spartax Chemicals), distilled over CaH_2 and stored in a Young's tube under N_2. The sparteine free base readily absorbs atmospheric carbon dioxide (CO_2) and should be stored in a Young's tube under argon/N_2 at −20 °C. Petrol refers to the fraction of petroleum ether boiling at 40 – 60 °C. Anhydrous THF, CH_2Cl_2, toluene, *n*-hexane, acetonitrile and Et_2O were dried by passing through a modified Grubbs system of alumina columns, manufactured by Anhydrous Engineering, stored over 3Å molecular sieves (25% of total volume) and were transferred under N_2 *via* syringe. Benzyl alcohol was distilled over CaH_2 and was transferred under N_2 *via* syringe.

Synthetic General Procedures

General Procedure 1 (GP1): Lithiation–borylation

Stannane **3.29** (*R* or *S* enantiomers, respectively 1.30 – 2.30 eq.) was transferred to a flame dried schlenk tube via syringe and stirred under vacuum for 10 min to remove any air introduced during the weighing process. The stannane was dissolved in anhydrous Et_2O (0.30 M) and cooled to −78 °C (colourless solution). *n*BuLi (1.60 M in *n*-hexane, 1.3 – 2.25 eq.) was added dropwise and the reaction mixture was stirred at this temperature for 1 – 2 h (when Sn-Li exchange takes place the reaction mixture will be bright yellow). Boronic ester (1 M in anhydrous Et_2O, 1.00 eq.) was added dropwise (4 mL/hr) to the reaction mixture at −78 °C and the reaction was stirred at this temperature for 10 min – 1 h. The cooling bath was removed and the reaction was stirred at the desired solvent, time and temperature for 1,2 migration (see below for time and temperature guide for 1,2-migration). The reaction was filtered through a plug of wetted (Et_2O) silica (~ 2 cm depth) to give a pale-yellow solution. The silica was washed with Et_2O, which was removed *in vacuo* to give crude boronic ester. The crude boronic ester could be re-dissolved in anhydrous Et_2O for further homologations or purified by flash column chromatography.

1,2-Migration Time Guide

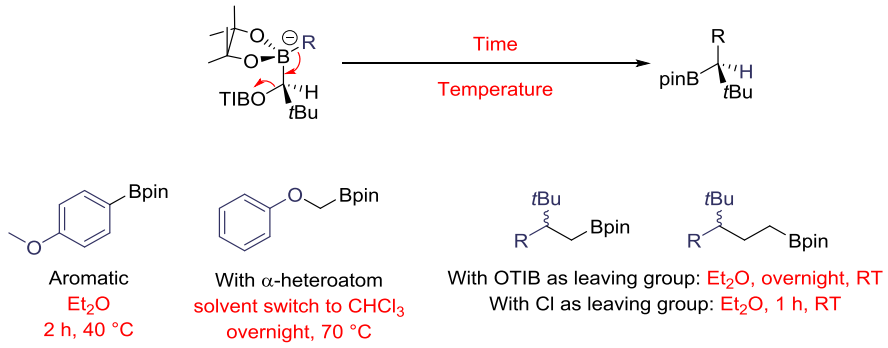

General Procedure 2 (GP2): Matteson Homologation

Small scale (~0.2 mmol of boronic ester) procedure[94]

A solution of boronic ester (0.2 M in anhydrous Et_2O, 1.00 eq.) and bromochloromethane (3.00 eq.) was cooled to −78 °C. *n*BuLi (1.6 M in *n*-hexane, 2.50 eq.) was **slowly** added (1.2 mL/hr) to the reaction mixture and the mixture was stirred at −78 °C for 20 min. After 20 min the reaction was warmed to ambient temperature and was stirred for a further 1 h. The reaction

mixture was filtered through a plug of wetted (Et_2O) silica (~ 1.5 cm depth) to give a colourless solution. The silica was washed with Et_2O and solvent was removed *in vacuo* to give crude boronic ester. The crude boronic ester could be re-dissolved in anhydrous Et_2O for further homologations or purified by flash column chromatography.

Large scale (> 0.5 mmol of boronic ester) procedure

A solution of boronic ester (0.15 – 0.20 M in anhydrous Et_2O, 1.00 eq.) and bromochloromethane (3.00 eq.) was cooled to –95 °C (MeOH/liquid N_2). *n*BuLi (1.6 M in *n*-hexane, 2.50 eq.) was added (2.00 mL/hr) to the reaction mixture and the mixture was stirred at –95 °C for 1.5 h. After 1.5 h the reaction was warmed to ambient temperature and was stirred for a further 1 h. The reaction mixture was filtered through a plug of wetted (Et_2O) silica (~ 1.5 cm depth) to give a colourless solution. The silica was washed with Et_2O and solvent was removed *in vacuo* to give crude boronic ester. The crude boronic ester could be re-dissolved in anhydrous Et_2O for further homologations or purified by flash column chromatography.

General Procedure 3 (GP3): Amination of boronic esters using a modified literature procedure[116]

Potassium *tert* butoxide (5.00 eq.) was added to a flame-dried sample vial containing boronic ester (1.00 eq.) followed by the addition of anhydrous toluene (0.15 M) and $MeONH_2$ (5.00 eq.). The vial was sealed and heated at 100 °C with stirring overnight. (The reaction turned from colourless to a milky suspension). A solution of aqueous NaOH (3.00 M) was added to the reaction and stirred for 10 min. The layers were separated, and the aqueous layer was extract by EtOAc (5 mL × 3). The organic layers were combined, dried over $MgSO_4$ and solvent was removed *in vacuo*. The crude mixture was dissolved in anhydrous THF followed by the addition of Boc_2O (1.5 eq.) and reaction was stirred at ambient temperature for 5 h. Purification of the crude material by flash column chromatography gave pure products.

General Procedure 4 (GP4): Boc-protection of carbamates using a modified literature procedure.[143]

A solution of carbamate (1.00 eq.) in anhydrous THF (0.30 M) was cooled to −78 °C followed by the dropwise addition of *n*BuLi (1.6 M, 1.00 eq.). After 20 min the reaction was warmed to

0 °C followed by the addition of Boc_2O (1.50 eq.) and a solution of DMAP (.001 eq.) in anhydrous THF (0.50 M). After 20 min the reaction was warmed to ambient temperature and stirred overnight. The reaction was quenched by the addition of water and Et_2O. The phases were separated and the aqueous layer was extracted with EtOAc (3 mL × 3). The organic extracts were combined, dried over $MgSO_4$ and solvent was removed *in vacuo*. Purification of the crude material by flash column chromatography gave pure products.

General Procedure 5 (GP5): Deprotection of benzyl protecting group.

Carbamate (1 eq.) was dissolved in ethanol (0.25 M) followed by the addition of Pd/C (10% wt, 10 mol%). The reaction was stirred under H_2 atmosphere overnight. The crude residue was filtered through a short pad of wetted celite (EtOH) and solvent was removed *in vaco*. Purification of the crude material gave the corresponding alcohols**.**

General Procedure 6 (GP6): Stahl oxidation of alcohols.[139]

Solid $Cu(MeCN)_4OTf$ (5 – 10 mol%), 4,4'-dimethoxy-2,2'-bipyridine (^{MeO}bpy, 5 mol%), ABNO (1 mol%), and NMI (10 mol%) were added to a solution of alcohol (1 eq.) in MeCN (0.5 M) in a sample vial. The addition of each catalytic component was followed by a rinse of MeCN (0.1 mL). The dark red solution was stirred at 950 RPM open to air at ambient temperature until all the alcohol was consumed, as indicated by TLC or LCMS analysis. Reaction completion was accompanied by a change in colour to blue/green. The reaction was filtered through a pad of wetted SiO_2 (MeCN) and solvent was removed *in vacuo*. Purification of the crude material gave the corresponding aldehydes.

General Procedure 7 (GP7): Pinnick oxidation of aldehydes.[178]

A solution of aldehyde (1.00 eq.) was stirred in *tert*-BuOH (0.05 M) at room temperature followed by the addition of 2-methyl-2-butene (50.00 eq.). The reaction was stirred at ambient temperature for 5 min followed by the dropwise addition of a solution of sodium chlorite (9.00 eq.), sodium phosphate monobasic (7.00 eq.) in water (500.00 eq.). The reaction mixture was stirred at room temperature for 4.5 h and *tert*-BuOH was removed *in vacuo*. The crude residue was diluted with water (2 mL) and was carefully acidified to pH ~5 with aqueous HCl (1 M).

The crude reaction mixture was extracted using EtOAc (5 mL × 4) and the organic phases were combined and dried over $MgSO_4$. Solvent was removed *in vacuo* to yield crude carboxylic acids, which were subjected to the subsequent transformations without purification.

General Procedure 8 (GP8): Methylation of carboxylic acids.[179]

(Trimethylsilyl)diazomethane (2.0 M in Et_2O, 1.00 eq.) was added to a solution of carboxylic acid (1.00 eq.) in 3:2 mixture of anhydrous methanol and toluene (0.10 M) at ambient temperature for 30 min. The reaction was quenched by the addition of water (0.5 mL) and ethyl acetate (1 mL). Two layers were separated and the aqueous layer was extracted by EtOAc (5 mL × 3). The organic layers were combined, washes with brine (5 mL), dried over $MgSO_4$ and solvent were removed *in vacuo*. Purification of the crude material by column chromatography gave the corresponding methyl esters.

General Procedure 9 (GP9): – Mono Boc deprotection.[180]

TFA (2.00 eq.) was added to a solution of bis-Boc carbamate (1.00 eq.) in DCM (0.15 M) at room temperature and the reaction was stirred for 4.5 h. Solvent was removed *in vacuo* and the crude material was purified by column chromatography to yield the corresponding carbamates.

Neopentyl 2,4,6-triisopropylbenzoate, 3.26

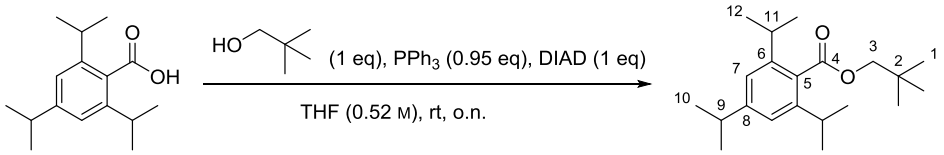

Diisopropyl azodicarboxylate (15.8 mL, 80.0 mmol) was added dropwise to a solution of 2,4,6-triisopropylbenzoic acid (19.8 g, 80.0 mmol), triphenyl phosphine (20.0 g, 76.0 mmol) and neopentyl alcohol (7.1 g, 80.0 mmol) in anhydrous THF (152 mL) at 0 °C. The reaction mixture was stirred at this temperature for 20 min before warming to room temperature and allowed to stir overnight. The reaction was quenched by the addition of saturated aqueous $NaHCO_3$ (120 mL) and H_2O (120 mL). The layers were separated and the aqueous layer was extracted with Et_2O (3 × 60 mL). The combined organic phase was dried over $MgSO_4$, filtered and concentrated *in vacuo* to give a pale yellow oil, which was then dried under high vacuum to yield a yellow solid. Pentane (300 mL) was added to the solid and the resulting suspension was passed through a short plug of SiO_2. The filtrate was concentrated *in vacuo* to give a pale oil. Purification by flash column chromatography (2:98, Et_2O:*n*-pentane) gave benzoate **3.26** (22.5 g, 70.0 mmol, 93%) as a colourless oil.

R_f (2 : 98 Et_2O : pentane) 0.29.

^{1}H NMR ($CDCl_3$, 500 MHz) δ 7.01 (2H, s, H_7), 3.98 (2H, s, H_3), 2.94-2.81 (3H, m, H_9 and H_{11}), 1.25 (6H, d, J = 7.0 Hz, H_{10}), 1.25 (12H, d, J = 6.8 Hz, H_{12}), 0.99 (9H, s, H_1).

^{13}C NMR ($CDCl_3$, 125 MHz) δ 171.5 (C_4), 150.0 (C_5), 144.8 (C_6), 131.0 (C_8), 120.9 (C_7), 74.9 (C_3), 34.5 (C_{11} or C_9), 31.7 (C_{11} or C_9), 31.2 (C_2), 26.7 (C_1), 24.3 (C_{12}), 24.1 (C_{10}).

IR (ν_{max}/cm^{-1}, neat): 2959, 2870, 1725, 1606.

HRMS (ESI$^+$): calc. for $C_{21}H_{34}O_2Na$ $[M+Na]^+$: 341.2451; found: 341.2452.

2,2-Dimethyl-1-(trimethylstannyl)propyl 2,4,6-triisopropylbenzoate, *rac*-**3.29**

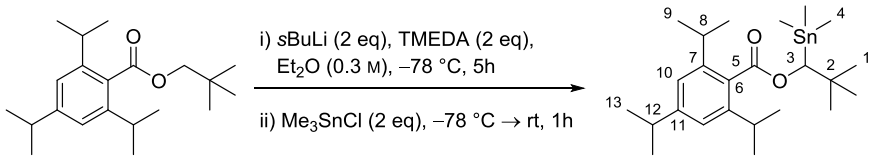

3.26 *rac*-**3.29**

A solution of benzoate **3.26** (1.26 g, 3.97 mmol) and TMEDA (0.77 mL, 7.94 mmol) in anhydrous Et_2O (14.0 mL) was cooled to –78 °C, followed by the dropwise addition of *sec*-BuLi (1.30 M in cyclohexane/ *n*-hexane (92/8), 6.1 mL. 7.94 mmol). The reaction was stirred at –78 °C for 5 h followed by the dropwise addition of Me_3SnCl (1.00 M in *n*-hexane, 7.94 mL, 7.94 mmol). The reaction was stirred at this temperature for 10 min before warming up to room temperature. After 1 hour the reaction was quenched by aqueous HCl (2.00 M, 14 mL) and left to stir for 20 min. The layers were separated and the organic layer was washed with HCl (2.00 M, 3 × 15 mL). The combined aqueous phases were extracted with Et_2O (3 × 15 mL). The combined organic phase was dried over $MgSO_4$ and concentrated *in vacuo* to give crude stannane as a clear oil. Purification by flash column chromatography (0.5:95.5, Et_2O:pentane) gave racemic stannane *rac*-**3.29** (1.58 g, 3.28 mmol, 83%) as a colourless oil. For characterisation data *vide infra.*

(*R*)-2,2-Dimethyl-1-(trimethylstannyl)propyl 2,4,6-triisopropylbenzoate, (*R*)-**3.29**

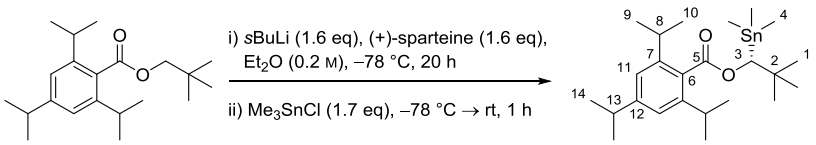

3.26 (*R*)-**3.29**

*s*BuLi (1.3 M in cyclohexane/ *n*-hexane (92/8), 33.80 mL, 43.90 mmol) was added to a solution of benzoate **3.26** (8.70 g, 27.50 mmol) and (+)-sparteine (10.10 mL, 43.90 mmol) in anhydrous Et_2O (137.00 mL) at –78 °C. The reaction was stirred at –78 °C for 20 h followed by the dropwise addition of Me_3SnCl (1.00 M in *n*-hexane, 46.70 mL, 46.70 mmol). The reaction was stirred at this temperature for 30 min before warming up to room temperature. After 1 hour the reaction was quenched by slow addition of 2 M HCl aqueous solution (150.00 mL) and left to stir for 20 min. The layers were separated and the organic layer was washed with 2M aqueous HCl (3 × 50 mL). The combined aqueous phases were extracted with Et_2O (3 × 100 mL). The combined organic phase was dried over $MgSO_4$ and concentrated *in vacuo* to give crude stannane as a clear oil. Purification by column chromatography (Biotage SNAP ultra 100g column, using a gradient elution of 2% toluene/pentane to 15% toluene/pentane) gave the *R* enantiomer of stannane **3.29** (11.9 g, 24.8 mmol, 92%, er 97:3) as a colourless oil.

The opposite enantiomer ((*S*)-**3.29**) was synthesised by using (–)-sparteine instead pf (+)-sparteine in identical yield and similar *er* (98:2). Stannanes used in this project were dried under high vacuum (1 mbar) at 40 °C with stirring overnight.

Note: it is essential to achieve a good conversion for desirable separation by column chromatography.

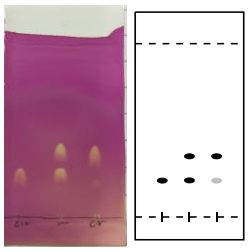

R_f (15 : 85 toluene : pentane) 0.35.

^{1}H NMR ($CDCl_3$, 500 MHz) δ 7.00 (2H, s, H_{11}), 5.03 (1H, s, J (^{1}H-$^{117/119}$Sn) = 14.5 Hz, H_3), 2.89 (3H, m, H_8 and H_{13}), 1.25 (12H, d, J = 6.9 Hz, H_9 and H_{10}), 1.22 (6H, d, J = 6.9 Hz, H_{14}), 1.02 (9H, s, H_1), 0.24 (9H, s, J(^{1}H-^{117}Sn) = 50.74 Hz, J(^{1}H-^{119}Sn) = 53.11 Hz, H_4).

^{13}C NMR ($CDCl_3$, 125 MHz) δ 171.1 (C_5), 149.9 (C_6), 145.3 (C_7), 130.8 (C_{12}), 121.1 (C_{11}), 84.1 (C_3, J(^{13}C-^{119}Sn) = 431.6 Hz, J(^{13}C -^{117}Sn) = 412.5 Hz), 36.45 (C_2), 34.3 (C_{13}), 31.4 (C_8),

28.3 (C_1, J(^{13}C -$^{117/119}$Sn = 21.5 Hz), 24.7 (C_9, C_{10} or C_{14}), 24.5 (C_9, C_{10} or C_{14}), 24.1 (C_9, C_{10} or C_{14}), –6.4 (C_4, J(^{13}C-^{119}Sn) = 324.6 Hz, J(^{13}C -^{117}Sn) = 309.8 Hz).

IR (ν_{max}/cm^{-1}, neat): 2959, 2929, 2868, 1708, 1607, 1250, 1075, 767, 525.

HRMS (ESI$^+$): calc. for $C_{24}H_{42}O_2{}^{119}SnNa$ $[M+Na]^+$: 505.2107; found 505.2106.

$[\alpha]_D^{20}$ –35 (*c* 1, $CHCl_3$) for (*R*)-isomer, +30 (*c* 1, $CHCl_3$) for (*S*)-isomer.

Chiral HPLC IB column with guard, 100% *n*-hexane, flow rate 0.9 mL/min, 210 nm, room temperature; t_R = 4.30 min (*R* enantiomer), 5.29 (*S* enantiomer).

er of (*R*)-isomer 97:3, er of (*S*)-isomer 98:2

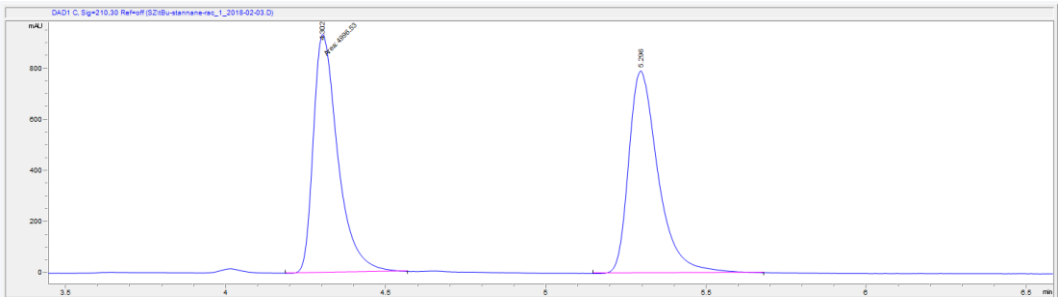

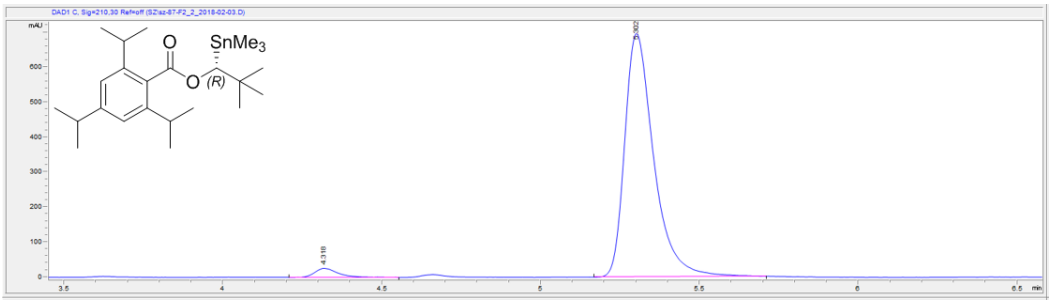

#	Time	Type	Area	Height	Width	Area%	Symmetry
1	4.318	VV R	140.4	26.3	0.0708	3.080	0.578
2	5.302	BV R	4418	695.5	0.0931	96.920	0.618

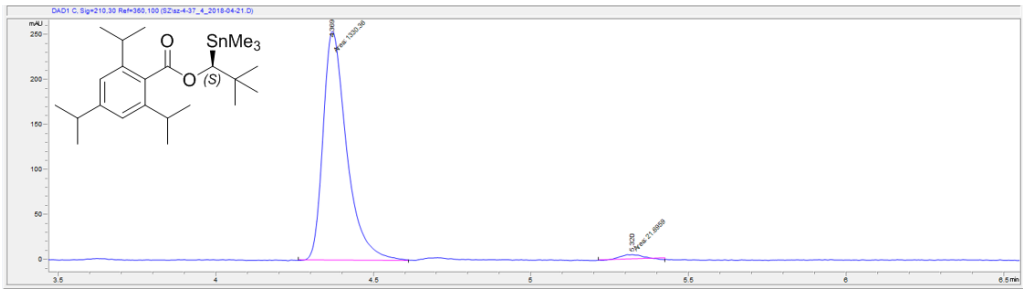

#	Time	Type	Area	Height	Width	Area%	Symmetry
1	4.369	MM	1330.4	254.8	0.087	98.395	0.623
2	5.32	MM	21.7	4.7	0.0765	1.605	1.291

Sparteine recovery [85]

The combined aqueous layers were made basic (brought to about pH 11) with NaOH ($20\%_{aq}$). The aqueous phase was extracted with Et_2O (3 × 100 mL). The combined aqueous layers were dried ($MgSO_4$), filtered and concentrated *in vacuo* to give crude (–)-sparteine. Distillation over CaH_2 (1.5 mbar, sparteine bp: 173 – 178 °C, oil bath: 150 °C) of the residual oil gave (–)-sparteine (90 %) as a colourless oil.

(*R*)-2,2'-(3,3-dimethylbutane-1,2-diyl)bis(4,4,5,5-tetramethyl-1,3,2-dioxaborolane), 3.42 and **(*S*)-2,2-dimethyl-1-(4,4,5,5-tetramethyl-1,3,2-dioxaborolan-2-yl)propyl 2,4,6-triisopropylbenzoate, 3.43**

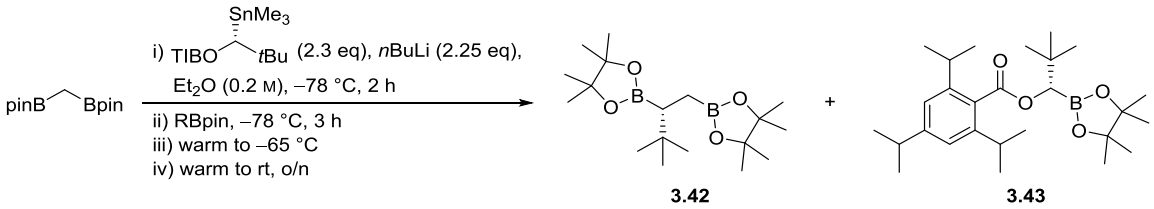

(*R*)-stannane **3.29** (206.60 mg, 0.43 mmol) was transferred to a flame dried Schlenk tube via syringe and stirred under vacuum for 5 min to remove any air introduced during the weighing process. The stannane was dissolved in anhydrous Et_2O (2.15 mL) and cooled to −78 °C (colourless solution). *n*BuLi (1.60 M in *n*-hexane, 0.26 mL, 0.42 mmol) was added dropwise and the reaction mixture was stirred at this temperature for 2 h. Diborylmethane (50.00 mg, 0.19 mmol) was dissolved in anhydrous Et_2O (0.60 mL) and the resulting solution was added dropwise (4.80 mL/hr) to the reaction mixture at −78 °C. The reaction was stirred at this temperature for 3 h then warmed −65 °C. After 40 min the reaction was warmed to room temperature and sttireed overnight. The reaction mixture was filtered through a plug of wetted (Et_2O) silica (~ 1.5 cm depth) to give a pale yellow solution. The silica was washed with Et_2O and solvent was removed *in vacuo* to give crude boronic esters. Purification by column chromatography (6:94, Et_2O: *n*-hexane) gave homologated boronic ester **3.42** (21.4 mg, .0.06 mmol, 33%) as an colourless oil and boronic ester **3.43** (27.2 mg, 0.06 mmol, 33%) as a white solid.

(*R*)-2,2'-(3,3-dimethylbutane-1,2-diyl)bis(4,4,5,5-tetramethyl-1,3,2-dioxaborolane), 3.42

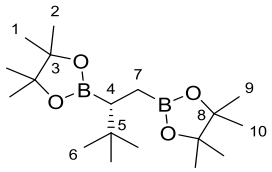

R_f (6 : 94 Et_2O : *n*-hexane) 0.19.

^{1}H NMR ($CDCl_3$, 500 MHz), δ1.25 (12H, s, H_1 and H_2 or H_9 and H_{10}), 1.22 (6H, s, $H_1/H_2/H_9/H_{10}$), 1.21 (6H, s, $H_1/H_2/H_9/H_{10}$), 0.99–0.93 (1H, m, H_4), 0.91 (9H, s, H_6), 0.86–0.78 (2H, m, H_7).

^{13}C NMR ($CDCl_3$, 125 MHz) δ 82.9 (C_3 or C_8), 82.8 (C_3 or C_8), 32.5 (C_5), 29.2 (C_6), 25.4 ($C_1/C_2/C_9/C_{10}$), 25.2($C_1/C_2/C_9/C_{10}$), 25.0($C_1/C_2/C_9/C_{10}$), 24.8($C_1/C_2/C_9/C_{10}$), carbons attached to boron (C_4 & C_7) were not observed due to quadrupolar relaxation.

^{11}B NMR ($CDCl_3$, 128 MHz) δ 33.41.

IR (ν_{max}/cm^{-1}, neat): 2977, 2867, 1466, 1388, 1369, 1311, 1142, 969.

$[\boldsymbol{\alpha}]_{\boldsymbol{D}}^{\boldsymbol{20}}$ −2 (*c* 1, $CHCl_3$).

HRMS (ESI^+): calc. for $C_{18}H_{36}B_2NaO_4$ $[M+Na]^+$: 361.2698; found: 361.2712.

(*S*)-2,2-dimethyl-1-(4,4,5,5-tetramethyl-1,3,2-dioxaborolan-2-yl)propyl 2,4,6-triisopropylbenzoate, 3.43

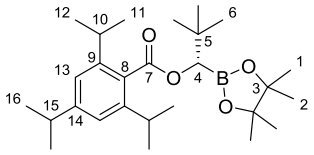

R_f (6 : 94 Et_2O : *n*-hexane) 0.3.

^{1}H NMR ($CDCl_3$, 500 MHz), δ 6.99 (2H, s, H_{13}), 3.83 (1H, s, H_4), 3.06 (2H, hept, J = 6.8 Hz, H_{10}), 2.89 (1H, hept, J = 7.1 Hz, H_{15}), 1.31 (6H, s, H_1 or H_2), 1.28 (6H, s, H_1 or H_2), 1.25 (6H, d, J = 6.9 Hz, $H_{11}/H_{12}/H_{16}$), 1.24 (6H, d, J = 6.6 Hz, $H_{11}/H_{12}/H_{16}$), 1.22 (6H, d, J = 6.8 Hz, $H_{11}/H_{12}/H_{16}$), 1.03 (9H, s, H_6).

^{13}C NMR ($CDCl_3$, 125 MHz) δ 172.6 (C_7), 149.9 (C_{14}), 145.4 (C_9), 130.6 (C_8), 120.9 (C_{13}), 83.9 (C_3), 75.9 (br, C_4), 34.5 (C_{15}), 32.8 (C_5), 30.9 (C_{10}), 27.5 (C_6), 25.08 (C_1/C_2), 25.08 (C_1/C_2), 24.6 (C_{16}), 24.3 (C_{11}/C_{12}), 24.1 (C_{11}/C_{12}).

^{11}B NMR ($CDCl_3$, 128 MHz) δ 30.88.

IR (ν_{max}/cm^{-1}, neat): 2952, 2927, 2868, 1705, 1372, 1338, 1143.

$[\boldsymbol{\alpha}]_{\boldsymbol{D}}^{\mathbf{20}}$ +12 (*c* 1, $CHCl_3$).

M.P. 97.5 – 98 °C (pentane).

HRMS (ESI^+): calc. for $C_{27}H_{45}BNaO_4$ $[M+Na]^+$: 467.3308; found: 467.3298.

2-(4-Methoxyphenyl)-4,4,5,5-tetramethyl-1,3,2-dioxaborolane, 3.20

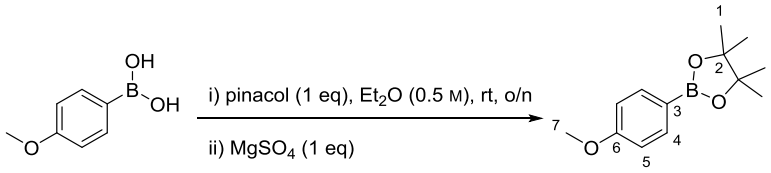

A solution of (4-methoxyphenyl)boronic acid (3.79 g, 25.00 mmol) and pinacol (2.95 g, 25.00 mmol) in anhydrous Et_2O (50.00 mL) was stirred at room temperature overnight. Flame dried $MgSO_4$ (3.00 g, 25.00 mmol) was added and stirring continued at room temperature for 2 h. The reaction mixture was filtered through celite and the filtrate was concentrated *in vacuo*. Purification by column chromatography (10:90, EtOAc:pentane) gave the product pinacol boronic ester **3.20** (5.57 g, 23.80 mmol, 95%) as a colourless oil.

Note: After cooling in the freezer overnight the product became an amorphous solid.

$\mathbf{R_f}$ (10 : 90 EtOAc : pentane) 0.7.

^{1}H NMR ($CDCl_3$, 400 MHz), δ 7.76 (2H, apparent d, J = 8.5 Hz, H_4/H_5), 6.90 (2H, apparent d, J = 8.5 Hz, H_4/H_5), 3.83 (3H, s, H_7), 1.33 (12H, s, H_1).

^{13}C NMR ($CDCl_3$, 101 MHz) δ 162.2 (C_6), 136.6 (C_4/C_5), 113.4 (C_4/C_5), 86.6 (C_2), 55.2 (C_7), 24.9(C_1), C_3 was not observed due to quadrupolar relaxation.

Analytical data were consistent with literature values.[181]

(*S*)-2-(1-(4-Methoxyphenyl)-2,2-dimethylpropyl)-4,4,5,5-tetramethyl-1,3,2-dioxaborolane, 3.47

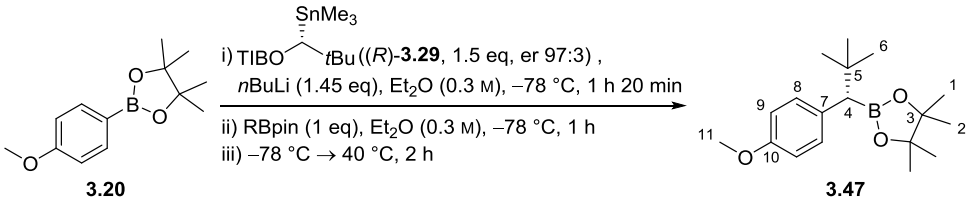

Prepared according to **GP1** using boronic ester **3.20** (48.00 mg, 0.20 mmol), *R* enantiomer of stannane (*R*)-**3.29** (148.00 mg, 0.31 mmol) and *n*BuLi (1.59 M in *n*-hexane, 0.19 mL, 0.29 mmol) in anhydrous Et_2O (1.00 mL, 0.30 M). The crude material was purified by flash column chromatography (2:98, Et_2O:*n*-hexane) to give homologated boronic ester **3.47** (61.00 mg, 0.20 mmol, 99%, *er* 98.7:1.3) as a colourless oil.

R_f (5 : 95 Et_2O : *n*-hexane): 0.25.

^{1}H NMR ($CDCl_3$, 400 MHz) δ 7.17 (2H, apparent d, J = 8.7 Hz, H_8/H_9), 6.79 (2H, apparent d, J = 8.7 Hz, H_8/H_9), 3.78 (3H, s, H_{11}), 2.15 (1H, s, H_4), 1.24 (6H, s, H_1/H_2), 1.21 (6H, s, H_1/H_2), 0.93 (9H, s, H_6).

^{13}C NMR ($CDCl_3$, 101 MHz) δ 157.6 (C_{10}), 132.5 (C_7), 132.1 (C_8/C_9), 113.0 (C_8/C_9), 83.0 (C_3), 55.2 (C_{11}), 33.3(C_5), 29.4 (C_6), 24.9, (C_1/C_2)24.8 (C_1/C_2), carbon attached to boron not observed due to quadrupolar relaxation.

IR (ν_{max}/cm^{-1}, neat): 2975, 2949, 2905, 2868, 1607, 1508, 1350, 1315, 1245, 1138.

$[\boldsymbol{\alpha}]_{\boldsymbol{D}}^{\boldsymbol{20}}$ +12 (*c* 1, $CHCl_3$).

HRMS (ESI$^+$): calc'd for $C_{18}H_{30}BO_3$ $[M+H]^+$ 305.2286; found 305.2295.

Boronic ester **3.47** was oxidised to the corresponding alcohol for chiral SFC analysis.

Chiral SFC IC column, iso 5%, 4 mL/min, 125 bar, co-solvent: MeOH; t_R (*R*-enantiomer) = 2.38 min, t_R (*S*-enantiomer) = 2.8 mins;

er 98.7:1.3

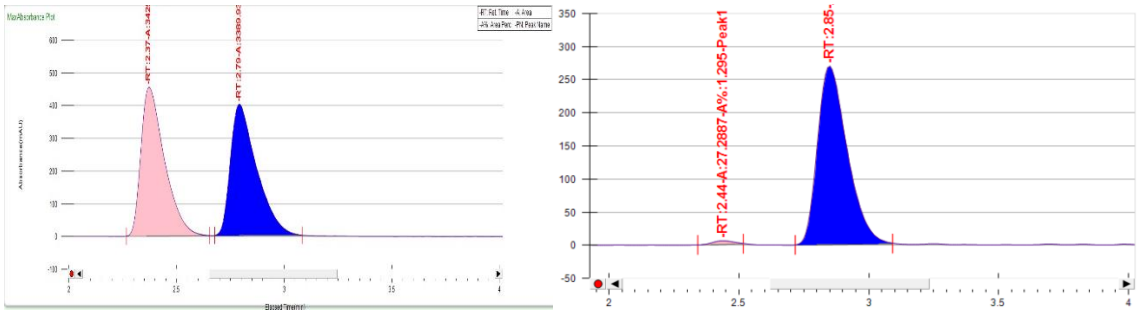

Peak Information

Peak No	% Area	Area	Ret. Time	Height	Cap. Factor
1	1.295	27.2887	2.44 min	5.1669	2440.6333
2	98.705	2079.8874	2.85 min	269.3946	2848.9667

(*S*)-2-(2-(4-Methoxyphenyl)-3,3-dimethylbutyl)-4,4,5,5-tetramethyl-1,3,2-dioxaborolane, 3.48

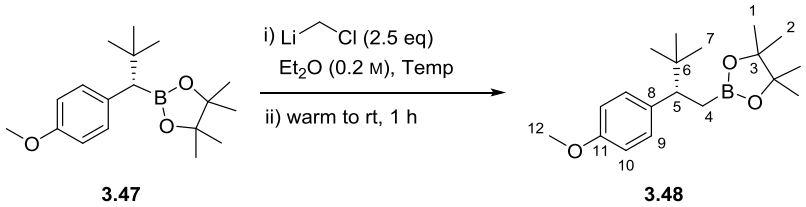

3.47 **3.48**

Small scale: performed according to **GP2** using boronic ester **3.47** (37.800 mg, 0.12 0mmol), bromochloromethane (0.025 mL, 0.370 mmol) and *n*BuLi (1.59 M in *n*-hexane, 0.200 mL, 0.310 mmol) in anhydrous Et_2O (0.500 mL) at −78 °C. Purification of the crude material by flash column chromatography (4:96, Et_2O : *n*-hexane) gave product **3.48** (35.000 mg, 0.110 mmol, 92%) as a colourless oil.

Large scale: performed according to **GP2** using boronic ester **3.47** (258.4 mg, 0.85 mmol), bromochloromethane (0.19 mL, 2.82 mmol) and *n*BuLi (1.6 M in *n*-hexane, 1.46 mL, 2.35 mmol) in anhydrous Et_2O (6.5 mL) at –95 °C. Purification of the crude material by flash column chromatography (4:96, Et_2O:*n*-hexane) gave product **3.48** (261.8 mg, 0.82 mmol, 88%) as a colourless oil.

$\mathbf{R_f}$ (5 : 95 Et_2O : *n*-hexane) 0.23.

^{1}H NMR ($CDCl_3$, 500 MHz) δ 7.08 (2H, apparent d, J = 8.7 Hz, H_9/H_{10}), 6.79 (2H, apparent d, J = 8.7 Hz, H_9/H_{10}), 3.77 (3H, s, H_{12}), 2.66 (1H, dd, J = 10.3, 7.1 Hz, H_5), 1.24-1.18 (2H, m, H_4), 0.98 (6H, s, H_1/H_2), 0.91 (6H, s, H_1/H_2), 0.84 (9H, s, H_7).

^{13}C NMR ($CDCl_3$, 125 MHz) δ 157.8 (C_{11}), 136.7 (C_8), 130.6 (C_9/C_{10}), 112.6 (C_9/C_{10}), 82.8 (C_3), 55.3 (C_{12}), 50.9 (C_5), 34.2 (C_6), 27.8 (C_7), 24.7 (C_1/C_2), 24.3 (C_1/C_2), 12.5 (C_4).

$[\boldsymbol{\alpha}]_{\boldsymbol{D}}^{\mathbf{20}}$ −26 (*c* 1, $CHCl_3$).

IR (ν_{max}/cm^{-1}, neat): 2965, 2834, 1610, 1511, 1365, 1244, 1144, 831.

HRMS (ESI^+): calc. for $C_{19}H_{31}BO_3Na$ $[M+Na]^+$: 341.2366. Found 341.2267.

2-((3*R*,5*S*)-5-(4-methoxyphenyl)-2,2,6,6-tetramethylheptan-3-yl)-4,4,5,5-tetramethyl-1,3,2-dioxaborolane, 3.19

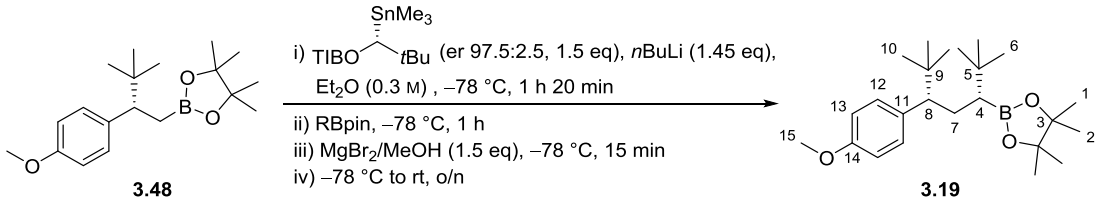

Prepared according to **GP1** using boronic ester **3.48** (48.0 mg, 0.20 mmol), (*R*)–enantiomer of stannane (*R*)-**3.29** (67.8 mg, 0.14 mmol) and *n*BuLi (1.59 M in *n*-hexane, 0.09 mL, 0.13 mmol) in anhydrous Et_2O (0.65 mL). $MgBr_2$/MeOH (1 M, 0.19 mL, 0.19 mmol) was added before warming the reaction mixture to room temperature. The crude material was purified by flash column chromatography (2:98 → 3:97, Et_2O:*n*-hexane) to give homologated boronic ester **3.19** (27.7 mg, 0.07 mmol, 76%, dr 95:5) as a colourless oil.

R_f (4 : 94 Et_2O : *n*-hexane) 0.22.

^{1}H NMR ($CDCl_3$, 500 MHz) δ 7.04 (2H, apparent d, J = 8.1 Hz, H_{12} or H_{13}), 6.76 (2H, apparent d, J = 8.5 Hz, H_{12} or H_{13}), 3.76 (3H, s, H_{15}), 2.15 (1H, dd, J= 10.2, 3.1 Hz, H_8), 1.89 (1H, dt, J= 14 Hz, 3.2 Hz, H_{7a} or H_{7b}), 1.8 (1H, ddd, J= 14, 10.2, 7.3 Hz, H_{7a} or H_{7b}), 1.08 (6H, s, H_1 or H_2), 1.02 (6H, s, H_1 or H_2), 0.94 (9H, s, H_6 or H_{10}), 0.83 (9H, s, H_6 or H_{10}), 0.58 (1H, dd, J= 7.2, 3.3 Hz, H_4).

^{13}C NMR ($CDCl_3$, 125 MHz) δ 157.9 (C_{14}), 135.9 (C_{11}), 130.7 (C_{12} or C_{13}), 113.0 (C_{12} or C_{13}), 82.79(C_3), 58.6 (C_8), 55.3 (C_{15}), 34.9(C_9), 33.5 (C_5), 30.4 (C_4), 29.6 (C_6 or C_{10}), 28.5 (C_6 or C_{10}), 27.5 (C_7), 25.4 (C_1 or C_2), 24.9 (C_1 or C_2).

$[\boldsymbol{\alpha}]_{\boldsymbol{D}}^{\boldsymbol{20}}$ +13 (*c* 0.98, $CHCl_3$).

IR (ν_{max}/cm^{-1}, neat): 2950, 2902, 2867, 1610, 1511, 1362, 1246, 1140, 831, 734, 561.

M.P. 66.2 – 66.8 °C (pentane).

HRMS (ESI$^+$) calc. for $C_{24}H_{41}BO_3Na$ $[M+Na]^+$: 411.3149. Found 411.3045.

2-((3*S*,5*S*)-5-(4-methoxyphenyl)-2,2,6,6-tetramethylheptan-3-yl)-4,4,5,5-tetramethyl-1,3,2-dioxaborolane, 3.44

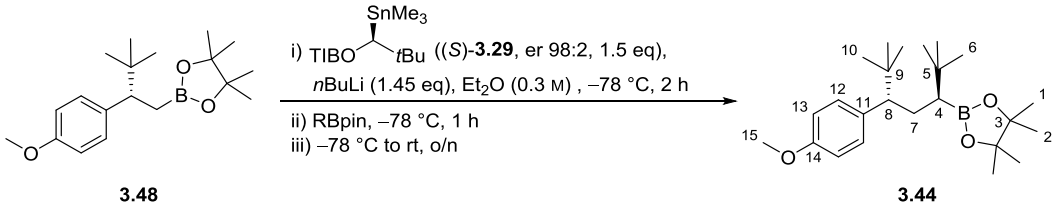

3.48 **3.44**

Prepared according to **GP1** using boronic ester **3.48** (30 mg, 0.13 mmol), (*S*)–enantiomer of stannane (*S*)-**3.29** (67.8 mg, 0.14 mmol) and *n*BuLi (1.59 M in *n*-hexane, 0.09 mL, 0.13 mmol) in anhydrous Et_2O (0.42 mL). The crude material was purified by flash column chromatography (2:98 → 3:97, Et_2O : *n*-hexane) to give the homologated boronic ester **3.44** (31.7 mg, 0.82 mmol, 87%, dr 95:5) as a colourless oil.

R_f (4:96, Et_2O : *n*-hexane): 0.22.

^{1}H NMR ($CDCl_3$, 500 MHz) δ 6.99 (2H, m, H_{12} or H_{13}), 6.77 (2H, apparent d, J = 8.8 Hz, H_{12} or H_{13}), 3.78 (3H, s, H_{15}), 2.10 (1H, dd, , J= 12.6, 2.5 Hz, H_8), 1.87 (1H, td, J= 12.6, 2.5 Hz, H_{7a} or $H7_b$), 1,70 (1H, td, J= 12.6, 2.6 Hz, H_{7a} or $H7_b$), 1.29 (6H, s, H_1 or H_2), 1.27 (6H, s, H_1 or H_2), 0.85 (9H, s, H_6 or H_{10}), 0.84 (9H, s, H_6 or H_{10}), 0.48 (1H, dd, J= 12.6, 2.6 Hz, H_4).

^{13}C NMR ($CDCl_3$, 125 MHz) δ 157.7 (C_{14}), 135.0 (C_{11}), 113.0 (C_{12} and C_{13}), 82.8 (C_3), 56.0 (C_{15}), 55.1 (C_8), 34.2 (C_9), 32.0 (C_5), 29.6(C_6 or C_{10}), 28.5(C_6 or C_{10}), 26.8 (C_7), 25.3 (C_1 or C_2), 25.1 (C_1 or C_2), C_4 was not observed due to quadrupolar relaxation.

IR (ν_{max}/cm^{-1}, neat): 2952, 1511, 1246, 1141, 830.

$[\boldsymbol{\alpha}]_{\boldsymbol{D}}^{\mathbf{20}}$ −35 (*c* 1, $CHCl_3$).

HRMS (ESI$^+$): calc'd for $C_{24}H_{42}BO_3$ $[M+Na]^+$: 389.3226; found: 389.3218.

Methoxyamine[94]

DIPEA (18.90 mL, 108.00 mmol) was added to a solution of methoxyamine hydrochloride (7.52 g, 90.00 mmol) in glycerol (40.00 mL). The reaction mixture was heated at 50 °C for 2 h. Methoxyamine (bp: 48–50 °C) was distilled from the reaction mixture (oil bath: 110 °C; distillation temperature: 40 °C) to give pure methoxyamine (2.6 g, 90 mmol, 61%) as a colourless liquid. Methoxyamine was stored at 4 °C under an atmosphere of nitrogen.

***tert*-butyl ((3*R*,5*S*)-5-(4-methoxyphenyl)-2,2,6,6-tetramethylheptan-3-yl)carbamate, 3.43**

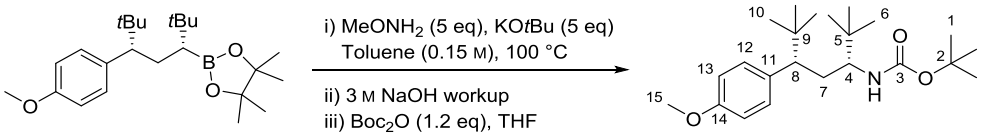

3.19 **3.43**

Prepared according to **GP3** using boronic ester **3.19** (50.0 mg, 0.13 mmol), $MeONH_2$ (30.5 mg, 0.65 mmol), KO*t*Bu (72.9 mg, 0.65 mmol) in anhydrous toluene (0.89 mL). The reaction mixture was then subjected to basic work up followed by Boc-protection using Boc_2O (33.7 mg, 0.15 mmol) in THF (0.65 mL). The crude material was purified by flash column chromatography (6:94, EtOAc:*n*-hexane) to give the carbamate **3.43** (22.5 mg, 0.068 mmol, 85%) as a colourless oil.

Note: After two days at room temperature the product became a white solid.

R_f (10:90, EtOAc:*n*-hexane, TLC visualised by ninhydrin stain): 0.25.

^{1}H NMR ($CDCl_3$, 500 MHz) δ 7.04 (2H, apparent d, J = 8.3 Hz, H_{12} or H_{13}), 6.78 (2H, apparent d, J = 8.3 Hz, H_{12} or H_{13}), 3.78 (3H, s, H_{15}), 3.68 (1H, d, J = 10 Hz, NH), 3.38 (1H, td, J = 10.8, 2.9 Hz, H_4), 2.31 (1H, dd, J = 8.1, 2.5 Hz, H_8), 2.14 (2H, dt, J = 14 Hz, 2.8 Hz, H_{7a} or H_{7b}), 1.48-1.41 (1H, m, H_{7a} or H_{7b}), 1.32 (9H, s, H_1), 0.85 (9H, s, H_6 or H_{10}), 0.83(9H, s, H_6 or H_{10}).

^{13}C NMR ($CDCl_3$, 125 MHz) δ 157.6 (C_{14}), 153.8 (C_3), 137.3 (C_{11}), 125.6 (C_{12} or C_{13}), 113.1 (C_{12} or C_{13}), 78.2 (C_2), 61.2 (C_4), 55.2 (C_{15}), 54.6 (C_8), 35.7 (C_5 or C_9), 34.9 (4 C_5 or C_9), 31.6 (C_7), 28.1 (C_6 or C_{10}), 26.41 (C_6 or C_{10}).

IR (ν_{max}/cm^{-1}, neat): 3665, 3453, 3372, 2960, 2870, 1698, 1510, 1364, 733.

$[\alpha]_D^{19.7}$: −22 (*c* 1, $CHCl_3$).

M.P. 64.5 – 65 °C (pentane).

HRMS (ESI^+): calc. for $C_{23}H_{39}NNaO_3$ $[M+Na]^+$: 400.2822; found: 400.2822.

2-((Benzyloxy)methyl)-4,4,5,5-tetramethyl-1,3,2-dioxaborolane, 3.59

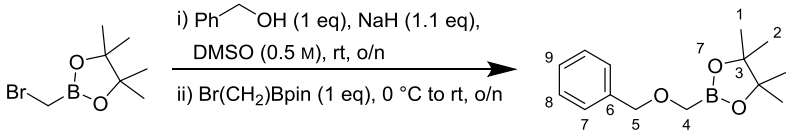

Sodium hydride 60% wt. (1.99 g, 49.80 mmol) was washed with anhydrous *n*-hexane three times under nitrogen atmosphere and dried under vacuum for 10 min. Anhydrous DMSO (90.50 mL, 0.50 M) was added followed by the addition of distilled benzyl alcohol (4.68 mL, 45.30 mmol, 1.00 eq) at room temperature and the reaction mixture was stirred overnight. 2-(Bromomethyl)-4,4,5,5-tetramethyl-1,3,2-dioxaborolane (10.00 g, 45.30 mmol) was added to the reaction mixture at 0 °C and the reaction was stirred at room temperature overnight. The reaction was quenched with saturated aqueous NH_4Cl (200 mL) followed by the addition of Et_2O (100 mL). The layers were separated and the aqueous layer was extracted with Et_2O (3 × 100 mL) and the combined organic layer was washed with brine (100 mL), dried over $MgSO_4$ and the solvent was removed *in vacuo*. The crude product was purified by distillation (1.10 mbar, 102 – 110 °C, oil bath 175 °C), re-dissolved in *n*-pentane and washed with H_2O three times to yield boronic ester **3.59** (8.22 g, 33.12 mmol, 73%) as a colourless oil.

^{1}H NMR ($CDCl_3$, 400 MHz), δ 7.38-7.27 (5H, m, H_7, H_8, H_9), 4.52 (2H, s, H_5), 3.28 (2H, s, H_4), 1.27 (12H, s, H_1, H_2).

^{13}C NMR ($CDCl_3$, 101 MHz) δ138.2 (C_6), 128.4 (C_7 and C_8), 127.7 (C_9), 84.0 (C_3), 75.9 (C_5), 57.3(br, C_4), 24.9 (C_1,C_2).

^{11}B NMR ($CDCl_3$, 128 MHz) δ 31.49.

IR (ν_{max}/cm^{-1}, neat): 2978, 2847, 1338, 1143, 1031, 957, 845, 735, 697.

HRMS (ESI^+): calc. for $C_{21}H_{34}O_2Na$ $[M+H]^+$: 249.1659; found: 249.1670.

(*S*)-2-(1-(Benzyloxy)-3,3-dimethylbutan-2-yl)-4,4,5,5-tetramethyl-1,3,2-dioxaborolane, 3.62

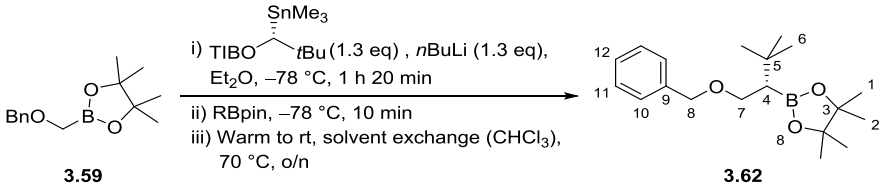

Prepared according to **GP1** using boronic ester **3.59** (1.00 g, 4.00 mmol), (*R*)–enantiomer of stannane (*R*)-**3.29** (2.90 g, 6.00 mmol) and *n*BuLi (1.60 M in *n*-hexane, 3.65 mL, 5.87 mmol) in anhydrous Et_2O (20.15 mL). The crude material was purified by flash column chromatography (3:97, Et_2O:*n*-hexane) to give the homologated boronic ester **3.62** (940.5 mg, 2.96 mmol, 73%) as a colourless oil.

R_f (4:96, Et_2O:*n*-hexane) 0.24.

^{1}H NMR ($CDCl_3$, 400 MHz), δ 7.35-7.28 (4H, m, H_{10}, H_{11}), 7.25-7.22 (1H, m, H_{12}), 4.49 (2H, s, H_8), 3.64 (1H, app. s, H_{7a} or H_{7b}), 3.63 (1H, app. d, J = 2.3 Hz, H_{7a} or H_{7b}), 1.37 (1H, dd, J = 9.1, 7.1 Hz H_4), 1.23 (12H, s, H_1, H_2), 0.97 (9H, s, H_6).

^{13}C NMR ($CDCl_3$, 101 MHz) δ139.1 (C_9), 128.2 (C_{11}), 127.5 (C_{10}), 127.2 (C_{12}), 83.0 (C_3), 73.1 (C_8), 70.4 (C_7), 37.34 (br, C_4), 31.3 (C_5), 30.1 (C_6), 25.0 (C_1 or C_2), 24.9(9) (C_1 or C_2).

^{11}B NMR ($CDCl_3$, 96 MHz): 33.07.

IR (ν_{max}/cm^{-1}, neat): 2955, 2867, 1454, 1370, 1142.

$[\boldsymbol{\alpha}]_{\boldsymbol{D}}^{\mathbf{23}}$ +6 (*c* 1, $CHCl_3$).

HRMS (ESI^+): calc. for $C_{19}H_{31}BO_3Na$ $[M+Na]^+$: 341.2262; found: 341.2262.

Boronic ester **3.62** was oxidised to the corresponding alcohol for chiral SFC analysis.

(*S*)-1-(Benzyloxy)-3,3-dimethylbutan-2-ol

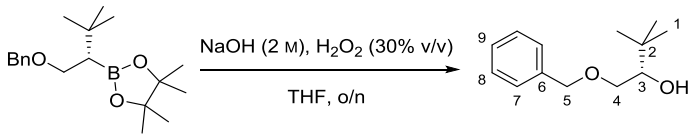

3.62

A mixture of boronic ester **3.62** containing an unknown impurity (combined weight 100 mg, < 0.31 mmol of the boronic ester) was dissolved in THF (1.5 mL) and cooled to 0 °C. A 2:1 mixture of NaOH (0.86 mL, 3 M in water) and hydrogen peroxide (0.43 mL, 30% aqueous solution *v*/*v*) was added to the reaction mixture. The mixture was warmed to room temperature and left to stir vigorously overnight. The reaction mixture was diluted with water (2 mL) and Et_2O (2 mL). The phases were separated and the aqueous later was extracted with Et_2O (3 × 10 mL) and the combined organic phase were washed with brine (5 mL), dried over $MgSO_4$ and concentrated *in vacuo*. Purification by flash column chromatography (10:90, Et_2O:*n*-hexane) gave the corresponding alcohol (39 mg, 0.19 mmol, > 62%) as a colourless oil.

R_f (10 : 90 Et_2O : *n*-hexane) 0.15.

^{1}H NMR ($CDCl_3$, 500 MHz), δ 7.35-7.28 (4H, m, H_7, H_8, H_9), 4.56 (2H, s, H_5), 3.63 (1H, dd, J = 9.2, 2.6 Hz, H_{4a} or H_{4b}), 3.52 (1H, dd, J = 9.1, 2.4 Hz, H_3), 3.39 (1H, t, J = 9.2 Hz, H_{4a} or H_{4b}), 2.46 (1H, s, OH), 0.92 (9H, s, H_1).

^{13}C NMR ($CDCl_3$, 125 MHz) δ 138.1 (C_6), 128.6 (C_9), 127.9 (C_7/C_8), 127.8 (C_7/C_8), 77.6 (C_3), 73.5 (C_5), 71.6 (C_4), 33.5 (C_2), 26.1 (C_1).

IR (ν_{max}/cm^{-1}, neat): 3482, 3030, 2954, 2869, 1453, 1364, 1074.

$[\boldsymbol{\alpha}]_{\boldsymbol{D}}^{\mathbf{22}}$ +22 (*c* 1, $CHCl_3$).

HRMS (ESI^+): calc. for $C_{19}H_{20}NaO_2$ $[M+Na]^+$: 231.1356; found: 231.1350.

Chiral SFC Whelk-01 column, iso 10%, 4 mL/min, 125 bar, co-solvent: 50% IPA/Hex; t_R (*S*-enantiomer) = 2.08 min, t_R (*R*-enantiomer) = 2.27 mins.

er 98:2

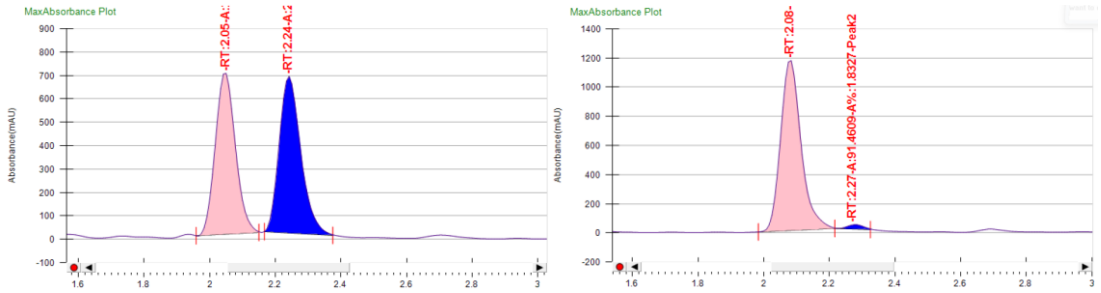

Peak Information

Peak No	% Area	Area	Ret. Time	Height	Cap. Factor
1	98.1673	4898.9892	2.08 min	1166.8221	0
2	1.8327	91.4609	2.27 min	29.4587	0

A side product **3.63** (28.00 mg, 0.08 mmol) was also isolated.

2-hydroxy-3,3-dimethyl-1-(2,4,6-triisopropylphenyl)butan-1-one, 3.63

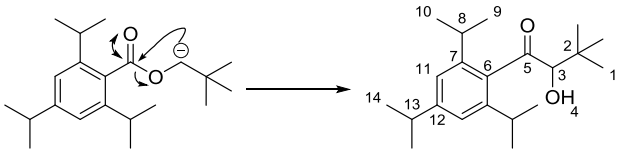

R_f (3:97, Et_2O:*n*-hexane) 0.11.

^{1}H NMR ($CDCl_3$, 400 MHz), δ 7.02 (2H, s, H_{11}), 4.24 (1H, d, J = 7.0 Hz, H_3), 3.57 (1H, d, J = 7.2 Hz, H_4), 2.88 (1H, hept, J = 6.9 Hz, H_{13}), 2.81 (2H, hept, J = 6.9 Hz, H_8), 1.28 – 1.20 (18 H, m, H_9, H_{10} and H_{14}), 0.89 (9H, s, H_1).

^{13}C NMR ($CDCl_3$, 100 MHz) δ 221.9 (C_5), 151.1 (C_{12}), 146.1 (C_6), 135.4 (C_7), 121.9 (C_{11}), 86.1 (C_3), 36.9 (C_2), 34.4 (C_{13}), 31.2 (C_8), 26.5 (C_1), 24.1 (C_9, C_{10} or C_{14}), 24.0 (C_9, C_{10} or C_{14}), 23.9 (C_9, C_{10} or C_{14}).

IR (ν_{max}/cm^{-1}, neat): 3481, 2961, 2870, 1707, 1677, 1461, 1364, 1264, 1080.

M.P.: 92 – 93 °C (pentane).

HRMS (ESI^+): calc. for $C_{21}H_{34}NaO_2$ $[M+Na]^+$: 341.2451; found: 241.2450.

(*S*)-2-(2-((Benzyloxy)methyl)-3,3-dimethylbutyl)-4,4,5,5-tetramethyl-1,3,2-dioxaborolane, 3.65

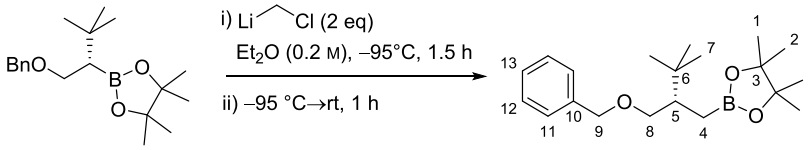

3.62 **3.65**

Small scale: performed according to **GP2** using boronic ester **3.62** (30.00 mg, 0.09 mmol), bromochloromethane (0.02 mL, 0.28 mmol) and *n*BuLi (1.55 M in *n*-hexane, 0.15 mL, 0.24 mmol) in anhydrous Et_2O (0.38 mL) at −78 °C. Purification of the crude material by flash column chromatography (5:95, Et_2O:*n*-hexane) gave product **3.65** (25.70 mg, 0.08 mmol, 89%) as a colourless oil.

Large scale: performed according to **GP2** using boronic ester **3.62** (398.40 mg, 1.25 mmol), bromochloromethane (0.24 mL, 3.75 mmol) and *n*BuLi (1.6 M in *n*-hexane, 1.96 mL, 3.13 mmol) in anhydrous Et_2O (5.09 mL) at –95 °C. Purification of the crude material by flash column chromatography (5:95, Et_2O:*n*-hexane) gave product **3.65** (358.80 mg, 1.07 mmol, 86%) as a colourless oil.

R_f (5:95, Et_2O:*n*-hexane) 0.24.

^{1}H NMR ($CDCl_3$, 500 MHz), δ 7.39-7.29 (4H, m, H_{11} and H_{12}), 7.28-7.23 (1H, m, H_{13}), 4.50 (2H, m, H_9), 3.58 (1H, dd, J = 8.9, 4.5 Hz, H_{8a} or H_{8b}), 3.18 (1H, t, J = 8.8 Hz, H_{8a} or H_{8b}), 1.80 (1H, ddt, J = 10, 8.6, 4.4 Hz, H_5), 1.21 (6H, s, H_1 or H_2), 1.20 (6H, s, H_1 or H_2), 0.90-0.82 (1H, m, H_{4a} or H_{4b}), 0.85 (9H, s, H_7), 0.71 (1H, dd, J = 15.3, 10 Hz, H_{4a} or H_{4b}).

^{13}C NMR ($CDCl_3$, 125 MHz) δ 139.1 (C_{10}), 128.4 (C_{12}), 127.7 (C_{11}), 127.4 (C_{13}) 82.8 (C_3), 72.99 (C_8 or C_9), 72.97 (C_8 or C_9), 44.7 (C_5), 32.8 (C_6), 27.9 (C_7), 25.1 (C_1 or C_2), 24.9 (C_1 or C_2), 11.1 (C_4).

IR (ν_{max}/cm^{-1}, neat): 2962, 2867, 1368, 1810, 1145, 1094, 733.

$[\boldsymbol{\alpha}]_{\boldsymbol{D}}^{\boldsymbol{20}}$ –2 (*c* 1, $CHCl_3$).

HRMS (ESI^+): calc. for $C_{20}H_{34}BO_3$ $[M+H]^+$: 333.2598; found: 333.2599.

2-((3*R*,5*S*)-5-((Benzyloxy)methyl)-2,2,6,6-tetramethylheptan-3-yl)-4,4,5,5-tetramethyl-1,3,2-dioxaborolane, 3.57

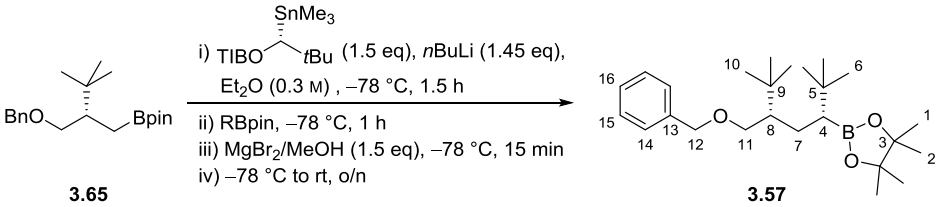

Prepared according to **GP1** using boronic ester **3.65** (748.20 mg, 2.25 mmol), *R* enantiomer of stannane (*R*)-**3.29** (1.63 g, 3.40 mmol) and *n*BuLi (1.53 M in *n*-hexane, 2.13 mL, 3.26 mmol) in anhydrous Et_2O (11.30 mL). $MgBr_2$/MeOH (1.00 M, 3.38 mL, 3.38 mmol) was added before warming the reaction mixture to room temperature. The crude material was purified by flash column chromatography (2:98 → 4:96, Et_2O:*n*-hexane) to give the homologated boronic ester **3.57** (624.00 mg, 1.55 mmol, 69%, dr 95:5) as a colourless oil.

R_f (4 : 96 Et_2O : *n*-hexane) 0.26.

^{1}H NMR ($CDCl_3$, 500 MHz), δ 7.36-7.29 (4H, m, H_{14} and H_{15}), 7.27-7.21 (1H, m, H_{16}), 4.45 (2H, s, H_{12a} and H_{12b}), 3.48 (1H, dd, *J* = 9.6, 5.9 Hz, H_{11a} or H_{11b}), 3.42 (1H, dd, *J* = 9.6, 3.9 Hz, H_{11a} or H_{11b}), 1.52 (1H, dt, *J* = 13.7, 4.1 Hz, H_{7a} or H_{7b}), 1.32-1.26 (1H, m, *J* = Hz, H_{7a} or H_{7b}), 1.20 (6H, s, H_1 or H_2), 1.22 (6H, s, H_1 or H_2), 1.21-1.17 (1H, m, H_8), 0.95 (9H, s, H_6 or H_{10}), 0.93 (9H, s, H_6 or H_{10}), 0.92-0.99 (m, 1H, H_4).

^{13}C NMR ($CDCl_3$, 125 MHz) δ 139.3 (C_{13}), 128.3 (C_{14} or C_{15}), 127.6 (C_{14} or C_{15}), 127.3 (C_{16}), 82.3 (C_3), 72.9 (C_{12}), 72.7 (C_{11}), 49.9 (C_8), 34.0 (C_5 or C_9) 33.12 (C_5 or C_9), 9.6 (C_6 or C_{10}), 28.6 (C_6 or C_{10}), 25.4 (C_1 or C_2), 24.9 (C_1 or C_2).

^{11}B NMR ($CDCl_3$, 128 MHz): δ 33.60.

IR (ν_{max}/cm^{-1}, neat): 2955, 2867, 1475, 1364, 1314, 1141, 1111, 695.

$[\alpha]_D^{21}$ –14 (*c* 1, $CHCl_3$).

HRMS (ESI^+): calc. for $C_{25}H_{43}BNaO_3$ $[M+Na]^+$: 425.3202; found: 425.3201.

***tert*-Butyl ((3*R*,5*S*)-5-((benzyloxy)methyl)-2,2,6,6-tetramethylheptan-3-yl)carbamate, 3.77**

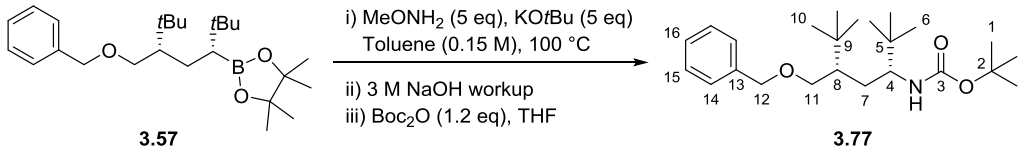

Prepared according to **GP3** using boronic ester **3.57** (557.7 mg, 1.39 mmol), $MeONH_2$ (0.36 mL, 6.95 mmol), KO*t*Bu (777.50 mg, 6.95 mmol) in anhydrous toluene (9.00 mL). The reaction mixture was subjected to basic work up followed by Boc-protection using Boc_2O (362.90 mg, 1.66 mmol) in THF (6.95 mL). The crude material was purified by flash column chromatography (5:95, Et_2O:*n*-hexane) to give carbamate **3.77** (468.10 mg, 1.20 mmol, 85%) as a white solid.

$\mathbf{R_f}$ (5 : 95 Et_2O : *n*-hexane) 0.25.

^{1}H NMR ($CDCl_3$, 500 MHz), δ 7.37-7.27 (4H, m, H_{14} and H_{15}), 7.31-7.27 (1H, m, H_{16}), 4.77 (1H, d, J = 9.2 Hz, NH), 4.54 (1H, d, J = 12.1 Hz, H_{12a} and H_{12b}), 4.44 (1H, d, J = 12.1 Hz, H_{12a} and H_{12b}), 3.59 (1H, dd, J = 9.0, 3.9 Hz, $H_{11a/b}$), 3.28 (1H, ddd, J = 12.1, 9.2, 3.0 Hz, H_4), 3.21 (1H, t, J = 9.1 Hz, $H_{11a/b}$), 1.71 (1H, ddd, J = 14.6, 5.0, 3.1 Hz, H_{7a} or H_{7b}), 1.42 (9H, s, H_1), 1.37 (1H, dq, J = 8.7, 3.9 Hz, H_8), 1.20 (1H, ddd, J = 14.6, 12.0, 3.4 Hz, H_{7a} or H_{7b}), 0.90 (9H, s, H_6), 0.87 (9H, s, H_{10}).

^{13}C NMR ($CDCl_3$, 125 MHz), δ 156.9 (C_3), 138.9 (C_{13}), 128.4 (C_{16}), 127.5 (C_{15}), 127.4 (C_{14}), 78.4 (C_2), 73.1 (C_{12}), 72.4 (C_{11}), 60.1 (C_4), 45.6 (C_8), 35.7 (C_5), 33.3 (C_9), 28.6 (C_1), 28.5 (C_7), 28.1 (C_{10}), 26.5 (C_6).

IR (ν_{max}/cm^{-1}, neat): 3395, 2951, 2869, 1715, 1503, 1363, 1169, 1049, 732, 697.

$[\boldsymbol{\alpha}]_{\boldsymbol{D}}^{\mathbf{20}}$ –17 (*c* 1, $CHCl_3$).

M.P. 44.4 – 45.4 °C (pentane).

HRMS (ESI$^+$): calc. for $C_{24}H_{41}NNaO_3$ $[M+Na]^+$: 414.2979; found: 414.2977.

***tert*-Butyl ((3*R*,5*S*)-5-(hydroxymethyl)-2,2,6,6-tetramethylheptan-3-yl)carbamate, 3.66**

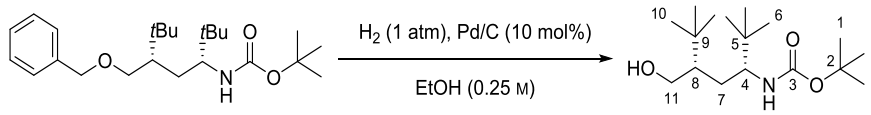

3.77 **3.66**

Prepared according to **GP5** using carbamate **3.77** (389.00 mg, 0.99 mmol), Pd/C (10% wt, 105.70 mg, 0.099 mmol) in EtOH (3.97 mL). Purification of the crude material by flash column chromatography (13:87, EtOAc:*n*-hexane) gave the *syn* alcohol **3.66** (244.7 mg, 0.81 mmol, 82%) as a white solid.

Rotamers were observed in both ^{1}H and ^{13}C NMR.

R_f (15 : 85 EtOAc : *n*-hexane) 0.23.

^{1}H NMR ($CDCl_3$, 400 MHz), δ 4.67 (1H, broad s, NH), 3.83 (1H, dd, J = 10.6, 3.7 Hz, H_{11a} or H_{11b}), 3.35 (1.5H, m, H_{11a} or H_{11b}, H_4 rotamer), 3.23 (0.5H, m, H_4 rotamer), 1.90 (broad s, OH), 1.76 (1H, m, H_{7a} or H_{7b}), 1.48-1.40 (9H, m, H_1), 1.22 (1H, m, H_8), 1.20 (1H, m, H_{7a} or H_{7b}), 0.91 (9H, s, H_{10}), 0.90 (9H, s, H_6).

^{13}C NMR ($CDCl_3$, 101 MHz) δ 156.9 (C_3), 78.9 (C_2), 64.3 (C_{11}), 61.7 (C_4 rotamer), 60.0 (C_4 rotamer), 48.9 (C_8 rotamer), 48.3 (C_8 rotamer), 35.6 (C_5), 33.5 (C_9), 29.1 (C_7), 28.6 (C_1), 28.2 (C_{10}), 26.6 (C_6).

IR (ν_{max}/cm^{-1}, neat): 3361, 2961, 2871, 1715, 1691, 1365, 1172, 1049.

$[\boldsymbol{\alpha}]_{\boldsymbol{D}}^{\boldsymbol{20}}$ +5 (*c* 1, $CHCl_3$).

M.P. 81.5 – 82.5 °C (pentane).

HRMS (ESI$^+$): calc. for $C_{17}H_{35}NNaO_3$ $[M+Na]^+$: 324.2509; found: 324.2529.

***tert*-Butyl (*R*)-2,4-di-tert-butyl-2,3-dihydro-1H-pyrrole-1-carboxylate**, **3.66**

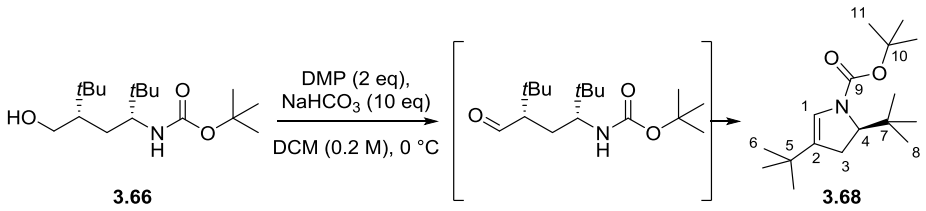

$NaHCO_3$ (83.60 mg, 1.00 mmol) was added to a solution of alcohol **3.66** (30.00 mg, 0.10 mmol) in anhydrous DCM (0.50 mL) at 0 °C. DMP (84.40 mg, 0.20 mmol) was added and the reaction was stirred at 0 °C for 3 h. The reaction mixture was diluted with EtOAc (2 mL) and quenched by the addition of saturated aqueous $Na_2S_2O_3$ (2 mL). The layers were separated and the aqueous layer was extracted with EtOAc (2 × 2 mL), dried over $MgSO_4$ and concentrated *in vacuo*. The crude material was purified by flash column chromatography (10:90, Et_2O:*n*-hexane) to give **3.68** (15.30 mg, 0.065 mmol, 65%) as a white solid.

R_f (10:90, Et_2O:*n*-hexane) 0.48.

^{1}H NMR ($CDCl_3$, 500 MHz), δ 6.34-5.98 (1H, m, H_1), 4.10-3.80 (1H, n, H_4), 2.71-2.56 (1H, m H_{3a} or H_{3b}), 2.30-2.16 (1H, d, J = 16.1 Hz, H_{3a} or H_{3b}), 1.48 (9H, s, H_{11}), 1.06 (9H, s, H_6), 0.85 (9H, s, H_8).

^{13}C NMR ($CDCl_3$, 125 MHz) δ 132.4 (C_2), 123.2 (C_1), 79.7 (C_{10}), 65.5 (C_4), 36.7 (C_7), 31.60 (C_3 and C_5), 29.1 (C_6), 28.6 (C_{11}), 26.1 (C_8), C_9 was not observed.

IR (ν_{max}/cm^{-1}, neat): 2953, 1705, 1382, 1125.

$[\boldsymbol{\alpha}]_{\boldsymbol{D}}^{\mathbf{23}}$ +190 (*c* 0.18, $CHCl_3$).

M.P. 69.9 – 70.9 °C (pentane).

HRMS (ESI$^+$): calc. for $C_{17}H_{31}NNaO_2$ $[M+Na]^+$: 304.2247; found: 304.2252.

***tert*-butyl ((3*R*,5*S*)-5-formyl-2,2,6,6-tetramethylheptan-3-yl) carbamate**, **3.67** and ***tert*-butyl (3*S*,5*R*)-3,5-di-tert-butyl-2-hydroxypyrrolidine-1-carboxylate**, **3.70**

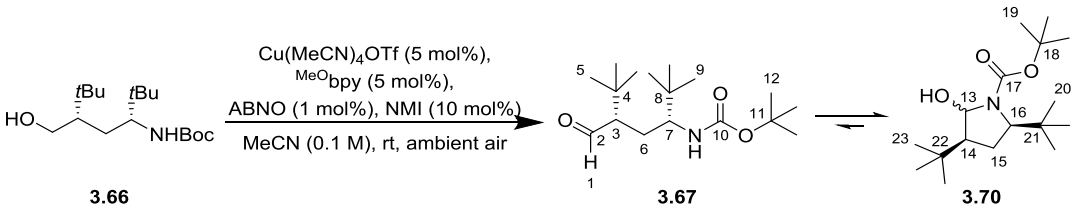

Prepared according to **GP6** using alcohol **3.66**(5.00 mg, 0.02 mmol), $Cu(MeCN)_4OTf$ (0.31 mg, 0.001 mmol), 4,4'-dimethoxy-2,2'-bipyridine (^{MeO}bpy, 0.18 mg, 0.001 mmol), ABNO (0.02 mg, 0.2 µmmol), and NMI (1.5 µL, 0.002 mmol) in MeCN (0.01 mL). The crude material was purified by flash column chromatography (5:95, EtOAc:*n*-hexane) to give product (4 mg, 0.013 mmol, 81%) as a 1 : 4 mixture of aldehyde **3.67** and hemiaminal **3.70** in $CDCl_3$.

$\mathbf{R_f}$ (5 : 95 EtOAc : *n*-hexane) 0.3.

^{1}H NMR ($CDCl_3$, 500 MHz), δ 9.89 (1H, d, J = 2.6 Hz, H_1), 5.57 (1H, m, H_{13}), 4.15 (1H, J = 10.8 Hz, NH), 3.79 (1H, t, J = 8.6 Hz, H_{16}), 3.31 (1H, td, J = 11.3, 3.1 Hz, H_7), 2.28 (1H, dt, J = 8.8, 2.4 Hz, H_3), 1.96 (1H, broad s, OH), 1.87 (2H, dd, J = 10.2, 8.3 Hz, H_{15}), 1.81 (1H, m, H_{6a}/H_{6b}), 1.68 (1H, m, H_{6a} or H_{6b}), 1.54 (1H, tdd, J = 10.4, 4.7 Hz, H_{14}), 1.49 (9H, s, H_{19}), 1.43 (9H, s, H_{12}), 1.04 (9H, s, H_{23}), 1.02 (9H, s, H_5), 0.94 (9H, s, H_{20}), 0.92 (9H, s, H_9).

^{13}C NMR ($CDCl_3$, 125 MHz) δ 206.5 (C_2), 156.5 (C_{17} and C_{10}), 86.5 (C_{13}), 80.2 (C_{18}), 79.2 (C_{11}), 65.8 (C_{16}), 60.1(9) (C_3 or C_7), 60.1(6) (C_3 or C_7), 53.4 (C_{14}), 35.5(C_{21}), 35.2(C_8), 34.8(C_4), 31.4(C_{22}), 28.9(C_{23}), 28.5(C_{12} and C_{19}), 28.1(C_5), 27.7(C_{20}), 26.5(C_9), 26.2(C_{15}), 25.4 (C_6).

IR (ν_{max}/cm^{-1}, neat): 3420, 2959, 1669, 1365, 1113.

HRMS (ESI$^+$): calc. for $C_{17}H_{32}NO_2$ $[M+H-H_2O]^+$: 282.2428; found: 282.2426.

Notes:

1. Due to the limited availability of the products, $[\boldsymbol{\alpha}]_{\boldsymbol{D}}^{\mathbf{20}}$ was not measured.

2. Extra signals observed in the NMR spectra (not included in the above assignments) were thought to be the diastereomer of the hemiaminal **3.70**, which arises from the epimer of the stereogenic centre at position 13. Although the intensities associated with these signals in the 2D spectra are too weak to reach an unequivocal assignment of the second diastereomer, further

oxidation of the products only gave the lactam, thus implying these minor signals corresponds to the diastereomer of hemiaminal **3.70**.

***tert*-Butyl (3*S*,5*R*)-3,5-di-*tert*-butyl-2-oxopyrrolidine-1-carboxylate**, **3.71**

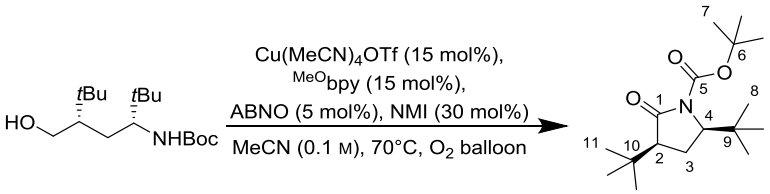

3.66 **3.71**

Solid $Cu(MeCN)_4OTf$ (4.39 mg, 0.012 mmol), 4,4'-dimethoxy-2,2'-bipyridine (^{MeO}bpy, 2.52 mg, 0.010 mmol), ABNO (0.33 mg, 0.002 mmol), and NMI (1.9 µL, 0.020 mmol) were added to a solution of alcohol **3.66** (70.20 mg, 0.230 mmol) in MeCN (2.33 mL) in a sample vial. The addition of each catalytic component was followed by a rinse of MeCN (0.15 mL). The dark red solution was purged with O_2 balloon and stirred at 950 RPM at 70°C for two h. All the catalytic components ($Cu(MeCN)_4OTf$, ^{MeO}bpy, ABNO and NMI) were reloaded every two h the reaction was stirred at 70°C with O_2 balloon for further 6 h until full conversion to the product was observed (monitored by LCMS analysis). The reaction was filtered through a pad of SiO_2 with MeCN wash and solvent was removed *in vacuo*. The crude material was purified by flash column chromatography (5:95, EtOAc:*n*-hexane) to give product **3.71** (44.8 mg, 0.15 mmol, 65%) as a white solid.

R_f (5:95, EtOAc:*n*-hexane) 0.32;

^{1}H NMR ($CDCl_3$, 500 MHz), δ 3.85 (1H, app. t, J = 8.5 Hz, H_4), 2.30 (1H, t, J = 11.3 Hz, H_2), 2.02 (1H, ddd, J = 13.2, 10.6, 8.2 Hz, H_{3a} or H_{3b}), 1.58 (1H, ddd, J = 13.2, 11.3, 8.9 Hz, H_{3a} or H_{3b}), 1.53 (9H, s, H_7), 1.05 (9H, s, H_{11}), 0.91 (9H, s, H_8).

^{13}C NMR ($CDCl_3$, 125 MHz) δ 176.2 (C_1), 153.1 (C_5), 83.2 (C_6), 62.0 (C_4), 51.7 (C_2), 36.1 (C_9), 32.7 (C_{10}), 28.0 (C_7), 27.6 (C_{11}), 26.7 (C_8), 22.8 (C_3).

IR (ν_{max}/cm^{-1}, neat): 2964, 1724, 1477, 1367, 1280, 1147.

$[\boldsymbol{\alpha}]_{\boldsymbol{D}}^{\mathbf{21}}$ +20 (*c* 1, $CHCl_3$).

M.P. 88.8 – 89.1 °C (pentane).

HRMS (ESI^+): calc. for $C_{17}H_{31}NNaO_3$ $[M+Na]^+$: 320.2196; found: 320.2203.

(3*S*,5*R*)-3,5-Di-*tert*-butylpyrrolidin-2-one, **3.76**

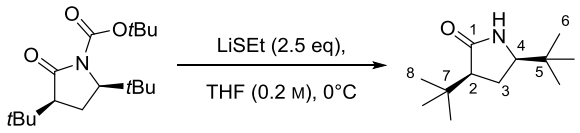

3.71 **3.76**

A solution of ethanethiol (4 μL, 0.06 mmol) in anhydrous THF (0.08 mL) was stirred at −78 °C followed by the dropwise addition of *n*BuLi (1.6 M in *n*-hexane, 0.03 mL) and stirred for 5 min. The reaction mixture was warming to 0°C and stirred for 15 min. A solution of lactam **3.71** (5.0 mg, 0.06 mmol) in anhydrous THF (0.1 mL) was cooled to −78 °C and added to the reaction mixture via syringe at 0 °C. The reaction was stirred at 0 °C overnight and quenched by the addition of 0.5 mL aqueous NaOH solution (1M) and 0.5 mL Et_2O. The reaction was stirred for 5 min and two phases were separated. The aqueous phase was extracted by Et_2O (1 mL × 3) and the organic phases were combined, dried over $MgSO_4$ and solvent was removed *in vacuo*. The crude material was purified by flash column chromatography (20:80, EtOAc:*n*-hexane) to give product **3.76** (1.9 mg, 0.01 mmol, 51%) as a white solid.

Note: Due to the limited amount of product, which was also being contaminated by BHT (from Et_2O), IR, $[\alpha]_D$ and melting point were not measured.

R_f (20:80, EtOAc:*n*-hexane) 0.15.

^{1}H NMR ($CDCl_3$, 500 MHz), δ 5.16 (1H, broad s, NH), 3.20 (1H, dd, J = 8.5, 4.8 Hz, H_4), 2.21 (1H, dd, J = 9.9, 7.2 Hz, H_2), 2.02-1.87 (2H, m, H_3), 1.03 (9H, s, H_8), 0.87 (9H, s, H_6).

^{13}C NMR ($CDCl_3$, 125 MHz) δ 178.85 (C_1), 61.0 (C_4), 50.2 (C_2), 34.5 (C_5), 33.2 (C_7), 27.5 (C_8), 25.6 (C_3), 25.4 (C_6).

HRMS (ESI^+): calc. for $C_{12}H_{23}NNaO$ $[M+Na]^+$: 220.1672; found: 220.1675.

***tert*-Butyl ((3*R*,5*S*)-5-(hydroxymethyl)-2,2,6,6-tetramethylheptan-3-yl) bis-carbamate, 3.78**

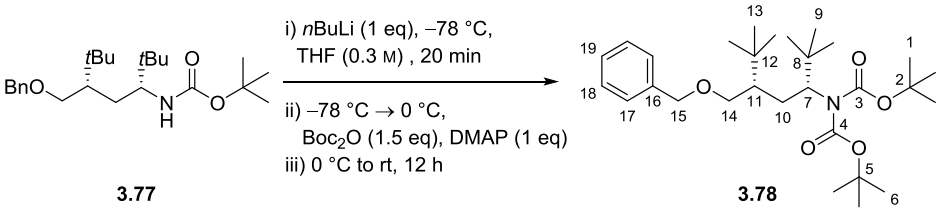

Prepared according to **GP4** using carbamate **3.77** (40.00 mg, 0.10 mmol), *n*BuLi (1.60 M, 0.06 mL, 0.10 mmol), DMAP (12.50 mg, 0.10 mmol), Boc_2O (33.70 mg, 0.15 mmol) in anhydrous THF (0.33 mL). Purification of the crude material by flash column chromatography (3:97, Et_2O:*n*-hexane) gave product **3.78** (39.00 mg, 0.08 mmol, 79%) as a colourless oil.

$\mathbf{R}_f$ (5:95, Et_2O:*n*-hexane) 0.48.

^{1}H NMR ($CDCl_3$, 500 MHz), δ 7.34-7.28 (4H, m, H_{17}, H_{18}), 7.26-7.22 (1H, m, H_{19}), 4.43 (2H, s, H_{15}), 4.02 (1H, dd, *J* = 9.6, 3.6 Hz, H_7), 3.55 (1H, dd, *J* = 10.1, 3.1 Hz, H_{14a} or H_{14b}), 3.50 (1H, dd, *J* = 10.1, 5.9 Hz, H_{14a} or H_{14b}), 1.98 (1H, ddd, *J* = 15.1, 9.6, 6.5 Hz, H_{10a} or H_{10b}), 1.69 (1H, dt, J = 15.2, 4.0 Hz, H_{10a} or H_{10b}), 1.48 (9H, s, H_1 or H_6), 1.47 (9H, s, H_1 or H_6), 1.37-1.31 (1H, m, H_{11}), 0.98 (9H, s, H_9), 0.96 (9H, s, H_{13}).

^{13}C NMR ($CDCl_3$, 125 MHz), δ 155.7 (C_4 or C_3), 153.9 (C_4 or C_3), 139.4 (C_{16}), 128.3 (C_{18}), 127.5 (C_{17}), 127.2 (C_{19}), 81.7 (C_2 or C_5), 81.6 (C_2 or C_5), 73.0 (C_{15}), 72.2 (C_{14}), 67.0 (C_7), 47.2 (C_{11}), 37.3 (C_8), 34.0 (C_{12}), 28.6 (C_{13}), 28.2 (C_1 or C_6), 28.1 (C_9), 28.0 (C_1 or C_6), 26.1 (C_{10}).

IR (ν_{max}/cm^{-1}, neat): 2960, 1870, 1744, 1700, 1366, 1334, 1147, 1113.

$[\boldsymbol{\alpha}]_{\boldsymbol{D}}^{\mathbf{20}}$ –4 (*c* 1, $CHCl_3$).

HRMS (ESI$^+$): calc. for $C_{29}H_{49}NNaO_5$ $[M+Na]^+$: 514.3503; found: 514.3510.

***tert*-Butyl ((3*R*,5*S*)-5-(hydroxymethyl)-2,2,6,6-tetramethylheptan-3-yl) bis-carbamate, 3.79**

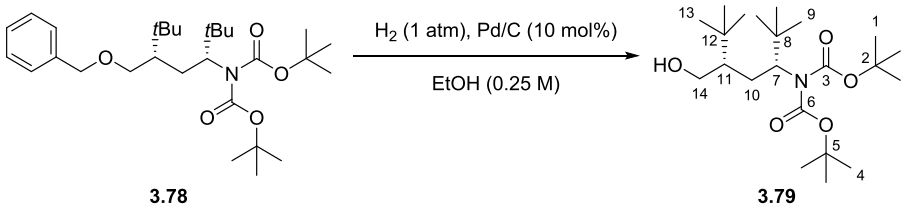

3.78 **3.79**

Prepared using **GP5** using Carbamate **3.78** (39.00 mg, 0.08 mmol), Pd/C (10% wt, 8.40 mg, 0.008 mmol) in ethanol (0.32 mL). Purification of the crude material by flash column chromatography (5:95, EtOAc:*n*-hexane) gave alcohol **3.79** (26.80 mg, 0.06 mmol, 84%) as a colourless oil.

$\mathbf{R}_f$ (5:95, EtOAc:*n*-hexane) 0.17.

^{1}H NMR ($CDCl_3$, 500 MHz), δ 4.07 (1H, dd, J = 12.4, 3.2 Hz, H_7), 3.70 (1H, d, J = 8.5 Hz, H_{14a} or H_{14b}), 3.45 (1H, dd, J = 10.9, 8.0 Hz, H_{14a} or H_{14b}), 3.30 (1H, s, OH), 2.09 (1H, ddd, J = 15.4, 12.4, 3.1 Hz, H_{10a} or H_{10b}), 1.74 (1H, ddd, J = 15.3, 6.6, 3.3 Hz, H_{10a} or H_{10b}), 1.49(5) (9H, s, H_1 or H_4) 1.49(3) (9H, s, H_1 or H_4), 1.24-1.18 (1H, m, H_{11}), 0.98 (9H, s, H_9), 0.92 (9H, s, H_{13}).

^{13}C NMR ($CDCl_3$, 125 MHz) δ 156.0 (C_3 or C_6), 155.0 (C_3 or C_6), 83.0 (C_2 or C_5), 81.9 (C_2 or C_5), 66.5 (C_7), 64.8 (C_{14}), 48.2 (C_{11}), 36.9 (C_8), 33.5 (C_{12}), 28.1 (C_{13}), 28.1 (C_1 or C_4), 27.7 (C_1 or C_4), 27.6 (C_9), 26.5 (C_{10}).

IR (ν_{max}/cm^{-1}, neat): 3512, 2964, 2872, 1736, 1695, 1367, 1338, 1173, 1145, 1114.

$[\boldsymbol{\alpha}]_{\boldsymbol{D}}^{\mathbf{20}}$ +68 (*c* 1, $CHCl_3$).

HRMS (ESI^+): calc. for $C_{22}H_{43}NNaO_5$ $[M+Na]^+$: 424.3033; found: 424.3039.

***tert*-Butyl ((3*R*,5*S*)-5-formyl-2,2,6,6-tetramethylheptan-3-yl) bis-carbamate, 3.80**

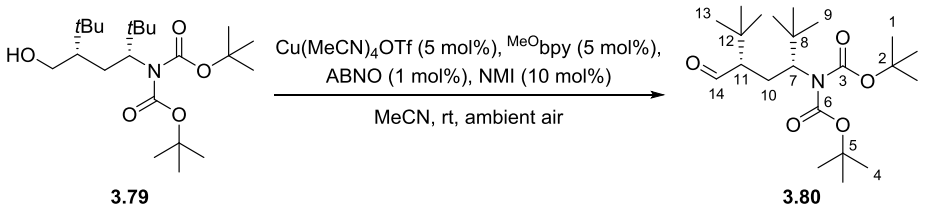

3.79 **3.80**

Prepared according to **GP6** using alcohol **3.79** (21 mg, 0.05 mmol), $Cu(MeCN)_4OTf$ (1.00 mg, 0.003 mmol), 4,4'-dimethoxy-2,2'-bipyridine (^{MeO}bpy, 0.57 mg, 0.003 mmol), ABNO (0.07 mg, 0.001 mmol), and NMI (0.4 µL, 0.01 mmol) in MeCN (0.1 mL). The crude material was purified by flash column chromatography (2:98, EtOAc:*n*-hexane) to give aldehyde **3.80** (15.60 mg, 0.04 mmol, 78%) as a colourless oil.

$\mathbf{R}_f$ (2:98, EtOAc:*n*-hexane) 0.19.

^{1}H NMR ($CDCl_3$, 500 MHz), δ 9.66 (1H, d, J = 4.8 Hz, H_{14}), 3.88 (1H, dd, J = 11.7, 3.0 Hz, H_7), 2.65 (ddd, J = 14.8, 11.8, 8.0 Hz, H_{10a} or H_{10b}), 1.90 (1H, ddd, J = 8.0, 4.9, 3.2 Hz, H_{11}), 1.74 (1H, dt, J = 14.8, 3.1, 3.1 Hz, H_{10a} or H_{10b}), 1.49 (9H, s, H_1 or H_6), 1.47 (9H, s, H_1 or H_6), 0.99 (9H, s, H_{13}), 0.98 (9H, s, H_9).

^{13}C NMR ($CDCl_3$, 125 MHz) δ 206.2 (C_{14}), 155.1 (C_3 or C_6), 154.1 (C_3 or C_6), 82.3 (C_2 or C_5), 82.0 (C_2 or C_5), 66.2 (C_7), 60.8 (C_{11}), 36.8 (C_8), 34.1 (C_{12}), 28.2 (C_1/C_4/C_9/C_{13}), 28.1(C_1/C_4/C_9/C_{13}), 27.9(C_1/C_4/C_9/C_{13}), 27.8(C_1/C_4/C_9/C_{13}), 23.7 (C_{10}).

IR (ν_{max}/cm^{-1}, neat): 2957, 2934, 2872, 1745, 1724, 1699, 1363, 1335, 1175, 1147, 1116.

$[\boldsymbol{\alpha}]_{\boldsymbol{D}}^{\mathbf{20}}$ +29 (*c* 0.62, $CHCl_3$).

HRMS (ESI$^+$): calc. for $C_{22}H_{41}NNaO_5$ $[M+Na]^+$: 422.2876; found: 422.2863.

(2*S*,4*R*)-4-(Bis-(*tert*-butoxycarbonyl)amino)-2-(*tert*-butyl)-5,5-dimethylhexanoic acid, 3.81

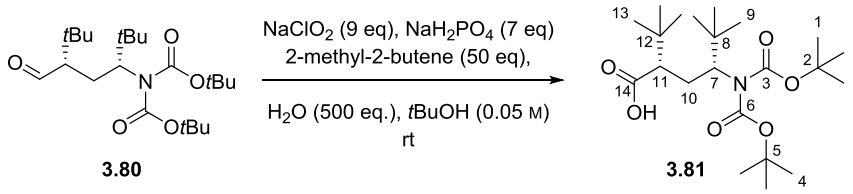

Prepared according to **GP7** using a solution of aldehyde **3.80** (15.60 mg, 0.04 mmol) in *t*BuOH (0.78 mL), 2-methyl-2-butene (0.21 mL, 1.95 mmol) and a solution of sodium chlorite (39.72 mg, 0.35 mmol) and sodium phosphate monobasic (32.80 mg, 0.27 mmol) in water (0.35 mL, 19.52 mmol) The crude material was subjected to subsequent transformations without purification.

Methyl(2*S*,4*R*)-4-(bis-(*tert*-butoxycarbonyl)amino)-2-(*tert*-butyl)-5,5-dimethylhexanoate, 3.82

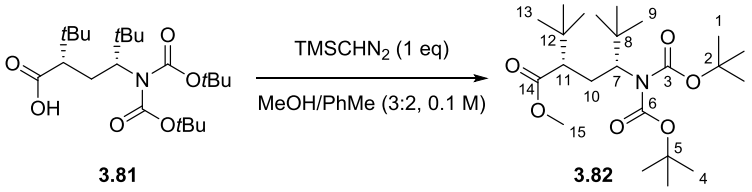

Prepared according to **GP8** using a solution of acid **3.81** (16.2 mg, 0.04 mmol) in anhydrous methanol (0.23 mL), toluene (0.16 mL) and (Trimethylsilyl)diazomethane (2.0 M in Et_2O, 0.02 mL, 0.04 mmol). Purification of the crude material by column chromatography (2:98, EtOAc:*n*-hexane) gave methyl ester **3.82** (13.4 mg, 0.03 mmol, 77%) as a colourless oil.

R_f (5:95, EtOAc:*n*-hexane) 0.37.

^{1}H NMR ($CDCl_3$, 500 MHz), δ 3.90 (1H, dd, J = 10.4, 3.2 Hz, H_7), 3.60 (3H, s, H_{15}), 2.44 (1H, ddd, J = 14.8, 10.4, 8.8 Hz, H_{10a} or H_{10b}), 2.12 (1H, dd, J = 8.9, 2.5 Hz, H_{11}), 1.78 (1H, dt, J = 14.8, 3.0 Hz, H_{10a} or H_{10b}), 1.49 (9H, s, H_1 or H_4), 1.48 (9H, s, H_1 or H_4),0.96 (9H, s, H_9 or H_{13}), 0.95 (9H, s, H_9 or H_{13}).

^{13}C NMR ($CDCl_3$, 125 MHz) δ 175.7 (C_{14}), 155.4 (C_6 or C_3), 153.5 (C_6 or C_3), 81.9 (C_2 or C_5), 51.4 (C_2 or C_5), 66.8 (C_7), 55.3 (C_{11}), 51.1 (C_{15}), 36.9 (C_8), 33.9 (C_{12}), 28.2 (C_1/C_4/C_9/C_{13}), 28.0 (C_1/C_4/C_9/C_{13}), 27.9 (C_1/C_4/C_9/C_{13}), 27.7 (C_1/C_4/C_9/C_{13}), 26.7 (C_{10}).

IR (ν_{max}/cm^{-1}, neat): 3961, 2930, 2872, 1736, 1702, 1367, 1340, 1146, 1112.

$[\boldsymbol{\alpha}]_{\boldsymbol{D}}^{\mathbf{20}}$ +10.5 (*c* 0.38, $CHCl_3$).

HRMS (ESI^+): calc. for $C_{22}H_{43}NNaO_6$ $[M+Na]^+$: 452.2983; found: 452.2990.

Methyl(2*S*,4*R*)-4-((*tert*-butoxycarbonyl)amino)-2-(*tert*-butyl)-5,5-dimethylhexanoate, 3.11

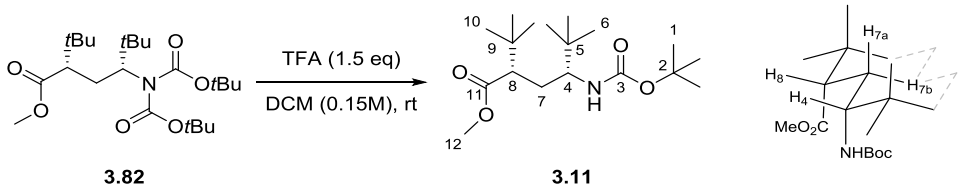

Prepared according to **GP9** using a solution of bis Boc **3.82** (35.30 mg, 0.08 mmol) in DCM (0.55 mL) and TFA (10 µL, 0.16 mmol) was added to a solution of in DCM (0.55 mL, 0.15 M). The crude material was purified by flash column chromatography (5:95, EtOAc:*n*-hexane) to give carbamate **3.11** (22.50 mg, 0.07 mmol, 85%) as a white solid.

Rotamers were observed in both ^{1}H and ^{13}C NMR.

R$_f$ (5 : 95 EtOAc : *n*-hexane) 0.22.

^{1}H NMR ($CDCl_3$, 500 MHz), δ 4.11 (0.84H, d, *J* = 10.5 Hz, NH rotamer), 3.79 (0.15H, d, *J* = 10.5 Hz, NH rotamer), 3.65 (2.45H, H_{12} rotamer) 3.63 (0.51H, H_{12} rotamer), 3.34 (0.88H, ddd, *J* = 11.4, 11.2, 3.5 Hz, H_4 rotamer), 3.17 (0.12H, ddd, *J* = 12.0, 11.9, 2.92 Hz, H_4 rotamer), 2.14 (0.85H, dd, *J* = 10.3, 1.6 Hz, H_8 rotamer), 2.05 (0.15H dd, *J* = 10.7, 1.7 Hz, H_8 rotamer), 1.79-1.74 (0.96H, ddd, *J* = 14.0, 3.6, 1.7 Hz, H_{7a} rotamer), 1.75-1.71 (1H, m, H_{7a} rotamer), 1.66 (1.42H, ddd, *J* = 14.0. 11.8, 10.3 Hz, H_{7b} rotamer), 1.62-1.55 (0.51H, m, H_{7b} rotamer), 1.46 (1.30H, s, H_1 rotamer), 1.42 (7.80H, s, H_1 rotamer), 0.93 (1.59H, s, H_{10} rotamer), 0.92 (7.41H, s, H_{10} rotamer), 0.89-0.85 (9H, m, H6).

^{13}C NMR ($CDCl_3$, 125 MHz) δ 177.7 (C_{11} rotamer), 176.9 (C_{11} rotamer), 156.0 (C_3 rotamer), 155.7 (C_3 rotamer), 79.5 (C_2 rotamer), 78.9 (C_2 rotamer), 62.1 (C_4 rotamer), 60.1 (C_4 rotamer), 54.9 (C_8 rotamer), 54.2 (C_8 rotamer), 51.5 (C_{12} rotamer), 51.4 (C_{12} rotamer), 35.4(9) (C_5 rotamer), 35.4(6) (C_5 rotamer), 33.6 (C_9 rotamer), 33.5 (C_9 rotamer), 28.7 (C_7 rotamer), 28.6 (C_1 rotamer), 28.5 (C_1 rotamer), 28.3 (C_7 rotamer), 27.8(1) (C_{10} rotamer), 27.7(9) (C_{10} rotamer), 26.4(2) (C_6 rotamer), 26.4(0) (C_6 rotamer).

IR (ν_{max}/cm^{-1}, neat): 3371, 2984, 2950, 1730, 1713, 1519, 1363, 1170, 1157, 1048.

$[\boldsymbol{\alpha}]_{\boldsymbol{D}}^{\boldsymbol{20}}$ –20 (*c* 0.2, $CHCl_3$).

M.P. 104.9 – 105.6 °C (pentane).

HRMS (ESI^+): calc. for $C_{18}H_{35}NNaO_4$ $[M+Na]^+$: 352.2458; found: 352.2450.

2-((3*S*,5*S*)-5-((Benzyloxy)methyl)-2,2,6,6-tetramethylheptan-3-yl)-4,4,5,5-tetramethyl-1,3,2-dioxaborolane, 3.83

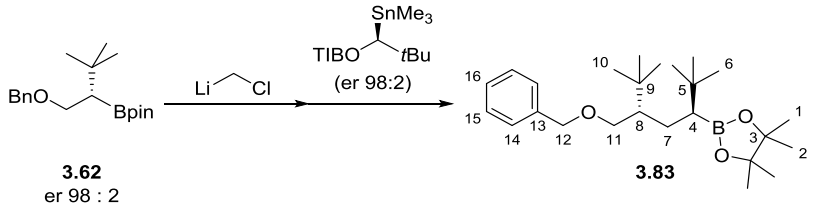

Boronic ester **3.62** (150 mg, 0.47 mmol) was subjected to two iterative homologations. After each homologation the crude mixture was filtered through a pad of wetted SiO_2 (Et_2O) and solvent was removed under reduced pressure to give the crude boronic ester for the subsequent reaction.

1st homologation (GP2): Performed using bromochloromethane (0.09 mL, 1.40 mmol) and *n*BuLi (1.65 M in *n*-hexane, 0.71 mL, 1.17 mmol) in anhydrous Et_2O (2.36 mL).

2nd homologation (**GP1**): Performed using (*S*)-**3.29** (340.3 mg, 0.71 mmol), *n*BuLi (1.65M in *n*-hexane, 0.42 mL, 0.68 mmol) in anhydrous Et_2O (1.6 mL).

The crude reaction mixture was purified by column chromatography (2:98, Et_2O:*n*-hexane) to yield the corresponding homologated boronic ester **3.83** (124.20 mg, 0.31 mmol, 66%, dr 96 : 4) as a waxy oil.

R_f (3 : 97 Et_2O : *n*-hexane) 0.22.

^{1}H NMR ($CDCl_3$, 500 MHz), δ 7.36-7.29 (2H, m, H_{14} and H_{15}), 7.27-7.22 (1H, m, H_{16}), 4.47-4.40 (2H, m, H_{12}), 3.50 (1H, dd, *J* = 10.1, 4.9 Hz, H_{11a} or H_{11b}), 3.42 (1H, dd, *J* = 10.1, 2.4 Hz, H_{11a} or H_{11b}), 1.54 (1H, td, *J* = 12.6, 1.9 Hz, H_{7a} or H_{7b}), 1.31 (1H, td, *J* = 12.3, 2.7 Hz, H_{7a} or H_{7b}), 1.24 (12H, s, H_1 and H_2), 1.04 (1H, ddt, *J* = 11.7, 4.5, 2.1 Hz, H_8), 0.96-0.93 (1H, m, H_4), 0.93(4) (9H, s, H_{10}), 0.93(0) (9H, s, H_6).

^{13}C NMR ($CDCl_3$, 125 MHz) δ 139.4 (C_{13}), 128.3 (C_{15}), 127.6 (C_{14}), 127.2 (C_{16}), 82.9 (C_3), 73.0 (C_{12}), 70.3 (C_{11}), 48.5 (C_8), 33.5 (C_5), 32.4 (C_9), 29.7 (C_{10}), 28.6 (C_6), 25.48(C_1 or C_2), 25.16 (C_1 or C_2), 24.5 (C_7), C_4 was not observed due to quadrupolar relaxation.

^{11}B NMR ($CDCl_3$, 128 MHz): δ 33.43.

IR (ν_{max}/cm^{-1}, neat): 2957, 2858, 1454, 1370, 1313, 1142, 695.

$[\boldsymbol{\alpha}]_{\boldsymbol{D}}^{\mathbf{21}}$ –29 (*c* 1, $CHCl_3$).

HRMS (ESI^+): calc. for $C_{25}H_{44}BO_3$ $[M+H]^+$: 403.3382; found: 403.3403.

***tert*-Butyl ((3*S*,5*S*)-5-((benzyloxy)methyl)-2,2,6,6-tetramethylheptan-3-yl)carbamate, 3.108**

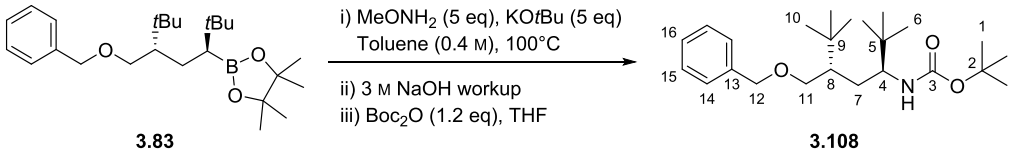

Prepared according to **GP3** using boronic ester **3.83** (124.20 mg, 0.31 mmol), $MeONH_2$ (0.01 mL, 1.85 mmol) and KO*t*Bu (207.80 mg, 1.85 mmol) in anhydrous toluene (3.10 mL). The reaction mixture was subjected to basic work up followed by Boc-protection using Boc_2O (101.00 mg, 0.46 mmol) in THF (1.55 mL). The crude material was purified by flash column chromatography (5:95, Et_2O:*n*-hexane) to give carbamate **3.108** (90.00 mg,0.23 mmol, 73%) as a viscous oil.

R_f (5:95, Et_2O:*n*-hexane) 0.23.

Rotamers were observed in both ^1H and ^{13}C NMR.

^{1}H NMR ($CDCl_3$, 500 MHz), δ 7.36-7.28 (4H, m, H_{14} and H_{15}), 7.27-7.22 (1H, m, H_{16}), 4.51-4.40 (2H, m, H_{12a} and H_{12b}), 4.19 (0.83H, d, J = 10.6 Hz, NH rotamer), 3.96 (0.17H, d, J = 10.8 Hz, NH rotamer), 3.62-3.54 (1.91H, m, $H11_a$ and $H11_b$ rotamer), 3.53-3.49 (0.20H, app. dd, J = 9.8, 3.7 Hz H_{11a} and H_{11b} rotamer), 3.49-3.38 (0.90H, td, J = 11.1, 1.8 Hz, H_4 rotamer), 3.44-3.34 (0.14H, m, H_4 rotamer), 1.75-1.68 (0.90H, ddd, J = 13.9, 10.6, 1.8 Hz, H_{7a} rotamer or H_{7b} rotamer), 1.68-1.62 (0.21H, m, H_{7a}/H_{7b} rotamer), 1.42 (9H, broad s, H_1), 1.38-1.32 (0.41H, m, H8 rotamer), 1.31-1.23 (0.64H, m, H8 rotamer), 1.12-1.02 (1H, m, H_{7a} rotamer or H_{7b} rotamer), 0.91(9H, broad s, H_{10}), 0.87 (9H, broad s, H_6).

^{13}C NMR ($CDCl_3$, 125 MHz), δ 156.7 (C_3 rotamer), 156.5 (C_3 rotamer), 139.3 (C_{13} rotamer), 139.1 (C_{13} rotamer), 128.3 (C_{15} rotamer), 128.3 (C_{15} rotamer), 127.6 (C_{14} rotamer), 127.4 (C_{14} rotamer), 127.3 (C_{16}), 75.6 (C_2 rotamer), 78.8 (C_2 rotamer), 73.3 (C_{12} rotamer), 73.2 (C_{12} rotamer), 70.5 (C_{11} rotamer), 70.2 (C_{11} rotamer), 58.9 (C_4 rotamer), 57.6 (C_4 rotamer), 45.1 (C_8 rotamer), 44.93 (C_8 rotamer), 35.3 (C_5 rotamer), 35.1 (C_5 rotamer), 33.0 (C_9), 28.6(4) (C_{10}), 28.6(2) (C_1), 28.6 (C_{10} rotamer or C_1 rotamer), 28.5 (C_{10} rotamer or C_1 rotamer), 28.3 (C_7 rotamer), 28.2 (C_7 rotamer), 26.5 (C_6).

IR (ν_{max}/cm^{-1}, neat): 3260, 2961, 1698, 1364, 1170, 1106, 733, 697.

$[\boldsymbol{\alpha}]_{\boldsymbol{D}}^{\boldsymbol{20}}$ –24 (*c* 1, $CHCl_3$).

HRMS (ESI^+): calc. for $C_{24}H_{41}NNaO_3$ $[M+Na]^+$: 414.2979; found: 414.2984.

***tert*-Butyl ((3*S*,5*S*)-5-((benzyloxy)methyl)-2,2,6,6-tetramethylheptan-3-yl) bis-carbamate, 3.109**

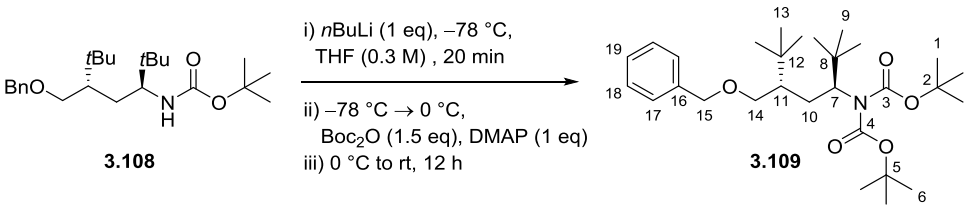

Prepared according to **GP4** using carbamate **3.108** (81.00 mg, 0.21 mmol) *n*BuLi (1.65 M in *n*-hexane, 0.13 mL, 0.21 mmol), Boc_2O (67.70 mg, 0.31 mmol), DMAP (25.30 mg, 0.21 mmol) in anhydrous THF (0.69 mL). Purification of the crude material by flash column chromatography (3:97, Et_2O:*n*-hexane) gave product **3.109** (56.6 mg, 0.12 mmol, 55 %, 97% yield BRSM) as a colourless liquid.

R_f (5:95, Et_2O:*n*-hexane) 0.47.

^{1}H NMR ($CDCl_3$, 500 MHz), δ 7.35-7.29 (4H, m, H_{17}, H_{18}), 7.26-7.22 (1H, m, H_{19}), 4.49 (1H, d, J = 12.1 Hz, $H15_a$ or $H15_b$), 4.44 (1H, d, J = 12.0 Hz, H_{15a} or H_{15b}), 4.02 (1H, dd, J = 12.1, 2.5 Hz, H_7), 3.59 (2H, d, J = 3.4 Hz, H_{14a} and H_{14b}), 2.19 (1H, ddd, J = 14.3, 12.2, 2.2 Hz, H_{10a} or H_{10b}), 1.60 (1H, ddd, J = 14.2, 11.5, 2.6 Hz, H_{10a} or H_{10b}), 1.48 (9H, s, H_1 or H_6), 1.47 (9H, s, H_1 or H_6), 1.19 (1H, dtd, J = 11.6, 3.4, 2.1 Hz, H_{11}), 0.97 (9H, s, H_9), 0.94 (9H, s, H_{13}).

^{13}C NMR ($CDCl_3$, 125 MHz), δ 156.2 (C_4 or C_3), 153.5 (C_4 or C_3), 139.4 (C_{16}), 128.3 (C_{18}), 127.5 (C_{17}), 127.2 (C_{19}), 81.6 (C_5 or C_2), 81.5 (C_5 or C_2), 73.18 (C_{15}), 69.6 (C_{14}), 64.5 (C_7), 45.1 (C_{11}), 36.5 (C_8), 33.3 (C_{12}), 28.9 (C_{13}), 28.2 (C_1/C_9/C_6), 28.1(4) (C_1/C_9/C_6), 28.1(0) (C_1/C_9/C_6), 23.6 (C_{10}).

IR (ν_{max}/cm^{-1}, neat): 2964, 1744, 1701, 1367, 1335, 1115, 905, 732, 649.

$[\boldsymbol{\alpha}]_{\boldsymbol{D}}^{\mathbf{20}}$ −18 (*c* 0.28, $CHCl_3$).

HRMS (ESI$^+$): calc. for $C_{29}H_{49}NNaO_5$ $[M+Na]^+$: 514.3503; found: 514.3483.

***tert*-Butyl ((3*S*,5*S*)-5-(hydroxymethyl)-2,2,6,6-tetramethylheptan-3-yl) bis-carbamate, 3.84**

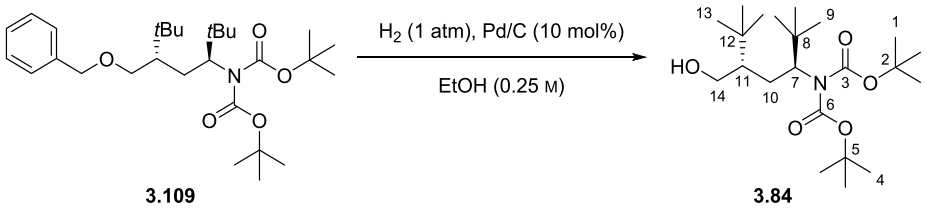

3.109 3.84

Prepared using **GP5** using **3.109** (56.60 mg, 0.12 mmol), Pd/C (12.30 mg, 10% wt, 10 mol%) in ethanol (0.46 mL). Purification of the crude material by flash column chromatography (5:95, EtOAc:*n*-hexane) gave alcohol **3.84** (32.00 mg, 0.08 mmol, 69%) as a colourless oil.

R$_f$ (5:95, EtOAc:*n*-hexane) 0.20.

^{1}H NMR ($CDCl_3$, 500 MHz), δ 4.01 (1H, dd, *J* = 12.4, 2.5 Hz, H_7), 3.77 (1H, dd, *J* = 11.9, 3.8 Hz, H_{14a} or H_{14b}), 3.56 (1H, dd, *J* = 11.9, 3.2 Hz, H_{14a} or H_{14b}), 2.23 (1H, ddd, *J* = 14.3, 12.4, 2.0 Hz, H_{10a} or H_{10b}), 2.24-2.13 (1H, br s, OH), 1.48 (9H, s, H_1 or H_4), 1.47 (9H, s, H_1 or H_4), 1.27 (1H, ddd, *J* = 14.3, 12.0, 2.6 Hz, H_{10a} or H_{10b}), 1.07 (1H, dtd, *J* = 12.0, 3.6, 2.0, H_{11}), 0.99 (9H, s, H_9), 0.92 (9H, s, H_{13}).

^{13}C NMR ($CDCl_3$, 125 MHz) δ 157.2 (C_3 or C_6), 153.0 (C_3 or C_6),82.4 (C_2 or C_5), 81.8 (C_2 or C_5), 65.0 (C_7), 63.9 (C_{14}), 48.9 (C_{11}), 36.5 (C_8), 33.2 (C_{12}), 28.3 (C_{13}), 28.2 (C_9), 28.1 (C_1 and C_4), 25.1 (C_{10}).

IR (ν_{max}/cm^{-1}, neat): 3503, 2959, 1744, 1699, 1366, 1333, 1172, 1147, 1132, 943.

$[\boldsymbol{\alpha}]_{\boldsymbol{D}}^{\mathbf{25}}$ +10 (*c* 1, $CHCl_3$).

HRMS (ESI$^+$): calc. for $C_{17}H_{36}NO_3$ $[M+H]^+$: 302.2690; found: 302.2697.

***tert*-Butyl ((3*S*,5*S*)-5-formyl-2,2,6,6-tetramethylheptan-3-yl) bis-carbamate, 3.110**

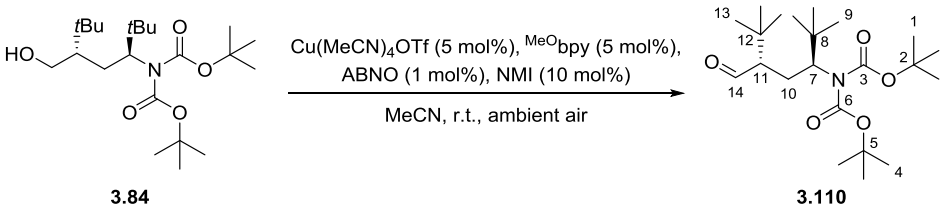

3.84 **3.110**

Prepared according to **GP6** using alcohol **3.84** (32.0 mg, 0.08 mmol), $Cu(MeCN)_4OTf$ (1.5 mg, 0.004 mmol), 4,4'-dimethoxy-2,2'-bipyridine (^{MeO}bpy, 0.9 mg, 0.004 mmol), ABNO (0.1 mg, 0.0008 mmol), and NMI (0.6 µL, 0.008 mmol) in MeCN (0.8 mL). The crude material was purified by flash column chromatography (5:95, EtOAc:*n*-hexane) to give aldehyde **3.110** (22.60 mg, 0.06 mmol, 71%) as a colourless oil.

$\mathbf{R_f}$ (5:95, EtOAc:*n*-hexane) 0.31.

^{1}H NMR ($CDCl_3$, 500 MHz), δ 9.82 (1H, d, J = 3.0 Hz, H_{14}), 3.65 (1H, dd, J =12.3, 2.9 Hz, H_7), 2.27-2.16 (2H, m, H_{10a} or H_{10b} and H_{11}), 1.91 (1H, ddd, J = 13.7, 11.3, 2.8, H_{10a} or H_{10b}), 1.48-1.46 (18H, m, H_1 and H_4), 1.00 (9H, s, H_9), 0.97 (9H, s, H_{13}).

^{13}C NMR ($CDCl_3$, 125 MHz) δ 206.4 (C_{14}), 155.5 (C_3 or C_6),153.4 (C_3 or C_6), 82.0 (C_2 or C_5), 81.8 (C_2 or C_5), 64.5 (C_7), 58.4 (C_{11}), 36.5 (C_8), 34.2 (C_{12}), 28.4 (C_1/C_4/C_9/C_{13}), 28.1(C_1/C_4/C_9/C_{13}), 28.0(7) (C_1/C_4/C_9/C_{13}), 27.9(8) (C_1/C_4/C_9/C_{13}), 21.90 (C_{10}).

IR (ν_{max}/cm^{-1}, neat): 2954, 1744, 1720, 1703, 1367, 1334, 1173, 1148, 1115.

$[\boldsymbol{\alpha}]_{\boldsymbol{D}}^{\mathbf{20}}$ +15 (*c* 1, $CHCl_3$).

HRMS (ESI$^+$): calc. for $C_{22}H_{41}NNaO_5$ $[M+Na]^+$: 422.2877; found: 422.2875.

(2*S*,4*S*)-4-(Bis-(*tert*-butoxycarbonyl)amino)-2-(*tert*-butyl)-5,5-dimethylhexanoic acid, 3.111

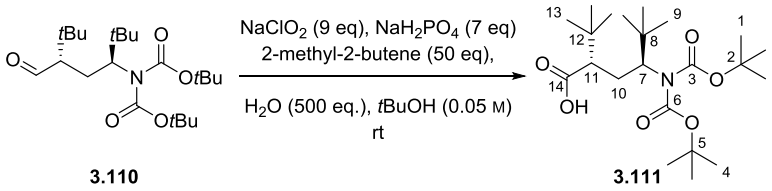

Prepared according to **GP7** using a solution of aldehyde **3.110** (22.60 mg, 0.06 mmol) in *t*BuOH (1.13 mL), 2-methyl-2-butene (0.30 mL, 2.83 mmol) and a solution of sodium chlorite (57.55 mg, 0.51 mmol) and sodium phosphate monobasic (47.50 mg, 0.40 mmol) in water (0.51 mL, 28.30 mmol) The crude material was subjected to subsequent transformations without purification.

Methyl (2*S*,4*S*)-4-(bis-(*tert*-butoxycarbonyl)amino)-2-(*tert*-butyl)-5,5-dimethylhexanoate, 3.110

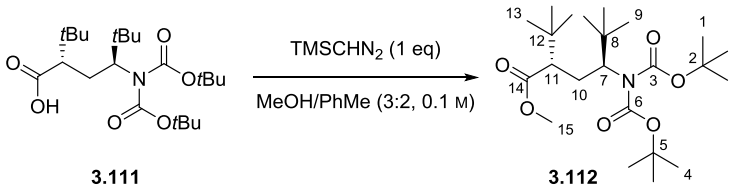

Prepared according to **GP8** using a solution of crude acid **3.111** in anhydrous methanol (0.35 mL), toluene (0.24 mL) and (Trimethylsilyl)diazomethane (2.0 M in Et_2O, 0.03 mL, 0.06 mmol). The crude material was subjected to subsequent transformations without purification.

Methyl (2*S*,4*S*)-4-((*tert*-butoxycarbonyl)amino)-2-(*tert*-butyl)-5,5-dimethylhexanoate, 3.12

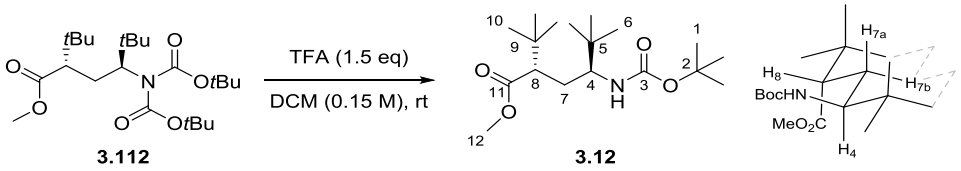

Prepared according to **GP9** using a solution of bis carbamate **3.112** (13.40 mg, 0.03 mmol) in DCM (0.21 mL) and TFA (5 µL, 0.06 mmol). The crude material was purified by flash column chromatography (5:95, EtOAc:*n*-hexane) to give carbamate **3.12** (7.40 mg, 0.002 mmol, 75%) as a colourless oil.

Rotamers were observed in both ^{1}H and ^{13}C NMR.

R$_f$ (5:95, EtOAc:*n*-hexane) 0.2.

^{1}H NMR ($CDCl_3$, 500 MHz), δ 4.15 (0.75H, d, *J* = 10.6 Hz, NH rotamer), 4.00 (0.25H, m, NH rotamer), 3.18 (0.73H, td, *J* = 11.6, 2.4 Hz, H_4 rotamer), 2.99 (0.30H, t, *J* = 11.2 Hz, H_4 rotamer), 2.34 (0.30H, dd, *J* = 12.2, 2.2 Hz, H_8 rotamer), 2.28 (0.74H, dd, J = 12.1, 2.5 Hz, H_8 rotamer), 1.97 (1H, ddd, *J* = 14.4, 12.1, 2.6 Hz, H_{7a} or H_{7b}), 1.46-1.43 (9H, m, H_1), 1.19 (1.10H, ddd, *J* = 13.9, 11.8, 2.6 Hz, H_{7a} rotamer or H_{7b} rotamer), 1.12 (0.66H, ddd, *J* = 13.7, 11.7, 2.3 Hz, H_{7a} rotamer or H_{7b} rotamer), 0.94-0.92 (9H, m, H_{10}), 0.88-0.86 (9H, m, H_6).

^{13}C NMR ($CDCl_3$, 125 MHz) δ 175.6 (C_{11} rotamer), 175.5 (C_{11} rotamer), 156.6 (C_3 rotamer), 156.0 (C_3 rotamer), 79.8 (C_2 rotamer), 78.9 (C_2 rotamer), 59.2 (C_4 rotamer), 57.3 (C_4 rotamer), 52.9 (C_8 rotamer), 52.8 (C_8 rotamer), 51.2 (C_{12} rotamer), 51.1 (C_{12} rotamer), 35.3 (C_5 rotamer), 35.2 (C_5 rotamer), 33.1 (C_9 rotamer), 33.0 (C_9 rotamer), 29.0 (C_7 rotamer), 28.6 (C_7 rotamer), 28.6 (C_1 rotamer), 28.4 (C_1 rotamer), 28.1 (C_{10}), 26.4 (C_6).

IR (ν_{max}/cm^{-1}, neat): 3256, 2955, 1732, 1699, 1385, 1355, 1174, 1049.

$[\boldsymbol{\alpha}]_{\boldsymbol{D}}^{\boldsymbol{20}}$ –46 (*c* 0.26, $CHCl_3$).

HRMS (ESI^+): calc. for $C_{18}H_{35}NNaO_4$ $[M+Na]^+$: 352.2458; found: 352.2476.

2-((3*R*,6*S*)-6-((Benzyloxy)methyl)-2,2,7,7-tetramethyloctan-3-yl)-4,4,5,5-tetramethyl-1,3,2-dioxaborolane, 3.91

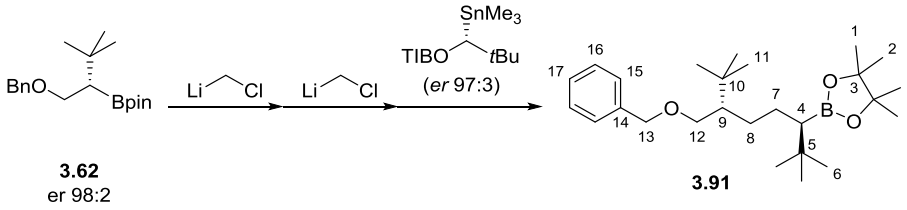

3.62
er 98:2

3.91

Boronic ester **3.62** (102.20 mg, 0.32 mmol) was subjected to three iterative homologations. After each homologation the crude mixture was filtered through a pad of wetted SiO_2 (Et_2O) and solvent was removed under reduced pressure to give the crude boronic ester for the subsequent reaction.

1st homologation (GP2): Performed using bromochloromethane (0.06 mL, 0.96 mmol) and *n*BuLi (1.65 M in *n*-hexane, 0.48 mL, 0.80 mmol) in anhydrous Et_2O (1.61 mL).

2nd homologation (GP2): Performed using bromochloromethane (0.06 mL, 0.96 mmol) and *n*BuLi (1.65 M in *n*-hexane, 0.48 mL, 0.80 mmol) in anhydrous Et_2O (1.61 mL).

3rd homologation (**GP1**): Performed using (*R*)-stannane **3.29** (215.10 mg, 0.46 mmol), *n*BuLi (1.65 M in *n*-hexane, 0.27 mL, 0.45 mmol) in anhydrous Et_2O (1.49 mL)

The crude reaction mixture was purified by column chromatography (3:97, Et_2O:*n*-hexane) to yield the corresponding homologated boronic ester **3.91** (37.00 mg, 0.09 mmol, 26%, dr 94:4) as a colourless oil.

R_f (3:97, Et_2O:*n*-hexane) 0.19.

^{1}H NMR ($CDCl_3$, 500 MHz), δ 7.35-7.29 (4H, m, H_{15} and H_{16}), 7.23-7.27 (1H, m, H_{17}), 4.49-4.42 (2H, m, H_{13}), 3.54 (1H, dd, J = 9.6, 4.7 Hz, H_{12a} or H_{12b}), 3.36 (1H, dd, J = 9.5, 4.8 Hz, H_{12a} or H_{12b}), 1.59 (1H, tt, J = 12.4, 4.0 Hz, H_{7a} or H_{7b}), 1.40 (1H, tdd, J = 12.6, 4.6, 2.9 Hz, H_{8a} or H_{8b}), 1.30 (1H, qd, J = 12.1, 4.6 Hz, H_{7a} or H_{7b}), 1.28-1.21 (1H, m, H_9), 1.25 (12H, s, H_1 and H_2), 1.13-1.01 (1H, dddd, J = 12.6, 12.0, 9.2, 4.0 Hz, H_{8a} or H_{8b}), 0.92 (9H, s, H_6), 0.90 (9H, s, H_{11}), 0.75 (1H, dd, J = 12.2, 3.4 Hz, H_4).

^{13}C NMR ($CDCl_3$, 125 MHz), δ 139.1 (C_{14}), 128.4 (C_{16}), 127.5 (C_{15}), 127.4 (C_{17}), 82.9 (C_3), 73.1 (C_{13}), 71.9 (C_{12}), 49.7 (C_9), 33.21 (C_{10}), 32.2 (C_5), 29.76 (C_6), 29.59 (C_8), 28.4 (C_{11}), 27.3 (C_7), 25.3 (C_1 or C_2), 25.1 (C_1 or C_2), C_4 not observed due to quadrupolar relaxation.

^{11}B NMR ($CDCl_3$, 128 MHz): δ 34.17.

IR (ν_{max}/cm^{-1}, neat): 2957, 2867, 1366, 1313, 1142, 696.

$[\boldsymbol{\alpha}]_{\boldsymbol{D}}^{\boldsymbol{24}}$ −3 (*c* 1, $CHCl_3$).

HRMS (ESI^+): calc. for $C_{26}H_{46}BO_3$ $[M+H]^+$: 417.3539; found: 417.3550.

***tert*-Butyl ((3*R*,6*S*)-6-((benzyloxy)methyl)-2,2,7,7-tetramethyloctan-3-yl)carbamate, 3.92**

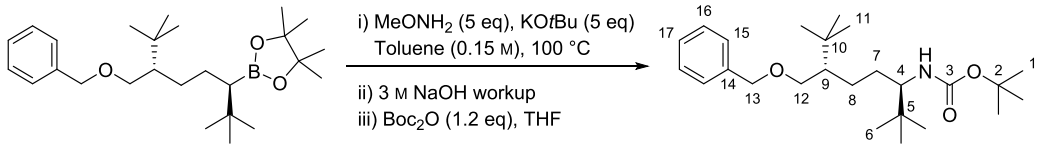

3.91 **3.92**

Prepared according to **GP3** using boronic ester **3.91** (43.60 mg, 0.10 mmol), KO*t*Bu (70.50 mg, 0.63 mmol) and $MeONH_2$ (0.03 mL, 0.63 mmol) in anhydrous toluene (0.70 mL). The reaction mixture was subjected to basic work up followed by Boc-protection using Boc_2O (27.40 mg, 0.13 mmol) in THF (0.70 mL). The crude material was purified by flash column chromatography (10:90, Et_2O:*n*-hexane) to give carbamate **3.92** (33.00 mg, 0.08 mmol, 77%) as a colourless oil.

R_f (10 : 90 Et_2O : *n*-hexane) 0.32;

Rotamers were observed in both ^1H and ^{13}C NMR.

^{1}H NMR ($CDCl_3$, 500 MHz), δ 7.35-7.29 (4H, m, H_{15}, H_{16}), 7.29-7.23 (1H, m, H_{17}), 4.46 (2H, m, H_{13a} and H_{13b}), 4.26 (0.80H, d, J = 10.4 Hz, NH rotamer), 4.01 (0.13H, d, J = 10.5 Hz, NH rotamer), 3.56 (1H, dd, J = 9.5, 4.0 Hz, H_{12a} or H_{12b}), 3.40-3.36 (0.15H, m, H_{12a} rotamer or H_{12b} rotamer), 3.34 (0.86H, dd, J = 9.5, 5.1 Hz, H_{12a} rotamer or H_{12b} rotamer), 3.25 (0.81H, td, J = 11.0, 2.3 Hz, H_4 rotamer), 3.16-3.07 (0.14H, m, H_4 rotamer), 1.88-1.79 (0.85H, m, H_{7a} rotamer or H_{7b} rotamer), 1.79-1.75 (0.11H, m, H_{7a} rotamer or H_{7b} rotamer), 1.62-1.54 (1H, m, H_{8a} or H_{8b}), 1.46 (1.4H, s, H_1 rotamer), 1.43 (7.5H, s, H_1 rotamer), 1.27-1.15 (2H, m, H9 and H_{8a} or H_{8b}), 1.04-0.94 (1H, m, H_{7a} or H_{7b}), 0.92-0.88 (9H, m, H_{11}), 0.86-0.84 (9H, br. s, H_6).

^{13}C NMR ($CDCl_3$, 125 MHz), δ 156.8 (C_3 rotamer), 156.5 (C_3 rotamer), 138.9 (C_{14}), 128.4 (C_{16}), 127.6 (C_{15}), 127.5 (C_{17}), 79.5 (C_2 rotamer), 78.7 (C_2 rotamer), 73.2 (C_{13}), 72.3 (C_{12} rotamer), 72.0 (C_{12} rotamer), 62.0 (C_4 rotamer), 60.2 (C_4 rotamer), 49.3 (C_9 rotamer), 49.1 (C_9 rotamer), 34.9 (C_5 rotamer), 34.9 (C_5 rotamer), 33.2 (C_{10}), 30.8 (C_7 rotamer), 30.6 (C_7 rotamer), 28.6 (C_1), 28.3 (C_{11} rotamer), 28.2 (C_{11} rotamer), 26.53 (C_8 or C_6), 26.5 (C_8 or C_6).

IR (ν_{max}/cm^{-1}, neat): 3451, 3360, 3265,2961, 2868, 1716, 1700, 1498, 1364, 1171, 734, 697.

$[\boldsymbol{\alpha}]_{\boldsymbol{D}}^{\boldsymbol{20}}$ −11 (*c* 1, $CHCl_3$).

HRMS (ESI^+): calc. for $C_{25}H_{43}NNaO_3$ $[M+Na]^+$: 428.3135; found: 428.3122.

***tert*-Butyl ((3*R*,6*S*)-6-(hydroxymethyl)-2,2,7,7-tetramethyloctan-3-yl)carbamate, 3.93**

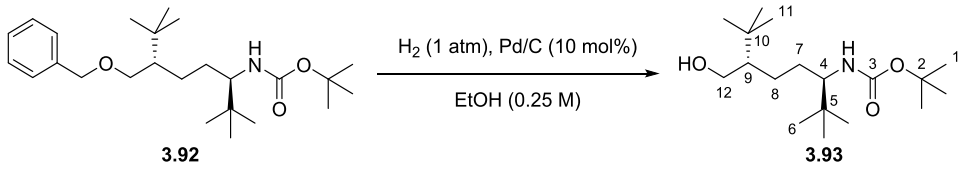

3.92 **3.93**

Prepared using **GP5** using **3.92** (34.30 mg, 0.08 mmol), Pd/C (8.70 mg, 10% wt, 10 mol%) in ethanol (0.30 mL). Purification of the crude material by flash column chromatography (10:90, EtOAc:*n*-hexane) gave alcohol **3.93** (21.00 mg, 0.07 mmol, 85%) as a colourless oil.

Note: After two days at room temperature the product became a white solid.

$\mathbf{R_f}$ (10:90, EtOAc:*n*-hexane) 0.18.

Rotamers were observed in both ^{1}H and ^{13}C NMR.

^{1}H NMR ($CDCl_3$, 500 MHz), δ 4.31 (0.87H, d, J = 10.5 Hz, NH rotamer), 4.14-4.08 (0.13H, m, NH rotamer), 3.83 (0.03H, dd, J = 10.5, 3.7 Hz, H_{12a} rotamer or H_{12b} rotamer), 3.76 (0.98H, dd, J = 11.2, 4.0 Hz, H_{12a} rotamer or H_{12b} rotamer), 3.57 (0.12H, dd, J = 11.2, 5.3 Hz, H_{12a} rotamer or H_{12b} rotamer), 3.48 (0.87H, dd, J = 11.2, 6.1 Hz, H_{12a} rotamer or H_{12b} rotamer), 3.31 (0.88H, td, J = 11.0, 2.2 Hz, H_4 rotamer), 3.14 (0.12, m, H_4 rotamer), 1.75 (1H, dddd, J = 13.8, 9.2, 7.2, 2.2 Hz, H_{7a} or H_{7b}), 1.67-1.61 (0.15H, m, H_{8a} rotamer or H_{8b} rotamer), 1.61-1.52 (1H, m, H_{8a} rotamer or H_{8b} rotamer), 1.46 (1.21H, s, H_1 rotamer), 1.43 (7.81H, s, H_1 rotamer), 1.28-1.19 (1.28H, m, H_{8a} rotamer or H_{8b} rotamer), 1.21-1.09 (0.12H, m, H_{8a} rotamer or H_{8b} rotamer), 1.16-0.98 (2H, m, H_9 and H_{7a} or H_{7b}), 0.91-0.89 (9H, br. s, H_{11}), 0.89-0.85 (9H, br. s, H_6).

^{13}C NMR ($CDCl_3$, 125 MHz) δ 156.9(5) (C_3 rotamer), 156.8(3) (C_3 rotamer), 76.7 (C_2 rotamer), 79.2 (C_2 rotamer), 64.2 (C_{12} rotamer), 63.9 (C_{12} rotamer), 61.7 (C_4 rotamer), 59.4 (C_4 rotamer), 51.5 (C_9 rotamer), 51.4 (C_9 rotamer), 35.0 (C_5 rotamer), 34.8 (C_5 rotamer), 33.4 (C_{10} rotamer), 33.2 (C_{10} rotamer), 30.9 (C_7 rotamer), 30.8 (C_7 rotamer), 28.6 (C_1), 28.3 (C_{11}), 26.5 (C_6); 25.6 (C_8 rotamer), 24.9 (C_8 rotamer).

IR (ν_{max}/cm^{-1}, neat): 3347, 2952, 1686, 1355, 1170, 1054.

$[\boldsymbol{\alpha}]_{\boldsymbol{D}}^{\mathbf{24}}$ +11.9 (*c* 0.84, $CHCl_3$).

M.P. 77.9 – 78.9 °C (pentane).

HRMS (ESI$^+$): calc. for $C_{18}H_{37}NNaO_3$ $[M+Na]^+$: 338.2666; found: 338.2671.

***tert*-Butyl ((3*R*,6*S*)-6-formyl-2,2,7,7-tetramethyloctan-3-yl)carbamate, 3.94**

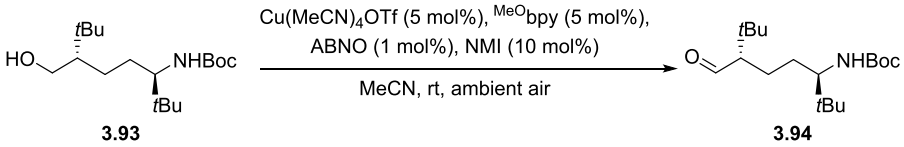

3.93 **3.94**

Prepared according to **GP6** using alcohol **3.93** (15.00 mg, 0.04 mmol), $Cu(MeCN)_4OTf$ (0.68 mg, 0.002 mmol), 4,4'-dimethoxy-2,2'-bipyridine (^{MeO}bpy, 0.39 mg, 0.002 mmol), ABNO (0.05 mg, 0.0004 mmol), and NMI (0.3 µL, 0.004 mmol) in MeCN (0.4 mL). The crude material was subjected to subsequent transformations without purification.

(2*S*,5*R*)-5-((*Tert*-butoxycarbonyl)amino)-2-(*tert*-butyl)-6,6-dimethylheptanoic acid, 3.113

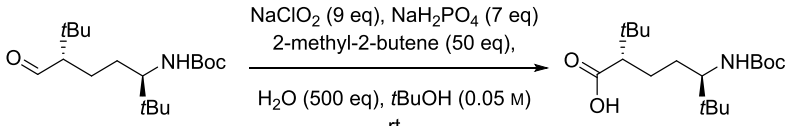

3.94 **3.113**

Prepared according to **GP7** using a solution of crude aldehyde **3.94** in *t*BuOH (0.72 mL), 2-methyl-2-butene (0.19 mL, 1.80 mmol) and a solution of sodium chlorite (36.64 mg, 0.32 mmol) and sodium phosphate monobasic (30.25 mg, 0.25 mmol) in water (0.32 mL, 28.30 mmol) The crude material was subjected to subsequent transformations without purification.

Methyl (2*S*,5*R*)-5-((*tert*-butoxycarbonyl)amino)-2-(*tert*-butyl)-6,6-dimethylheptanoate, 3.88

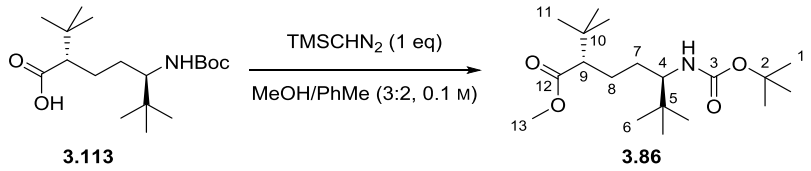

Prepared according to **GP8** using a solution of crude acid **3.113** in anhydrous methanol (0.20 mL), toluene (0.14 mL) and (trimethylsilyl)diazomethane (2.0 M in Et_2O, 0.02 mL, 0.04 mmol). Purification of the crude material by column chromatography (5:95, EtOAc:*n*-hexane) gave methyl ester **3.88** (12.40 mg, 0.036 mmol, 90%) as a white solid.

R_f (5:95, EtOAc:*n*-hexane) 0.24.

Rotamers were observed in both ^1H and ^{13}C NMR.

^1H NMR ($CDCl_3$, 500 MHz), δ 4.23 (0.77H, d, J = 10.6 Hz, NH rotamer), 4.05, (0.17H, d, J = 10.6 Hz, NH rotamer), 3.65 (3H, s, H_{13}), 3.27 (0.79H, td, J = 10.9, 2.1 Hz, H_4 rotamer), 3.15 (0.19H, m, H_4 rotamer), 2.07 (1H, dd, J = 11.7, 2.9 Hz, H_9), 1.70-1.50 (2H, m, H_{8a} and H_{8b}), 1.58-1.74 (1H, m, H_{7a}/H_{7b}), 1.47 (1.68H, s, H_1 rotamer), 1.44 (7.27H, s, H_1 rotamer), 0.93 (9H, s, H_{11}), 0.94-0.94 (1H, m, H_{7a}/H_{7b}), 0.85 (9H, s, H_6).

^{13}C NMR ($CDCl_3$, 125 MHz) δ 176.1 (C_{12} rotamer), 175.9 (C_{12} rotamer), 79.8 (C_2 rotamer), 78.9 (C_2 rotamer), 61.5 (C_4 rotamer), 59.7 (C_4 rotamer), 57.1 (C_9 rotamer), 56.7 (C_9 rotamer), 51.1 (C_{13}), 34.9 (C_5), 33.1 (C_{10}), 29.7 (C_7), 28.6 (C_1), 28.0 (C_{11}), 26.5 (C_6), 25.7 (C_8 rotamer), 25.4 (C_8 rotamer).

IR (ν_{max}/cm^{-1}, neat): 3391, 2957, 1707, 1517, 1152.

$[\boldsymbol{\alpha}]_{\boldsymbol{D}}^{\mathbf{23}}$ −10.5 (*c* 0.5, $CHCl_3$).

M.P. 99 – 100 °C (Et_2O).

HRMS (ESI^+): calc. for $C19H_{37}NNaO_4$ $[M+Na]^+$: 366.2614; found: 366.2616.

General computational procedures

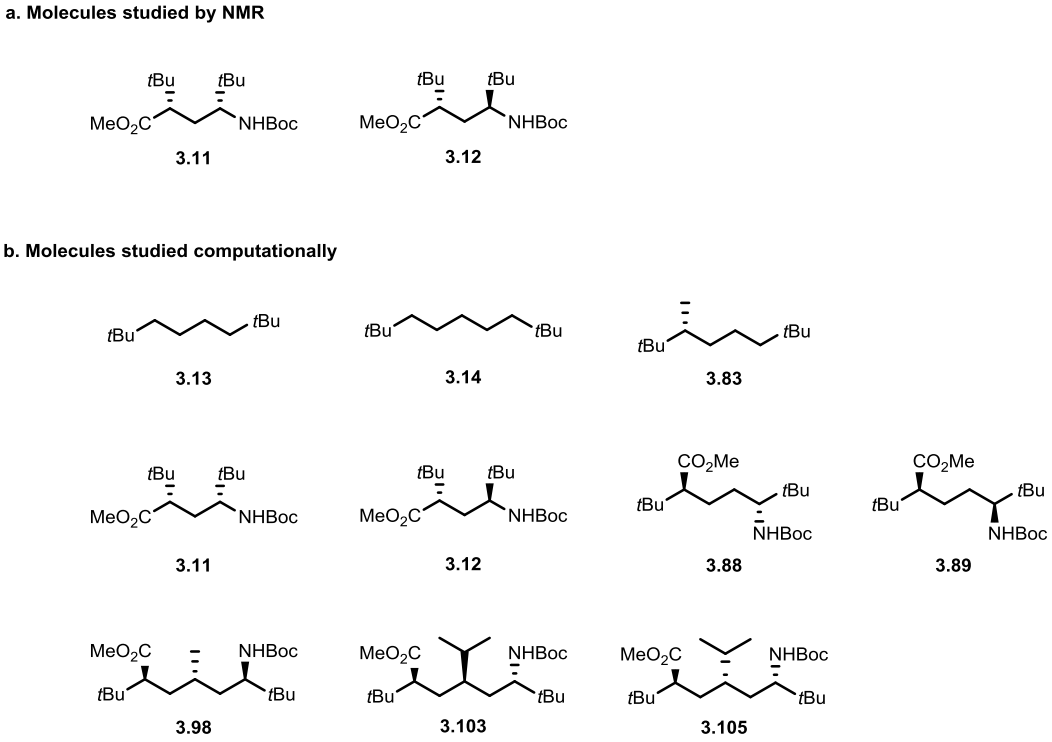

Figure 6.26: Compounds studied by NMR and computational modelling.

A Monte Carlo multiple minimum (MCMM)[63] conformational search was performed in implicit $CHCl_3$ using 500,000 iterations along with Merck Molecular Force Field (MMFFs)[61,170]. Structures were minimised using the truncated Newton Conjugate Gradients (TNCG) method with 500 iterations with a gradient convergence criteria of 0.05. Conformers within 21.0 kJ mol^{-1} of the lowest energy conformer found were stored.

All conformers found were subjected to DFT geometry optimisation and frequency calculations with the mPW1PW91 functional using the 6-311 G (d,p) basis set in implicit chloroform (IEFPCM, ε=4.71). The Boltzmann averaged chemical shifts, total spin-spin coupling constants and interproton distances were computed using the same DFT method using GIAO method. A keyword 'mixed' was also used to incorporate explicit mixing of core orbitals in the calculation of the fermi contact term.[160]

Conformer population and Boltzmann averaged NMR parameters were calculated using equations discussed previously (Equation 6.2 – 6.6).

Calculated data of 3.85

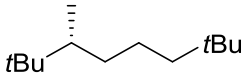

3.85

Table 6.59: DFT calculated energies (in kJ mol^{-1}) of **3.85** conformers.

Conformer	ΔG (kJ mol^{-1})	Population (298 K, %)
3.85-1	0.00	78.93%
3.85-2	3.96	15.97%
3.85-3	9.82	1.50%
3.85-4	10.11	1.33%
3.85-5	10.92	0.96%
3.85-6	12.02	0.61%
3.85-7	12.67	0.47%
3.85-8	14.48	0.23%

Calculated data of 3.88

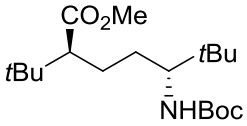

3.88

Table 6.60: DFT calculated energies (in kJ mol^{-1}) of **3.88** conformers.

Conformer	ΔG (kJ mol^{-1})	Population (298 K, %)
3.88-1	0.00	55.42%
3.88-2	2.51	20.09%
3.88-3	3.67	12.61%
3.88-4	5.55	5.90%
3.88-5	8.36	1.90%
3.88-6	10.01	0.97%
3.88-7	10.40	0.83%
3.88-8	11.00	0.65%
3.88-9	12.27	0.39%
3.88-10	13.53	0.23%
3.88-11	14.48	0.16%
3.88-12	14.72	0.15%
3.88-13	14.78	0.14%
3.88-14	15.24	0.12%
3.88-15	15.33	0.11%
3.88-16	15.45	0.11%

Calculated data of 3.89

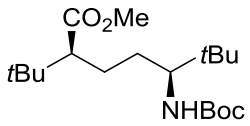

3.89

Table 6.61: DFT calculated energies (in kJ mol^{-1}) of **3.89** conformers.

Conformer	ΔG (kJ mol^{-1})	Population (298 K, %)
3.89-1	0.00	61.46%
3.89-2	2.13	26.04%
3.89-3	5.99	5.48%
3.89-4	7.58	2.88%
3.89-5	8.38	2.08%
3.89-6	11.33	0.63%
3.89-7	11.50	0.59%
3.89-8	12.60	0.38%
3.89-9	14.63	0.17%
3.89-10	16.62	0.07%
3.89-11	16.87	0.07%
3.89-12	17.34	0.06%
3.89-13	18.08	0.04%
3.89-14	18.64	0.03%
3.89-15	21.10	0.01%
3.89-16	23.24	0.01%

Calculated data of 3.98

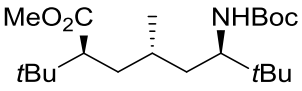

3.98

Table 6.62: DFT calculated energies (in kJ mol^{-1}) of **3.98** conformers.

Conformer	ΔG (kJ mol^{-1})	Population (298 K, %)
3.98-1	0.00	91.64%
3.98-2	7.19	5.03%
3.98-3	9.61	1.89%
3.98-4	14.32	0.28%
3.98-5	14.52	0.26%
3.98-6	15.05	0.21%
3.98-7	15.22	0.20%
3.98-8	16.90	0.10%
3.98-9	17.69	0.07%
3.98-10	17.75	0.07%

3.98-11	17.80	0.07%
3.98-12	18.07	0.06%

Calculated data of 3.103

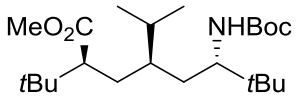

3.103

Table 6.63: DFT calculated energies (in kJ mol^{-1}) of **3.103** conformers.

Conformer	ΔG (kJ mol^{-1})	Population (298 K, %)
3.103-1	0.00	54.77%
3.103-2	2.06	23.88%
3.103-3	3.14	15.43%
3.103-4	8.27	1.94%
3.103-5	10.48	0.80%
3.103-6	10.70	0.73%
3.103-7	11.61	0.50%
3.103-8	11.68	0.49%
3.103-9	11.70	0.49%
3.103-10	12.15	0.41%
3.103-11	12.94	0.29%
3.103-12	13.16	0.27%

Calculated data of 3.105

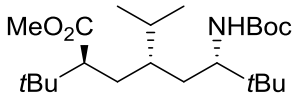

3.105

Table 6.64: DFT calculated energies (in kJ mol^{-1}) of **3.105** conformers.

Conformer	ΔG (kJ mol^{-1})	Population (298 K, %)
3.105-1	0.00	30.34%
3.105-2	0.78	22.17%
3.105-3	1.93	13.93%
3.105-4	1.93	13.92%
3.105-5	4.36	5.22%
3.105-6	6.62	2.10%
3.105-7	7.25	1.62%
3.105-8	7.27	1.61%
3.105-9	7.43	1.51%
3.105-10	7.57	1.43%
3.105-11	8.18	1.12%

3.105-12	8.63	0.93%
3.105-13	8.63	0.93%
3.105-14	9.60	0.63%
3.105-15	10.11	0.51%
3.105-16	11.10	0.34%
3.105-17	11.11	0.34%
3.105-18	11.49	0.29%
3.105-19	12.38	0.20%
3.105-20	13.49	0.13%
3.105-21	13.68	0.12%
3.105-22	14.66	0.08%

General NMR procedures

All NMR spectra were recorded in $CDCl_3$. ^1H-^1H scalar coupling constants were measured manually from multiplets in ^1H spectra. ^1H-^{13}C scalar coupling constants of both U-shaped and L-shaped molecules (**3.11** and **3.12**, respectively) were measured from the Accordion In-Phase and Anti Phase (IPAP) HSQMBC NMR spectra (12 scans, 1600 f1 increments and 8192 t2 data points, f1 spectra width 190.2 ppm (23923Hz), f2 spectra width 10 ppm (5005Hz), matching J_{LR} from 3Hz to 8 Hz.)[174] The spectra were processed using methods as discussed in the experimental section of Chapter 2.

NMR data of U-shaped molecule (3.11)

Table 6.65: Experimental $^nJ_{HH}$ values (in Hz) and Boltzmann averaged calculated $^nJ_{HH}$ (in Hz) before for **3.11** with Deviations (Dev, in Hz), Mean Absolute Deviations (MAD, in Hz), Standard Deviations (StDev, in Hz) and χ^2 (reduced) values (χ^2 (red.)).

H_A	H_B	Exp. $^nJ_{HH}$/ Hz	Calc. $^nJ_{HH}$/Hz	Deviation/Hz
NH	H_4	10.80	11.86	1.06
H_4	H_{7a}	3.30	4.00	0.70
H_4	H_{7b}	11.40	13.10	1.70
H_8	H_{7a}	1.54	0.99	−0.55
H_8	H_{7b}	10.47	11.14	0.67
			MAD	0.94
			StDev	0.82
			χ^2 (red.)	1.31

Table 6.66: Experimental $^nJ_{CH}$ values (in Hz) and Boltzmann averaged calculated $^nJ_{CH}$ (in Hz) before for **3.11** with Deviations (Dev, in Hz), Mean Absolute Deviations (MAD, in Hz), Standard Deviations (StDev, in Hz) and χ^2 (reduced) values (χ^2 (red.)).

H	C	Exp. $^nJ_{HH}$/ Hz	Calc. $^nJ_{HH}$/Hz	Deviation/Hz
H_{12}	C_{11}	3.83	4.10	0.27
H_8	C_{11}	7.48	8.02	0.54
H_{7a}	C_{11}	8.97	9.38	0.40
H_{7b}	C_{11}	4.66	5.19	0.52
H_4	C_3	3.39	3.89	0.50
H_{7a}	C3	1.59	1.09	−0.50
NH	C_4	2.95	2.97	0.02
H_8	C_4	4.38	4.58	0.20
H_{7b}	C_4	5.54	5.77	0.23
H_{12}	C_8	1.61	0.39	−1.22
H_4	C_8	2.90	2.58	−0.31
H_{7a}	C_8	4.19	4.20	0.01
H_{7b}	C_8	4.63	4.87	0.24

H_{10}	C_8	3.94	3.96	0.02
H_4	C_5	3.62	3.85	0.23
H_6	C_5	3.96	3.60	−0.36
H_8	C_9	4.93	5.06	0.13
H_{7a}	C_9	3.66	4.24	0.58
H_{10}	C_9	3.92	3.66	−0.26
H_4	C_7	4.43	4.95	0.52
H_8	C_7	3.82	3.82	0.00
H_8	C_{10}	3.35	3.45	0.10
H_4	C_6	2.98	3.10	0.12
			MAD	0.32
			StDev	0.41
			χ^2 (red.)	0.18

NMR data of L-shaped molecule (3.12)

Table 6.67: Experimental $^nJ_{HH}$ values (in Hz) and Boltzmann averaged calculated $^nJ_{HH}$ (in Hz) before for **3.12** with Deviations (Dev, in Hz), Mean Absolute Deviations (MAD, in Hz), Standard Deviations (StDev, in Hz) and χ^2 (reduced) values (χ^2 (red.)).

H_A	**H_B**	**Exp. $^nJ_{HH}$/ Hz**	**Calc. $^nJ_{HH}$/Hz**	**Deviation/Hz**
NH	H_4	10.64	11.69	1.05
H_4	H_{7a}	11.56	13.03	1.47
H_4	H_{7b}	2.40	3.03	0.63
H_8	H_{7a}	2.55	2.31	−0.24
H_8	H_{7b}	12.10	12.82	0.72
			MAD	0.82
			StDev	0.63
			χ^2 (red.)	1.06

Table 6.68: Experimental $^nJ_{CH}$ values (in Hz) and Boltzmann averaged calculated $^nJ_{CH}$ (in Hz) before for **3.12** with Deviations (Dev, in Hz), Mean Absolute Deviations (MAD, in Hz), Standard Deviations (StDev, in Hz) and χ^2 (reduced) values (χ^2 (red.)).

H	**C**	**Exp. $^nJ_{HH}$/ Hz**	**Calc. $^nJ_{HH}$/Hz**	**Deviation/Hz**
H_{12}	C_{11}	3.81	4.12	0.31
H_8	C_{11}	7.33	7.92	0.59
H_{7b}	C_{11}	3.14	3.48	0.34
H_{7a}	C_{11}	9.88	10.63	0.75
H_4	C_3	3.49	3.99	0.50
H_{7b}	C_3	1.44	1.21	−0.22
NH	C_4	2.78	2.96	0.18
H_8	C_4	2.94	2.91	−0.02
H_{7b}	C_4	1.81	1.74	−0.07
H_{7a}	C_4	6.05	5.89	−0.16

H_{12}	C_8	1.29	0.39	−0.90
H_4	C_8	3.08	2.73	−0.35
H_{7b}	C_8	5.18	5.61	0.44
H_{7a}	C_8	3.39	3.19	−0.21
H_{10}	C_8	3.70	4.00	0.30
H_4	C_5	3.98	4.11	0.13
H_{7b}	C_5	1.42	1.02	-0.40
H_{7a}	C_5	1.60	1.61	0.01
H_6	C_5	3.78	3.60	−0.18
H_8	C_9	4.90	4.87	−0.03
H_{7b}	C_9	1.69	1.17	−0.52
H_{7b}	C_9	2.33	1.17	−1.16
H_{10}	C_9	3.91	3.67	−0.24
H_4	C_7	4.28	4.47	0.19
H_8	C_7	3.78	4.17	0.39
H_8	C_{10}	3.48	3.35	−0.13
H_4	C_6	3.22	3.15	−0.07
			MAD	0.33
			StDev	0.43
			χ^2 (red.)	0.19

X-ray structure of U-shaped molecule 3.11

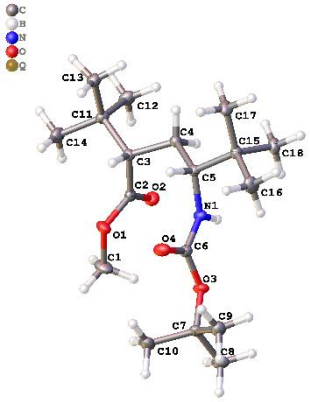

Table 6.69: Crystal data and structure refinement for 3.11

Identification code	**3.11**
Empirical formula	$C_{18}H_{35}NO_4$
Formula weight	329.47
Temperature/K	100(2)
Crystal system	orthorhombic
Space group	$C222_1$
a/Å	10.6107(2)
b/Å	19.1802(4)
c/Å	19.7887(4)
α/°	90
β/°	90
γ/°	90
Volume/Å^3	4027.30(14)
Z	8
ρ_{calc}g/cm^3	1.087
μ/mm^{-1}	0.075
F(000)	1456.0
Crystal size/mm^3	0.435 × 0.378 × 0.282
Radiation	MoKα (λ = 0.71073)
2Θ range for data collection/°	4.116 to 55.776
Index ranges	$-13 \leq h \leq 13$, $-25 \leq k \leq 22$, $-26 \leq l \leq 26$
Reflections collected	18725
Independent reflections	4819 [R_{int} = 0.0437, R_{sigma} = 0.0394]
Data/restraints/parameters	4819/0/222
Goodness-of-fit on F^2	1.025

Final R indexes [I>=2σ (I)]	R_1 = 0.0363, wR_2 = 0.0801
Final R indexes [all data]	R_1 = 0.0454, wR_2 = 0.0844
Largest diff. peak/hole / e Å^{-3}	0.24/-0.20

Table 6.70: Fractional Atomic Coordinates (×10^4) and Equivalent Isotropic Displacement Parameters (Å^2×10^3) for **3.11**. U_{eq} is defined as 1/3 of of the trace of the orthogonalised U_{IJ} tensor.

Atom	***x***	***y***	***z***	**U(eq)**
O1	4266.5(12)	5679.0(7)	6395.2(6)	19.9(3)
O2	5539.7(12)	5647.1(7)	5487.2(6)	19.8(3)
O3	2729.0(11)	4017.6(7)	5717.1(6)	17.9(3)
O4	3341.4(12)	3888.5(8)	6817.3(6)	22.1(3)
N1	4765.4(14)	4040.7(8)	5967.7(8)	15.1(3)
C1	3315(2)	5977.9(12)	5961.3(10)	28.5(5)
C2	5359.2(17)	5525.9(9)	6080.1(9)	15.5(4)
C3	6316.8(16)	5215.5(9)	6559.4(8)	13.6(3)
C4	6818.1(17)	4522.7(9)	6274.9(9)	15.6(4)
C5	5892.5(16)	3919.1(9)	6378.9(9)	14.3(4)
C6	3590.8(16)	3972.4(9)	6222.7(8)	15.6(4)
C7	1404.0(17)	3834.6(10)	5855.2(9)	17.5(4)
C8	800.9(18)	3890.2(11)	5160.2(10)	23.8(4)
C9	1318.4(19)	3088.6(10)	6114.0(10)	23.1(4)
C10	816.9(18)	4353.5(11)	6339.0(10)	24.5(4)
C11	7366.2(17)	5763.7(10)	6724.6(9)	16.7(4)
C12	8215.5(19)	5909.4(11)	6116.4(9)	23.3(4)
C13	8164.7(19)	5485.4(10)	7309.2(9)	21.4(4)
C14	6744(2)	6445.2(10)	6957.5(10)	24.9(4)
C15	6460.1(17)	3182.2(9)	6255.7(9)	16.2(4)
C16	5429(2)	2631.0(10)	6363.0(11)	25.5(4)
C17	7516.6(19)	3045.1(10)	6769.7(10)	22.4(4)
C18	6987(2)	3109.0(10)	5537.9(9)	22.4(4)

Table 6.71: Anisotropic Displacement Parameters ($Å^2×10^3$) for **3.11**. The Anisotropic displacement factor exponent takes the form: $-2\pi^2[h^2a^{*2}U_{11}+2hka^*b^*U_{12}+\ldots]$.

Atom	U_{11}	U_{22}	U_{33}	U_{23}	U_{13}	U_{12}
O1	16.9(6)	24.7(7)	18.1(7)	1.3(6)	0.2(5)	7.8(6)
O2	21.3(7)	23.4(7)	14.6(6)	2.7(5)	-1.5(5)	0.5(6)
O3	10.3(6)	26.4(7)	17.0(6)	3.4(5)	0.1(5)	-2.4(5)
O4	16.3(6)	33.6(8)	16.5(6)	3.3(6)	0.9(5)	-1.2(6)
N1	13.8(7)	20.7(8)	10.8(7)	2.9(6)	-0.5(6)	-0.9(6)
C1	21.4(10)	38.0(13)	26.1(10)	6.5(9)	-3.2(8)	12.8(9)
C2	17.0(9)	11.8(8)	17.5(8)	-1.2(7)	-0.3(7)	-0.6(7)
C3	13.7(8)	14.7(9)	12.5(8)	1.7(7)	0.7(7)	0.6(7)
C4	14.6(9)	14.7(9)	17.6(9)	0.3(7)	0.9(7)	0.9(7)
C5	13.5(8)	15.9(9)	13.5(8)	1.1(7)	0.7(6)	0.5(7)
C6	15.4(9)	15.5(9)	15.9(9)	1.7(7)	-0.4(7)	-1.0(7)
C7	10.4(8)	21.3(10)	20.8(9)	-0.1(7)	3.0(7)	-1.4(7)
C8	15.9(9)	31.2(11)	24.2(10)	1.2(9)	-2.9(8)	-2.9(8)
C9	21.9(10)	20.7(10)	26.6(10)	-0.9(8)	1.6(9)	-2.7(8)
C10	15.8(9)	25.6(11)	32.1(11)	-6.5(9)	2.4(8)	-1.1(8)
C11	17.5(9)	15.1(9)	17.5(9)	1.5(7)	-1.6(7)	-2.8(7)
C12	23.1(10)	24.7(10)	22.1(9)	3.4(8)	-0.8(8)	-7.3(8)
C13	21.6(10)	22.6(10)	20.0(9)	-0.6(8)	-3.6(8)	-1.3(8)
C14	29.0(11)	15.7(10)	30.0(11)	-2.9(8)	-5.5(9)	-1.4(8)
C15	18.7(9)	14.9(9)	15.1(8)	0.1(7)	0.3(7)	-0.1(7)
C16	27.6(11)	15.6(10)	33.1(11)	1.3(8)	5.2(9)	-3.2(8)
C17	26.8(10)	18.5(10)	21.7(9)	0.6(8)	-4.5(9)	6.9(8)
C18	29.8(11)	18.8(10)	18.5(9)	-2.3(8)	2.1(8)	4.2(8)

Table 6.72: Bond Lengths for **3.11**.

Atom	Atom	Length/Å	Atom	Atom	Length/Å
O1	C1	1.444(2)	C4	C5	1.532(3)
O1	C2	1.349(2)	C5	C15	1.556(2)
O2	C2	1.211(2)	C7	C8	1.521(3)
O3	C6	1.358(2)	C7	C9	1.522(3)
O3	C7	1.475(2)	C7	C10	1.515(3)

O4	C6	1.217(2)	C11	C12	1.529(3)
N1	C5	1.465(2)	C11	C13	1.530(3)
N1	C6	1.351(2)	C11	C14	1.535(3)
C2	C3	1.512(2)	C15	C16	1.536(3)
C3	C4	1.538(2)	C15	C17	1.536(3)
C3	C11	1.566(2)	C15	C18	1.533(2)

Table 6.73: Bond Angles for **3.11**.

Atom	Atom	Atom	Angle/°	Atom	Atom	Atom	Angle/°
C2	O1	C1	114.37(14)	O3	C7	C9	110.06(15)
C6	O3	C7	119.35(13)	O3	C7	C10	110.66(15)
C6	N1	C5	122.02(14)	C8	C7	C9	110.19(16)
O1	C2	C3	111.92(14)	C10	C7	C8	110.63(16)
O2	C2	O1	122.81(16)	C10	C7	C9	112.35(16)
O2	C2	C3	125.23(17)	C12	C11	C3	112.18(15)
C2	C3	C4	110.05(14)	C12	C11	C13	109.42(15)
C2	C3	C11	110.14(14)	C12	C11	C14	109.53(16)
C4	C3	C11	114.24(14)	C13	C11	C3	108.50(15)
C5	C4	C3	112.45(14)	C13	C11	C14	107.95(15)
N1	C5	C4	109.17(14)	C14	C11	C3	109.18(15)
N1	C5	C15	111.94(14)	C16	C15	C5	109.15(15)
C4	C5	C15	114.66(14)	C16	C15	C17	108.06(15)
O4	C6	O3	125.06(16)	C17	C15	C5	109.53(14)
O4	C6	N1	125.08(16)	C18	C15	C5	111.70(14)
N1	C6	O3	109.86(14)	C18	C15	C16	108.96(16)
O3	C7	C8	102.53(14)	C18	C15	C17	109.37(16)

Table 6.74: Hydrogen Atom Coordinates (Å×10^4) and Isotropic Displacement Parameters (Å^2×10^3) for **3.11**.

Atom	*x*	*y*	*z*	U(eq)
H1A	3131.15	5654.85	5590.5	43
H1B	3622.21	6420.16	5776.09	43
H1C	2545.41	6061.42	6223.01	43
H3	5868.87	5107.54	6991.57	16

H4A	6985.51	4578.07	5785.69	19
H4B	7626.22	4408.14	6499.02	19
H5	5619.97	3935.39	6862.37	17
H8A	911.45	4364.5	4985.73	36
H8B	-100.43	3784.51	5194.57	36
H8C	1203	3557.53	4852.29	36
H9A	1793.38	2779.49	5812.98	35
H9B	433.6	2942.54	6125.13	35
H9C	1673.18	3063.55	6570.65	35
H10A	1184.78	4293.09	6789.43	37
H10B	-94.66	4274.6	6361.59	37
H10C	980.73	4828.39	6178.82	37
H12A	8601.35	5472.84	5963.34	35
H12B	8877.61	6239.23	6246.7	35
H12C	7711.69	6109.39	5749.36	35
H13A	7610.7	5333	7676.93	32
H13B	8724.12	5855.1	7473.19	32
H13C	8670.62	5089.92	7152.04	32
H14A	6246.87	6641.61	6585.98	37
H14B	7396.78	6778.83	7092.09	37
H14C	6190.39	6350.3	7343.19	37
H16A	5053.01	2691.99	6811.39	38
H16B	5800.57	2164.38	6329.91	38
H16C	4777.21	2684.96	6016.35	38
H17A	8215.33	3368.19	6687.1	34
H17B	7816.14	2564.37	6721.55	34
H17C	7192.13	3115.36	7228.35	34
H18A	6315.13	3198.39	5209.37	34
H18B	7313.18	2635.55	5473.97	34
H18C	7669.73	3446.27	5471.53	34
H1	4840(20)	4087(11)	5548(11)	21(6)

Chapter 4

General computational procedures

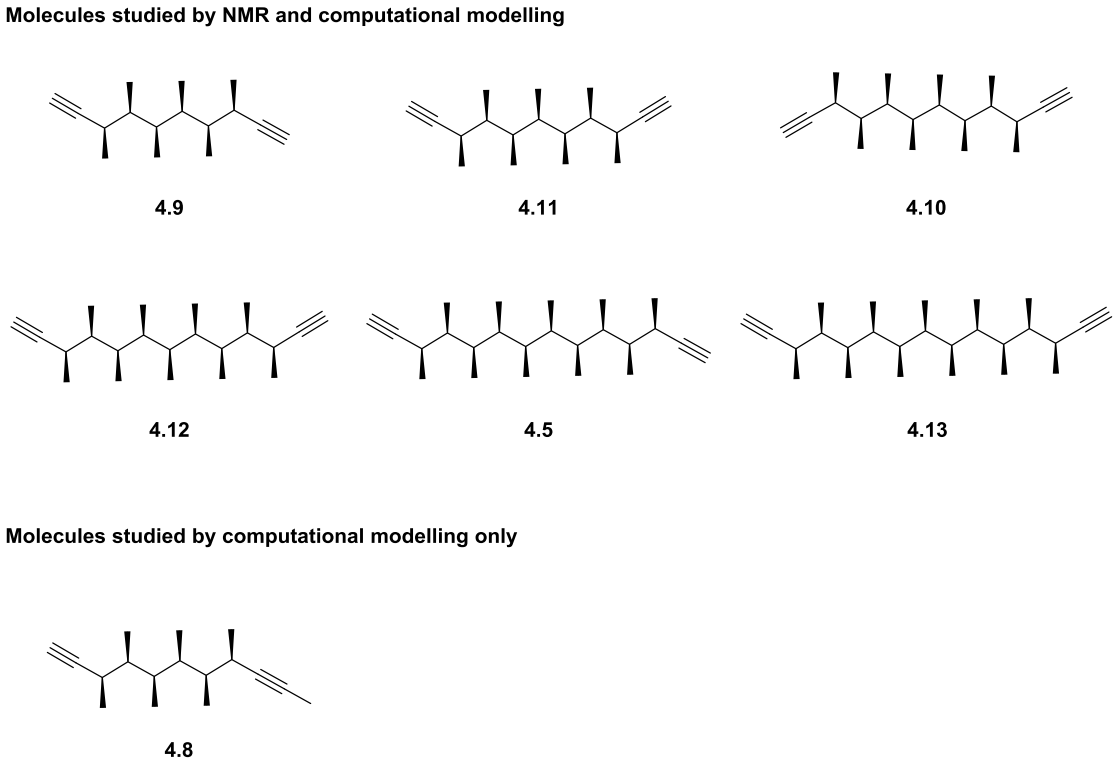

Figure 6.27: Compounds studied by computational modelling and NMR spectroscopy.

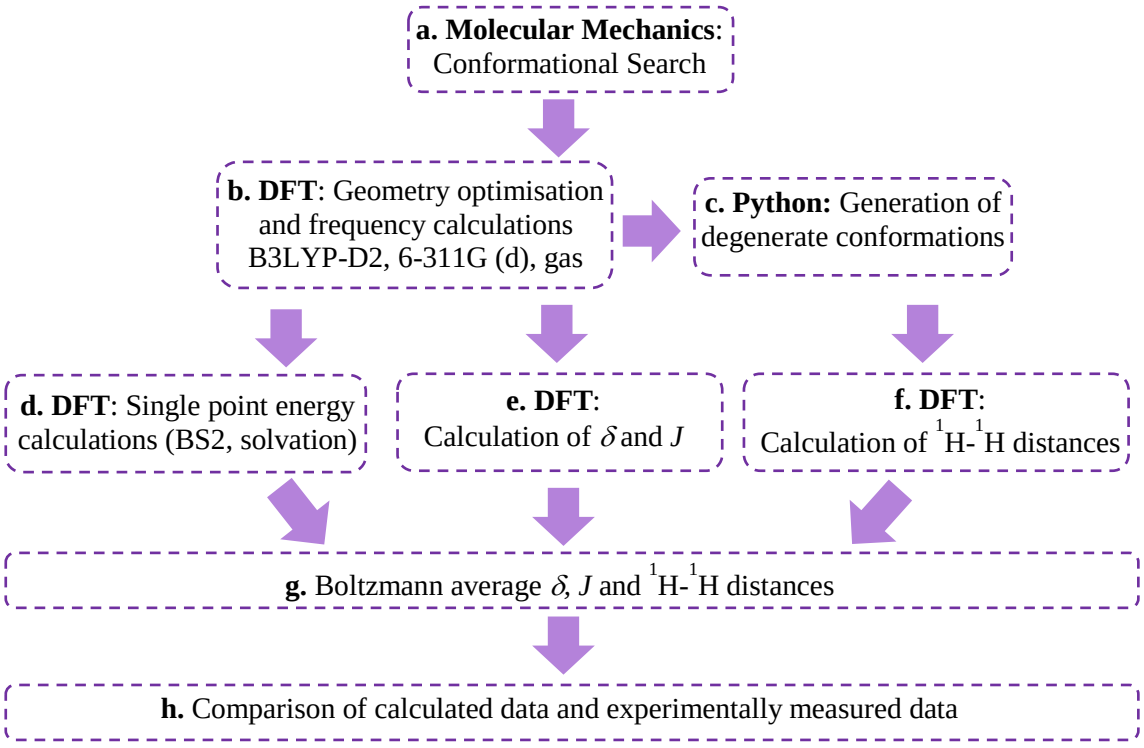

Figure 6.28: Computational workflow used in chapter 4.

Here is a description of the computational procedures for each stage (**a** to **f**, Figure 6.28) of the workflow.

Stage a, Molecular mechanics (MM) conformational search.

A Monte Carlo multiple minimum (MCMM)[63] conformational search was performed in implicit $CHCl_3$ using 500,000 iterations along with Merck Molecular Force Field (MMFFs)[61,170]. Structures were minimised using the truncated Newton Conjugate Gradients (TNCG) method with 500 iterations with a gradient convergence criteria of 0.05. Conformers within 21.0 kJ mol^{-1} of the lowest energy conformer found were stored.

Stage b, Density Functional Theory (DFT) geometry optimisation and frequency calculations.

All conformers found were subjected to DFT geometry optimisation and frequency calculations using the B3LYP-D2 functional and the 6-311 G (d) basis set (Basis set 1, BS1) in gas phase unless stated otherwise.

Stage c, Generation of degenerate conformations (for *C2* symmetric molecules only)

Degenerate conformations were generated using a python script which swap the xyz coordinates of equivalent nuclei.

```
# Atom_swapper.sh
# Will Gerrard  (wg12385@bristol.ac.uk)
#
# Script for swapping atom coordinates in gaussian .com files
# Usage: python atom_swapper.py File1 File2
# Where File1 is a list of atom numbers to be swapped in two column, comma
separated format
# And File2 is a gaussian .com file
#
#

from __future__ import print_function
import sys
import numpy as np

def isnum(s):
    try:
        float(s)
    except:
        return(False)
    else:
        return(True)


try:
    swapfile = sys.argv[1]
except:
    print("Usage: python atom_swapper.py < file1: list of atoms to swap >
< file2: gaussian .com file >")

try:
```

```
    comfile = sys.argv[2]
except:
    print("Usage: python atom_swapper.py < file1: list of atoms to swap >
< file2: gaussian .com file >")

swap_pairs = []

pairs = 0

with open(swapfile, "r") as f:
  for line in f:
    items = line.split(",")
    if len(items) >= 2:
        if isnum(items[0]) and isnum(items[1]):
            swap_pairs.append(line)
            pairs += 1

swap_array = np.zeros((pairs, 2), dtype=np.int64)


for k in range(0, pairs):
    pair = swap_pairs[k].split(',')
    a = pair[0]
    b = pair[1].split("\\")
    b = b[0]

    swap_array[k][0] = int(a)-1
    swap_array[k][1] = int(b)-1

ln = 0

com_lines = []
atoms = 0


with open(comfile, "r") as f:
    for line in f:
        com_lines.append(line)
        ln += 1
        items = line.split()
        if len(items) > 2:
            if not isnum(items[0]) and ( isnum(items[1]) and
isnum(items[2]) and isnum(items[3])):
                if atoms == 0:
                    start_line = ln - 1
                else:
                    end_line = ln - 1
                atoms += 1

swap_array = swap_array + start_line

line_order = np.zeros((ln), dtype=np.int64)

for i in range(0, ln):
    line_order[i] = i

for p in range(pairs):
    line_order[swap_array[p][0]] = swap_array[p][1]
    line_order[swap_array[p][1]] = swap_array[p][0]

outfile = "swapped_" + comfile

with open(outfile, "w") as f:
    for i in range(0, ln):
        print(com_lines[line_order[i]], end='', file=f)

print("Done")
```

Stage d, DFT single point energy calculations.

In order to obtain a more accurate description of conformer energies, additional single point calculations were performed using the BS1 optimised geometries. The effect of a larger basis set on conformer energy was evaluated by performing single point calculations using B3LYP-D2 functional and 6-311G (d,p) basis set (BS2) in gas phase. Solvation effects were also evaluated by performing single point calculations using B3LYP-D2 with the Integral Equation Formalism Polarizable Continuum Model (IEF-PCM) continuum dielectric solvation model using toluene as solvent (ε = 2.3741).

Stage e and f, Calculation of NMR properties (δ, J and interproton NOE-distances)

The magnetic shielding tensor and total nuclear spin-spin coupling constants of low energy conformers with a combined population of greater than 90%, based on their free energies (see below), were computed with GIAO (gauge-independent atomic orbitals) with mPW1PW91 functional using the 6-311G (d, p) basis set[173] with toluene as solvent (IEF-PCM). In order to maximise the accuracy of scalar coupling constant prediction, in particular for ^{1}H-^{13}C couplings, the Gaussian keyword "mixed" was used to incorporate more explicit mixing of core orbitals as described by Bally T. and Rablen P[160]. Interproton distances were extracted from the BS1 optimised geometries for all conformers (100% population) to obtain the Boltzmann averaged ^{1}H-^{1}H distances. Cartesian coordinates for all conformers subjected to NMR calculations can be found at the CD attached to this thesis

Calculation of estimated Gibbs free energies ($\Delta G_{est}^{\mathbf{BS2,toluene}}$) and Boltzmann population

The nature of the stationary point and the Gibbs free energy of each conformer were calculated using a lower basis set (BS1) and the effect of a higher basis set (BS2) and solvation (toluene) on energies were incorporated by single point calculations. Gibbs free energies (in kJ mol^{-1}) of each conformer ($G_{est}^{\mathrm{BS2,toluene}}$, in kJ mol^{-1}) were estimated according to

$$G_i^{\mathrm{BS2,toluene}} = E_i^{\mathrm{BS2,gas}} + (G_i^{\mathrm{BS1,gas}} - E_i^{\mathrm{BS1,gas}}) + (E_i^{\mathrm{BS1,toluene}} - E_i^{\mathrm{BS1,gas}}) \qquad \textbf{Equation 6.10}$$

where $G_i^{\mathrm{BS1,gas}}$ is the Gibbs free energy of conformer *i* with basis set 1 in gas phase, $E_i^{\mathrm{BS1,gas}}$ is the potential energy of conformer *i* with basis set 1 in gas phase, $E_i^{\mathrm{BS2,gas}}$ is single point energy of conformer *i* with basis set 2 in gas phase, $E_i^{\mathrm{BS1,toluene}}$ is the single point energy of conformer *i* with basis set 1 in toluene. This approximation of Gibbs free energies is based on

the assumption that the change in basis set and solvation has minimal impact on the change in both zero point energy correction and entropy ($G_i^{\mathrm{BS1,gas}} - E_i^{\mathrm{BS1,gas}}$, **Equation 6.10**).

The estimated Gibbs free energies ($G^{\mathrm{BS2,toluene}}$) of each conformer were then used in the Boltzmann analysis of population according to

$$p_i = \frac{g e^{-\frac{\Delta G_i^{\mathrm{BS2,toluene}}}{RT}}}{\sum_{i=1}^{n} g e^{-\frac{\Delta G_i^{\mathrm{BS2,toluene}}}{RT}}} \qquad \textbf{Equation 6.11}$$

where $\Delta G_i^{\mathrm{BS2,toluene}}$ is the estimated Gibbs free energy (relative to the global minimum, in kJ mol^{-1}) of conformer i, *R* is the Boltzmann constant (8.314 × 10^{-3} kJ mol^{-1}), *T* is temperature of the system (298K) and *g* is the degeneracy of conformer i. *g* equals to 2 for all *C2* symmetric compounds (**4.9**, **4.10** and **4.5**) and equals to 1 for all *meso* compounds (**4.11**, **4.12** and **4.13**).

χ^2 Analysis

Table 6.75: A summary of estimated standard deviations for comparison between computed and experimental chemical shifts, scalar coupling constants and ^{1}H-^{1}H distances

NMR properties	Typical standard deviations
δH	0.15 ppm[77,79]
δC	1.5 ppm[79]
$^nJ_{HX}$ (X=H or C)	1 Hz [44]
r_{noe}	3.5%[54]

Table 6.76: A summary of values of *n* and *m* used to calculate χ2(reduced) values.

Compounds	***n***			
	δ_H	δ_C	$^nJ_{HH}$	r_{eff}
4.9	7	8	5	6
4.11	9	10	7	22
4.10	9	10	7	21
4.12	-	-	-	19
4.5	11	12	9	28
4.13	-	-	-	12
m	1			

Calculation of Boltzmann averaged ^{1}H-^{1}H effective distances

Boltzmann averaged distances from one proton (H_A) to another proton (H_B) were calculated according to:

$$r_{eff(HA-H_B,calc)} = (\sum_i ((r_{H_{A,i}-H_{B,i}})^{-6} + (r_{H_{A,i}-H_{B\prime,i}})^{-6} + (r_{H_{A\prime,i}-H_{B,i}})^{-6} + (r_{H_{A\prime,i}-H_{B\prime,i}})^{-6}) \times p_i)^{-\frac{1}{6}}$$ **Equation 6.12**

where $r_{H_{A,i}-H_{B,i}}$, $r_{H_{A,i}-H_{B\prime,i}}$, $r_{H_{A\prime,i}-H_{B,i}}$ and $r_{H_{A\prime,i}-H_{B\prime,i}}$ are the computed ^{1}H-^{1}H distances (in Å) of equivalent pairs of protons in conformer *i*, and p_i is the Boltzmann population of conformer *i*.

To Boltzmann average the effective distances from a single proton (H_A) to a methyl group (H_C, CH_3), the following equation is used:

$$r_{eff(HA-H_B,calc)} = (\sum_i ((r_{H_{A,i}-H_{C1,i}})^{-6} + (r_{H_{A,i}-Hc_{2,i}})^{-6} + (r_{H_{A,i}-H_{C3,i}})^{-6} + (r_{H_{A,i}-H_{C1\prime,i}})^{-6} + (r_{H_{A,i}-H_{C2\prime,i}})^{-6} + (r_{H_{A,i}-H_{C3\prime,i}})^{-6} + (r_{H_{A\prime,i}-H_{C1,i}})^{-6} + (r_{H_{A\prime,i}-H_{C2,i}})^{-6} + (r_{H_{A\prime,i}-H_{C3,i}})^{-6} + (r_{H_{A\prime,i}-H_{C1-eq,i}})^{-6} + (r_{H_{A\prime,i}-H_{C2\prime,i}})^{-6} + (r_{H_{A\prime,i}-H_{C3\prime,i}})^{-6}) \times p_i)^{-\frac{1}{6}}$$ **Equation 6.13**

where $r_{HA,i-H_{C1},i}$ is the computed ^{1}H-^{1}H distances from proton H to one of the equivalent protons of the methyl group, $r_{HA,i-H_{C2},i}$ and $r_{HA,i-H_{C3},i}$is the computed ^{1}H-^{1}H distances from proton H the other two of the equivalent protons of the methyl group. The dash (eg. HA') represents the corresponding chemically equivalent protons of either the single proton, or the equivalent protons of the methyl group.

To Boltzmann average the effective distances from one methyl group (H_C, CH_3) to another methyl group (H_D, CH_3), the following equation is used:

$$r_{eff(H_B-H_c,calc)} = (\sum_i ((r_{H_{C1,i}-H_{D1,i}})^{-6} + (r_{H_{C1,i}-H_{D2,i}})^{-6} + (r_{H_{C1,i}-H_{D3,i}})^{-6} + (r_{H_{C2,i}-H_{D1,i}})^{-6} + (r_{H_{C2,i}-H_{D2,i}})^{-6} + (r_{H_{C2,i}-H_{D3,i}})^{-6} + (r_{H_{C3,i}-H_{D1,i}})^{-6} + (r_{H_{C3,i}-H_{D2,i}})^{-6} + (r_{H_{C3,i}-H_{D3,i}})^{-6} + (r_{H_{C1,i}-H_{D1\prime,i}})^{-6} + (r_{H_{C1,i}-H_{D2\prime,i}})^{-6} + (r_{H_{C1,i}-H_{D3\prime,i}})^{-6} + (r_{H_{C2,i}-H_{D1\prime,i}})^{-6} + (r_{H_{C2,i}-H_{D2\prime,i}})^{-6} + (r_{H_{C2,i}-H_{D3\prime,i}})^{-6} + (r_{H_{C3,i}-H_{D1\prime,i}})^{-6} + (r_{H_{C3,i}-H_{D2\prime,i}})^{-6} + (r_{H_{C3,i}-H_{D3\prime,i}})^{-6} + (r_{H_{C1\prime,i}-H_{D1,i}})^{-6} + (r_{H_{C1\prime,i}-H_{D2,i}})^{-6} + (r_{H_{C1\prime,i}-H_{D3,i}})^{-6} + (r_{H_{C2\prime,i}-H_{D1,i}})^{-6} + (r_{H_{C2\prime,i}-H_{D2,i}})^{-6} + (r_{H_{C2\prime,i}-H_{D3,i}})^{-6} + (r_{H_{C3\prime,i}-H_{D1,i}})^{-6} + (r_{H_{C3\prime,i}-H_{D2,i}})^{-6} + (r_{H_{C3\prime,i}-H_{D3,i}})^{-6} + ((r_{H_{C1\prime,i}-H_{D1\prime,i}})^{-6} + (r_{H_{C1\prime,i}-H_{D2\prime,i}})^{-6} + (r_{H_{C1\prime,i}-H_{D3\prime,i}})^{-6} + (r_{H_{C2\prime,i}-H_{D1\prime,i}})^{-6} +$$

$$(r_{H_{C2\prime,i}-H_{D2\prime,i}})^{-6} + (r_{H_{C2\prime,i}-H_{D3\prime,i}})^{-6} + (r_{H_{C3\prime,i}-H_{D1\prime,i}})^{-6} + (r_{H_{C3\prime,i}-H_{D2\prime,i}})^{-6} + (r_{H_{C3\prime,i}-H_{D3\prime,i}})^{-6}) \times p_i)^{-\frac{1}{6}}$$ **Equation 6.14**

where H_{C-1}, H_{C-2} and H_{C-3} represent the three equivalent protons of one methyl group, and H_{D-1}, H_{D-2} and H_{D-3} represent the three equivalent protons of the other methyl group. The dash (eg. C1') represents the corresponding chemically equivalent protons.

Calculated data for 4.9-4.13.

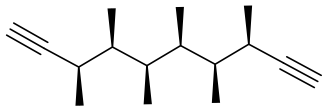

4.9

Table 6.77: Calculated energies (in kJ mol^{-1}) and DFT calculated population for all conformers of **4.9**.

Conformer	$\Delta E^{\text{MMFFs, gas}}$	$\Delta E^{\text{BS1, gas}}$	$\Delta G^{\text{BS1, gas}}$	$\Delta E^{\text{BS2, gas}}$	$\Delta E^{\text{BS1, toluene}}$	$\Delta G_{\text{est.}}^{\text{BS2,toluene}}$	Population (%)/$\Delta G_{\text{est.}}^{\text{BS2,MeOH}}$
4.9-1	0.00	0.94	5.04	0.82	0.35	4.33	5.49%
4.9-2	1.51	0.00	0.00	0.00	0.00	0.00	31.53%
4.9-3	5.85	4.90	3.55	5.57	4.79	4.12	5.98%
4.9-4	8.22	5.92	7.51	5.81	5.72	7.21	1.72%
4.9-5	10.88	12.31	14.54	12.29	11.78	13.99	0.11%
4.9-6	10.90	6.85	10.96	6.59	6.55	10.41	0.47%
4.9-7	11.86	8.49	7.58	9.10	8.32	8.03	1.23%
4.9-8	12.64	7.87	11.46	8.16	7.56	11.44	0.31%
4.9-9	13.27	10.90	15.02	10.72	10.06	14.01	0.11%
4.9-10	13.50	8.49	7.58	9.10	8.32	8.03	1.23%
4.9-11	14.19	10.12	10.62	10.45	9.96	10.78	0.41%
4.9-12	14.26	12.92	13.87	13.65	12.30	13.98	0.11%
4.9-13	14.71	10.76	14.61	10.72	10.54	14.34	0.10%
4.9-14	14.84	12.76	11.71	13.25	12.35	11.79	0.27%
4.9-15	15.27	7.44	14.66	7.47	7.30	14.56	0.09%
4.9-16	16.56	16.35	18.12	16.86	15.72	17.99	0.02%
4.9-17	16.63	14.93	18.09	15.30	14.70	18.22	0.02%
4.9-18	17.34	13.97	13.87	14.25	13.76	13.94	0.11%
4.9-19	17.43	17.76	21.97	17.73	17.10	21.29	0.01%
4.9-20	18.35	12.92	13.87	13.65	12.30	13.98	0.11%
4.9-21	18.88	13.12	10.83	13.50	12.83	10.92	0.38%

4.9-22	18.91	21.78	22.87	22.52	20.73	22.56	0.00%
4.9-23	19.75	14.26	16.15	14.35	14.17	16.15	0.05%
4.9-24	19.94	17.37	21.20	17.65	17.06	21.18	0.01%
4.9-25	20.32	19.78	22.17	20.33	19.14	22.07	0.00%
4.9-26	20.35	16.04	16.31	16.62	15.64	16.49	0.04%
4.9-27	20.37	15.15	14.49	15.71	15.00	14.90	0.08%
4.9-28	20.48	25.08	28.57	25.04	24.04	27.48	0.00%
4.9-29	20.72	17.71	23.13	17.89	16.71	22.32	0.00%

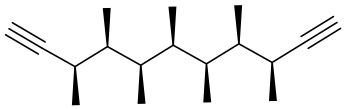

4.11

Table 6.78: Calculated energies (in kJ mol^{-1}), DFT calculated population and conformer population after NOE-refinement for all conformers of **4.11**.

Conformer	$\Delta E^{\text{MMFFs, gas}}$	$\Delta E^{\text{BS1, gas}}$	$\Delta G^{\text{BS1, gas}}$	$\Delta E^{\text{BS2, gas}}$	$\Delta E^{\text{BS1, toluene}}$	$\Delta G_{\text{est.}}^{\text{BS2,toluene}}$	Population (%) / $\Delta G_{\text{est.}}^{\text{BS2,MeOH}}$	Cluster	Population after refinement (%) $\Sigma(\Delta\Delta G)^2$ =100
4.11-1	0.00	0.00	0.00	0.00	0.00	0.00	31.47%	Cluster 1	22.31%
4.11-2	0.01	0.00	0.00	0.00	0.00	0.00	31.47%	Cluster 1	22.31%
4.11-3	7.11	5.86	8.74	5.91	5.79	8.73	0.93%	Cluster 2	0.14%
4.11-4	7.14	5.86	8.74	5.91	5.79	8.73	0.93%	Cluster 2	0.14%
4.11-5	10.00	12.84	17.20	12.93	12.35	16.79	0.04%	Cluster 12	0.03%
4.11-6	10.01	12.84	17.20	12.93	12.35	16.79	0.04%	Cluster 12	0.03%
4.11-7	11.25	6.74	5.58	6.64	7.02	5.76	3.08%	Cluster 3	1.22%
4.11-8	11.26	6.74	5.58	6.64	7.02	5.76	3.08%	Cluster 3	1.22%
4.11-9	12.02	10.22	3.40	10.32	10.12	3.38	8.03%	Cluster 2	1.20%
4.11-10	12.03	10.22	3.39	10.32	10.12	3.37	8.06%	Cluster 2	1.20%
4.11-11	12.81	10.33	10.22	10.48	10.13	10.17	0.52%	Cluster 8	0.49%
4.11-12	12.82	10.33	10.22	10.48	10.13	10.17	0.52%	Cluster 8	0.49%
4.11-13	13.21	10.33	10.68	10.33	10.12	10.48	0.46%	Cluster 9	0.34%
4.11-14	13.21	10.33	10.68	10.33	10.12	10.48	0.46%	Cluster 9	0.34%
4.11-15	13.53	8.19	6.93	8.53	8.57	7.65	1.43%	Cluster 4	12.43%
4.11-16	13.54	8.19	6.93	8.53	8.57	7.65	1.43%	Cluster 4	12.43%
4.11-17	13.66	11.75	8.47	12.47	11.56	8.99	0.83%	Cluster 7	9.25%

4.11-18	13.67	11.75	8.47	12.47	11.56	8.99	0.83%	Cluster 7	9.25%
4.11-19	13.83	12.63	13.21	12.96	12.16	13.07	0.16%	Cluster 15	0.31%
4.11-20	13.83	12.63	13.21	12.96	12.16	13.07	0.16%	Cluster 15	0.31%
4.11-21	14.02	13.94	14.24	14.21	13.44	14.01	0.11%	Cluster 12	0.09%
4.11-22	14.02	13.94	14.24	14.21	13.44	14.01	0.11%	Cluster 12	0.09%
4.11-23	14.03	13.94	14.24	14.21	13.44	14.01	0.11%	Cluster 12	0.09%
4.11-24	15.83	15.18	11.95	15.95	14.72	12.26	0.22%	Cluster 11	0.23%
4.11-25	15.84	15.18	11.95	15.95	14.72	12.26	0.22%	Cluster 11	0.23%
4.11-26	16.10	6.90	7.81	7.14	7.55	8.69	0.94%	Cluster 6	0.57%
4.11-27	16.11	6.90	7.81	7.14	7.55	8.69	0.94%	Cluster 6	0.57%
4.11-28	16.31	14.05	15.71	14.14	13.84	15.58	0.06%	Cluster 17	0.05%
4.11-29	16.32	14.05	15.71	14.14	13.84	15.58	0.06%	Cluster 17	0.05%
4.11-30	16.55	10.98	7.38	11.94	11.29	8.66	0.95%	Cluster 5	0.74%
4.11-31	16.56	10.98	7.38	11.94	11.29	8.66	0.95%	Cluster 5	0.74%
4.11-32	16.65	14.76	12.94	15.39	15.12	13.93	0.11%	Cluster 14	0.14%
4.11-33	16.66	14.76	12.94	15.39	15.12	13.93	0.11%	Cluster 14	0.14%
4.11-34	16.78	13.99	12.74	15.00	14.13	13.89	0.12%	Cluster 13	0.10%
4.11-35	16.79	13.99	12.74	15.00	14.13	13.89	0.12%	Cluster 13	0.10%
4.11-36	17.92	11.92	11.13	11.78	12.17	11.25	0.33%	Cluster 10	0.20%
4.11-37	17.93	11.92	11.13	11.78	12.17	11.25	0.33%	Cluster 10	0.20%
4.11-38	18.85	19.80	21.15	20.98	19.54	22.07	0.00%	Cluster 20	0.00%
4.11-39	18.85	19.80	21.15	20.98	19.54	22.07	0.00%	Cluster 20	0.00%
4.11-40	18.89	19.70	22.38	20.03	19.04	22.05	0.00%	Cluster 21	0.00%
4.11-41	18.89	19.70	22.38	20.03	19.04	22.05	0.00%	Cluster 21	0.00%
4.11-42	19.61	15.81	17.62	15.79	15.53	17.34	0.03%	Cluster 19	0.03%
4.11-43	19.61	15.81	17.62	15.79	15.53	17.34	0.03%	Cluster 19	0.03%
4.11-44	20.47	13.46	14.53	13.94	13.66	15.21	0.07%	Cluster 16	0.06%
4.11-45	20.48	13.46	14.53	13.94	13.66	15.21	0.07%	Cluster 16	0.06%
4.11-46	20.60	16.33	16.87	17.03	16.01	17.25	0.03%	Cluster 18	0.03%
4.11-47	20.60	16.33	16.87	17.03	16.01	17.25	0.03%	Cluster 18	0.03%

Conformer	Population after refinement (%) $\Sigma(\Delta\Delta G)^2$ =225	Population after refinement (%) $\Sigma(\Delta\Delta G)^2$ =625	Conformer	$\Sigma(\Delta\Delta G)^2$ =225	$\Sigma(\Delta\Delta G)^2$ =625
4.11-1	11.57%	9.06%	**4.11**-27	0.63%	0.55%
4.11-2	11.57%	9.06%	**4.11**-28	0.05%	0.04%
4.11-3	0.09%	0.05%	**4.11**-29	0.05%	0.04%
4.11-4	0.09%	0.05%	**4.11**-30	0.47%	0.92%
4.11-5	0.02%	0.01%	**4.11**-31	0.47%	0.92%
4.11-6	0.02%	0.01%	**4.11**-32	0.19%	14.40%
4.11-7	1.32%	1.06%	**4.11**-33	0.19%	14.40%
4.11-8	1.32%	1.06%	**4.11**-34	0.08%	0.07%
4.11-9	0.76%	0.42%	**4.11**-35	0.08%	0.07%
4.11-10	0.77%	0.42%	**4.11**-36	0.17%	0.10%
4.11-11	0.27%	0.26%	**4.11**-37	0.17%	0.10%
4.11-12	0.27%	0.26%	**4.11**-38	0.00%	0.00%
4.11-13	0.23%	0.11%	**4.11**-39	0.00%	0.00%
4.11-14	0.23%	0.11%	**4.11**-40	0.00%	0.00%
4.11-15	19.63%	7.38%	**4.11**-41	0.00%	0.00%
4.11-16	19.63%	7.38%	**4.11**-42	0.02%	0.02%
4.11-17	3.67%	5.35%	**4.11**-43	0.02%	0.02%
4.11-18	3.67%	5.35%	**4.11**-44	0.06%	0.04%
4.11-19	10.47%	9.99%	**4.11**-45	0.06%	0.04%
4.11-20	10.47%	9.99%	**4.11**-46	0.03%	0.02%
4.11-21	0.06%	0.04%	**4.11**-47	0.03%	0.02%
4.11-22	0.06%	0.04%			
4.11-23	0.06%	0.04%			
4.11-24	0.16%	0.09%			
4.11-25	0.16%	0.09%			
4.11-26	0.63%	0.55%			

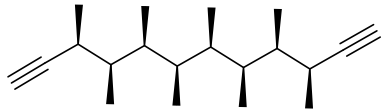

4.10

Table 6.79: Calculated energies (in kJ mol^{-1}) and DFT calculated population for all conformers of **4.10**.

Conformer	$\Delta E^{\text{MMFFs, gas}}$	$\Delta E^{\text{BS1, gas}}$	$\Delta G^{\text{BS1, gas}}$	$\Delta E^{\text{BS2, gas}}$	$\Delta E^{\text{BS1, toluene}}$	$\Delta G_{\text{est.}}^{\text{BS2,toluene}}$	Population (%)/$\Delta G_{\text{est.}}^{\text{BS2,MeOH}}$
4.10-1	0.00	2.10	5.63	2.10	1.49	5.02	4.13%
4.10-2	1.07	0.00	0.00	0.00	0.00	0.00	31.41%
4.10-3	8.24	5.38	8.49	5.40	5.32	8.43	1.04%
4.10-4	8.38	6.48	3.76	7.68	6.34	4.83	4.46%
4.10-5	10.54	6.55	11.99	6.42	6.30	11.62	0.29%
4.10-6	11.17	12.56	14.56	12.66	12.06	14.16	0.10%
4.10-7	12.36	10.89	13.26	10.84	10.12	12.44	0.21%
4.10-8	12.42	9.91	16.62	9.72	9.10	15.60	0.06%
4.10-9	12.51	10.06	9.69	10.21	9.88	9.67	0.63%
4.10-10	13.60	9.01	10.44	9.39	8.78	10.60	0.43%
4.10-11	13.72	10.50	8.72	10.63	10.31	8.66	0.95%
4.10-12	14.07	7.88	7.88	8.65	7.96	8.73	0.92%
4.10-13	14.38	10.67	7.67	11.68	10.43	8.44	1.04%
4.10-14	14.42	10.67	7.67	11.68	10.43	8.45	1.04%
4.10-15	14.59	12.26	13.67	12.53	11.81	13.49	0.14%
4.10-16	14.60	13.87	13.04	14.20	13.39	12.88	0.17%
4.10-17	15.37	13.68	20.08	14.05	13.54	20.32	0.01%
4.10-18	15.98	11.67	11.52	11.69	11.59	11.46	0.31%
4.10-19	16.06	10.91	7.40	11.32	10.71	7.61	1.45%
4.10-20	16.19	8.79	11.95	8.92	8.72	12.02	0.25%
4.10-21	16.75	13.81	11.72	14.92	13.41	12.43	0.21%
4.10-22	17.12	15.45	16.11	15.78	14.94	15.93	0.05%

4.10-23	17.22	14.44	13.30	14.48	14.24	13.13	0.16%
4.10-24	18.48	16.10	18.68	16.95	15.47	18.91	0.02%
4.10-25	18.77	14.98	13.75	15.10	14.78	13.66	0.13%
4.10-26	18.96	18.58	13.75	18.63	18.04	13.26	0.15%
4.10-27	19.55	22.01	23.57	22.60	21.02	23.16	0.00%
4.10-28	19.84	19.79	21.31	20.06	19.18	20.96	0.01%
4.10-29	20.01	15.55	17.22	15.69	15.27	17.07	0.03%
4.10-30	20.18	11.80	16.35	12.46	11.48	16.68	0.04%
4.10-31	20.59	14.69	12.56	15.36	14.47	13.01	0.16%

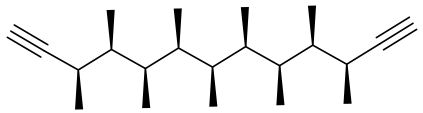

4.12

Table 6.80: Calculated energies (in kJ mol^{-1}), DFT calculated population and conformer population after NOE-refinement for all conformers of **4.12**.

Conformer	$\Delta E^{\text{MMFFs, gas}}$	$\Delta E^{\text{BS1, gas}}$	$\Delta G^{\text{BS1, gas}}$	$\Delta E^{\text{BS2, gas}}$	$\Delta E^{\text{BS1, toluene}}$	$\Delta G_{\text{est.}}^{\text{BS2,toluene}}$	Population (%) /$\Delta G_{\text{est.}}^{\text{BS2,MeOH}}$	Cluster	Population after refinement (%)
4.12-1	0.00	0.00	0.00	0.00	0.00	0.00	20.63%	Cluster 1	16.82%
4.12-2	0.03	0.00	0.00	0.00	0.00	0.00	20.63%	Cluster 1	16.82%
4.12-3	7.82	6.12	6.71	6.08	6.05	6.60	1.44%	Cluster 8	1.35%
4.12-4	7.82	6.12	6.71	6.08	6.05	6.60	1.44%	Cluster 8	1.35%
4.12-5	9.18	7.29	3.42	8.34	7.13	4.32	3.61%	Cluster 1	2.94%
4.12-6	9.21	7.29	3.42	8.34	7.13	4.32	3.61%	Cluster 1	2.94%
4.12-7	10.02	7.67	7.02	7.58	7.52	6.78	1.34%	Cluster 8	1.25%
4.12-8	10.03	7.67	7.02	7.58	7.52	6.78	1.34%	Cluster 8	1.25%
4.12-9	10.74	5.32	3.68	5.17	5.67	3.87	4.32%	Cluster 3	0.69%
4.12-10	10.75	5.32	3.68	5.17	5.67	3.87	4.32%	Cluster 3	0.69%
4.12-11	10.75	13.39	16.07	13.44	12.83	15.57	0.04%	Cluster 23	0.02%
4.12-12	10.76	13.39	16.07	13.44	12.83	15.57	0.04%	Cluster 23	0.02%
4.12-13	11.74	9.09	8.56	9.22	8.88	8.48	0.67%	Cluster 12	0.33%
4.12-14	11.77	9.09	8.56	9.22	8.88	8.48	0.67%	Cluster 12	0.33%
4.12-15	12.15	8.92	6.65	8.72	8.69	6.22	1.67%	Cluster 7	0.24%
4.12-16	12.15	8.92	6.65	8.72	8.69	6.22	1.67%	Cluster 7	0.24%
4.12-17	12.20	4.13	4.83	4.04	5.03	5.65	2.11%	Cluster 5	12.33%
4.12-18	12.22	4.13	4.83	4.04	5.03	5.65	2.11%	Cluster 5	12.33%
4.12-19	12.32	11.64	13.21	11.74	11.16	12.81	0.12%	Cluster 23	0.07%
4.12-20	12.32	11.64	13.21	11.74	11.16	12.81	0.12%	Cluster 23	0.07%

4.12-21	12.46	9.15	9.20	9.14	9.01	9.05	0.53%	Cluster 15	0.29%
4.12-22	12.46	9.15	9.20	9.14	9.01	9.05	0.53%	Cluster 15	0.29%
4.12-23	13.12	10.84	10.17	10.41	10.55	9.45	0.45%	Cluster 17	0.17%
4.12-24	13.12	10.84	10.17	10.41	10.55	9.45	0.45%	Cluster 17	0.17%
4.12-25	13.36	10.33	14.82	10.27	9.89	14.31	0.06%	Cluster 28	0.03%
4.12-26	13.36	10.33	14.81	10.27	9.89	14.30	0.06%	Cluster 28	0.03%
4.12-27	13.58	8.72	9.02	8.80	8.24	8.63	0.63%	Cluster 14	0.13%
4.12-28	13.60	8.72	9.02	8.80	8.24	8.64	0.63%	Cluster 14	0.13%
4.12-29	13.67	11.51	13.40	11.74	11.01	13.12	0.10%	Cluster 24	0.05%
4.12-30	13.69	11.51	13.40	11.74	11.01	13.12	0.10%	Cluster 24	0.05%
4.12-31	13.83	4.18	8.09	4.24	4.14	8.11	0.78%	Cluster 10	0.18%
4.12-32	13.83	4.18	8.09	4.24	4.14	8.11	0.78%	Cluster 10	0.18%
4.12-33	13.96	7.54	6.26	8.00	7.87	7.04	1.20%	Cluster 6	0.57%
4.12-34	13.97	7.54	6.26	8.00	7.87	7.04	1.20%	Cluster 6	0.57%
4.12-35	14.50	3.57	10.92	3.85	3.07	10.70	0.27%	Cluster 18	0.09%
4.12-36	14.50	3.57	10.92	3.85	3.07	10.70	0.27%	Cluster 18	0.09%
4.12-37	14.64	6.19	3.07	6.93	6.84	4.45	3.42%	Cluster 2	1.50%
4.12-38	14.66	6.19	3.07	6.93	6.84	4.45	3.42%	Cluster 2	1.50%
4.12-39	14.80	10.23	7.95	10.02	10.00	7.51	1.00%	Cluster 9	0.22%
4.12-40	14.82	10.23	7.95	10.02	10.00	7.51	1.00%	Cluster 9	0.22%
4.12-41	15.21	3.57	10.92	3.85	3.07	10.70	0.27%	Cluster 18	0.09%
4.12-42	15.21	3.57	10.92	3.85	3.07	10.70	0.27%	Cluster 18	0.09%
4.12-43	15.28	10.87	10.76	11.74	10.66	11.42	0.20%	Cluster 8	0.19%
4.12-44	15.29	10.87	10.76	11.74	10.66	11.42	0.20%	Cluster 8	0.19%
4.12-45	15.45	12.41	13.11	12.80	12.82	13.92	0.07%	Cluster 22	0.04%
4.12-46	15.45	12.41	13.11	12.80	12.82	13.92	0.07%	Cluster 22	0.04%
4.12-47	15.48	3.57	10.92	3.85	3.07	10.70	0.27%	Cluster 18	0.09%
4.12-48	15.50	12.83	15.79	12.85	12.64	15.61	0.04%	Cluster 30	0.02%
4.12-49	15.50	3.57	10.92	3.85	3.07	10.70	0.27%	Cluster 18	0.09%
4.12-50	15.51	12.83	15.79	12.85	12.64	15.61	0.04%	Cluster 30	0.02%
4.12-51	16.04	9.81	4.70	10.21	10.14	5.43	2.30%	Cluster 4	8.20%

4.12-52	16.05	9.81	4.70	10.21	10.14	5.43	2.30%	Cluster 4	8.20%
4.12-53	16.20	11.60	13.89	11.97	11.55	14.22	0.07%	Cluster 25	0.03%
4.12-54	16.21	11.60	13.89	11.97	11.55	14.22	0.07%	Cluster 25	0.03%
4.12-55	16.41	6.89	8.83	7.02	7.41	9.48	0.45%	Cluster 13	0.12%
4.12-56	16.42	6.89	8.83	7.02	7.41	9.48	0.45%	Cluster 13	0.12%
4.12-57	16.72	13.99	9.99	14.41	14.07	10.50	0.30%	Cluster 16	0.12%
4.12-58	16.73	13.99	9.99	14.41	14.07	10.50	0.30%	Cluster 16	0.12%
4.12-59	17.45	18.74	17.57	18.84	17.97	16.89	0.02%	Cluster 36	0.01%
4.12-60	17.47	18.74	17.57	18.84	17.97	16.89	0.02%	Cluster 36	0.01%
4.12-61	17.70	14.62	12.82	15.57	14.10	13.24	0.10%	Cluster 21	0.06%
4.12-62	17.72	14.62	12.82	15.57	14.10	13.24	0.10%	Cluster 21	0.06%
4.12-63	18.07	12.64	11.95	13.84	12.62	13.13	0.10%	Cluster 16	0.04%
4.12-64	18.08	12.64	11.95	13.84	12.62	13.13	0.10%	Cluster 16	0.04%
4.12-65	18.17	18.80	21.72	19.06	18.16	21.34	0.00%	Cluster 39	0.00%
4.12-66	18.17	18.80	21.72	19.06	18.16	21.34	0.00%	Cluster 39	0.00%
4.12-67	18.37	14.17	13.91	13.95	13.87	13.39	0.09%	Cluster 26	0.04%
4.12-68	18.37	14.17	13.91	13.95	13.87	13.39	0.09%	Cluster 26	0.04%
4.12-69	18.50	11.23	12.04	11.10	11.52	12.21	0.15%	Cluster 19	0.06%
4.12-70	18.51	11.23	12.04	11.10	11.52	12.21	0.15%	Cluster 19	0.06%
4.12-71	18.58	12.35	15.34	12.20	12.20	15.04	0.05%	Cluster 29	0.02%
4.12-72	18.59	12.35	15.34	12.20	12.20	15.04	0.05%	Cluster 29	0.02%
4.12-73	18.72	12.64	11.95	13.84	12.62	13.13	0.10%	Cluster 16	0.04%
4.12-74	18.76	11.63	14.49	12.06	11.61	14.90	0.05%	Cluster 27	0.02%
4.12-75	18.77	11.63	14.49	12.06	11.61	14.90	0.05%	Cluster 27	0.02%
4.12-76	18.85	15.77	16.83	15.34	15.44	16.06	0.03%	Cluster 34	0.01%
4.12-77	18.87	15.77	16.83	15.34	15.44	16.06	0.03%	Cluster 34	0.01%
4.12-78	19.17	20.15	19.45	20.74	19.77	19.66	0.01%	Cluster 31	0.00%
4.12-79	19.17	20.15	19.45	20.74	19.77	19.66	0.01%	Cluster 31	0.00%
4.12-80	19.19	10.06	8.49	11.25	10.59	10.22	0.33%	Cluster 4	1.19%
4.12-81	19.20	10.06	8.49	11.25	10.59	10.22	0.33%	Cluster 4	1.19%
4.12-82	19.91	14.94	16.47	14.89	14.68	16.17	0.03%	Cluster 33	0.01%

4.12-83	19.92	14.94	16.47	14.89	14.68	16.17	0.03%	Cluster 33	0.01%
4.12-84	20.05	9.58	12.12	10.18	9.78	12.92	0.11%	Cluster 20	0.05%
4.12-85	20.06	9.58	12.12	10.18	9.78	12.92	0.11%	Cluster 20	0.05%
4.12-86	20.15	5.02	8.48	5.46	5.86	9.75	0.40%	Cluster 11	0.24%
4.12-87	20.16	5.02	8.48	5.46	5.86	9.75	0.40%	Cluster 11	0.24%
4.12-88	20.18	16.26	21.10	16.29	15.63	20.50	0.01%	Cluster 38	0.00%
4.12-89	20.19	16.26	21.10	16.29	15.63	20.50	0.01%	Cluster 38	0.00%
4.12-90	20.40	14.54	20.73	14.24	14.04	19.93	0.01%	Cluster 37	0.00%
4.12-91	20.41	14.54	20.73	14.24	14.04	19.93	0.01%	Cluster 37	0.00%
4.12-92	20.74	16.05	17.46	16.17	15.82	17.34	0.02%	Cluster 35	0.01%
4.12-93	20.77	16.05	17.46	16.17	15.82	17.34	0.02%	Cluster 35	0.01%
4.12-94	20.82	16.30	16.37	16.42	15.97	16.16	0.03%	Cluster 32	0.01%
4.12-95	20.83	16.30	16.37	16.42	15.97	16.16	0.03%	Cluster 32	0.01%
4.12-96	20.91	20.19	15.97	21.59	19.83	17.01	0.02%	Cluster 31	0.01%
4.12-97	20.91	20.19	15.97	21.59	19.83	17.01	0.02%	Cluster 31	0.01%

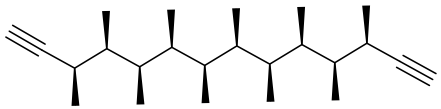

4.5

Table 6.81: Calculated energies (in kJ mol^{-1}) and DFT calculated population (BS1: B3LYP-D2 6-311G (d), BS2: B3LYP-D2 6-311G (d,p)) for all conformers of **4.5**.

Conformer	$\Delta E^{\text{MMFFs, gas}}$	$\Delta E^{\text{BS1, gas}}$	$\Delta G^{\text{BS1, gas}}$	$\Delta E^{\text{BS2, gas}}$	$\Delta E^{\text{BS1, toluene}}$	$\Delta G_{\text{est.}}^{\text{BS2,toluene}}$	Population (%)/$\Delta G_{\text{est.}}^{\text{BS2,MeOH}}$
4.5-1	0.00	3.02	4.33	3.00	2.38	3.67	6.73%
4.5-2	1.03	0.00	0.00	0.00	0.00	0.00	29.62%
4.5-3	8.76	8.05	7.45	8.05	7.91	7.32	1.54%
4.5-4	10.08	6.14	4.34	7.59	5.96	5.62	3.06%
4.5-5	10.84	7.58	12.38	7.51	7.31	12.03	0.23%
4.5-6	10.89	8.05	7.45	8.05	7.91	7.32	0.00%
4.5-7	11.02	9.37	11.32	10.33	8.54	11.46	0.29%
4.5-8	11.04	9.03	13.92	8.89	8.20	12.94	0.16%
4.5-9	11.73	13.55	14.22	13.64	13.05	13.81	0.11%
4.5-10	12.73	11.70	12.82	11.71	10.88	12.00	0.23%
4.5-11	12.86	9.50	9.32	9.64	9.31	9.28	0.70%
4.5-12	12.88	9.40	8.88	9.26	9.22	8.54	0.94%
4.5-13	13.26	12.10	11.61	12.26	11.65	11.32	0.31%
4.5-14	13.97	8.93	9.19	9.14	8.51	8.98	0.79%
4.5-15	14.25	7.88	8.74	8.21	7.45	8.63	0.91%
4.5-16	14.41	9.97	13.64	10.43	9.76	13.89	0.11%
4.5-17	14.56	7.38	9.96	8.19	7.50	10.90	0.36%
4.5-18	14.57	9.42	8.32	9.70	9.19	8.36	1.01%
4.5-19	14.68	11.47	12.90	11.78	11.02	12.77	0.17%
4.5-20	15.09	13.96	18.48	14.34	13.80	18.70	0.02%
4.5-21	15.19	13.54	15.44	13.83	13.02	15.22	0.06%

4.5-22	15.47	8.30	10.98	9.38	7.93	11.69	0.26%
4.5-23	15.57	9.63	11.36	10.25	9.20	11.56	0.28%
4.5-24	15.62	8.30	10.98	9.38	7.93	11.69	0.00%
4.5-25	15.99	9.05	15.31	9.26	9.00	15.48	0.06%
4.5-26	16.09	10.00	7.38	11.23	9.82	8.43	0.98%
4.5-27	16.57	13.41	13.21	13.46	13.27	13.11	0.15%
4.5-28	16.71	12.53	13.21	12.60	12.42	13.16	0.15%
4.5-29	17.64	19.74	24.32	20.19	18.76	23.80	0.00%
4.5-30	18.02	13.50	14.27	13.48	13.31	14.05	0.10%
4.5-31	18.19	13.50	14.26	13.48	13.31	14.05	0.10%
4.5-32	18.62	13.41	13.50	14.77	12.96	14.40	0.09%
4.5-33	19.01	14.36	14.78	14.25	14.08	14.40	0.09%
4.5-34	19.24	15.94	21.22	15.88	14.99	20.21	0.01%
4.5-35	19.28	19.07	20.93	19.36	18.49	20.63	0.01%
4.5-36	19.62	19.56	22.09	19.71	18.99	21.66	0.00%
4.5-37	19.66	14.61	16.64	15.66	14.00	17.09	0.03%
4.5-38	20.06	10.82	14.53	11.55	10.44	14.87	0.07%
4.5-39	20.24	15.23	16.80	15.36	15.01	16.70	0.03%
4.5-40	20.33	14.13	17.05	14.21	13.63	16.64	0.04%
4.5-41	20.42	17.49	21.05	17.66	16.97	20.70	0.01%
4.5-42	20.56	16.34	18.24	16.44	15.91	17.91	0.02%
4.5-43	20.69	11.45	13.75	12.65	11.36	14.85	0.07%
4.5-44	20.86	11.45	13.75	12.65	11.36	14.85	0.07%
4.5-45	20.94	20.92	19.65	21.00	20.29	19.11	0.01%

Table 6.82: Calculated energies (in kJ mol^{-1}) and DFT calculated energies and population for all conformers of **4.5**.

Functional	**mPW1PW91**								**B3LYP**			
Basis set	**6-31G (d)**		**6-311G (d)**		**6-311G (d,p)**		**6-311+G (d,p)**		**6-311G (d)**		**6-311G (d) toluene**	
Conformer	***ΔG***	**Population**	***ΔG***	**Population**	***ΔG***	**Population**	***ΔG***	**Population**	***ΔG***	**Population**	***ΔG***	**Pop.**
4.5-1	8.65	0.71%	6.41	1.77%	7.92	0.91%	6.95	1.33%	8.91	0.71%	9.70	0.68%
4.5-2	0.82	16.74%	0.00	23.54%	0.00	22.38%	0.00	22.10%	0.00	25.83%	0.00	34.00%
4.5-3	7.15	1.30%	7.72	1.04%	7.91	0.92%	8.26	0.79%	6.87	1.61%	8.57	1.07%
4.5-4	0.00	23.30%	1.70	11.85%	1.32	13.14%	1.09	14.22%	3.37	6.61%	3.95	6.90%
4.5-5	11.04	0.27%	19.96	0.01%	11.59	0.21%	11.33	0.23%	13.36	0.12%	14.84	0.08%
4.5-6	7.15[a]	-	7.04	1.37%	8.10	0.85%	8.32	0.77%	6.87[a]	-	8.57	0.00%
4.5-7	10.01	0.41%	9.85	0.44%	9.55	0.47%	8.96	0.59%	10.40	0.39%	11.38	0.34%
4.5-8	14.74	0.06%	13.61	0.10%	14.72	0.06%	14.45	0.06%	13.36	0.12%	13.11	0.17%
4.5-9	15.16	0.05%	14.35	0.07%	13.75	0.09%	13.61	0.09%	14.51	0.07%	14.20	0.11%
4.5-10	17.30	0.02%	15.46	0.05%	16.30	0.03%	15.54	0.04%	15.23	0.06%	14.95	0.08%
4.5-11	6.19	1.91%	5.70	2.35%	5.47	2.46%	5.47	2.43%	8.32	0.90%	8.39	1.15%
4.5-12	6.37	1.78%	5.15	2.95%	4.15	4.18%	4.44	3.68%	7.17	1.43%	8.16	1.26%
4.5-13	11.29	0.24%	10.17	0.39%	10.79	0.29%	10.16	0.37%	2.60	9.02%	10.20	0.55%
4.5-14	11.96	0.19%	10.16	0.39%	10.92	0.27%	10.48	0.32%	12.16	0.19%	10.20	0.55%
4.5-15	11.42	0.23%	10.54	0.33%	12.43	0.15%	12.26	0.16%	13.79	0.10%	13.38	0.15%
4.5-16	13.90	0.08%	11.45	0.23%	13.96	0.08%	13.64	0.09%	13.69	0.10%	14.08	0.12%
4.5-17	11.95	0.19%	11.53	0.22%	11.80	0.19%	12.11	0.17%	14.74	0.07%	15.64	0.06%
4.5-18	11.59	0.22%	10.75	0.31%	11.09	0.25%	11.21	0.24%	12.85	0.14%	12.93	0.18%
4.5-19	15.41	0.05%	14.07	0.08%	14.67	0.06%	14.19	0.07%	14.44	0.08%	14.63	0.09%
4.5-20	19.69	0.01%	18.06	0.02%	19.96	0.01%	19.12	0.01%	22.09	0.00%	22.11	0.00%

4.5-21	19.77	0.01%	17.30	0.02%	18.24	0.01%	18.11	0.01%	19.48	0.01%	18.75	0.02%
4.5-22	13.60	0.10%	13.08	0.12%	13.52	0.10%	12.99	0.12%	15.09	0.06%	15.77	0.06%
4.5-23	13.60[a]	-	13.08[a]	-	13.52[a]	0.00%	12.99	0.12%	15.09[a]	-	15.77[a]	-
4.5-24	13.60[a]	-	13.08	0.00%	13.52[a]	-	12.99	0.12%	15.09[a]	-	15.77[a]	-
4.5-25	21.94	0.00%	21.21	0.00%	21.45	0.00%	21.03	0.00%	21.25	0.00%	23.64	0.00%
4.5-26	6.86	1.46%	7.04[a]	-	6.46	1.64%	7.32	1.15%	8.21	0.94%	10.19	0.56%
4.5-27	14.15	0.08%	13.59	0.10%	13.40	0.10%	13.53	0.09%	12.03	0.20%	10.63	0.46%
4.5-28	19.51	0.01%	12.20	0.17%	9.02	0.59%	19.69	0.01%	14.53	0.07%	15.51	0.06%
4.5-29	24.68	0.00%	23.17	0.00%	23.75	0.00%	22.80	0.00%	22.30	0.00%	21.88	0.00%
4.5-30	15.21	0.05%	16.10	0.04%	15.98	0.04%	16.08	0.03%	14.53[a]	-	13.20	0.16%
4.5-31	15.21[a]	-	16.10[a]	-	15.98[a]	-	16.08[a]	-	14.53[a]	-	13.20	0.16%
4.5-32	11.65	0.21%	11.05	0.27%	11.69	0.20%	10.94	0.27%	10.18	0.42%	11.02	0.40%
4.5-33	13.19	0.11%	12.67	0.14%	13.29	0.10%	13.16	0.11%	13.68	0.10%	14.22	0.11%
4.5-34	22.99	0.00%	23.57	0.00%	23.90	0.00%	23.61	0.00%	25.62	0.00%	24.51	0.00%
4.5-35	20.39	0.01%	19.89	0.01%	19.98	0.01%	19.52	0.01%	19.18	0.01%	19.17	0.01%
4.5-36	23.83	0.00%	24.77	0.00%	22.11	0.00%	21.68[a]	-	17.77	0.02%	21.70	0.01%
4.5-37	20.48	0.01%	20.57	0.01%	21.23	0.00%	20.66	0.01%	21.84	0.00%	21.91	0.00%
4.5-38	17.92	0.02%	20.05	0.01%	17.59	0.02%	18.11	0.01%	18.29	0.02%	17.39	0.03%
4.5-39	13.77	0.09%	14.10	0.08%	13.68	0.09%	13.98	0.08%	11.70	0.23%	12.21	0.25%
4.5-40	21.32	0.00%	20.51	0.01%	20.93	0.00%	20.79	0.01%	22.41	0.00%	23.60	0.00%
4.5-41	21.09	0.00%	20.36	0.01%	20.18	0.01%	19.86	0.01%	19.50	0.01%	19.27	0.01%
4.5-42	17.16	0.02%	16.52	0.03%	16.41	0.03%	16.40	0.03%	18.28	0.02%	18.58	0.02%
4.5-43	14.87	0.06%	14.96	0.06%	14.81	0.06%	14.45	0.06%	12.52	0.16%	14.67	0.09%
4.5-44	14.87[a]	-	14.97	0.06%	14.81[a]	-	14.45[a]	-	12.53	0.16%	14.67[a]	-
4.5-45	23.83[a]	-	22.65	0.00%	22.11[a]	-	21.68[a]	-	23.60	0.00%	21.97	0.00%

a: Degenerate conformers were removed for Boltzmann population calculations

(Table 6.82 continued)

Functional	**M06-2X**				**B3LYP-D2**			
Basis set	**6-31G (d)**		**6-311G (d)**		**6-31G (d)**		**6-311G (d)**	
Conformer	***ΔG***	**Population**	***ΔG***	**Population**	***ΔG***	**Population**	***ΔG***	**Population**
4.5-1	8.46	0.97%	7.18	1.57%	5.50	2.19%	4.33	5.06%
4.5-2	0.00	29.58%	0.00	28.38%	0.00	20.22%	0.00	29.11%
4.5-3	8.45	0.97%	10.37	0.43%	4.07	3.91%	7.45	1.43%
4.5-4	3.15	8.30%	2.45	10.56%	2.87	6.33%	4.34	5.04%
4.5-5	13.22	0.14%	13.16	0.14%	10.60	0.28%	12.38	0.20%
4.5-6	5.73	2.93%	7.37	1.45%	4.12	3.83%	7.45[a]	-
4.5-7	13.70	0.12%	13.50	0.12%	11.01	0.24%	11.32	0.30%
4.5-8	14.00	0.10%	13.58	0.12%	12.58	0.13%	13.92	0.11%
4.5-9	18.96	0.01%	19.79	0.01%	13.60	0.08%	14.22	0.09%
4.5-10	16.50	0.04%	18.09	0.02%	14.85	0.05%	12.82	0.16%
4.5-11	8.93	0.80%	7.97	1.13%	9.39	0.46%	9.32	0.67%
4.5-12	8.01	1.17%	6.41	2.13%	7.89	0.84%	8.88	0.81%
4.5-13	13.15	0.15%	13.90	0.10%	11.39	0.20%	11.61	0.27%
4.5-14	9.68	0.59%	9.58	0.59%	7.70	0.90%	9.19	0.71%
4.5-15	8.43	0.98%	8.10	1.08%	6.81	1.29%	8.74	0.85%
4.5-16	16.29	0.04%	17.06	0.03%	12.03	0.16%	13.64	0.12%
4.5-17	9.99	0.52%	10.87	0.35%	8.14	0.76%	9.96	0.52%
4.5-18	10.11	0.50%	10.76	0.37%	5.87	1.89%	8.32	1.01%
4.5-19	11.94	0.24%	13.50	0.12%	12.99	0.11%	12.90	0.16%
4.5-20	18.42	0.02%	17.85	0.02%	17.57	0.02%	18.48	0.02%

4.5-21	17.62	0.02%	18.27	0.02%	13.90	0.07%	15.44	0.06%
4.5-22	13.45	0.13%	12.80	0.16%	8.98	0.54%	10.98	0.35%
4.5-23	13.45[a]	-	12.80[a]	-	10.54	0.29%	11.36	0.30%
4.5-24	13.45[a]	-	12.80[a]	-	8.98[a]	-	10.98[a]	-
4.5-25	16.64	0.04%	16.81	0.03%	12.89	0.11%	15.31	0.06%
4.5-26	8.60	0.92%	9.44	0.63%	4.27	3.61%	7.38	1.48%
4.5-27	15.40	0.06%	16.10	0.04%	12.22	0.15%	13.21	0.14%
4.5-28	16.22	0.04%	18.22	0.02%	9.87	0.37%	13.21	0.14%
4.5-29	25.60	0.00%	25.82	0.00%	24.58	0.00%	24.32	0.00%
4.5-30	13.90	0.11%	16.79	0.03%	12.27	0.14%	14.27	0.09%
4.5-31	13.90[a]	-	16.79[a]	-	12.28	0.14%	14.26	0.09%
4.5-32	12.92	0.16%	13.61	0.12%	12.79	0.12%	13.50	0.13%
4.5-33	12.48	0.19%	14.52	0.08%	12.75	0.12%	14.78	0.07%
4.5-34	23.29	0.00%	22.98	0.00%	20.96	0.00%	21.22	0.01%
4.5-35	22.83	0.00%	22.25	0.00%	21.15	0.00%	20.93	0.01%
4.5-36	27.10	0.00%	27.88	0.00%	19.79	0.01%	22.09	0.00%
4.5-37	18.40	0.02%	19.27	0.01%	15.51	0.04%	16.64	0.04%
4.5-38	19.36	0.01%	20.59	0.01%	12.44	0.13%	14.53	0.08%
4.5-39	16.19	0.04%	15.54	0.05%	15.83	0.03%	16.80	0.03%
4.5-40	18.54	0.02%	18.72	0.01%	15.61	0.04%	17.05	0.03%
4.5-41	21.29	0.01%	22.09	0.00%	19.83	0.01%	21.05	0.01%
4.5-42	18.84	0.01%	18.78	0.01%	16.94	0.02%	18.24	0.02%
4.5-43	16.06	0.05%	16.56	0.04%	11.84	0.17%	13.75	0.11%
4.5-44	16.06[a]	-	16.56[a]	-	11.84[a]	-	13.75	0.11%
4.5-45	23.40	0.00%	25.51	0.00%	18.90	0.01%	19.65	0.01%

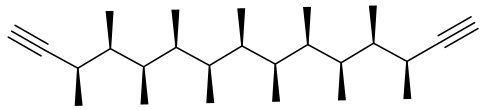

4.13

Table 6.83: Calculated energies (in kJ mol^{-1}), DFT calculated population and conformer population after NOE-refinement for all conformers of **4.13**.

Conformer	$\Delta E^{\text{MMFFs, gas}}$	$\Delta E^{\text{BS1, gas}}$	$\Delta G^{\text{BS1, gas}}$	$\Delta E^{\text{BS2, gas}}$	$\Delta E^{\text{BS1, toluene}}$	$\Delta G_{\text{est.}}^{\text{BS2,toluene}}$	Population (%) /$\Delta G_{\text{est.}}^{\text{BS2,MeOH}}$	Cluster	Population after refinement (%)
4.13-1	0.00	3.65	0.00	3.07	3.34	0.00	11.90%	Cluster 1	14.8%
4.13-2	0.02	3.65	0.00	3.07	3.34	0.00	11.90%	Cluster 1	14.8%
4.13-3	7.54	10.28	6.58	9.66	9.85	6.43	0.89%	Cluster 9	0.4%
4.13-4	7.54	10.28	6.58	9.66	9.85	6.43	0.89%	Cluster 9	0.4%
4.13-5	8.77	1.52	4.19	0.40	1.10	3.54	2.85%	Cluster 4	1.4%
4.13-6	8.77	1.52	4.19	0.40	1.10	3.54	2.84%	Cluster 4	1.4%
4.13-7	9.80	10.84	7.70	10.24	10.33	7.47	0.58%	Cluster 11	0.2%
4.13-8	9.80	10.84	7.70	10.24	10.33	7.47	0.58%	Cluster 11	0.2%
4.13-9	9.84	10.84	7.70	10.24	10.33	7.47	0.58%	Cluster 11	0.2%
4.13-10	10.00	10.84	7.70	10.24	10.33	7.47	0.58%	Cluster 11	0.2%
4.13-11	10.41	17.27	14.94	16.81	16.40	14.50	0.03%	Cluster 41	0.0%
4.13-12	10.43	17.27	14.94	16.81	16.40	14.50	0.03%	Cluster 41	0.0%
4.13-13	10.87	10.44	12.77	9.72	9.93	12.44	0.08%	Cluster 28	0.0%
4.13-14	10.88	10.44	12.77	9.72	9.93	12.44	0.08%	Cluster 28	0.0%
4.13-15	10.92	9.29	4.06	10.04	8.77	5.19	1.46%	Cluster 7	24.3%
4.13-16	10.98	9.05	6.79	8.35	9.08	7.01	0.70%	Cluster 10	0.4%
4.13-17	10.99	9.05	6.79	8.35	9.08	7.01	0.70%	Cluster 10	0.4%
4.13-18	11.01	9.29	4.07	10.04	8.77	5.19	1.46%	Cluster 7	24.3%
4.13-19	11.26	10.48	10.93	9.77	9.99	10.62	0.16%	Cluster 23	0.1%
4.13-20	11.26	10.48	10.93	9.77	9.99	10.62	0.16%	Cluster 23	0.1%

4.13-21	11.82	9.63	10.91	9.01	8.86	10.41	0.18%	Cluster 20	0.1%
4.13-22	11.82	9.63	10.91	9.01	8.86	10.41	0.18%	Cluster 20	0.1%
4.13-23	12.21	14.71	13.72	14.26	13.90	13.36	0.05%	Cluster 33	0.0%
4.13-24	12.22	14.71	13.72	14.26	13.90	13.36	0.05%	Cluster 33	0.0%
4.13-25	12.27	12.70	13.59	12.24	12.17	13.50	0.05%	Cluster 36	0.0%
4.13-26	12.28	12.70	13.59	12.24	12.17	13.50	0.05%	Cluster 36	0.0%
4.13-27	12.88	12.40	10.58	11.81	11.92	10.41	0.18%	Cluster 19	0.1%
4.13-28	12.89	12.40	10.58	11.81	11.92	10.41	0.18%	Cluster 19	0.1%
4.13-29	13.19	9.70	10.16	9.44	8.87	9.97	0.21%	Cluster 18	0.1%
4.13-30	13.19	9.70	10.16	9.44	8.87	9.97	0.21%	Cluster 18	0.1%
4.13-31	13.30	13.89	12.41	13.80	13.12	12.45	0.08%	Cluster 29	0.0%
4.13-32	13.68	12.25	15.91	11.19	11.68	15.17	0.03%	Cluster 35	0.0%
4.13-33	13.69	12.25	15.91	11.19	11.68	15.17	0.03%	Cluster 35	0.0%
4.13-34	13.75	0.00	0.94	0.00	0.00	1.83	5.68%	Cluster 3	0.7%
4.13-35	13.75	0.00	0.94	0.00	0.00	1.83	5.68%	Cluster 3	0.7%
4.13-36	14.08	10.00	0.41	9.64	9.80	0.74	8.84%	Cluster 2	1.6%
4.13-37	14.10	10.00	0.41	9.64	9.80	0.74	8.83%	Cluster 2	1.6%
4.13-38	14.25	15.23	16.31	14.84	14.42	16.00	0.02%	Cluster 49	0.0%
4.13-39	14.26	15.23	16.31	14.84	14.42	16.00	0.02%	Cluster 49	0.0%
4.13-40	14.59	11.75	9.27	11.12	11.62	9.40	0.27%	Cluster 17	0.1%
4.13-41	14.60	11.29	7.09	11.21	11.30	7.91	0.49%	Cluster 13	0.3%
4.13-42	14.61	11.75	9.27	11.12	11.62	9.40	0.27%	Cluster 17	0.1%
4.13-43	14.61	11.29	7.09	11.21	11.30	7.91	0.49%	Cluster 13	0.3%
4.13-44	14.78	11.24	3.15	10.99	11.31	3.86	2.51%	Cluster 5	1.2%
4.13-45	14.79	11.24	3.15	10.99	11.31	3.86	2.51%	Cluster 5	1.2%
4.13-46	14.93	6.20	9.57	5.45	5.74	9.25	0.28%	Cluster 16	0.2%
4.13-47	14.94	6.20	9.58	5.45	5.74	9.26	0.28%	Cluster 16	0.2%
4.13-48	14.98	8.74	4.54	8.95	9.11	6.02	1.05%	Cluster 8	0.6%
4.13-49	14.99	8.74	4.54	8.95	9.11	6.02	1.05%	Cluster 8	0.6%
4.13-50	15.26	8.37	11.35	7.21	7.80	10.51	0.17%	Cluster 21	0.1%
4.13-51	15.29	8.37	11.35	7.21	7.80	10.51	0.17%	Cluster 21	0.1%

4.13-52	15.29	14.86	15.46	14.68	15.02	16.33	0.02%	Cluster 50	0.0%
4.13-53	15.30	14.86	15.46	14.68	15.02	16.33	0.02%	Cluster 50	0.0%
4.13-54	15.32	14.58	13.20	14.32	14.35	13.60	0.05%	Cluster 37	0.0%
4.13-55	15.33	14.58	13.20	14.32	14.35	13.60	0.05%	Cluster 37	0.0%
4.13-56	15.55	14.86	13.71	14.24	14.35	13.48	0.05%	Cluster 35	0.0%
4.13-57	15.55	14.86	13.71	14.24	14.35	13.48	0.05%	Cluster 35	0.0%
4.13-58	15.75	10.09	5.27	10.17	9.85	5.99	1.06%	Cluster 2	0.2%
4.13-59	15.86	8.51	3.30	9.22	8.39	4.79	1.72%	Cluster 6	0.7%
4.13-60	15.87	8.51	3.30	9.22	8.39	4.79	1.72%	Cluster 6	0.7%
4.13-61	16.04	10.00	11.56	9.55	10.22	12.23	0.09%	Cluster 27	0.0%
4.13-62	16.05	10.00	11.56	9.55	10.22	12.23	0.09%	Cluster 27	0.0%
4.13-63	16.13	0.00	0.94	0.00	0.00	1.83	5.68%	Cluster 3	0.7%
4.13-64	16.15	0.00	0.94	0.00	0.00	1.83	5.68%	Cluster 3	0.7%
4.13-65	16.19	16.62	16.14	16.05	16.06	15.89	0.02%	Cluster 48	0.0%
4.13-66	16.20	16.62	16.14	16.05	16.06	15.89	0.02%	Cluster 48	0.0%
4.13-67	16.36	11.49	12.33	11.79	10.68	12.72	0.07%	Cluster 30	0.0%
4.13-68	16.38	11.49	12.33	11.79	10.68	12.72	0.07%	Cluster 30	0.0%
4.13-69	16.99	15.90	14.83	15.26	15.27	14.44	0.03%	Cluster 40	0.0%
4.13-70	17.00	15.90	14.83	15.26	15.27	14.44	0.03%	Cluster 40	0.0%
4.13-71	17.10	13.55	7.46	14.07	13.01	8.34	0.41%	Cluster 14	0.2%
4.13-72	17.11	13.55	7.46	14.07	13.01	8.34	0.41%	Cluster 14	0.2%
4.13-73	17.76	21.21	19.66	21.11	20.58	19.83	0.00%	Cluster 57	0.0%
4.13-74	17.78	21.21	19.66	21.11	20.58	19.83	0.00%	Cluster 57	0.0%
4.13-75	17.83	9.05	7.43	8.37	8.93	7.53	0.57%	Cluster 12	0.3%
4.13-76	17.84	9.05	7.43	8.37	8.93	7.53	0.57%	Cluster 12	0.3%
4.13-77	18.34	10.31	18.48	9.37	9.42	17.54	0.01%	Cluster 54	0.0%
4.13-78	18.35	10.31	18.48	9.37	9.42	17.54	0.01%	Cluster 54	0.0%
4.13-79	18.65	13.33	18.13	12.12	12.67	17.16	0.01%	Cluster 52	0.0%
4.13-80	18.66	14.93	13.16	14.25	14.87	13.32	0.05%	Cluster 32	0.0%
4.13-81	18.67	13.33	18.13	12.12	12.67	17.16	0.01%	Cluster 52	0.0%
4.13-82	18.67	14.93	13.16	14.25	14.87	13.32	0.05%	Cluster 32	0.0%

4.13-83	18.67	16.33	17.62	15.61	15.72	17.19	0.01%	Cluster 53	0.0%
4.13-84	18.68	16.33	17.62	15.61	15.72	17.19	0.01%	Cluster 53	0.0%
4.13-85	18.88	22.76	21.30	22.44	21.80	20.90	0.00%	Cluster 59	0.0%
4.13-86	18.88	22.76	21.30	22.44	21.80	20.90	0.00%	Cluster 59	0.0%
4.13-87	19.33	17.45	15.55	16.86	16.78	15.19	0.03%	Cluster 46	0.0%
4.13-88	19.33	17.45	15.55	16.86	16.78	15.19	0.03%	Cluster 46	0.0%
4.13-89	19.61	16.99	11.22	17.60	16.16	11.90	0.10%	Cluster 26	0.1%
4.13-90	19.62	16.99	11.22	17.60	16.16	11.90	0.10%	Cluster 26	0.1%
4.13-91	19.78	22.21	25.23	21.66	21.20	24.55	0.00%	Cluster 61	0.0%
4.13-92	19.78	22.21	25.23	21.66	21.20	24.55	0.00%	Cluster 61	0.0%
4.13-93	19.83	14.57	12.69	15.40	14.29	14.14	0.04%	Cluster 39	0.0%
4.13-94	19.85	14.57	12.68	15.40	14.29	14.14	0.04%	Cluster 39	0.0%
4.13-95	19.86	18.46	14.97	18.09	17.95	14.99	0.03%	Cluster 45	0.0%
4.13-96	19.88	18.46	14.97	18.09	17.95	14.99	0.03%	Cluster 45	0.0%
4.13-97	19.92	6.05	10.92	6.22	5.90	11.83	0.10%	Cluster 25	0.1%
4.13-98	19.93	6.05	10.92	6.22	5.90	11.83	0.10%	Cluster 25	0.1%
4.13-99	19.97	18.29	14.21	18.45	17.75	14.72	0.03%	Cluster 44	0.0%
4.13-100	19.98	18.29	14.21	18.45	17.75	14.72	0.03%	Cluster 44	0.0%
4.13-101	20.19	14.57	12.68	15.40	14.29	14.14	0.04%	Cluster 39	0.0%
4.13-102	20.25	17.47	14.53	17.26	16.95	14.70	0.03%	Cluster 43	0.0%
4.13-103	20.25	17.47	14.53	17.26	16.95	14.69	0.03%	Cluster 42	0.0%
4.13-104	20.28	17.75	22.02	16.65	17.06	21.13	0.00%	Cluster 60	0.0%
4.13-105	20.28	17.75	22.02	16.65	17.06	21.13	0.00%	Cluster 60	0.0%
4.13-106	20.30	11.66	12.25	11.79	11.57	13.18	0.06%	Cluster 31	0.0%
4.13-107	20.31	11.66	12.25	11.79	11.57	13.18	0.06%	Cluster 31	0.0%
4.13-108	20.38	14.23	10.97	13.85	13.99	11.25	0.13%	Cluster 24	0.1%
4.13-109	20.39	14.23	10.97	13.85	13.99	11.25	0.13%	Cluster 24	0.1%
4.13-110	20.45	4.54	6.21	4.17	6.25	8.44	0.39%	Cluster 15	0.2%
4.13-111	20.46	4.54	6.21	4.17	6.25	8.44	0.39%	Cluster 15	0.2%
4.13-112	20.58	16.16	12.41	15.43	16.04	12.46	0.08%	Cluster 29	0.0%
4.13-113	20.59	16.16	12.41	15.43	16.04	12.46	0.08%	Cluster 29	0.0%

4.13-114	20.60	5.86	9.95	5.66	5.76	10.55	0.17%	Cluster 22	0.1%
4.13-115	20.61	16.16	12.41	15.43	16.04	12.46	0.08%	Cluster 29	0.0%
4.13-116	20.61	5.86	9.95	5.66	5.76	10.55	0.17%	Cluster 22	0.1%
4.13-117	20.75	17.52	17.29	17.29	17.24	17.68	0.01%	Cluster 56	0.0%
4.13-118	20.76	17.52	17.29	17.29	17.24	17.68	0.01%	Cluster 56	0.0%
4.13-119	20.80	18.69	16.77	18.09	18.13	16.51	0.02%	Cluster 51	0.0%
4.13-120	20.81	18.31	21.23	17.43	17.45	20.38	0.00%	Cluster 58	0.0%
4.13-121	20.81	18.31	21.24	17.43	17.45	20.38	0.00%	Cluster 58	0.0%
4.13-122	20.82	18.69	16.77	18.09	18.13	16.51	0.02%	Cluster 51	0.0%
4.13-123	20.84	11.04	11.29	12.07	11.27	13.44	0.05%	Cluster 34	0.0%
4.13-124	20.88	17.46	15.34	16.96	17.34	15.62	0.02%	Cluster 47	0.0%
4.13-125	20.88	11.04	11.29	12.07	11.27	13.44	0.05%	Cluster 34	0.0%
4.13-126	20.89	17.46	15.34	16.96	17.34	15.62	0.02%	Cluster 47	0.0%
4.13-127	20.92	17.52	17.54	16.90	17.32	17.62	0.01%	Cluster 55	0.0%
4.13-128	20.92	17.52	17.54	16.90	17.32	17.62	0.01%	Cluster 55	0.0%
4.13-129	20.97	15.53	13.67	15.29	15.29	14.09	0.04%	Cluster 38	0.0%
4.13-130	20.97	15.53	13.67	15.29	15.29	14.09	0.04%	Cluster 38	0.0%

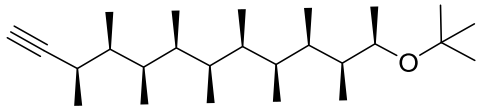

4.15

Table 6.84: Calculated energies (in kJ mol^{-1}), DFT calculated population and conformer population after NOE-refinement for all conformers of **4.15**.

Conformer	$\Delta E^{\text{MMFFs, gas}}$	$\Delta E^{\text{BS1, gas}}$	$\Delta G^{\text{BS1, gas}}$	$\Delta E^{\text{BS2, gas}}$	$\Delta E^{\text{BS1, toluene}}$	$\Delta G_{\text{est.}}^{\text{BS2,toluene}}$	Population (%)/$\Delta G_{\text{est.}}^{\text{BS2,MeOH}}$
4.15-1	0.00	5.82	4.67	5.77	4.11	7.96%	5.82
4.15-2	4.99	0.00	0.00	0.00	0.00	41.85%	0.00
4.15-3	10.31	7.48	5.16	7.54	5.54	4.47%	7.48
4.15-4	10.65	12.00	13.00	11.82	12.14	0.31%	12.00
4.15-5	10.96	10.85	10.52	10.69	10.22	0.67%	10.85
4.15-6	11.78	12.13	13.03	11.92	12.19	0.31%	12.13
4.15-7	11.80	13.95	13.78	14.25	13.62	0.17%	13.95
4.15-8	12.60	10.81	8.18	10.90	7.89	1.73%	10.81
4.15-9	12.66	6.05	8.48	6.04	8.42	1.40%	6.05
4.15-10	13.00	14.39	13.78	14.31	13.09	0.21%	14.39
4.15-11	13.07	14.16	12.02	14.22	11.27	0.44%	14.16
4.15-12	13.16	9.37	7.12	9.56	7.75	1.83%	9.37
4.15-13	13.39	9.58	7.25	9.83	7.20	2.29%	9.58
4.15-14	14.01	7.59	9.41	7.91	9.39	0.94%	7.59
4.15-15	14.29	6.68	2.40	8.05	3.38	10.69%	6.68
4.15-16	14.31	12.75	12.49	13.12	12.77	0.24%	12.75
4.15-17	14.39	8.59	8.40	9.14	8.64	1.28%	8.59
4.15-18	14.92	12.49	7.09	12.69	7.25	2.24%	12.49
4.15-19	15.07	13.87	14.58	14.09	14.19	0.14%	13.87
4.15-20	15.16	8.69	7.80	8.84	7.89	1.73%	8.69
4.15-21	15.22	6.05	8.48	6.04	8.42	1.40%	6.05
4.15-22	15.30	10.38	9.10	11.17	10.18	0.69%	10.38

4.15-23	15.45	17.01	14.83	17.33	15.13	0.09%	17.01
4.15-24	15.63	16.43	13.74	16.63	13.56	0.17%	16.43
4.15-25	15.66	13.01	18.40	13.11	18.04	0.03%	13.01
4.15-26	15.83	8.59	8.40	9.14	8.64	0.00%	8.59
4.15-27	15.90	12.09	12.04	12.18	12.20	0.30%	12.09
4.15-28	16.00	8.68	9.60	9.63	10.34	0.64%	8.68
4.15-29	16.12	12.09	13.71	11.93	13.50	0.18%	12.09
4.15-30	16.70	16.68	13.16	17.37	13.41	0.19%	16.68
4.15-31	16.84	9.32	10.59	9.48	10.58	0.58%	9.32
4.15-32	17.02	16.68	13.16	17.37	13.41	0.19%	16.68
4.15-33	17.22	14.52	13.03	14.78	13.84	0.16%	14.52
4.15-34	17.48	12.56	13.05	12.85	12.95	0.22%	12.56
4.15-35	17.66	7.67	11.46	7.77	12.05	0.32%	7.67
4.15-36	17.86	2.70	6.59	3.45	7.89	1.73%	2.70
4.15-37	17.86	10.36	11.64	10.43	11.65	0.38%	10.36
4.15-38	17.98	11.90	7.11	13.40	8.16	1.55%	11.90
4.15-39	18.06	22.63	21.17	23.07	20.83	0.01%	22.63
4.15-40	18.21	13.59	12.92	13.61	13.23	0.20%	13.59
4.15-41	18.31	16.02	18.95	16.31	19.15	0.02%	16.02
4.15-42	18.32	12.39	14.90	12.57	14.65	0.11%	12.39
4.15-43	18.37	11.29	13.71	11.62	13.61	0.17%	11.29
4.15-44	18.41	2.70	6.59	3.45	7.89	0.00%	2.70
4.15-45	18.45	12.51	8.41	13.62	9.66	0.84%	12.51
4.15-46	18.57	3.96	10.47	4.28	10.40	0.63%	3.96
4.15-47	18.72	7.00	11.79	8.16	12.59	0.26%	7.00
4.15-48	19.05	11.26	11.21	11.76	11.16	0.46%	11.26
4.15-49	19.24	15.71	16.15	15.74	16.41	0.06%	15.71
4.15-50	19.42	4.54	14.00	4.93	14.36	0.13%	4.54
4.15-51	19.47	8.83	8.61	9.82	9.14	1.04%	8.83
4.15-52	19.51	23.75	18.43	24.63	18.44	0.02%	23.75
4.15-53	19.51	8.83	8.61	9.82	9.15	1.04%	8.83

4.15-54	19.60	18.79	19.31	18.70	18.43	0.02%	18.79
4.15-55	19.76	15.09	13.31	15.12	13.53	0.18%	15.09
4.15-56	19.77	16.12	15.77	16.24	15.42	0.08%	16.12
4.15-57	20.26	10.62	5.00	11.78	5.84	3.97%	10.62
4.15-58	20.39	13.08	16.59	13.19	16.53	0.05%	13.08
4.15-59	20.43	16.27	14.10	16.62	14.04	0.14%	16.27
4.15-60	20.48	13.68	11.45	14.03	11.51	0.40%	13.68
4.15-61	20.62	19.48	15.99	19.96	15.37	0.08%	19.48
4.15-62	20.77	13.51	12.94	14.21	13.43	0.18%	13.51
4.15-63	20.91	15.52	13.18	15.73	13.78	0.16%	15.52

Population refinement of *meso* compounds (4.11, 4.12 and 4.13) based on ^{1}H-^{1}H distances

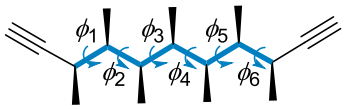

4.11

Table 6.85: Dihedral cluster of **4.11** with initial DFT energy derived population, NOE-refined $\Delta\Delta G$ (in kJ mol^{-1}) and NOE-refined population for each cluster.

Cluster	Φ_1	Φ_2	Φ_3	Φ_4	Φ_5	Φ_6	Initial Population	NOE–refined $\Delta\Delta G$/kJ mol^{-1} $\Sigma(\Delta\Delta G)^2$ =100	NOE–Refined Population $\Sigma(\Delta\Delta G)^2$ =100
1	*ap*	*g*+	*ap*	*g*+	*ap*	*g*+	62.95%	0.83	44.62%
	g−	*ap*	*g*−	*ap*	*g*−	*ap*			
2	*ap*	*g*+	*ap*	*g*+	*ap*	*g*−	17.94%	4.69	2.68%
	g+	*ap*	*g*−	*ap*	*g*−	*ap*			
3	*g*−	*ap*	*g*−	*ap*	−*ac*	*g*−	6.16%	2.28	2.43%
	g+	+*ac*	*ap*	*g*+	*ap*	*g*+			
4	*g*−	+*ac*	*ap*	*g*+	*ap*	*g*+	2.86%	−5.38	24.87%
	g−	*ap*	*g*−	*ap*	−*ac*	*g*+			
5	*g*−	*ap*	−*ac*	*g*+	*ap*	*g*+	1.91%	0.60	1.48%
	g−	*ap*	*g*−	+*ac*	*ap*	*g*+			
6	*g*−	*ap*	*g*−	*ap*	*g*−	*g*−	1.88%	1.21	1.14%
	g+	*g*+	*ap*	*g*+	*ap*	*g*+			
7	*g*+	+*ac*	*g*−	*ap*	*g*−	*ap*	1.67%	−5.98	18.49%
	ap	*g*+	*ap*	*g*+	−*ac*	*g*−			
8	*ap*	*g*+	*ap*	+*ac*	*ap*	*g*+	1.04%	0.13	0.97%
	g−	*ap*	−*ac*	*ap*	*g*−	*ap*			
9	*g*−	*ap*	*g*−	*ap*	−*ac*	*ap*	0.91%	0.74	0.67%
	ap	+*ac*	*ap*	*g*+	*ap*	*g*+			

10	*g+*	*+ac*	*ap*	*g+*	*ap*	*g−*	0.67%	1.25	0.40%
	g+	*ap*	*g−*	*ap*	*−ac*	*ap*			
11	*ap*	*g+*	*ap*	*g+*	*−ac*	*ap*	0.44%	−0.15	0.47%
	ap	*+ac*	*g−*	*ap*	*g−*	*ap*			
12	*ap*	*ap*	*g−*	*ap*	*g−*	*ap*	0.40%	0.49	0.33%
	g−	*ap*	*g−*	*+ac*	*ap*	*g−*			
13	*g+*	*ap*	*−ac*	*g+*	*ap*	*g+*	0.23%	0.41	0.19%
	g−	*ap*	*g−*	*ap*	*g−*	*g+*			
14	*g−*	*g+*	*ap*	*g+*	*ap*	*g+*	0.23%	−0.50	0.28%
	ap	*g+*	*ap*	*+ac*	*g−*	*ap*			
15	*ap*	*g+*	*−ac*	*ap*	*g−*	*ap*	0.32%	−1.63	0.61%
	ap	*g+*	*ap*	*g+*	*ap*	*ap*			
16	*g+*	*ap*	*g−*	*ap*	*−ac*	*g+*	0.14%	0.25	0.12%
	g−	*+ac*	*ap*	*g+*	*ap*	*g−*			
17	*ap*	*g+*	*ap*	*+ac*	*ap*	*g−*	0.12%	0.20	0.11%
	g+	*ap*	*−ac*	*ap*	*g−*	*ap*			
18	*ap*	*g−*	*ap*	*g+*	*ap*	*g+*	0.06%	0.13	0.06%
	g−	*ap*	*g−*	*ap*	*g+*	*ap*			
19	*g+*	*ap*	*g−*	*ap*	*−ac*	*ap*	0.06%	0.18	0.05%
	ap	*+ac*	*ap*	*g+*	*ap*	*g−*			
20	*g−*	*ap*	*g−*	*ap*	*ap*	*ap*	0.01%	0.02	0.01%
	ap	*ap*	*ap*	*g+*	*ap*	*g+*			
21	*ap*	*g+*	*ap*	*+ac*	*ap*	*ap*	0.01%	0.02	0.01%
	ap	*ap*	*−ac*	*ap*	*g−*	*ap*			

Cluster	NOE−refined $\Delta\Delta G$/kJ mol^{-1} $\Sigma(\Delta\Delta G)^2$=225	NOE−Refined Population $\Sigma(\Delta\Delta G)^2$=225	NOE−refined $\Delta\Delta G$/kJ mol^{-1} $\Sigma(\Delta\Delta G)^2$=625	NOE−Refined Population $\Sigma(\Delta\Delta G)^2$=625
1	2.41	23.13%	0.89	18.75%
2	5.76	1.71%	8.71	0.23%
3	2.03	2.64%	4.40	0.44%
4	−6.55	39.26%	−6.65	17.88%
5	1.67	0.94%	−0.18	0.87%
6	0.91	1.27%	−1.33	1.37%
7	−3.74	7.34%	−7.10	12.50%
8	1.59	0.53%	2.82	0.14%
9	1.63	0.46%	4.61	0.06%
10	1.58	0.34%	4.30	0.05%
11	0.72	0.32%	2.94	0.06%
12	1.24	0.24%	3.42	0.04%
13	0.76	0.17%	2.20	0.04%
14	−1.40	0.39%	−14.00	27.54%
15	−10.41	20.93%	−12.34	19.93%
16	0.41	0.11%	1.97	0.03%
17	0.54	0.09%	1.77	0.02%
18	0.33	0.05%	1.02	0.02%
19	0.36	0.05%	1.81	0.01%
20	0.06	0.01%	0.35	0.00%
21	0.08	0.01%	0.39	0.00%

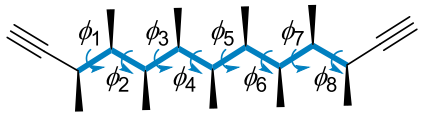

4.12

Table 6.86: Dihedral cluster of **4.12** with initial DFT energy derived population, NOE-refined $\Delta\Delta G$ (in kJ mol^{-1}) and NOE-refined population for each cluster.

Cluster	Φ_1	Φ_2	Φ_3	Φ_4	Φ_5	Φ_6	Φ_7	Φ_8	Initial Population	NOE–refined $\Delta\Delta G$/kJ mol^{-1}	NOE–Refined Population
1	*ap*	*g*+	*ap*	*g*+	*ap*	*g*+	*ap*	*g*+	48.48%	−1.33	39.52%
	g−	*ap*	*g*−	*ap*	*g*−	*ap*	*g*−	*ap*			
2	*g*−	*ap*	*g*−	+*ac*	*ap*	*g*+	*ap*	*g*+	6.85%	0.21	3.00%
	g−	*ap*	*g*−	*ap*	−*ac*	*g*+	*ap*	*g*+			
3	*g*+	+*ac*	*ap*	*g*+	*ap*	*g*+	*ap*	*g*+	8.64%	2.72	1.38%
	g−	*ap*	*g*−	*ap*	*g*−	*ap*	−*ac*	*g*−			
4	*g*−	*ap*	−*ac*	*g*+	*ap*	*g*+	*ap*	*g*+	5.26%	−4.98	18.77%
	g−	*ap*	*g*−	*ap*	*g*−	+*ac*	*ap*	*g*+			
5	*ap*	*g*+	*ap*	*ap*	*g*−	+*ac*	*ap*	*g*+	4.21%	−6.21	24.67%
	g−	*ap*	−*ac*	*g*+	*ap*	*ap*	*g*−	*ap*			
6	*g*−	+*ac*	*ap*	*g*+	*ap*	*g*+	*ap*	*g*+	2.41%	0.01	1.14%
	g−	*ap*	*g*−	*ap*	*g*−	*ap*	−*ac*	*g*+			
7	*ap*	*g*+	*ap*	+*ac*	*ap*	*g*+	*ap*	*g*+	3.35%	2.95	0.49%
	g−	*ap*	*g*−	*ap*	−*ac*	*ap*	*g*−	*ap*			
8	*ap*	*g*+	*ap*	*g*+	*ap*	*g*+	*ap*	*g*−	5.96%	−1.68	5.59%
	g+	*ap*	*g*−	*ap*	*g*−	*ap*	*g*−	*ap*			
9	*ap*	*g*+	*ap*	*ap*	*g*−	+*ac*	*ap*	*g*−	1.99%	1.96	0.43%
	g+	*ap*	−*ac*	*g*+	*ap*	*ap*	*g*−	*ap*			
10	*ap*	*g*+	*ap*	*ap*	*g*−	*g*+	*ap*	*g*+	1.56%	1.74	0.37%
	g−	*ap*	*g*−	*g*+	*ap*	*ap*	*g*−	*ap*			

11	*g*−	*ap*	−*ac*	*g*+	*g*+	*g*+	*ap*	*g*+	0.80%	−0.51	0.47%
	g−	*ap*	*g*−	*g*−	*g*−	+*ac*	*ap*	*g*+			
12	*ap*	*g*+	*ap*	*g*+	*ap*	+*ac*	*ap*	*g*+	1.35%	−0.08	0.66%
	g−	*ap*	−*ac*	*ap*	*g*−	*ap*	*g*−	*ap*			
13	*g*+	*g*+	*ap*	*g*+	*ap*	*g*+	*ap*	*g*+	0.90%	1.38	0.25%
	g−	*ap*	*g*−	*ap*	*g*−	*ap*	*g*−	*g*−			
14	*ap*	*g*+	*ap*	+*ac*	*g*−	*ap*	*g*−	*ap*	1.26%	2.01	0.27%
	ap	*g*+	*ap*	*g*+	−*ac*	*ap*	*g*−	*ap*			
15	*ap*	+*ac*	*ap*	*g*+	*ap*	*g*+	*ap*	*g*+	1.07%	−0.37	0.59%
	g−	*ap*	*g*−	*ap*	*g*−	*ap*	−*ac*	*ap*			
16	*g*+	*ap*	*ap*	*g*+	*ap*	*g*+	*ap*	*g*+	0.90%	0.49	0.35%
	g−	*ap*	*g*−	*ap*	*g*−	*ap*	*ap*	*g*−			
17	*ap*	*g*+	*ap*	*ap*	*g*+	*g*+	*ap*	*g*+	0.91%	0.62	0.34%
	g−	*ap*	*g*−	*g*−	*ap*	*ap*	*g*−	*ap*			
18	*ap*	*g*+	−*ac*	*g*+	*ap*	*ap*	*g*−	*ap*	1.65%	0.94	0.54%
	ap	*g*+	*ap*	*ap*	*g*−	+*ac*	*g*−	*ap*			
19	*g*+	+*ac*	*ap*	*g*+	*ap*	*g*+	*ap*	*g*−	0.30%	0.48	0.12%
	g+	*ap*	*g*−	*ap*	*g*−	*ap*	−*ac*	*g*−			
20	*g*+	+*ac*	*g*−	+*ac*	*ap*	*g*+	*ap*	*g*+	0.22%	0.16	0.10%
	g−	*ap*	*g*−	*ap*	−*ac*	*g*+	−*ac*	*g*−			
21	*ap*	+*ac*	*g*−	*ap*	*g*−	*ap*	*g*−	*ap*	0.20%	−0.44	0.11%
	ap	*g*+	*ap*	*g*+	*ap*	*g*+	−*ac*	*ap*			
22	*g*−	*ap*	*g*−	*ap*	*g*−	*ap*	*g*−	*g*+	0.15%	−0.12	0.07%
	g−	*g*+	*ap*	*g*+	*ap*	*g*+	*ap*	*g*+			
23	*ap*	*ap*	*g*−	*ap*	*g*−	*ap*	*g*−	*ap*	0.31%	−0.57	0.19%
	ap	*g*+	*ap*	*g*+	*ap*	*g*+	*ap*	*ap*			
24	*ap*	*g*+	−*ac*	*ap*	*g*−	*ap*	*g*−	*ap*	0.21%	−0.24	0.11%
	ap	*g*+	*ap*	*g*+	*ap*	+*ac*	*g*−	*ap*			

25	*ap*	*g+*	*ap*	*ap*	*+ac*	*g+*	*ap*	*g+*	0.13%	−0.09	0.07%
	g−	*ap*	*g−*	*−ac*	*ap*	*ap*	*g−*	*ap*			
26	*ap*	*g+*	*ap*	*+ac*	*ap*	*g+*	*ap*	*g−*	0.19%	0.52	0.07%
	g+	*ap*	*g−*	*ap*	*−ac*	*ap*	*g−*	*ap*			
27	*ap*	*g+*	*ap*	*ap*	*g−*	*ap*	*ap*	*g+*	0.10%	0.01	0.05%
	g−	*ap*	*ap*	*g+*	*ap*	*ap*	*g−*	*ap*			
28	*ap*	*g+*	*ap*	*ap*	*g−*	*ap*	*g−*	*ap*	0.13%	0.06	0.06%
	ap	*g+*	*ap*	*g+*	*ap*	*ap*	*g−*	*ap*			
29	*ap*	*g+*	*ap*	*ap*	*g−*	*ap*	*−ac*	*g−*	0.10%	0.10	0.04%
	g+	*+ac*	*ap*	*g+*	*ap*	*ap*	*g−*	*ap*			
30	*ap*	*g+*	*ap*	*g+*	*ap*	*+ac*	*ap*	*g−*	0.08%	0.03	0.04%
	g+	*ap*	*−ac*	*ap*	*g−*	*ap*	*g−*	*ap*			
31	*ap*	*ap*	*ap*	*g+*	*ap*	*g+*	*ap*	*g+*	0.06%	−0.11	0.03%
	g−	*ap*	*g−*	*ap*	*g−*	*ap*	*ap*	*ap*			
32	*ap*	*g−*	*ap*	*g+*	*ap*	*g+*	*ap*	*g+*	0.06%	0.18	0.03%
	g−	*ap*	*g−*	*ap*	*g−*	*ap*	*g+*	*ap*			
33	*ap*	*+ac*	*ap*	*g+*	*ap*	*g+*	*ap*	*g−*	0.06%	0.05	0.03%
	g+	*ap*	*g−*	*ap*	*g−*	*ap*	*−ac*	*ap*			
34	*ap*	*g+*	*ap*	*ap*	*g+*	*g+*	*ap*	*g−*	0.06%	0.09	0.03%
	g+	*ap*	*g−*	*g−*	*ap*	*ap*	*g−*	*ap*			
35	*ap*	*g+*	*ap*	*ap*	*+ac*	*g+*	*ap*	*g−*	0.04%	−0.01	0.02%
	g+	*ap*	*g−*	*−ac*	*ap*	*ap*	*g−*	*ap*			
36	*ap*	*ap*	*−ac*	*g+*	*ap*	*ap*	*g−*	*ap*	0.05%	0.00	0.02%
	ap	*g+*	*ap*	*ap*	*g−*	*+ac*	*ap*	*ap*			
37	*ap*	*g+*	*ap*	*g+*	*ap*	*+ac*	*g+*	*ap*	0.01%	0.04	0.01%
	ap	*g−*	*−ac*	*ap*	*g−*	*ap*	*g−*	*ap*			
38	*ap*	*+ac*	*ap*	*g+*	*ap*	*ap*	*g−*	*ap*	0.01%	0.00	0.00%
	ap	*g+*	*ap*	*ap*	*g−*	*ap*	*−ac*	*ap*			

39	*ap*	*ap*	*−ac*	*ap*	*g−*	*ap*	*g−*	*ap*	0.01%	0.00	0.00%
	ap	*g+*	*ap*	*g+*	*ap*	*+ac*	*ap*	*ap*			

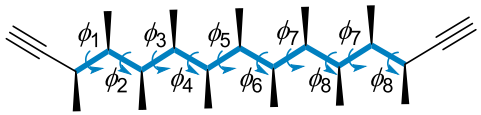

4.13

Table 6.87: Dihedral cluster of **4.13** with initial DFT energy derived population, NOE-refined $\Delta\Delta G$ (in kJ mol^{-1}) and NOE-refined population for each cluster.

Cluster	Φ_1	Φ_2	Φ_3	Φ_4	Φ_5	Φ_6	Φ_7	Φ_8	Φ9	Φ_{10}	Initial Population	NOE−refined $\Delta\Delta G$/kJ mol^{-1}	NOE−Refined
1	*g−*	*ap*	*g−*	*ap*	*g−*	*ap*	*g−*	*ap*	*g−*	*ap*	23.81%	−2.04	29.58%
	ap	*g+*	*ap*	*g+*	*ap*	*g+*	*ap*	*g+*	*ap*	*g+*			
2	*g−*	*ap*	*g−*	*ap*	*−ac*	*g+*	*ap*	*g+*	*ap*	*g+*	18.72%	2.72	3.40%
	g−	*ap*	*g−*	*ap*	*g−*	*+ac*	*ap*	*g+*	*ap*	*g+*			
3	*g−*	*ap*	*g−*	*ap*	*ap*	*g+*	*−ac*	*g+*	*ap*	*g+*	22.73%	3.86	2.60%
	g−	*ap*	*g−*	*+ac*	*g−*	*ap*	*ap*	*g+*	*ap*	*g+*			
4	*g−*	*ap*	*g−*	*ap*	*ap*	*g+*	*−ac*	*ap*	*g−*	*ap*	5.69%	0.24	2.82%
	ap	*g+*	*ap*	*+ac*	*g−*	*ap*	*ap*	*g+*	*ap*	*g+*			
5	*g−*	*ap*	*g−*	*ap*	*g−*	*ap*	*g−*	*+ac*	*ap*	*g+*	5.01%	0.23	2.50%
	g−	*ap*	*−ac*	*g+*	*ap*	*g+*	*ap*	*g+*	*ap*	*g+*			
6	*g−*	*ap*	*g−*	*ap*	*−ac*	*g+*	*−ac*	*g+*	*ap*	*g+*	3.44%	0.72	1.40%
	g−	*ap*	*g−*	*+ac*	*g−*	*+ac*	*ap*	*g+*	*ap*	*g+*			
7	*g−*	*ap*	*g−*	*+ac*	*g−*	*+ac*	*g−*	*ap*	*g−*	*ap*	2.93%	−8.46	48.66%
	ap	*g+*	*ap*	*g+*	*−ac*	*g+*	*−ac*	*g+*	*ap*	*g+*			
8	*g−*	*+ac*	*g−*	*+ac*	*ap*	*g+*	*ap*	*g+*	*ap*	*g+*	2.09%	0.01	1.14%
	g−	*ap*	*g−*	*ap*	*g−*	*ap*	*−ac*	*g+*	*−ac*	*g+*			

9	*ap*	*g+*	*ap*	*g+*	*ap*	*g+*	*ap*	*g+*	*ap*	*g−*	1.77%	0.62	0.75%
	g+	*ap*	*g−*	*ap*	*g−*	*ap*	*g−*	*ap*	*g−*	*ap*			
10	*g−*	*ap*	*g−*	*ap*	*g−*	*ap*	*g−*	*ap*	*−ac*	*g−*	1.40%	0.06	0.75%
	g+	*+ac*	*ap*	*g+*	*ap*	*g+*	*ap*	*g+*	*ap*	*g+*			
11	*g+*	*+ac*	*g−*	*ap*	*g−*	*ap*	*g−*	*ap*	*g−*	*ap*	2.33%	0.70	0.96%
	ap	*g+*	*ap*	*g+*	*ap*	*g+*	*ap*	*g+*	*−ac*	*g−*			
12	*g+*	*+ac*	*ap*	*+ac*	*g−*	*ap*	*ap*	*g+*	*ap*	*g+*	1.14%	0.12	0.59%
	g−	*ap*	*g−*	*ap*	*ap*	*g+*	*−ac*	*ap*	*−ac*	*g−*			
13	*g−*	*ap*	*g−*	*ap*	*g−*	*ap*	*g−*	*ap*	*−ac*	*g+*	0.98%	−0.29	0.60%
	g−	*+ac*	*ap*	*g+*	*ap*	*g+*	*ap*	*g+*	*ap*	*g+*			
14	*ap*	*g+*	*ap*	*g+*	*−ac*	*g+*	*−ac*	*g+*	*−ac*	*g−*	0.82%	0.06	0.44%
	g+	*+ac*	*g−*	*+ac*	*g−*	*+ac*	*g−*	*ap*	*g−*	*ap*			
15	*g−*	*ap*	*g−*	*ap*	*ap*	*g+*	*−ac*	*ap*	*−ac*	*g+*	0.79%	−0.05	0.44%
	g−	*+ac*	*ap*	*+ac*	*g−*	*ap*	*ap*	*g+*	*ap*	*g+*			
16	*g−*	*ap*	*g−*	*ap*	*ap*	*g+*	*g−*	*ap*	*g−*	*ap*	0.57%	−0.05	0.32%
	ap	*g+*	*ap*	*g+*	*g−*	*ap*	*ap*	*g+*	*ap*	*g+*			
17	*g−*	*ap*	*g−*	*ap*	*ap*	*g+*	*ap*	*g+*	*ap*	*g+*	0.54%	0.24	0.27%
	g−	*ap*	*g−*	*ap*	*g−*	*ap*	*ap*	*g+*	*ap*	*g+*			
18	*ap*	*g+*	*ap*	*g+*	*ap*	*+ac*	*g−*	*ap*	*g−*	*ap*	0.43%	−0.01	0.23%
	ap	*g+*	*ap*	*g+*	*−ac*	*ap*	*g−*	*ap*	*g−*	*ap*			
19	*ap*	*+ac*	*ap*	*g+*	*ap*	*g+*	*ap*	*g+*	*ap*	*g+*	0.36%	−0.02	0.20%
	g−	*ap*	*g−*	*ap*	*g−*	*ap*	*g−*	*ap*	*−ac*	*ap*			
20	*ap*	*g+*	*ap*	*g+*	*ap*	*g+*	*−ac*	*ap*	*g−*	*ap*	0.36%	0.03	0.19%
	ap	*g+*	*ap*	*+ac*	*g−*	*ap*	*g−*	*ap*	*g−*	*ap*			
21	*g+*	*ap*	*g−*	*ap*	*ap*	*g+*	*−ac*	*ap*	*g−*	*ap*	0.34%	0.13	0.18%
	ap	*g+*	*ap*	*+ac*	*g−*	*ap*	*ap*	*g+*	*ap*	*g−*			
22	*g+*	*+ac*	*g−*	*+ac*	*g−*	*ap*	*ap*	*g+*	*ap*	*g+*	0.34%	0.31	0.16%
	g−	*ap*	*g−*	*ap*	*ap*	*g+*	*−ac*	*g+*	*−ac*	*g−*			

23	*ap*	*g+*	*ap*	*+ac*	*ap*	*g+*	*ap*	*g+*	*ap*	*g+*	0.33%	0.11	0.17%
	g−	*ap*	*g−*	*ap*	*g−*	*ap*	*−ac*	*ap*	*g−*	*ap*			
24	*g+*	*ap*	*g−*	*ap*	*g−*	*+ac*	*ap*	*g+*	*ap*	*g+*	0.25%	0.19	0.13%
	g−	*ap*	*g−*	*ap*	*−ac*	*g+*	*ap*	*g+*	*ap*	*g−*			
25	*g+*	*ap*	*g−*	*ap*	*ap*	*g+*	*−ac*	*g+*	*ap*	*g+*	0.20%	0.17	0.10%
	g−	*ap*	*g−*	*+ac*	*g−*	*ap*	*ap*	*g+*	*ap*	*g−*			
26	*ap*	*+ac*	*g−*	*+ac*	*g−*	*+ac*	*g−*	*ap*	*g−*	*ap*	0.20%	−0.02	0.11%
	ap	*g+*	*ap*	*g+*	*−ac*	*g+*	*−ac*	*g+*	*−ac*	*ap*			
27	*g−*	*ap*	*g−*	*ap*	*g−*	*ap*	*g−*	*ap*	*g−*	*g−*	0.17%	−0.03	0.09%
	g+	*g+*	*ap*	*g+*	*ap*	*g+*	*ap*	*g+*	*ap*	*g+*			
28	*ap*	*g+*	*ap*	*g+*	*ap*	*+ac*	*ap*	*g+*	*ap*	*g+*	0.16%	0.04	0.08%
	g−	*ap*	*g−*	*ap*	*−ac*	*ap*	*g−*	*ap*	*g−*	*ap*			
29	*g+*	*+ac*	*g−*	*ap*	*g−*	*ap*	*g−*	*ap*	*−ac*	*g−*	0.23%	0.11	0.12%
	g+	*+ac*	*ap*	*g+*	*ap*	*g+*	*ap*	*g+*	*−ac*	*g−*			
30	*ap*	*g+*	*ap*	*+ac*	*g−*	*+ac*	*g−*	*+ac*	*g−*	*ap*	0.14%	−0.01	0.08%
	ap	*g+*	*−ac*	*g+*	*−ac*	*g+*	*−ac*	*ap*	*g−*	*ap*			
31	*g−*	*ap*	*g−*	*ap*	*g−*	*ap*	*−ac*	*g+*	*−ac*	*g−*	0.12%	0.05	0.06%
	g+	*+ac*	*g−*	*+ac*	*ap*	*g+*	*ap*	*g+*	*ap*	*g+*			
32	*g+*	*ap*	*g−*	*ap*	*g−*	*ap*	*g−*	*ap*	*−ac*	*g−*	0.11%	0.06	0.06%
	g+	*+ac*	*ap*	*g+*	*ap*	*g+*	*ap*	*g+*	*ap*	*g−*			
33	*ap*	*g+*	*ap*	*g+*	*ap*	*g+*	*ap*	*g+*	*−ac*	*ap*	0.11%	0.03	0.06%
	ap	*+ac*	*g−*	*ap*	*g−*	*ap*	*g−*	*ap*	*g−*	*ap*			
34	*g−*	*ap*	*−ac*	*g+*	*ap*	*g+*	*−ac*	*g+*	*ap*	*g+*	0.10%	−0.02	0.06%
	g−	*ap*	*g−*	*+ac*	*g−*	*ap*	*g−*	*+ac*	*ap*	*g+*			
35	*g−*	*ap*	*g−*	*ap*	*ap*	*g−*	*g−*	*ap*	*g−*	*ap*	0.15%	−0.02	0.09%
	ap	*g+*	*ap*	*g+*	*g+*	*ap*	*ap*	*g+*	*ap*	*g+*			
36	*g−*	*ap*	*−ac*	*ap*	*g−*	*ap*	*g−*	*ap*	*g−*	*ap*	0.10%	−0.05	0.06%
	ap	*g+*	*ap*	*g+*	*ap*	*g+*	*ap*	*+ac*	*ap*	*g+*			

37	*g+*	*ap*	*−ac*	*g+*	*ap*	*g+*	*ap*	*g+*	*ap*	*g+*	0.10%	0.04	0.05%
	g−	*ap*	*g−*	*ap*	*g−*	*ap*	*g−*	*+ac*	*ap*	*g−*			
38	*g−*	*ap*	*g−*	*ap*	*g−*	*+ac*	*ap*	*g+*	*ap*	*g−*	0.08%	0.06	0.04%
	g+	*ap*	*g−*	*ap*	*−ac*	*g+*	*ap*	*g+*	*ap*	*g+*			
39	*g−*	*ap*	*g−*	*+ac*	*g−*	*+ac*	*g−*	*+ac*	*ap*	*g−*	0.12%	0.02	0.06%
	g+	*ap*	*−ac*	*g+*	*−ac*	*g+*	*−ac*	*g+*	*ap*	*g+*			
40	*g+*	*ap*	*g−*	*ap*	*−ac*	*ap*	*g−*	*ap*	*g−*	*ap*	0.07%	0.04	0.04%
	ap	*g+*	*ap*	*g+*	*ap*	*+ac*	*ap*	*g+*	*ap*	*g−*			
41	*ap*	*g+*	*ap*	*g+*	*ap*	*g+*	*ap*	*g+*	*ap*	*+ac*	0.07%	0.00	0.04%
	−ac	*ap*	*g−*	*ap*	*g−*	*ap*	*g−*	*ap*	*g−*	*ap*			
42	*g−*	*ap*	*g−*	*ap*	*ap*	*g+*	*ap*	*+ac*	*g−*	*ap*	0.06%	0.00	0.03%
	ap	*g+*	*−ac*	*ap*	*g−*	*ap*	*ap*	*g+*	*ap*	*g+*			
43	*ap*	*g+*	*ap*	*g+*	*ap*	*g+*	*−ac*	*g+*	*−ac*	*ap*	0.08%	0.02	0.04%
44	*g−*	*+ac*	*ap*	*+ac*	*g−*	*ap*	*g−*	*ap*	*g−*	*ap*	0.06%	−0.02	0.03%
	ap	*g+*	*ap*	*g+*	*ap*	*g+*	*−ac*	*ap*	*−ac*	*g+*			
45	*ap*	*g+*	*ap*	*g+*	*ap*	*g+*	*−ac*	*ap*	*−ac*	*g−*	0.06%	0.00	0.03%
	g+	*+ac*	*ap*	*+ac*	*g−*	*ap*	*g−*	*ap*	*g−*	*ap*			
46	*g−*	*ap*	*g−*	*ap*	*g−*	*ap*	*g−*	*+ac*	*g+*	*ap*	0.05%	0.04	0.03%
	ap	*g−*	*−ac*	*g+*	*ap*	*g+*	*ap*	*g+*	*ap*	*g+*			
47	*g+*	*+ac*	*ap*	*+ac*	*ap*	*g+*	*ap*	*g+*	*ap*	*g+*	0.04%	0.01	0.02%
	g−	*ap*	*g−*	*ap*	*g−*	*ap*	*−ac*	*ap*	*−ac*	*g−*			
48	*ap*	*g+*	*ap*	*g+*	*ap*	*g+*	*ap*	*+ac*	*ap*	*g−*	0.04%	0.00	0.02%
	g+	*ap*	*−ac*	*ap*	*g−*	*ap*	*g−*	*ap*	*g−*	*ap*			
49	*ap*	*g+*	*−ac*	*ap*	*g−*	*ap*	*g−*	*ap*	*g−*	*ap*	0.04%	−0.02	0.02%
	ap	*g+*	*ap*	*g+*	*ap*	*g+*	*ap*	*+ac*	*g−*	*ap*			
50	*g−*	*g+*	*ap*	*g+*	*ap*	*g+*	*ap*	*g+*	*ap*	*g+*	0.03%	−0.02	0.02%
	g−	*ap*	*g−*	*ap*	*g−*	*ap*	*g−*	*ap*	*g−*	*g+*			
	ap	*+ac*	*ap*	*g+*	*ap*	*g+*	*ap*	*g+*	*ap*	*g−*			

51	*g+*	*ap*	*g−*	*ap*	*g−*	*ap*	*g−*	*ap*	*−ac*	*ap*	0.03%	0.01	0.02%
52	*−ac*	*ap*	*g−*	*ap*	*ap*	*g+*	*−ac*	*ap*	*g−*	*ap*	0.02%	0.00	0.01%
	ap	*g+*	*ap*	*+ac*	*g−*	*ap*	*ap*	*g+*	*ap*	*+ac*			
53	*ap*	*g+*	*ap*	*+ac*	*ap*	*g+*	*ap*	*g+*	*ap*	*g−*	0.02%	0.02	0.01%
	g+	*ap*	*g−*	*ap*	*g−*	*ap*	*−ac*	*ap*	*g−*	*ap*			
54	*ap*	*g+*	*ap*	*g+*	*g+*	*g+*	*−ac*	*ap*	*g−*	*ap*	0.02%	−0.01	0.01%
	ap	*g+*	*ap*	*+ac*	*g−*	*g−*	*g−*	*ap*	*g−*	*ap*			
55	*g−*	*ap*	*g−*	*ap*	*g−*	*ap*	*ap*	*g+*	*ap*	*g−*	0.02%	0.02	0.01%
	g+	*ap*	*g−*	*ap*	*ap*	*g+*	*ap*	*g+*	*ap*	*g+*			
56	*g−*	*ap*	*−ac*	*ap*	*g−*	*ap*	*ap*	*g+*	*ap*	*g+*	0.02%	0.00	0.01%
	g−	*ap*	*g−*	*ap*	*ap*	*g+*	*ap*	*+ac*	*ap*	*g+*			
57	*−ac*	*ap*	*−ac*	*g+*	*ap*	*g+*	*ap*	*g+*	*ap*	*g+*	0.01%	0.00	0.00%
	g−	*ap*	*g−*	*ap*	*g−*	*ap*	*g−*	*+ac*	*ap*	*+ac*			
58	*ap*	*g+*	*ap*	*g+*	*ap*	*g+*	*ap*	*+ac*	*g+*	*ap*	0.01%	0.00	0.00%
	ap	*g−*	*−ac*	*ap*	*g−*	*ap*	*g−*	*ap*	*g−*	*ap*			
59	*−ac*	*ap*	*−ac*	*ap*	*g−*	*ap*	*g−*	*ap*	*g−*	*ap*	0.01%	0.00	0.00%
	ap	*g+*	*ap*	*g+*	*ap*	*g+*	*ap*	*+ac*	*ap*	*+ac*			
60	*ap*	*g+*	*ap*	*g+*	*g+*	*ap*	*ap*	*g+*	*ap*	*g−*	0.00%	0.00	0.00%
	g+	*ap*	*g−*	*ap*	*ap*	*g−*	*g−*	*ap*	*g−*	*ap*			
61	*−ac*	*ap*	*g−*	*ap*	*−ac*	*ap*	*g−*	*ap*	*g−*	*ap*	0.00%	0.00	0.00%
	ap	*g+*	*ap*	*g+*	*ap*	*+ac*	*ap*	*g+*	*ap*	*+ac*			

NMR procedures

All NMR spectra were recorded in toluene-d_6.^{1}H-^{1}H scalar coupling constants were measured manually from multiplets in ^{1}H spectra. ^{1}H-^{13}C scalar coupling constants of were measured from the Accordion In-Phase and Anti Phase (IPAP) HSQMBC NMR spectra (12 scans, 1600 f1 increments and 8192 t2 data points, f1 spectra width 160.3 ppm (20161Hz), f2 spectra width 10 ppm (5005Hz), matching J_{LR} from 3Hz to 8 Hz.)[174] The spectra were processed using methods as discussed in the experimental section of Chapter 2.

The interproton distances of were determined using Equation 6.9[52], the 1D DPFGSE NOESY and 1D chemical shift selective filtered (CSSF) NOESY. PANIC was applied as discussed previously using the integrations in Table 6.88.

Table 6.88: A summary of PANIC integration values used in this study. Protons being irradiated are highlighted in blue.

Protons being irradiated	Number of protons being irradiated	PANIC integration values of irradiated peaks
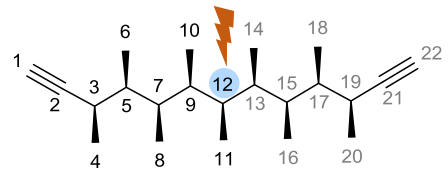 **4.12**	1	1000
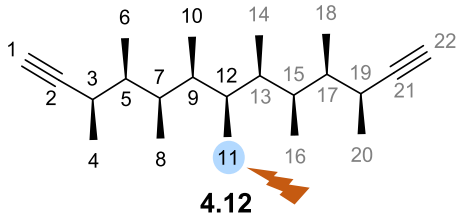 **4.12**	3	3000
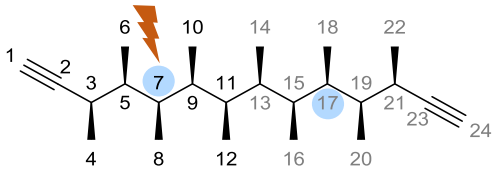 **4.5**	2	2000
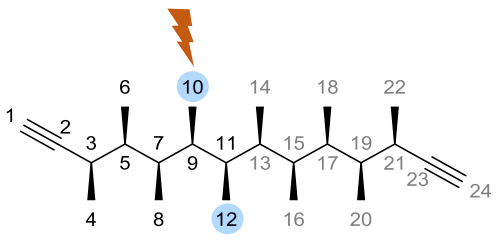 **4.5**	6	6000

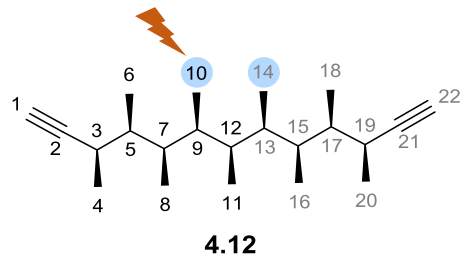

4.12

NMR experimental data.

***C2* symmetric compounds (4.9, 4.10 and 4.5).**

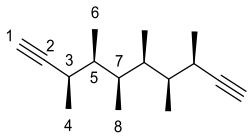

4.9

Table 6.89: Assignment table for **4.9**.

Proton	Exp. δ_H, Mult. (*J*/Hz)	Calc. δ_H, Multi. (*J*/Hz)
H_1	1.83, d (2.4)	1.78, d (4.21)
H_3	2.21, dqd (9.2, 6.9, 2.4)	2.39, dqd (9.42, 6.98, 4.21)
H_4	1.09, d (6.9)	1.18, d (6.98)
H_5	1.63, dqd (9.4, 6.9, 2.5)	1.47, dqd (9.42, 7.00, 4.16)
H_6	0.76, d (6.9)	0.79, d (7.00)
H_7	1.94, m	1.86, dqd (9.49, 7.01, 4.16)
H_8	0.76, d (6.5)	0.77, d (7.01)

Table 6.90: Calculated Boltzmann averaged ^{1}H chemical shifts (δ_H) and experimental ^{1}H chemical for **4.9** with Mean Absolute Deviations (MAD, in ppm), Standard Deviations (StDev, in ppm) and χ^2 (reduced) values (χ^2 (red.)).

Proton	Experimental δ_H /ppm	Calc. δ_H /ppm	Deviations/ppm
H_1	1.83	1.78	-0.05
H_3	2.21	2.39	0.18
H_4	1.09	1.18	0.09
H_5	1.63	1.47	-0.16
H_6	0.77	0.79	0.02
H_7	1.94	1.86	-0.08
H_8	0.76	0.77	0.01
		MAD	0.09
		StDev	0.11
		χ^2 (red.)	1.31

Table 6.91: Calculated Boltzmann averaged ^{13}C chemical shifts (δ_C) and experimental ^{13}C chemical for **4.9** with Mean Absolute Deviations (MAD, in ppm), Standard Deviations (StDev, in ppm) and χ^2 (reduced) values (χ^2 (red.)).

Carbon	Experimental δ_C /ppm	Calc. δ_C /ppm	Deviations/ppm
C_1	69.54	70.76	1.22
C_2	88.67	87.67	-1.00
C_3	29.98	30.05	0.07
C_4	18.87	18.98	0.11
C_5	38.94	39.15	0.21
C_6	11.15	11.30	0.15
C_7	37.10	37.05	-0.05
C_8	11.65	10.95	-0.70
		MAD	0.44
		StDev	0.66
		χ^2 (red.)	0.19

Table 6.92: Experimental $^nJ_{HH}$ values (in Hz) and Boltzmann averaged calculated $^nJ_{HH}$ (in Hz) before for **4.9** with Deviations (Dev, in Hz), Mean Absolute Deviations (MAD, in Hz), Standard Deviations (StDev, in Hz) and χ^2 (reduced) values (χ^2 (red.)).

H	Coupled H	Exp. $^nJ_{HH}$/Hz	Calc. $^nJ_{HH}$/Hz	Deviation/Hz
H_1	H_3	2.40	4.21	-*
H_3	H_4	6.90	6.98	0.08
H_3	H_5	9.20	9.42	0.22
H_5	H_6	6.90	7.00	0.10
H_5	H_7	2.50	4.16	1.66
H_7	H_8	6.50	7.01	0.51
			MAD	0.51
			StDev	0.66
			χ^2 (red.)	0.77
*$^4J_{H1H3}$ was not used for comparison.				

Table 6.93: Experimental ^1H-^1H distances derived from 1D DPFGSE NOESY and CSSF NOESY spectra and the Boltzmann averaged computed ^1H-^1H distances for **4.9** with Mean Absolute Deviations (MAD), Standard Deviations (StDev) and χ^2 (reduced) values (χ^2 (red.)).

H_A	H_B	η_{eff}	Experimental r_{eff}/Å	Calculated r_{eff}/Å	% Error
H_3	H_7	14.02	2.18	2.37	8.5%
H_7	H_5	16.98	2.11	2.11	0.1%
H_7	H_4	7.17	2.44	2.34	-3.9%
H_5	H_4	16.94	2.11	2.12	0.2%
H_4	H_3	24.46 (ref)	1.99	1.93	-3.1%

H_4	**H_6**	36.89	1.86	1.82	-1.7%
				MAD	2.92%
				StDev	1.84%
				χ^2 (red.)	1.64

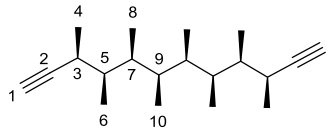

4.10

Table 6.94: Assignment table for **4.10**.

Proton	Exp. δ_H, Mult. (J/Hz)	Calc. δ_H, Multi. (J/Hz)
H_1	1.84, d (2.4)	1.83, d (4.0)
H_3	2.22, dqd (9.2, 6.9, 2.4)	2.43, dqd (9.1, 6.6, 4.0)
H_4	1.10, d (6.9)	1.20, d (6.6)
H_5	1.67, dqd (9.2, 6.9, 3.4)	1.55, dqd (9.1, 6.7, 3.5)
H_6	0.70, d (6.9)	0.79, d (6.7)
H_7	2.05, dqd (8.5, 6.8, 3.4)	1.98, dqd (8.6, 6.7, 3.5)
H_8	0.75, d (6.8)	0.76, d (6.7)
H_9	1.49, m	1.30, dqd (8.6, 6.7, 4.2)
H_{10}	0.88, d (6.7)	0.83, d (6.7)

Table 6.95: Calculated Boltzmann averaged ^{1}H chemical shifts (δ_H) and experimental ^{1}H chemical for **4.10** with Mean Absolute Deviations (MAD, in ppm), Standard Deviations (StDev, in ppm) and χ^2 (reduced) values (χ^2 (red.)).

Proton	Experimental δ_H /ppm	Calc. δ_H /ppm	Deviation/ppm
H_1	1.84	1.83	-0.01
H_3	2.22	2.43	0.21
H_4	1.10	1.20	0.10
H_5	1.67	1.55	-0.12
H_6	0.70	0.79	0.09
H_7	2.05	1.98	-0.07
H_8	0.75	0.76	0.01
H_9	1.49	1.31	-0.18
H_{10}	0.88	0.83	-0.05
		MAD	0.09
		StDev	0.12
		χ^2 (red.)	1.47

Table 6.96: Calculated Boltzmann averaged ^{13}C chemical shifts (δ_C) and experimental ^{13}C chemical for **4.10** with Mean Absolute Deviations (MAD, in ppm), Standard Deviations (StDev, in ppm) and χ^2 (reduced) values (χ^2 (red.)).

Carbon	Experimental δ_C/ppm	Calc. δ_C/ppm	Deviation/ppm
C_1	69.63	70.82	1.22
C_2	88.61	87.59	-1.01
C_3	30.10	30.04	-0.06

C_4	18.86	19.03	0.13
C_5	38.77	39.13	0.33
C_6	11.41	11.80	0.40
C_7	37.07	37.25	0.15
C_8	11.88	11.24	-0.66
C_9	35.78	35.57	-0.23
C_{10}	11.65	11.43	-0.27
		MAD	0.45
		StDev	0.61
		χ^2 (red.)	0.17

Table 6.97: Experimental $^{n}J_{HH}$ values (in Hz) and Boltzmann averaged calculated $^{n}J_{HH}$ (in Hz) before for **4.10** with Deviations (Dev, in Hz), Mean Absolute Deviations (MAD, in Hz), Standard Deviations (StDev, in Hz) and χ^2 (reduced) values (χ^2 (red.)).

H	Coupled H	Exp. $^{n}J_{HH}$/Hz	Calc. $^{n}J_{HH}$/Hz	Deviation/Hz
H_1	**H_3**	2.44	4.20	-
H_3	**H_4**	6.87	6.97	0.10
H_3	**H_5**	9.15	9.50	0.35
H_5	**H_6**	6.87	7.05	0.18
H_5	**H_7**	3.40	3.72	0.32
H_7	**H_8**	6.83	7.01	0.18
H_7	**H_9**	8.45	9.00	0.55
H_9	**H_{10}**	6.68	6.99	0.31
			MAD	0.12
			StDev	0.14
			χ^2 (red.)	0.02
*$^{4}J_{H1H3}$ was not used for comparison.				

Table 6.98: Experimental ^{1}H-^{1}H distances derived from 1D DPFGSE NOESY and CSSF NOESY spectra and the Boltzmann averaged computed ^{1}H-^{1}H distances for **4.10** with Mean Absolute Deviations (MAD), Standard Deviations (StDev) and χ^2 (reduced) values (χ^2 (red.)).

H_A	H_B	η_{eff}	Exp. r_{eff}/Å	Calc. r_{eff}/Å	% Error
H_3	**H_7**	7.96	2.49	2.73	9.3%
H_3	**H_9**	15.70	2.22	2.53	13.0%
H_3	**H_8**	33.70	1.96	1.91	−2.4%
H_3	**H_6**	19.94	2.13	2.17	1.6%
H_7	**H_5**	16.37	2.21	2.22	0.7%
H_7	**H_4**	9.86	2.40	2.45	2.2%
H_7	**H_{10}**	57.27	1.79	1.80	0.8%
H_7	**H_6**	7.15	2.53	2.58	1.9%
H_5	**H_9**	88.59	1.66	1.84	10.0%
H_5	**H_4**	25.82	2.04	2.14	4.8%

H_5	**H_{10}**	19.72	2.14	1.96	−8.7%
H_5	**H_8**	6.94	2.55	2.55	0.3%
H_9	**H_8**	27.66	2.15	2.05	−4.8%
H_9	**H_6**	37.98	1.92	1.81	−5.6%
H_4	**H_3**	39.74 (Ref)	1.90	1.93	0.0%
H_4	**H_6**	49.37	1.83	1.83	−0.4%
H_{10}	**H_9**	28.06	2.02	1.88	−6.8%
H_{10}	**H_8**	48.44	1.84	1.77	−3.9%
H_8	**H_7**	33.32	1.96	1.89	−3.5%
H_8	**H_6**	41.08	1.89	1.84	−2.8%
H_6	**H_5**	28.97	2.01	1.90	−5.3%
				MAD	4.25%
				StDev	5.37%
				χ^2 (red.)	2.60

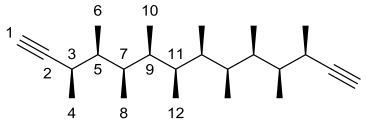

4.5

Table 6.99: Assignment table for **4.5**.

Proton	Exp. δ_H, Mult. (J/Hz)	Calc. δ_H, Multi. (J/Hz)
H_1	1.85, d (2.38)	1.73 d (4.18)
H_3	2.24, dqd (9.23, 6.88, 2.38)	2.89 dqd (9.06, 7.00, 4.18)
H_4	1.11, d (6.88)	1.15 d (7.00)
H_5	1.71, dqd (9.23, 6.78, 3.3)	1.66 dqd (9.06, 7.05, 3.91)
H_6	0.74 , d (6.78)	0.99 d (7.05)
H_7	2.05, dqd (8.6, 6.76, 3.3)	1.70 dqd (8.71, 6.96, 3.91)
H_8	0.77, d (6.76)	0.86 d (6.96)
H_9	1.52, dqd (8.6, 6.78, 3.2)	1.33 dqd (8.71, 6.99, 4.73)
H_{10}	0.81, d (6.78)	0.76 d (6.99)
H_{11}	1.62, m	1.41 dqd (8.20, 6.99, 4.73)
H_{12}	0.87, app. d (6.2)	0.82 d (7.05)

Table 6.100: Calculated Boltzmann averaged ^{1}H chemical shifts (δ_H) and experimental ^{1}H chemical for **4.5** with Mean Absolute Deviations (MAD, in ppm), Standard Deviations (StDev, in ppm) and χ^2 (reduced) values (χ^2 (red.)).

Proton	Exp. δ_H/ppm	Calc. δ_H/ppm	Deviations/ppm
H_1	1.85	1.85	0.00
H_3	2.24	2.53	0.29
H_4	1.11	1.21	0.10
H_5	1.71	1.64	-0.07
H_6	0.74	0.83	0.09
H_7	2.05	1.96	-0.09
H_8	0.77	0.79	0.02
H_9	1.52	1.39	-0.13
H_{10}	0.81	0.84	0.03
H_{11}	1.62	1.42	-0.20
H_{12}	0.87	0.84	-0.03
		MAD	0.09
		StDev	0.13
		χ^2 (red.)	1.73

Table 6.101: Calculated Boltzmann averaged ^{13}C chemical shifts (δ_C) and experimental ^{13}C chemical for **4.5** with Mean Absolute Deviations (MAD, in ppm), Standard Deviations (StDev, in ppm) and χ^2 (reduced) values (χ^2 (red.)).

Carbon	Exp. δ_C/ppm	Calc. $\delta_C$ppm	Deviations/ppm
C_1	69.92	70.70	0.78
C_2	88.68	88.03	−0.65
C_3	30.10	29.61	−0.49
C_4	18.79	18.60	−0.19
C_5	38.82	39.12	0.30
C_6	11.58	12.05	0.47
C_7	37.21	37.40	0.19
C_8	11.90	11.83	−0.07
C_9	35.72	35.88	0.18
C_{10}	12.02	12.00	−0.02
C_{11}	35.71	35.59	−0.11
C_{12}	11.84	11.45	−0.39
		MAD	0.32
		StDev	0.41
		χ^2 (red.)	0.08

Table 6.102: Experimental $^nJ_{HH}$ values (in Hz) and Boltzmann averaged calculated $^nJ_{HH}$ (in Hz) before for **4.5** with Deviations (Dev, in Hz), Mean Absolute Deviations (MAD, in Hz), Standard Deviations (StDev, in Hz) and χ^2 (reduced) values (χ^2 (red.)).

H	Coupled H	Exp. $^nJ_{HH}$/Hz	Calc. $^nJ_{HH}$/Hz	Deviations/Hz
H_1	**H_3**	2.38	4.18	*
H_3	**H_4**	6.88	7.00	0.12
H_3	**H_5**	9.23	9.06	−0.17
H_5	**H_6**	6.78	7.05	0.27
H_5	**H_7**	3.30	3.91	0.61
H_7	**H_8**	6.76	6.96	0.20
H_7	**H_9**	8.60	8.71	0.11
H_9	**H_{10}**	6.78	6.99	0.21
H_9	**H_{11}**	3.20	4.73	1.53
H_{11}	**H_{12}**	6.20	6.99	0.79
			MAD	0.44
			StDev	0.51
			χ^2 (red.)	0.44
*$^4J_{H1H3}$ was not used for comparison.				

Table 6.103: Experimental ^1H-^1H distances derived from 1D DPFGSE NOESY and CSSF NOESY spectra and the Boltzmann averaged computed ^1H-^1H distances using B3LYP-D2 6-311 G(d) optimised

geometries and conformer energies corrected after single point energy calculations for **4.5** with Mean Absolute Deviations (MAD), Standard Deviations (StDev) and χ^2 (reduced) values (χ^2 (red.)).

H_A	H_B	η_{eff}	Exp. r_{eff}/ Å	Calc r_{eff}/ Å	% error
H_3	H_9	23.05	2.17	2.36	8.47%
H_3	H_4	40.57	1.98	1.93	−2.41%
H_3	H_8	37.63	2.00	1.93	−3.75%
H_3	H_6	23.67	2.16	2.21	2.13%
H_7	H_3	7.02	2.65	2.71	2.45%
H_7	H_5	21.95	2.19	2.27	3.48%
H_7	H_{11}	33.44	2.04	2.26	10.06%
H_7	H_4	11.15	2.45	2.41	−1.47%
H_7	H_{12}	47.30	1.93	1.90	−1.34%
H_7	H_{10}	27.44	2.11	2.14	1.59%
H_7	H_6	7.43	2.62	2.51	−4.53%
H_5	H_{11}	98.74	1.70	1.87	9.51%
H_5	H_9	11.59	2.43	2.50	2.68%
H_5	H_4	34.67	2.03	2.18	7.35%
H_5	H_{12}	17.53	2.27	2.08	−9.02%
H_5	H_{10}	15.59	2.32	2.30	−0.96%
H_5	H_8	8.13	2.58	2.50	−3.11%
H_5	H_6	36.88	2.01	1.93	−4.06%
H_{11}	H_{10}	49.18	1.91	1.88	−1.64%
H_{11}	H_8	11.62	2.43	2.25	−7.68%
H_{11}	H_6	12.83	2.39	2.32	−3.19%
H_9	H_{12}	19.25	2.24	2.19	−2.18%
H_9	H_{10}	52.58	1.89	1.78	−5.94%
H_9	H_8	34.52	2.03	2.15	5.92%
H_9	H_6	43.82	1.95	1.96	0.29%
H_4	H_3	47.72 (Ref)	1.92	1.93	0.30%
H_4	H_6	58.48	1.86	1.83	−1.66%
H_{12}	H_{11}	68.29	1.81	1.81	−0.35%
				MAD	3.84%
				StDev	4.92%
			–	**χ^2 (red.)**	1.97

Table 6.104: Experimental ^{1}H-^{1}H distances derived from 1D DPFGSE NOESY and CSSF NOESY spectra and the Boltzmann averaged computed ^{1}H-^{1}H using different DFT methods for **4.5** with Mean Absolute Deviations (MAD), Standard Deviations (StDev) and χ^2 (reduced) values (χ^2 (red.)).

	Functional	**MMFFs**			**mPW1PW91**					
	Basis set	**-**			**6-31G (d)**			**6-311G (d)**		
H_A	**H_X**	Exp *r* /Å	Calc./ Å	% error[a]	Exp *r* /Å	Calc./ Å	% error[a]	Exp *r* /Å	Calc./ Å	% error[a]
H_3	**H_9**	2.24	2.00	−11.32%	2.26	2.92	25.71%	2.25	2.72	19.24%
H_3	**H_4**	2.03	1.92	−5.71%	2.05	1.92	−6.53%	2.04	1.92	−6.11%
H_3	**H_8**	2.06	2.17	5.08%	2.08	1.92	−8.08%	2.07	1.92	−7.35%
H_3	**H_6**	2.23	2.45	9.67%	2.25	2.20	−2.37%	2.24	2.20	−1.63%
H_7	**H_3**	2.73	2.77	1.69%	2.75	2.57	−6.90%	2.74	2.59	−5.61%
H_7	**H_5**	2.25	2.45	8.23%	2.28	2.26	−0.57%	2.26	2.26	−0.36%
H_7	**H_{11}**	2.10	1.99	−5.67%	2.12	2.30	8.20%	2.11	2.27	7.45%
H_7	**H_4**	2.52	2.19	−14.10%	2.55	2.78	8.57%	2.54	2.65	4.50%
H_7	**H_{12}**	1.98	2.07	4.12%	2.00	1.90	−5.01%	1.99	1.88	−5.96%
H_7	**H_{10}**	2.17	2.34	7.39%	2.19	2.22	1.17%	2.18	2.23	2.32%
H_7	**H_6**	2.70	2.27	−17.12%	2.73	2.80	2.55%	2.71	2.73	0.80%
H_5	**H_{11}**	1.75	2.11	18.22%	1.77	1.79	0.78%	1.76	1.79	1.45%
H_5	**H_9**	2.51	2.80	11.04%	2.53	2.23	−12.51%	2.52	2.31	−8.54%
H_5	**H_4**	2.09	2.43	14.99%	2.11	2.19	3.56%	2.10	2.19	4.06%
H_5	**H_{12}**	2.34	2.54	8.30%	2.36	2.40	1.51%	2.35	2.37	0.90%
H_5	**H_{10}**	2.39	2.05	−15.01%	2.41	2.44	1.05%	2.40	2.25	−6.29%
H_5	**H_8**	2.66	2.28	−15.50%	2.69	2.78	3.57%	2.67	2.73	2.09%
H_5	**H_6**	2.07	1.91	−7.65%	2.09	1.92	−8.40%	2.08	1.92	−7.89%
H_{11}	**H_{10}**	1.97	1.98	0.65%	1.99	1.89	−5.34%	1.98	1.89	−4.58%
H_{11}	**H_8**	2.51	1.97	−23.84%	2.53	2.82	10.79%	2.52	2.66	5.50%

H_{11}	**H_6**	2.46	2.71	9.56%	2.49	2.61	4.81%	2.48	2.55	2.94%
H_9	**H_{12}**	2.30	1.91	−18.83%	2.33	2.58	10.18%	2.32	2.47	6.54%
H_9	**H_{10}**	1.95	1.87	−4.11%	1.97	1.85	−6.41%	1.96	1.85	−5.66%
H_9	**H_8**	2.09	2.35	11.87%	2.11	2.22	4.83%	2.10	2.22	5.37%
H_9	**H_6**	2.01	2.21	9.48%	2.03	1.91	−5.84%	2.02	1.91	−5.68%
H_4	**H_3**	1.98	1.92	−3.00%	2.00	1.92	−3.82%	1.99	1.92	−3.40%
H_4	**H_6**	1.91	1.89	−1.50%	1.93	1.83	−5.26%	1.92	1.84	−4.53%
H_{12}	**H_{11}**	1.87	1.84	−1.35%	1.88	1.81	−3.96%	1.87	1.80	−4.10%
			MAD	9.89%		**MAD**	6.01%		**MAD**	5.07%
			StDev	6.83%		**StDev**	7.89%		**StDev**	7.92%
			χ^2(red.)	11.57		**χ^2(red.)**	5.08		**χ^2(red.)**	3.20
	Functional	**mPW1PW91**						**B3LYP**		
	Basis set	**6-311G(d,p)**			**6-311G+(d,p)**			**6-311G(d)**		
H_A	**H_X**	Exp *r* /Å	Calc./ Å	% error[a]	Exp *r* /Å	Calc./ Å	% error[a]	Exp *r* /Å	Calc./ Å	% error[a]
H_3	**H_9**	2.25	2.88	24.67%	2.25	2.76	20.58%	2.27	2.96	26.37%
H_3	**H_4**	2.04	1.92	−6.09%	2.04	1.92	−6.11%	2.07	1.93	−6.93%
H_3	**H_8**	2.07	1.91	−7.86%	2.07	1.90	−8.65%	2.09	1.93	−7.80%
H_3	**H_6**	2.24	2.19	−2.12%	2.24	2.19	−2.19%	2.26	2.22	−1.95%
H_7	**H_3**	2.74	2.60	−5.39%	2.74	2.61	−4.89%	2.77	2.52	−9.20%
H_7	**H_5**	2.26	2.25	−0.81%	2.26	2.25	−0.86%	2.29	2.25	−1.64%
H_7	**H_{11}**	2.11	2.31	9.00%	2.11	2.32	9.31%	2.13	2.44	13.48%
H_7	**H_4**	2.54	2.68	5.47%	2.54	2.72	6.86%	2.56	2.68	4.44%
H_7	**H_{12}**	1.99	1.87	−6.48%	1.99	1.89	−5.44%	2.01	1.88	−6.57%
H_7	**H_{10}**	2.18	2.23	2.21%	2.18	2.18	−0.17%	2.20	2.16	−1.84%
H_7	**H_6**	2.71	2.78	2.56%	2.71	2.76	1.56%	2.74	2.82	2.88%
H_5	**H_{11}**	1.76	1.78	0.77%	1.76	1.78	0.71%	1.78	1.78	−0.04%

H_5	**H_9**	2.52	2.30	−9.07%	2.52	2.35	−7.11%	2.54	2.46	−3.42%
H_5	**H_4**	2.10	2.18	3.63%	2.10	2.18	3.74%	2.12	2.21	3.99%
H_5	**H_{12}**	2.35	2.36	0.20%	2.35	2.30	−2.15%	2.38	2.33	−2.03%
H_5	**H_{10}**	2.40	2.28	−4.91%	2.40	2.43	1.52%	2.42	2.41	−0.33%
H_5	**H_8**	2.67	2.77	3.70%	2.67	2.75	2.95%	2.70	2.82	4.37%
H_5	**H_6**	2.08	1.92	−7.89%	2.08	1.92	−7.77%	2.10	1.93	−8.60%
H_{11}	**H_{10}**	1.98	1.88	−5.03%	1.98	1.87	−5.83%	2.00	1.88	−6.11%
H_{11}	**H_8**	2.52	2.78	9.77%	2.52	2.70	7.14%	2.54	2.87	12.05%
H_{11}	**H_6**	2.48	2.53	2.12%	2.48	2.51	1.46%	2.50	2.52	0.76%
H_9	**H_{12}**	2.32	2.54	9.08%	2.32	2.50	7.57%	2.34	2.58	9.69%
H_9	**H_{10}**	1.96	1.85	−5.67%	1.96	1.83	−6.54%	1.98	1.84	−7.36%
H_9	**H_8**	2.10	2.22	5.34%	2.10	2.18	3.72%	2.12	2.16	1.92%
H_9	**H_6**	2.02	1.89	−6.43%	2.02	1.91	−5.37%	2.04	1.96	−4.15%
H_4	**H_3**	1.99	1.92	−3.38%	1.99	1.92	−3.40%	2.01	1.93	−4.23%
H_4	**H_6**	1.92	1.84	−4.58%	1.92	1.83	−4.80%	1.94	1.86	−4.34%
H_{12}	**H_{11}**	1.87	1.80	−3.95%	1.87	1.81	−3.75%	1.89	1.80	−5.32%
			MAD	5.65%		**MAD**	5.08%		**MAD**	5.78%
			StDev	7.35%		**StDev**	6.02%		**StDev**	7.92%
			χ^2(red.)	4.41		**χ^2(red.)**	3.47		**χ^2(red.)**	5.12
	Functional	**B3LYP**			**M06-2X**					
	Basis set	**6-311 G(d) toluene (IEFPCM)**			**6-31G (d)**			**6-311G (d)**		
H_A	**H_X**	Exp *r* /Å	Calc./ Å	% error[a]	Exp *r* /Å	Calc./ Å	% error[a]	Exp *r* /Å	Calc./ Å	% error[a]
H_3	**H_9**	2.27	2.94	25.48%	2.22	2.83	23.83%	2.22	2.77	22.01%
H_3	**H_4**	2.07	1.93	−7.18%	2.02	1.93	−4.84%	2.02	1.93	−4.88%
H_3	**H_8**	2.10	1.90	−9.58%	2.05	1.90	−7.44%	2.05	1.91	−7.26%
H_3	**H_6**	2.26	2.19	−3.50%	2.21	2.20	−0.84%	2.21	2.20	−0.67%

H_7	**H_3**	2.77	2.65	−4.61%	2.71	2.60	−4.03%	2.71	2.60	−4.18%
H_7	**H_5**	2.29	2.24	−2.34%	2.24	2.26	0.72%	2.24	2.25	0.56%
H_7	**H_{11}**	2.14	2.46	14.00%	2.09	2.40	13.88%	2.09	2.38	12.83%
H_7	**H_4**	2.57	2.80	8.52%	2.51	2.63	4.67%	2.51	2.73	8.33%
H_7	**H_{12}**	2.02	1.89	−6.62%	1.97	1.89	−4.32%	1.97	1.90	−3.57%
H_7	**H_{10}**	2.21	2.15	−2.76%	2.16	2.12	−2.10%	2.16	2.11	−2.33%
H_7	**H_6**	2.75	2.81	2.35%	2.69	2.71	0.88%	2.69	2.68	−0.12%
H_5	**H_{11}**	1.79	1.78	−0.33%	1.75	1.79	2.60%	1.75	1.80	3.26%
H_5	**H_9**	2.55	2.51	−1.47%	2.49	2.35	−5.82%	2.49	2.32	−7.36%
H_5	**H_4**	2.13	2.18	2.53%	2.08	2.16	3.82%	2.08	2.16	3.92%
H_5	**H_{12}**	2.38	2.32	−2.61%	2.33	2.12	−9.14%	2.33	2.14	−8.25%
H_5	**H_{10}**	2.43	2.53	4.21%	2.37	2.46	3.40%	2.37	2.46	3.38%
H_5	**H_8**	2.71	2.82	3.99%	2.65	2.71	2.46%	2.65	2.69	1.80%
H_5	**H_6**	2.10	1.93	−8.71%	2.06	1.93	−6.57%	2.06	1.92	−6.68%
H_{11}	**H_{10}**	2.00	1.87	−7.00%	1.96	1.87	−4.91%	1.96	1.87	−4.44%
H_{11}	**H_8**	2.55	2.86	11.55%	2.49	2.68	7.35%	2.49	2.64	5.65%
H_{11}	**H_6**	2.51	2.50	−0.13%	2.45	2.43	−1.00%	2.45	2.40	−1.99%
H_9	**H_{12}**	2.34	2.59	9.90%	2.29	2.50	8.70%	2.29	2.47	7.52%
H_9	**H_{10}**	1.98	1.84	−7.62%	1.94	1.78	−8.25%	1.94	1.79	−7.74%
H_9	**H_8**	2.13	2.15	1.17%	2.08	2.12	1.79%	2.08	2.13	2.23%
H_9	**H_6**	2.04	1.94	−5.35%	2.00	1.94	−2.94%	2.00	1.93	−3.45%
H_4	**H_3**	2.02	1.93	−4.47%	1.97	1.93	−2.13%	1.97	1.93	−2.18%
H_4	**H_6**	1.95	1.85	−5.24%	1.90	1.84	−3.62%	1.90	1.83	−3.90%
H_{12}	**H_{11}**	1.90	1.80	−5.45%	1.86	1.79	−3.33%	1.86	1.80	−3.28%
			MAD	6.02%		**MAD**	5.19%		**MAD**	5.14%
			StDev	8.00%		**StDev**	7.17%		**StDev**	6.83

			χ^2(red.)	5.22		**χ^2(red.)**	4.13			**χ^2(red.)**	3.81
	Functional	**B3LYP-D2**									
	Basis set	**6-31G (d)**			**6-311G (d)**						
H_A	**H_X**	Exp *r* /Å	Calc./ Å	% error[a]	Exp *r* /Å	Calc./ Å	% error[a]				
H_3	**H_9**	2.19	2.54	14.62%	2.18	2.54	15.13%				
H_3	**H_4**	1.99	1.93	−3.21%	1.98	1.93	−2.69%				
H_3	**H_8**	2.02	1.95	−3.44%	2.01	1.95	−2.92%				
H_3	**H_6**	2.18	2.19	0.40%	2.17	2.19	0.92%				
H_7	**H_3**	2.67	2.70	1.11%	2.66	2.70	1.62%				
H_7	**H_5**	2.21	2.27	2.59%	2.20	2.27	3.10%				
H_7	**H_{11}**	2.06	2.26	9.22%	2.05	2.26	9.74%				
H_7	**H_4**	2.47	2.32	−6.44%	2.46	2.32	−5.92%				
H_7	**H_{12}**	1.94	1.91	−1.63%	1.93	1.91	−1.11%				
H_7	**H_{10}**	2.13	2.17	1.95%	2.12	2.17	2.46%				
H_7	**H_6**	2.64	2.59	−2.10%	2.63	2.59	−1.58%				
H_5	**H_{11}**	1.72	1.84	6.68%	1.71	1.84	7.19%				
H_5	**H_9**	2.46	2.29	−6.81%	2.44	2.29	−6.29%				
H_5	**H_4**	2.05	2.16	5.41%	2.04	2.16	5.93%				
H_5	**H_{12}**	2.29	2.12	−7.91%	2.28	2.12	−7.40%				
H_5	**H_{10}**	2.34	2.34	0.27%	2.33	2.34	0.78%				
H_5	**H_8**	2.61	2.60	−0.41%	2.59	2.60	0.11%				
H_5	**H_6**	2.03	1.92	−5.09%	2.01	1.92	−4.57%				
H_{11}	**H_{10}**	1.93	1.89	−2.30%	1.92	1.89	−1.79%				
H_{11}	**H_8**	2.45	2.42	−1.47%	2.44	2.42	−0.96%				
H_{11}	**H_6**	2.41	2.36	−2.27%	2.40	2.36	−1.75%				
H_9	**H_{12}**	2.26	2.31	2.52%	2.25	2.31	3.04%				

H_9	**H_{10}**	1.91	1.79	−6.32%	1.90	1.79	−5.80%			
H_9	**H_8**	2.05	2.17	5.62%	2.04	2.17	6.13%			
H_9	**H_6**	1.97	1.93	−2.06%	1.96	1.93	−1.54%			
H_4	**H_3**	1.94	1.93	−0.50%	1.93	1.93	0.02%			
H_4	**H_6**	1.88	1.85	−1.49%	1.87	1.85	−0.97%			
H_{12}	**H_{11}**	1.83	1.81	−1.05%	1.82	1.81	−0.54%			
			MAD	3.74%		**MAD**	3.54%			
			StDev	5.05%		**StDev**	4.80%			
			χ^2(red.)	2.08		**χ^2(red.)**	1.88			

Data for *meso* compounds (4.11, 4.12 and 4.13)

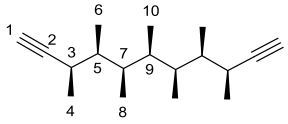

4.11

Table 6.105: Calculated Boltzmann averaged ^{1}H chemical shifts (δ_H) and experimental ^{1}H chemical for **4.11** with Mean Absolute Deviations (MAD, in ppm), Standard Deviations (StDev, in ppm) and χ^2 (reduced) values (χ^2 (red.)).

		DFT population		***M* and *P* helices only, 1:1**	
H	**Exp δ_H/ppm**	**Calc. δ_H/ppm**	**Deviations/ppm**	**Calc. δ_H/ppm**	**Deviations/ppm**
H_1	1.83	1.75	-0.08	1.75	-0.08
H_3	2.37	2.62	0.25	2.62	0.25
H_4	1.04	1.07	0.03	1.06	0.02
H_5	1.62	1.49	-0.13	1.52	-0.10
H_6	0.79	0.84	0.05	0.82	0.03
H_7	1.8	1.64	-0.16	1.61	-0.19
H_8	0.76	0.89	0.13	0.88	0.12
H_9	1.24	1.13	-0.11	1.14	-0.10
H_{10}	0.7	0.71	0.01	0.74	0.04
		MAD	0.11	**MAD**	0.10
		StDev	0.14	**StDev**	0.13
		χ^2 (red.)	1.82	**χ^2 (red.)**	1.8

Table 6.106: Calculated Boltzmann averaged ^{1}H chemical shifts (δ_C) and experimental ^{13}C chemical for **4.11** with Mean Absolute Deviations (MAD, in ppm), Standard Deviations (StDev, in ppm) and χ^2 (reduced) values (χ^2 (red.)).

		DFT population		***M* and *P* helices only, 1:1**	
C	**Exp δC/ppm**	**Calc. δ_C/ppm**	**Deviations/ppm**	**Calc. δ_C/ppm**	**Deviations/ppm**
C_3	29.08	29.08	0.00	28.79	-0.29
C_4	17.02	17.20	0.18	17.02	0.00
C_5	39.40	39.73	0.33	39.65	0.25
C_6	12.39	12.92	0.53	12.72	0.33
C_7	36.09	36.13	0.04	36.93	0.84
C_8	11.38	11.45	0.07	11.56	0.18
C_9	36.80	36.34	-0.46	35.89	-0.91
C_{10}	11.72	11.02	-0.70	11.31	-0.41
		MAD	0.29	**MAD**	0.40

		StDev	0.40	**StDev**	0.50
		χ^2 (red.)	0.07	**χ^2 (red.)**	0.13

Table 6.107: Experimental $^{n}J_{HH}$ values (in Hz) and Boltzmann averaged calculated $^{n}J_{HH}$ (in Hz) before for **4.11** with Deviations (Dev, in Hz), Mean Absolute Deviations (MAD, in Hz), Standard Deviations (StDev, in Hz) and χ^2 (reduced) values (χ^2 (red.)).

			DFT population		***M* and *P* helices only, 1:1**	
H_A	**H_B**	**Exp. $^{n}J_{HH}$/Hz**	**Calc. $^{n}J_{HH}$/Hz**	**Deviations/Hz**	**Calc. $^{n}J_{HH}$/Hz**	**Deviations/Hz**
H_3	**H_4**	6.99	7.13	0.14	7.10	0.11
H_3	**H_5**	6.90	6.54	-0.36	7.00	0.10
H_5	**H_6**	6.80	7.00	0.20	6.96	0.16
H_5	**H_7**	5.40	5.79	0.39	6.51	1.11
H_7	**H_8**	6.80	6.99	0.19	6.95	0.15
H_7	**H_9**	6.70	6.94	0.24	7.08	0.38
H_9	**H_{10}**	6.80	7.04	0.24	6.97	0.17
			MAD	0.25	**MAD**	0.31
			StDev	0.24	**StDev**	0.36
			χ^2 (red.)	0.08	**χ^2 (red.)**	0.24

Table 6.108: Experimental ^{1}H-^{1}H distances derived from 1D DPFGSE NOESY and CSSF NOESY spectra and the Boltzmann averaged computed ^{1}H-^{1}H distances for **4.11** with Mean Absolute Deviations (MAD), Standard Deviations (StDev) and χ^2 (reduced) values (χ^2 (red.)).

		r_{eff}^{-6}, DFT population			***M* and *P* helices only, 1:1**		
H	**H**	**Exp r_{eff}/Å**	**Calc r_{eff}/Å**	**% Error**	**Exp r_{eff}/Å**	**Calc r_{eff}/Å**	**% Error**
H3	**H5**	2.31	2.29	−0.7%	2.32	2.35	1.0%
H3	**H9**	1.87	2.10	11.3%	1.88	2.06	8.9%
H_3	**H_6**	2.19	2.25	2.6%	2.21	2.31	4.5%
H_3	**H_8**	2.09	2.11	0.7%	2.11	2.04	−3.2%
H_3	**H_{10}**	2.49	2.28	−8.7%	2.50	2.18	−13.8%
H_7	**H_3**	2.42	2.76	12.9%	2.44	2.77	12.9%
H_7	**H_4**	2.14	2.06	−4.0%	2.15	2.14	−0.3%
H_7	**H_{10}**	2.24	2.33	3.9%	2.25	2.28	1.4%
H_7	**H_8**	1.86	1.77	−5.0%	1.88	1.78	−5.2%
H_7	**H_6**	2.11	2.11	−0.1%	2.12	2.07	−2.5%
H_5	**H_9**	2.36	2.58	8.8%	2.38	2.91	20.0%
H_5	**H_4**	2.14	2.17	1.3%	2.15	2.29	6.1%
H_5	**H_{10}**	2.11	2.11	0.0%	2.12	2.08	−2.1%
H_5	**H_8**	2.08	2.03	−2.3%	2.09	1.97	−5.6%

H_9	**H_8**	2.25	2.32	3.2%	2.26	2.28	0.6%
H_9	**H_6**	2.19	2.15	−2.2%	2.21	2.12	−4.2%
H_9	**H_4**	2.56	2.33	−9.4%	2.58	2.32	−10.6%
H_4	***H_3***	*1.93*	*1.92*	*−0.5%*	1.95	1.93	−0.9%
H_4	**H_6**	1.83	1.79	−2.4%	1.84	1.73	−6.2%
H_4	**H_8**	2.82	2.57	−9.1%	2.83	2.86	0.8%
H_8	**H_7**	1.76	1.77	0.6%	1.77	1.78	0.4%
H_8	**H_{10}**	1.84	1.82	−0.7%	1.85	1.83	−0.7%
			MAD	4.10%		**MAD**	5.1%
			StDev	5.96%		**StDev**	7.4%
			χ^2 (red.)	3.76		**χ^2 (red.)**	6.08

Table 6.109: Experimental δ_H values (in ppm) and population refined (using different constraints) Boltzmann averaged calculated δ_H (in ppm) for **4.11** with Deviations (Dev, in ppm), Mean Absolute Deviations (MAD, in ppm), Standard Deviations (StDev, in ppm) and χ^2 (reduced) values (χ^2 (red.))

		Refined population, Sum($\Delta\Delta G^2$) = 100		**Refined population, SUM($\Delta\Delta G^2$) = 225**		**Refined population, SUM(($\Delta\Delta G^2$) = 625**	
Proton	**Exp δ_H/ppm**	**Calc. δ_H/ppm**	**Dev./ppm**	**Calc. δ_H/ppm**	**Dev./ppm**	**Calc. δ_H/ppm**	**Dev./ppm**
H_1	1.83	1.75	-0.08	1.74	-0.09	1.77	-0.06
H_3	2.37	2.58	0.21	2.59	0.22	2.60	0.23
H_4	1.04	1.09	0.05	1.07	0.03	1.05	0.01
H_5	1.62	1.46	-0.16	1.45	-0.17	1.47	-0.15
H_6	0.79	0.81	0.02	0.82	0.03	0.76	-0.03
H_7	1.8	1.72	-0.08	1.68	-0.12	1.53	-0.27
H_8	0.76	0.87	0.11	0.85	0.09	0.84	0.08
H_9	1.24	1.15	-0.09	1.24	0.00	1.46	0.22
H_{10}	0.7	0.72	0.02	0.70	0.00	0.68	-0.02
		MAD	0.09	**MAD**	0.08	**MAD**	0.12
		StDev	0.12	**StDev**	0.12	**StDev**	0.16
		χ^2 (red.)	1.34	**χ^2 (red.)**	1.4	**χ^2 (red.)**	2.6

Table 6.110: Experimental δ_C values (in ppm) and population refined (using different constraints) Boltzmann averaged calculated δ_C (in ppm) for **4.11** with Deviations (Dev, in ppm), Mean Absolute Deviations (MAD, in ppm), Standard Deviations (StDev, in ppm) and χ^2 (reduced) values (χ^2 (red.))

		Refined population, Sum($\Delta\Delta G^2$) = 100		**Refined population, Sum($\Delta\Delta G^2$) = 225**		**Refined population, Sum($\Delta\Delta G^2$) = 625**	
Carbon	**Exp δ_C/ppm**	**Calc. δ_C/ppm**	**Dev./ppm**	**Calc. δ_C/ppm**	**Dev./ppm**	**Calc. δ_C/ppm**	**Dev./ppm**
C_1	69.27	68.71	-0.56	66.72	-2.55	68.30	-0.97

C_2	88.94	86.02	-2.92	83.84	-5.10	85.88	-3.06
C_3	29.08	29.11	0.03	28.85	-0.23	28.85	-0.23
C_4	17.02	17.46	0.44	17.20	0.18	17.22	0.20
C_5	39.40	39.39	-0.01	39.36	-0.04	39.39	-0.01
C_6	12.39	12.84	0.45	13.17	0.78	12.88	0.49
C_7	36.09	35.11	-0.98	35.57	-0.52	36.79	0.70
C_8	11.38	10.91	-0.47	11.25	-0.13	11.40	0.02
C_9	36.80	37.64	0.84	37.45	0.65	36.23	-0.57
C_{10}	11.72	11.43	-0.29	11.03	-0.69	11.11	-0.61
		MAD	0.70	**MAD**	1.09	**MAD**	0.69
		StDev	1.05	**StDev**	1.78	**StDev**	1.06
		χ^2 (red.)	0.55	**χ^2 (red.)**	1.70	**χ^2 (red.)**	0.58

Table 6.111: Experimental $^{n}J_{HH}$ values (in Hz) and population refined (using different constraints) Boltzmann averaged calculated $^{n}J_{HH}$ values (in Hz) for **4.11** with Deviations (Dev, in Hz), Mean Absolute Deviations (MAD, in Hz), Standard Deviations (StDev, in Hz) and χ^2 (reduced) values (χ^2 (red.))

			Refined population, Sum($\Delta\Delta G^2$) = 100		**Refined population, Sum($\Delta\Delta G^2$) = 225**		**Refined population, Sum($\Delta\Delta G^2$) = 625**	
H_A	**H_B**	**Exp. $^{n}J_{HH}$/Hz**	**Calc. $^{n}J_{HH}$ /Hz**	**Deviation/Hz**	**Calc. $^{n}J_{HH}$/Hz**	**Deviation/Hz**	**Calc. $^{n}J_{HH}$ /Hz**	**Deviation/Hz**
H_3	**H_4**	6.99	7.09	0.10	7.09	0.10	7.14	0.15
H_3	**H_5**	6.90	7.07	0.17	7.24	0.34	6.95	0.05
H_5	**H_6**	6.80	7.06	0.26	7.05	0.25	7.08	0.28
H_5	**H_7**	5.40	5.07	-0.33	5.55	0.15	6.54	1.14
H_7	**H_8**	6.80	7.10	0.30	7.16	0.36	7.09	0.29
H_7	**H_9**	6.70	6.95	0.25	6.21	-0.49	5.92	-0.78
H_9	**H_{10}**	6.80	7.03	0.23	7.12	0.32	7.00	0.20
			MAD	0.23	**MAD**	0.29	**MAD**	0.41

			StDev	0.22	**StDev**	0.30	**StDev**	0.56
			χ^2 (red.)	0.07	**χ^2 (red.)**	0.11	**χ^2 (red.)**	0.36

Table 6.112: Experimental effective ^{1}H-^{1}H distances (r_{eff}, in Å) and population refined (using different constraints) Boltzmann averaged calculated ^{1}H-^{1}H distances (r_{eff}, in Å) for **4.11** with Deviations (Dev), Mean Absolute Deviations (MAD), Standard Deviations (StDev) and χ^2 (reduced) values (χ^2 (red.))

		Refined population, Sum($\Delta\Delta G^2$) = 100			**Refined population, Sum($\Delta\Delta G^2$) = 225**			**Refined population, Sum($\Delta\Delta G^2$) = 625**		
H	**H**	**Exp r_{eff}/Å**	**Calc r_{eff}/Å**	**% Error**	**Exp r_{eff}/Å**	**Calc r_{eff}/Å**	**% Error**	**Exp r_{eff}/Å**	**Calc r_{eff}/Å**	**% Error**
H_3	**H_5**	2.33	2.31	−0.8%	2.34	2.35	0.6%	2.34	2.35	0.5%
H_3	**H_9**	1.89	2.15	13.0%	1.90	2.10	10.3%	1.90	2.07	8.6%
H_3	**H_6**	2.21	2.22	0.4%	2.22	2.26	1.5%	2.22	2.20	−0.9%
H_3	**H_8**	2.11	2.09	−1.1%	2.12	2.10	−1.0%	2.12	2.14	0.8%
H_3	**H_{10}**	2.51	2.44	−2.7%	2.52	2.45	−3.0%	2.52	2.49	−1.0%
H_7	**H_3**	2.44	2.63	7.2%	2.46	2.52	2.7%	2.46	2.44	−0.6%
H_7	**H_4**	2.16	2.06	−4.4%	2.17	2.10	−2.9%	2.17	2.10	−3.3%
H_7	**H_{10}**	2.26	2.35	4.0%	2.27	2.40	5.8%	2.27	2.38	4.6%
H_7	**H_8**	1.88	1.79	−5.2%	1.89	1.79	−5.3%	1.89	1.79	−5.4%
H_7	**H_6**	2.13	2.15	0.8%	2.14	2.14	0.2%	2.14	2.11	−1.4%
H_5	**H_9**	2.38	2.43	1.8%	2.40	2.36	−1.4%	2.40	2.45	2.3%
H_5	**H_4**	2.16	2.15	−0.2%	2.17	2.22	2.3%	2.17	2.23	2.9%
H_5	**H_{10}**	2.13	2.15	1.0%	2.14	2.15	0.7%	2.14	2.11	−1.1%
H_5	**H_8**	2.09	2.07	−1.1%	2.10	2.09	−0.7%	2.10	2.10	−0.1%
H_9	**H_8**	2.27	2.34	3.1%	2.28	2.39	5.0%	2.28	2.38	4.2%
H_9	**H_6**	2.21	2.15	−2.9%	2.22	2.20	−1.0%	2.22	2.22	−0.2%
H_9	**H_4**	2.59	2.54	−1.9%	2.60	2.54	−2.3%	2.60	2.60	0.0%
H_4	***H_3***	*1.95*	*1.92*	*−1.4%*	1.96	1.89	−3.4%	1.96	1.89	−3.4%

H_4	**H_6**	1.84	1.80	−2.6%	1.85	1.81	−2.5%	1.85	1.80	−2.7%
H_4	**H_8**	2.84	2.68	−5.8%	2.85	2.77	−3.0%	2.85	2.82	−1.2%
H_8	**H_7**	1.78	1.79	0.4%	1.79	1.79	0.3%	1.79	1.79	0.2%
H_8	**H_{10}**	1.85	1.81	−2.1%	1.86	1.82	−2.3%	1.86	1.82	−2.4%
			MAD	2.9%		**MAD**	2.7%		**MAD**	2.2%
			StDev	4.2%		**StDev**	3.6%		**StDev**	3.1%
			χ^2 (red.)	1.94		**χ^2 (red.)**	1.42		**χ^2 (red.)**	1.05

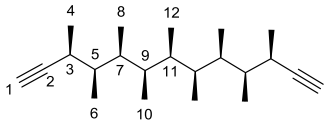

4.12

Table 6.113: Experimental ^{1}H-^{1}H distances derived from 1D DPFGSE NOESY and CSSF NOESY spectra and the Boltzmann averaged computed ^{1}H-^{1}H distances for **4.12** with Mean Absolute Deviations (MAD), Standard Deviations (StDev) and χ^2 (reduced) values (χ^2 (red.)).

		DFT calculated population			**Refined population, Sum($\Delta\Delta G^2$) ≤ 100**		
H_A	**H_B**	**Exp r_{eff}/Å**	**Calc r_{eff}/Å**	**% Error**	**Exp r_{eff}/Å**	**Calc r_{eff}/Å**	**% Error**
H_3	**H_9**	1.90	2.11	10.7%	1.90	2.10	10.3%
H_3	**H_6**	2.32	2.28	−1.8%	2.32	2.30	−0.8%
H_7	**H_3**	2.58	2.70	4.7%	2.58	2.68	4.1%
H_7	**H_9**	1.85	1.97	6.3%	1.85	1.92	3.6%
H_7	**H_4**	2.29	2.15	−6.2%	2.29	2.19	−4.2%
H_5	**H_9**	2.32	2.39	3.2%	2.32	2.30	−0.6%
H_5	**H_4**	2.22	2.25	1.6%	2.22	2.28	2.6%
H_{11}	**H_7**	2.43	2.44	0.5%	2.43	2.45	1.0%
H_{11}	**H_5**	1.90	2.04	6.9%	1.90	2.10	10.1%
H_9	**H_7**	1.81	1.97	8.7%	1.81	1.92	6.0%
H_9	**H_4**	2.62	2.35	−10.7%	2.62	2.38	−9.7%
H_4	**H_3**	2.01	1.92	−4.6%	2.01	1.93	−4.4%
H_{12}	**H_5**	2.51	2.28	−9.5%	2.51	2.40	−4.3%
H_{12}	**H_{11}**	2.31	2.16	−6.6%	2.31	2.16	−6.5%
H_{12}	**H_9**	2.27	2.35	3.3%	2.27	2.36	3.8%
H_6	**H_3**	2.26	2.28	0.8%	2.26	2.30	1.8%
H_6	**H_7**	2.21	2.29	3.4%	2.21	2.22	0.6%
H_6	**H_{11}**	2.75	2.50	−9.6%	2.75	2.56	−7.2%
H_6	**H_4**	1.92	1.85	−3.8%	1.92	1.83	−4.8%
			MAD	5.4%		**MAD**	4.5%
			StDev	6.5%		**StDev**	5.6%
			χ^2 (red.)	3.4		**χ^2 (red.)**	2.6

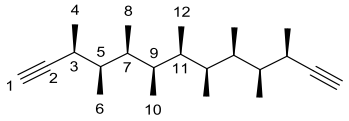

4.13

Table 6.114: Experimental ^{1}H-^{1}H distances derived from 1D DPFGSE NOESY and CSSF NOESY spectra and the Boltzmann averaged computed ^{1}H-^{1}H distances for **4.13** with Mean Absolute Deviations (MAD), Standard Deviations (StDev) and χ^2 (reduced) values (χ^2 (red.)).

			DFT calculated population		**Refined population, Sum($\Delta\Delta G^2$) ≤ 100**		
H_A	**H_B**	**Exp r_{eff}/Å**	**Calc r_{eff}/Å**	**Exp r_{eff}/Å**	**Calc r_{eff}/Å**	**Exp r_{eff}/Å**	**Calc r_{eff}/Å**
H_3	**H_9**	1.90	2.33	20.1%	1.90	2.04	7.1%
H_7	**H_3**	2.52	2.73	7.9%	2.52	2.60	2.9%
H_7	**H_4**	2.28	2.37	3.9%	2.28	2.14	-6.5%
H_5	**H_9**	2.41	2.54	5.3%	2.41	2.44	1.2%
H_5	**H_4**	2.19	2.15	-2.3%	2.19	2.29	4.1%
H_9	**H_4**	2.69	2.72	0.9%	2.69	2.66	-1.3%
H_4	**H_3**	2.00	1.93	-3.4%	2.00	1.93	-3.4%
H_{12}	**H_5**	2.40	2.07	-14.9%	2.40	2.30	-4.0%
H_{12}	**H_9**	2.17	2.25	3.6%	2.17	2.21	2.0%
H_6	**H_3**	2.27	2.21	-2.8%	2.27	2.33	2.5%
H_6	**H_7**	2.33	2.50	6.8%	2.33	2.39	2.7%
H_6	**H_4**	1.96	1.79	-8.6%	1.96	1.82	-6.9%
			MAD	6.7%		**MAD**	3.7%
			StDev	8.9%		**StDev**	4.4%
			χ^2 (red.)	6.6		**χ^2 (red.)**	1.6

NMR data of 4.15

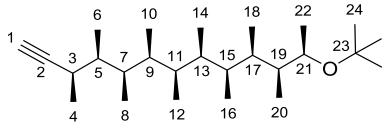

4.15

Table 6.115: Experimental $^{n}J_{HH}$ values (in Hz) and Boltzmann averaged calculated $^{n}J_{HH}$ (in Hz) before for **4.15** with Deviations (Dev, in Hz), Mean Absolute Deviations (MAD, in Hz), Standard Deviations (StDev, in Hz) and χ^2 (reduced) values (χ^2 (red.)).

H	Coupled H	Exp. $^{n}J_{HH}$/Hz	Calc. $^{n}J_{HH}$/Hz	Deviations/Hz
H_3	**H_1**	2.50	4.20	1.70*
H_3	**H_4**	6.90	7.02	0.12
H_3	**H_5**	7.80	8.95	1.15
H_5	**H_6**	6.80	7.07	0.27
H_5	**H_7**	4.20	3.60	−0.60
H_7	**H_8**	6.90	7.01	0.11
H_7	**H_9**	7.30	8.92	1.62
H_9	**H_{10}**	6.80	7.02	0.22
H_9	**H_{11}**	4.20	4.20	0.00
H_{15}	**H_{17}**	7.20	8.98	1.78
H_{17}	**H_{18}**	6.81	7.05	0.24
H_{17}	**H_{19}**	4.80	3.31	−1.49
H_{19}	**H_{20}**	6.80	7.29	0.49
			MAD	0.69
			StDev	0.91
			χ^2 (red.)	0.93
*$^{4}J_{H1H3}$ was not used for comparison.				

Table 6.116: Experimental ^{1}H-^{1}H distances derived from 1D DPFGSE NOESY and CSSF NOESY spectra and the Boltzmann averaged computed ^{1}H-^{1}H distances for **4.15** with Mean Absolute Deviations (MAD), Standard Deviations (StDev) and χ^2 (reduced) values (χ^2 (red.)).

H_A	H_B	η_{eff}	Exp. r_{eff}/Å	Calc. r_{eff}/Å	% Error
H_{21}	**H_{17}**	8.49	2.61	2.85	8.8%
H_{21}	**H_{19}**	12.58	2.45	2.71	0.0%
H_{21}	**H_{24}**	37.02	2.04	1.90	−7.5%
H_{21}	**H_{22}**	19.28	2.28	2.17	−4.9%
H_{21}	**H_{18}**	13.47	2.42	2.22	−8.5%
H_3	**H_7**	4.73	2.88	3.06	5.9%
H_3	**H_5**	7.65	2.66	2.75	3.2%
H_3	**H_9**	19.81	2.27	2.76	19.6%
H_3	**H_4**	18.76 (reference)	2.29	2.16	−5.7%
H_3	**H_8**	15.62	2.36	2.19	−7.6%

H_7	**H_5**	9.61	2.56	2.54	−0.7%
H_7	**H_9**	6.38	2.74	2.82	3.0%
H_7	**H_4**	7.46	2.67	2.63	−1.7%
H_7	**H_8**	19.21	2.28	2.16	−5.5%
H_9	**H_5**	5.18	2.84	2.87	1.1%
H_9	**H_4**	3.85	2.98	3.22	7.6%
H_9	**H_8**	12.65	2.45	2.46	0.6%
				MAD	5.74%
				StDev	7.52%
				χ^2 (red.)	4.63

Chapter 7 References

(1) Barton, D. H. *Experientia* **1950**, *8*, 316.
(2) Eliel, E. L. *J. Chem. Educ.* **1975**, *52*, 762.
(3) Anslyn, E. V.; Dougherty, D. A. *Modern Physical Organic Chemistry*; University Science Books: United States of America, 2006.
(4) Clayden, J.; Greeves, N.; Warren, S.; Wothers, P. *Organic Chemistry*; 1st edition ed.; OUP Oxford: United States, 2001.
(5) Tsuzuki, S.; Schafer, L.; Goto, H.; Jemmis, E. D.; Hosoya, H.; Siam, K.; Tanabe, K.; Psawa, E. *J. Am. Chem. Soc.* **1991**, *113*, 4665.
(6) Wang, X.; Erickson, S. D.; Iimori, T.; Still, W. C. *J. Am. Chem. Soc.* **1992**, *114*, 4128.
(7) Iimoria, T.; Ericksona, S. D.; Rheingoldb, A. L.; Still, W. C. *Tetrahedron Lett.* **1989**, *30*, 6947.
(8) Burns, M.; Essafi, S.; Bame, J. R.; Bull, S. P.; Webster, M. P.; Balieu, S.; Dale, J. W.; Butts, C. P.; Harvey, J. N.; Aggarwal., V. K. *Nature* **2014**, *513*, 183.
(9) Broeker, J. L.; Hoffmann, R. W.; Houk, K. N. *J. Am. Chem. Soc.* **1991**, *113*, 5006.
(10) Hoffmann, R. W. *Chem. Rev.* **1989**, *89*, 1841.
(11) Hoffmann, R. W.; Schopfer, U.; Stahl, M. *Tetrahedron Lett.* **1997**, *38*, 4055.
(12) Song, Z.; Lohseb, A. G.; Hsung, R. P. *Nat. Prod. Rep.* **2009**, *26*, 560.
(13) Hoffmann, R. W. *Angew. Chem. Int. Ed.* **2000**, *39*, 2054.
(14) Brooks, H. A.; Gardner, D.; Poyser, J. P.; King, T. J. *J. Antibiot.* **1984**, *37*, 1501.
(15) Thiehoff, C.; Rey, Y. P.; Gilmour, R. *Isr. J. Chem.* **2017**, *57*, 92.
(16) Hunter, L. *Beilstein J. Org. Chem.* **2010**, *6*, 38.
(17) O'Hagan, D. *J. Org. Chem.* **2012**, *77*, 3689.
(18) Rablen, P. R.; Hoffmann, R. W.; Hrovat, D. A.; Borden, W. T. *J. Chem. Soc., Perkin Trans. 2* **1999**, *0*, 1719.
(19) Masoud, G. N.; Li, W. *Acta Pharm Sin B.* **2015**, *5*, 378.
(20) Hon, W.; Wilson, M. I.; Harlos, K.; Claridge, T. D. W.; Schofield, C. J.; Pugh, C. W.; Maxwell, P. H.; Ratcliffe, P. J.; Stuart, D. I.; Jones, E. Y. *Nature* **2002**, *417*, 975.
(21) Fujimori, D. G. *Nat. Chem. Bio.* **2009**, *5*, 202.
(22) Wu, D.; Tian, A. *J. Phys. Chem. A* **1998**, *102*, 9901.
(23) Hunter, L.; Kirsch, P.; Slawin, A. M. Z.; O'Hagan, D. *Angew. Chem. Int. Ed.* **2009**, *48*, 5457.
(24) Baker, E. N.; Hubbard, R. E. *Prog. Biophys. Mol. Biol.* **1984**, *44*, 97.
(25) O'Hagana, D. *Chem. Soc. Rev.* **2008**, *37*, 308.
(26) Tsuzuki, S.; Fujii, A. *Phy. Chem. Chem. Phys.* **2008**, *10*, 2584.
(27) D.Rychnovsky, S.; J.Skalitzky, D. *Tetrahedron Lett.* **1990**, *31*, 945.
(28) Rychnovsky, S. D.; Richardson, T. I.; Rogers, B. N. *J. Org. Chem.* **1997**, *62*, 2925.
(29) Lee, J.; Kobayashi, Y.; Tezuka, K.; Kishi, Y. *Org. Lett.* **1999**, *1*, 2181.
(30) Fidanze, S.; Song, F.; Szlosek-Pinaud, M.; Small, P. L. C.; Kishi, Y. *J. Am. Chem. Soc.* **2001**, *123*, 10117.
(31) Kobayashi, Y.; Tan, C.-H.; Kishi, Y. *Helvetica Chimica Acta* **2000**, *83*, 2562.
(32) Kobayashi, Y.; Tan, C.-H.; Kishi, Y. *J. Am. Chem. Soc.* **2001**, *123*, 2076.
(33) Grkovic, T.; Blees, J. S.; Colburn, N. H.; Schmid, T.; Thomas, C. L.; Henrich, C. J.; McMahon, J. B.; Gustafson, K. R. *J. Nat. Prod.* **2011**, *74*, 1015.
(34) Wang, Y.; O'Doherty, G. A. *J. Am. Chem. Soc.* **2013**, *135*, 9334.
(35) Phuwapraisirisan, P.; Matsunaga, S.; Fusetani, N. *Org. Lett.* **2005**, *7*, 2233.
(36) Karplus, M. *J. Am. Chem. Soc.* **1963**, *85*, 2870.
(37) Haasnoot, C. A. G.; Leeuw, F. A. A. M. d.; Altona, C. *Tetrahedron* **1980**, *36*, 2783.
(38) Palermo, G.; Riccio, R.; Bifulco, G. *J. Org. chem.* **2010**, *75*, 1982.

(39) Contreras, R. H.; Peralta, J. E. *Prog. Nucl. Magn. Reson. Spectrosc.* **2000**, *37*, 321.
(40) Claridge, T. D. W. *High-Resolution NMR Techniques in Organic Chemistry*; 2nd ed.; Elsevier Science: Oxford, UK, 2009.
(41) Foroozandeh, M.; Adams, R. W.; Kiraly, P.; Nilssona, M.; Morrisa, G. A. *Chem. Commun.* **2015**, *51*, 15410.
(42) Parella, T.; Espinosa, J. F. *Nuclear Magnetic Resonance Spectroscopy* **2013**, *73*, 17.
(43) Krishnamurthy, V. V. *J. Magn. Reson. A.* **1996**, *121*, 33.
(44) Dickson, C. L.; Blundell, C. D.; Butts, C. P.; Felton, A.; Jeffreys, A.; Takacs, Z. *Analyst* **2017**, *142*, 621.
(45) Matsumori, N.; Kaneno, D.; Murata, M.; Nakamura, H.; Tachibana, K. *J. Org. Chem.* **1999**, *64*, 866.
(46) Bifulco, G.; Dambruoso, P.; Gomez-Paloma, L.; Riccio, R. *Chem. Rev.* **2007**, *107*, 3744.
(47) Wu, M.; Okino, T.; Nogle, L. M.; Marquez, B. L.; Williamson, R. T.; Sitachitta, N.; Berman, F. W.; Murray, T. F.; McGough, K.; Jacobs, R.; Colsen, K.; Asano, T.; Yokokawa, F.; Shioiri, T.; Gerwick, W. H. *J. Am. Chem. Soc.* **2000**, *122*, 12041.
(48) Ciminiello, P.; Dell'Aversano, C.; Fattorusso, E.; Forino, M.; Magno, S.; Rosa, M. D.; Ianaro, A.; Poletti, R. *J. Am. Chem. Soc.* **2002**, *124*, 13114.
(49) Nouls, J. C.; Binst, G. V.; Martin, R. H. *Tetrahedron Lett.* **1967**, *41*, 4065.
(50) Bell, R. A.; Osakwe, E. N. C. *Chem. Commun.* **1968**, 1093.
(51) Butts, C. P.; Jones, C. R.; Towers, E. C.; Flynn, J. L.; Appleby, L.; Barron, N. J. *Org. Biomol. Chem.* **2011**, *9*, 177.
(52) Jones, C. R.; Butts, C. P.; Harvey, J. N. *Beilstein J. Org. Chem.* **2011**, *7*, 145.
(53) Hu, H.; Krishnamurthy, K. *Journal of Magnetic Resonance* **2006**, *182*, 173.
(54) Butts, C. P.; Jones, C. R.; Harvey, J. N. *Chem. Commun.* **2011**, *47*, 1193.
(55) Lipsitz, R. S.; Tjandra, N. *Annu. Rev. Biophys. Biomol. Struct.* **2004**, *33*, 387.
(56) Kummerlo¨we, G.; Luy, B. *Residual Dipolar Couplings for the Configurational and Conformational Analysis of Organic Molecules*; Elsevier, 2009; Vol. 68.
(57) Hallwass, F.; Schmidt, M.; Sun, H.; Mazur, A.; Kummerlöwe, G.; Luy, B.; Navarro‐Vázquez, A.; Griesinger, C.; Reinscheid, U. M. *Angew. Chem. Int. Ed.* **2011**, *50*, 9487.
(58) Hehre, W. J. *A Guide to Molecular Mechanics and Quantum Chemical Calculations*; Wavefunction, Inc.: United States of America, 2003.
(59) Allinger, N. L. *J. Am. Chem. Soc.* **1977**, *99*, 8127.
(60) Allinger, N. L.; Yuh, Y. H.; Lii, J. H. *J. Am. Chem. Soc.* **1989**, *111*, 8551.
(61) Halgren, T. A. *J. Comp. Chem.* **1996**, *17*, 490.
(62) Leach, A. R.; Gillet, V. J. *An Introduction to Chemoinformatics*; Revised edition ed.; Springer: Dordrecht, Netherlands, 2007.
(63) Chang, G.; Guida, W. C.; Still, W. C. *J. Am. Chem. Soc.* **1989**, *111*, 4379.
(64) Young, D. *Computational chemistry. A Practical Guide for Applying Techniques to Real World Problems*; John Wiley & Sons, Inc.: Canada, 2001.
(65) Schrödinger, E. *Phys. Rev.* **1926**, *28*, 1049.
(66) Jain, A.; Shin, Y.; Persson, K. A. *Nature Reviews Materials* **2016**, *1*, 1.
(67) Born, M.; Oppenheimer, J. R. *Annalen der Physik* **1927**, *389*, 457.
(68) Hohenberg, P.; Khon, W. *Phys. Rev.* **1964**, *136*, B864.
(69) Kohn, W.; Sham, L. J. *Phys. Rev.* **1965**, *140*, A1133.
(70) Becke, A. D. *J. Chem. Phys.* **1993**, 98.
(71) Adamo, C.; Barone, V. *J. Chem. Phys.* **1998**, *108*, 664.
(72) Sperger, T.; Sanhueza, I. A.; Schoenebeck, F. *Acc. Chem. Res.* **2016**, *49*, 1311.
(73) Cheeseman, J. R.; Trucks, G. W.; Keith, T. A.; Frisch, M. J. *J. Chem. Phys.* **1996**, *104*, 5497.

(74) Lodewyk, M. W.; Soldi, C.; Jones, P. B.; Olmstead, M. M.; Rita, J.; Shaw, J. T.; Tantillo, D. J. *J. Am. Chem. Soc.* **2012**, *134*, 18550.
(75) Feliciano, A. S.; Medarde, M.; Miguel-del-Corral, J. M.; Aramburu, A.; Gordaliza, M.; Barreroa, A. F. *Tetrahedron Lett.* **1989**, *30*, 2851.
(76) Saya, J. M.; Vos, K.; Kleinnijenhuis, R. A.; Maarseveen, J. H. v.; Ingemann, S.; Hiemstra, H. *Org. Lett.* **2015**, *17*, 3892.
(77) Smith, S. G.; Goodman, J. M. *J. Am. Chem. Soc.* **2010**, *132*, 12946.
(78) Grimblat, D. N.; Sarotti, D. A. M. *Chem. Eur. J.* **2016**, *22*, 12246.
(79) Grimblat, N.; Zanardi, M. M.; Sarotti, A. M. *J. Org. Chem.* **2015**, *80*, 12526.
(80) Chini, M. G.; Jones, C. R.; Zampella, A.; D'Auria, M. V.; Renga, B.; Fiorucci, S.; Butts, C. P.; Bifulco, G. *J. Org. Chem.* **2012**, 1489.
(81) Scott, H. K.; Aggarwal, V. K. *Chem. Eur. J.* **2011**, *17*, 13124.
(82) Sandford, C.; Aggarwal, V. K. *Chem. Commun.* **2017**, *53*, 5481.
(83) Aggarwal, V. K.; Fang, G. Y.; Ginesta, X.; Howells, D. M.; Zaja, M. *Pure Appl. Chem.* **2006**, *78*, 215.
(84) Matteson, D. S.; Ray, R.; Rocks, R. R.; Tsai, D. J. S. *Organometallics* **1983**, *2*, 1536.
(85) Matteson, D. S.; Ray, R. *J. Am. Chem. Soc.* **1980**, *102*, 7590.
(86) Matteson, D. S.; Majumdar, D. *Organometallics* **1983**, *2*, 1529.
(87) Matteson, D. S.; Majumdar, D. *J. Am. Chem. Soc.* **1980**, *102*.
(88) Matteson, D. S. *J. Org. Chem.* **2013**, *78*, 10009.
(89) Matteson, D. S. *Acc. Chem. Res.* **1988**, *21*, 294.
(90) Beckmann, E.; Desai, V.; Hoppe, D. *Synlett* **2004**, *13*, 2275.
(91) Besong, G.; Jarowicki, K.; Kocienski, P. J.; Sliwinskia, E.; Boyleb, F. T. *Org. Biomol. Chem.* **2006**, *4*, 2193.
(92) Webster, M. PhD Thesis, University of Bristol, 2010.
(93) Beak, P.; Carter, L. G. *J. Org. Chem.* **1981**, *46*, 2363.
(94) Balieu, S.; Hallett, G. E.; Burns, M.; Bootwicha, T.; Studley, J.; Aggarwal, V. K. *J. Am. Chem. Soc.* **2015**, *137*, 4398.
(95) Tripathi, A.; Schofield, M. M.; Chlipala, G. E.; Schultz, P. J.; Yim, I.; Newmister, S. A.; Nusca, T. D.; Scaglione, J. B.; Hanna, P. C.; Tamayo-Castillo, G.; Sherman, D. H. *J. Am. Chem. Soc.* **2014**, *134*, 1579; erratum **2014**, *136*, 10541.
(96) Steele, A. D.; Ernouf, G.; Lee, Y. E.; Wuest, W. M. *Org. Lett.* **2018**, *20*, 1126.
(97) Guchhait, S.; Chatterjee, S.; Ampapathi, R. S.; Goswami, R. K. *J. Org. Chem.* **2017**, *82*, 2414.
(98) Cimino, P.; Bifulco, G.; Evidente, A.; Abouzeid, M.; Riccio, R.; Gomez-Paloma, L. *Org. Lett.* **2002**, *4*, 2779.
(99) Lodewyk, M. W.; Siebert, M. R.; Tantillo, D. J. *Chem. Rev.* **2012**, *112*, 1839.
(100) Halgren, T. A. *J. Comp. Chem.* **1999**, *20*, 720.
(101) Micco, S. D.; Zampella, A.; D'Auria, M. V.; Festa, C.; Marino, S. D.; Riccio, R.; Butts, C. P.; Bifulco, G. *Beilstein J. Org. Chem.* **2013**, *9*, 2940.
(102) Rohr, K.; Herre, R.; Mahrwald, R. *J. Org. Chem.* **2009**, *74*, 3744.
(103) Ruiz, J.; Karre, N.; Roisnel, T.; Chandrasekhar, S.; Grée, R. *Eur. J. Org. Chem.* **2016**, 773.
(104) Reddy, G. P.; Murthy, A. S.; Reddy, J. S.; lDas, S.; Roisnel, h.; S.Yadav, J.; Chandrasekhar, S.; Grée, R. *Tetrahedron Lett.* **2014**, *55*, 365.
(105) Sellars, J. D.; Steel, P. G. *Tetrahedron* **2009**, *65*, 5588.
(106) Ichibakase, T.; Nakajima, M. *Org. Lett.* **2011**, *13*, 1579.
(107) Willoughby, P. H.; Jansma, M. J.; Hoye, T. R. *Nature Protocols* **2014**, *9*, 643.
(108) Maestro, version 9.2, Schrödinger, LLC, New York, NY, 2011

(109) Liu, Y.; Saurí, J.; Mevers, E.; Peczuh, M. W.; Hiemstra, H.; Clardy, J.; Martin, G. E.; Williamson, R. T. *Science* **2017**, *356*, eaam5349.
(110) Alder, R. W.; Maunder, C. M.; Orpen, A. G. *Tetrahedron Lett.* **1990**, *31*, 6717.
(111) Alder, R. W.; Allen, P. R.; Anderson, K. R.; Butts, C. P.; Khosravi, E.; Martin, A.; Maunder, C. M.; Orpen, A. G.; Pourcain, C. B. S. *J. Chem. Soc., Perkin Trans. 2* **1998**, *0*, 2083.
(112) Hoffmann, R. W.; Göttlich, R.; Schopfer, U. *Eur. J. Org. Chem.* **2001**, *2001*, 1865.
(113) Hoffmann, R. W.; Stahl, M.; Schopfer, U.; Frenking, G. *Chem. Eur. J.* **1998**, *4*, 559.
(114) Dufourcq, J.; Clin, B.; Lemanceau, B. *Febs Letters* **1972**, *22*, 205.
(115) Mlynarski, S. N.; Karns, A. S.; Morken, J. P. *J. Am. Chem. Soc.* **2012**, *134*, 16449.
(116) Edelstein, E. K.; Grote, A. C.; Palkowitz, M. D.; Morken, J. P. *Synlett* **2018**, *29*, 1749.
(117) Zweifel, G.; Arzoumanian, H.; Whitney, C. C. *J. Am. Chem. Soc.* **1967**, *89*, 3652.
(118) Roesner, S.; Blair, D. J.; Aggarwal, V. K. *Chem. Sci.* **2015**, *6*, 3718.
(119) Carlsen, P. H. J.; Katsuki, T.; Martin, V. S.; Sharpless, K. B. *J. Org. Chem.* **1981**, *46*, 3936.
(120) Fournier, A. M.; Clayden, J. *Org. Lett.* **2012**, *14*, 142.
(121) Hoppe, D.; Hense, T. *Angew. Chem. Int. Ed. Engl.* **1997**, *36*, 2282.
(122) Hoppe, D.; Felix, M.; Brüggemann, M. *Organolithiums in Enantioselective Synthesis*; Springer: Heidelberg, 2003.
(123) Beckmann, E.; Hoppe, D. *Synthesis* **2005**, *2*, 217.
(124) Beak, P.; McKinnie, B. G. *J. Am. Chem. Soc.* **1977**, *99*, 5213.
(125) Beak, P.; Baillargeon, M.; Carter, L. G. *J. Org. Chem.* **1978**, *43*, 4255.
(126) Würthwein, E.-U.; Behrens, K.; Hoppe, D. *Chem. Eur. J.* **1999**, *5*, 3459.
(127) Mykura, R. C.; Veth, S.; Varela, A.; Dewis, L.; Farndon, J. J.; Myers, E. L.; Aggarwal, V. K. *J. Am. Chem. Soc.* **2018**, *140*, 14677.
(128) Graña, P.; Paleo, M. R.; Sardina, F. J. *J. Am. Chem. Soc.* **2002**, *124*, 12511.
(129) Casoni, G.; Kucukdisli, M.; Fordham, J. M.; Burns, M.; Myers, E. L.; Aggarwal, V. K. *J. Am. Chem. Soc.* **2017**, *139*, 11877.
(130) Bagustski, V.; French, R. M.; Aggarwal, V. K. *Angew. Chem. Int. Ed.* **2010**, *49*, 5142.
(131) Watson, C. G.; Balanta, A.; Elford, T. G.; Essafi, S.; Harvey, J. N.; Aggarwal, V. K. *J. Am. Chem. Soc.* **2014**, *136*, 17370.
(132) Ho, O. C.; Soundararajan, R.; Lu, J.; Matteson, D. S.; Wang, Z.; Chen, X.; Wei, M.; Willett, R. D. *Organometallics* **1995**, *14*, 2855.
(133) Matteson, D. S.; Soundararajan, R.; Ho, O. C.; Gatzweiler, W. *Organometallics* **1996**, *15*, 152.
(134) Struth, F. R.; Hirschhäuser, C. *Eur. J. Org. Chem.* **2016**, 958.
(135) Varela, A.; Garve, L. K. B.; Leonori, D.; Aggarwal, V. K. *Angew. Chem. Int. Ed.* **2017**, *56*, 2127.
(136) Fawcett, A.; Nitsch, D.; Ali, M.; Bateman, J. M.; Myers, E. L.; Aggarwal, V. K. *Angew. Chem. Int. Ed.* **2016**, *55*, 14663.
(137) Vedrenne, E.; Wallner, O. A.; Vitale, M.; Schmidt, F.; Aggarwal, V. K. *Org. Lett.* **2009**, *11*, 165.
(138) Cauwberghs, S.; Clercq, P. J. D.; Tinant, B.; Declercq, J. P. *Tetrahedron Lett.* **1988**, *29*, 2493.
(139) Steves, J. E.; Stahl, S. S. *J. Am. Chem. Soc.* **2013**, *135*, 15742.
(140) Evanseck, J. D.; Blake, J. F.; Jorgensen, W. L. *J. Am. Chem. Soc.* **1987**, *109*, 2349.
(141) Evans, D. A.; Briton, T. C.; Ellman, J. A. *Tetrahedron Lett.* **1987**, *28*, 6141.
(142) Evans, D. A.; Wu, L. D.; Wiener, J. J. M.; Johnson, J. S.; Ripin, D. H. B.; Tedrow, J. S. *J. Org. Chem.* **1999**, *64*, 6411.
(143) Chandrasekhar, S.; Mahipal, B.; Kavitha, M. *J. Org. Chem.* **2009**, *74*, 9531.

(144) Zangger, K.; Armitage, I. M. *Magn. Reson. Chem.* **2000**, *38*, 452.
(145) Hughes, S. J.; Ciulli, A. *Essays Biochem.* **2017**, *61*, 505.
(146) Zengerle, M.; Chan, K.-H.; Ciulli, A. *ACS Chem. Biol.* **2015**, *10*, 1770.
(147) Snir, Y.; Kamien, R. D. *Science* **2005**, *307*, 1067.
(148) Edwards, T. A.; Wilson, A. J. *Amino Acids* **2011**, *41*, 734.
(149) Megens, R. P.; Roelfes, G. *Chem. Eur. J.* **2011**, *17*, 8514.
(150) Azzarito, V.; Long, K.; Murphy, N. S.; Wilson, A. J. *Nat. Chem.* **2013**, *5*, 161.
(151) Yashima, E.; Maeda, K.; Iida, H.; Furusho, Y.; Nagai, K. *Chem. Rev.* **2009**, *109*, 6102.
(152) Yamamoto, T.; Yamada, T.; Nagata, Y.; Suginome, M. *J. Am. Chem. Soc.* **2010**, *132*, 7899.
(153) Poli, M. D.; Zawodny, W.; Quinonero, O.; Lorch, M.; Webb, S. J.; Clayden, J. *Science* **2016**, *352*, 575.
(154) Dolain, C.; Jiang, H.; Léger, J.-M.; Guionneau, P.; Huc, I. *J. Am. Chem. Soc.* **2005**, *127*, 12943.
(155) Trudeau, S.; Morgan, J. B.; Shrestha, M.; Morken, J. P. *J. Org. Chem.* **2005**, *70*, 9538.
(156) Wang, Y.; Noble, A.; Myers, E. L.; Aggarwal, V. K. *Angew. Chem. Int. Ed.* **2016**, *55*, 4270.
(157) Buevich, A. V.; Chan, T.-M.; Wang, C. H.; McPhail, A. T.; Ganguly, A. K. *Magn. Reson. Chem.* **2005**, *43*, 187.
(158) Gaussian 09, Revision D.01, Frisch, M. J.; Trucks, G. W.; Schlegel, H. B.; Scuseria, G. E.; M. A. Robb, J. R. C.; G. Scalmani, V. B.; Mennucci, B.; Petersson, G. A.; Nakatsuji, H.; Caricato, M.; X. Li, H. P. H.; Izmaylov, A. F.; J. Bloino, G. Z.; Sonnenberg, J. L.; M. Hada, M. E.; K. Toyota, R. F.; J. Hasegawa, M. I.; T. Nakajima, Y. H.; O. Kitao, H. N.; Vreve, T.; Montgomery, J. A.; Jr., J. E. P.; Ogliaro, F.; Bearpark, M.; Heyd, J. J.; Brothers, E.; Kudin, K. N.; Staroverov, V. N.; Kobayashi, R.; Norman, J.; Raghavachari, K.; Rendell, A.; Burant, J. C.; Iyengar, S. S.; Tomasi, J.; Cossi, M.; Rega, N.; Millam, J. M.; Klene, M.; Knox, J. E.; Cross, J. B.; Bakken, V.; Adamo, C.; Jaramillo, J.; Gomperts, R.; Stratmann, R. E.; Yazyev, O.; Austin, A. J.; Cammi, R.; Pomelli, C.; Ochterski, J. W.; Martin, R. L.; Morokuma, K.; Zakrzewski, V. G.; G. A. Voth, P. S.; Dannenberg, J. J.; Dapprich, S.; Daniels, A. D.; Farkas, Ö.; Foresman, J. B.; Ortiz, J. V.; Cioslowski, J.; Fox, D. J., Gaussian, Inc., Wallingford CT, 2009
(159) Levy, R. M.; Bassolino, D. A.; Kitchen, D. B.; Pardi, A. *Biochemistry* **1989**, *28*, 9361.
(160) Bally, T.; Rablen, P. R. *J. Org. Chem.* **2011**, *76*, 4818.
(161) Aguilar, J. A.; Colbourne, A. A.; Cassani, J.; Nilsson, M.; Morris, G. A. *Angew. Chem. Int. Ed.* **2012**, *51*, 6460.
(162) Mohamadi, F.; Richards, N. G. J.; Guida, W. C.; Liskamp, R.; Lipton, M.; Caufield, C.; Chang, G.; Hendrickson, T.; Still, W. C. *J. Comput. Chem.* **1990**, *11*, 440.
(163) Bruker, SAINT+ Integration Engine, Data Reduction Software, , Bruker Analytical X-ray Intruments Inc., Madison, WI, USA, 2007
(164) Bruker, SADABS, Bruker AXS area detector scaling and absorption correction, Bruker Analytical X-ray Instruments Inc., Madison, Winsconsin, USA, 2001
(165) Palatinus, L.; Chapuis, G. *J. Appl. Crystallogr.* **2007**, *40*, 786.
(166) Palatinus, L.; Prathapa, S. J.; Smaalen, S. v. *J. Appl. Crystallogr.* **2012**, *45*, 575.
(167) Sheldrick, G. M. *Acta Cryst.* **2008**, *A64*, 112.
(168) Sheldrick, G. M. *Acta Crystallogr. C* **2015**, *71*, 3.
(169) Dolomanov, O. V.; Bourhis, L. J.; Gildea, R. J.; Howard, J. A. K.; Puschmann, H. *J. Appl. Crystallogr.* **2009**, *42*, 339.
(170) Halgren, T. A. *J. Comp. Chem.* **1999**, *20*, 730.
(171) Marten, B.; Kim, K.; Cortis, C.; Friesner, R. A.; Murphy, R. B.; Ringnalda, M. N.; Sitkoff, D.; Honig, B. *J. Phys. Chem.* **1996**, *100*, 11775.

(172) Tannor, D. J.; Marten, B.; Murphy, R.; Friesner, R. A.; Sitkoff, D.; Nicholls, A.; Honig, B.; Ringnalda, M.; Goddard, W. A. *J. Am. Chem. Soc.* **1994**, *116*, 11875.
(173) Micco, S. D.; Chini, M. G.; Riccio, R.; Bifulco, G. *Eur. J. Org. Chem.* **2010**, *2010*, 1411.
(174) Zangger, K.; Armitage, I. M. *Magn. Reson. Chem.* **2000**, *38*, 452.
(175) Macura, S.; Farmer, B. T.; Brown, L. R. *J. Magn. Reson.* **1986**, *70*, 493.
(176) Esposito, G.; Pastore, A. *J. Magn. Reson.* **1988**, *76*, 331.
(177) Burchat, A. F.; Chong, J. M.; Nielsen, N. *Journal of Organometallic Chemistry* **1997**, *542*, 281.
(178) Pelsˇs, A.; Gandhamsetty, N.; Smith, J. R.; Mailhol, D.; Silvi, M.; Watson, A. J. A.; Perez-Powell, I.; PrØvost, S.; Schützenmeister, N.; Moore, P. R.; Aggarwal, V. K. *Chem. Eur. J.* **2018**, *24*, 9542.
(179) Kühnel, E.; Laffan, D. D. P.; Lloyd‐Jones, G. C.; Campo, T. M. d.; Shepperson, I. R.; Slaughter, J. L. *Angew. Chem. Int. Ed.* **2007**, *46*, 7075.
(180) Risgaard, R.; Nielsen, S. D.; Hansen, K. B.; Jensen, C. M.; Nielsen, B.; Traynelis, S. F.; Clausen, R. P. *J. Med. Chem.* **2013**, *56*, 4071.
(181) Stymiest, J. L.; Gagutski, V.; French, R. M.; Aggarwal, V. K. *Nature* **2008**, *456*, 778.